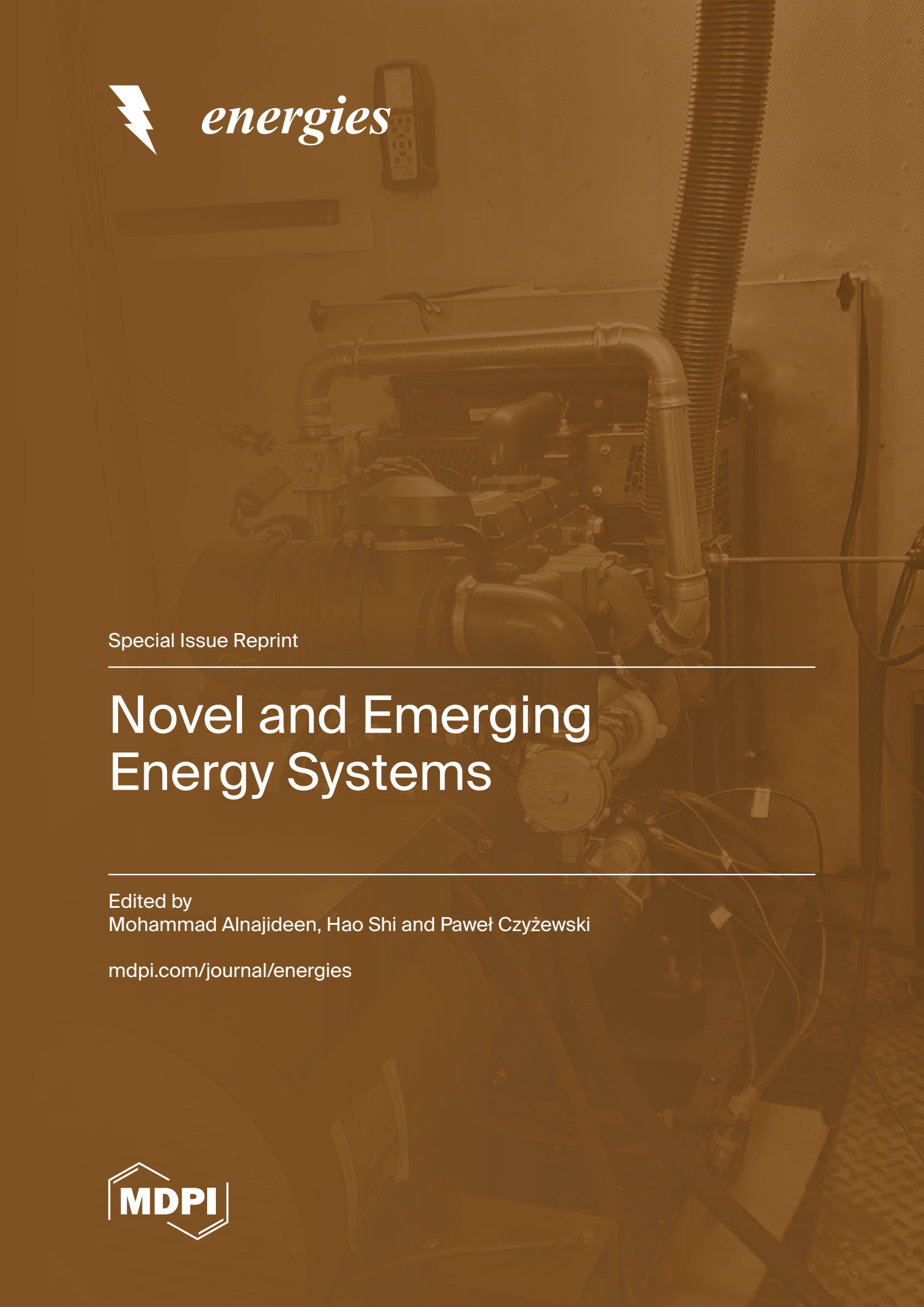


energies

Special Issue Reprint

Novel and Emerging Energy Systems

Edited by
Mohammad Alnajideen, Hao Shi and Paweł Czyżewski

mdpi.com/journal/energies

MDPI

Novel and Emerging Energy Systems

Novel and Emerging Energy Systems

Guest Editors

Mohammad Alnajideen
Hao Shi
Paweł Czyżewski

MDPI

Basel • Beijing • Wuhan • Barcelona • Belgrade • Novi Sad • Cluj • Manchester

Guest Editors

Mohammad Alnajideen
College of Physical Sciences and Engineering
Cardiff University
Cardiff
UK

Hao Shi
The Institute of Reactive Flows and Diagnostics
Technical University of Darmstadt
Darmstadt
Germany

Paweł Czyżewski
Institute of Thermal Science
Poznan University of Technology
Poznan
Poland

Editorial Office

MDPI AG
Grosspeteranlage 5
4052 Basel, Switzerland

This is a reprint of the Special Issue, published open access by the journal *Energies* (ISSN 1996-1073), freely accessible at: https://www.mdpi.com/journal/energies/special_issues/VD6I541880.

For citation purposes, cite each article independently as indicated on the article page online and as indicated below:

Lastname, A.A.; Lastname, B.B. Article Title. *Journal Name* **Year**, *Volume Number*, Page Range.

ISBN 978-3-7258-9069-9 (Hbk)
ISBN 978-3-7258-9070-5 (PDF)
https://doi.org/10.3390/books978-3-7258-9070-5

Cover image courtesy of Mohammad Alnajideen

© 2026 by the authors. Articles in this reprint are Open Access and distributed under the Creative Commons Attribution (CC BY) license. The reprint as a whole is distributed by MDPI under the terms and conditions of the Creative Commons Attribution-NonCommercial-NoDerivs (CC BY-NC-ND) license (https://creativecommons.org/licenses/by-nc-nd/4.0/).

Contents

About the Editors . . . . . **vii**

Preface . . . . . **ix**

Lukasz Pawlik, Jacek Lukasz Wilk-Jakubowski, Krzysztof Podosek and Grzegorz Wilk-Jakubowski
Machine Learning-Driven Advancements in Electric Motorcycles: A Systematic Review of Electric Motors, Energy Storage, Charging Technologies, and Electronic Components
Reprinted from: *Energies* **2025**, *18*, 4529, https://doi.org/10.3390/en18174529 . . . . . **1**

Jakub Katerla and Krzysztof Sornek
Biomass for Residential Heating: A Review of Technologies, Applications, and Sustainability Aspects
Reprinted from: *Energies* **2025**, *18*, 5875, https://doi.org/10.3390/en18225875 . . . . . **40**

Qiyan Wang, Kosala Gunawardane and Li Li
A Review of Multi-Port Converter Architecture in Hydrogen-Based DC Microgrid
Reprinted from: *Energies* **2025**, *18*, 6487, https://doi.org/10.3390/en18246487 . . . . . **79**

Ahmad Mohamed S. H. Al-Moftah, Mohammad Alnajideen, Fatima Alafifi, Pawel Czyzewski, Hao Shi, Mohammad Alherbawi, et al.
Economic Feasibility of Using Municipal Solid Waste and Date Palm Waste for Clean Energy Production in Qatar
Reprinted from: *Energies* **2025**, *18*, 988, https://doi.org/10.3390/en18040988 . . . . . **111**

Elisabeta Spunei, Dorian Anghel, Gheorghe Liuba, Cristian Paul Chioncel and Mihaela Martin
Study on Determining the Efficiency of a High-Power Hydrogenerator Using the Calorimetric Method
Reprinted from: *Energies* **2025**, *18*, 4813, https://doi.org/10.3390/en18184813 . . . . . **133**

Sadiq Muhammad, Saher Javaid, Iacovos Ioannou, Yuto Lim, and Yasuo Tan
Mitigating Energy Losses Under Incremental Load Variations in Distributed Power-Flow Systems While Ensuring User Comfort
Reprinted from: *Energies* **2025**, *18*, 5716, https://doi.org/10.3390/en18215716 . . . . . **160**

Abdulaziz Aborujilah, Mohammed Al-Sarem and Marwan Alabed Abu-Zanona
Forecast-Driven Climate Control for Smart Greenhouses: Energy Optimization Using LSTM Model
Reprinted from: *Energies* **2025**, *18*, 5821, https://doi.org/10.3390/en18215821 . . . . . **197**

Ali Soleimani, Paul Davidsson, Reza Malekian and Romina Spalazzese
Multi-Criteria Model Predictive Controller for Hybrid Heating Systems in Buildings
Reprinted from: *Energies* **2025**, *18*, 5839, https://doi.org/10.3390/en18215839 . . . . . **217**

Martyna Szatkowska, Piotr Szatkowski, Katarzyna Suchorowiec, Ewelina Radomska and Kinga Pielichowska
Carbon Black–Enhanced Polyethylene Wax Phase Change Materials for Efficient Photothermal Energy Conversion and Storage in Mobile Heating Systems
Reprinted from: *Energies* **2026**, *19*, 1162, https://doi.org/10.3390/en19051162 . . . . . **240**

Pawel Czyzewski, Przemyslaw Matuszak, Marcelina Malecka, Joanna Jojka, Ahmad M. S. H. Al-Moftah, Hao Shi, et al.
Effect of Illumination Colour on the Growth and Energetic Properties of *Chlorella vulgaris* for Bioenergy Applications
Reprinted from: *Energies* **2026**, *19*, 1572, https://doi.org/10.3390/en19061572 . . . . . **262**

About the Editors

Mohammad Alnajideen

Mohammad Alnajideen is a research fellow (=Senior Lecturer) and manager of the Centre of Excellence on Ammonia Technologies at the School of Engineering, Cardiff University. His research interests include renewable energy systems, ammonia and hydrogen technologies, alternative fuels, combustion, gas turbines, internal combustion engines, combined heat and power, thermodynamic cycles, solar energy and integrated low carbon energy systems. He is Principal Investigator of the AgriCHP project and has contributed to major research programmes focused on ammonia and hydrogen applications in engines, turbines and thermal energy systems, including SAFE and OceanREFuel. He has more than fifteen years of academic, industrial and research experience and has led the development of experimental facilities, academic and industrial collaborations, and multidisciplinary energy projects. He is a chartered engineer and a fellow of the Higher Education Academy, and his achievements include peer reviewed publications, editorial leadership, research supervision, international collaboration and the development of patented solar energy technology.

Hao Shi

Hao Shi is a Research Fellow at Cambridge CARES in Singapore, where he works on the HYCOMBS project in collaboration with Tohoku University. His research interests include ammonia and hydrogen combustion, renewable energy, engine combustion and optical diagnostics. His work investigates fuel injection, turbulent flow, flame behaviour and emissions in advanced engines using techniques such as particle image velocimetry, laser induced fluorescence and tuneable diode laser absorption spectroscopy. He obtained his doctorate in mechanical engineering from King Abdullah University of Science and Technology in 2022, subsequently conducted postdoctoral research at Cardiff University, and was awarded a research fellowship by the Alexander von Humboldt Foundation. He has also carried out research at the Reactive Flows and Diagnostics group at the Technical University of Darmstadt.

Paweł Czyżewski

Paweł Czyżewski is a researcher and assistant professor at the Institute of Thermal Energy, Faculty of Environmental Engineering and Energy, Poznan University of Technology. His research interests include the thermochemical conversion of solid fuels, biomass and waste gasification, pyrolysis, synthesis gas cleaning and conditioning, biogas production, alternative fuels, hydrogen carriers and the combustion of gaseous fuels. He has contributed to research and industrial projects on emissions reduction in large gas engines, the combustion characteristics of gaseous fuels, Fischer Tropsch synthesis and the energy conversion of biomass and refuse derived fuels. His achievements include research placements at the Royal Institute of Technology in Stockholm and at Bioenergy 2020 plus in Austria, where he investigated biomass gasification, synthesis gas reforming and gas cleaning. He is also a member of the Polish Combustion Institute.

Preface

The transition towards sustainable, secure and efficient energy systems requires the development of technologies that can respond to environmental, economic and operational challenges. This Reprint brings together research addressing recent advances in renewable energy integration, energy conversion, hydrogen technologies, energy storage, intelligent control, resource recovery and energy use across industrial, agricultural and building applications.

The purpose of this Reprint is to present a multidisciplinary view of emerging energy systems and to demonstrate how experimental research, numerical modelling, optimisation and techno economic assessment can support their practical development. The collected studies reflect the growing need to improve energy efficiency, reduce emissions, increase system flexibility and make better use of renewable and recovered resources.

This Reprint was prepared to provide researchers, engineers, industry professionals, policymakers and postgraduate students with a useful overview of current approaches and applications in the energy field. It is intended to support further scientific investigation, encourage collaboration across disciplines and contribute to the development and deployment of reliable and environmentally responsible energy solutions.

We would like to thank all authors for their valuable contributions and the reviewers for their careful assessment and constructive comments. We also acknowledge the editorial team for their support throughout the preparation of this Reprint.

Mohammad Alnajideen, Hao Shi, and Paweł Czyżewski
Guest Editors

energies

MDPI

Systematic Review

Machine Learning-Driven Advancements in Electric Motorcycles: A Systematic Review of Electric Motors, Energy Storage, Charging Technologies, and Electronic Components

Lukasz Pawlik [1,*], Jacek Lukasz Wilk-Jakubowski [1,2,*], Krzysztof Podosek [3] and Grzegorz Wilk-Jakubowski [2,4]

[1] Department of Information Systems, Kielce University of Technology, 7 Tysiąclecia Państwa Polskiego Ave., 25-314 Kielce, Poland
[2] Institute of Crisis Management and Computer Modelling, 28-100 Busko-Zdrój, Poland; grzegorzwilkjakubowski@wp.pl
[3] Department of Automotive Engineering and Transport, Kielce University of Technology, 7 Tysiąclecia Państwa Polskiego Ave., 25-314 Kielce, Poland; k.podosek@tu.kielce.pl
[4] Institute of Internal Security, Old Polish University of Applied Science, 49 Ponurego Piwnika Str., 25-666 Kielce, Poland
* Correspondence: lpawlik@tu.kielce.pl (L.P.); jwilk@tu.kielce.pl (J.L.W.-J.)

Abstract

The integration of artificial intelligence (AI) and machine learning (ML) technologies is rapidly transforming the design, operation, and optimization of electric motorcycles. This review analyzes research published between 2015 and 2024, focusing on how ML algorithms enhance performance, energy efficiency, diagnostics, and charging strategies across four key domains: electric motors, energy storage, charging systems, and electronic components. The review highlights state-of-the-art solutions such as torque and range prediction using LSTM/GRU models, predictive maintenance via CNNs and autoencoders, energy flow control in hybrid battery–supercapacitor systems using reinforcement learning, and federated learning for privacy-preserving embedded applications. Comparative insights reveal quantifiable performance gains over traditional methods, while integrated frameworks are proposed for linking ML diagnostics, Vehicle-to-Grid (V2G) functionalities, and renewable energy integration. The paper concludes with targeted recommendations for future research, including lightweight edge-deployable models, Explainable AI for safety-critical applications, and the fusion of intelligent charging with eco-design principles, aiming to enable intelligent, sustainable, and high-performance electric motorcycle systems.

Keywords: electric motorcycles; electric motors; energy storage; battery charging; electrical components; energy efficiency; sustainability

1. Introduction

In recent years, there has been a dynamic increase in interest in electric vehicles (EVs), primarily driven by the depletion of fossil fuel resources and growing environmental awareness related to the reduction in air pollution emissions [1–6]. Particular attention from researchers and manufacturers has been directed toward electric motorcycles, which offer an alternative to conventional internal combustion engine vehicles due to their higher energy efficiency, quiet operation, and the ability to recover energy during braking [7–9].

A significant technological challenge lies in the development of efficient electric motors and appropriate control strategies. The most commonly used technologies include brushless DC (BLDC) motors and switched reluctance (SRM) motors, which differ in efficiency,

weight, and the cost of materials used in their construction [10–12]. Permanent magnet synchronous motors (PMSMs) are also widely adopted due to their high efficiency and compatibility with field-oriented control (FOC) methods [13–16].

In parallel with hardware advancements, the last decade has seen a rapid expansion in the use of artificial intelligence (AI) and machine learning (ML) methods for modeling, control, diagnostics, and energy management in electric motorcycles. These algorithms have enabled more accurate representation of nonlinear drive characteristics, real-time optimization of control parameters, predictive maintenance of motors and battery systems, and adaptive charging management—often surpassing the capabilities of conventional approaches [17–24].

Energy storage remains a crucial issue. Although lithium-ion batteries are widely used, they are characterized by limited lifespan due to degradation caused by temperature and charging cycles [25–29]. Hybrid solutions are being developed, such as systems combining high-energy-density batteries with supercapacitors, which enable efficient management of peak power demands and extend battery life [17,18,30]. In this context, ML-supported Battery Management Systems (BMSs) are increasingly important, enabling accurate state-of-charge (SoC) and state-of-health (SoH) estimation, as well as adaptive control to extend service life [31–34].

Battery charging for electric motorcycles involves the development of both traditional wired and innovative wireless technologies. Vehicle-to-Grid (V2G) systems are gaining importance, enabling power grid stabilization and cost optimization during operation [25,35–37]. Integration with renewable energy sources, such as photovoltaic and wind installations, further contributes to the reduction of CO_2 emissions and the overall cost of battery charging [38–43]. Predictive and adaptive charging strategies, supported by ML algorithms, have been demonstrated to improve efficiency and flexibility in grid-connected and off-grid scenarios [44–49].

Another important aspect is the development of electric motorcycle components, including traction inverters, which must be modular, reliable, and energy-efficient to meet diverse technical requirements [19,50–52]. Recent research increasingly combines modern power electronics, such as silicon carbide (SiC)-based converters, with ML-based diagnostic systems to enable early fault detection and self-adaptive performance optimization [53–60]. Ensuring high comfort and safety for users is equally essential, which can be achieved through optimized suspension design, technical diagnostics, and effective energy management strategies [44,45,53,61].

In addition to advancements in electric motors, energy storage, charging technologies, and electronic components, recent studies have also focused on dynamic control challenges and socio-technical innovations specific to electric motorcycles. For example, slip ratio control algorithms that incorporate camber angle have been shown to improve posture stabilization and steering operability in two-wheel drive configurations, while sensorless, open-loop traction strategies in all-wheel drive systems can enhance stability under low-adhesion conditions. Structural optimization methods, such as topology-optimized chassis design, address the integration of battery packs without compromising strength or handling. Furthermore, research on the spatial optimization of charging station placement and the development of mobile application-based battery swapping platforms illustrates the growing role of digital tools and infrastructure planning. These developments indicate that the design of next-generation electric motorcycles requires a holistic approach, integrating vehicle dynamics, mechanical design, energy management, and user-oriented services into a unified and adaptive e-mobility ecosystem.

The aim of this article is to provide a comprehensive review of modern technological solutions used in electric motorcycles—from motors and energy storage systems to charging methods and supporting components—focusing on performance optimization, predictive diagnostics, and intelligent energy management. The authors analyze current challenges and highlight future development directions that may contribute to the widespread adoption of this type of vehicle.

This review places a particular emphasis on the integration of AI/ML techniques across all four domains, analyzing their role in control, diagnostics, and energy optimization of electric motorcycles.

2. Materials and Methods

This study adopts a systematic review approach focused on analyzing the literature published between 2015 and 2024. The selection of publications was conducted using the Scopus, IEEE Xplore, and Web of Science databases, based on keyword queries such as Electric Motorcycles, Electric Motors, Energy Storage, Battery Charging, Electrical Components, Energy Efficiency, and Sustainability. A total of 101 articles were included for analysis, meeting the following inclusion criteria: English language, topic relevance (electric motorcycles), and full-text availability. Review articles and popular science literature were excluded.

Document classification was carried out manually, based on abstracts and full texts, with articles categorized into four main areas: electric motors, energy storage, battery charging, and electrical components. A taxonomy-based qualitative analysis was employed to identify occurrences of terms related to energy efficiency and sustainability. The geographical distribution of publications and chronological trends in technological development were also examined.

Quantitative analysis was performed on technical parameters such as motor efficiency, battery energy density, and charging times.

Based on the conducted literature review, five key research questions were formulated:

1. Which type of electric motor (BLDC, SRM, PMSM) is the most efficient in terms of energy performance and production cost for electric motorcycles?
2. What energy storage technologies offer the best balance between performance, safety, and battery lifespan?
3. Does the implementation of hybrid energy storage systems (e.g., battery-supercapacitor combinations) significantly improve electric motorcycle performance?
4. Which charging technologies (wired, wireless, V2G) best meet user requirements and effectively support integration with the power grid and renewable energy sources?
5. What are the optimal configurations of electric motorcycle components—particularly traction inverters—in terms of modularity, reliability, and energy efficiency?

2.1. Article Selection and Research Category Definition

The literature review was conducted using the Scopus database based on queries including the terms Electric Motorcycles, Electric Motors, Energy Storage, Battery Charging, Electrical Components, Energy Efficiency, and Sustainability, covering the period from 2015 to 2024. The selected articles were grouped into four main research categories based on Scopus keywords: electric motors, energy storage, battery charging, and electrical components, with additional consideration given to energy efficiency and sustainability aspects.

The assignment of publications to each category was based on Scopus keyword classification, while the categorization for the Research Methodology section was performed manually through full-text analysis of the articles.

The following query was used:

TITLE-ABS-KEY("Electric Motorcycles") AND PUBYEAR > 2014 AND PUBYEAR < 2025 AND (EXCLUDE (SUBJAREA,"BIOC") OR EXCLUDE (SUBJAREA,"NEUR") OR EXCLUDE (SUBJAREA,"MULT") OR EXCLUDE (SUBJAREA,"AGRI") OR EXCLUDE (SUBJAREA,"PSYC") OR EXCLUDE (SUBJAREA,"ARTS") OR EXCLUDE (SUBJAREA,"MEDI") OR EXCLUDE (SUBJAREA,"CHEM") OR EXCLUDE (SUBJAREA,"ECON") OR EXCLUDE (SUBJAREA,"EART") OR EXCLUDE (SUBJAREA,"CENG") OR EXCLUDE (SUBJAREA,"BUSI") OR EXCLUDE (SUBJAREA,"PHYS")) AND (LIMIT-TO (LANGUAGE,"English")) AND (EXCLUDE (DOCTYPE,"tb")) AND (LIMIT-TO (EXACTKEYWORD,"Electric Motors") OR LIMIT-TO (EXACTKEYWORD,"Traction Motors") OR LIMIT-TO (EXACTKEYWORD,"Electric Traction") OR LIMIT-TO (EXACTKEYWORD,"Reluctance Motors") OR LIMIT-TO (EXACTKEYWORD,"Electric Drives") OR LIMIT-TO (EXACTKEYWORD,"Energy Storage") OR LIMIT-TO (EXACTKEYWORD,"Secondary Batteries") OR LIMIT-TO (EXACTKEYWORD,"Lithium-ion Batteries") OR LIMIT-TO (EXACTKEYWORD,"Supercapacitor") OR LIMIT-TO (EXACTKEYWORD,"Battery Pack") OR LIMIT-TO (EXACTKEYWORD,"Electric Batteries") OR LIMIT-TO (EXACTKEYWORD,"Battery") OR LIMIT-TO (EXACTKEYWORD,"Hybrid Energy Storage Systems") OR LIMIT-TO (EXACTKEYWORD,"Charging (batteries)") OR LIMIT-TO (EXACTKEYWORD,"Battery Management Systems") OR LIMIT-TO (EXACTKEYWORD,"Regenerative Braking") OR LIMIT-TO (EXACTKEYWORD,"Charging Station") OR LIMIT-TO (EXACTKEYWORD,"Battery Swapping") OR LIMIT-TO (EXACTKEYWORD,"Battery Chargers") OR LIMIT-TO (EXACTKEYWORD,"Permanent Magnets") OR LIMIT-TO (EXACTKEYWORD,"Electric Inverters") OR LIMIT-TO (EXACTKEYWORD,"DC-DC Converters") OR LIMIT-TO (EXACTKEYWORD,"Digital Storage"))

In the next stage, selection was carried out based on the results of the Scopus database query, which initially yielded 194 publications published between 2015 and 2024, written in English and classified within subject areas such as Engineering, Energy, Computer Science, Mathematics, Social Sciences, Environmental Science, Materials Science, and Decision Sciences. To narrow the thematic scope, the keywords Electric Motorcycles, Electric Motors, Energy Storage, Battery Charging, Electrical Components, Energy Efficiency, and Sustainability were applied. Non-technical fields (e.g., biochemistry, psychology, arts, medicine) were excluded during the filtering of Scopus subdisciplines.

The titles and abstracts of the publications were extracted from the Scopus database and filtered using technical and thematic criteria. The initial set of 194 publications was reduced to 101 items by applying an additional keyword filter in Scopus. This process followed steps inspired by the PRISMA guidelines, including identification, screening, and eligibility assessment.

Furthermore, the full texts of the publications were manually reviewed to confirm compliance with the adopted analytical criteria. Titles and abstracts underwent initial screening to remove duplicates as well as review and popular science articles. Subsequently, full texts were manually verified, resulting in a refined set of 101 articles meeting the required technical and thematic standards.

The selected articles were assigned to two main thematic categories based on content analysis: (1) E-mobility Technologies—encompassing electric motors, energy storage, battery charging, and electrical components; (2) Engineering and Optimization—focusing on energy efficiency, sustainability, design, and methodological analysis, including topology, simulation, and the finite element method.

A geographical analysis of author affiliations was performed for countries including Canada, India, Indonesia, Italy, Japan, Malaysia, South Korea, Spain, Thailand, the

United Kingdom, and the United States, enabling an assessment of the global distribution of research.

A visualization of the literature selection stages, applied filtering criteria, and the main classification directions is presented in Figure 1, which also illustrates the thematic distribution of the analyzed publications. The final set of 101 articles was considered representative for the subsequent review analysis.

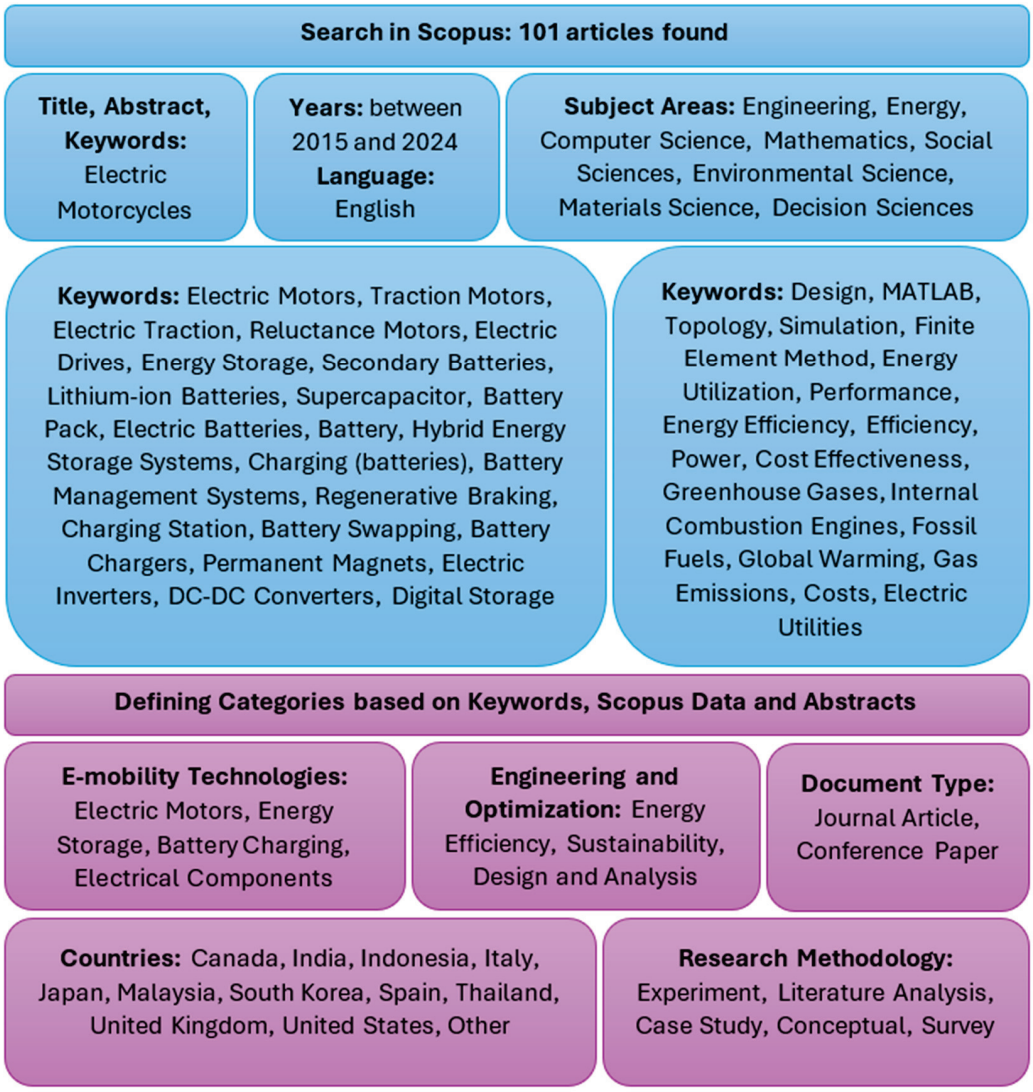


Figure 1. Data collection and preparation workflow.

2.2. Classification Criteria

As part of the literature review, 194 documents were identified in the Scopus database using a query combining the terms Electric Motorcycles, Electric Motors, Energy Storage, Battery Charging, Electrical Components, Energy Efficiency, and Sustainability. The results were limited to publications from 2015 to 2024, written in English, and classified within the subject areas of Engineering, Energy, Computer Science, Mathematics, Social Sciences, Environmental Science, Materials Science, and Decision Sciences. The query was subsequently refined by adding keywords from the Engineering and Optimization group, including Design, MATLAB, Topology, Simulation, Finite Element Method, Energy Utilization, Performance, Energy Efficiency, Efficiency, Power, Cost Effectiveness, Greenhouse

Gases, Internal Combustion Engines, Fossil Fuels, Global Warming, Gas Emissions, Costs, and Electric Utilities. This refinement reduced the dataset to 101 documents.

Further narrowing was achieved by excluding literature from non-technical domains (e.g., AGRI, PSYC, ARTS, MEDI, ECON, EART, CENG, BUSI, PHYS), thereby ensuring high topical relevance.

For the purposes of further analysis, five classification criteria were adopted: thematic group, country of author affiliation, document type, research methodology, and keyword set.

The first criterion, thematic grouping, distinguished two main categories:

1. E-mobility Technologies:
    - Electric Motors
    - Energy Storage
    - Battery Charging
    - Electrical Components
2. Engineering and Optimization:
    - Energy Efficiency
    - Sustainability
    - Design and Analysis

The second criterion concerned the country of author affiliation, determined based on Scopus bibliographic data and including, among others, Canada, India, Indonesia, Italy, Japan, Malaysia, South Korea, Spain, Thailand, the United Kingdom, and the United States. Remaining countries were grouped under the category "Other".

The third criterion was document type, encompassing journal articles and conference papers.

The fourth criterion referred to research methodology, identified through content analysis and including experimental approaches, literature reviews, case studies, conceptual works, and surveys.

The fifth criterion was based on the keywords used in the publications, which were grouped into the main categories of E-mobility Technologies and Engineering and Optimization, allowing for the inclusion of diverse research approaches.

By applying these well-defined criteria, a comprehensive and comparative analysis of research on electric motorcycle technologies was made possible, forming the foundation for the conclusions drawn in this review. This approach ensured methodological consistency and transparency throughout the literature review process. The classification results are presented in tabular form in Section 3 and discussed in the context of technological and geographical trends.

2.3. Data Processing and Analysis

The bibliographic data retrieved from the Scopus database, comprising 101 scientific publications that met the established thematic, linguistic, and temporal criteria, underwent a process of standardization and preparation for analysis.

In the initial phase, manual verification of titles, abstracts, and keywords was conducted, and each publication was assigned at least one classification category based on keywords and source metadata. The categories identified included e-mobility technologies (electric motors, energy storage, battery charging, electrical components) and engineering and optimization (energy efficiency, sustainability, design and analysis).

Additionally, the type of document (journal article, conference paper), country of author affiliation (including Canada, India, Indonesia, Italy, Japan, Malaysia, South Korea,

Spain, Thailand, the United Kingdom, and the United States), and research methodology (experiment, literature review, case study, conceptual paper, survey) were classified.

Data processing and visualization were carried out using Python 3.12, along with the Pandas 2.2.2, Matplotlib 3.8.4, and NumPy 1.26.4 libraries. The data were imported into a local PostgreSQL 16.2 database, in which relational tables were created to store information on authors, affiliations, keywords, publication year, and DOI identifiers. SQL queries enabled cross-sectional thematic analyses and comparisons across selected categories.

Geographical analysis enabled the identification of publication distribution by country and the most active research institutions. To monitor temporal developments, a year-by-year analysis covering the period 2015–2024 was conducted, allowing the identification of trends and research dynamics in the field of e-mobility technologies.

Network graphs generated using VOSviewer 1.6.20 were employed to visualize the co-occurrence of keywords.

Through the synergy of programming tools, database systems, and manual classification, an in-depth insight into the structure and development directions of research on electric motorcycles and related technologies was obtained.

2.4. Review Protocol and Publication Quality

To ensure transparency and reproducibility of the procedure, the selection and inclusion process was organized in accordance with the PRISMA (Preferred Reporting Items for Systematic Reviews and Meta-Analyses) protocol. The diagram illustrates the four fundamental stages of the process:

- Identification—A total of 194 records were identified in the Scopus database based on search criteria related to titles, abstracts, and keywords associated with electric motorcycles.
- Screening—After removing duplicates (n = 0), a preliminary screening of titles and abstracts was conducted (n = 194), resulting in the exclusion of 93 records that did not meet the study's inclusion criteria.
- Eligibility—101 full-text articles were assessed for substantive relevance to the defined research scope. No further exclusions were necessary at this stage.
- Included—All 101 articles were ultimately included in the qualitative synthesis.

The selection process is illustrated in Figure 2, which provides a structured overview of the flow from initial identification to final inclusion, helping to clarify both the rigor and transparency of the review methodology.

The second part of the analysis focused on the thematic classification of publication content based on keywords and abstracts. VOSviewer was used to identify dominant concepts and term co-occurrence networks, which allowed for the extraction of key research topics. The analysis revealed two main thematic axes: e-mobility technologies and energy efficiency and optimization. Within the first axis, categories related to electric motors, energy storage, battery charging, and electrical components were identified. The second axis included topics such as energy efficiency, sustainability, system design, and performance analysis.

Geographical classification was based on the affiliations of the authors of each publication. The most frequently represented countries included Indonesia, Japan, the United Kingdom, the United States, Canada, Italy, Thailand, India, Malaysia, South Korea, and Spain. Publications from countries with only a single representation were grouped under the category "Other." This distinction enabled the identification of geographical centers with the highest research activity in the field of electric motorcycles.

Documents were also classified by publication type: journal articles and conference papers.

The research methodology was determined based on abstract content and full-text analysis, considering five categories: experimental studies, literature reviews, case studies, conceptual papers, and survey-based research.

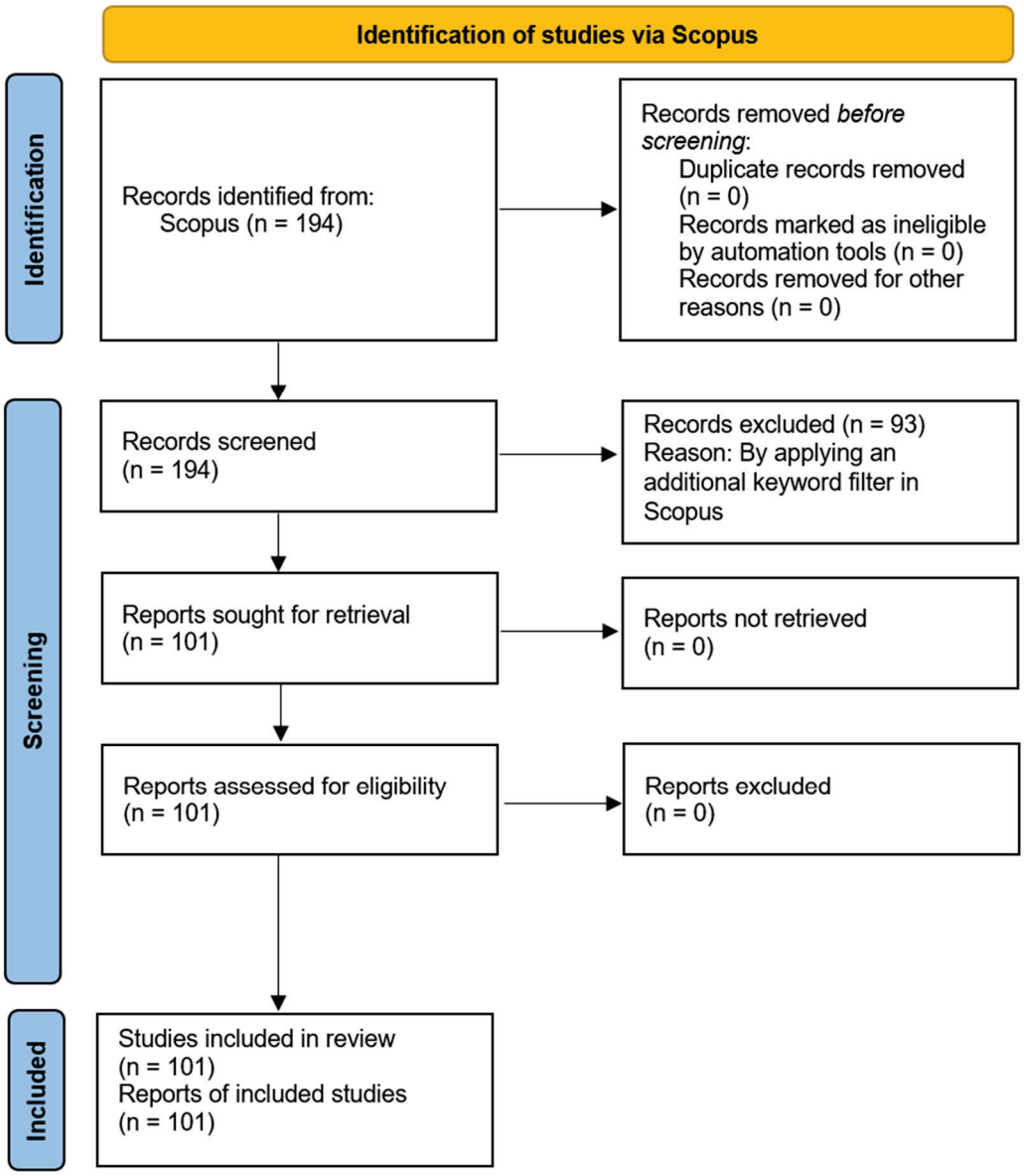


Figure 2. PRISMA flow diagram illustrating the literature selection process, including the stages of identification, screening, eligibility assessment, and final inclusion of publications for the review.

For the purposes of this classification, the data were manually verified by two independent reviewers, who assigned categories based on predefined criteria. In cases of disagreement, consensus was reached through discussion. This approach ensured consistency in classification and enabled a multidimensional analysis of the literature, encompassing technical, geographical, and methodological aspects.

The categorization described was based not only on the presence of specific terms but also on their frequency and position within the keyword co-occurrence network, as visualized in the keyword density map presented in Figure 3. This analysis facilitated the identification of the most frequently addressed research areas as well as existing knowledge gaps requiring further investigation.

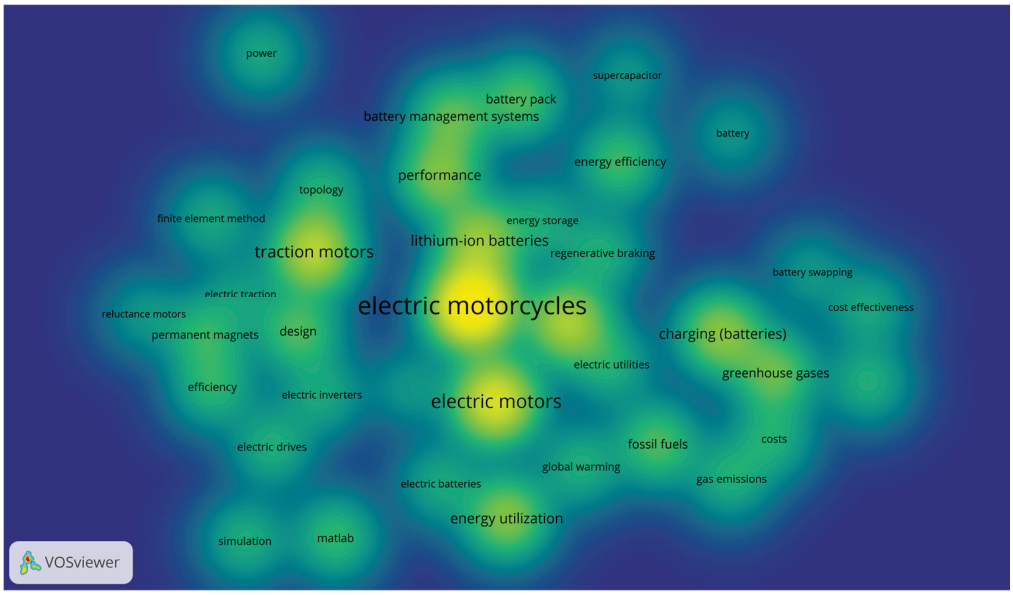


Figure 3. Term density map generated using VOSviewer 1.6.20 software [62].

The density analysis generated in VOSviewer presents the distribution and frequency of key terms within the corpus of 101 publications on electric motorcycles. The map uses a color scale ranging from blue (low frequency), through green (moderate frequency), to yellow (high frequency), enabling rapid identification of the most significant concepts.

At the center of the diagram is the term "electric motorcycles", surrounded by a yellow area indicating the highest term density, which reflects its dominant role in the analyzed dataset. Closely surrounding it are "electric motors" and "lithium-ion batteries", which also appear with high intensity (green-to-yellow areas), highlighting strong research interest in electric drives and energy storage systems.

In the upper-left section of the map, a thematic cluster is distinguished that relates to drive system design, including terms such as "traction motors", "reluctance motors", "permanent magnets", and "finite element method". This cluster reflects intensive exploration of motor types, and the methods used to analyze their properties.

The lower section of the diagram features terms like "energy utilization" and "electric drives", indicating research focused on optimizing system efficiency.

The right-hand side of the map contains environmentally and logistically oriented terms such as "charging (batteries)", "greenhouse gases", "gas emissions", and "cost effectiveness". These appear in green shades, suggesting a moderate frequency of occurrence and growing interest in the environmental and economic impacts of electromobility.

Smaller, blue areas of the map include simulation tools ("simulation", "MATLAB"), electrical components ("electric inverters"), and battery management topics ("battery management systems", "battery pack"), underlining the multidisciplinary nature of the research.

The entire map illustrates the complex structure of electric motorcycle research, where clear concentration around core topics related to hardware, energy systems, and environmental impact enables the identification of primary development directions and research gaps.

Interpreting this network reveals not only the key research domains but also potential thematic gaps—for example, the relatively low number of connections between the "battery management systems" cluster and "blockchain" may indicate the need for more in-depth

exploration of distributed ledger technologies in the context of energy management in electric vehicles.

Thus, Figure 4 provides a visual perspective on the structure and complexity of the analyzed literature, supporting a quick understanding of inter-topic relationships and highlighting areas for further investigation.

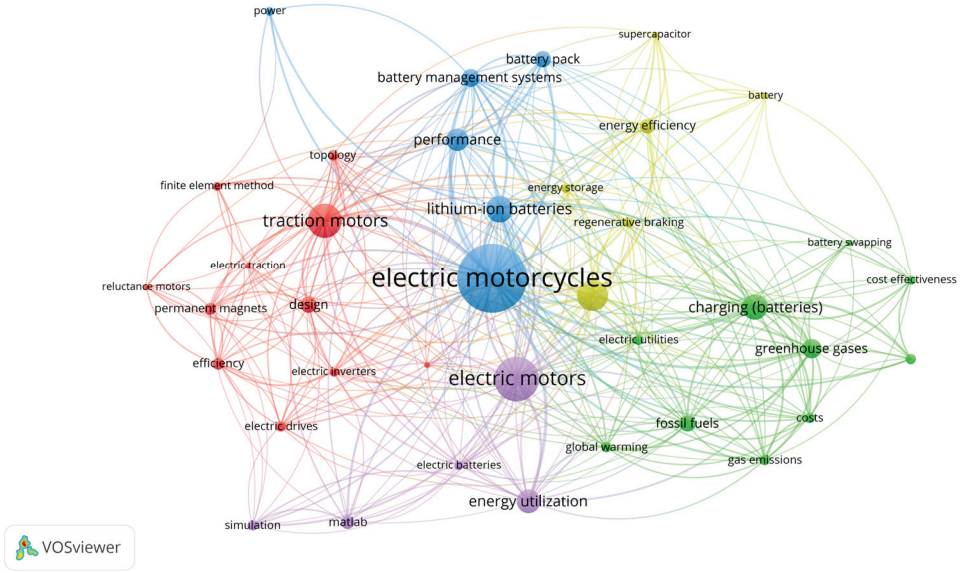


Figure 4. Network map of terms visualizing interrelationships and thematic clusters identified in the analyzed publications, generated using VOSviewer 1.6.20 software [62].

The network diagram generated in VOSviewer illustrates the co-occurrence relationships among 28 key terms extracted from the corpus of 101 publications. The size of each node corresponds to the frequency of the term in the analyzed dataset, while the thickness and length of the links represent the strength and frequency of co-occurrence between term pairs. The colors of nodes and edges indicate thematic clusters automatically detected by the VOSviewer algorithm.

Blue cluster (center, largest node "electric motorcycles"): The central node of the network is "electric motorcycles", reflecting its dominant role in the literature. It is directly connected to terms such as "lithium-ion batteries", "performance", and "battery management systems", highlighting a close relationship between research on electric drivetrains, energy storage, and battery management systems.

Purple cluster (bottom of the diagram): Nodes such as "electric motors", "energy utilization", "electric batteries", "simulation", and "MATLAB" form a distinct research area focused on modeling, numerical simulations, and the analysis of energy-efficient drive systems. The thick link between "electric motors" and "energy utilization" indicates a frequent co-occurrence of these topics in the literature.

Red cluster (upper left area): The term "traction motors" serves as the central node in a cluster centered on technical discussions related to traction motors, including "reluctance motors" and "permanent magnets". The presence of "finite element method" and "topology" in the same cluster suggests the widespread use of FEM and topology optimization methods in motor design research.

Green cluster (right area): This segment of the network focuses on environmental and operational topics, including "charging (batteries)", "greenhouse gases", "gas emissions", "cost effectiveness", "battery swapping", and "electric utilities". The links between these

nodes indicate an interdisciplinary approach that integrates charging technology with environmental impact and cost analysis.

Yellow cluster (upper right section): A smaller but distinct cluster surrounding "energy efficiency", "battery pack", and "supercapacitor" reflects growing interest in research aimed at improving energy efficiency and designing advanced storage systems, including hybrid battery–supercapacitor architectures.

This network structure enables an understanding of how core technical topics (drivetrains, batteries, simulations) connect with environmental and economic concerns (emissions, costs, energy services) and reveals both strong and weaker thematic interrelations. The network diagram (Figure 4) facilitates the rapid identification of central research areas and their interconnections.

The bibliographic references marked as [4–24,28–34,36,37,39–49,51–60,63–112] were included in the final dataset for the systematic review, allowing readers to clearly distinguish the core set of analyzed studies from supporting or contextual literature.

3. State of the Art: Review from 2015 to 2024

This section presents an overview of the most significant research advancements in the field of electric motorcycles and related technologies between 2015 and 2024. The analysis includes studies focused on the design of drivetrain systems, including hybrid and fully electric powertrains utilizing PMSM, BLDC, and SRM machines, as well as advanced traction inverters. Particular emphasis is placed on research into energy storage systems—from lithium-ion battery packs and hybrid configurations with supercapacitors, to battery capacity selection methodologies and strategies for managing temperature and state of charge, often implemented in modular BMS architectures.

Another important research stream involves modeling and simulation (MATLAB/Simulink, FEM, VOSviewer) aimed at evaluating performance, energy efficiency, and vehicle dynamics, alongside experimental studies that validate simulation outcomes.

Attention has also been drawn to the development of charging infrastructure—ranging from low-cost grid- and photovoltaic-based stations, to range-extending devices and the economic and environmental aspects of charging within the broader context of global electromobility trends.

Finally, the chapter discusses modern approaches to speed control and ride safety, including adaptive neuro-fuzzy systems, predictive control, and optimal control methods, collectively providing a comprehensive picture of research into electric motorcycles.

3.1. Application of Machine Learning Algorithms in Modeling and Control of Electric Motors

In the past decade, there has been a rapid development in the application of machine learning (ML) algorithms for modeling and controlling electric motors used in electric vehicles, particularly in electric motorcycles. These algorithms have enabled more accurate representation of the nonlinear characteristics of drives, real-time dynamic control, and increased energy efficiency and component lifespan.

Field-Oriented Control (FOC) was applied to a PMSM, demonstrating its superiority over other methods in terms of smooth operation and torque ripple reduction [13]. A modular, scalable inverter was developed in, optimized for efficiency and compatibility with various motor types [19]. Study [20] combined artificial neural networks (ANN) with a genetic algorithm (GA), resulting in significant improvements in energy efficiency and range for electric scooters.

Optimal control models were employed to enhance the driving strategy of a racing motorcycle in [64]. Predictive models such as LSTM and fuzzy logic systems were used

in [17], where a hybrid energy management system (HESS) was developed to predict power distribution between the battery and supercapacitors.

Motor temperature prediction models under variable load were introduced in, which could be developed using nonlinear regression or deep neural networks (DNN) [65]. Study [18] focused on structural optimization of motorcycle frames, highlighting the potential of PSO algorithms for designing lightweight yet robust structures. Alternative drive architectures and the impact of gear selection and energy recovery mechanisms on the energy efficiency of electric motorcycles were analyzed in [8,31,51,52]. In contrast, [28,67,69,71] focused on structural optimization—from cooling systems to frame geometries—using ML algorithms for simulation and design optimization.

The use of real-world data also played a significant role. In [68], motor operating parameters were modeled using LabVIEW, suggesting their potential use as input for predictive ML models. Electric motorcycle riding patterns were classified in based on GPS and accelerometer data, supporting dynamic optimization of drive operations using algorithms such as SVM or XGBoost [73].

Hybrid models (e.g., ANFIS) were proposed in [21], where features of fuzzy systems and neural networks were combined for precise BLDC motor control. Study [14] analyzed telemetry data from races, indicating the potential for integrating video data with ML to model power profiles. The effectiveness of classifiers in predicting motor faults based on vibration signals using CNNs and autoencoders was demonstrated in [6,77].

The use of XGBoost and Random Forest algorithms to assess energy efficiency in motorcycles was presented in [9,79], while LSTM and GRU models for torque prediction were described in [22,82]. FOC and DTC were compared as drive control strategies in [15], emphasizing the possibility of hybridization supported by learning algorithms.

Control systems based on adaptive ML algorithms that adjust to changing road conditions were analyzed in [23,42,52]. Reinforcement Learning was applied for real-time motor control in [24], whereas [86] presented the application of federated learning to update ML models without transmitting raw data to the cloud. The concept of distributed learning of predictive models in environments with limited connectivity was developed in [43,87,88]. In [21,91–93] the importance of data security and privacy was emphasized in locally trained models, including the use of homomorphic encryption and differential privacy.

Further studies such as [37,89,90] utilized sensor data topologies from IPM and SRM drives for dynamic predictive model training. The impact of optimizing input data (e.g., driving trajectory, mass, battery state) on the accuracy of ML models was analyzed in [91].

The use of classifiers to identify load types and recognize terrain conditions was described in [18,95,96], while ensemble learning methods to improve model accuracy and robustness were presented in [98,99]. Additional ensemble learning techniques and bagging methods were proposed in [97,100–102] for load and operating condition classification, as well as improved robustness of models to noisy or incomplete data. Finally, in [12,60,103,104,112], signal transformation techniques (e.g., FFT, DWT) were applied to improve the quality of input data used in predictive ML models.

In addition to the previously described ML applications in controlling PMSMs, BLDC motors, and SRM motors, significant contributions address dynamic challenges specific to electric motorcycles. For instance, a slip ratio control algorithm explicitly considering the camber angle was developed for a two-wheel drive electric motorcycle, improving posture stabilization and steering operability by adapting control strategies to the unique dynamics of single-track vehicles [31,113]. A similar approach, but implemented in an all-wheel drive architecture, was presented in a study proposing a sensorless, open-loop traction strategy. Simulation results demonstrated that such an AWD configuration can sig-

nificantly enhance stability and performance, particularly under low-adhesion conditions. Recent work has also explored the integration of advanced sensing solutions to monitor dynamic and electrical parameters in real time [114], as well as optimizing control electronics to reduce switching losses in motorcycle drive controllers [77,115]. These examples illustrate how ML-driven and advanced control methods are increasingly adapted to the specific dynamic requirements of electric motorcycles, expanding current research on drive architecture optimization.

In summary, research from 2015 to 2024 demonstrated a significant expansion in the use of ML in controlling electric motorcycle drives—from traditional regression algorithms to deep networks, reinforcement learning, and federated learning. Their effectiveness depended on data quality, feature selection, and implementation capabilities in embedded systems. Table 1 presents a summary of the types of machine learning algorithms and their applications in E-mobility technologies.

Table 1. Types of Machine Learning Algorithms and Their Applications in the Prediction of E-mobility Technologies.

Type of ML Algorithm	Application	Example Publications
Linear/Nonlinear Regression	Prediction of energy consumption, torque, motor temperature	[9,13,65]
Neural Networks (ANN, DNN)	Drive behavior modeling, parameter estimation, adaptive control	[20–22,89]
Genetic Algorithms (GA)	Optimization of drive configuration and control parameters	[20,39,91]
XGBoost, Random Forest	Efficiency prediction, driving style classification, operational data analysis	[9,73,79,95]
SVM	Driving pattern classification, road condition detection	[18,23,73]
LSTM, GRU	Range, torque, SoC prediction, time series control	[22,64,82,86]
Fuzzy Logic/ANFIS	Fuzzy drive control, adaptation to operating conditions	[17,21,23]
CNN	Classification of acoustic, image, vibration data, sensor data analysis	[14,37,77]
Autoencoders	Fault and anomaly detection in motors	[6,98]
Reinforcement Learning	Real-time drive control learning	[24,103]
Federated Learning	Remote ML model training without data centralization	[12,86]
Ensemble Learning	Improving classifier accuracy and robustness	[60,99]

The application of machine learning (ML) algorithms in modeling and controlling electric motors in electric vehicles has become one of the key tools supporting the development of electromobility. ML has enabled precise mapping of the nonlinear characteristics of drive systems, real-time adaptive control parameters depending on driving conditions, and predictive management of motor operating parameters. Particularly effective results have been demonstrated with the implementation of neural networks, genetic algorithms, LSTM, CNN, SVM, and hybrid methods based on Fuzzy Logic and ANFIS.

The research addressed both structural and operational aspects—from drive system design optimization to torque and speed control, and real-time anomaly detection. ML algorithms have also enabled the integration of data from sensors, GPS systems, video, and accelerometers, facilitating adaptive and autonomous control of PMSM, BLDC, SRM, and other motor types. Additionally, ML has shown potential for deployment in embedded systems, opening paths for commercial smart drive solutions.

An illustrative example of combining structural optimization with intelligent control is presented in the design and optimization of an external-rotor switched reluctance motor (SRM) for an electric scooter, where Finite Element Analysis (FEA) and Particle Swarm Optimization (PSO) were applied to increase the average torque and reduce copper losses [91,116]. Such optimized motor configurations can be further integrated with

predictive ML models, enabling adaptive adjustment of operating parameters in real time based on load, temperature, and riding conditions [117]. This approach reflects the broader trend of merging mechanical design optimization with data-driven control strategies to simultaneously improve drivetrain efficiency and durability.

In summary, machine learning has significantly enhanced the precision, responsiveness, and energy efficiency of electric drive systems. Further development should focus on improving model robustness, reducing computational requirements, and integrating with comprehensive vehicle energy and safety management systems.

3.2. Algorithms for Control and Prediction in Energy Management Systems of Electric Vehicles and Grid Integration

With the increasing demand for intelligent and flexible power systems in electromobility, machine learning (ML) algorithms have begun to play a vital role in energy management systems (EMS) and the integration of electric vehicles with power grid infrastructure. Their application has enabled energy demand forecasting, charging schedule optimization, integration with renewable energy sources (RES), and minimization of operating costs and CO_2 emissions.

Study [63] analyzed the process of energy recovery during vehicle braking, where sensor data could be used in ML models to predict the recovered power under various driving conditions. In [10], PV system selection for EVs was analyzed using probabilistic distributions, indicating the potential for extending the approach with ML algorithms to dynamically predict energy supply and demand.

In [7], SVM and k-NN were used to forecast grid loads resulting from mass EV charging. A similar approach was taken in [30], where urban electric vehicle fleet data was used to predict instantaneous energy demand. Study [44] proposed a cost optimization model for charging under dynamic tariffs, which could be enhanced with boosting and logistic regression for improved precision.

Network integration issues were addressed in [45,46], which demonstrated the potential of dynamically managing power based on predictions using LSTM and XGBoost models. In [32,47], the impact of EV integration with RES on microgrid stability was analyzed, suggesting the implementation of predictive ML algorithms using weather and historical data.

In [40,70,72] reinforcement learning was used for energy management strategies and adaptive neural networks to independently tailor energy management strategies based on user profiles. Federated learning models described in [41,75] enabled model training on vehicles without transmitting raw data to the cloud, enhancing privacy and system security.

Ensemble learning for battery health classification, lifespan estimation, and replacement timing was presented in [33,34,53,55]. The use of autoencoders and signal transformation to improve data quality in energy management was described in [5,56,76]. Additional studies [4,54,57,74] introduced advanced signal processing techniques from sensors—including DWT, STFT, and nonlinear filtering—which significantly improved ML input data quality for energy management and fault detection.

In subsequent research [9,11,58,59,78–80] the focus was on real-time prediction of battery and supercapacitor behavior. It was shown that LSTM, GRU, and CNN enabled accurate estimation of SoC, SoH, and thermal control of battery packs, contributing to increased lifespan and efficiency. Complementary studies [30,80,81,83] addressed battery state monitoring using fuzzy logic models, Kalman filters, and adaptive neural networks, improving SoH prediction accuracy under real-world conditions.

A notable example of advanced energy management in electric motorcycles is provided by the optimal control of fuel consumption in a hybrid motorcycle equipped with three power sources: an internal combustion engine, an electric motor, and an integrated starter generator (ISG). The study compared two energy management strategies—Rule-Based Control (RBC) and the Equivalent Consumption Minimization Strategy (ECMS)—and quantified measurable reductions in fuel consumption [80]. These findings demonstrate that, even in complex multi-source configurations, substantial efficiency gains can be achieved through the appropriate selection of control strategies, particularly when supported by data-driven prediction from real-world driving cycles. Integrating such solutions with ML approaches, such as reinforcement learning, could further enhance the system's ability to adapt in real time to user profiles, road conditions, and charging infrastructure availability.

Publications [16,48,49,84,85] analyzed multipoint vehicle charging strategies using real-time data from chargers and vehicles. ML algorithms were used to predict peak demand, optimize power allocation, and reduce operational costs.

Finally, in [31,107–111], attempts were made to integrate ML with next-generation energy control systems based on distributed architectures, cloud computing, and neural networks processing sensor, weather, and tariff data in real time. Studies [105,106] further explored control in modern EMSs, describing dynamic power allocation and energy quality control using agent-based decision systems and peer-to-peer topologies. Table 2 provides a comprehensive summary of the different application areas for machine learning in E-mobility energy management systems.

Table 2. Types of Machine Learning Algorithms and Their Applications in the Prediction of E-Mobility Energy Management Systems.

Application Area	Objective/Function	Applied ML Algorithms	Publications
Energy Demand Prediction	Estimating instantaneous and long-term energy consumption by EVs	LSTM, XGBoost, regression, SVM	[7,30,63,78,79]
Charging Optimization	Power management, dynamic tariffs, charging schedules	Reinforcement Learning, boosting, CNN	[16,44,48,49]
Integration with RES (Renewable Energy Sources)	Matching PV/wind supply to EV demand	LSTM, hybrid models	[10,45–47]
Battery Diagnostics and Durability	Estimating SoH, SoC, life cycle, replacement timing	Autoencoders, ensemble, GRU	[33,34,53,58,59]
Predictive Systems in Microgrids	Load stabilization, overload and fault detection	SVM, k-NN, predictive models	[5,7,32,72]
Distributed and Private Learning	Model training without data transfer (privacy-aware EMS)	Federated Learning, edge ML	[41,75,107]
Energy Data Transformation	Improving data quality for ML (FFT, DWT, PCA)	CNN, autoencoders, PCA	[6,56,76,112]
Dynamic Control with Sensor Data	Real-time management based on GPS, IMU, thermometers, power sensors	Deep Learning, Reinforcement Learning	[40,72,85,109]

In the context of EMS optimization, research on the thermal management of a swappable lithium-ion battery pack for an electric motorcycle demonstrated that an air-cooling system could improve cell performance by up to 12% [29]. The integration of such cooling systems with ML-based predictive control enables proactive regulation of battery temperature and state-of-charge (SoC), extending battery lifespan and enhancing operational safety.

Another relevant consideration is the mechanical integration of the battery pack into the motorcycle chassis. A topology-optimized frame design, providing a lightweight yet stiff structure while accommodating the battery safely, addresses this challenge [96].

When combined with predictive EMS algorithms, such design solutions enable the creation of lightweight, efficient, and service-friendly electric motorcycles ready for seamless integration with microgrids and Vehicle-to-Grid (V2G) systems.

The application of machine learning algorithms in energy management systems for electric vehicles and their integration with the grid has enabled the development of intelligent, adaptive, and highly efficient solutions. By utilizing models such as LSTM, GRU, CNN, and XGBoost, it has become possible to accurately predict energy consumption, battery state-of-charge and state-of-health (SoC/SoH), as well as dynamically control the charging process. These algorithms also support energy management in grid conditions—allowing for power balancing, minimization of overloads, and adaptation to variable tariffs and weather conditions. Increasingly important are locally trained models (federated learning), which protect data privacy and enhance the security of EMSs.

Research conducted between 2015 and 2024 highlights the growing significance of deep learning and ensemble methods in the field of electric vehicle energy management. Particular attention is being paid to the development of robust, energy-efficient models deployable in embedded systems and microgrids. Future research should focus on improving model transparency (Explainable AI), resistance to interference, and adaptability to changing user conditions—elements that are essential for the widespread integration of ML in modern energy management systems within e-mobility.

Beyond purely technical optimization, machine learning can also support policy-making and infrastructure planning in the electric motorcycle domain. For example, a recent study examining the effectiveness of policies for developing the battery swapping service industry in Indonesia applied a system dynamics model to evaluate the impact of subsidies, standardization, and other regulatory measures. The findings suggest that well-designed policy instruments can accelerate technology adoption and reduce entry barriers for service providers—an approach that can be enhanced by ML-driven scenario simulations to forecast adoption rates and economic outcomes [21].

In addition, optimizing the spatial placement of electric motorcycle charging stations has been demonstrated in a case study from Surakarta, Indonesia, where centrality index and scalogram calculations were used to identify station locations that maximize accessibility and public benefit [118]. When combined with ML-based predictive models incorporating traffic density, population distribution, and charging patterns, such spatial analyses can significantly improve the efficiency and user experience of charging networks [75].

Furthermore, the concept of Tukerin, a mobile application-based marketplace for electric motorcycle battery swapping, illustrates how digital platforms can address key adoption barriers such as range anxiety and long charging times [119,120]. By integrating this type of platform with demand prediction and energy management systems powered by ML, it becomes possible to optimize battery inventory, reduce wait times, and coordinate with Vehicle-to-Grid (V2G) operations [6].

Incorporating such socio-technical innovations into the architecture of energy management systems (EMS) for electric motorcycles bridges technical optimization (charging strategies, demand prediction) with infrastructure and policy considerations, creating a holistic and adaptive ecosystem for sustainable e-mobility growth.

3.3. ML Algorithms in Control and Prediction Within Electric Vehicle Energy Management Systems and Their Integration with the Grid

With the development of electromobility and the increasing demand for intelligent, self-adaptive, and efficient control systems, energy management, and optimization of

charging infrastructure, machine learning (ML) algorithms are becoming the foundation of modern engineering solutions. Future ML applications in this domain will focus on deeper integration with distributed technologies, improved model interpretability, and adaptation to variable operational and environmental conditions.

One of the key areas of development is federated learning, which enables training ML models without transferring raw data to the cloud. This allows user privacy to be preserved while still improving predictive models—an essential aspect for deploying ML in network-connected vehicle systems [41,75,107]. Such models can be dynamically updated at the level of an individual vehicle or fleet, increasing local autonomy and system resilience.

Another significant trend is the development of energy-efficient algorithms optimized for edge computing. ML models implemented directly in onboard controllers of motorcycles and other EVs must be characterized by low power consumption and high resilience to disturbances, especially in rough terrain or urban traffic overloads [66–68]. For this purpose, lightweight neural networks, compressed deep models, and self-adaptive systems capable of real-time operation are being developed.

Reinforcement learning is also becoming an important direction, enabling control and energy management systems to learn optimal strategies based on experience and environmental feedback [43,70,72,109]. For example, such models can be used for continuous optimization of power distribution between the battery and supercapacitors in HESSs, taking into account driving style, predicted road conditions, and charging infrastructure availability.

As the number of electric vehicles grows, intelligent charging management and operating cost optimization are also advancing. Algorithms such as XGBoost, LSTM, and CNN allow highly accurate forecasting of energy demand—even under variable tariffs, power limits, and irregular usage patterns [39,79,81]. Integration with renewable energy sources (RES), microgrids, and dynamic charging stations requires not only prediction but also real-time response, which can be achieved through hybrid ML models.

Predictive maintenance systems are also receiving increasing attention, enabling early detection of irregularities in motors, batteries, and electronic components. The use of autoencoders, recurrent neural networks, and ensemble learning makes it possible to identify subtle changes in measurement signals before they result in failure [41,63,65,71,74]. These models support maintenance planning, improve safety, and reduce unplanned downtimes.

A vital area of development is data fusion from multiple sources—onboard sensors, GPS, weather data, energy tariffs, and contextual user information. The application of deep neural networks (DNN) and dimensionality reduction methods allows for building complex yet efficient predictive models that are robust to disturbances and measurement imperfections [6,71,112].

Explainable AI (XAI) also plays a key role—referring to algorithms whose operations can be understood by end users or system operators. Transparency of ML models will be critical for their certification, deployment in safety-critical environments, and for building trust in autonomous technologies. Transparent models will find use in energy safety management systems and automated decision-support systems [40,52,54,82].

In the coming years, ML is expected to be increasingly integrated with cloud-based architectures, IoT, and distributed systems. These solutions will form the foundation of fully intelligent EV fleet management systems, integrating energy management, technical maintenance, and adaptive drive control within one cohesive environment.

3.4. Summary of the Analysis in Relation to Key Research Questions

In the context of electric motor efficiency used in electric motorcycles, the most optimal solution in terms of energy performance remains the Permanent Magnet Synchronous Motor (PMSM). These motors are characterized by high power density and efficiency, making them an attractive choice for premium and sport segments. Their advantages also include low noise levels and favorable control characteristics under variable operating conditions [14,67,68,73]. While Brushless DC motors (BLDC) are slightly less efficient, they are simpler in design, cheaper to manufacture, and easier to maintain, making them ideal for more economical vehicle models [13,15]. Switched Reluctance Motors (SRM), on the other hand, are notable for their high durability and resistance to external factors, although their development is limited by noise emission challenges and complex control characteristics [23,91].

In the field of energy storage technologies, lithium-ion cells remain the dominant solution due to their favorable capacity-to-weight ratio, long lifecycle, and good thermal performance [64–66]. Safer alternatives include LFP cells and solid-state electrolyte systems, which offer higher thermal stability and lower fire risk, although often at the expense of energy density [39,45,51]. Increasing attention is being given to advanced Battery Management Systems (BMS) supported by ML algorithms, which enable predictive control of battery parameters and monitoring of their condition [32,46].

The use of Hybrid Energy Storage Systems (HESS), integrating batteries with supercapacitors, significantly enhances the performance of electric motorcycles, especially in the context of regenerative braking and the delivery of high instantaneous power during acceleration. Such systems increase the lifespan of the main battery pack by reducing peak loads [31,47,70]. Combined with ML algorithms, they enable dynamic energy flow management by adapting to riding style, road conditions, and the vehicle's energy demand [40,71,72,109].

In the field of charging technologies, wired charging systems still dominate, offering the highest efficiency and broad compatibility with existing energy infrastructure [48,85]. However, wireless charging systems are gaining interest, particularly for urban fleets where convenience, automation, and minimal physical interaction become key advantages [16,83,85]. A particularly promising development direction is Vehicle-to-Grid (V2G) technology, which allows bidirectional energy flow and turns motorcycles into active participants in the power grid. Although this technology is still in the early stages of deployment, its potential for integration with renewable energy sources and local microgrids is significant [32,33,41].

Optimal configurations of electric motorcycle components, especially traction inverters, should be based on solutions that ensure high energy conversion efficiency, low switching losses, and resistance to electromagnetic interference [121]. In this context, modern inverters built using SiC transistors and multilevel architectures are particularly effective [27,53–57]. Contemporary design approaches also emphasize system modularity and the integration of ML-based diagnostic systems, which enable predictive fault detection, autonomous component switching, and drive configuration adjustment to operating conditions [58–60]. Furthermore, with the advancement of AI technologies and models, research is being conducted on the potential use of acoustic waves for extinguishing flames from various fuels and substances, which in the future may find application in both individual and public transport. Research in this area is the subject of numerous scientific efforts worldwide, e.g., [122–131].

In conclusion, the literature indicates that the future of electric motorcycles will depend on the synergistic development of high-performance PMSMs, advanced and safe

energy storage technologies, flexible charging solutions, and ML-supported control systems. Thoughtful integration of these components into a coherent, scalable technical architecture will allow for the creation of more reliable, economical, and sustainable mobility solutions.

4. Results and Analysis

This chapter presents a detailed statistical analysis of 101 scientific publications in the field of electromobility, published across two five-year periods: 2015–2019 and 2020–2024. The analysis covered four main dimensions: document types (conference papers and journal articles), technological domains (electric drivetrains, energy storage, battery charging, electrical components), engineering and optimization topics (energy efficiency, sustainability, design and analysis), and applied methodological approaches (experiment, literature review, case study, conceptual approach, and survey-based research).

Additionally, a geographical comparison was conducted based on the authors' country affiliations, and chi-square tests were applied to evaluate the statistical significance of observed differences. The results are presented in the form of tables, charts, and heatmaps, enabling the identification of dominant research trends, development directions, and areas requiring further investigation.

Based on the presented chart (Figure 5), it was shown that the number of conference papers increased from 21 in the period 2015–2019 to 48 in 2020–2024 (an increase of approximately 129%), while journal articles were recorded in quantities of 14 and 18, respectively (an increase of approximately 29%). The chart suggests that research findings were primarily disseminated through scientific conferences, highlighting the importance of rapid knowledge exchange. At the same time, the growing number of peer-reviewed journal articles indicates an increasing emphasis on formal validation of results.

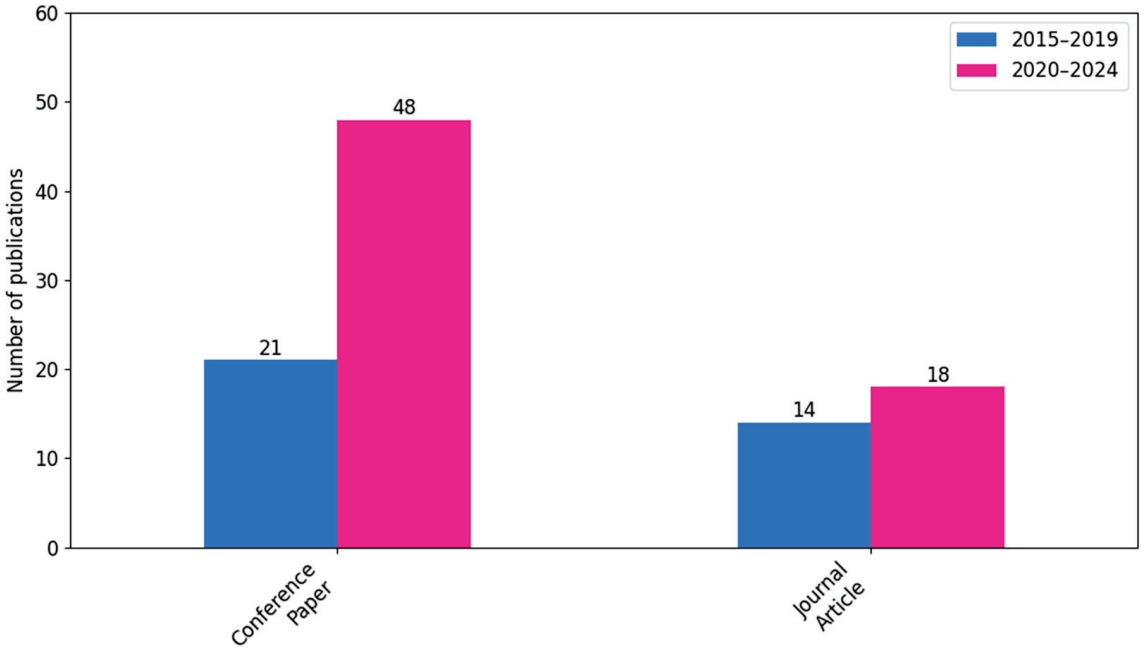


Figure 5. Document types.

The rise in the share of conference publications, alongside a moderate increase in journal articles, may be interpreted as a sign of intensified research dialog and a thematic shift from exploratory phases toward more established knowledge.

Figure 6 presents a comparison of the number of publications in four key areas of e-mobility technologies—electric drivetrains, energy storage, battery charging, and electrical components—across two consecutive five-year periods. In the area of electric drivetrains, the number of publications increased from 26 to 31 (an increase of approximately 19%). In the energy storage segment, the number of studies rose from 13 to 33 (approximately 154% growth). The most significant increase was observed in the field of battery charging, where the number of publications grew from 7 to 27 (an increase of approximately 286%). In contrast, the area of electrical components showed only a minimal change, with publications increasing from 9 to 10 (about 11% growth).

This publication dynamics structure is interpreted as a shift in research focus toward storage efficiency and fast charging, while interest in supporting components appears to have stabilized.

The marked growth in publications on battery charging between 2015 and 2019 and 2020–2024 reflects not only the expansion of charging infrastructure but also the rise in ML-assisted strategies for optimizing charging schedules, reducing costs under dynamic tariffs, and enabling V2G functionality [44–49]. In contrast, the modest increase in electrical component research suggests that while hardware improvements (e.g., SiC inverters) remain important, the integration of predictive diagnostics and adaptive control algorithms is an emerging but less explored area [53–60].

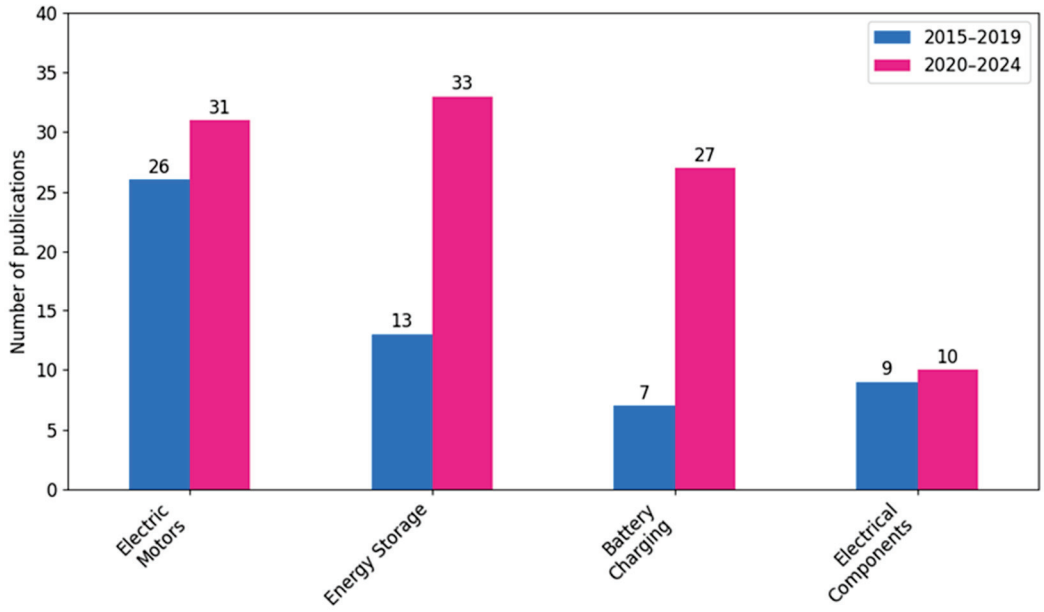


Figure 6. Number of publications in the field of e-mobility technologies in the periods 2015–2019 and 2020–2024.

Figure 7 presents a comparison of the number of publications in three thematic categories related to engineering and optimization—energy efficiency, sustainability, and design and analysis—across the periods 2015–2019 and 2020–2024. In the first category, the number of studies increased from 15 to 41, representing a growth of approximately 173%. In the case of sustainability, no increase was recorded, with the number remaining constant at 20 (0% growth). In contrast, the design and analysis category saw an increase from 13 to 20 publications, corresponding to a growth of approximately 54%.

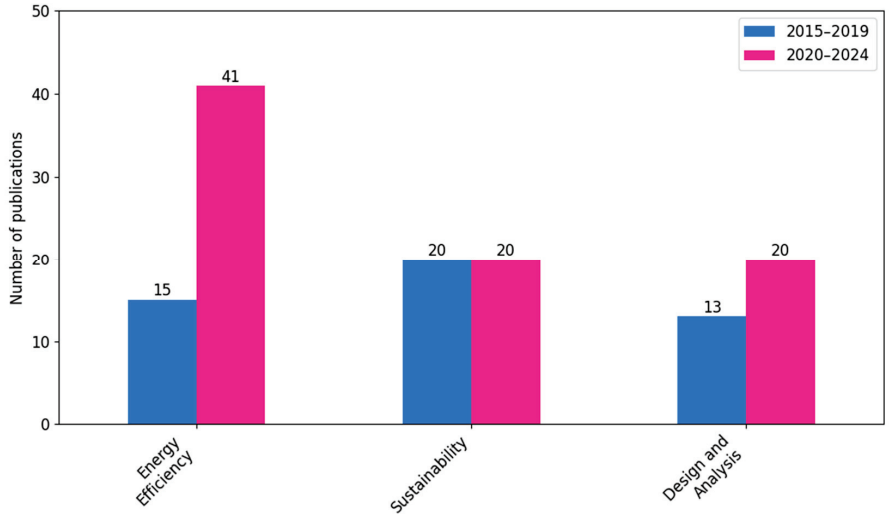


Figure 7. Number of publications in engineering and optimization categories in the periods 2015–2019 and 2020–2024.

This trend indicates an intensification of research in energy efficiency and a strengthening of the role of design, while interest in sustainability-related issues appears to have stabilized.

The dominance of energy efficiency as a research theme aligns with the deployment of AI/ML models aimed at reducing energy losses in motors, optimizing energy flow in HESS configurations, and improving the accuracy of SoC/SoH estimation [17,32–34,40,46,70,72]. The stable number of sustainability-focused studies indicates that environmental lifecycle assessments are not growing at the same pace as performance-focused research, despite the potential of ML to optimize design for recyclability and eco-efficiency [58,59].

Figure 8 compares the number of publications across five research methodology categories—experimental studies, literature analysis, case studies, conceptual approaches, and survey-based research—across two consecutive five-year periods. For experimental methods, the number of publications increased from 18 to 38 (a growth of approximately 111%), while literature analysis rose from 9 to 25 (around 178%). In the case study category, the number of publications increased from 8 to 12 (50%), whereas conceptual approaches grew from 26 to 45 (about 73%). Only the survey category experienced a decline, dropping from 2 to 1 publication (a 50% decrease).

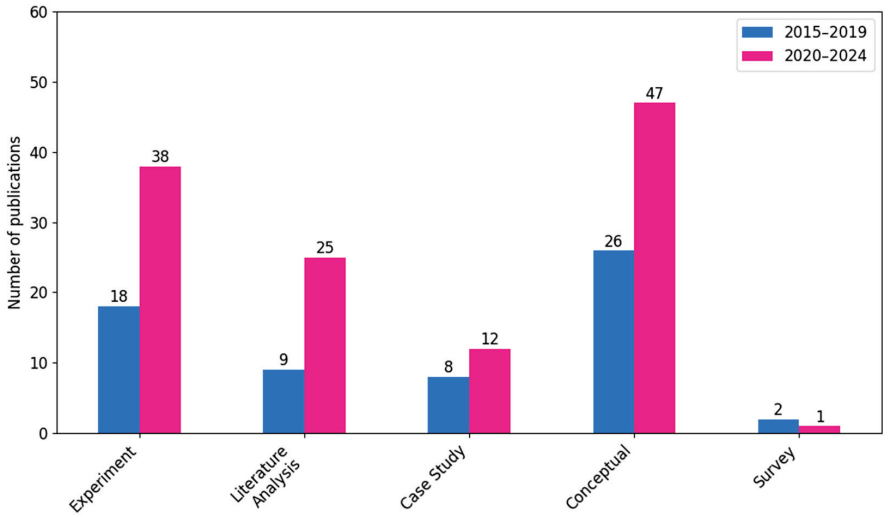


Figure 8. Number of publications by research methodology in the periods 2015–2019 and 2020–2024.

This pattern indicates a clear shift in emphasis toward experimental research and theoretical modeling, accompanied by a reduced reliance on survey-based methods.

The sharp increase in literature analysis publications corresponds to the systematic mapping of AI/ML applications across electric motorcycle subsystems, allowing researchers to identify high-impact algorithmic trends. The growth in experimental studies demonstrates a shift toward real-world validation of ML-based control and diagnostic systems, though survey-based research remains rare, limiting user feedback integration into AI-enabled designs.

Table 3 presents a summary of 101 publications in the field of electromobility, divided into two time periods (2015–2019 and 2020–2024). The analysis covers four main dimensions: document type (Conference Paper vs. Journal Article), technological domains (Electric Motors, Energy Storage, Battery Charging, Electrical Components), optimization topics (Energy Efficiency, Sustainability, Design and Analysis), and research methodology (Experiment, Literature Analysis, Case Study, Conceptual, Survey).

Table 3. Publications by year in all categories.

Name	2015–2019	2020–2024	All Years	Share [%]
Total	35	66	101	100.0
Document Type				
Conference Paper	21	48	69	68.32
Journal Article	14	18	32	31.68
E-mobility Technologies				
Electric Motors	26	31	57	56.44
Energy Storage	13	33	46	45.54
Battery Charging	7	27	34	33.66
Electrical Components	9	10	19	18.81
Engineering and Optimization				
Energy Efficiency	15	41	56	55.45
Sustainability	20	20	40	39.6
Design and Analysis	13	20	33	32.67
Research Methodology				
Experiment	18	38	56	55.45
Literature Analysis	9	25	34	33.66
Case Study	8	12	20	19.8
Conceptual	26	47	73	72.28
Survey	2	1	3	2.97

In addition, statistical significance of differences between categories was assessed using the chi-square test within the groups "Technologies and Infrastructure" and "Research Methodology."

Furthermore, chi-square statistical tests were applied across four groups: (1) Document Type, (2) E-mobility Technologies, (3) Engineering and Optimization, (4) Research Methodology.

Based on Table 3, a detailed, multidimensional analysis of the distribution of 101 scientific publications in the field of electromobility was carried out, covering two time periods: 2015–2019 (35 publications) and 2020–2024 (66 publications). The analysis included four main dimensions: document type, technological domain, optimization topics, and adopted research methodology. The obtained results were subjected to statistical verification using the chi-square test.

In the Document Type category, two groups were distinguished: Conference Paper and Journal Article. Conference papers accounted for 69 publications (68.32%), with 21 published before 2019 and 48 between 2020 and 2024. Journal articles were recorded in 32 cases (31.68%), including 14 in the first period and 18 in the second. It was observed that the share of journal articles increased by over 28% between the two periods, which may reflect the growing importance of peer review and the increasing stability of research findings.

The E-mobility Technologies analysis was divided into four subcategories: Electric Motors, Energy Storage, Battery Charging, and Electrical Components. Electric Motors were addressed in 57 publications (26 in 2015–2019; 31 in 2020–2024; 56.44%), indicating sustained interest in electric drive design and performance. Energy Storage appeared in 46 studies (13 + 33; 45.54%), with a significant increase in the second period, likely due to advancements in battery technologies. Battery Charging was the focus of 34 publications (7 + 27; 33.66%), reflecting growing challenges in charging infrastructure. Electrical Components were included in 19 studies (9 + 10; 18.81%), suggesting that hardware elements are less frequently explored, although they remain critical to system reliability.

In the Engineering and Optimization area, three key topics were identified: Energy Efficiency was covered in 56 publications (15 + 41; 55.45%), emphasizing the priority of optimizing energy consumption in EV systems. Sustainability appeared in 40 papers (20 + 20; 39.60%), indicating consistent interest in environmental aspects and component life cycles. Design and Analysis was the subject of 33 publications (13 + 20; 32.67%), highlighting the complexity of design and simulation processes necessary for developing safe and efficient solutions.

The Research Methodology distribution included five research approaches, with a dominance of experimental and conceptual studies: Experimental methods were used in 56 publications (18 + 38; 55.45%), reflecting high engagement in prototype testing and lab validation. Conceptual approaches were found in 73 publications (26 + 47; 72.28%), emphasizing the development of analytical and simulation-based models. Literature Analysis appeared in 34 papers (9 + 25; 33.66%), indicating strong foundations in review-based research. Case Studies were applied in 20 publications (8 + 12; 19.80%), while Survey-based studies were noted in only 3 cases (2 + 1; 2.97%), suggesting limited use of fieldwork and user feedback.

Chi-square tests were used to verify the significance of differences in four groups: for Document Type, the result was $\chi^2 = 1.17$ (df = 1; $p = 0.28$); for E-mobility Technologies, $\chi^2 = 8.09$ (df = 3; $p = 0.04$), indicating statistically significant differences between subcategories. In Engineering and Optimization, $\chi^2 = 5.47$ (df = 2; $p = 0.06$); in Research Methodology, $\chi^2 = 2.78$ (df = 4; $p = 0.60$), showing no statistically significant differences.

Key conclusions from the analysis include:

1. Conference Papers dominate the electromobility research space, reflecting the role of rapid dissemination of preliminary results at conferences;
2. Within E-mobility Technologies, Electric Motors and Energy Storage are the most frequently represented topics, while Electrical Components receive comparatively less attention;

3. In Engineering and Optimization, Energy Efficiency holds central importance, reflecting the dominance of research focused on energy performance;
4. In Research Methodology, experimental and conceptual studies account for more than two-thirds of all approaches, emphasizing the parallel development of practical testing and theoretical modeling.

Based on Table 4, "Publications by E-mobility Technologies in other categories", a detailed analysis of the 101 scientific publications in the electromobility domain was conducted, with classification according to four technology categories: Electric Motors (57), Energy Storage (46), Battery Charging (34), and Electrical Components (19). Publications were assigned to two main thematic groups: Engineering and Optimization and Research Methodology.

Additionally, statistical analysis using the chi-square test was performed in two groups: (1) Engineering and Optimization, (2) Research Methodology.

In the Engineering and Optimization area, three subcategories were analyzed. For Energy Efficiency, 56 publications were identified, including 27 related to Electric Motors, 27 to Energy Storage, 20 to Battery Charging, and 10 to Electrical Components. The topic of Sustainability was addressed in 40 publications (21, 15, 14, and 5, respectively, for each of the listed technologies). Within Design and Analysis, 33 articles were identified, of which 25 focused on Electric Motors, 13 on Energy Storage, 6 on Battery Charging, and 11 on Electrical Components. This distribution indicates strong interest in optimizing drivetrains and storage systems, with moderate attention to design-related aspects and relatively lower engagement in research on electrical components.

Table 4. Publications by E-mobility Technologies in other categories.

Name	Electric Motors	Energy Storage	Battery Charging	Electrical Components	Total
Total	57	46	34	19	101
Engineering and Optimization					
Energy Efficiency	27	27	20	10	56
Sustainability	21	15	14	5	40
Design and Analysis	25	13	6	11	33
Research Methodology					
Experiment	31	28	19	13	56
Literature Analysis	21	14	10	8	34
Case Study	9	9	6	2	20
Conceptual	38	31	27	16	73
Survey	3	0	1	0	3

In the Research Methodology group, five research approaches were compared. A total of 56 studies were classified under Experiment, of which 31 focused on Electric Motors, 28 on Energy Storage, 19 on Battery Charging, and 13 on Electrical Components. Literature Analysis included 34 publications (21, 14, 10, and 8 for the respective technologies).

Case Study was used in 20 studies, particularly involving Electric Motors and Battery Charging (9 and 6 cases, respectively), while Energy Storage appeared in 3 and Electrical Components in 2. Conceptual approaches were applied in 73 articles, with notable inclusion of Electric Motors (38), Energy Storage (31), Battery Charging (27), and Electrical Components (16). Survey appeared infrequently—in only 3 publications, primarily in the context of Electric Motors and Battery Charging. A clear dominance of Conceptual and Experimental approaches was observed, while Survey and Case Study methods were

used less frequently. For the Engineering and Optimization group, the chi-square test yielded $\chi^2 = 8.69$ (df = 6; $p = 0.19$), indicating no statistically significant differences in the distribution of publications across technological subcategories. Similarly, in the Research Methodology group, the result was $\chi^2 = 5.78$ (df = 12; $p = 0.93$), confirming no significant differences in the choice of research methods.

From the analysis, the following conclusions can be drawn:

1. Electric Motors technology was the most frequently addressed in both optimization and methodological studies, which may indicate the central role of drivetrains in the development of electromobility.
2. Energy Storage ranked just behind drivetrains, underscoring the importance of storage systems in EV design.
3. Battery Charging and Electrical Components were represented to a lesser extent, suggesting the need for further research in charging infrastructure and electronic componentry.
4. The absence of statistically significant differences suggests a relatively even distribution of research interest across technologies in the context of both optimization and methodology.

Figure 9 presents a comparison of the number of publications across two five-year periods, categorized by the authors' country of affiliation. For Indonesia, the number of publications increased from 2 to 18, representing the most significant change in the dataset. In the case of Japan, the number of studies remained constant at 5, while in the United Kingdom, it rose from 3 to 6. The United States saw a modest increase from 3 to 4 publications, while Canada and Thailand maintained stable levels of 3 and 3, respectively. Italy's publication count increased from 2 to 4, and India recorded a rise from 0 to 5. A decrease from 3 to 2 publications was registered for Malaysia, while both South Korea and Spain experienced an increase from 2 to 3 publications. For the "Other" category, the number of studies rose from 9 to 15.

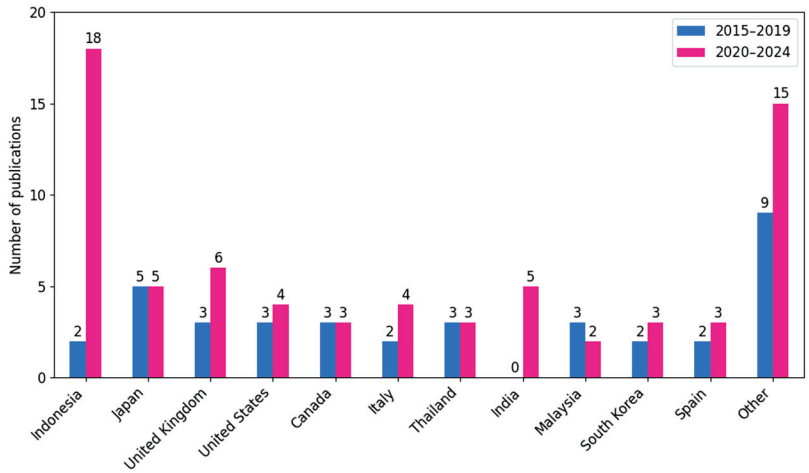


Figure 9. Distribution of studies by application areas.

This dynamic indicates a shift in research activity toward regions with a growing presence in the field of electromobility literature.

Based on Table 5, the distribution of 101 publications in the field of electromobility is presented according to the authors' country of affiliation across the two periods (2015–2019 and 2020–2024), showing each country's percentage share and the result of a chi-square test verifying the significance of observed changes.

Table 5. Publications by year in Countries.

Country	2015–2019	2020–2024	All Years	Share [%]
All countries	35	66	101	100.0
Indonesia	2	18	20	19.8
Japan	5	5	10	9.9
United Kingdom	3	6	9	8.91
United States	3	4	7	6.93
Canada	3	3	6	5.94
Italy	2	4	6	5.94
Thailand	3	3	6	5.94
India	0	5	5	4.95
Malaysia	3	2	5	4.95
South Korea	2	3	5	4.95
Spain	2	3	5	4.95
Other	9	15	24	23.76

To assess whether the changes in the number of publications across individual countries between the periods 2015–2019 and 2020–2024 were statistically significant, a chi-square test was applied.

- Chi-square value (χ^2): 12.22
- Degrees of freedom: 11
- *p*-value: 0.35

Since the *p*-value exceeded the significance threshold of 0.05, no statistically significant association was found between the year of publication and the authors' country of affiliation.

The analysis included 101 publications, with 35 published in 2015–2019 and 66 in 2020–2024. The largest share of studies was attributed to Indonesia (20; 19.8%), where the number of publications increased from 2 to 18 across the two timeframes. Japan ranked second with an even distribution (5 + 5; 9.9%), while the United Kingdom followed in third place (3 + 6; 8.91%). The United States had 7 publications (3 + 4; 6.93%), and Canada published 6 (3 + 3; 5.94%), reflecting the relative stability of their contributions. A similar number of studies (6; 5.94%) was observed in Italy and Thailand, while India, Malaysia, South Korea, and Spain each accounted for 5 publications (4.95%). The "Other" category, comprising 24 papers (23.76%), indicates significant involvement from smaller research centers.

The analysis leads to the following conclusions:

1. Indonesia emerged as the leading research hub during the analyzed period, accounting for nearly 20% of all publications.
2. Japan and the UK maintained steady levels of research activity, possibly reflecting stable research funding.
3. The increase in India's output from 0 to 5 publications suggests a dynamic growth in scientific engagement in South Asia.
4. Countries with a moderate contribution, such as Canada, Italy, and Thailand, maintained a consistent level of output, possibly due to established research strategies.

5. The high proportion of papers classified under "Other" reflects growing geographical diversity and increasing activity of smaller research institutions worldwide—possibly the result of intentional research policy initiatives.

The presented heatmap (Figure 10) illustrates the distribution of publications by research methodology (experiment, literature review, case study, conceptual approach, survey) in the context of four e-mobility technologies (electric motors, energy storage, battery charging, electrical components).

The most frequently employed research methodology was experimental studies, highlighting the importance of practical validation of technological solutions. This group included:

- 31 publications related to electric motors,
- 28 analyses of energy storage,
- 19 studies focused on battery charging,
- 13 works addressing electrical components.

Literature analysis was identified as the second most commonly used method, with 21 publications on electric motors, 14 on energy storage, 10 on battery charging, and 8 on electrical components. Case studies were relatively rare—conducted in 9 studies on motors and storage, 6 on charging, and only 2 on components—indicating limited documentation of real-world implementations. Conceptual approaches proved essential for theoretical development, as evidenced by 38 publications on electric motors, 31 on energy storage, 27 on battery charging, and 16 on electrical components. Surveys were used sporadically—3 times in the context of motors, once in charging, and none for storage or components.

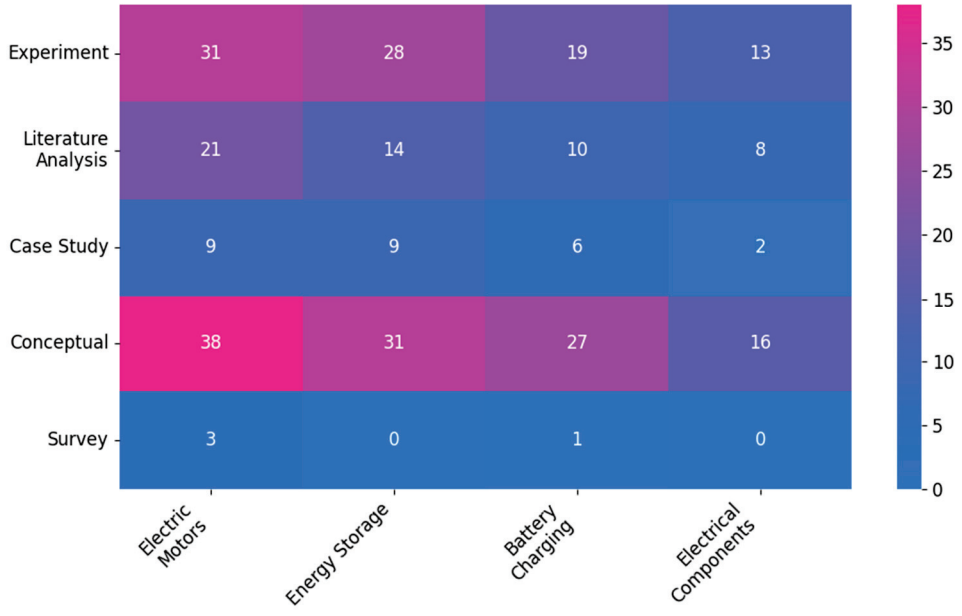


Figure 10. Heatmap of research methodology scope and e-mobility technologies.

This methodological structure is considered to reflect the advanced stage of e-mobility technology development, where practical testing and conceptual framework development go hand in hand. The limited number of case studies and surveys suggests a gap, particularly in documenting implementations and gathering user data. Literature analysis, meanwhile, is seen as the foundation for building a robust theoretical base, enabling the

generation of new hypotheses. The presented distribution may serve to guide future research directions by identifying both methodological and technological gaps.

The presented heatmap (Figure 11) illustrates the relationship between three categories of engineering and optimization topics and four e-mobility technologies. Each cell contains the number of publications in which a given topic (energy efficiency, sustainability, design and analysis) is linked to a specific technology (electric motors, energy storage, battery charging, electrical components). This enables the identification of the most frequently explored thematic combinations in the reviewed literature.

Energy efficiency was identified as the most frequently represented category within engineering and optimization, highlighting its central role in e-mobility research. This group included:

- 27 publications related to electric motors,
- 27 studies on energy storage,
- 20 papers on battery charging,
- 10 publications concerning electrical components.

Such high values were interpreted as a concentration of scientific efforts on optimizing energy consumption in the core elements of EV systems, with gradually decreasing attention given to auxiliary components.

Sustainability was the second most prominent category, with:

- 21 publications focused on electric motors,
- 15 on energy storage,
- 14 on battery charging,
- 5 related to electrical components.

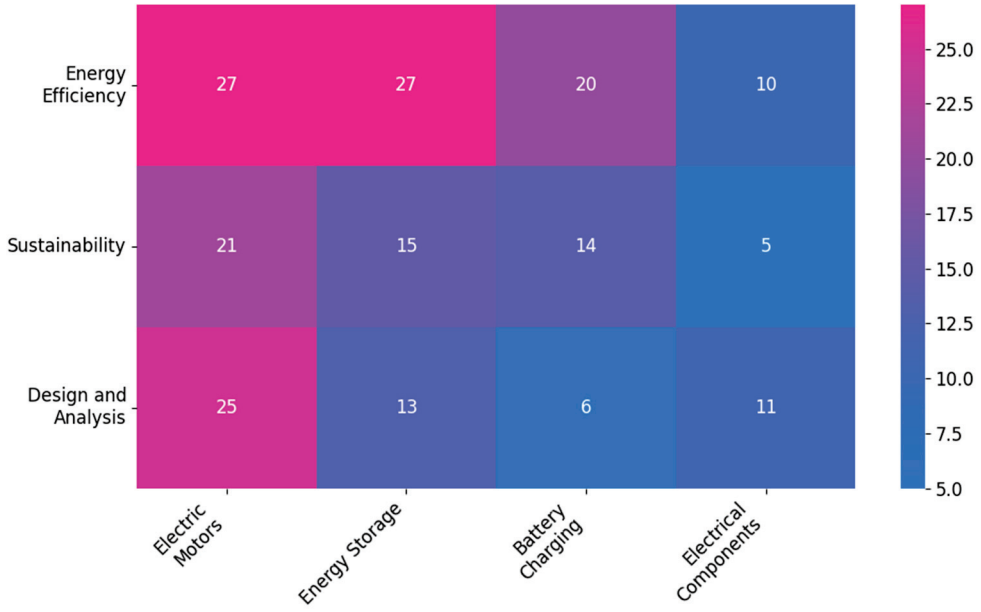


Figure 11. Heatmap of relationships between engineering and optimization categories and e-mobility technologies.

The moderate level of attention given to charging and components was seen as a signal of the need for deeper investigation into the environmental impact and life cycle of e-mobility technologies.

In the area of design and analysis, the following numbers were observed:

- 25 publications on electric motors,

- 13 on energy storage,
- 6 on battery charging,
- 11 on electrical components.

This varied distribution reflects the growing importance of interdisciplinary simulation and modeling methods in the integration of different technologies.

In summary, energy efficiency clearly dominated the reviewed literature, while interest in sustainability and in design and analysis was more evenly balanced across studies on electric motors. The least attention was paid to electrical components.

The analysis of 101 scientific publications in the field of electromobility revealed a clear increase in research activity in the period 2020–2024 compared to 2015–2019. Conference papers remained the dominant form of publication, underscoring the importance of rapid dissemination in a rapidly evolving field. At the same time, the growing share of peer-reviewed journal articles reflects the scientific community's pursuit of formal validation and stabilization of results.

Among the technological areas, electric drivetrains and energy storage attracted the greatest interest. The most dynamic growth in the number of publications was observed in the field of battery charging, likely due to increasing demands on charging infrastructure. Electrical components, while essential for EV system reliability, were relatively less represented in the literature.

Engineering-related topics focused primarily on energy efficiency, appearing in over half of the analyzed studies. Although sustainability and design/analysis were also present, they appeared to a lesser extent. This distribution suggests a practical orientation in research, with energy savings being treated as a top priority in e-mobility systems.

From a methodological perspective, experimental and conceptual approaches were dominant, indicating simultaneous development of both practical solutions and theoretical models. Literature reviews and case studies played a supplementary role, while survey-based research was marginal. This methodological structure suggests that research in this domain is still rarely conducted with direct user participation or in the context of real-world implementations.

Geographically, the largest increase in the number of publications was observed in Indonesia, which emerged as the leading contributor to electromobility research. Japan, the United Kingdom, and the United States maintained consistent levels of activity. At the same time, the number of publications from previously less-represented countries increased, suggesting growing internationalization of research and rising interest in e-mobility across developing regions.

In conclusion, this chapter reveals the dynamic scientific development in the field of electromobility, with a clear shift in research focus toward energy storage, battery charging, and energy efficiency. The dominance of experimental and conceptual methods, along with the limited use of applied approaches, points to the potential for further exploration in areas related to implementation and end-user perspectives.

5. Discussion and Future Work

Table 6 summarizes the most relevant machine learning (ML) trends identified across the four main technological domains of electric motorcycles. For each domain, key ML algorithms are listed alongside reported performance benefits, major technical challenges, and suggested future research directions. The synthesis highlights that, while ML has achieved measurable gains—such as improved torque control in motors, higher accuracy in battery state estimation, and cost-optimized charging—challenges remain in terms of computational efficiency, model generalization, and infrastructure readiness. Addressing these gaps,

particularly through lightweight models, federated learning, and Explainable AI (XAI), will be essential for large-scale deployment in commercial electric motorcycle systems.

Table 6. Summary of ML-driven trends, benefits, challenges, and future directions across technology domains.

Domain	Key ML Algorithms	Reported Benefits	Main Challenges	Future Directions
Electric Motors	LSTM, ANFIS, RL, SVM	+3–5% efficiency, torque ripple reduction, improved adaptability	Computational load, large datasets required	Lightweight hybrid control models for embedded systems
Energy Storage	CNN, Ensemble, GRU, Kalman filters	SoC/SoH error $\leq$ 2%, extended battery lifespan	Sensor noise, temperature sensitivity	Federated BMS learning, thermal-aware predictive models
Charging and V2G	RL, LSTM, Boosting, SVM	Reduced charging cost/time, improved grid stability	Infrastructure readiness, interoperability issues	Hybrid scheduling combining V2G, RES, and HESS
Electronic Components	Autoencoders, CNN, Decision Trees	Early fault detection, reduced downtime	Generalization across platforms, limited datasets	XAI-based diagnostics, adaptive fault-tolerant control

The comparative overview in Table 7 reveals several key cross-domain patterns:

1. AI/ML penetration is highest in control and prediction tasks. PMSMs and energy storage show the most mature applications, where LSTM, ANFIS, and CNN architectures deliver measurable performance gains.
2. Data quality and computational constraints remain universal bottlenecks, limiting real-time deployment in embedded systems.
3. Charging and V2G applications are emerging as high-growth areas, but infrastructure readiness and interoperability remain barriers.
4. Electronic components lag in research intensity, although ML-based diagnostics have demonstrated clear benefits in fault detection and maintenance reduction.
5. Future directions converge toward integrated, lightweight, and explainable models, suggesting a shift from isolated component optimization toward fully connected, AI-driven motorcycle architectures.

Table 7. Comparative performance of major ML algorithms in the four key technological domains.

Domain	ML Algorithms	Application	Measured Effect	Representative Sources
Electric Motors	LSTM, ANFIS, RL, SVM	Torque control, ripple reduction, load adaptation	+3–5% efficiency, 8–12% torque ripple reduction, 10–15% faster dynamic response	[14,17,20–24]
Energy Storage	CNN, Ensemble, GRU, Kalman filters	SoC/SoH estimation, degradation forecasting	$\leq$2% SoC error, 5–10% longer lifespan, >90% fault prediction accuracy	[32–34,46,53,58,59]
Charging and V2G	RL, LSTM, Boosting, SVM	Cost/time optimization, renewable integration	10–15% faster charging, 5–12% cost reduction, 8–10% peak load reduction	[16,44,46–49]
Electronic Components	Autoencoders, CNN, Decision Trees	Inverter diagnostics, fault prediction	>95% fault detection accuracy, 10–20% downtime reduction	[53–60]

As summarized in Table 6, the systematic literature review conducted for the period 2015–2024 revealed that electric motorcycles are becoming an increasingly important component of electromobility, with technological development focused around four key areas: electric motors, energy storage, charging systems, and electronic components. Across

these domains, the integration of artificial intelligence (AI) and machine learning (ML) has emerged as a unifying factor, enhancing control precision, predictive maintenance capabilities, and overall system efficiency.

5.1. Key Findings and Discussion

In the context of electric motor efficiency, Permanent Magnet Synchronous Motors (PMSMs) remain the most attractive option in terms of energy performance and controllability, particularly when combined with ML-enhanced control strategies such as LSTM-assisted Field-Oriented Control and adaptive neuro-fuzzy inference systems. These approaches have been shown to reduce torque ripple, improve dynamic response, and adapt to variable load conditions better than conventional methods. Brushless DC motors (BLDC) and Switched Reluctance Motors (SRM) remain relevant for cost-sensitive applications, where ML-based optimization can mitigate their inherent disadvantages, such as acoustic noise and complex torque profiles.

For energy storage technologies, lithium-ion cells continue to dominate due to their favorable capacity-to-weight ratio and thermal performance. However, ML-supported Battery Management Systems (BMS) now play a key role in maximizing their lifespan and reliability, providing accurate state-of-charge (SoC) and state-of-health (SoH) estimation, as well as adaptive control to mitigate degradation. Hybrid Energy Storage Systems (HESS), integrating batteries with supercapacitors, further benefit from reinforcement learning and predictive algorithms to optimize energy flow during acceleration and regenerative braking.

Regarding charging technologies, wired systems currently offer the highest efficiency and compatibility, but wireless and Vehicle-to-Grid (V2G) solutions are gaining traction. In particular, ML-based charging optimization—using reinforcement learning, LSTM forecasting, and boosting algorithms—enables intelligent scheduling under dynamic tariffs, integration with renewable energy sources, and grid load balancing. Although V2G for motorcycles remains at an early stage, predictive and adaptive algorithms hold significant potential for future deployment.

For electronic components, modern traction inverters built with SiC transistors and multilevel architectures are delivering higher conversion efficiencies and lower switching losses. ML-driven diagnostics embedded in these components allow for early fault detection, autonomous component switching, and adaptive performance tuning, directly improving system reliability and reducing downtime.

5.2. Future Research Directions

Future research should focus on the following strategic directions:

- Integrated AI/ML Architectures—Developing unified control frameworks that combine motor drive optimization, energy storage management, charging control, and fault diagnostics within a single intelligent system.
- Lightweight and Energy-Efficient Models—Designing ML algorithms optimized for embedded controllers with strict computational and power constraints, enabling real-time operation in edge environments.
- Explainable AI (XAI)—Increasing the interpretability of ML models to improve user trust, support certification processes, and ensure safe deployment in safety-critical functions.
- Federated Learning and Privacy-Preserving Systems—Enabling collaborative training of ML models across fleets without transmitting raw operational data, thereby enhancing security and scalability.

- Advanced Hybrid Energy Management—Integrating fast charging, V2G capabilities, and HESS within a single ML-optimized framework to improve flexibility, sustainability, and cost-effectiveness.
- Eco-Design Integration—Combining sustainable materials and lightweight construction with intelligent control systems to reduce lifecycle environmental impact. Standardized Performance Benchmarks—Establishing common metrics for evaluating ML-based solutions in electric motorcycles to facilitate cross-study comparisons and industrial adoption.

By pursuing these directions, future electric motorcycles can evolve into fully intelligent platforms capable of continuous self-optimization, predictive adaptation to environmental and operational conditions, and seamless integration with the wider energy ecosystem. This convergence of hardware innovation and AI/ML-driven intelligence represents a decisive step toward achieving the twin goals of high performance and environmental sustainability in the electromobility sector.

6. Conclusions

This review has provided a comprehensive analysis of technological advancements in electric motorcycles between 2015 and 2024, focusing on four main domains: electric motors, energy storage, charging technologies, and electronic components. As highlighted in Table 6 and further discussed in the preceding section, the integration of artificial intelligence (AI) and machine learning (ML) into these domains is no longer a peripheral trend but a central driver of innovation.

The findings confirm that PMSMs deliver the highest efficiency and controllability among electric motor types, especially when combined with ML-enhanced control strategies. Lithium-ion batteries remain the dominant energy storage technology, with ML-supported Battery Management Systems significantly improving state estimation accuracy and extending service life. Hybrid Energy Storage Systems (HESSs) demonstrate strong potential for enhancing performance, particularly when paired with predictive ML-based energy flow control. Charging technologies are evolving beyond traditional wired solutions toward intelligent, ML-driven wireless and Vehicle-to-Grid (V2G) systems, enabling adaptive integration with renewable energy sources. Modern electronic components—such as SiC-based inverters—combined with embedded ML diagnostics are improving fault detection, operational safety, and system adaptability.

Across all domains, ML enables higher efficiency, predictive capabilities, and adaptive control; however, most implementations remain focused on individual subsystems rather than integrated architectures. The absence of standardized performance benchmarks limits comparability and hinders large-scale adoption.

The future trajectory of electric motorcycle development will depend on advancing integrated AI/ML architectures, deploying lightweight and energy-efficient models for embedded systems, implementing Explainable AI for transparency and trust, and combining eco-design principles with intelligent energy management. These advancements will be critical to achieving the twin objectives of high performance and environmental sustainability.

In conclusion, the convergence of hardware innovation and AI/ML-driven intelligence represents a transformative shift in electric motorcycle design. By uniting advances in motor technology, energy storage, charging systems, and electronic components under an integrated, intelligent framework, the industry can accelerate the transition toward smarter, more efficient, and more sustainable mobility solutions.

Author Contributions: Conceptualization, G.W.-J., K.P. and J.L.W.-J.; methodology, L.P. and J.L.W.-J.; software, L.P.; validation, L.P.; formal analysis, J.L.W.-J.; investigation, L.P.; resources, L.P.; data curation, L.P.; writing—original draft preparation, J.L.W.-J., G.W.-J., K.P. and L.P.; final writing—review and editing, J.L.W.-J.; visualization, L.P.; supervision, J.L.W.-J., G.W.-J. and K.P.; project administration, J.L.W.-J.; funding acquisition, J.L.W.-J. All authors have read and agreed to the published version of the manuscript.

Funding: This research received no external funding.

Data Availability Statement: The original contributions presented in this study are included in the article. Further inquiries can be directed to the corresponding author.

Conflicts of Interest: The authors declare no conflicts of interest.

References

1. Dhandapani, S.; Raja, T.; Murugan, V.; Selvaraj, J.; Rathinasamy, V. Comprehensive Review on Evolution, Progression, Design, and Exploration of Electric Bicycle. *Arch. Motoryz.* **2024**, *105*, 5–43. [CrossRef]
2. Borucka, A.; Stopka, O.; Kozłowski, E. Analysis of Electric Vehicles in the Context of the World's Largest Economies. *Arch. Motoryz.* **2024**, *106*, 65–82. [CrossRef]
3. Lewicki, W. The Case Study of the Impact of the Costs of Operational Repairs of Cars on the Development of Electromobility in Poland. *Arch. Motoryz.* **2017**, *78*, 107–116. [CrossRef]
4. Carranza, G.; Do Nascimiento, M.; Fanals, J.; Febrer, J.; Valderrama, C. Life Cycle Assessment and Economic Analysis of the Electric Motorcycle in the City of Barcelona and the Impact on Air Pollution. *Sci. Total Environ.* **2022**, *821*, 153419. [CrossRef]
5. Tuayharn, K.; Kaewtatip, P.; Ruangjirakit, K.; Limthongkul, P. ICE Motorcycle and Electric Motorcycle: Environmental and Economic Analysis. In *SAE Technical Paper, Proceedings of the 11th International Conference on Automotive Engineering, Cuernavaca, Mexico, 24–27 November 2015*; SAE International: Warrendale, PA, USA, 2015.
6. Antika, C.F.; Angrendo, J.L.; Anggatama, R.; Muljartono, J.G.; Kurniadi, F.I. Tukerin: Battery Exchange for Electric Motorcycles. In Proceedings of the 6th International Conference of Computer and Informatics Engineering (IC2IE), Lombok, Indonesia, 14–15 September 2023; pp. 157–162.
7. Montesinos-Miracle, D.; Ruiz-Bassols, T. Regenerative Braking in Electric Scooters. In Proceedings of the 19th European Conference on Power Electronics and Applications (EPE ECCE Europe), Warsaw, Poland, 11–14 September 2017.
8. Boretti, A. Comparison of Electric and Internal Combustion Engine SuperSport Bikes. *Energy Technol.* **2023**, *11*, 2300226. [CrossRef]
9. Samii, A.; Lotfi, F.; Taghirad, H.D. Optimization of Battery Life and State of the Charge in an Electric Motorcycle Braking System. In Proceedings of the 9th RSI International Conference on Robotics and Mechatronics (ICRoM), Tehran, Iran, 17–19 November 2021; pp. 203–209.
10. Ramadhan, M.R.; Asfani, D.A.; Made Yulistya Negara, I.; Nugraha, Y.U. Performance Comparison of BLDC and SRM on Electric Motorcycle. In Proceedings of the 7th International Conference on Electrical, Electronics and Information Engineering: Technological Breakthrough for Greater New Life (ICEEIE), Malang, Indonesia, 2 October 2021.
11. Christyono, Y.; Adi Soetrisno, Y.A.; Surya Pratama, A.F. Design Analysis of Brushless Direct Current Motors Made of Copper and Aluminum Conductors for Better Performance and Cost-Effectiveness. In Proceedings of the 11th International Conference on Information Technology, Computer and Electrical Engineering (ICITACEE), Semarang, Indonesia, 29–30 August 2024; pp. 82–89.
12. Kachapornkul, S.; Pupadubsin, R.; Somsiri, P.; Jitkreeyarn, P.; Tungpimolrut, K. Performance Improvement of a Switched Reluctance Motor and Drive System Designed for an Electric Motorcycle. *Energies* **2022**, *15*, 694. [CrossRef]
13. Alagmy, A.R.; El-Morsy, A.I.; Matar, O.; Elagamy, Y.; Algohary, M.; Sameh, R.; Ethman, Y.; Kaddah, S.S.; Badr, B.M. Modelling and Design of Motor Drive System for Electric Motorcycles. In Proceedings of the 24th International Middle East Power System Conference (MEPCON), Mansoura, Egypt, 19–21 December 2023.
14. Alagmy, A.R.; Sarhan, M.M.; Matar, O.; Elagamy, Y.; Khattab, M.H.; Bekhit, M.M.; Mashaly, A.; Abdelkader, A.; Kaddah, S.S.; Badr, B.M. Design and Development of Drivetrain System for Electric Motorcycles. In Proceedings of the 25th International Middle East Power System Conference (MEPCON), Cairo, Egypt, 17–19 December 2024.
15. Fernandez, E.; Coello, M. Comparative Analysis of Control Techniques in Drive Systems for Electric Motorcycle. In Proceedings of the 6th International Youth Conference on Energy (IYCE), Budapest, Hungary, 21–24 June 2017.
16. Teixeira Paula, G.; Boffino Almeida Monteiro, J.R.; Eugenio Portes Almeida, T.; Patricio Santana, M. Different Slot Configurations for Direct-Drive PM Brushless Machines. *IEEE Lat. Am. Trans.* **2015**, *13*, 634–639. [CrossRef]
17. Baumann, M.; Buchholz, M.; Dietmayer, K. Investigations on a Hybrid Energy Storage System for an All-Wheel Driven Motorcycle. In Proceedings of the EVS—International Electric Vehicle Symposium and Exhibition, Stuttgart, Germany, 9–11 October 2017.

18. Goussian, A.; LeBel, F.-A.; Trovão, J.P.; Boulon, L. Passive Hybrid Energy Storage System Based on Lithium-Ion Capacitor for an Electric Motorcycle. *J. Energy Storage* **2019**, *25*, 100884. [CrossRef]
19. Rafiezadeh, R.; Busquets-Monge, S.; Alepuz, S. Optimized Modular Design of Neutral-Point-Clamped Traction Inverters for Multiple Electric Vehicles. In Proceedings of the AEIT International Conference on Electrical and Electronic Technologies for Automotive (AEIT AUTOMOTIVE), Modena, Italy, 17–19 July 2023.
20. Hieu, L.T.; Lim, O.T. A Deep Learning Approach to Optimize the Performance and Power Demand of Electric Scooters under the Effect of Operating and Structure Parameters. *Energies* **2024**, *17*, 427. [CrossRef]
21. Setiawan, A.D.; Zahari, T.N.; Anderson, K.; Moeis, A.O.; Hidayatno, A. Examining the Effectiveness of Policies for Developing Battery Swapping Service Industry. *Energy Rep.* **2023**, *9*, 4682–4700. [CrossRef]
22. De Gaetano, D.; Golovanov, D.; Sala, G.; Galassini, A.; Degano, M.; Mahmoud, H.; Gerada, C. Advantages of a Double Three-Phase Winding Layout for a Dual Rotor e-Bike Motor Considering Third Current Harmonic Injection Technique. In Proceedings of the IEEE Transportation Electrification Conference & Expo (ITEC), Chicago, IL, USA, 23–26 June 2020; pp. 1159–1164.
23. Caliwag, A.C.; Lim, W. Hybrid VARMA and LSTM Method for Lithium-Ion Battery State-of-Charge and Output Voltage Forecasting in Electric Motorcycle Applications. *IEEE Access* **2019**, *7*, 59680–59689. [CrossRef]
24. Zhang, H.; Hua, W.; Wu, Z. Modular Spoke-Type Permanent-Magnet Machine for In-Wheel Traction Applications. *IEEE Trans. Ind. Electron.* **2018**, *65*, 7648–7659. [CrossRef]
25. Christoforidis, C.; Christakis, I.; Kotzasavva, F.; Fousekis, G.; Rimpas, D. Electric Vehicles Charging Stations and Their Influence on the Electricity Utility Grid. *Arch. Motoryz.* **2025**, *107*, 102–126. [CrossRef]
26. Małek, A.; Taccani, R. Innovative Approach to Electric Vehicle Diagnostics. *Arch. Motoryz.* **2021**, *92*, 49–67. [CrossRef]
27. Małek, A.; Taccani, R. Long-Term Test of an Electric Vehicle Charged from a Photovoltaic Carport. *Arch. Motoryz.* **2019**, *86*, 55–63. [CrossRef]
28. Arifwardana, J.F.; Rushadiawan, I.P.; Tjahjana, D.D.D.P.; Nizam, M.; Putra, M.R.A. Experimental of Heat Generation on Electric Motorcycle NMC and LiFePO4 Battery Pack. In Proceedings of the 7th International Conference on Electric Vehicular Technology (ICEVT), Bali, Indonesia, 14–16 September 2022; pp. 173–176.
29. Rushadiawan, I.P.; Arifwardana, J.F.; Tjahjana, D.D.D.P.; Nizam, M.; Putra, M.R.A. Analysis of Li-Ion Battery Pack Performance Air Cooling Battery Compartment on a Swappable Battery of Electric Motorcycle. In Proceedings of the 7th International Conference on Electric Vehicular Technology (ICEVT), Bali, Indonesia, 14–16 September 2022; pp. 185–188.
30. Henderson, T. Sealed Lead Acid Battery and Supercapacitor Power Configurations for Electric Drag Racing. In Proceedings of the IEEE Green Technologies Conference (GreenTech), Oklahoma City, OK, USA, 1–3 April 2020; pp. 16–20.
31. Abumi, T.; Murakami, T. Posture Stabilization of Two-Wheel Drive Electric Motorcycle by Slip Ratio Control Considering Camber Angle. In Proceedings of the IEEE International Conference on Mechatronics (ICM), Nagoya, Japan, 6–8 March 2015; pp. 353–358.
32. Putra, M.R.A.; Tjahjana, D.D.D.P.; Nizam, M.; Arifin, Z. Performance Analysis in Eddy Current Brake at Different Temperatures Using the Finite Element Method. In Proceedings of the 7th International Conference on Electric Vehicular Technology (ICEVT), Bali, Indonesia, 14–16 September 2022; pp. 169–172.
33. Kaneko, K.; Omori, H.; Morizane, T.; Kimura, N.; Nakaoka, M.; Mekhilef, S. A Study of Balancer-Less EDLC Stack in a New Power Electric Motor-Driven Capacitor Scooter System. In Proceedings of the Asian Conference on Energy, Power and Transportation Electrification (ACEPT), Singapore, 24–26 October 2017; pp. 1–6.
34. Rifa'I, A.F.; Rudiansyah, H.; Milanto, R. Design and Implementation of Auto-Limit Riding Speed System for Electric Motorcycles Based on Battery Level with Fuzzy PID. In Proceedings of the International Conference on Electric Vehicular Technology (ICEVT), Bali, Indonesia, 14–16 September 2022; pp. 27–33.
35. Stańczyk, T.L.; Hyb, L. Technological and Organisational Challenges for E-Mobility. *Arch. Motoryz.* **2019**, *84*, 57–70. [CrossRef]
36. Ananwattanaporn, S.; Ngaopitakkul, A.; Jettanasen, C. Power Quality and Break-Even Points in the Use of Electric Motorcycles in the Case of the Thailand Residential Building. *Sustainability* **2024**, *16*, 212. [CrossRef]
37. Wong, H.-W.; Ieong, C.-F.; Lam, C.-S. Optimizing Inductive Power Transfer Circular Pad Coils for Electric Vehicles Using Multi-Objective Particle Swarm Optimization. In Proceedings of the IECON 2023—49th Annual Conference of the IEEE Industrial Electronics, Society, Singapore, 16–19 September 2023.
38. Małek, A.; Marciniak, A.; Bartnik, G. The Selection of an Electric Vehicle for the Existing Photovoltaic System—Case Study in Polish Climatic Conditions. *Arch. Motoryz.* **2024**, *103*, 38–56. [CrossRef]
39. Niyonsaba, J.D.; De Dieu Samvura, J.; Bikorimana, J.M.V. Integration of Electric Motorcycle Charging Station Based on PV System in Kigali City. In Proceedings of the IEEE Southern Power Electronics Conference (SPEC), Kigali, Rwanda, 6–9 December 2021.
40. Huu, D.N.; Ngoc, V.N. A Research on the Trend of Transport Electrification in Vietnam and the Feasibility of PV-Integrated Charging Station for Electric Two-Wheelers at Electric Power University. In Proceedings of the International Conference on Power, Energy and Electrical Engineering (CPEEE), Shiga, Japan, 26–28 February 2021; pp. 255–260.

41. Wayan Adiyasa, I.; Rasid, M.A.H.B.; Wayan Warsita, I.; Arifin, Z.; Dwipayana, A.D.; Suteja, R.P. Identification of Computation of Solar and Wind Energy Potential for Off-Grid Electric Motorcycle Battery Charging Stations. In Proceedings of the International Conference on Smart-Green Technology in Electrical and Information Systems (ICSGTEIS), Badung, Bali, Indonesia, 2–4 November 2023; pp. 208–213.
42. Clairand, J.-M.; Rodríguez-García, J.; Álvarez-Bel, C. Electric Vehicle Charging Strategy for Isolated Systems with High Penetration of Renewable Generation. *Energies* **2018**, *11*, 3188. [CrossRef]
43. Changoluisa, L.F.; Zapata, M. Design and Implementation of Wind-Powered Charging System to Improve Electric Motorcycle Autonomy. In *Computational Science and Its Applications–ICCSA 2023, Proceedings of the International Conference on Computational Science and Its Applications, Athens, Greece, 3–6 July 2023*; Gervasi, O., Murgante, B., Taniar, D., Apduhan, B.O., Braga, A.C., Garau, C., Stratigea, A., Eds.; Lecture Notes in Computer Science; Springer: Cham, Switzerland, 2023; Volume 13956, pp. 55–66.
44. Villamizar, D.P.; Prada, S.R. Computer Aided Methodology for the Optimization of an Electric Motorcycle Suspension. In Proceedings of the ASME International Mechanical Engineering Congress and Exposition, Salt Lake City, UT, USA, 11–14 November 2019; Volume 4.
45. Canilang, H.M.O.; Caliwag, A.C.; Lim, W. Design of Modular BMS and Real-Time Practical Implementation for Electric Motorcycle Application. *IEEE Trans. Circuits Syst. II Express Briefs* **2022**, *69*, 519–523. [CrossRef]
46. Kastner, M.; Friedl, H.; Hubmann, C.; Falk, P.; Graf, B. Development of Smart Drive 48V E-Motorcycle. In Proceedings of the 26th Small Powertrains and Energy Systems Technology Conference, Himeji, Japan, 31 October–3 November 2022.
47. Luzardo, E.J.; Galluzzi, R.; Escobar, G.; Juarez, J. Comparative Study of Interior Permanent-Magnet Synchronous Motor Topologies for Motorcycle Traction Application. In Proceedings of the International Symposium Electromobility (ISEM), Monterrey, Mexico, 26–28 October 2023.
48. Farzaneh, A.; Farjah, E. Analysis of Road Curvature's Effects on Electric Motorcycle Energy Consumption. *Energy* **2018**, *151*, 160–166. [CrossRef]
49. Kirca, M.C.; McGordon, A.; Dinh, T.Q. Rapid Decision-Making Tool for Electric Powertrain Sizing for Motorcycles during New Product Development. *Energies* **2024**, *17*, 330. [CrossRef]
50. Frej, D.P.; Ludwinek, K. Analysis of Road Accidents in 2002–2019 on the Example of Poland. *Arch. Motoryz.* **2020**, *89*, 5–18. [CrossRef]
51. Shu, Z.; Chen, W.; Fengfa, Y.; Yijie, W.; Alonso, J.M. A 500-kHz ZVS Class-E Type DC-DC Converter with Two Anti-Series Mosfets Topology. *IEEE Trans. Power Electron.* **2023**, *38*, 10810–10820. [CrossRef]
52. Fernandez, E.; Coello, M.; Rockwood, R. Optimization of Weight-Volume in Impedance Network SiC Converter for Electric Motorcycle. In Proceedings of the IEEE Fourth Ecuador Technical Chapters Meeting (ETCM), Guayaquil, Ecuador, 11–15 November 2019.
53. Khoa, N.X.; Kien, N.T.; Vinh, N.T.; Hung, C.D. Study the Effect of Transmission Ratios on the Electric Motorbike's Performance through a Simulation Model. In Proceedings of the International Conference on Green Technology and Sustainable Development (GTSD), Nha Trang City, Vietnam, 29–30 July 2022; pp. 47–51.
54. Blissett, J.; Degano, M.; Gimeno-Fabra, M.; Wheeler, P. Design of Electrical System for Racing Electric Motorcycles. In Proceedings of the International Conference on Electrical Systems for Aircraft, Railway, Ship Propulsion and Road Vehicles & International Transportation Electrification Conference (ESARS-ITEC), Toulouse, France, 2–4 November 2016.
55. Sakai, M.; Takeshita, T. Energy Management System of Electric Motorcycles for Power Boost. In Proceedings of the IEEE International Conference Renewable Energy Research and Applications (ICRERA), Oshawa, ON, Canada, 29 August–1 September 2023; pp. 140–145.
56. Setiawan, A.D. Modelling Battery Swapping Industry Development Strategy to Support Net Zero Emissions Transition. *S. Afr. J. Ind. Eng.* **2024**, *35*, 1–12. [CrossRef]
57. Conto, C.; Bianchi, N. Design of Electric Motor for E-Bike Application. In Proceedings of the IEEE International Electric Machines & Drives Conference (IEMDC), San Francisco, CA, USA, 15–18 May 2023.
58. Dora, R.; Mulla, G.B. Materials for E-Bike and End to End Design Aspects. *Mater. Today* **2023**, *92*, 1374–1380. [CrossRef]
59. Sakai, M.; Takeshita, T. Power Control Using Sub-Battery for Electric Motorcycle. In Proceedings of the International Conference on Electrical Machines Systems (ICEMS), Fukuoka, Japan, 26–29 November 2024; pp. 3757–3762.
60. Sakai, M.; Takeshita, T. SOC-Based Mode Switching in Hybrid Battery Systems for Electric Motorcycles. In Proceedings of the International Conference on Renewable Energy Research and Applications (ICRERA), Nagasaki, Japan, 9–13 November 2024; pp. 1232–1237.
61. Podosek, K.; Šarić, Ž.; Zuska, A. Test Bench for the Assessment of Vibrations Occurring in Motorcycles. *Arch. Motoryz.* **2022**, *95*, 65–78. [CrossRef]

62. van Eck, N.J.; Waltman, L. Software Survey: VOSviewer, a Computer Program for Bibliometric Mapping. *Scientometrics* **2010**, *84*, 523–538. [CrossRef]
63. Morandin, M.; Ferrari, M.; Bolognani, S. Power-Train Design and Performance of a Hybrid Motorcycle Prototype. *IEEE Trans. Ind. Appl.* **2015**, *51*, 2216–2226. [CrossRef]
64. Dal Bianco, N.; Lot, R.; Matthys, K. Lap Time Simulation and Design Optimisation of a Brushed DC Electric Motorcycle for the Isle of Man TT Zero Challenge. *Veh. Syst. Dyn.* **2018**, *56*, 27–54. [CrossRef]
65. Khanna, Y.; D'Arpino, M.; Ramesh, P. Design Methodology for Energy Storage System in Motorsports Using Statistical Analysis of Mission Profile. In Proceedings of the WCX SAE World Congress Experience, Detroit, MI, USA, 5–7 April 2022.
66. Adiyasa, I.W.; Wijaya, F.D.; Firmansyah, E. Analysis of Fuel and Energy Consumption Using the Torque Assist on Single Cylinder ICE. In Proceedings of the International Conference on Information Technology and Electrical Engineering (ICITEE), Bali, Indonesia, 23–25 October 2024; pp. 422–427.
67. Suryoatmojo, H.; Pratomo, D.R.; Ridwan, M.; Riawan, D.C.; Setijadi, E.; Mardiyanto, R. Robust Speed Control of Brushless Dc Motor Based on Adaptive Neuro Fuzzy Inference System for Electric Motorcycle Application. *Int. J. Innov. Comput. Inf. Control* **2020**, *16*, 415–428. [CrossRef]
68. Reckziegel, S.; Guerrero, A.; Arzamendia, M. Analysis and Design of a Functional Electric Motorcycle Prototype. In Proceedings of the IEEE Chilean Conference on Electrical, Electronics Engineering, Information and Communication Technologies (CHILECON), Valparaíso, Chile, 6–9 December 2021.
69. Maghfiroh, H.; Hermanu, C.; Ibrahim, M.H.; Nizam, M. Low Cost Charging Station for Electric Vehicle: Design and Prototyping. In Proceedings of the International Conference on Electric Vehicular Technology (ICEVT), Bali, Indonesia, 18–21 November 2019; pp. 20–24.
70. LeBel, F.A.; Pelletier, L.; Messier, P.; Trovão, J.P. Battery Pack Sizing Method—Case Study of an Electric Motorcycle. In Proceedings of the IEEE Vehicle Power and Propulsion Conference (VPPC), Chicago, IL, USA, 27–30 August 2018.
71. Sadiq, M.M.; Abro, G.E.M.; Yazsid, A.Z.S.M.; Zulkifli, S.A.M. Development of Range Enhancement Device for Personal Electric Mobility. In Proceedings of the International Conference on Electric Vehicular Technology (ICEVT), Bali, Indonesia, 14–16 September 2022; pp. 144–152.
72. Bui, T.M.N.; Subari, M.A.B.; Dinh, T.Q. Real-Time Prediction of Remaining Driving Range for Electric Motorcycle Applications. *IEEE Trans. Intell. Transp. Syst.* **2024**, *25*, 18171–18184. [CrossRef]
73. Faraji-Niri, M.; Dinh, T.Q.; Marco, J. Riding Pattern Identification by Machine Learning for Electric Motorcycles. In Proceedings of the International Conference on Mechatronics Technology (ICMT), Singapore, 18–22 December 2021.
74. Brodsky, P.; Fan, G.; Canova, M. Battery Pack Design and Optimization for the OSU Buckeye Current 2016 Electric Racing Motorcycle. In Proceedings of the International Conference on Electrical Systems for Aircraft, Railway, Ship Propulsion and Road Vehicles & International Transportation Electrification Conference (ESARS-ITEC), Toulouse, France, 2–4 November 2016.
75. Istiqomah, S.; Sutopo, W.; Hisjam, M.; Wicaksono, H. Optimizing Electric Motorcycle-Charging Station Locations for Easy Accessibility and Public Benefit: A Case Study in Surakarta. *World Electr. Veh. J.* **2022**, *13*, 232. [CrossRef]
76. Benecki, K.; Prins, R. Design of a Laboratory Electric Vehicle Powertrain System. In Proceedings of the Systems and Information Engineering Design Symposium (SIEDS), Charlottesville, VA, USA, 28 April 2017; pp. 44–49.
77. Lot, R.; Del Rosso, V.; Boria, S.; Andreucci, A.; Nardini, A.; Ranalli, A. A Sensorless Traction Strategy for All-Wheel Drive Electric Motorcycles. *Veh. Syst. Dyn.* **2022**, *60*, 3668–3693. [CrossRef]
78. Rinaldi, S.; Pasetti, M.; Musatti, A. Retrofitting Existing Charging Stations for Light Mobility: Enhancing Infrastructure to Support Sustainable Transportation. In Proceedings of the International Conference on Electrical, Computer and Energy Technologies (ICECET), Cape Town, South Africa, 16–17 November 2023.
79. Guerra, E. Electric Vehicles, Air Pollution, and the Motorcycle City: A Stated Preference Survey of Consumers' Willingness to Adopt Electric Motorcycles in Solo, Indonesia. *Transp. Res. Part Transp. Environ.* **2019**, *68*, 52–64. [CrossRef]
80. Wu, C.-H.; Xu, Y.-X. The Optimal Control of Fuel Consumption for a Heavy-Duty Motorcycle with Three Power Sources Using Hardware-in-the-Loop Simulation. *Energies* **2019**, *13*, 22. [CrossRef]
81. Abu Hanifah, R.; Toha, S.F.; Mohamad Hanif, N.H.H.; Kamisan, N.A. Electric Motorcycle Modeling for Speed Tracking and Range Travelled Estimation. *IEEE Access* **2019**, *7*, 26821–26829. [CrossRef]
82. Amilia, N.; Palinrungi, Z.; Vanany, I.; Arief, M. Designing an Optimized Electric Vehicle Charging Station Infrastructure for Urban Area: A Case Study from Indonesia. In Proceedings of the IEEE 25th International Conference on Intelligent Transportation Systems (ITSC), Macau, China, 8–12 October 2022; pp. 2812–2817.
83. Matsuda, Y.; Murase, T.; Kawai, D. The Feasibility Study of a Design Concept of Electric Motorcycle. In Proceedings of the JSAE/SAE 2015 International Powertrains, Fuels & Lubricants Meeting, Kyoto, Japan, 1–4 September 2015.

84. de Assis Brasil Weber, N.; da Rocha, B.P.; Smith Schneider, P.; Daemme, L.C.; de Arruda Penteado Neto, R. Energy and Emission Impacts of Liquid Fueled Engines Compared to Electric Motors for Small Size Motorcycles Based on the Brazilian Scenario. *Energy* **2019**, *168*, 70–79. [CrossRef]
85. Zahrina, N.; Hidayatno, A.; Setiawan, A.D. Model Conceptualization of Battery Swapping Industry Development Using System Dynamics. In Proceedings of the 3rd Asia Pacific Conference on Research in Industrial and Systems Engineering (APCORISE), Depok, Indonesia, 16 June 2020; pp. 129–134.
86. Hicham, C.; Nasri, A.; Harrouz, A.; Kayisli, K. A Novel Control Approach of Multi Motor Electric Scooter Drive. In Proceedings of the International Conference on Renewable Energy Research and Applications (ICRERA), Istanbul, Turkey, 26–29 September 2021; pp. 362–369.
87. Sulthan, S.M.; Mohammed Mansoor, O.; Laila, D.S.; Sri Revathi, B.; Aziz, A.A.B.A. Modeling, Design, and Implementation of Electric Tri-Wheeler. In Proceedings of the Innovations in Power and Advanced Computing Technologies (i-PACT), Kuala Lumpur, Malaysia, 8–10 December 2023.
88. Kawai, D.; Matsuda, Y.; Murase, T. A Study of Function Control in the Electric Motorcycle. In Proceedings of the JSAE/SAE 2015 Small Engine Technologies Conference & Exhibition, Osaka, Japan, 17–19 November 2015.
89. Sakai, M.; Takeshita, T. Hybrid Battery System of Electric Motorcycles for Power Boost during High-Speed Driving. In Proceedings of the Energy Conversion Congress & Expo Europe (ECCE), Darmstadt, Germany, 2–6 September 2024.
90. Kammuang-lue, N.; Pattana, S.; Wiratkasem, K. Draft of the MEPS and HEPS for Two-Wheel Electric Motorcycles in Thailand. *Energy Rep.* **2020**, *6*, 851–855. [CrossRef]
91. Sandesh, B.B.; Jogi, A.; Pitchaimani, J.; Gangadharan, K.V. Design and Optimization of an External-Rotor Switched Reluctance Motor for an Electric Scooter. *Mater. Today Proc.* **2023**, *in press*. [CrossRef]
92. Pelletier, L.; LeBel, F.-A.; Rubio, R.G.; Roux, M.-A.; Trovão, J.P. Design of a High Performance Battery Pack as a Constraint Satisfaction Problem. In Proceedings of the IEEE Vehicle Power Propulsion Conference (VPPC), Chicago, IL, USA, 27–30 August 2018.
93. Kerdlap, P.; Gheewala, S.H. Electric Motorcycles in Thailand: A Life Cycle Perspective. *J. Ind. Ecol.* **2016**, *20*, 1399–1411. [CrossRef]
94. Zhou, S.; Dinh, T.Q.; Zhu, T.; Kirca, M.C.; McGordon, A. Impact of Riding Posture and Regenerative Braking on Electric Motorcycle Energy Consumption. In Proceedings of the IEEE Vehicle Power Propulsion Conference (VPPC), Milan, Italy, 24–27 October 2023.
95. Elbeshbeshy, A.M.; Matar, O.; Shawky, A.; Alaaeldin, A.; Faiod, H.S.; Gomaa, M.A.; Ahmed, H.A.; Shaheen, A.G.; Kaddah, S.S.; Badr, B.M. Design and Development of a Low-Cost Battery System for Electric Motorcycles. In Proceedings of the International Middle East Power System Conference (MEPCON), Mansoura, Egypt, 19–21 December 2023.
96. Ahmad, M.I.; Dorlikar, P. Chassis Design with Integrated Battery Pack Space for Electric Motorcycle. In *Advances in Energy Technology*; Bansal, R.C., Agarwal, A., Jadoun, V.K., Eds.; Lecture Notes in Electrical Engineering; Springer: Singapore, 2022; Volume 766, pp. 339–349.
97. Chen, S.-Y.; Lin, F.-J.; Pu, T.-A. Hierarchical Power Management System for a Fuel Cell/Battery Hybrid Electric Scooter. *IEEE Trans. Transp. Electrif.* **2024**, *10*, 4583–4593. [CrossRef]
98. Ngoc, P.T.K. Policy Measure to Promote Electric Mobility in Emerging Cities. In *CIGOS 2021, Emerging Technologies and Application for Green Infratructure*; Ha-Minh, C., Tang, A.M., Bui, T.Q., Vu, X.H., Huynh, D.V.K., Eds.; Lecture Notes in Civil Engineering; Springer: Singapore, 2021; Volume 203, pp. 1683–1691.
99. Stincescu, T.; Zhao, R.; Ballantyne, E.E.F.; Stone, D.A.; Foster, M.P. Matlab-Based High-Performance Electric Motorbike Energy Model, Utilising Video Data. In Proceedings of the 16th International Conference on Ecological Vehicles and Renewable Energies (EVER), Monte Carlo, Monaco, 5–7 May 2021.
100. Jagadan, G.; Sourav, U.K.; Chathayil, V.; Kumar, R.S.; Manjunath, V. Design of LLC Resonant Converter for High Efficiency EV Charging. In Proceedings of the IEEE Global Conference on Computing, Power and Communication Technologies (GlobConPT), New Delhi, India, 23–25 September 2022.
101. Carvalho, J.; Sousa, T.J.C.; Pedrosa, D. Traction and Charging Systems for an Electric Motorcycle. In *Sustainable Energy for Smart Cities, Proceedings of the International Conference on Sustainable Energy for Smart Cities, Online, 24–26 November 2021*; Afonso, J.L., Monteiro, V., Pinto, J.G., Eds.; Lecture Notes of the Institute for Computer Sciences, Social Informatics and Telecommunications Engineering; Springer: Cham, Switzerland, 2022; Volume 425, pp. 157–172.
102. Wonia, A.; Wonia, M.; Piotrowski, R. Control of a Nonlinear and Linearized Model of Self-Balancing Electric Motorcycle. In *Advanced, Contemporary Control*; Bartoszewicz, A., Kabzinski, J., Kacprzyk, J., Eds.; Springer: Cham, Switzerland, 2020; Volume 1196, pp. 360–371.

103. Firmansyah, A.I.; Supriatna, N.K.; Gunawan, Y.; Setiadanu, G.T. Performance Testing of Electric Motorcycle Conversion. In Proceedings of the 7th International Conference on Electric Vehicular Technology (ICEVT), Bali, Indonesia, 14–16 September 2022; pp. 165–168.
104. Jusoh, L.I.; Sulaiman, E. Analysis and Performance of 4S-8P Permanent Magnet Flux Switching Motors (PMFSM) for Electric Bicycle Applications. In Proceedings of the 5th IET International Conference on Clean Energy and Technology (CEAT2018), Kuala Lumpur, Malaysia, 5–6 September 2018.
105. Prianjani, D.; Sutopo, W.; Hisjam, M.; Pujiyanto, E. Sustainable Supply Chain Planning for Swap Battery System: Case Study Electric Motorcycle Applications in Indonesia. *IOP Conf. Ser. Mater. Sci. Eng.* **2019**, *495*, 012081. [CrossRef]
106. Nguyen, V.-T.; Hwang, P.; Huynh, T. Computational Analysis on Hybrid Electric Motorcycle with Front Wheel Electric Motor Using Lithium Ion Battery. In Proceedings of the International Conference on System Science and Engineering (ICSSE), Ho Chi Minh City, Vietnam, 21–23 July 2017; pp. 355–359.
107. Farzaneh, A.; Farjah, E. A Novel Smart Energy Management System in Pure Electric Motorcycle Using COA. *IEEE Trans. Intell. Veh.* **2019**, *4*, 600–608. [CrossRef]
108. Albana, M.H.; Guntur, H.L.; Putra, A.B.K. The Effect of Grooves on the In-Wheel Motor Cover of an Electric Scooter to Increase the Heat Transfer Process. In Proceedings of the International Conference on Computer Science, Information Technology and Engineering (ICCoSITE), Jakarta, Indonesia, 16 February 2023; pp. 84–89.
109. Ruensumruay, S.; Pattaraprakorn, W.; Chutiprapat, V.; Bhasaputra, P. The Study on the Effect of Electric Motorcycle to Energy Consumption in Thailand. In Proceedings of the 13th International Conference on Electrical Engineering/Electronics, Computer, Telecommunications and Information Technology (ECTI-CON), Chiang Mai, Thailand, 28 June–1 July 2016.
110. Yuniarto, M.N.; Wiratno, S.E.; Nugraha, Y.U.; Sidharta, I.; Nasruddin, A. Modeling, Simulation, and Validation of An Electric Scooter Energy Consumption Model: A Case Study of Indonesian Electric Scooter. *IEEE Access* **2022**, *10*, 48510–48522. [CrossRef]
111. Abumi, T.; Murakami, T. Posture Stabilization Control of Two-Wheel Drive Electric Motorcycle with Assistant Pendulum for Rider Motion. In Proceedings of the 5th Asia International Symposium on Mechatronics (AISM 2015), Guilin, China, 7–10 October 2015.
112. Lawrence, M.D.; Siavoshani, S. Step by Step Conversion of ICE Motorcycle to a BEV Configuration. In Proceedings of the WCX SAE World Congress Experience, Online, 16–18 June 2020.
113. Del Rosso, V.; Andreucci, A.; Boria, S.; Corradini, M.L.; Giambo, R.; Ranalli, A. Self-Balancing Two-Wheel Drive Electric Motorcycle Modelling and Control: Preliminary Results. In Proceedings of the 5th International Conference on Control, Decision and Information Technologies (CoDIT), Thessaloniki, Greece, 10–13 April 2018; pp. 358–363.
114. Lee, C.-Y.; Chen, C.-H.; Lee, T.-J.; Cheong, J.-S.; Liu, Y.-C.; Chen, Y.-C. Flexible Five-in-One Microsensor for Real-Time Wireless Microscopic Diagnosis inside Electric Motorcycle Fuel Cell Stack Range Extender. *Micromachines* **2021**, *12*, 103. [CrossRef]
115. Soomro, H.A.; Md Khir, M.H.B.; Azrin, B.M.; Zulkifli, S.; Abualnaeem, M.M. Impact of Switching Frequency on Power Loss in GaN-Based Motor Drive for Electric Motorcycle and Comparative Analysis with Si-MOSFET. In Proceedings of the IEEE Symposium on Industrial Electronics & Applications (ISIEA), Kuala Lumpur, Malaysia, 6–7 July 2024.
116. Andrada, P. Comparison between a Surface Permanent Magnet Synchronous Motor and a Segmented Stator Switched Reluctance Motor with Aluminum Windings for Light Electric Traction. *Renew. Energy Power Qual. J.* **2024**, *22*, 1–5. [CrossRef]
117. Kawashima, K.; Omori, H.; Kimura, N.; Morizane, T. A New Ultra-Capacitor Driven Dynamic WPT Scooter System. In Proceedings of the 8th International Conference on Renewable Energy Research and Applications (ICRERA), Brasov, Romania, 3–6 November 2019; pp. 767–772.
118. Fahma, F.; Sutopo, W.; Pujiyanto, E.; Nizam, M. Technological-Based Interoperability for Electric Motorcycle Swappable Battery: State of the Art and Future Research Agenda. In *Advances in Manufacturing Processes and Smart Manufactuing Systems, Proceedings of the Global Congress on manufacturing and Management, Kuching, Malaysia, 4–7 December 2023*; Kurniawan, D., Nor, F.M., Eds.; Lecture Notes in Networks and Systems; Springer: Cham, Switzerland, 2024; Volume 1214, pp. 194–210.
119. Idamsyah, A.; Setiawan, A.D. Developing a Sustainable Green Battery Swapping Industry Model: A Conceptual Framework. In Proceedings of the 4th Asia Pacific Conference on Research in Industrial and Systems Engineering: Building Business Resilience to Face the Challenge in Pandemic Era (APCORISE), Depok, Indonesia, 25 May 2021; pp. 499–505.
120. Park, Y.; Zu, S.; Xie, C.; Lee, H.; Cheong, T.; Lu, Q.-C.; Xu, M. Smart Battery Swapping Control for an Electric Motorcycle Fleet with Peak Time Based on Deep Reinforcement Learning. *IEEE Trans. Intell. Transp. Syst.* **2024**, *25*, 20175–20189. [CrossRef]
121. Wilk-Jakubowski, J.L.; Pawlik, L.; Frej, D.; Wilk-Jakubowski, G. Data-Driven Computational Methods in Fuel Combustion: A Review of Applications. *Appl. Sci.* **2025**, *15*, 7204. [CrossRef]
122. Porowski, R.; Gieras, M. *Laboratorium Spalania*; Oficyna Wydawnicza Politechniki Warszawskiej: Warsaw, Poland, 2018; ISBN 978-83-7814-706-0.

123. Wilk-Jakubowski, J.L.; Yılmaz-Atay, H. A Review of Environmentally Friendly Approaches in Fire Extinguishing: From Chemical Sciences to Innovations in Electrical Engineering. *Polymers* **2022**, *14*, 1224. [CrossRef]
124. Wilk-Jakubowski, J. Acoustic Firefighting Method on the Basis of European Research: A Review. *Akustika* **2023**, *46*, 31–45. [CrossRef]
125. Shevchenko, R.I.; Strelets, V.M.; Loboichenko, V.M.; Pruskyi, A.V.; Myroshnyk, O.N.; Kamyshentsev, G.V. Review of Up-to-Date Approaches for Extinguishing Oil and Petroleum Products. *SOCAR Proc.* **2021**, 169–174. [CrossRef]
126. Loboichenko, V.; Wilk-Jakubowski, G.; Wilk-Jakubowski, J.L.; Ciosmak, J. Application of Low-Frequency Acoustic Waves to Extinguish Flames on the Basis of Selected Experimental Attempts. *Appl. Sci.* **2024**, *14*, 8872. [CrossRef]
127. Vovchuk, T.; Wilk-Jakubowski, J.; Telelim, V.; Loboichenko, V.; Shevchenko, R.; Shevchenko, O.; Tregub, N. Investigation of the Use of the Acoustic Effect in Extinguishing Fires of Oil and Petroleum Products. *SOCAR Proc.* **2021**, 24–31. [CrossRef]
128. Loboichenko, V.; Wilk-Jakubowski, J.; Wilk-Jakubowski, G.; Harabin, R.; Shevchenko, R.; Strelets, V.; Levterov, A.; Soshinskiy, A.; Tregub, N.; Antoshkin, O. The Use of Acoustic Effects for the Prevention and Elimination of Fires as an Element of Modern Environmental Technologies. *Environ. Clim. Technol.* **2022**, *26*, 319–330. [CrossRef]
129. Loboichenko, V.; Wilk-Jakubowski, J.L.; Levterov, A.; Wilk-Jakubowski, G.; Statyvka, Y.; Shevchenko, O. Using the Burning of Polymer Compounds to Determine the Applicability of the Acoustic Method in Fire Extinguishing. *Polymers* **2024**, *16*, 3413. [CrossRef]
130. Wilk-Jakubowski, J.; Wilk-Jakubowski, G.; Loboichenko, V. Experimental Attempts of Using Modulated and Unmodulated Waves in Low-Frequency Acoustic Wave Flame Extinguishing Technology: A Review of Selected Cases. *Stroj. Vestn. J. Mech. Eng.* **2024**, *70*, 270–281. [CrossRef]
131. Wilk-Jakubowski, J.L.; Loboichenko, V.; Divizinyuk, M.; Wilk-Jakubowski, G.; Shevchenko, R.; Ivanov, S.; Strelets, V. Acoustic Waves and Their Application in Modern Fire Detection Using Artificial Vision Systems: A Review. *Sensors* **2025**, *25*, 935. [CrossRef]

Disclaimer/Publisher's Note: The statements, opinions and data contained in all publications are solely those of the individual author(s) and contributor(s) and not of MDPI and/or the editor(s). MDPI and/or the editor(s) disclaim responsibility for any injury to people or property resulting from any ideas, methods, instructions or products referred to in the content.

energies

MDPI

Review

Biomass for Residential Heating: A Review of Technologies, Applications, and Sustainability Aspects

Jakub Katerla and Krzysztof Sornek *

Department of Sustainable Energy Development, Faculty of Energy and Fuels, AGH University of Krakow, al. A. Mickiewicza 30, 30-059 Krakow, Poland; katerla@agh.edu.pl
* Correspondence: ksornek@agh.edu.pl

Abstract

Biomass has long been a major source of energy for residential heating and, in recent decades, has regained attention as a renewable alternative to fossil fuels. This review explores the current state and prospects of domestic biomass-based heating technologies, including biomass-fired boilers, local space heaters, and hybrid systems that integrate biomass with complementary renewable energy sources to deliver heat, electricity, and cooling. The review was conducted to identify key trends, performance data, and innovations in conversion technologies, fuel types, and efficiency enhancement strategies. The analysis highlights that biomass is increasingly recognized as a viable energy carrier for energy-efficient, passive, and nearly zero-energy buildings, particularly in cold climates where heating demand remains high. The analysis of the available studies shows that modern biomass-fired systems can achieve high energy performance while reducing environmental impact through advanced combustion control, optimized heat recovery, and integration with low-temperature heating networks. Overall, the findings demonstrate that biomass-based technologies, when designed and sourced efficiently and sustainably, can play a significant role in decarbonizing the residential heating sector and advancing nearly zero-energy building concepts.

Keywords: biofuels; biomass; biomass-appliances; pellet boiler; wood-fired boiler; local space heaters; micro-scale cogeneration; CHP; nearly zero energy buildings; NZEBs

1. Introduction

The inhabitants of Earth are facing climate change, which affects them through rising average global temperatures and more frequent extreme weather events. One of the main reasons responsible for the situation is the emission of greenhouse gases and other pollutants into the atmosphere. The European Union (EU) bodies decided to react and established challenging goals for the first half of the 21st century. The target for 2030 was to reduce net greenhouse gas emissions by at least 55% by 2030 compared to 1990 levels [1]. The European Commission proposed an amendment to the EU Climate Law, setting a new 2040 goal: a 90% reduction in net greenhouse gas emissions relative to 1990 levels. The ultimate goal is to achieve climate neutrality by 2050. Such action will lead not only to a less polluted atmosphere and reduced negative climate effects, but also to the diversification of heating systems for citizens and their independence from fossil fuel supplies. Apart from emission reduction, the objectives of the EU Climate Law are to monitor progress on the actions taken and take further action if needed, provide predictability for investors and other

economic actors, and ensure that the transition to climate neutrality is irreversible [1]. The assumptions and motives behind the EU legislation are clear; however, the evolving nature of the restrictions and the pace of their implementation can be particularly challenging for end-users and manufacturers of heating systems. In EU countries, the residential sector accounted for 26.2% of final energy consumption [2]. The majority of household energy use was attributed to space heating (62.5%) and domestic hot water preparation (15.1%). Natural gas and electricity were the dominant energy sources, accounting for 29.5% and 25.9% of residential demand, respectively. Renewable energy sources accounted for 23.5%, petroleum products for 10.3%, and derived heat for 8.5%. Solid fossil fuels made up the smallest share, at just 2.2% of the sector's energy use (see Figure 1).

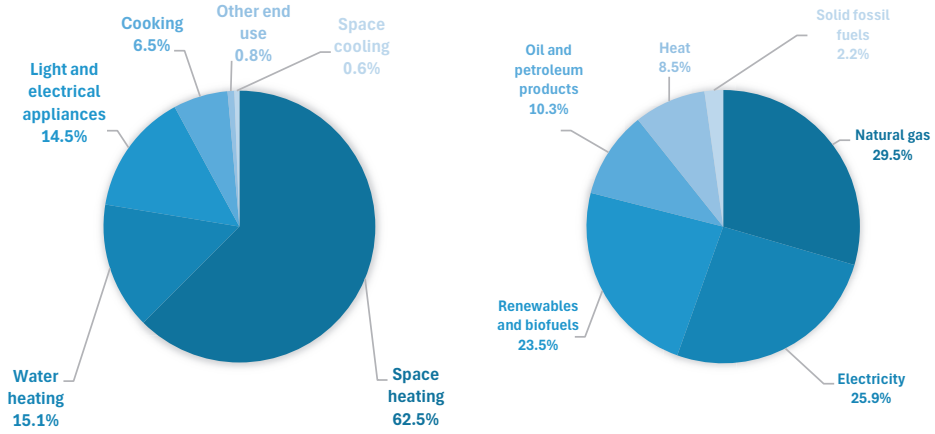


Figure 1. Final energy consumption in the residential sector by usage (**a**) and fuel (**b**) in 2023 (adopted from [2]).

When adapting to new regulations and reducing fossil fuel use, the only way forward is to implement systems powered by renewable energy sources (RES), including biomass, solar, wind, geothermal, and combined systems. Since biomass is considered a zero-carbon dioxide-emissions fuel option, it plays a key role in the energy sector's decarbonization. In the EU, almost a quarter of the final energy consumption in the residential sector in 2023 came from renewables and biofuels [2]. In less developed countries, the importance of biomass is even greater. According to the World Health Organization (WHO), over three billion people in developing countries use solid biomass for cooking and heating [3]. In 2020, over 11 million households in the U.S. (almost 9%) used wood as a fuel, mostly for heating [4].

The term "biomass" is broad and encompasses a wide range of fuels. Biomass is produced by plants and animals as organic matter. Vassilev et al. [5] divided biomass into six main groups:

- Wood and woody biomass;
- Herbaceous and agricultural biomass;
- Aquatic biomass;
- Animal and human biomass wastes;
- Contaminated biomass and industrial biomass wastes (semi-biomass);
- Biomass mixtures.

The primary biomass sources include agricultural and forestry residues, animal residues, sewage, algae, and aquatic crops [6]. Among the biomass fuels used in residential applications, the most common are wood logs, pellets (and briquettes), wood chips,

straw, husks, and shells, as shown in Figure 2. The decisive factor in choosing fuel is price and availability, as well as ease of storage and preparation.



Figure 2. Typical biomass fuels used in residential applications: (**a**) wood logs, (**b**) pellets, (**c**) wood chips, (**d**) straw, (**e**) shells, and (**f**) husks. Source: Author's own elaboration, created in Canva (based on materials provided under the Canva License Agreement).

Biomass can be converted into energy, fuels, and chemicals through several thermochemical processes, notably combustion, pyrolysis, and gasification (see Figure 3). Combustion involves the complete oxidation of biomass in the presence of excess oxygen, producing heat, carbon dioxide, and water, making it an ideal process for direct energy generation. In contrast, pyrolysis is the thermal decomposition of biomass in the absence of oxygen, yielding a mixture of solid char, liquid bio-oil, and gaseous products. This method is versatile and supports bio-refinery applications, depending on whether slow or fast pyrolysis is employed. Gasification operates under limited oxygen conditions at high temperatures to convert biomass into syngas—a mixture of carbon monoxide, hydrogen, and methane—which can be used for electricity generation, heat production, or as a precursor for chemical synthesis [7].

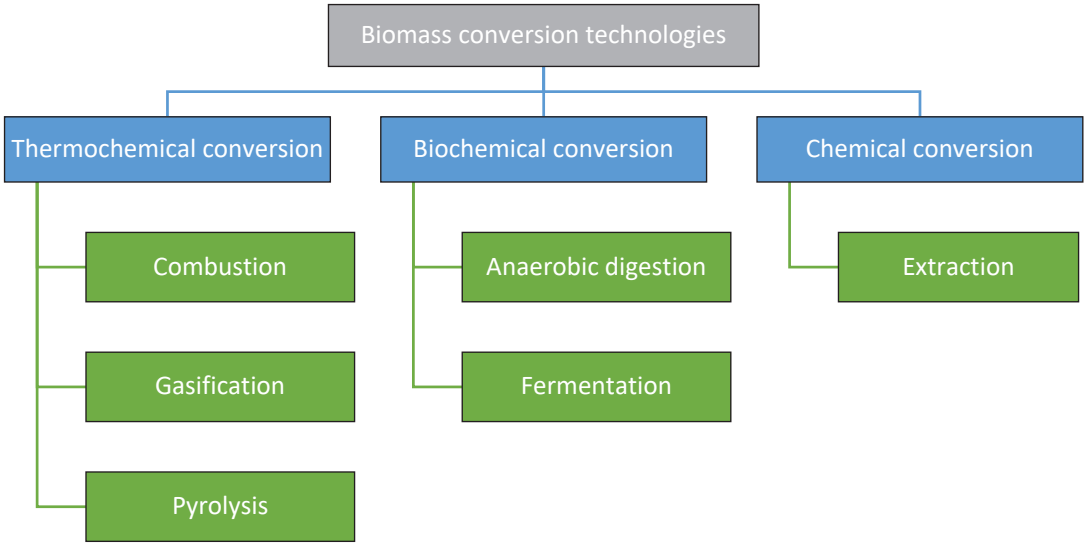


Figure 3. Biomass conversion technologies (adopted from [8]).

The Global Bioenergy Statistics Report (11th edition) [9] noted that in 2022, renewable energy sources, including biofuels, accounted for 14.3% of the global energy supply. In

2021, bioenergy contributed 96% of renewable heat, mostly in Europe (80%). The global domestic supply of biomass reached almost 54 EJ [GBS], and the IRENA report [10] predicts that by 2030, the global total biomass supply in primary energy terms will range from 97 to 147 EJ/year, primarily from agricultural residues and wastes. The supply potential of forest products, including forestry residues, is 27–43 EJ/year. From the EUBIA (European Biomass Industry Association) report: the technical potential for the EU-27 is estimated at around 200 Mtoe/year (i.e., ~8.4 EJ/year) in the short term (2020), with the possibility of doubling this to 400 Mtoe/year (~16.8 EJ/year) by 2050 [11]. Biomass is a fuel available in almost every inhabited region of the world. Due to its high moisture content (when harvested fresh) and relatively low calorific value, it is used locally, thereby ensuring energy security and independence from other energy carriers.

This review summarizes the current state of the art in biomass technologies used for residential heating. It presents the developed technologies and new directions for development, including mixed systems that combine traditional biomass use with other energy systems to produce not only heat but also electricity, cooling, and desalinated water. In this context, biomass can also be considered a part of energy-saving, passive, and nearly zero-energy buildings (NZEBs), especially in cold regions. NZEBs are defined as buildings with very high energy performance whose nearly zero or very low remaining energy demand is covered to a very significant extent by on-site or nearby renewables [12]. They represent a key strategy for mitigating the environmental footprint of the built environment. To support their development, building optimization has emerged as a powerful tool for evaluating design alternatives and identifying configurations that achieve zero-energy performance. This approach involves formulating and minimizing objective functions that encompass energy metrics (e.g., thermal demand, renewable energy yield, and efficiency gains), environmental indicators (e.g., CO_2 emissions), and economic criteria (e.g., life-cycle cost, net present value, and capital investment) [13]. Consequently, NZEBs integrate advanced energy-efficient systems—including HVAC, lighting, and appliances—alongside renewable energy technologies to meet their operational demands sustainably. Given the high share of heating in final energy consumption in buildings, integrating biomass-fired sources into NZEBs is a promising option for meeting building energy demands with minimal environmental impact. Biomass, as a controllable and carbon-neutral energy source, serves as an effective complement to variable renewables, such as solar and wind—especially in regions with pronounced seasonal fluctuations and during periods of high thermal demand. To enhance operational flexibility and overall system efficiency, biomass is increasingly being integrated into hybrid configurations that primarily combine solar thermal collectors, electric heat pumps, and thermal energy storage (TES). Against this backdrop, the present article is original in relation to the extant literature, offering a new approach to the issues surrounding nearly zero-energy buildings.

2. Methodology

This review aims to provide a comprehensive examination of the current state of research on biomass-fired heating systems, technological progress, and the potential for their integration into nearly zero-energy buildings through combining them with other systems. To ensure credibility and clarity, a systematic approach was adopted to select and analyze the literature. The review was organized into three stages: gathering and retrieving the literature, analyzing its content, and discussing domain knowledge.

2.1. Criteria Applied to Ensure the Credibility and Clarity of the Review

The literature was collected from leading academic databases, including Scopus, Web of Science, ScienceDirect, IEEE Xplore, and EBSCO, and was further supplemented with information from carefully selected, topic-relevant websites. The following criteria were applied to refine the literature selection:

- Peer-reviewed sources (journal articles and conference proceedings) were preferred—116 (92.1% of all references);
- Studies published within the last ten years were primarily considered, including 107 Articles: 77 from 2020 to 2025 and 30 from 2015 to 2019;
- Articles from well-established publishers were mainly cited, including Elsevier, MDPI, IEEE, Wiley, Springer Nature, Frontiers, and IOPscience.

2.2. The Main Stages of the Literature Review Process

The review spans a broad temporal scope, with an emphasis on recent publications to accurately reflect the current state of the art. A limited number of earlier studies were also included to provide essential historical and conceptual context. The literature review process was conducted in several stages:

- Initial screening—titles and abstracts were reviewed to assess the relevance of each work to the research topic;
- Evaluation—full-text articles were analyzed to identify significant scientific and technical contributions, methodologies, and findings;
- Classification and usage—key insights were categorized into thematic groups and integrated into the corresponding sections of the review.

2.3. Keyword Selection

To conduct a comprehensive literature search across the selected databases, a set of keywords and their combinations was formulated using Boolean operators (“AND”, “OR”) to ensure precision and coverage. The selected terms included the following: residential heating, biomass, biofuel, pellet, wood, straw, biomass combustion, biomass-fired boilers, pellet boilers, wood boilers, wood chip boilers, logwood gasification boilers, straw-fired boilers, local space heaters, wood stove, biomass hybrid systems, emission reduction, combustion optimization, automation, control systems, CFD modelling, micro-CHP, co-generation, thermoelectric generators, TEG, Stirling engines, NZEB, nearly zero-energy buildings, renewable energy integration, solar–biomass hybrid systems, heat pump integration, among others. These terms were combined and refined iteratively to capture a broad yet relevant range of studies related to domestic biomass-based heating technologies, including biomass-fired boilers, local space heaters, and hybrid systems that integrate biomass with complementary renewable energy sources to deliver heat, electricity, and cooling. Furthermore, Figure 4 shows the co-occurrence visualization created from keywords identified in the cited references. Based on occurrence, the keywords with the highest weight are as follows: biomass, biomass combustion, and wood stove.

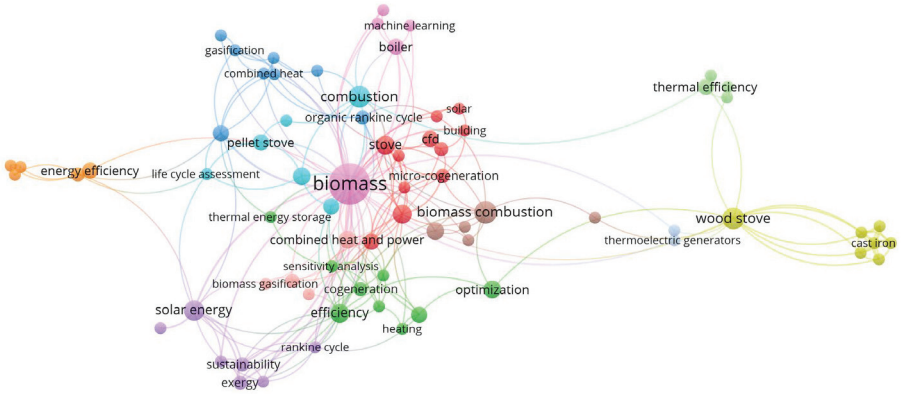


Figure 4. Keyword co-occurrence visualization (map generated in VOSviewer 1.6.20).

2.4. Limitations of the Review

The following limitations were identified during the literature collection and review process:

- Language bias—the review focuses exclusively on publications written in English and may therefore omit relevant studies published in other languages;
- Source scope—mainly peer-reviewed scientific papers were included, potentially excluding valuable insights from technical reports and other non-academic sources;
- Search methodology—reliance on keyword-based searches may have unintentionally excluded certain relevant studies due to variations in terminology and indexing practices.

3. Biomass-Fired Heating Systems—State of the Art

Biomass-fired heating systems are the oldest and most common technologies in use. However, new solutions and applications emerge in industry and the literature every year. Biomass is considered CO_2-neutral and readily available, making it an attractive and important source of heat. Wood and other woody biomass were burned in ineffective stoves, fireplaces, and kitchens for many years. In most cases, the heat was transferred directly via infrared radiation and convection. According to Garrison [14], the first central-heating systems appeared in Germany in the 1870s. The majority of appliances used at present can be divided into boilers and local space heaters (including stoves and fireplaces). Because the first group of heating systems are located in the utility room, they also serve an aesthetic function. The second group can be characterized by higher efficiency and fewer emissions, as the combustion process can be easily controlled and automated when pellets and wood chips are used. Boilers transfer heat only to the water, while local space heaters can employ different methods of heat transfer, including water heat exchangers. Today, these systems are being developed and are becoming increasingly effective and emitting less pollution.

3.1. Pellet Boilers

Pellets are made of compressed solid biomass, usually in the form of small cylindrical rods with a diameter of 6 mm. Such a structure enables effective and stable transport (with a retort feeder or a gutter feeder) and provides good control of the combustion process. The moisture and ash contents are low, and the pellets meet the required standards. Their repeatable shape and composition make supply and operation easier. The primary disadvantage of using pellets as a fuel source is the associated cost of biomass milling, compression, packaging, and other related processes.

Pellet boilers are biomass heating systems that use wood pellets as a renewable fuel, offering a sustainable alternative to fossil-fuel boilers in residential, commercial, and district heating applications. The technology has undergone significant development in recent decades, driven by concerns over energy security, climate policies, and the push toward low-carbon heating solutions [15]. At present, automatic pellet boilers are gaining popularity among homeowners of detached homes, thanks to their straightforward design and ease of use. These systems typically feature a pellet storage tank and a heat exchanger equipped with a burner, linked together by a fuel delivery mechanism. The most common type of feeder is the screw feeder, which transports pellets into the combustion chamber using a rotating spiral. An alternative is the piston feeder, which delivers a fixed quantity of fuel with each stroke. Piston feeders offer greater versatility, as they can accommodate a wider range of fuel types—including pellets, granular coal, shredded straw, and wood chips [16]. An example of a pellet-fired boiler is shown in Figure 5.



Figure 5. An example of the pellet boiler tested at the Centre of Sustainable Development and Energy Saving AGH WGGiOŚ "Miękinia" [17].

Pellet boilers, among the cleanest solid-fuel heating systems, produce the lowest levels of air pollutants among boiler types. Nevertheless, the complete elimination of harmful substances in flue gases remains unattainable. Most pellet boilers currently available fall into the fifth class—the highest category—under the PN-EN 303-5:2012 standard [18]. For a 20 kW unit in this class, the minimum required efficiency is 88%. According to PN-EN 303-5:2012, the maximum permissible emissions for automatic biomass boilers are as follows (adjusted to 10% oxygen concentration in flue gas): carbon monoxide (CO) at 500 mg/m^3, organic gaseous carbon (OGC) at 20 mg/m^3, and particulate matter at 40 mg/m^3. These boilers also comply with the Ecodesign directive and are rated A+ for energy efficiency under Commission Delegated Regulation (EU) No 811/2013. In terms of nominal heating capacity, pellet boilers achieve efficiencies exceeding 90% [16,17].

Considering their functional advantages, pellet boilers are increasingly used in hybrid systems (e.g., combined with solar thermal collectors or heat pumps) and in district heating networks. In the context of Positive Energy Districts (PEDs), pellet boilers can complement heat pumps and other renewable energy sources, such as wind and solar, by providing dispatchable thermal energy.

3.2. Wood Chip Boilers

Wood chips differ significantly from pellets because of their irregular shape and size, and their variable moisture, ash, and heating value contents. These features also pose

challenges for the fuel supply mechanism and combustion process control, resulting in higher emissions (especially particulate matter, or PM) and lower efficiency. Despite this, automatic fuel feeding is still possible due to their small size and fragmentation. Wood chips are significantly cheaper than pellets and more easily accessible, as they can be produced independently.

Wood chip boilers are a mature form of biomass combustion technology that are widely applied in district heating systems, public buildings, and industrial facilities, particularly across Europe and North America. Unlike pellet boilers, which rely on standardized, densified fuel, wood chip boilers use locally sourced, less-processed biomass, often originating from forestry residues, thinning operations, or sawmill by-products. Modern wood chip boilers employ moving grate or stoker combustion systems, combined with multi-stage air injection and flue gas cleaning technologies (e.g., cyclones, electrostatic precipitators). Efficiency typically ranges between 85% and 94%, but emissions remain highly dependent on fuel properties and operational settings [19,20]. Therefore, emissions control remains a central challenge. Rector et al. [21] found particulate emissions from a chip boiler to be significantly higher those from an oil boiler, while Trojanowski et al. [22] demonstrated that pre-treating chips via hot water extraction reduced particulate emissions considerably. These findings have underscored the importance of fuel preparation, automation, and emissions control systems in enhancing environmental performance. An example of a 50 kW boiler and fuel storage used by Tucki et al. [23] for the combustion of wood chips is shown in Figure 6.



Figure 6. An example of a 50 kW boiler and a fuel storage with a mixer, filled with pine chips [23].

3.3. Logwood Gasification Boilers

Logwood fuel refers to natural firewood logs that are cut, split, and seasoned. It is one of the oldest and most traditional heating fuels, valued for its wide availability and ability to produce a steady, high heat output when properly prepared. Hardwoods such as oak, ash, and beech are generally preferred due to their higher energy density and cleaner combustion. The quality of logwood fuel depends heavily on its moisture content. Freshly cut wood must be dried for one to two years until it reaches a moisture content of approximately 20% or less. Well-seasoned logs burn more efficiently, release more heat, and produce less smoke and creosote buildup in chimneys.

Logwood gasification boilers are biomass combustion systems designed to convert solid wood logs into combustible gas (syngas) before final combustion. This process enhances efficiency and reduces emissions compared to conventional basic wood boilers. Gasification involves the partial oxidation of wood at high temperatures, generating gases

such as CO, H_2, and CH_4, which are then combusted in a secondary combustion zone. These systems typically employ a two-stage combustion process: a gasification stage (pyrolysis and partial oxidation) that produces combustible gases and a combustion stage where these gases are burned with excess air to achieve complete oxidation. This configuration enables the more complete combustion of volatile components released from the wood, thereby significantly reducing unburned volatile emissions and particulate matter. As a result, logwood gasifiers emit lower levels of volatile organic compounds (VOCs), carbon monoxide (CO), and particulates compared to simple wood boilers—especially under optimal operating conditions. Real-world emissions studies of modern biomass boilers have shown that newer designs produce lower levels of CO, organic gases, and total suspended particles than older units [24]. In well-engineered systems, thermal efficiencies can be significantly higher than those of basic wood boilers. However, actual performance depends strongly on wood moisture, load conditions, and the sophistication of the control systems [25]. An example of a 23 kW logwood gasification boiler used in the tests described by Valicek et al. [25] is shown in Figure 7.



Figure 7. An example of a boiler for the gasification of wood pieces with a nominal heat output of 23 kW, used in tests conducted by Valicek et al. [25].

3.4. Straw Boilers

Straw, the residual stalks of cereal crops (e.g., wheat, barley, rice, oat), is an abundant agricultural biomass resource, especially in agricultural regions. As a low-cost, regionally available fuel, straw has been explored as a feedstock for boilers and combustion systems aiming to provide heat or combined heat and power. However, its combustion presents distinct challenges due to its high ash, alkali, silica, and chlorine contents, as well as its low bulk density. Although environmental aspects are considered, the high ash content poses a significant risk of deposits and corrosion in the boiler and ducts. Straw ash has a low softening temperature, and it is crucial not to exceed this temperature during operation.

Straw-fired boilers currently available on the market include several types: batch boilers designed for the periodic, cyclic combustion of baled straw; systems that utilize ground straw combustion through the "burning cigar" method for continuous operation; and automatic units capable of burning chopped straw into 5–10 cm pieces, also operating continuously. The typical power output of batch straw-fired boilers ranges from 40 to 700 kW, making them well-suited for generating low-temperature heat for space heating and domestic hot water systems, as well as for specialized settings such as greenhouses, drying facilities, and distilleries. In such cases, beyond conventional heating boilers, oil-fired air heaters are also commonly employed, using thermal oil as the working medium,

heated to 150–200 °C [26]. An example of a 100 kW straw-fired cogeneration boiler is shown in Figure 8.



Figure 8. An example of a 100 kW straw boiler adapted to an experimental CHP system [27].

3.5. Local Space Heaters

Local space heaters, i.e., stoves and fireplaces, are the most popular home heating appliances, as most of them do not require electricity and their operation is entirely user-dependent. By acquiring inexpensive fuel, users become completely independent of external energy sources, bringing them closer to the original use of fire. Local space heaters hearths can be divided into those with and without a grate. Hearth grates are typically used in fireplaces and freestanding stoves (and boilers), and allow for continuous ash removal but result in lower combustion temperatures and, consequently, lower efficiency. Fuel loads in fireplaces are frequent, occurring approximately once per hour, and are small, ranging from 1 to 3 kg. In grateless hearths found in heat-storage stoves and traditional tiled stoves, the combustion temperature is significantly higher, and the accumulative mass of the appliance allows for heat storage, significantly increasing efficiency. Wood loads are large, typically 5–20 kg, and infrequent, occurring once to three times per day. An example of wood stoves with a heating power of up to 20 kW, used in studies conducted by Motyl et al. [28], is shown in Figure 9.



Figure 9. An example of wood stoves with a heating power of up to 20 kW, used in studies conducted by Motyl et al. [28].

3.6. Summary of the Available Biomass-Fired Appliances and Future Perspectives

The biomass-fired appliances discussed are widely deployed and contribute significantly to energy security and independence. A general comparison of pellet boilers, gasification boilers, wood chip boilers, straw boilers, and local space heaters is presented

in Table 1. However, to enhance the efficiency and environmental performance of biomass utilization, further technological advancements are essential, particularly those aimed at reducing air pollution and minimizing fuel waste. Reducing air pollution is critical to meet the emission requirements in Table 2. In this context, Section 4 explores several strategies to improve the biomass-fired appliances, including the optimization of combustion chamber geometry, refinement of combustion process control, implementation of technologies to reduce solid and gaseous emissions, and integration of combined heat and power (CHP) solutions. Section 5 shifts focus to the incorporation of biomass technologies within nearly zero-energy buildings, emphasizing synergies with heat pumps and solar thermal systems. These integrated approaches enable more effective energy use in residential applications.

Table 1. General summary of the available biomass-fired appliances.

Parameter	Pellet Boilers	Gasification Boilers	Wood Chip Boilers	Straw Boilers	Local Space Heaters
Typical fuel	Wood pellets	Seasoned logwood	Wood chips, forest residues	Cereal/wheat straw in the form of bales	Seasoned logwood, briquette

Table 1. *Cont.*

Parameter	Pellet Boilers	Gasification Boilers	Wood Chip Boilers	Straw Boilers	Local Space Heaters
Automation level	High (fuel feed conveyors, ash removal, control systems)	Moderate (batch-fed, downdraft gasification)	Moderate (fuel feed conveyors, fuel variability is an issue)	Low (manual feed and ignition in domestic appliances)	Low (manual feed, manual or automated air control)
Efficiency and emissions	High efficiency, over 90% (over 100% for condensing technologies), and low emissions	Gasification allows for more complete combustion and lower emissions compared to simple wood-fired boilers, efficiency of over 90%	Efficiency can be good (over 90%), but emissions and operational stability depend on fuel quality	It can be efficient (up to 80–90%), but issues of ash handling, slagging, corrosion, and variable moisture are more severe	Tend to have lower efficiencies (80–90%) and higher particulate emissions unless they are modern, well-regulated units
Scale suitability	Good for residential to medium-sized heating loads	Suitable for residential to small industrial scale	Better at larger scales (e.g., district heating, larger buildings)	Well-suited to agricultural or rural heating installations	For individual rooms or localized heating
Ash, slagging, corrosion risks	Pellets generally yield low ash and a predictable ash composition, with less slag	Lower slagging compared to direct combustion, but gasification may produce tars or condensable species	Wood chips can contain more contaminants (bark, soil) that increase ash and fouling risks	Straw contains high potassium, chlorine, silica, etc., leading to high corrosion, fouling, and ash slagging issues	Ash and soot accumulation is simpler but may be frequent; the risk of creosote and particulate emissions is higher
Capital cost and economics	Moderate to high capital cost (250–500 EUR/kW), but more automation reduces labor cost	Higher capital for gasification chamber, controls, and often integrated thermal storage (300–600 EUR/kW)	Capital cost rises with handling systems, fuel processing, and emission controls (300–600 EUR/kW)	Capital cost is high for reliable systems with ash handling and corrosion protection (400–800 EUR/kW)	Lower capital cost for a stove or heater, but less economical when scaled up (400–1000 EUR/kW)
Environmental and regulatory considerations	Emissions must meet standards; pellet boilers can do well in regulated environments	Gasification is favorable because of lower particulate level and unburned emissions	Emissions depend on fuel handling, particulate controls, and boiler design	Straw combustion emissions are more challenging to control	Tighter emissions constraints under many jurisdictions

Table 2. Emission requirements for biomass-fired appliances.

Parameter	Boilers ≤ 20 kW (COMMISSION REGULATION (EU) 2015/1189 of 28 April 2015) [29]		Local Space Heaters (COMMISSION REGULATION (EU) 2015/1185 of 24 April 2015) [29]	
	Automatically Stoked	Manually Stoked	Using Solid Fuel Other than Compressed Wood in the Form of Pellets	Using Compressed Wood in the Form of Pellets
Seasonal space heating energy efficiency, %	≥75	≥75	≥65	≥79
Particulate matter (PM), mg/m^3	≤40	≤60	≤40	≤20
Organic gaseous compounds (OGC), mg/m^3	≤20	≤30	≤120	≤60
Carbon monoxide (CO), mg/m^3	≤500	≤700	≤1500	≤300
Nitrogen oxides (NO_x), mg/m^3	≤200	≤200	≤200	≤200

4. Technological Advances in Biomass-Fired Heating Systems

To meet stringent EU regulations and evolving societal expectations, biomass-based heating systems must become increasingly safe for both human health and the environment, while also offering greater versatility and user convenience. This presents a significant challenge for manufacturers and researchers. Due to its heterogeneous structure and composition, biomass fuel tends to emit relatively high levels of solid and gaseous pollutants, prompting intensive efforts to develop effective technologies for reducing emissions.

A growing trend in the sector is the automation of biomass appliances, which enhances user control while minimizing direct contact with hot surfaces or open flames—an important factor in improving safety and usability. One promising direction in local space heater design is the integration of heat-storing materials. While this concept has historical roots in traditional tiled stoves, modern materials and configurations are being developed to better align with the thermal characteristics of contemporary, well-insulated buildings. Furthermore, biomass heating appliances are increasingly integrated into hybrid energy systems that provide not only space heating, but also electricity generation, cooling, and even water desalination. Biomass appliances demonstrate strong potential in micro-scale cogeneration systems, particularly when combined with thermoelectric generators (TEGs), Stirling engines (SEs), Organic Rankine Cycle (ORC) units, and internal combustion engines (ICEs). On the other hand, in the context of nearly zero-energy buildings, particular attention is given to the combination of biomass-fired appliances with solar thermal systems and heat pumps, which are already widely adopted in the residential sector.

4.1. Emission Reduction Technologies

Pollutants emitted during biomass combustion can be divided into two groups: gaseous and particulate. Gaseous pollutants include CO, NO_x, and hydrocarbons (HC), including polycyclic aromatic hydrocarbons (PAHs). Increased CO and HC emissions result from incomplete fuel combustion and poor process organization. Flame cooling, on the other hand, increases PAH levels in flue gases. NO_x produced during biomass combustion comprises approximately 90% NO and 10% NO_2. The majority of these are fuel nitrogen. NO_x produced during the thermal mechanism is negligible due to the low combustion temperature (<1600 °C).

Solid pollutants include inorganic pollutants (such as ash) and organic pollutants (including soot, coke, organic condensates, tar, and polycyclic aromatic hydrocarbons, or

PAHs). A short residence time in the combustion chamber is considered the primary cause of organic particle emissions. A distinction is also made between primary particles, formed in the combustion chamber, and secondary particles, produced by gas-phase condensation or atmospheric reactions, such as secondary organic aerosols (SOA). A significant characteristic that distinguishes solid pollutants is their size: PM10 (diameter $\leq$ 10 μm), PM2.5 (diameter $\leq$ 2.5 μm), PM1 (diameter $\leq$ 1 μm), and ultrafine particles (UFP) (diameter $\leq$ 0.1 μm). The smaller the particles, the deeper they can reach in the human respiratory system.

4.1.1. Particle Emission Reduction

An important part of developing biomass technologies for residential heating is considering external factors that influence pollutant emissions, such as filters, collectors, and catalysts. Suhonen et al. [30] designed a high-temperature electric soot collector to reduce particle emissions in a logwood-fired masonry heater. The device was an insulated high-voltage electrode that generates an electric field and is installed in a firebox. Particles with electrical charges were collected on the electrode and oxidized at high temperatures, leading to a reduction in fine particle emissions (of 45% in this case). Moreover, this construction could be implemented in existing appliances. Kantová et al. [31] tested different fuel (pellet) dosage-to-supply/standmill ratios in an automatic pellet boiler. The authors also designed a four-tube precipitator to improve particle separation ability. The dosage system did not significantly affect emissions; however, the precipitator achieved a high collection efficiency of 79–90% across all dosage settings. A novel PM emission reduction system, the passive cyclone abatement system (PCAS), was designed by Coccia et al. [32] for residential pellet stoves. The system could capture PM with quantities exceeding 10 mg/MJ and diameters mostly exceeding 10 μm. The PCAS was considered versatile and could be mounted on other residential heating appliances. Bianchini et al. [33] achieved a particulate matter removal efficiency of 95%. The device applied for this purpose was a bubble-column scrubber integrated with a biomass boiler for residential heating. A similar solution dedicated to a pellet boiler was proposed by Blumberga et al. [33]. The 'fog unit' was supposed to capture PM, and water was recirculated. The authors claimed that the PM removal efficiency depends on inlet water temperature, outlet gas temperature, droplet velocity, and droplet holdup. Butcher and Trojanowski [34] proposed a method to reduce particulate emissions from residential wood pellet boilers by adding external thermal storage. Such a solution enabled elongation of the total cycle period of the boiler from 23 to 228 min. This resulted in an efficiency increase from 56% to 74% and a 66% reduction in particulate emissions. A Thermal Energy Storage (TES) tank in combination with a biomass boiler was also studied by Wang et al. [35]. A broad range of boiler nominal outputs and heat demand profiles was investigated, and the authors found a linear correlation between the optimized TES tank volume and the boiler's nominal capacity. Moreover, it was stated that the average building heat demand is around 45% of the boiler's nominal capacity. Considering methods for reducing particulate matter emissions, Ozgen et al. [36] discussed various options for pellet boilers. A summary of these methods is provided in Figure 10.

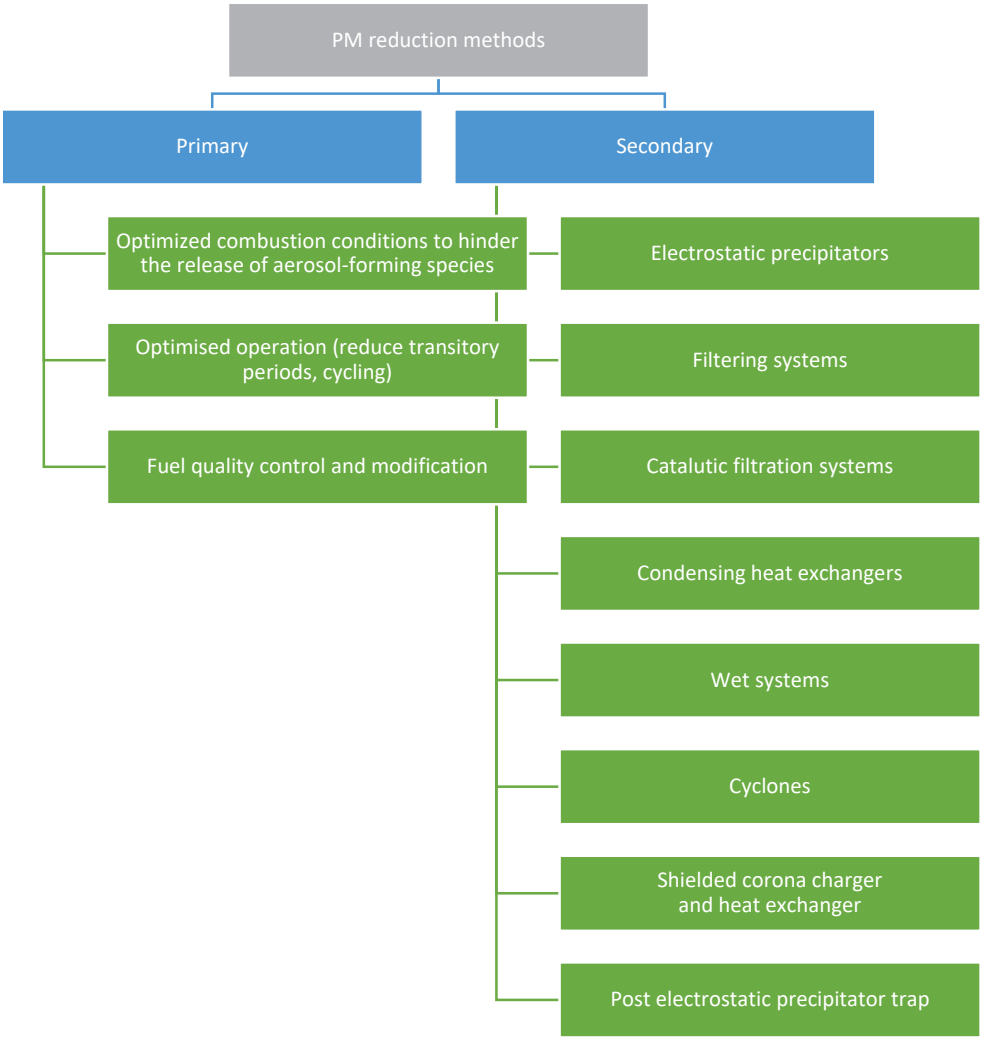


Figure 10. Division of particulate matter emission reductions from pellet boilers, according to Ozgen [36].

4.1.2. Methods for the Reduction of Gaseous Pollutant Emissions

Since reducing air pollutant emissions (especially PM, but also CO and NO_x) remains of high interest, the authors develop a broad range of methods to achieve this goal. Many of them focus on dividing the inlet air entering the combustion chamber into primary and secondary air. Different placements and designs of air nozzles are studied. The researchers attempt to divide the entire combustion process into two separate stages: gasification and combustion of the generated gas. Moreover, automatic control of the combustion process and appliance operation is investigated; however, this is not straightforward in batch log combustion, where conditions are less steady than in pellet boilers. Energy storage is a possible way to reduce emissions per unit of energy. More direct solutions are, for instance, flue gas recirculation or dosing the reductive agent. In this context, Lamberg et al. [37] proposed a hybrid slow heat-release stove for residential heating that can burn both wood logs and wood pellets. The work focused on particle and gaseous emissions, reporting 92% reductions in fine particle emissions and 65% reductions in CO emissions from pellets compared to wood logs. Moreover, it was noted that most particle emissions occur at the beginning of the combustion process, whereas CO emissions are observed at its end. An intelligent model to control the combustion process was developed by Loprete et al. [38]. This controlled incoming air to improve stove performance. The system considered stove temperature, weight, and

airflow rates to estimate instantaneous efficiency, stoichiometry, and the moisture content of the wood. The control algorithm used these parameters to optimize the air input. Eo et al. [39] improved the thermal efficiency of the wood pellet boiler by optimizing the inlet air flow and quality. To improve contact between fuel and oxygen and increase the reaction rate, a nozzle-type burner pin was designed. The vortex generator was applied to enhance mixing in the combustion chamber and achieve higher temperatures. A system using a LiBr solution for air dehumidification and preheating was developed. When both solutions were applied together, the boiler's efficiency increased from 73.11% to 78.89%. The inlet air parameters for the wood pellet boiler were also investigated by Zadravec et al. [40]. The authors studied the primary air/secondary air (PA/SA) ratio, infiltration ratio, and global excess air. It was found that, for reducing gaseous emissions, the optimal PA/SA ratio was 0.53, with an O_2 concentration of 5.26%. Deng et al. [41] analyzed the relationship between inlet air (primary and secondary) and the performance and pollutant emissions of the biomass stove. The authors created an air supply control system with different parameters set for airflow rate and PA/SA ratios. The results showed that the optimal air supply was 184 L/min, with a PA/SA ratio ranging from 4:6 to 6:4. Furthermore, Polonini et al. [42] tested a flue gas recirculation (FGR) system in a pellet stove to reduce combustion emissions (see Figure 11). The inclusion of that system resulted in 80% lower CO_2 emissions, 45% lower PM emissions, and 11% lower NO_x emissions. The authors emphasized the FGR system's ability to reduce emissions, particularly with extreme O_2 contents.

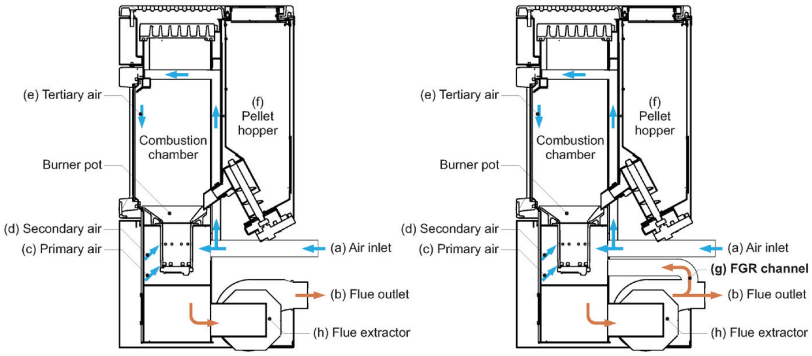


Figure 11. Scheme of the pellet stove without FGR system (**left**) and scheme of the pellet stove with FGR system (**right**) [42].

Kardaś et al. [43] tested a two-stage pellet combustion process: first, gasification, and second, oxidation of the gasification products in a boiler. The authors tested different constructions for pellet burners with high- and low-secondary-air nozzles and compared them with a typical retort burner. The version with low-secondary-air nozzles resulted in 74% lower CO emissions compared to the retort burner and 36% lower PM emissions. It was noted that the distance from the secondary nozzles to the gasifying section is crucial for the burner's operation and its ability to reduce pollutant emissions. Carvalho et al. [44] mounted an external chimney component around the existing chimney of a traditional wood stove for preheating one of two air inlet streams. This division helped increase efficiency and reduce CO. Horvat et al. [45] performed experimental and numerical tests of a biomass domestic boiler using a combustion intensifier (CI) within the conventional combustion system and rotary pellet burner. Two variants of CI were tested: honeycomb-structured ceramic CI and a parallel V-corrugated metal plate CI. The authors noted a 30% reduction in CO emissions in both experimental and simulated tests. Lower dust and NO_x emissions, as well as higher efficiency, were also reported. The solution was recognized as suitable for installation in almost every residential heating appliance. A selective non-catalytic reduction mechanism

was applied by Ciupek [46]. This work aimed to reduce NO_x emissions from a biomass boiler by utilizing an aqueous urea solution. The solution was dosed into the combustion chamber, and a flue gas analysis was performed. The authors observed a 43% decrease in NO_x at the highest dosing rate. However, an increase in CO emissions was observed due to process cooling and incomplete oxidation. The optimal dosing conditions were evaluated to minimize PM and NO_x emissions simultaneously. Sturmlechner et al. [47] investigated the potential to reduce pollutant emissions through user training. The results are promising, and the desired reduction was observed across all parameters studied, especially BaP. The authors suggest repeating the training in reasonable intervals.

Several solutions for biomass-fired heating in a single-family house were simulated in TRNSYS by Marigo et al. [48]. They considered a gas boiler system with radiators as terminal units, a pellet stove (with and without an air-ducting system), a wood-log stove, and a mix of the above seven configurations. The energy analysis was evaluated based on ideal space heating needs, final energy demand, and primary energy consumption. The authors claimed that biomass stoves, especially wood-burning stoves, are often oversized for the rooms they are located in due to difficulties controlling thermal output. A pellet stove, a gas boiler, and a radiator system provide similar final energy levels, and the wood stove provided an increase of 21% for the electric heater and 9% for the gas boiler. In the case of primary energy, combining the gas heating with wood stoves was similar to a gas boiler system.

On the other hand, Szramowiat-Sala et al. [49] studied emissions from wood combustion in domestic heating units, focusing on PM and gaseous pollutants across three combustion phases: firing, combustion, and post-combustion. Measurements included fuel mass loss, gas concentrations (CO_2, CO, O_2, SO_2), and PM sampling for chemical analysis. The use of an accumulation layer reduced emissions of NO, NO_x, and SO_2, but increased CO and PM levels. PAH analysis revealed that acenaphthene and benzo[a]pyrene (BaP) were most prevalent, with BaP concentrations peaking during the post-combustion phase. The accumulation layer helped lower BaP emissions during ignition, highlighting its potential for emission control. Ozgen et al. [50] highlighted key factors influencing NO_x emissions from biomass combustion in domestic heating. As was discussed, NO_x formation was primarily driven by fuel-bound nitrogen (fuel-N), with higher fuel-N content leading to lower conversion efficiency. Non-woody biomass, typically rich in fuel-N, requires effective emission control strategies. However, applying NO_x reduction techniques to small-scale systems was challenging due to technical limitations and high costs. Air staging is commonly used, but it may increase CO emissions, requiring careful balancing. Operational parameters, such as air distribution, residence time, and temperature, also play a crucial role in this context; however, small appliances often lack sufficient chamber size for optimal NO_x reduction. Compared to fossil fuels, biomass systems emit more NO_x and particulate matter, underscoring the need for LCA. In this context, NO_x emissions from small wood-burning room heaters were investigated using CFD modeling of a 5 kW natural-draft stove by Bugge et al. [51]. In the analyzed setup, primary air was introduced through bottom slots, secondary air through rear wall openings, and flushing air was directed vertically above the front glass window. Unlike conventional boiler air staging, this configuration allowed for secondary air injection before the complete mixing of fuel gases with primary air. The study demonstrated a notable reduction in NO_x emissions at a primary excess air ratio of 0.8, suggesting that staged air combustion can effectively lower NO_x emissions, even in compact residential stoves. Another study examined the performance of a lambda-sensor-controlled 15 kW pellet boiler. The authors discussed lambda control as an efficient way to reduce NO_x emissions, especially for non-woody biomass fuels, without compromising complete combustion [52]. Vodička et al. [53] presented an experimental

study on reducing NO_x emissions through staged oxygen injection during the oxy-fuel combustion of lignite and wood pellets in a 30 kW bubbling fluidized bed. By varying the ratio of secondary to primary oxygen while maintaining constant flue gas oxygen levels and bed temperature, the authors achieved up to 50% NO_x reduction at ratios of 0.5 for lignite and 1.0 for wood. The staged injection also significantly increased freeboard temperatures, reaching a maximum of 950 °C. The findings confirmed that oxygen staging is an effective strategy for NO_x mitigation and may support the use of non-selective catalytic reduction in fluidized bed systems. A summary of the literature positions discussed in this review, focusing on gaseous pollutants and effectiveness improvement, is presented in Table 3.

Table 3. Summary of cited items considering gaseous pollutants and effectiveness improvements.

Reference	Parameter Improved	Method	Fuel/Appliance
Lamberg et al. [37]	CO and PM	Fuel change	Wood and pellet/slow heat release stove
Loprete et al. [38]	Efficiency	Air inlet control	Wood/stove
Eo et al. [39]	Efficiency	Air inlet design	Pellet/boiler
Zadravec et al. [40]	CO, NO_x, efficiency	Air inlet control	Pellet/boiler
Deng et al. [41]	CO, NO_x, and PM	Air inlet control	Pellet/stove
Polonini et al. [42]	CO, NO_x, and PM	Flue gas recirculation	Pellet/stove
Kardaś et al. [43]	CO and PM	Combustion phasing	Pellet/boiler
Carvalho et al. [44]	CO and efficiency	Air inlet preheating	Wood/stove
Horvat et al. [45]	CO, NO_x, PM and efficiency	Combustion control	Pellet/boiler
Ciupek et al. [46]	NO_x	Reducing solution dosing	Pellet/boiler
Sturmlechner et al. [47]	BaP	User training	Wood/stove
Szramowiat-Sala et al. [49]	NO_x, BaP, and SO_2	Accumulation layer	Wood/fireplace
Bugge et al. [51]	NO_x	Air staging	Biomass/stove
Carvalho et al. [52]	NO_x	Air inlet control	Pellet/boiler
Vodicka et al. [53]	NO_x	Oxygen staging	Lignite and pellet/fluidized bed

Computational Fluid Dynamics (CFD) is a valuable tool that reduces the cost of experimental facilities, tests, and work time. Researchers use this tool for various purposes, including simulating combustion and heat transfer processes in biomass heating appliances. Scharler et al. [54] developed a 3D model of a wood stove, accompanied by a 1D model of a wood log. The authors report a satisfactory reconstruction of wood batch combustion, including CO emissions, O_2 content in the flue gas, and chimney temperatures. Szubel et al. [55] demonstrated a validated CFD model for optimizing straw-fired batch boilers. The developed model successfully identified repeatable combustion stages, enabling the observation of phenomena that are difficult to measure directly, such as the dynamics of straw gasification. It revealed that primary air distribution has a strong impact on the heterogeneous burnout rate of straw. In contrast, secondary air injection plays a crucial role in shaping combustion dynamics and must be considered in chamber design and control algorithms. Among the tested configurations, the variant with centrally positioned secondary air inlets proved the most effective, reducing stack losses by up to 33% compared to other configurations. In this case, incomplete combustion losses were reduced experimentally by 43% and in simulations by 18.2% compared to the worst-performing variant, while thermal

efficiency improved by 45.7%. These improvements also enabled a reduction in blower fan power, resulting in lower energy consumption and reduced emissions. Furthermore, Bianco et al. [56] employed CFD analysis to design an air manifold for a biomass-fired batch boiler, thereby improving combustion. The proposed solutions were based on minimizing the entropy generation rate by rounding manifold corners. Design improvements have enhanced air velocity distribution, resulting in more uniform conditions within the combustion chamber. Chen et al. [57] and Luo et al. [58] investigated soot formation in wood stoves. The papers noted that the quantity of soot depends on the number of logs and the distance between them, as well as on the air inlet parameters and the construction. Zlateva et al. [59] investigated the combustion of mixed biomass pellets in a domestic boiler, combining experimental flue gas measurements with CFD simulations. The simulations provided insights into temperature distribution, flue gas flow, and turbulence behavior within the combustion chamber. A key focus was the influence of primary-to-secondary air ratios on combustion quality, emissions, and thermal performance. Optimizing air distribution proved effective in improving combustion and reducing pollutant emissions. Findings showed that a 60/40 air distribution ratio enhances combustion efficiency and significantly reduces emissions—CO by 12% and NO_x by 27%. The results underscored the viability of mixed biomass pellets as a sustainable fuel alternative, contingent on the precise control of combustion parameters.

4.2. Combustion and Control Advances

Conventional biomass appliances typically rely on manual operation, with the operator's experience guiding adjustments. This method is labor-intensive and often results in inefficient resource use. To address the specific operational dynamics of biomass appliances, various attempts have been made to develop efficient control strategies for different types of biomass-fired units. In addition to control strategies, various measures are being implemented to enhance the efficiency and environmental performance of boilers and local space heaters. These include the use of thermal storage systems and integration with broader building infrastructure.

4.2.1. Automatic Control for Biomass-Fired Appliances

Álvarez-Murillo et al. [60] designed a control system using a programmable logic controller (PLC) to improve combustion in biomass stoves. PLC-controlled air and pellet supply systems provide higher efficiency and lower CO emissions. Different types of biomass fuels have been investigated. The highest power output was achieved with poplar pellets (8.77 kW) and the lowest with holm oak pellets (5.66 kW). The combination of automatic air supply control with an oxidizing catalyst was applied to the commercial fireplace and tested by Zhang et al. [61]. The authors burned batches of wood logs, and the control system operated based on signals: catalyst temperature, residual oxygen concentration, and CO/HC content in the exhaust. Motor-driven shutters controlled the inlet air streams. The results are very promising—the solutions provided reduced CO and PM emissions and increased efficiency. The same effect was achieved by Illerup et al. [62] after developing an automatically controlled system. The control parameters were oxygen concentration, flue gas temperature, and room temperature. In this case, air was supplied by three separate ducts and controlled with valves. Mižáková et al. [63] explored advanced methods for monitoring and controlling biomass combustion in small and medium-scale boilers, emphasizing not only O_2 concentration in flue gas but also CO emission trends. The developed control algorithms dynamically assessed the relationship between CO and O_2 levels, aiming to minimize oxygen concentration and reduce energy

losses while keeping CO emissions within legal limits. The system proved effective with wood chips containing 35–45% moisture and up to 50% across various wood types, such as fir, beech, and oak. The authors in Ref. [64] investigated methods to reduce CO emissions during wood combustion in an accumulation-type stove-fireplace (SFA). The study first compared the combustion characteristics of beech wood of varying quality and then tested different control strategies for SFA operation. A prototype controller was developed using O_2 and CO signals to regulate air throttles. The results confirmed that the system can meet the performance criteria set by BImSchV 2 and Ecodesign standards. Ye et al. [65] developed an advanced biomass boiler controller that utilizes embedded and wireless communication technologies, enabling local and remote control, data archiving, and signal monitoring. Designed for practical use, this system employed a fuzzy PID control strategy to enhance energy efficiency and real-time performance. Extensive testing confirmed the reliability of its electronics and software. The solution also proved cost-effective by reducing labor, time, and resource demands, indicating strong potential for widespread practical application. Pitel and Mižák [66] introduced new control algorithms for woodchip-fired boilers to achieve complete combustion with minimal excess air. Cost-effective CO and O_2 sensors were selected to enable application in small-scale systems. Monitoring results from two boiler types confirmed the successful design and implementation of the automated biomass combustion control strategy. Miranda et al. [67] proposed a system that provided reliable and precise data, enabling a detailed analysis of combustion variables across different fuels and operating regimes. Its modular design enabled the integration of additional sensors (e.g., CO_2 and incomplete combustion probes), making it a versatile tool for future studies on adapting conventional boilers for multi-fuel use. He et al. [68] introduced a predictive model, FOD-BP-ACO, designed to optimize control parameters in biomass boilers. The model used k-means clustering to classify operational states based on boundary parameters, including steam drum pressure, feedwater flow rate, and unit load. One of the key improvements was the application of delay parameter compensation, which reduced the model's average relative error by 25.78%, demonstrating a significant enhancement in prediction accuracy. Numerical simulation and experimental validation of a pellet boiler were performed by Chen et al. [69]. The authors explored the optimal operating parameters. The balanced particle diameter and inlet air temperature were noted. The optimal negative pressure was set at 50 Pa. The effect of inlet air relative humidity was also investigated, reaching the optimal value at 50%.

4.2.2. Heat Accumulation

Despite numerous advantages, heat production in residential appliances—fireplaces and stoves—brings some challenges due to their discontinuous operation and, thus, transient heat emissions from the appliance or heat exchangers. The solution to this problem is to introduce heat storage. Heat storage materials based on fireclay have been known for centuries and are still in use, especially in Europe. Thus, stove-fireplaces with heat accumulation systems (SFA)—which blend the aesthetics of fireplaces with the functionality of traditional storage stoves—are gaining popularity. These systems store the heat generated from wood combustion in an accumulation heat exchanger, releasing it gradually for up to 12 h after the fire has gone out. Their thermal efficiency reaches around 90%, largely due to automated combustion control. Advanced optimizers regulate both the air supply to the furnace and the flue gas temperature within the exchanger, helping to prevent tar condensation, which can occur with low exhaust temperatures. Airflow is managed through one or more proportionally opening choke valves, which are adjustable from 0% to 100%. The air enters through multiple inlets, ensuring the thorough mixing of wood gasification

byproducts with oxygen, resulting in clean and efficient biomass combustion [70]. An example of a stove-fireplace with heat accumulation is shown in Figure 12.



Figure 12. An example of a stove-fireplace with heat accumulation [71].

Szubel et al. [72] performed both an experimental and a numerical analysis of an accumulative heat exchanger connected to a residential heating fireplace. Apart from insignificant divergences, the proposed model can be applied to heating appliance design. The ability and effectiveness of the accumulative heat exchanger in improving efficiency and reducing heat losses were highlighted. Furthermore, the study conducted by Żołądek et al. [73] identified operational differences among the accumulative wood stove, the steel stove with accumulation, and the traditional steel wood stove. Comparative analysis focused on the temperature distribution across the external surfaces of each unit and the corresponding energy transfer to the heated space. The surface temperature analysis revealed that the average temperature of a traditional steel stove was approximately 1.5 times higher than that of a steel stove equipped with an accumulation layer, and nearly three times higher than that of an accumulative stove. However, in terms of total heat transfer through the side walls, the accumulative stove demonstrated the highest output, at 14.6 MJ. In comparison, the steel stove with accumulation yielded the lowest, at 7.4 MJ. These findings were particularly relevant for energy-efficient and passive buildings, where minimizing overheating and maintaining thermal comfort are critical. On the other hand, as house insulation levels increase, there is a need to develop materials or other solutions that maintain stable heat release. Such a solution in the form of latent heat storage (LHS) has been proposed by Kristjansson et al. [74]. The authors simulated the use of phase change materials (PCMs) with different properties in combination with a wood stove using a numerical model. It was found that LHS predominates over sensible heat storage when stable heat release is required. Skreiberg et al. [75] used Erythritol as a PCM in a simulation of a cast iron stove to improve heat release performance. A 43% reduction in average (53% reduction in peak) heat emission was reported during the combustion cycle. Sevault et al. [76] performed a simulation using the same PCM. Still, they were located between the walls of coaxial cylinders placed above the outlet of the flue gases from the wood stove. The material released the heat over 6–10 h. The authors highlighted the potential issue of material degradation when burning multiple consecutive batches. Cablé et al. [77] performed a numerical analysis of a system combining a wood and a pellet stove, equipped with a heat exchanger and mechanical ventilation with heat recovery. Scenarios for different climate conditions were considered. The proposed solution significantly increased comfort in the rooms. Moreover, the heat exchanger recovered up to 611 kWh from the wood stove and up to 1281 kWh from the pellet stove over the space-heating season. An innovative heat exchanger was developed by Gallardo et al. [78]. The introduced solution could be

applied in domestic heating and hot water appliances. The computational model of the heat exchanger showed increases in turbulent intensity, flue gas velocity, and residence time, leading to a higher total heat transfer rate.

4.2.3. Combined Heat and Power Generation

Biomass serves as a viable fuel source for combined heat and power (CHP) technologies, which not only deliver heat and electricity simultaneously but also significantly enhance process efficiency—from 30–35% up to 80% [79]. A range of micro-scale CHP technologies is discussed in the literature, including thermoelectric generators (TEGs), Stirling engines (SEs), Organic Rankine Cycle (ORC), fuel cells (FCs), and internal combustion engines (ICEs) [80].

Thermoelectric Generators: One way to use the heat produced by residential appliances (fireplaces and stoves) is to generate electricity with thermoelectric generators (TEGs). This topic seems to be interesting, especially for off-grid areas and suburbs. Moreover, such a solution is a good answer for power outages during the heating season, as it can keep them operating or facilitate a safe shutdown. TEGs are devices that capture waste heat and transform part of it into usable electrical energy. Their operation is based on the Seebeck effect—a phenomenon where a temperature difference between two dissimilar metals or semiconductors generates a voltage. When these materials are connected in a closed circuit, the resulting voltage drives a continuous electric current through the system. TEGs can be used in various applications, including biomass-fired appliances. They can be mounted on the bodies of stoves and boilers, or on a flue gas channel, and utilize waste heat that would otherwise be removed to the atmosphere (see Figure 13). In this context, implementing TEGs can improve the energy efficiency of biomass-fired devices.



Figure 13. A view of the steel stove with TEGs mounted on its rear wall (**a**,**b**) and flue gas channel (**c**) [81].

Najjar and Kseibi [82] carried out an analysis of a multi-purpose stove integrated with 12 TE modules. Their design featured an aerodynamically optimized combustor, a finned TEG base plate, a cooker, and a water heater for space heating. The system achieved a peak power output of approximately 7.88 W using fuels such as wood, manure, or peat, with an average overall stove efficiency of around 60%. Patowary and Baruah [83] conducted preliminary tests on a TEG-equipped cookstove, demonstrating its ability to produce 2.7 W of electrical power—sufficient to light a 3 W LED bulb. Guoneng et al. [84] developed and tested a micro-CHP system based on a TEG capable of delivering over 200 W of electrical power and more than 9.8 kW of thermal energy. The authors integrated a strategy encompassing heat collection, TEG wiring, power conditioning and storage, and temperature regulation. The system achieved a heat-collection efficiency of 34.16%, power-generation efficiency of 0.87%, and thermoelectric efficiency of 2.49%. Manfrida and Talluri [85] performed an exergy analysis of a thermoelectric wood fireplace, revealing an overall efficiency of 36.2%, with flue gases contributing the most to useful exergy. Sensitivity analysis revealed that a higher heat input improved exergy efficiency,

whereas increasing the fireplace height reduced it due to a lower flame temperature. The number of TE modules had minimal impact, as electricity accounted for only 2% of total exergy output. Sornek et al. [86] studied three types of TEGs—one with air and two with water cooling types, with matched output powers of 45, 100, and 350 W, respectively. The highest power was achieved by a 100 W water-cooled TEG, yielding 31.2 W; however, an air-cooled 45 W TEG had the highest power-to-nominal power ratio, reaching 41.7%. Moreover, the authors claimed that water cooling is recommended due to the lower temperatures of TEG's cold side. Tambunan et al. [87] also mounted an air-cooled TEG on the wall of the biomass stove. During the experiments, various types of biomass were tested, and for each, the electrical voltage generated was measured. The results showed that the electricity generated is not proportional to the fuel's heating value. TEG with a matched power of 28.8 W was constructed and mounted on the flue gas chimney by Sornek and Papis-Frączek [88]. The tests were conducted in a wood-fired stove, with a fuel load of 8 kg of pinewood. The maximum power recorded was 15.9 W. The authors noted that the tested TEG version can enable self-sufficient stove operation. The same conclusion was reached in the work of Obernberger et al. [89]. In both works, the authors also performed CFD simulations. Baldini et al. [90] designed a heat flux concentrator to intensify heat transfer to the TEG modules using water cooling in the fireplace. In a 26 kW fireplace, 140 W of thermoelectric power could be produced. A CHP system consisting of TEG modules and a solid-fuel stove was also applied by Montecucco et al. [91]. TEG modules were located on the top of the stove and charged a lead-acid battery. However, the average electricity production was 27 W, and the TEG efficiency was around 5%. Another combination of TEG modules with a biomass-fired heating appliance was studied by Usón et al. [92]. In this work, a biomass boiler was equipped with TEG modules installed in its upper part. The maximum generated power during the test was almost 70 W (tap-water cooling). The authors identified ash deposition on TEG modules, resulting in significantly lower temperatures and power output.

Stirling Engines: A Stirling engine is a closed heat engine in which the working medium (usually a gas, such as helium, hydrogen, or air) circulates between hot and cold zones. The following heating and cooling compress and expand the gas, causing the piston to move and generating mechanical work. A characteristic element of the design is a regenerator—a heat exchanger that temporarily stores thermal energy and returns it, increasing the cycle's efficiency. A Stirling engine can utilize any external heat source (e.g., biomass combustion, solar concentrators, or waste heat), operates very quietly, and has a potentially high efficiency approaching the limits of the Carnot cycle. In this context, a proposed method for integrating a Stirling engine with a biomass-fired unit is shown in Figure 14.

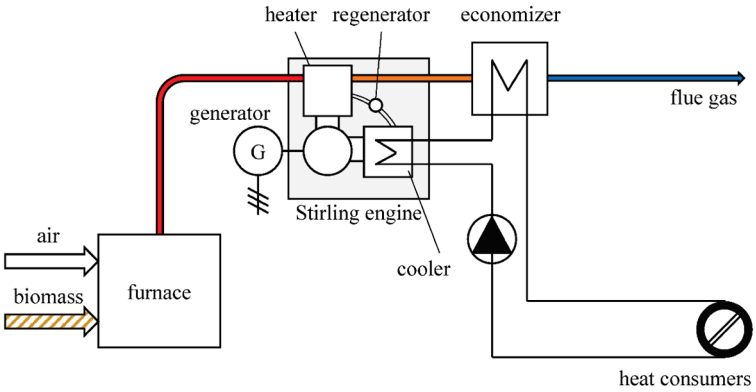


Figure 14. A biomass cogeneration unit with a Stirling engine [93].

Considering practical examples, Cardozo and Malmquist [94] tested a facility comprising a commercial wood pellet burner (20 kW), a prototype Stirling engine (1 kW), and a residential boiler (20 kW). The fuels used were wood and sugar cane bagasse pellets. Bagasse pellets produced more ash, which accumulates on the heat exchanger, thereby decreasing the efficiency of a Stirling engine CHP system compared to wood pellets. Kramens et al. [95] conducted experiments with a solid-biomass micro-CHP unit using a Stirling engine. The results showed that, from 1 kg of wood, 2.23 kWh of thermal energy and 7.84 kWh of electrical energy can be generated. Voronca et al. [93] tested the biomass Stirling micro-cogeneration device to assess its performance. Three heat transfer fluid flow rates and three thermal power outputs were set during the experiments. In the tested micro-CHP system, the DHW temperature was set to 60 °C. An increase in this temperature prevented the medium from absorbing the full thermal power. This caused the device to heat to 75 °C, triggering partial-load mode and reducing electricity production. Furthermore, an improved system—a biomass (wood pellet)-fueled micro-CHP unit—was tested by Borisov et al. [96]. This consisted of a Stirling engine, a two-stage vortex combustion chamber, an enhanced recuperator, and a waste heat-utilizing heat exchanger. The vortex application enhanced mixing in the combustion chamber and improved afterburning in the secondary chamber. The enlarged recuperator area led to a more uniform temperature field and a higher gas temperature. The proposed modifications enabled a 75% increase in the efficiency of a micro-CHP unit, while the Stirling engine achieved 14.8%.

Organic Rankine Cycles: The Organic Rankine Cycle (ORC) is a modification of the classic Rankine Cycle that uses an organic fluid with a lower boiling point instead of water and steam. This enables the efficient conversion of low-temperature heat, such as that from biomass, geothermal energy, exhaust gases, or waste heat, into electricity. In the ORC, the working fluid is heated in a heat exchanger until it reaches its boiling point, at which point it subsequently evaporates. The steam then drives a turbine coupled to a generator, after which it is condensed and returned to the pump, completing the cycle. ORC technology is characterized by high reliability, quiet operation, and the ability to utilize moderate-temperature distributed heat sources, making it an attractive option in renewable energy and energy recovery applications, including biomass-fired appliances. A simplified layout of the biomass-boiler micro-ORC system is shown in Figure 15.

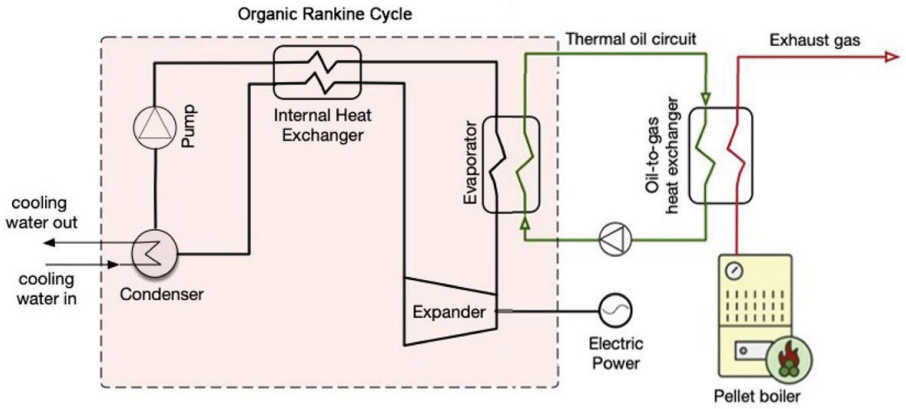


Figure 15. Simplified layout of the biomass-boiler micro-ORC system [97].

Algieri and Morrone [98] investigated a biomass boiler-driven ORC for domestic use as a micro-scale CHP generation system. Three organic fluids were examined, and the feasibility of regeneration was evaluated. The results showed that the choice of organic working fluid is a crucial factor for system performance. The authors achieved a thermal

power of over 14.8 kW (including electric power of 2.2–5.0 kW) for cogeneration. The system was considered a promising solution for small-scale residential applications. Villarino et al. [99] tested four different types of residual biomass in the 60 kW boiler combined with an ORC module. The net electrical power obtained during the test ranged from 3.33 to 3.60 kW, depending on the fuel. The authors report cogeneration yields of nearly 96% under the applied conditions. Furthermore, Falbo et al. [97] performed experimental studies on the energy performance of a biomass-fired recuperative ORC system. The highest net electric power was 2.3 kW (the highest pump speed was 2000 rpm, and the thermal oil temperature was 152.2 °C). The maximum electric efficiency of 8.55% was achieved at a pump speed of 1000 rpm, resulting in a net power output of 1.37 kW. The authors claimed that adjusting the pump speed is crucial for maximizing ORC performance and ensuring proper superheating of the working fluid.

Internal Combustion Engines: Gasification is a thermo-chemical process during which the initial fuel (biomass) is converted into gaseous fuels or chemical feedstock. The reaction is endothermic (requires heat) and takes place in a reducing (oxygen-deficient) atmosphere. Depending on costs and desired products, various media can be used in the process, including air, oxygen, subcritical steam, and mixtures [100].

Among other examples, the system proposed by Wang et al. [101] was driven by a gas-fired boiler, with gas generated from biomass in a biomass gasifier. The water vapor produced in the boiler was used in the CCHP system, which comprised a pumpless power cycle for electricity, a diffusion–absorption refrigeration cycle for cold energy, and heat exchangers for supplying domestic heat. The results indicated that the system is sufficient to meet the energy requirements of a single-family household, with power, cooling, and heating capacities ranging from 400 to 650 W, 500 to 900 W, and 1000 to 5000 W, respectively. The highest obtained energy efficiency was 55.26%. As the heat source temperature increases and the ambient temperature decreases, the system's thermal efficiency improves, resulting in lower costs and reduced CO_2 emissions. The optimal distribution ratios for cooling, heating, and power were studied, and in winter, the highest efficiency was achieved with a 0:5:5 ratio. In the summer, the worst-case scenario was 1.5:1.7.5. Similarly, Sunil et al. [102] developed a hot-water generation system based on a gasifier. The system significantly reduced pollutant emissions and achieved a thermal efficiency twice that of a conventional system with a gasifier and a separate hot water generator. The authors stated that this solution has high potential for residential applications. A single-family house with an area of 240 m^2 was studied by Malaguti et al. [103]. The simulation, conducted using TRNSYS 17, features a small-scale gasifier power plant with 15 kW of electrical power and 20 kW of thermal power. The house has a diesel oil boiler, and a simulation was performed to validate the dynamic model. After that, the biomass boiler and, finally, the two micro-CHP gasifiers were simulated. A biomass boiler is more efficient than diesel oil and costs approximately one-third as much. The micro-CHP gasifier system has lower thermal efficiency due to energy consumption for gasification. It also has a higher fuel cost and consumes electrical energy. On the other hand, it is possible to sell the electrical energy to the electrical grid and heat the house without additional costs. Furthermore, Caliano et al. [104] designed a biomass-fired trigeneration system with thermal energy storage, comprising a CHP unit, an absorption chiller, an auxiliary gas boiler, and electrical chillers. The model referred to a residential multi-apartment building that provided electricity to the external grid, hot water for domestic use, and heating or cooling, depending on the season. The authors evaluated the impact of the incentive for electricity generation on the results, finding that it significantly influences the size of the thermal energy storage system, the absorption chiller, and the cold thermal energy storage system. However, unlike the absorption chiller,

the size of the thermal energy storage system did not significantly affect the economic efficiency of the CCHP process. The authors considered integrating a cold thermal energy storage system as a viable economic solution.

The examples discussed demonstrate the high potential of biomass appliances as a heat source for combined heat and power generation. For small-scale applications, these systems can be used in residential, off-grid, and agricultural and commercial settings. The advantages and disadvantages of biomass-driven CHP systems are shown in Table 4.

Table 4. Comparison of technologies integrated with biomass-driven CHP.

Biomass-Driven CHP Technology	Electrical Efficiency	CHP System Efficiency	Advantages	Limitations
TEG modules	5–10%	90–100%	Power generation in off-grid areas or during power outages; utilization of waste heat; low maintenance; quiet operation	Selection of proper mounting location; efficient cooling needed; possible PM deposition decreases heat transfer; low power generation efficiency
Stirling engines	12–30%	65–90%	Quiet, smooth operation (no combustion in the cylinder)	Requires a stable heat supply; PM deposition on the heat exchanger decreases heat transfer
ORC	1.3–20.1%	70–100%	Stable, mature technology on an industrial scale; possible operation with low temperature heat (100–300 °C)	Complex construction and high specific costs on a small scale
Internal combustion engines	18–23%	75–85%	Highest electrical efficiency on a small scale; mature technology; widely available; fast load response; good regulation	Complex batch operation; continuous operation requires management of excess heat

5. Integration of Biomass into NZEBs

The transition toward NZEBs requires integrating renewable energy sources and high-efficiency thermal systems to meet building energy demands with minimal environmental impact. Biomass, as a dispatchable, carbon-neutral energy carrier, offers a valuable complement to intermittent renewables such as solar and wind, particularly in climates with significant seasonal variability and during peak thermal demand. To enhance system flexibility and performance, biomass is increasingly deployed in hybrid configurations alongside solar thermal collectors, electrically driven heat pumps, and TES. These multivalent systems enable dynamic load management, improved combustion conditions, and higher shares of renewable energy. In particular, bivalent-parallel and bivalent-series arrangements allow for strategic operation: the former prioritizes heat pumps above a switchover temperature with biomass support during peak loads, while the latter utilizes heat pumps for preheating and biomass for final temperature elevation or thermal pasteurization. Effective integration requires the careful selection of bivalence points, weather-compensated control algorithms, and stratified storage design to minimize cycling losses, enhance overall system efficiency, and reduce pollutant emissions associated with frequent ignition or idle phases of solid-fuel appliances.

5.1. Integration of Biomass Appliances with Heat Pumps

Integrating biomass boilers with electrically or thermally driven heat pumps leverages the high seasonal efficiency of heat pumps operating at low supply temperatures while preserving the flexibility of biomass systems to cover peak demand and cold-weather conditions. Two main configurations are commonly used. In bivalent-parallel systems, the heat pump operates as the primary heat source above a defined switchover temperature, with the biomass boiler supplementing during peak loads. In bivalent-series systems, the heat pump preheats a stratified thermal buffer, and the biomass unit raises the temperature to the final setpoint or performs thermal pasteurization. Optimizing the bivalence point, applying weather-compensated control strategies, and using stratified thermal storage help minimize cycling of both units, enhance overall system efficiency, and reduce pollutant emissions typically associated with frequent ignition or idle phases of solid-fuel appliances.

Bellos et al. [105] investigated a biomass-driven absorption heat pump for heating and cooling a simulated 400 m^2 residential building in Athens, Greece. The system was based on a single-effect LiBr–H_2O absorption chiller, modified to provide winter heating, and was coupled, for the first time, with a biomass boiler. Compared with conventional oil boiler and electric heat pump setups, the proposed system achieved 10.8% lower operational costs, a 4.8% reduction in primary energy demand, and notable reductions in CO_2 emissions. An experimental facility consisting of a pellet boiler and a hydrothermal heat pump was developed by Lee et al. [106] for smart farm heating. In comparison with a pellet boiler alone, the hybrid system offers higher thermal efficiency and lower operating costs. Uche et al. [107] simulated several systems—including an air-to-water heat pump, a biomass boiler, and their integration—for a residential building of 150 m^2 in Spain. The hybrid system was found to be more effective in terms of energy efficiency, economics, and environmental considerations. The authors also studied different configurations of hybrid heat pump systems. In a serial system, an 8 kW pump yields the best results, while in a parallel system, a 4 kW pump performs better. The pump size also affects the number of on/off cycles for both the pump and the biomass boiler. In Ref. [108], the previous system was further analyzed, highlighting its dependence on the climate zone. Moreover, the authors emphasized the importance of building insulation in reducing costs.

Hebenstreit et al. [109] evaluated an active condensation system designed to recover heat from biomass boiler flue gases by integrating a quench unit with a compression heat pump. The system was modeled using mass and energy balances and assessed across four Austrian-based test cases: two pellet boilers (10 kW and 100 kW) and two wood chip boilers (100 kW and 10 MW). The results indicated reductions in operating costs of 2% to 13% and improvements in primary energy efficiency of 3% to 21%. Westerlund et al. [110] tested a novel energy recovery method that also reduces particulate emissions from flue gas in small biofuel boilers. By integrating an open absorption system into the heat production unit, both environmental impact and thermal efficiency were improved. Over a 2-year experimental period, the system achieved a 33–44% reduction in flue gas particle emissions compared to conventional setups. Additionally, when using wet biofuels, heat output increased by 40%, demonstrating the dual benefit of enhanced performance and lower emissions.

Although there are few studies on single houses, there are a few on district-scale solutions. For example, Drofenik et al. [111] examined a hybrid energy system that combines a micro-CHP unit (16 kW thermal power, 6.5 kW electrical power) fueled by biogas from local food waste with a heat pump (6.5 kW electrical input, 28.5 kW thermal output). Designed for integration into existing heating networks in Slovenian communities of up

to 40,000 households, the system primarily targets DHW supply while replacing fossil-based sources. A simulation of a 3300-household community conducted with Aspen Plus showed that the hybrid setup can deliver more than twice the thermal output compared to the standalone micro-CHP. Economic analysis revealed a payback period of 7.2 years at a heat price of 80 EUR/MWh, which could be reduced to 3 years when scaled to serve 40,000 households. Hou et al. [112] conducted a performance and cost analysis of a centralized hybrid heating system serving a rural community in eastern China, with an annual heating demand of approximately 2 GWh. The system comprises a 310 kW geothermal heat pump, a 251 kW air-source heat pump, a 500 kW biomass boiler, and a thermal storage tank. Using TRNSYS simulations, the study compared the hybrid configuration to the standalone operation of each device. Over a one-year simulation, the heat supply distribution was 47% from the geothermal heat pump, 35% from the BB, and 18% from the air-source heat pump. The hybrid system demonstrated superior economic and energy performance, reducing operating costs by 9.6%, 14.2%, and 11.7% compared to the standalone geothermal heat pump, air-source heat pump, and biomass boiler, respectively. It also achieved the lowest power consumption, requiring only 34.3% of the biomass fuel compared to the standalone biomass boiler. Carotenuto et al. [113] developed a hybrid energy model for a low-temperature district heating and cooling system in Pozzuoli, Italy, integrating solar thermal, geothermal energy, and a wood-chip biomass boiler as an auxiliary source. The system was evaluated on both energy and economic grounds. Energy analysis revealed that the combined use of geothermal and solar sources is sufficient to meet winter heating demands. However, during summer, the biomass boiler becomes essential to achieve the elevated set-point temperatures required to operate an adsorption chiller for cooling. The system demonstrated solar thermal efficiency exceeding 40% and achieved primary energy savings of up to 75%.

5.2. Integration of Biomass Appliances with Solar Energy

In general, there are two basic options for integrating biomass-fired appliances and solar energy devices: combining them with solar thermal or photovoltaic systems. In solar–biomass combined systems, solar thermal energy is prioritized to charge a stratified storage tank, meeting domestic hot water (DHW) needs and space heating requirements during the shoulder seasons. The biomass boiler complements the system by meeting residual demand and peak loads in winter. Advanced hydraulic configurations—featuring multi-port stratified tanks and external heat exchangers—maximize solar contribution while ensuring efficient biomass combustion through longer, hotter, and less frequent firing cycles. Control strategies that postpone biomass activation until specific tank node temperatures drop below set thresholds help minimize fuel use and emissions, while maintaining DHW hygiene through periodic thermal pasteurization. On the other hand, PV installations can offset electrical auxiliaries (such as fans, augers, and pumps) and supply heat to heat pumps or biomass-fired boilers. When PV surpluses occur, power-to-heat via heat pumps (rather than resistive dumping) typically yields higher exergy efficiency. Dispatch strategies benefit from price-aware control that coordinates PV availability, battery state of charge, heat-pump COP, and biomass firing constraints. Furthermore, the combination of solar and biomass technologies is gaining popularity, particularly with different types of tri- and polygeneration systems. This approach enables the design of self-sufficient residential buildings that use renewable energy sources. Below, the innovative systems proposed in recent years are discussed.

Zhang et al. [114] presented a comprehensive analytical and experimental investigation of a solar/biomass space-heating system integrating microchannel solar thermal

panels and a biomass boiler, supported by a dedicated control algorithm. The system enabled the coordinated use of solar and biomass energy to maintain indoor thermal comfort. Experimental testing was conducted in situ, and data analysis using the Grubbs method yielded equations for solar panel thermal efficiency and the heat conversion factor of the combined storage/exchange tank. Annual performance was simulated in EnergyPlus for a 100 m^2 residential building, yielding a total heating-season demand of 24.3 GJ and an annual energy requirement of 35.91 GJ. Solar energy contributed 63.31% of the total energy, while biomass accounted for 36.69%. Compared to conventional systems, the proposed hybrid configuration demonstrated superior energy conversion and utilization performance, offering both economic and environmental benefits. The hot-water and space-heating system for the Hammam building in Marrakesh, Morocco, was proposed by Krarouch et al. [115]. The small pellet boiler was combined with three types of solar thermal systems (evacuated tube, flat plate, and parabolic trough collectors). The simulation was created using TRNSYS, and the model's thermodynamic efficiency, environmental impact, and profitability were assessed. Furthermore, the authors reported that hemp insulation on walls and roofs reduced heating demand by 36%. The optimal collector areas were 204 m^2 for parabolic trough collectors (PTC), 224 m^2 for flat plate collectors (FPC), and 300 m^2 for evacuated tube collectors (ETC). Such areas have the lowest levelized cost of heat (LCOH), at 0.0755, 0.0696, and 0.0642 USD/kWh, respectively. For the optimal system, the annual solar fractions were 36%, 42%, and 57%, respectively. In conclusion, the most effective configuration was a combination of evacuated tube collectors, resulting in an annual CO_2 reduction of 656 tons and a payback period of almost 5 years. A hybrid solar–biomass micro-CHP system designed to meet the thermal and electrical energy demands of ten apartments in a multi-family building in Athens was proposed by Skiadopoulos et al. [116]. The components of the unit were a biomass boiler, evaporated tube collectors (ETC), a partially evaporating Organic Rankine Cycle PEORC engine (prime mover), a natural gas boiler, a thermal energy storage tank, and an air-cooled condenser. ETCs are the main heat source, and the biomass boiler takes over when evaporator operation is insufficient in the PEORC. The thermal energy storage tank was designed to compensate for differences between the heat generated by the building and its space heating demand. For the computational analysis of the unit, a numerical model was developed, and the techno-economic performance and environmental impact of the system were assessed. The simulation results were promising—over 97% of annual space heating demand and over a quarter of electricity demand were covered by RES. Collectors provided 10.81% of the energy needed for micro-CHP operation during the heating period. Moreover, the application of the micro-CHP system has a positive environmental impact, reducing the annual carbon footprint by 31.22 kg CO_2-eq. per m^2 and saving 46.58 kWh of primary energy per m^2. Nonetheless, the authors emphasized the need for further research, including system behavior during startups and shutdowns, the application of numerical models across various locations, and the establishment of an experimental facility. The evacuated-tube solar thermal collectors were also chosen by Prieto et al. [117] for a simulated hybrid system to heat and cool a greenhouse in Spain. The system, composed of solar thermal collectors, a biomass boiler, and an air-cooled absorption chiller, controlled the greenhouse environment. Based on a validated model (using the TRNBuild tool), the annual heating and cooling demands were calculated at 26.37 kWh/m^2 and 61.97 kWh/m^2, respectively. Due to the excessively high temperatures from May to October, the greenhouse is forced to stop production. However, the proposed system can operate year-round. During spring and autumn, the collector's heat output exceeds demand and could be used for other purposes or for better control of conditions. What is important is that the annual solar energy share was almost 55% and

that for 4 months it reached 100%. In July and August, it slightly exceeded 40%, raising questions about the profitability of greenhouse operations during these months (due to high biomass consumption). It was also suggested that a water tank is crucial during the winter months, as available solar energy and heating demand are significantly limited.

Borri et al. [118] performed the Life Cycle Assessment of an innovative solar–biomass hybrid system for residential applications—SolBio-Rev. This project was EU-funded and supports the development of solar–biomass systems to provide heating, cooling, domestic hot water, and electricity. The authors focused on a multi-family house located in a continental climate, based on questionnaires collected for each component. IPCC (GWP100a) and ReCiPe were chosen as indicators for the evaluation on environmental impact. The system configuration consisted of solar collectors with integrated thermoelectric generators, short-term storage, and a thermal buffer tank; a reversible heat pump/ORC; a biomass boiler; and a dry cooler. The impact of each component was reported with and without considering the operational phase. The components with the greatest impact during manufacturing were the dry cooler, solar collectors, and a reversible heat pump/ORC. The highest share of CO_2 emissions occurred during the operational phase. To reduce the total impact, the efficiency of components and the share of energy supplied by renewables should be increased. The authors claimed that removing solar collectors decreases the environmental impact during manufacturing; however, increased energy consumption for heating during operation offsets this reduction, resulting in a net increase in environmental impact.

Liu et al. [119] proposed a novel hybrid energy system that combines biomass torrefaction, a biomass gasification subsystem, solar heat collection, and absorption refrigeration technology, providing cooling, heating, hot water, and gas supply for a building with an area of 4000 m^2. The authors studied various operating parameters and their effects on gasification products and conducted an economic analysis. The solar system consisted of a metal heat pipe vacuum collector tube with a collecting area of 560 m^2. The biomass raw material used in the tests was corn straw. The impact of torrefaction temperature on the composition of the gasification gas was studied. With increasing temperature, the content of CO and CH_4 increased, while H_2 and CO_2 decreased, improving the gasification process and the quality of the gasification gas and reducing tar content. The ratio of steam to biomass was also studied, and an increase in H_2 and CO_2 content was reported with an increase in the ratio from 0.4 to 1.6. Moreover, exergy and economic analysis were combined to assess the system exergy flow cost and calculate the unit exergy cost of system products. The results showed that the biomass gasifier accounted for almost 50% of the total exergy loss in the gasification system, and the gas boiler accounted for almost 25%. According to the economic analysis, the proposed system's payback period was 2.89 years. The authors summarized the analysis by calculating the energy and carbon dioxide emissions savings of over 1 million MJ and over 550 tons, respectively, over its lifespan. Such a conclusion demonstrates this system's economic and practical value for people's health, environmental protection, and energy conservation.

The system, comprising a photovoltaic-thermal (PVT) collector, a biomass-fired vapor-compression desalination system, and a floor heating system, was simulated by Zhu et al. [120]. The PVT collector supplied both thermal and electrical energy, and hot water was transported into a storage tank equipped with a heat exchanger. During periods of insufficient PVT collector operation, the biomass boiler supplied heat to the VC desalination system and the floor heating system. The heat was transferred from the PVT collectors to the storage tank heat exchanger, and then the temperature was increased in the biomass boiler to meet the system's thermal energy requirements.

The system's simulation was performed using TRNSYS 18 software to evaluate its performance under various conditions, thereby maximizing efficiency and effectiveness. The authors recognized the system's advantages, including its independence from the grid and its ability to provide freshwater in Riyadh, Doha, and Abu Dhabi. The system also provided heat for residential heating, which is another factor that increases living comfort, as indicated by the PMV and PPD metrics. Moreover, the system's ability to provide electrical energy for the desalination process was assessed. The factor calculated for assessment was the Power Ratio, defined as the ratio of the electrical power generated by the PVT collector to the electrical energy required by the desalination system. The highest average Power Ratio, at 2.35, was reported for Riyadh. Shirazi et al. [121] modeled a residential building of ten apartments in Toronto, Canada, and designed separate systems: a biomass-driven system and a solar-based system integrated with an air-to-water heat pump, both equipped with a thermal energy storage tank. The primary objective was to develop an automation system that manages energy transfer between the system, the grid, and the building. Efficiency, CO_2 emissions, capital costs, and the levelized cost of energy were evaluated. The biomass system has lower energy costs—36.7 USD/MWh—than the solar-heat pump system (78.9 USD/MWh). Moreover, the biomass system was 36% more efficient. The authors noted that a decrease in room temperature at night can reduce energy consumption and CO_2 emissions by 60.3 MWh and 21.1 t annually, respectively (at a 4 °C decrease). It was also found that the excess electrical energy from the solar system could be sold to the grid for almost a quarter of the year. Furthermore, Nami et al. [122] proposed and analyzed a solar-assisted, biomass-based, tri-generation system designed to meet domestic energy needs, which was evaluated using thermodynamic and sustainability metrics. The system integrated gas and steam turbines for electricity generation, while a chiller and auxiliary heat exchanger utilized residual thermal energy for cooling and heating. A pressurized water circuit recovered waste heat from the steam condenser and concentrated photovoltaic units to support space heating. Exergy analysis identified key sources of irreversibility within the system, and parametric studies assessed the impact of seasonal conditions and design variables. The system demonstrated the capacity to deliver 1 MW of electricity, 1241 kW of space heating, 101.5 kW of domestic hot water, and 55.35 kW of cooling.

A brief summarization of the discussed solar–biomass integrated technologies is shown in Table 5.

Table 5. Summary of the discussed solar–biomass integrated technologies.

Reference	Type of Solar–Biomass System	Type of Research	Components of the System
Zhang et al. [114]	Space heating	Experimental and simulation	Micro-channel solar thermal panel array, a biomass boiler, and a dedicated control algorithm.
Krarouch et al. [115]	Hot water and space heating	Simulation	Small biomass pellet boilers in combination with three types of solar thermal systems (evacuated tube, flat plate, and parabolic trough collectors).
Skiadopoulos et al. [116]	cogeneration	Simulation	Biomass boiler, evaporated tube collectors (ETC), partially evaporating Organic Rankine Cycle PEORC engine (prime mover), natural gas boiler, thermal energy storage tank, and an air-cooled condenser.

Table 5. *Cont.*

Reference	Type of Solar–Biomass System	Type of Research	Components of the System
Prieto et al. [117]	Heating and cooling	Simulation	Evacuated-tube solar thermal collectors, a biomass boiler, and an air-cooled absorption chiller with ammonia/lithium nitrate as a working mixture.
Borri et al. [118]	trigeneration	Simulation (LCA)	Solar collectors with integrated thermoelectric generators, short-term storage and thermal buffer tank, reversible heat pump/ORC; biomass boiler and dry cooler.
Liu et al. [119]	trigeneration	Simulation	Biomass torrefaction reactor, biomass gasification subsystem, solar heat collectors, and absorption refrigerator.
Zhu et al. [120]	trigeneration	Simulation, partially experimental	Photovoltaic-thermal (PVT) collector, a biomass boiler, a vapor-compression (VC) desalination system, and a floor heating system, along with auxiliary components such as pumps, heat exchangers, a storage tank, and a battery.
Nami et al. [122]	Heating, cooling, and power	Simulation	Gas turbine, a steam Rankine power block, a chiller unit, concentrated photovoltaic thermal (CPVT) panels, and an auxiliary heat exchanger.
Palomba et al. [123]	heating, cooling, and DHW	Simulation	Solar thermal collectors with thermoelectric generators; a sorption module; a reversible heat pump/ORC, and a biomass boiler.
Altayib and Dincer [124]	Heating, power, and freshwater	Simulation	Multi-staged steam Rankine Cycle, with the steam generator energized via heat transfer from hot biomass combustion gases and hot solar thermal oil, and a multi-effect desalination unit energized with thermal energy recovered from hot flue gases.
Wang et al. [125]	Heating, cooling, and power	Simulation	PVT panels, cogenerating heating and electricity, a biomass-fired heater, two heat exchangers connected to either radiator for space heating or the double-effect absorption chiller for space cooling, and a thermal energy storage tank.
Sabbaghi et al. [126]	Heating, cooling, and power	Simulation	Solar thermal collector, a biomass-fired boiler, heat recovery exchangers, a turbine, a condenser, an evaporator, a pump, and an ejector.

6. Future Challenges and Chances

Since many of the examples discussed in this paper are mature and widely available—such as pellet boilers, wood-chip boilers, logwood gasification boilers, straw boilers, and local space heaters—there are also numerous technologies currently under development. The exact Technology Readiness Level (TRL) depends on individual factors. For instance, when considering extending the functionality of biomass-fired appliances through combined heat and power generation, both emerging and commercially available solutions can be identified. Furthermore, although simple integrations of biomass-fired appliances with heat pumps, solar thermal collectors, or photovoltaic modules are already commercialized, various research efforts aim to further enhance these systems by incorporating electricity generation (e.g.,

through thermoelectric generators or Organic Rankine Cycle units) or cooling functionalities. These options are at different stages of technological maturity. As indicated in this review, the analyzed examples can generally be classified between TRL 2 (where basic principles have been studied) and TRL 7 (where a working model or prototype has been demonstrated in an operational environment). Despite this progress, many areas within biomass-fired appliances for the residential sector remain worthy of future investigation.

The further development of biomass technologies is facing numerous challenges. Older local space heaters and boilers account for the majority of PM2.5 emissions into the atmosphere, posing a risk to human health. Many biomass-fired appliances are manually loaded, requiring frequent user intervention. Even automatically supplied pellets or wood chips need to be periodically loaded into the storage tank. Staying on the topic of fuel, biomass, as a low-energy-density fuel, requires significant storage volume and proper seasoning and preparation. For city residents, such a challenge may be unmanageable. Biomass-driven cogeneration units usually have low electrical efficiency (<10%) and high costs. Nevertheless, various opportunities should be specified. Reducing emissions from biomass-fired appliances can achieve near-zero emissions. Several emission reduction methods have already been described in this review. In the context of local space heaters, a periodic pellet gasifier can be integrated into a traditional combustion chamber, enabling the combustion of in situ-generated wood gas, thereby significantly reducing pollutant emissions and increasing efficiency [71]. To avoid conflict with the food industry and forestry, the emphasis should be on developing biomass fuels from waste and residues, including food waste. Another potential improvement is the application of AI-assisted modeling to optimize combustion and heat transfer in heating installations. A general summary of the challenges and opportunities of biomass residential technologies is presented in Table 6.

Table 6. Summary of challenges and opportunities of biomass residential technologies.

Challenges	Explanation	Chances	Explanation
Air quality	Legacy stoves and boilers remain a major source of PM2.5	Near-zero-emission	Pellet boilers with ESPs and catalytic afterburners are expected to dominate new installations
User effort	Manual logwood boilers require frequent handling; pellet systems reduce, but do not eliminate, maintenance	Fuel diversification	Agro-pellets and residue-based fuels are under development, though ash and slagging issues remain
Logistics	Fuel storage underscores can be a barrier in urban areas	Smart controls	AI-driven combustion optimization
Economics	Higher capital costs compared to fossil fuel boilers and heat pumps; competitiveness depends on fuel prices and subsidies	Hybridization	Coupling with PV + batteries for energy self-sufficiency
Residential CHP	Low electrical efficiencies (<10%) and high costs limit current market uptake	Residential CHP	Further R&D on Stirling engines and thermoelectric modules is expected, with a focus on reliability, cost reduction, and integration with smart grids.
Environmental law	Strict regulations concerning efficiency and emission levels	Policy push	National subsidy schemes and replacement programs, accelerating turnover from old, polluting appliances to modern low-emission systems.

The energy potential of biomass enables the development of a wide range of projects that aim to generate both heat and electricity. Solid biomass can be directly converted into stoves, boilers, and CHP units. At the same time, biochemical and thermochemical processes enable the production of gaseous fuels, such as biogas and syngas, as well as liquid biofuels, including bioethanol and biodiesel [127]. These diverse conversion pathways make biomass a versatile energy carrier that can meet demand at various scales. One particularly effective strategy for harnessing local biomass resources is their integration into decentralized energy systems, such as individual buildings equipped with modern biomass boilers or pellet stoves, as well as collective solutions organized within local energy clusters. Such clusters can optimize resource use by balancing supply and demand among multiple users, improving efficiency and resilience. In this context, the concept of Nearly Zero-Energy Districts (NZEDs) is especially relevant, as biomass can complement other renewable sources—such as solar and wind—by providing dispatchable, low-carbon heat and power, thereby enhancing the overall sustainability and self-sufficiency of urban and rural communities alike [128]. General recommendations for the further development of biomass-fired applications are summarized in Table 7.

Table 7. General recommendations for the further development of biomass-fired applications.

Technology	Recommendation
Emission reduction technologies	Numerical simulations for construction improvements, machine learning
Combustion and control advances	Optimization by means of AI-assisted tools, machine learning in combustion process control
Biomass-driven cogeneration	Heat-transfer improvements for higher efficiency of the unit and power generation, integration with smart grids
Integration with heat pumps	Optimizing the bivalence point, applying weather-compensated control strategies, and using stratified thermal storage
Integration with solar energy	Development of multi-port stratified tanks and external heat exchangers, improvements in control strategies

7. Conclusions

Solid biomass remains an important energy source for many households worldwide. Due to its wide availability, wood remains irreplaceable in many regions. However, since the dangers associated with biomass combustion—mainly gaseous pollutants and particulate matter—are well known, there is a need to develop existing technologies further and design new systems.

The papers selected for this review are clearly related to household appliances used primarily for heating. The existing biomass technologies are summarized first, covering boilers and local space heaters. The review then focuses on advances in biomass-fired heating systems, including methods to reduce pollutant emissions, improve combustion and control, and develop integrated cogeneration capabilities. Finally, the integration of biomass into nearly zero-energy buildings is discussed, distinguishing between systems combined with heat pumps and those integrated with solar energy. Biomass appliances—which are becoming increasingly cleaner, more efficient, and less maintenance-intensive—are meeting legal and social requirements while competing with modern heating technologies. The

continuous development of established systems, along with their proposed combinations and integration with other technologies, highlights their ongoing potential and relevance. The final section analyzes current challenges and future opportunities, outlining directions for further development.

Biomass heating technologies have traditionally faced challenges such as fuel storage and preparation, appliance maintenance, and relatively low efficiency. Nevertheless, the literature provides solutions for each of these issues. The authors identify opportunities to enhance operational independence through automation and the development of micro-CHP technologies, thereby increasing energy security. AI-assisted tools and numerical simulations are also considered promising for improving the design and performance of future biomass technologies.

Author Contributions: Conceptualization, J.K. and K.S.; methodology, J.K. and K.S.; formal analysis, J.K.; investigation, J.K.; writing—original draft preparation, J.K. and K.S.; writing—review and editing, J.K. and K.S.; supervision, K.S.; project administration, K.S. All authors have read and agreed to the published version of the manuscript.

Funding: This work was carried out under Subvention no. 16.16.210.476 from the Faculty of Energy and Fuels, the AGH University of Krakow. This research project was partly supported by the program "Excellence initiative—research university" for the AGH University.

Data Availability Statement: No new data were created or analyzed in this study.

Conflicts of Interest: The authors declare no conflict of interest.

References

1. Regulation (EU) 2021/1119 of the European Parliament and of the Council of 30 June 2021. Available online: https://eur-lex.europa.eu/eli/reg/2021/1119/oj/eng (accessed on 19 September 2025).
2. Eurostat Energy Consumption in Households. Available online: https://ec.europa.eu/eurostat/statistics-explained/SEPDF/cache/58200.pdf (accessed on 19 September 2025).
3. IARC Working Group on the Evaluation of Carcinogenic Risks to Humans. Household Use of Solid Fuels and High-Temperature Frying. *IARC Monogr. Eval. Carcinog. Risks Hum.* **2010**, *95*, 1.
4. U.S. Energy Information Administration Residential Energy Consumption Survey 2020, Housing Characteristics. 2022. Available online: https://www.eia.gov/consumption/residential/data/2020/ (accessed on 19 September 2025).
5. Vassilev, S.V.; Baxter, D.; Andersen, L.K.; Vassileva, C.G.; Morgan, T.J. An Overview of the Organic and Inorganic Phase Composition of Biomass. *Fuel* **2012**, *94*, 1–33. [CrossRef]
6. Tursi, A. A Review on Biomass: Importance, Chemistry, Classification, and Conversion. *Biofuel Res. J.* **2019**, *6*, 962–979. [CrossRef]
7. Ali, F.; Dawood, A.; Hussain, A.; Alnasir, M.H.; Khan, M.A.; Butt, T.M.; Janjua, N.K.; Hamid, A. Fueling the Future: Biomass Applications for Green and Sustainable Energy. *Discov. Sustain.* **2024**, *5*, 156. [CrossRef]
8. Di Fraia, S.; Shah, M.; Vanoli, L. Biomass Polygeneration Systems Integrated with Buildings: A Review. *Sustainability* **2024**, *16*, 1654. [CrossRef]
9. World Bioenergy Association. *Global Bioenergy Statistics Report 2024*, 11th ed.; World Bioenergy Association: Stockholm, Sweden, 2024; p. 45.
10. Nakada, S.; Saygin, D.; Gielen, D. Global Bioenergy Supply and Demand Projections. A Working Paper for REmap 2030. *Irena* **2014**, *5*, 88.
11. EUBIA Bioenergy Production Potential. Available online: https://www.eubia.org/cms/wiki-biomass/bioenergy-production-potential/ (accessed on 29 September 2025).
12. Nearly-Zero Energy and Zero-Emission Buildings. Available online: https://energy.ec.europa.eu/topics/energy-efficiency/energy-performance-buildings/nearly-zero-energy-and-zero-emission-buildings_en (accessed on 29 September 2025).
13. Harkouss, F.; Fardoun, F.; Biwole, P.H. Optimization Approaches and Climates Investigations in NZEB—A Review. *Build. Simul.* **2018**, *11*, 923–952. [CrossRef]
14. Garrison, F.H. The History of Heating, Ventilation Andd Lighting. *N. Y. Acad. Med.* **1927**, *III*, 57–67. [CrossRef]
15. Sikkema, R.; Steiner, M.; Junginger, M.; Hiegl, W.; Hansen, M.T.; Faaij, A. The European Wood Pellet Markets: Current Status and Prospects for 2020. *Biofuels Bioprod. Biorefining* **2011**, *5*, 250–278. [CrossRef]

16. Nocoń, A.; Jachimowski, A.; Koniuch, W.; Pełka, G.; Luboń, W.; Kubarek, P.; Jach-Nocoń, M.; Dawiec, D. Analysis of the Energy and Emission Performance of an Automatic Biomass Boiler in the Context of Efficient Heat Management. *Energies* **2024**, *17*, 5885. [CrossRef]
17. Jach-Nocoń, M.; Pełka, G.; Luboń, W.; Mirowski, T.; Nocoń, A.; Pachytel, P. An Assessment of the Efficiency and Emissions of a Pellet Boiler Combusting Multiple Pellet Types. *Energies* **2021**, *14*, 4465. [CrossRef]
18. *PN-EN 303-5:2012*; Heating Boilers. Heating Boilers for Solid Fuels, Manually and Automatically Stoked, Nominal Heat Output of up to 500 kW. Terminology, Requirements, Testing and Marking. Polish Committee for Standardization: Warsaw, Poland, 2012.
19. Schön, C.; Kuptz, D.; Mack, R.; Zelinski, V.; Loewen, A.; Hartmann, H. Influence of Wood Chip Quality on Emission Behaviour in Small-Scale Wood Chip Boilers. *Biomass Convers. Biorefinery* **2019**, *9*, 71–82. [CrossRef]
20. Lee, H.H.; Kang, S.B.; Choi, J.J.; Youn, Y.J.; Kim, K.W.; Jeong, M.S.; Byeon, J.K. Co-Firing Combustion Characteristics of Woodchips and Spent Mushroom Substrates in a 400 kWth Stoker-Type Boiler. *Energies* **2022**, *15*, 9096. [CrossRef]
21. Rector, L.; Miller, P.J.; Snook, S.; Ahmadi, M. Comparative Emissions Characterization of a Small-Scale Wood Chip-Fired Boiler and an Oil-Fired Boiler in a School Setting. *Biomass Bioenergy* **2017**, *107*, 254–260. [CrossRef]
22. Trojanowski, R.; Butcher, T.; Fthenakis, V. The Impact of Fuel Type and Burn Phase on Combustion-Related Emissions and Efficiency of Woodchip-Fired Boilers. *Energy Fuels* **2024**, *38*, 21308–21321. [CrossRef]
23. Tucki, K.; Orynycz, O.; Wasiak, A.; Swic, A.; Mieszkalski, L.; Wichlacz, J. Low Emissions Resulting from Combustion of Forest Biomass in a Small Scale Heating Device. *Energies* **2020**, *13*, 5495. [CrossRef]
24. Hopan, F.; Chmelář, M.; Kremer, J.; Dej, M.; Vojtíšek-Lom, M.; Vicente, E.D.; Ryšavý, J.; Krpec, K.; Kuboňová, L.; Molčanov, A.; et al. In-Situ Investigation of Real-World Emissions from 111 Measurements on Solid Fuel Household Boilers. *Sci. Total Environ.* **2025**, *981*, 179564. [CrossRef]
25. Valíček, J.; Palková, Z.; Harničárová, M.; Kušnerová, M.; Lukáč, O. Thermal and Performance Analysis of a Gasification Boiler and Its Energy Efficiency Optimization. *Energies* **2017**, *10*, 1066. [CrossRef]
26. Sornek, K.; Filipowicz, M. A Study of the Applicability of a Straw-Fired Batch Boiler as a Heat Source for a Small-Scale Cogeneration Unit. *Chem. Process Eng.-Inz. Chem. I Proces.* **2016**, *37*, 503–515. [CrossRef]
27. Sornek, K. Prototypical Biomass-Fired Micro-Cogeneration Systems—Energy and Ecological Analysis. *Energies* **2020**, *13*, 3909. [CrossRef]
28. Motyl, P.; Wikło, M.; Bukalska, J.; Piechnik, B.; Kalbarczyk, R. A New Design for Wood Stoves Based on Numerical Analysis and Experimental Research. *Energies* **2020**, *13*, 1028. [CrossRef]
29. Commission Regulation (EU) 2015/1185 of 24 April 2015 implementing Directive 2009/125/EC of the European Parliament and of the Council with regard to ecodesign requirements for solid fuel local space heaters. *Off. J. Eur. Union* **2015**, *193*, 1–19.
30. Suhonen, H.; Laitinen, A.; Kortelainen, M.; Koponen, H.; Kinnunen, N.; Suvanto, M.; Tissari, J.; Sippula, O. Novel Fine Particle Reduction Method for Wood Stoves Based on High-Temperature Electric Collection of Naturally Charged Soot Particles. *J. Clean. Prod.* **2021**, *312*, 127831. [CrossRef]
31. Kantová, N.Č.; Backa, A.; Čaja, A.; Jandačka, J. Effect of Fuel Feeding Cycle Adjustments on Emissions in Spruce Pellet Combustion with the Application of a Four-Tube Electrostatic Precipitator. *Sci. Rep.* **2025**, *15*, 25988. [CrossRef]
32. Coccia, V.; Temporim, R.B.L.; Paglianti, A.; Di Giuseppe, A.; Cotana, F.; Nicolini, A. Energy and Environmental Valorisation of Residual Wood Pellet by Small Size Residential Heating Systems. *Sustainability* **2025**, *17*, 3814. [CrossRef]
33. Blumberga, D.; Priedniece, V.; Kalniņš, E.; Kirsanovs, V.; Veidenbergs, I. Small Scale Pellet Boiler Gas Treatment in Fog Unit. *Int. J. Energy Environ. Eng.* **2021**, *12*, 191–202. [CrossRef]
34. Butcher, T.A.; Trojanowski, R. Effect of Thermal Storage on the Emissions and Efficiency Performance of a Wood-Pellet-Fired Residential Boiler. *ACS Omega* **2020**, *5*, 28517–28528. [CrossRef]
35. Wang, K.; Satyro, M.A.; Taylor, R.; Hopke, P.K. Thermal Energy Storage Tank Sizing for Biomass Boiler Heating Systems Using Process Dynamic Simulation. *Energy Build.* **2018**, *175*, 199–207. [CrossRef]
36. Ozgen, S. Methods for Particulate Matter Emission Reduction from Pellet Boilers. *Biomass Convers. Biorefinery* **2024**, *14*, 8189–8213. [CrossRef]
37. Lamberg, H.; Sippula, O.; Tissari, J.; Virén, A.; Kaivosoja, T.; Aarinen, A.; Salminen, V.; Jokiniemi, J. Operation and Emissions of a Hybrid Stove Fueled by Pellets and Log Wood. *Energy Fuels* **2017**, *31*, 1961–1968. [CrossRef]
38. Loprete, J.; Trojanowski, R.; Butcher, T.; Longtin, J.P.; Assanis, D. Automated, Intelligently Modulating Stoves (Aims) to Reduce Residential Space Heating Emissions. In Proceedings of the 8th Thermal and Fluids Engineering Conference (TFEC), College Park, MD, USA, 26–29 March 2023; Begellhouse: Danbury, CT, USA, 2023; pp. 183–191.
39. Eo, J.W.; Kim, M.J.; Jeong, I.S.; Cho, L.H.; Kim, S.J.; Park, S.; Kim, D.H. Enhancing Thermal Efficiency of Wood Pellet Boilers by Improving Inlet Air Characteristics. *Energy* **2021**, *228*, 120475. [CrossRef]

40. Zadravec, T.; Rajh, B.; Kokalj, F.; Samec, N. Influence of Air Staging Strategies on Flue Gas Sensible Heat Losses and Gaseous Emissions of a Wood Pellet Boiler: An Experimental Study. *Renew. Energy* **2021**, *178*, 532–548. [CrossRef]
41. Deng, M.; Li, P.; Shan, M.; Yang, X. Optimizing Supply Airflow and Its Distribution between Primary and Secondary Air in a Forced-Draft Biomass Pellet Stove. *Environ. Res.* **2020**, *184*, 109301. [CrossRef]
42. Polonini, L.F.; Petrocelli, D.; Lezzi, A.M. The Effect of Flue Gas Recirculation on CO, PM and NOx Emissions in Pellet Stove Combustion. *Energies* **2023**, *16*, 954. [CrossRef]
43. Kardaś, D.; Wantuła, M.; Pieter, S.; Kazimierski, P. Effect of Separating Air into Primary and Secondary in an Integrated Burner Housing on Biomass Combustion. *Energies* **2024**, *17*, 4648. [CrossRef]
44. Carvalho, R.L.; Vicente, E.D.; Tarelho, L.A.C.; Jensen, O.M. Wood Stove Combustion Air Retrofits: A Low Cost Way to Increase Energy Savings in Dwellings. *Energy Build.* **2018**, *164*, 140–152. [CrossRef]
45. Horvat, I.; Dović, D.; Filipović, P. Numerical and Experimental Methods in Development of the Novel Biomass Combustion System Concept for Wood and Agro Pellets. *Energy* **2021**, *231*, 120929. [CrossRef]
46. Ciupek, B. Emission of Nitrogen Oxides (NOx) from a Heating Boiler Fuelled by Woody and Non-Woody Biomass Pellets Supplied with an Aqueous Solution of Urea. *Biomass Bioenergy* **2025**, *202*, 108202. [CrossRef]
47. Sturmlechner, R.; Schmidl, C.; Klauser, F.; Kirchsteiger, B.; Kasper-Giebl, A. Potential of User Training for Reducing Emissions of Firewood Stoves. *Atmos. Environ. X* **2024**, *23*, 100287. [CrossRef]
48. Marigo, M.; Zulli, F.; Bordignon, S.; Carnieletto, L.; Emmi, G.; De Carli, M. Energy Analysis of a Wood or Pellet Stove in a Single-Family House Equipped with Gas Boiler and Radiators. *Build. Simul.* **2022**, *15*, 1577–1593. [CrossRef]
49. Szramowiat-Sala, K.; Korzeniewska, A.; Sornek, K.; Marczak, M.; Wierońska, F.; Berent, K.; Gołaś, J.; Filipowicz, M. The Properties of Particulate Matter Generated during Wood Combustion in In-Use Stoves. *Fuel* **2019**, *253*, 792–801. [CrossRef]
50. Ozgen, S.; Cernuschi, S.; Caserini, S. An Overview of Nitrogen Oxides Emissions from Biomass Combustion for Domestic Heat Production. *Renew. Sustain. Energy Rev.* **2021**, *135*, 110113. [CrossRef]
51. Bugge, M.; Skreiberg, Ø.; Haugen, N.E.L.; Carlsson, P.; Houshfar, E.; Løvås, T. Numerical Simulations of Staged Biomass Grate Fired Combustion with an Emphasis on NOx Emissions. *Energy Procedia* **2015**, *75*, 156–161. [CrossRef]
52. Carvalho, L.; Wopienka, E.; Pointner, C.; Lundgren, J.; Verma, V.K.; Haslinger, W.; Schmidl, C. Performance of a Pellet Boiler Fired with Agricultural Fuels. *Appl. Energy* **2013**, *104*, 286–296. [CrossRef]
53. Vodička, M.; Hrdlička, J.; Skopec, P. Experimental Study of the NOX Reduction through the Staged Oxygen Supply in the Oxy-Fuel Combustion in a 30 KWth Bubbling Fluidized Bed. *Fuel* **2021**, *286*, 119343. [CrossRef]
54. Scharler, R.; Gruber, T.; Ehrenhöfer, A.; Kelz, J.; Bardar, R.M.; Bauer, T.; Hochenauer, C.; Anca-Couce, A. Transient CFD Simulation of Wood Log Combustion in Stoves. *Renew. Energy* **2020**, *145*, 651–662. [CrossRef]
55. Szubel, M.; Papis-Frączek, K.; Podlasek, S. Impact of the Air Supply System Configuration on the Straw Combustion in Small Scale Batch-Boiler—Experimental and Numerical Studies. *Renew. Energy* **2024**, *220*, 119540. [CrossRef]
56. Bianco, V.; Szubel, M.; Matras, B.; Filipowicz, M.; Papis, K.; Podlasek, S. CFD Analysis and Design Optimization of an Air Manifold for a Biomass Boiler. *Renew. Energy* **2021**, *163*, 2018–2028. [CrossRef]
57. Chen, T.; Sjöblom, J.; Ström, H. Numerical Investigations of Soot Generation during Wood-Log Combustion. *Appl. Energy* **2022**, *325*, 119841. [CrossRef]
58. Luo, H.; Du, Y.; Lin, W. CFD Modeling of a Modern Wood Stove—Soot Formation. *Renew. Energy* **2024**, *232*, 121054. [CrossRef]
59. Zlateva, P.; Terziev, A.; Krumov, K.; Murzova, M.; Mileva, N. Research on the Combustion of Mixed Biomass Pellets in a Domestic Boiler. *Fuels* **2025**, *6*, 40. [CrossRef]
60. Álvarez-Murillo, A.; González González, J.F.; Piquer Carapeto, J.; Nogales-Delgado, S. Control System Modification of a 5-KW Pellet Stove: Study and Analysis. *Appl. Sci.* **2024**, *14*, 8224. [CrossRef]
61. Zhang, X.; Ojha, B.; Bichlmaier, H.; Hartmann, I.; Kohler, H. Extensive Gaseous Emissions Reduction of Firewood-Fueled Low Power Fireplaces by a Gas Sensor Based Advanced Combustion Airflow Control System and Catalytic Post-Oxidation. *Sensors* **2023**, *23*, 4679. [CrossRef]
62. Illerup, J.B.; Hansen, B.B.; Lin, W.; Nickelsen, J.; Pedersen, V.H.; Eskerod, B.; Dam-Johansen, K. Performance of an Automatically Controlled Wood Stove: Thermal Efficiency and Carbon Monoxide Emissions. *Renew. Energy* **2020**, *151*, 640–647. [CrossRef]
63. Mižáková, J.; Piteľ, J.; Hošovský, A.; Pavlenko, I.; Ochowiak, M.; Khovanskyi, S. Biomass Combustion Control in Small and Medium-Scale Boilers Based on Low Cost Sensing the Trend of Carbon Monoxide Emissions. *Processes* **2021**, *9*, 2030. [CrossRef]
64. Sornek, K.; Filipowicz, M.; Rzepka, K. Study of Clean Combustion of Wood in a Stove-Fireplace with Accumulation. *J. Energy Inst.* **2017**, *90*, 613–623. [CrossRef]
65. Ye, C.; Xu, W.; Jiang, Y.; Mu, Z.; Cui, Z.; Wu, H.; Liu, S. Design of the Control and Remote Monitoring Energy System Based on an Embedded Biomass Boiler. *Front. Energy Res.* **2024**, *12*, 1–8. [CrossRef]
66. Pitel, J.; Mižák, J. Cost Effective Biomass Combustion Process Control. *IFAC Proc. Vol.* **2012**, *8*, 616–620. [CrossRef]

67. Miranda, M.T.; Montero, I.; Sepúlveda, F.J.; Arranz, J.I.; Rojas, C.V. Design and Implementation of a Data Acquisition System for Combustion Tests. *Energies* **2017**, *10*, 630. [CrossRef]
68. He, J.; Zhang, J.; Wang, L.; Hu, X.; Xue, J.; Zhao, Y.; Wang, X.; Dong, C. Optimizing the Controlling Parameters of a Biomass Boiler Based on Big Data. *Energies* **2023**, *16*, 7783. [CrossRef]
69. Chen, Y.; Zhang, T.; Cai, J.; Shi, Z.; Ma, T.; Lu, X.; Wang, Z.; Zheng, Z.; Xiao, J.; Chen, Y. Numerical Optimization and Experimental Study of a Biomass Pellet Stove. *Energy* **2025**, *336*, 138412. [CrossRef]
70. Sornek, K.; Filipowicz, M.; Rzepka, K. The Development of a Thermoelectric Power Generator Dedicated to Stove-Fireplaces with Heat Accumulation Systems. *Energy Convers. Manag.* **2016**, *125*, 185–193. [CrossRef]
71. Cebud Website. Available online: www.cebud.eu (accessed on 29 September 2025).
72. Szubel, M.; Bianco, V.; Filipowicz, M.; Saj, A.; Cecconi, C.; Kravets, A. Experimental and Numerical Studies of Accumulation Heat Exchangers for Thermal Retrofitting of Buildings. *Energy Build.* **2022**, *261*, 111990. [CrossRef]
73. Żołądek, M.; Sornek, K.; Boroń, A.; Nabożna, S.; Filipowicz, M. The Use of IR Thermography for Testing Operation Parameters of Plate Steel and Accumulative Wood Stoves. *Monit. Meas. Autom.* **2017**, *63*, 162–165.
74. Kristjansson, K.; Næss, E.; Skreiberg, Ø. Dampening of Wood Batch Combustion Heat Release Using a Phase Change Material Heat Storage: Material Selection and Heat Storage Property Optimization. *Energy* **2016**, *115*, 378–385. [CrossRef]
75. Skreiberg, Ø.; Georges, L. Wood Stove Material Configurations for Increased Thermal Comfort. *Energy Procedia* **2017**, *142*, 488–494. [CrossRef]
76. Sevault, A.; Soibam, J.; Haugen, N.E.L.; Skreiberg, Ø. Investigation of an Innovative Latent Heat Storage Concept in a Stovepipe. *Chem. Eng. Trans.* **2018**, *65*, 25–30. [CrossRef]
77. Cablé, A.; Georges, L.; Peigné, P.; Skreiberg; Druette, L. Evaluation of a New System Combining Wood-Burning Stove, Flue Gas Heat Exchanger and Mechanical Ventilation with Heat Recovery in Highly-Insulated Houses. *Appl. Therm. Eng.* **2019**, *157*, 113693. [CrossRef]
78. Gallardo, S.; Farías, O.; Cornejo, P.; Cuevas, C.; Valín, M.; Jimenez, J. Improving the Performance of a Condensing Heat Exchanger for Biomass Combustion at Household Scale. *Renew. Energy* **2024**, *228*, 120628. [CrossRef]
79. Vlad, A.-V.; Tirnovan, R.-A.; Sabou, D.; Maris, I.; Blidar, O.-C.; Muresan, A. A Review of Residential Micro–Combined Heat and Power Systems Based on Renewable Energy. In Proceedings of the 2021 9th International Conference on Modern Power Systems (MPS), Cluj-Napoca, Romania, 16 June 2021; IEEE: Piscataway, NJ, USA, 2021; pp. 1–7.
80. Brandoni, C.; Arteconi, A.; Ciriachi, G.; Polonara, F. Assessing the Impact of Micro-Generation Technologies on Local Sustainability. *Energy Convers. Manag.* **2014**, *87*, 1281–1290. [CrossRef]
81. Sornek, K. Study of Operation of the Thermoelectric Generators Dedicated to Wood-Fired Stoves. *Energies* **2021**, *14*, 6264. [CrossRef]
82. Najjar, Y.S.H.; Kseibi, M.M. Heat Transfer and Performance Analysis of Thermoelectric Stoves. *Appl. Therm. Eng.* **2016**, *102*, 1045–1058. [CrossRef]
83. Patowary, R.; Baruah, D.C. Feasibility Study of TEG-Integrated Biomass Cook Stove for Electrical Power Generation Specific to Rural Areas with Inadequate Electricity. *Energy Sources Part A Recover. Util. Environ. Eff.* **2023**, *45*, 5714–5735. [CrossRef]
84. Guoneng, L.; Youqu, Z.; Hongkun, L.; Jiangen, H.; Jian, L.; Wenwen, G. Micro Combined Heat and Power System Based on Stove-Powered Thermoelectric Generator. *Renew. Energy* **2020**, *155*, 160–171. [CrossRef]
85. Manfrida, G.; Talluri, L. Exergy Analysis of a Wood Fireplace Coupled with Thermo-Electric Modules. *Proceedings* **2020**, *58*, 10. [CrossRef]
86. Sornek, K.; Filipowicz, M.; Żołądek, M.; Kot, R.; Mikrut, M. Comparative Analysis of Selected Thermoelectric Generators Operating with Wood-Fired Stove. *Energy* **2019**, *166*, 1303–1313. [CrossRef]
87. Tambunan, B.H.; Simanjuntak, J.P.; Koto, I. The Use of Thermo Electric Generator to Utilize the Waste Heat from the Biomass Stove into Electricity. *J. Phys. Conf. Ser.* **2022**, *2193*, 012045. [CrossRef]
88. Sornek, K.; Papis-Frączek, K. Numerical and Experimental Analysis of a Prototypical Thermoelectric Generator Dedicated to Wood-Fired Heating Stove. *Micromachines* **2023**, *14*, 145. [CrossRef]
89. Obernberger, I.; Weiß, G.; Kössl, M. Development of a New Micro CHP Pellet Stove Technology. *Biomass Bioenergy* **2018**, *116*, 198–204. [CrossRef]
90. Baldini, A.; Cerofolini, L.; Fiaschi, D.; Manfrida, G.; Talluri, L. Thermodynamic Assessment on the Integration of Thermo-Electric Modules in a Wood Fireplace. *Civ. Environ. Eng. Rep.* **2019**, *29*, 218–235. [CrossRef]
91. Montecucco, A.; Siviter, J.; Knox, A.R. Combined Heat and Power System for Stoves with Thermoelectric Generators. *Appl. Energy* **2017**, *185*, 1336–1342. [CrossRef]
92. Usón, S.; Royo, J.; Canalís, P. Integration of Thermoelectric Generators in a Biomass Boiler: Experimental Tests and Study of Ash Deposition Effect. *Renew. Energy* **2023**, *214*, 395–406. [CrossRef]

93. Voronca, Ș.-D.; Siroux, M.; Darie, G. Experimental Characterization of Transitory Functioning Regimes of a Biomass Stirling Micro-CHP. *Energies* **2022**, *15*, 5547. [CrossRef]
94. Cardozo, E.; Malmquist, A. Performance Comparison between the Use of Wood and Sugarcane Bagasse Pellets in a Stirling Engine Micro-CHP System. *Appl. Therm. Eng.* **2019**, *159*, 113945. [CrossRef]
95. Kramens, J.; Vīgants, E.; Liepiņš, I.; Vernieks, L.; Terjanika, V. Research of a Biomass Boiler with Stirling Engine Microgeneration Unit. *Environ. Clim. Technol.* **2021**, *25*, 587–599. [CrossRef]
96. Borisov, I.; Khalatov, A.; Paschenko, D. The Biomass Fueled Micro-Scale CHP Unit with Stirling Engine and Two-Stage Vortex Combustion Chamber. *Heat Mass Transf. Und Stoffuebertragung* **2022**, *58*, 1091–1103. [CrossRef]
97. Falbo, L.; Algieri, A.; Morrone, P.; Perrone, D. Experimental Investigation into the Energy Performance of a Biomass Recuperative Organic Rankine Cycle (ORC) for Micro-Scale Applications in Design and Off-Design Conditions. *Energies* **2025**, *18*, 3201. [CrossRef]
98. Algieri, A.; Morrone, P. Energetic Analysis of Biomass-Fired ORC Systems for Micro-Scale Combined Heat and Power (CHP) Generation. A Possible Application to the Italian Residential Sector. *Appl. Therm. Eng.* **2014**, *71*, 751–759. [CrossRef]
99. Villarino, Y.T.; Rial, L.P.; Rodríguez-Abalde, Á. Assessment of a Residual Biomass Micro-Combined Heat and Power System Based on an Organic Rankine Cycle Coupled to a Boiler. *J. Environ. Manag.* **2022**, *301*, 113832. [CrossRef]
100. Basu, P. *Biomass Gasification and Pyrolysis*; Academic Press: Burlington, MA, USA, 2010; ISBN 9780080878737.
101. Wang, Z.X.; Li, H.Y.; Zhang, X.F.; Wang, L.W.; Du, S.; Fang, C. Performance Analysis on a Novel Micro-Scale Combined Cooling, Heating and Power (CCHP) System for Domestic Utilization Driven by Biomass Energy. *Renew. Energy* **2020**, *156*, 1215–1232. [CrossRef]
102. Sunil; Sinha, R.; Chaitanya, B.; Rajan, B.K.; Agarwal, A.; Thakur, A.D.; Raj, R. Design, Fabrication, and Performance Evaluation of a Novel Biomass-Gasification-Based Hot Water Generation System. *Energy* **2019**, *185*, 148–157. [CrossRef]
103. Malaguti, V.; Lodi, C.; Sassatelli, M.; Pedrazzi, S.; Allesina, G.; Tartarini, P. Dynamic Behavior Investigation of a Micro Biomass CHP System for Residential Use. *Int. J. Heat Technol.* **2017**, *35*, S172–S178. [CrossRef]
104. Caliano, M.; Bianco, N.; Graditi, G.; Mongibello, L. Design Optimization and Sensitivity Analysis of a Biomass-Fired Combined Cooling, Heating and Power System with Thermal Energy Storage Systems. *Energy Convers. Manag.* **2017**, *149*, 631–645. [CrossRef]
105. Bellos, E.; Lykas, P.; Tzivanidis, C. Theoretical Analysis of a Biomass-Driven Single-Effect Absorption Heat Pump for Heating and Cooling Purposes. *Appl. Syst. Innov.* **2022**, *5*, 99. [CrossRef]
106. Lee, C.G.; Cho, L.H.; Park, S.; Kim, S.J.; Jeong, I.S.; Kim, M.J.; Kim, D.H. Smart Farm Heating Using a Hybrid Pellet Boiler–Hydrothermal Heat Pump System. *J. Biosyst. Eng.* **2022**, *47*, 233–247. [CrossRef]
107. Uche, J.; Tajik Jamalabad, M.; Martínez, A. Configurational Design of a Hybrid System Based on an Air–Water Heat Pump and Biomass Boiler for a Rural Dwelling. *Appl. Sci.* **2024**, *14*, 9840. [CrossRef]
108. Uche, J.; Jamal-Abad, M.T.; Martínez-Gracia, A. Evaluating the Efficiency, Economics, and Environmental Impact of Hybrid Heat Pumps Assisted by Biomass Boilers for Spanish Climate Zones. *Energy* **2025**, *325*, 136180. [CrossRef]
109. Hebenstreit, B.; Schnetzinger, R.; Ohnmacht, R.; Höftberger, E.; Lundgren, J.; Haslinger, W.; Toffolo, A. Techno-Economic Study of a Heat Pump Enhanced Flue Gas Heat Recovery for Biomass Boilers. *Biomass Bioenergy* **2014**, *71*, 12–22. [CrossRef]
110. Westerlund, L.; Hermansson, R.; Fagerström, J. Flue Gas Purification and Heat Recovery: A Biomass Fired Boiler Supplied with an Open Absorption System. *Appl. Energy* **2012**, *96*, 444–450. [CrossRef]
111. Drofenik, J.; Urbancl, D.; Goričanec, D.; Kravanja, Z.; Novak Pintarič, Z. Food Waste to Energy through Innovative Coupling of CHP and Heat Pump. *Energies* **2023**, *16*, 3344. [CrossRef]
112. Hou, S.; Guo, J.; Yu, Z.; Zhang, L.; Sun, J. Optimization of Biomass Energy Coupled Multi-Source Heat Pumps Cooperative Heating System: A Case Study. *Energy Sources Part A Recover. Util. Environ. Eff.* **2023**, *45*, 8153–8166. [CrossRef]
113. Carotenuto, A.; Figaj, R.D.; Vanoli, L. A Novel Solar-Geothermal District Heating, Cooling and Domestic Hot Water System: Dynamic Simulation and Energy-Economic Analysis. *Energy* **2017**, *141*, 2652–2669. [CrossRef]
114. Zhang, X.; Yang, J.; Fan, Y.; Zhao, X.; Yan, R.; Zhao, J.; Myers, S. Experimental and Analytic Study of a Hybrid Solar/Biomass Rural Heating System. *Energy* **2020**, *190*, 116392. [CrossRef]
115. Krarouch, M.; Allouhi, A.; Hamdi, H.; Outzourhit, A. Energy, Exergy, Environment and Techno-Economic Analysis of Hybrid Solar-Biomass Systems for Space Heating and Hot Water Supply: Case Study of a Hammam Building. *Renew. Energy* **2024**, *222*, 119941. [CrossRef]
116. Skiadopoulos, A.; Kosmadakis, G.; van Heule, X.; Lecompte, S.; De Paepe, M.; Manolakos, D. Hybrid Solar-Biomass Residential Micro—Combined Heat and Power Systems Driven by the Partially Evaporating Organic Rankine Cycle—A Case Study in Southern Europe. *Therm. Sci. Eng. Prog.* **2024**, *55*, 102906. [CrossRef]
117. Prieto, J.; Ajnannadhif, R.M.; Fernández-del Olmo, P.; Coronas, A. Integration of a Heating and Cooling System Driven by Solar Thermal Energy and Biomass for a Greenhouse in Mediterranean Climates. *Appl. Therm. Eng.* **2023**, *221*, 119928. [CrossRef]

118. Borri, E.; Charalampidis, A.; Palomba, V.; Zsembinszki, G.; Frazzica, A.; Karellas, S.; Cabeza, L.F. Environmental Impact of an Innovative Solar-Biomass Hybrid System for Residential Applications. *Renew. Energy* **2025**, *239*, 122138. [CrossRef]
119. Liu, Y.; Bi, D.; Yin, M.; Zhang, K.; Liu, H.; Liu, S. Modeling and Exergy-Economy Analysis of Residential Building Energy Supply Systems Combining Torrefied Biomass Gasification and Solar Energy. *Therm. Sci. Eng. Prog.* **2024**, *50*, 102584. [CrossRef]
120. Zhu, J.; Kumar Nutakki, T.U.; Singh, P.K.; Abdullaeva, B.S.; Zhou, X.; Fouad, Y.; Alzubaidi, L.H. Sustainable Off-Grid Residential Heating and Desalination: Integration of Biomass Boiler and Solar Energy with Environmental Impact Analysis. *J. Build. Eng.* **2024**, *87*, 109035. [CrossRef]
121. Shirazi, P.; Behzadi, A.; Ahmadi, P.; Rosen, M.A.; Sadrizadeh, S. Comparison of Control Strategies for Efficient Thermal Energy Storage to Decarbonize Residential Buildings in Cold Climates: A Focus on Solar and Biomass Sources. *Renew. Energy* **2024**, *220*, 119681. [CrossRef]
122. Nami, H.; Anvari-Moghaddam, A.; Nemati, A. Modeling and Analysis of a Solar Boosted Biomass-Driven Combined Cooling, Heating and Power Plant for Domestic Applications. *Sustain. Energy Technol. Assess.* **2021**, *47*, 101326. [CrossRef]
123. Palomba, V.; Borri, E.; Charalampidis, A.; Frazzica, A.; Cabeza, L.F.; Karellas, S. Implementation of a Solar-Biomass System for Multi-Family Houses: Towards 100% Renewable Energy Utilization. *Renew. Energy* **2020**, *166*, 190–209. [CrossRef]
124. Altayib, K.; Dincer, I. Design and Evaluation of a New Solar-Biomass Based Energy System for a Small Sustainable Residential Community. *J. Clean. Prod.* **2022**, *369*, 133275. [CrossRef]
125. Wang, D.; Almojil, S.F.; Ahmed, A.N.; Chaturvedi, R.; Almohana, A.I. An Intelligent Design and Environmental Consideration of a Green-Building System Utilizing Biomass and Solar Having a Bidirectional Interaction with the Grid to Achieve a Sustainable Future. *Sustain. Energy Technol. Assess.* **2023**, *57*, 103287. [CrossRef]
126. Sabbaghi, M.A.; Soltani, M.; Fraser, R.; Dusseault, M.B. Emergy-Based Exergoeconomic and Exergoenvironmental Assessment of a Novel CCHP System Integrated with PEME and PEMFC for a Residential Building. *Energy* **2024**, *305*, 132301. [CrossRef]
127. Wądrzyk, M.; Katerla, J.; Janus, R.; Lewandowski, M.; Plata, M.; Korzeniowski, Ł. High-Energy-Density Hydrochar and Bio-Oil from Hydrothermal Processing of Spent Coffee Grounds—Experimental Investigation. *Energies* **2024**, *17*, 6446. [CrossRef]
128. Mirowski, T.; Kubica, K. Rola Biomasy w Lokalnych Klastrach Energetycznych. *Polityka Energ. Energy Policy J.* **2016**, *19*, 125–138.

Disclaimer/Publisher's Note: The statements, opinions and data contained in all publications are solely those of the individual author(s) and contributor(s) and not of MDPI and/or the editor(s). MDPI and/or the editor(s) disclaim responsibility for any injury to people or property resulting from any ideas, methods, instructions or products referred to in the content.

energies

MDPI

Review

A Review of Multi-Port Converter Architecture in Hydrogen-Based DC Microgrid

Qiyan Wang, Kosala Gunawardane * and Li Li

School of Electrical and Data Engineering, Faculty of Engineering and IT, University of Technology Sydney, Sydney 2007, Australia; qiyan.wang-1@student.uts.edu.au (Q.W.); li.li@uts.edu.au (L.L.)
* Correspondence: kosala.gunawardane@uts.edu.au

Abstract

With the rapid advancement of hydrogen-based direct current microgrid (H_2-DCMG) technology, multi-port converters (MPCs) have emerged as the pivotal interface for integrating renewable power generation, energy storage, and diverse DC loads. This paper systematically reviews the current research status and development trends of isolated and non-isolated MPC topologies within hydrogen-based DC microgrids. Firstly, it analyses the interface requirements for typical distributed energy sources (DER) such as photovoltaics (PV), wind turbines (WT), fuel cells (FC), battery energy storage (BESS), proton exchange membrane electrolyzers (PEMEL), and supercapacitors (SC). Secondly, it classifies and evaluates existing MPC topologies, clarifying the structural characteristics, technical advantages, and challenges faced by each type. Results indicate that non-isolated topologies offer advantages such as structural simplicity, high efficiency, and high power density, making them more suitable for residential and small-scale microgrid applications. Isolated topologies, conversely, provide electrical isolation and modular scalability, rendering them appropriate for high-voltage electrolytic hydrogen production and industrial scenarios with stringent safety requirements. Finally, the paper identifies current research gaps and proposes that future efforts should focus on exploring topology optimization, system integration design, and reliability enhancement.

Keywords: hydrogen-based DC microgrid; distributed energy sources; multi-port DC–DC converter; topology-derived architecture; high voltage gain

1. Introduction

The current global energy system faces multiple challenges, including excessive consumption of traditional energy sources, environmental pollution, and rising carbon emissions. To address these issues, numerous countries and regions have reached a consensus in recent years, committing to achieving net zero targets [1]. According to the International Energy Agency's (IEA) 2025 report, the growth rate of energy sources represented by renewables has risen to 38%, making it the world's fastest growing energy category [2]. This indicates that modern power systems are gradually shifting from centralized supply architectures towards more environmentally friendly and sustainable distributed energy frameworks. Within this context of energy transition, microgrids are one of the key developmental trends.

A microgrid is a small-scale power system that typically comprises energy sources, loads, energy storage systems, distribution networks, protective equipment, and control

systems. Its primary objective is to ensure stable power, voltage, and frequency within the system [3]. As illustrated in Figure 1, certain microgrids may connect to the main grid via a static transfer switch (STS) at a public coupling point (PCC). From the perspective of the main grid, a microgrid can be regarded as a single controllable unit. It exports power to the main grid during generation surpluses and imports power from the main grid during generation shortfalls. Furthermore, the microgrid can actively disconnect from the main grid to achieve independent operation in the event of power quality deterioration or if faults occur. Currently, microgrids possessing independent operation capabilities are attracting increasing attention and are commonly referred to as island, standalone, or self-sufficient microgrids.

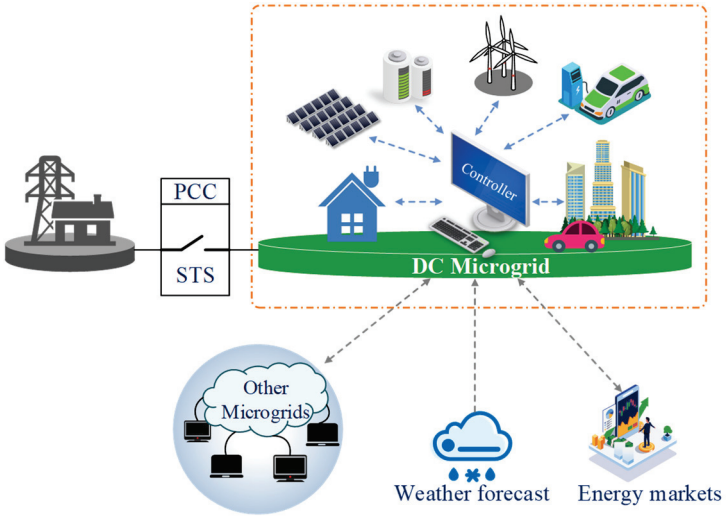


Figure 1. Typical architecture of DC microgrid.

Many mainstream renewable energy technologies, such as PV and FC, inherently generate direct current (DC) power. Additionally, modern electrical devices, including electric vehicles, computing equipment, and LED lighting systems, typically require DC input [4]. This inherent alignment between generation and consumption has led to increasing interest in DC microgrids, which feature simpler architectures and eliminate the need for complex synchronization controls. Furthermore, the adoption of DC microgrids substantially reduces the number of energy conversion stages relative to conventional AC microgrids [5]. This simplification lowers system energy losses and enhances overall energy efficiency.

However, due to the inherent intermittency and randomness of renewable energy sources (RES), their output alone is insufficient to consistently and reliably meet load demands. Consequently, energy storage systems have become essential components in DC microgrids. Of current technologies, chemical batteries represented by lithium-ion types have been widely adopted for short- and medium-term energy storage scenarios, benefiting from their high energy density and rapid response capability [6]. Nevertheless, the suitability of these batteries is constrained by factors including self-discharge characteristics, substantial initial investments, and ongoing maintenance expenses when meeting seasonal and long-term storage demands [7].

Against the backdrop of growing demand for long-term energy storage, hydrogen storage technologies have attracted considerable attention in recent years. Hydrogen features high energy density, zero emissions, long-term economic storage capability, and low maintenance costs, effectively addressing the shortcomings of existing long-duration

storage technologies [8]. In hydrogen-based DC microgrid energy storage systems, surplus renewable electricity is converted into hydrogen gas through proton exchange membrane electrolyzers (PEMEL), subsequently reconverted into electrical energy via FC as required. This process facilitates efficient, clean, and long-term energy storage and supply.

Figure 2 illustrates a representative hydrogen-based DC microgrid architecture that integrates generation units, storage units, and loads. These components are controlled via individual power converters and connected to a common DC bus for energy distribution and transmission. This approach has garnered attention for its plug-and-play functionality and strong scalability. However, as the number of integrated units increases, employing multiple individual converters significantly increases the structural complexity of the overall system, thereby posing considerable control challenges and reducing operational efficiency.

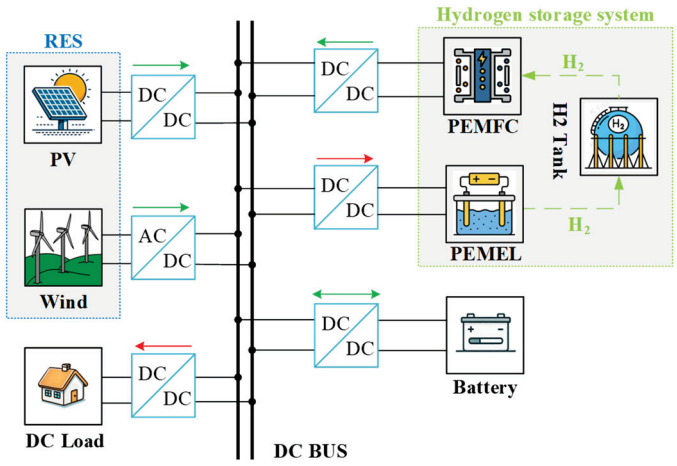


Figure 2. Single-converter architecture for hydrogen-based DC microgrid.

To achieve more efficient coordinated control and flexible integration of diverse energy sources and energy storage devices within DC microgrids, the development of novel power electronics interface technologies has emerged as a research priority. As illustrated in Figure 3, multi-port converters (MPC) have garnered significant attention from both academia and industry in recent years. This is due to their ability to simultaneously integrate renewable energy generation units and energy storage units, flexibly control power flow between ports, and enable modular system design.

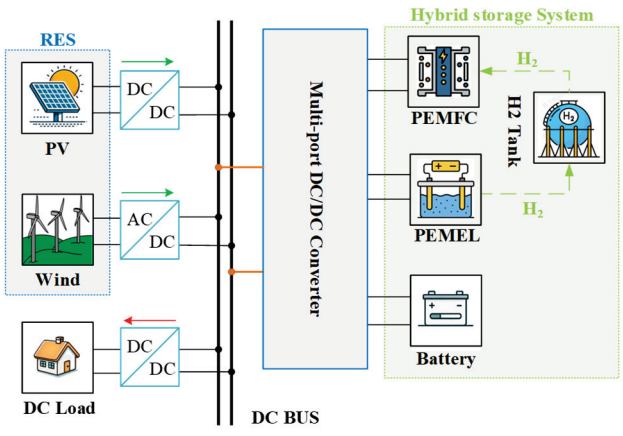


Figure 3. Integrated multi-port converter architecture for hydrogen-based DC microgrid.

Compared with conventional architectures that employ multiple individual converters, multi-port converter-based microgrids offer a more compact and integrated system design. This configuration effectively reduces the number of voltage conversion stages in renewable energy systems, leading to lower system complexity, smaller physical scale, and reduced construction costs [9]. In addition, certain multi-port converter topologies can provide electrical isolation between ports when required, thereby enhancing the operational safety of distributed energy systems.

The primary objective of this paper is to review the characteristics of mainstream distributed energy sources (DER) within a hydrogen-based DC microgrid, the requirements they impose on multi-port converters, and the predominant topologies of multi-port converters in current research. Specifically, it covers the technical features, advantages, and application challenges of both isolated and non-isolated architectures, whilst analyzing their applicable scenarios to clarify future research directions and technological development opportunities.

2. Classification of DER Types

In hydrogen-based DC microgrids, typical DERs include renewable generation units such as PV, WT, and FC. DERs also comprise energy storage subsystems, including BESS and PEMEL. Since these DERs differ in their operation characteristics, it is necessary to examine their power flow pathways, dynamic response behaviors, and power quality requirements in order to define the functional specifications that multi-port power converters must satisfy. This section classifies DERs according to their functional roles within the microgrid and reviews the characteristics of each category.

2.1. Photovoltaic Generation Unit

As shown in Figure 4, the PV port exhibits stochastic power variability and strong I-V nonlinearity, which complicate DC bus regulation and multi-port power coordination [10]. Operating the array consistently at its maximum power point is essential; however, converter-induced current/voltage ripple and transient disturbances can displace the operating point from the MPP, degrading energy capture [11]. A pronounced voltage-level mismatch also exists: PV modules provide low and variable DC (often <60 V), whereas building/campus DC buses commonly run at ~380–400 V, necessitating high and controllable step-up conversion with good efficiency over a wide input range [12]. Consequently, stand-alone PV rarely satisfies the load alone and is typically coordinated with BESS/FC/SC to stabilize net power and bus voltage within multi-port architectures.

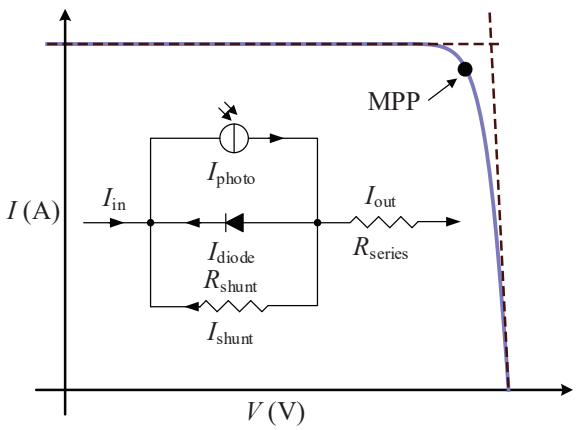


Figure 4. I-V Characteristic curve and equivalent circuit model for PV.

Accordingly, the PV interface within MPC-based microgrids should meet the following standards:

(1) **High-gain step-up with wide input operability**: It should deliver a sufficient conversion ratio and efficiency across irradiance/temperature-driven voltage spread to match the DC bus; isolation may be adopted when voltage matching and safety margins require it;
(2) **Low input-current ripple**: Maintaining low input-current ripple effectively suppresses ripple-induced deviations from the maximum power point (MPP), thus stabilizing power extraction efficiency from the PV port;
(3) **Fast dynamic response**: A fast, well-damped transient response limits disturbances propagated to the DC bus during multi-port coordination, preventing PV-side dynamic interactions from exacerbating DC bus voltage fluctuations.

2.2. Wind Generation Unit

Wind turbine (WT) generation units, commonly integrated within hydrogen-based DC microgrids, produce variable-frequency AC voltage that requires rectification and voltage step-up before feeding into the DC bus. However, the inherent stochastic nature of wind introduces unpredictable dynamics, leading to frequent DC link voltage fluctuations and degraded power quality. Although the mechanical inertia of turbines slightly buffers transient power variations, this natural damping alone cannot fully mitigate the rapid electrical fluctuations induced by wind speed changes [13]. Consequently, these residual electrical disturbances require precise converter controls to maintain stable DC bus operation and suppress voltage deviations. Additionally, the type of rectifier employed influences ripple characteristics. Multi-pulse diode or thyristor rectifiers generate low-frequency ripple components related to pulse number, while PWM active rectifiers shift the ripple into the switching frequency band [14]. Furthermore, converter topologies capable of extracting maximum power over a broad operating range are essential to achieve efficient power transfer and voltage-level matching.

Accordingly, the WT interface within MPC-based microgrids should meet the following standards:

(1) **AC/DC–DC/DC interface conversion**: The WT port should include an AC–DC rectifier followed by a regulated DC–DC stage that converts the variable-frequency low-voltage output of the generator to the specified DC bus voltage level. Topology selection should cover the full generator voltage range and meet the bus regulation target.
(2) **Maximum power extraction and power smoothing**: The WT port should implement MPPT and coordinate with energy storage units to limit DC bus deviation and meet dynamic performance criteria during wind variations.
(3) **High gain and wide operating range**: The WT port should provide a high, controllable step-up ratio across a wide input voltage range to achieve the required gain at moderate duty cycle while constraining device voltage stress and input current ripple.

2.3. Fuel Cell Generation Unit

Fuel cells (FC) convert stored hydrogen into electrical energy and serve as critical generation units in hydrogen-based DC microgrids. However, they exhibit slow dynamic response and pronounced V–I nonlinearity owing to inherent electrochemical polarization effects [15]. Therefore, FC faces challenges in providing instantaneous high-power support. PEMFCs behave as low-voltage sources with voltage droop under a rising current. Because a single cell typically operates at around 0.6–0.7 V, stacks deliver only tens of volts,

necessitating high step-up DC–DC conversion to meet typical DC bus requirements [16]. Achieving this with a conventional boost converter requires operation at high-duty cycles, which significantly elevates device stress and switching/conduction losses. Simultaneously, the FC-side input current must increase to maintain bus power, exacerbating ripples, EMI, and thermal management burdens. To sustain this higher power, the front-end step-up stage necessarily draws a more pulsating input current under finite inductance and high-duty cycles. This amplifies both low-frequency and switching band components, which raise FC losses, hasten degradation at high currents, and couple onto the DC bus to impair power quality [17].

Accordingly, FC port design within MPC architectures should ensure the following:

(1) **Unidirectional energy flow design**: As PEMFCs function as energy-supplying sources, their interface converters should exhibit unidirectional power flow characteristics, delivering energy from the fuel cell to the DC bus;
(2) **High-gain, high-current conversion design**: As PEMFCs operate under voltage depression and large average current conditions, their interface converters should feature high-gain and high-current capability with low input-current ripple, maintaining efficiency and operational safety;
(3) **Ripple mitigation and EMI control design**: As PEMFCs are sensitive to harmonics and ripple currents, their interface converters should include effective filtering, modulation schemes, and operating mode selection to minimize ripple-induced losses and prevent DC bus contamination;
(4) **Transient buffering and coordinated control design**: As PEMFCs exhibit slow dynamic response, their interface converters should incorporate transient buffering mechanisms and coordinated control with energy storage units to limit direct load impact on the stack and reduce DC bus regulation burdens.

2.4. Battery Storage Unit

In hydrogen-based DC microgrids, battery energy storage (BESS) provides bidirectional buffering that stabilizes the DC bus and smooths renewable variability. However, characteristics of BESS impose fundamental limits. Self-discharge undermines long-duration large-scale storage, while repeated cycling causes capacity fade and increases internal resistance; moreover, terminal voltage and impedance vary with state of charge and temperature [18]. These behaviors impose stringent requirements for the converter port. First, the BESS terminal voltage varies widely with SOC, temperature, and aging, while the DC bus voltage of the microgrid is maintained around a nominal setpoint. Consequently, the interface must furnish efficient wide-range buck–boost regulation to manage voltage mismatch across operating conditions [19]. Second, BESSs are sensitive to superimposed current ripple originating from source/load fluctuations (low frequency) and switching actions (high frequency); without proper mitigation, this ripple elevates internal heating, accelerates capacity fades and increases impedance. These effects propagate disturbances to the DC bus, degrading overall power quality [20]. Third, parallel packs exhibit module heterogeneity (capacity, impedance, temperature, aging); without robust current sharing, current limiting, and SOC balancing, circulating currents and uneven distribution arise, causing localized hot spots, reduced usable capacity, and accelerated degradation [21].

Accordingly, the BESS interface within MPC-based microgrids should meet the following standards:

(1) **Bidirectional power flow and DC-link stabilization**: The BESS interface should support bidirectional energy exchange, enabling charge and discharge coordination

to buffer renewable and load fluctuations while maintaining fast, well-damped DC bus voltage regulation;

(2) **High-efficiency wide-range power conversion**: The converter must sustain high efficiency across a broad input–output voltage span, accommodating variations in battery SOC and temperature while matching the fixed high DC bus voltage level;

(3) **Ripple suppression and lifetime enhancement**: Effective ripple reduction is required to minimize battery current ripple, thereby mitigating thermal stress and aging effects while preserving DC bus power quality.

2.5. Electrolyzer Unit

PEMEL is an energy consumption unit in the hydrogen DC microgrid, functioning as a load that draws electrical energy from the microgrid and outputs hydrogen energy. The hydrogen production rate of a PEMEL is approximately linearly proportional to its input DC, making current become the primary control variable [22]. PEMEL features rapid start-up and ramping capabilities, enabling power adjustments within seconds to minutes. While this flexibility aids in matching renewable energy fluctuations, it also introduces reliability concerns. Frequent dynamic loading accelerates membrane and electrode degradation, and sudden pressure fluctuations impose mechanical stresses that impair performance [23]. These operational characteristics influence the design of interface converters. Since a single PEMEL stack typically operates around 30 V, a step-down from the DC bus voltage is required [24]. Consequently, conventional single-stage buck converters operate at very small duty ratios, which results in narrow control margins, higher switching and conduction losses, and increased inductor and bus current ripple [25]. Therefore, due to the nonlinear I–V characteristics of the electrolyzer stack and its sensitivity to current ripple, superimposition can shift the operating point and reduce efficiency. Furthermore, long-term ripple exposure increases both contact resistance and high-frequency resistance, so the ripple must be tightly limited [26]. Rapid tracking of dispatch commands remains essential. To safely achieve this rapid response, ramp rates and operational constraints must be explicitly defined. Otherwise, renewable power fluctuations may propagate into the stack, reducing hydrogen production during transient periods and increasing safety risks.

Considering the operational characteristics and limitations of PEMEL units, the following specific requirements should be addressed when designing the associated interface converters:

(1) **Wide voltage range and high step-down capability**: The PEMEL interface converter must accommodate wide input voltages and achieve a high step-down ratio, often requiring multi-stage or specialized topologies due to efficiency constraints of traditional single-stage buck converters;

(2) **Current ripple control**: The PEMEL interface should minimize output current ripple using advanced filtering, interleaved structures, or multiphase techniques to enhance electrolysis efficiency and extend component lifetime;

(3) **Appropriate dynamic response control**: The PEMEL interface converter requires suitable dynamic responsiveness to rapidly implement system energy scheduling instructions, effectively stabilizing current variations without compromising hydrogen production efficiency or component lifespan.

2.6. Supercapacitor Storage Unit

Supercapacitors provide millisecond-level response and low ESR, which enables short-term buffering to smooth power and voltage in DC microgrids. They compensate for the

slower dynamics of distributed energy resources, improving transient ride-through and system stability [27]. These benefits also introduce converter design burdens that arise from the device's dynamics. The terminal voltage varies widely with state of charge. The interface must operate across a broad input range and maintain an adequate conversion ratio. Operation near extreme duty cycles can reduce efficiency and narrow control stability margins [28]. Because the ESR of the SC is very low, the SC behaves almost like a short circuit at a low SOC (near-zero terminal voltage) when connected to the DC bus. A similar condition occurs when the converter's voltage or current setpoint is stepped upward. In both cases, the resulting surge current and high di/dt elevate stress on semiconductors and the DC bus, potentially causing fluctuations or instability in the DC bus voltage. Frequent high-current cycling further increases current stress and complicates thermal management, and inadequate regulation can aggravate transient bus deviations and degrade power quality. In practice, these effects appear as bus voltage ripple and as nonlinear V–I deviations linked to SOC-dependent voltage and controller saturation near operating limits [29].

Therefore, when connecting SC to a hydrogen-based DC microgrid, the design of the interface converter needs to focus on meeting the following performance requirements:

(1) **Bidirectional power flow capability**: Supercapacitors can both absorb energy from the DC bus for charging and release energy to the bus for discharging. Therefore, the interface converter must support the bidirectional flow of energy between the bus and the supercapacitor;
(2) **Wide range of voltage**: The terminal voltage of the SC varies significantly with SOC; therefore, the interface converter should possess the capability to operate across a wide input voltage range to ensure effective voltage boosting and stable operation under low-voltage SC conditions;
(3) **High surge current tolerance**: SC can instantly provide/absorb large currents, so their interface converters must have corresponding high surge current carrying capacity. Topologies such as multi-phase interleaved parallel connection can be used to reduce current ripple and device stress, ensuring operational stability during charging and discharging;
(4) **High efficiency and fast dynamic response**: The interface converter needs to have high efficiency to reduce energy loss caused by frequent charging and discharging. At the same time, it should achieve fast dynamic response to effectively suppress transient power fluctuations and improve the overall operational stability of the microgrid.

Based on the above analysis, Table 1 summarizes the power flow characteristics, critical operational issues, and corresponding interface design requirements of various distributed energy resources in hydrogen-based DC microgrids.

The diversity of the above-mentioned distributed energy resources places demands on power electronic interfaces in terms of multi-port connectivity and flexible power allocation. From the perspective of power flow, the microgrid incorporates unidirectional generation-only sources (e.g., PV, WT, and FC), load-only or energy-consuming units (e.g., PEMEL), and bidirectional storage units capable of charging and discharging (e.g., BESS and SC). In particular, the hydrogen-based energy system integrates PEMFC generation units and PEMEL electrolysis units to achieve energy storage and utilization. It is noteworthy that PEMEL differs from other common distributed energy generation units by typically employing buck converters for its interface, whereas common generation units usually require boost converters. Consequently, the design of multi-port converters must address both the diversity of interfacing ports and the complexity inherent in system integration. Detailed

converter topologies and corresponding design considerations will be comprehensively discussed in the architecture review of multi-port converters.

Table 1. Characteristics and interface requirements of distributed energy resources.

Type	Flow	Output	Issues	Requirements
PV	Unidirectional	DC output/intermittent/ nonlinear I-V/ low voltage	DC bus deviation Multi-port coordination Inaccurate MPPT	High step-up MPPT Low input ripple Fast dynamics
WT	Unidirectional	Variable-freq AC/rectified then boosted/ inertia smoothing	DC bus deviation Power quality concern Inaccurate MPPT	MPPT + smoothing high gain/input filtering and damping
FC	Unidirectional	DC output; low voltage; high current/slow dynamics/nonlinear I-V	Slow dynamics Ripple and EMI	High-gain boost/low input ripple/ transient buffering
BESS	Bidirectional	Rapid absorb/release; wide voltage range	High requirement for ripple Wide voltage conversion Pack imbalance	Bidirectional DC–DC/ripple suppression/ Fast stabilization
PEMEL	Load-only consumer	DC load/low voltage/high current/H_2 rate ~ current/fast response	Ripple-sensitive Dynamic ramp rate control	Wide input range/high step-down/ripple control/ramp rate limit
SC	Bidirectional	ms-level response/ low ESR SOC-dependent voltage	Current stress/Transient bus deviation	Wide voltage operation/proper power regulation/ Moderate dynamics

3. Multi-Port Converter Architecture

In this section, the MPCs are systematically classified according to the structure presented in Figure 5. MPCs are first categorized into non-isolated and isolated types based on the presence of galvanic isolation. Non-isolated MPCs are further subdivided into three groups according to their port configurations: multi-input multi-output (MIMO), multi-input single-output (MISO), and single-input multi-output (SIMO). These groups can also be categorized according to their circuit characteristics into configurations such as input-series output-parallel (ISOP), input-parallel output-series (IPOS), input-parallel output-parallel (IPOP), input-series output-series (ISOS). Isolated MPCs are divided into two groups based on transformer implementations: multi-winding transformer-derived (MWTD) architectures, which inherently increase the number of ports by adding transformer windings; and topology-derived (TD) architectures, which utilize transformers with a fixed winding configuration. It is notable that TD architectures offer extensive composability by integrating non-isolated stages. Specifically, various non-isolated MISO topologies can be flexibly connected to the transformer's primary side, while multiple SIMO topologies can be attached to its secondary side. This configurational flexibility of TD is indicated by dashed connections in Figure 5. Subsequent sections provide a detailed discussion of representative circuits, their key characteristics, and specific application scenarios based on this classification framework.

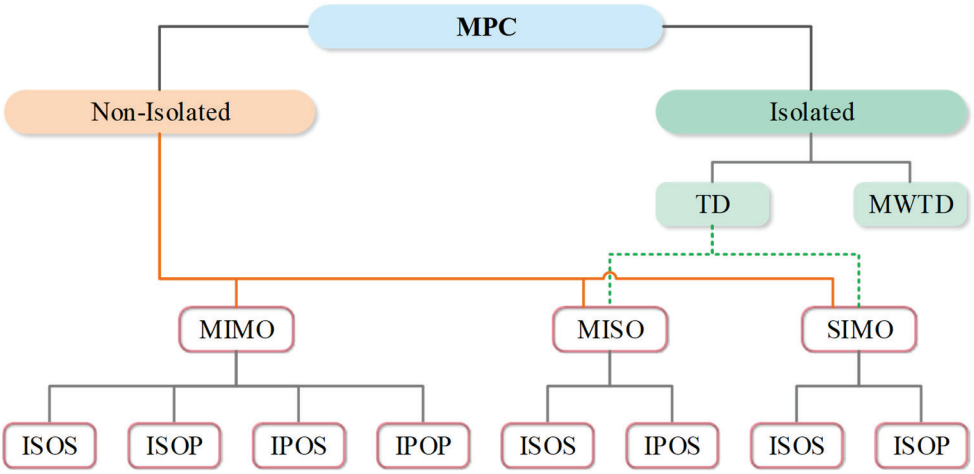


Figure 5. Classification framework of multi-port converter architectures.

3.1. Non-Isolated Multi-Port Converter Architecture

3.1.1. Multi-Input Single-Output

Series expansion

The fundamental design concept of the non-isolated "Series expansion" multi-input single-output (MISO) converter is to series-connect multiple DC sources through individual unidirectional diodes ahead of a common power stage. The shared post-stage then performs energy processing and voltage regulation. The topology can be directly obtained by extending classical single-input converters: Figure 6a shows the buck-derived multi-port converter [30], and Figure 6b shows the boost-derived multi-port converter [31]. The series diode network decouples the sources and suppresses reverse currents, while the back end shares the magnetic and filtering components, keeping the hardware scale and control organization within practical bounds. Consequently, this architecture is suitable for source-side voltage stacking with centralized post-stage regulation.

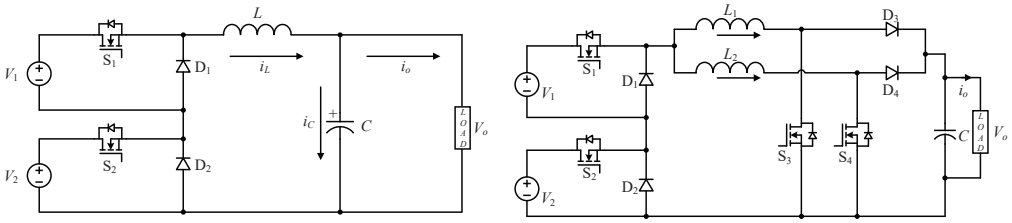


Figure 6. Series expansion MISO architecture: (**a**) Buck-derived; (**b**) Boost-derived.

For non-isolated "diode-series-extended" MISO MPCs, current key research focuses primarily on optimizing devices and operating modes for higher efficiency and lower ripple, including introducing continuous input/output current paths and phase management in boost-type MISO to reduce source-side current ripple and improve static/dynamic performance metrics [32,33]; and small-signal modeling and multi-switch coordination control in buck-type MISOs to mitigate stability and dynamic performance issues arising from multiple input duty cycle coupling [34,35]. To accommodate high-gain and wide-range bus requirements, multi-stage MISO boost/buck configurations have emerged, embedding high-gain switching networks within conventional boost/buck power stages to enhance boost/buck ratios while limiting device stress [36,37]. To further reduce device stress and input-side ripple, some implementations employ multi-phase interleaving at

each input port alongside common-source coupling inductors, canceling ripple and sharing current [38,39]. Throughout these evolutions, the core characteristic of "front-end diode-based input decoupling together with a single shared output power stage" has been maintained at the circuit level.

Parallel expansion

The concept of parallel-expanded MISO multi-port converters involves the establishment of multiple independent input ports by configuring the input stages in parallel at the front end of the primary power stage. Each port employs its intrinsic power conversion unit to feed into a common filtering network or DC bus, which is regulated by a centralized voltage controller. Figure 7a illustrates a typical parallel-type multi-port converter topology derived from boost converters, in which currents from multiple input ports converge at the common output capacitor [40]. Figure 7b demonstrates another parallel-type multi-port configuration evolved from Ćuk converters [41]; each parallel input port independently couples to a shared output stage through its dedicated Ćuk power stage, utilizing energy transfer capacitors and inductors to achieve port decoupling while concurrently sharing the post-stage filtering network. Such parallel integration approaches offer distinct advantages in terms of reduced component count, compact size, and enhanced energy integration capability.

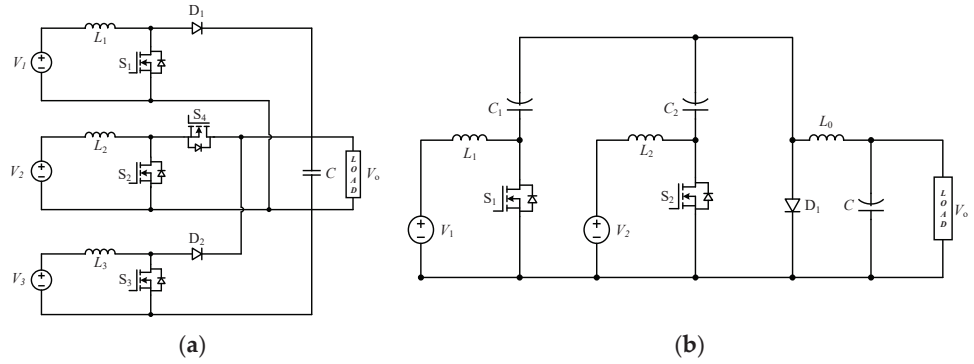


Figure 7. Parallel expansion MISO architecture: (**a**) boost-derived; (**b**) Ćuk-derived.

Current research on non-isolated "parallel expansion type" MISO MPCs is described in the following. At the circuit level, studies aim to enhance the voltage gain and efficiency of parallel connected systems through high-gain and high-power density designs. Typical approaches include combining parallel MISO-Boost topologies with multiple boost stages and coupled inductors to achieve higher voltage gains. Using soft switching technologies such as ZVS can reduce switching losses and device stress, improving power density while maintaining multi-port parallel integration [42,43]. For sources sensitive to current ripple, such as fuel cells, research has been conducted on reducing source-side ripple through phase-interleaved parallel connection and superimposing ripple compensation networks. At the same time, the structural advantages of continuous input current in Ćuk/SEPIC/modified ZSI and other similar topologies are utilized to further reduce ripple and EMI [44–46]. Some studies have explored the integration of passive resonant components into parallel-extended MISO MPC topologies. This technique broadens the ZVS operating range and effectively reduces input/output ripple currents without introducing additional active auxiliary switches, thereby improving the overall operational efficiency and reliability of the MPC [47,48]. In summary, current research for non-isolated parallel-extended MISO MPCs focuses on improving overall boosting performance and efficiency through advanced high-gain, high-power density designs, and reducing input ripple and

EMI by means of phase interleaving and ripple compensation networks. The soft-switching operational range can be extended further by passive resonant elements to further enhance system efficiency and reliability.

In the application of a hydrogen-based DC microgrid, the MISO architecture effectively integrates various distributed energy sources such as FC, PV, BESS, and SC, and uniformly connects them to a common DC bus. Of these, the interleaved boost topology has been applied to fuel cell applications, using ripple compensation and phase interleaving techniques to reduce the current ripple at the FC port, thereby improving the operating efficiency and stability of the fuel cell [33,46]. Furthermore, novel three-input boost topologies have been developed for hybrid scenarios involving PV, FC and BESS, facilitating flexible power allocation and coordinated control among multiple input ports through a unified voltage boost stage. This approach effectively addresses the demands of multi-source integration and dynamic power management within hydrogen-based DC microgrids [49,50]. Additionally, continuous current topologies such as Ćuk, SEPIC, and modified ZSI have been investigated due to their inherent smooth and continuous input–output current characteristics. These topologies effectively mitigate current ripple impacts on electrolyzers and fuel cells, thereby extending equipment lifespan and enhancing overall system efficiency [51,52].

3.1.2. Single-Input Multi-Output

Series expansion

The fundamental concept of the non-isolated "series-expanded" MPC topology is to connect multiple output stages in series on the DC side after the primary power stage, with energy transfer units following a single input source. Each stage is independently regulated, and its outputs are added in series on the DC side to form an expandable high-level bus. Figure 8 shows a non-isolated "back-end series expansion type" SIMO DC/DC converter topology based on a switched-capacitor-integrated boost architecture [53]. The input voltage V_i is uniformly switched by a common main switch S_1, and the back end consists of several repeated port power units that supply energy to corresponding output ports $V_{o1} \sim V_{on}$. The ground potential of each port equals the cumulative voltages of all preceding lower stages. The voltage at each port is sustained by local energy storage components and regulated individually via timing control. This topology embodies the characteristics of "shared front-end and back-end series expansion", addressing both multiple outputs and device multiplexing capability.

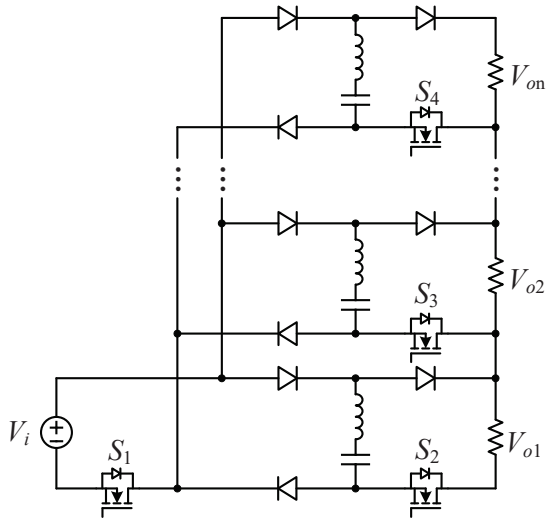


Figure 8. Boost-derived series expansion SIMO topology.

Current research on the non-isolated "series expansion type" SIMO MPC focuses on the following points. (1) Series cascaded structures based on voltage multipliers/switched capacitors: Recent studies integrate multi-stage voltage multipliers into conventional boost-type converters, forming non-isolated multi-output architectures characterized by multi-stage cascading and multi-port outputs. Such topologies achieve high voltage gain and port scalability while distributing device voltage stress across multiple stages [54,55]. However, critical challenges involve balancing the number of multiplier stages against efficiency, ripple, capacitor RMS currents, and energy redistribution losses among stages. (2) Hybrid inductor–capacitor structures with fewer active switches: Mixed "switched capacitor and switched inductor" structures generate multiple series outputs using a reduced number of active devices. Certain designs achieve multi-stage voltage stacking using a single PWM or single-switch driver, thereby reducing drive complexity and cost, while constraining the main switch voltage stress to a single-stage level [54]. However, Limitations of this approach include diode conduction losses and capacitor stresses arising from charge–discharge processes in voltage multiplier stages, necessitating careful consideration of device selection and thermal management. (3) Symmetrical multi-port topologies for bipolar DC buses: A "single-input/multi-output" configuration has emerged to serve bipolar low-voltage DC buses. Such structures inherently facilitate voltage self-balancing or simplify the balancing between positive and negative poles, thereby reducing the need for additional balancing converters [56].

Parallel expansion

The fundamental concept of the non-isolated "parallel-expanded" SIMO multi-port converter involves connecting multiple independent rectification and filtering branches in parallel at the output side after a single input power stage. Each branch takes energy from shared switches and rectification nodes, establishing the required DC voltage on its own branch to form multiple outputs. This structure reuses front-end devices, facilitates port expansion, and decouples each output through its own filtering network, allowing independent voltage levels to be set for each port. Figure 9 illustrates a boost-based non-isolated "parallel-expanded" SIMO multi-port converter topology [57]. A single input source V_s transfers energy through the input inductor L_1, which is centrally modulated by the main switching network. The output side consists of two parallel branches. The upper branch charges the capacitor C_1 through the diode D to form the first output V_{o1}. The lower branch extracts energy directly from the switching node and is filtered by L_2 and C_2 to yield the second output V_{o2}. The two outputs share the front stage but are not connected in series, reflecting the structural feature of "front stage sharing and back-end parallel expansion".

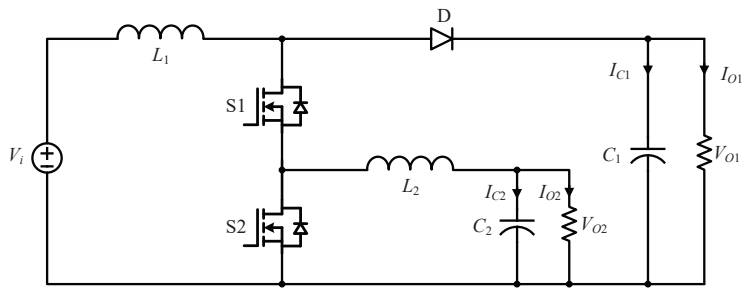


Figure 9. Boost-derived parallel expansion SIMO topology.

Existing research mainly focuses on three technical paths. (1) Incorporation of Coupled Inductor and SC/SL Units: To achieve a broader output range, recent studies integrate

coupled inductors and switched capacitor/switched inductor units into the SIMO back-end branches, enabling multiple buck–boost outputs simultaneously at relatively low-duty cycles [58,59]. However, trade-offs must be carefully managed regarding device stress and circulating currents. (2) Multiphase interleaving and soft-switching/resonant techniques: Recent studies have employed phase interleaving to reduce source side/bus ripple and improve transient performance under multi-phase superposition [57,60]. Meanwhile, introducing soft switching paths such as LLC and active clamping to achieve ZVS/ZCS can simultaneously reduce commutation loss and device stress, as well as improve efficiency [61,62]. (3) Energy buffering and decoupling strategies: As the number of output ports increases, the conduction time slot allocated to each individual port becomes restricted, exacerbating the trade-offs between transient and steady-state performance. The inherent "duty-cycle and inductor-charging sequence constraint" represents a structural limitation in SIMO converters. Recent studies have addressed this issue by integrating intermediate energy storage stages, energy-holding paths, or equivalent buffering units within the converter topology [63,64]. These methods effectively alleviate structural constraints, enhance each port's energy self-regulation capability, reduce cross-port interference, and significantly improve transient load response performance.

In hydrogen-based DC microgrid applications, non-isolated SIMO MPC architecture has been utilized to couple PV sources, DC buses, and electrolyzers. A non-isolated multi-port buck–boost architecture employs a two-phase interleaved boost mode to feed PV-generated power into the DC bus and utilizes a two-phase interleaved buck mode during the inductor energy release phase to supply power to the PEMEL, achieving coordinated allocation between PV-powered hydrogen production and bus power supply [65,66]. Additionally, a phase-interleaved SEPIC–Ćuk combined SIMO topology integrates bipolar bus outputs using a single switch, significantly reducing device count while balancing power distribution between positive and negative buses, which is particularly suited for low-voltage, compact hydrogen microgrid deployments [56]. A multi-port buck-based SIMO topology tailored for electric vehicles has also been investigated, achieving flexible multi-port power distribution with a single inductor and a minimal number of switches [67,68]. These advancements indicate significant advantages and broad engineering application potential for non-isolated SIMO topologies in hydrogen microgrids.

3.1.3. Multi-Input Multi-Output

Non-isolated MIMO DC–DC converters can achieve energy routing and voltage regulation for multiple-source and multiple-load scenarios within single-stage or reduced-stage power conversion structures. By deploying scalable energy transfer units (comprising inductors/capacitors combined with switches/diodes) at both the input and output sides, these converters enable independent or semi-independent regulation for each port while sharing magnetic and filtering components. Fundamentally, the design seeks a balance between port-decoupling capability and device/control complexity. Regardless of whether the input and output ports adopt series or parallel expansion methods, the system essentially forms a modulated energy channel matrix. Therefore, cross-regulation suppression, dynamic response, efficiency, and device stress must be cohesively addressed in design and control. Based on the modular interconnection methods (series or parallel) at the input and output sides, these topologies can be classified into four categories: ISOS, ISOP, IPOP, and IPOS. Figure 10a shows the energy convergence and current sharing of various DC sources at the front end of IPOS through diodes/switches connected to a common inductor. The back end uses cascaded switch capacitor units/stacked voltage outputs, allowing multiple output terminals to be connected in series in voltage to achieve high boost ratios

and multiple voltage levels, while the device voltage stress is shared by cascading. This structure is particularly suitable for scenarios where low-voltage high-current sources are paralleled and converged, and the load side requires high bus voltage or multiple voltage levels [69]. However, it requires addressing voltage balance and dynamic sharing among cascaded capacitors/modules. Figure 10b can be equivalently regarded as an ISOS/bipolar DC bus implementation, where multiple power units are series-connected at the input side to withstand high voltage, while their outputs are series-connected between the positive and negative poles to form a ± bipolar DC bus (with the midpoint stabilized by DC link capacitors). This configuration facilitates the use of lower-voltage-rated devices under high-voltage input/output conditions and increases power density [70]. However, it requires simultaneous management of input voltage balancing and output voltage balancing constraints.

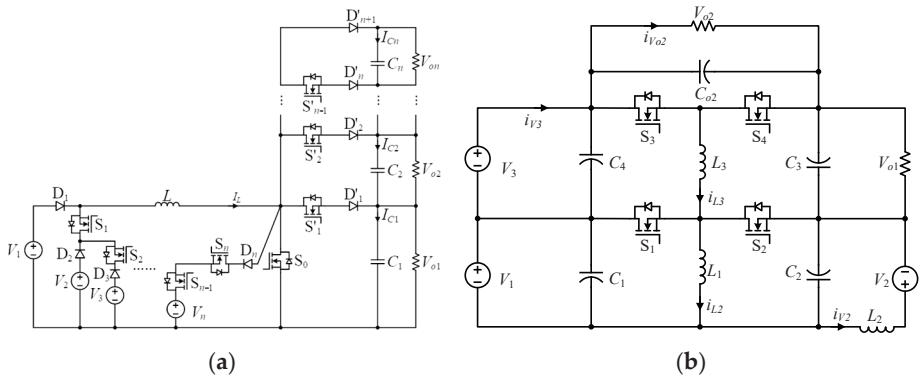


Figure 10. MIMO architectures: (**a**) Boost-derived IPOS topology; (**b**) buck–boost ISOS topology.

Recent research on multi-input multi-output (MIMO) DC–DC converters primarily focuses on the following themes. (1) Multi-port power/voltage/current balancing and decoupling control: Input voltage sharing (IVS) and output current/voltage sharing (OCS/OVS) within series parallel topologies (such as ISOP, ISOS, and IPOS) involve strong coupling and multiple interdependent links. Existing research has developed generalized control methods and stability designs for IVS and OCS/OVS [71]. However, when the system scales with increased ports or stages, coupled with device aging-induced parameter drift and asymmetric loading conditions, a unified and verifiable process for ensuring consistency in current/voltage sharing and fault-tolerant operation remains to be established. (2) High voltage gain combined with low device stress: To accommodate high-voltage DC buses or multi-level loads, existing research on non-isolated MIMO topologies has introduced voltage multiplier cells, coupled inductors, and phase-shifted or interleaved structures to achieve high voltage gain under low-duty cycles while effectively reducing device stress and conduction losses [72]. (3) Cross-port coupling and multi-objective control: Multi-input multi-output topologies inherently lead to energy interactions between sources and sources, sources and loads, as well as among loads, requiring power management to balance system efficiency, dynamic performance, and storage lifetime. Some studies have addressed this issue by adopting model predictive control (MPC) and hierarchical control strategies, achieving notable progress [73]. However, a scalable control framework remains insufficiently developed.

In the hydrogen DC microgrid, the non-isolated MIMO multi-port topology can connect the DER to the unipolar or ±bus uniformly to reduce cascading transformation and facilitate centralized energy management. For example, a PV–FC four-port DIDO interface designed for a 48 V bipolar bus employs a single inductor and two switches to achieve

polarity voltage regulation and MPPT for PV. This configuration significantly reduces the component count and control complexity, with its performance validated through prototype experiments [72]. Recent engineering-oriented MIMO solutions have further achieved high-gain capability and low component stress through independent port duty-cycle control, improving energy transfer from low-voltage sources to high-voltage buses and enhancing decoupling and controllability of critical ports like FCs and electrolyzers [74]. Furthermore, a 250 W MIMO prototype has demonstrated practical utility in isolated and remote microgrid applications, effectively mitigating cross-regulation issues and maintaining high efficiency with fewer components [71]. Additionally, continuous-current topologies such as Ćuk, SEPIC, and their combined multi-output variants have been extensively investigated. These topologies demonstrate effective ripple suppression that slows FC and electrolyzer aging while facilitating flexible bipolar or multi-level DC bus architectures [75]. Similar non-isolated multi-port structures have been experimentally validated in electric vehicles, highlighting their promising application potential in hydrogen-integrated EV scenarios [76].

3.2. Isolated Multi-Port Converter Architecture

Isolated multiport converters are built around a transformer that provides galvanic isolation and thereby electrically decouples the ports. Based on current trends in topology evolution, the isolated MPC architecture can be broadly classified into two categories. The first is the topology-derived type, where the transformer retains a fixed number of windings, and multiple DC ports are obtained by flexibly combining or reconfiguring these windings with an external power stage. The primary advantages of this category of converter are the scalability and flexibility of the power stage topology. Research in this field typically focuses on achieving efficient multi-port power conversion, enhancing energy density, and optimizing component sharing. The second category is the multi-winding transformer-derived type, which increases the number of transformer windings to expand the number of ports. Typical examples of this category include the Triple Active Bridge (TAB) and Multi-Active Bridge (MAB) topologies. Research on this type of topology primarily focuses on transformer design, optimization of coupling effects between windings, and improvements in energy transfer efficiency.

3.2.1. Topology-Derived Type

In the isolated "topology-derived" MPC, DC ports are expanded by flexibly reconfiguring the power stage at the transformer port without altering the number of windings in the isolation transformer. Currently, there are two representative approaches in hydrogen-based DC microgrids. The first employs a single two-winding isolation transformer as the sole isolation path, with multiple power stages (such as full-bridge/half-bridge, resonant, or current-source units) interfaced around the same high-frequency link. This approach creates multiple branch ports on both sides of the transformer, thus facilitating port decoupling and high design portability. Figure 11 illustrates a topology-derived isolated DC–DC converter that implements primary-side parallel aggregation, single-transformer isolation, and a post-stage bipolar DC bus [77]. Three generic sources are interfaced through input capacitors and inductors to function as independently dispatchable current-type ports, with their currents aggregated at a common node. The combined current excites a primary full bridge $S_1 - S_4$ via a DC-blocking/energy transfer branch (C_3, L_3) and a single transformer, providing high-frequency galvanic isolation, voltage scaling, and a wide soft-switching window. In the second approach, a synchronous full bridge $S'_1 - S'_4$ followed by L_4 forms

a bipolar DC bus. An active midpoint balancer (switch S_v with diodes D_{a-d}) equalizes the two rails so that the output voltages V_{o1} and V_{o2} remain under load asymmetry.

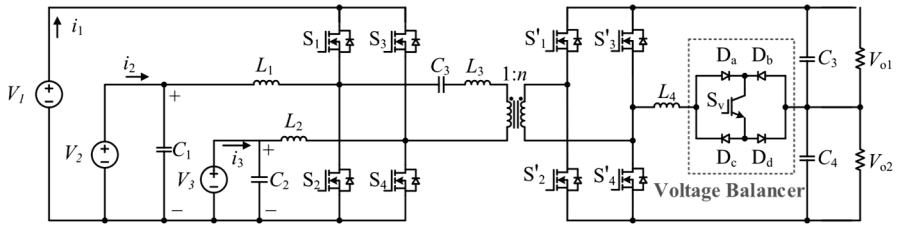


Figure 11. Topology-derived isolated MIMO topology.

Another approach adopts a modular structure composed of standardized submodules with high-frequency isolation as basic building blocks. Each submodule comprises a primary-side power stage (full bridge/half bridge, resonant, or DAB), a dual-winding high-frequency transformer (MFT), and a secondary-side rectifier/active bridge with a filter network. Multi-port expansion is achieved by adding or reconfiguring submodules and interconnecting their inputs or outputs through series or parallel arrangements to form multiple DC ports. Figure 12 illustrates a typical topology for this configuration, employing the ISOS modular structure paradigm, where identical isolated submodules are series-stacked on both the input and the output to increase the voltage rating [78]. In each submodule, there features a voltage-source full bridge on the primary side, driving the isolation transformer via leakage/resonant inductors L_1 and L'_1. Phase-shift modulation achieves voltage matching while extending the ZVS operating range of primary-side components. On the secondary side, the full-bridge diodes rectify the high-frequency voltage into pulsating DC. This can be combined with phase-interleaved rectification to further suppress ripple and reduce filter size, thereby allowing linear scaling of the number of ports and the rated voltage with the module count.

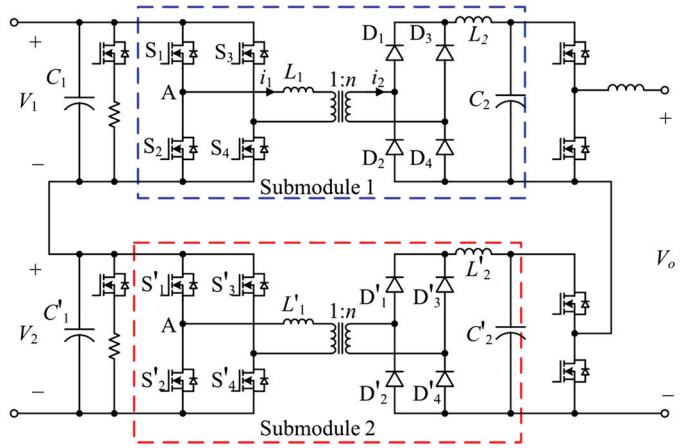


Figure 12. Topology-derived isolated MISO modular topology.

Within the family of single-transformer, two-winding high-frequency-link architectures, research has progressed from early three-port/multi-port full-bridge structures to derivative designs that incorporate buck/boost branches, voltage-multiplying or rectification networks, and resonant elements on the primary/secondary sides [79,80]. Furthermore, some designs extend the port and broaden the soft-switching operating range without adding windings, thereby reducing the voltage/current stress of the component and backflow power [81,82]. Typical approaches include introducing LCL/LLC resonant

branches or voltage-doubling rectification within dual-winding structures to suppress voltage/current stresses and broaden the soft-switching range, whilst mitigating port coupling and circulating current issues arising from shared magnetic flux [83,84]. However, the inherent challenges remain in cross-port power decoupling, leakage inductance selection, and magnetic–electrical co-design to balance efficiency and power density.

Along with the modular architecture, research converges on a multi-module structure with series/parallel networking. ISOS, ISOP, IPOS, and IPOP arrangements enable scalable voltage and current ratings while distributing device voltage stress [85,86]. However, this introduces challenges of input voltage sharing, output current sharing, and dynamic consistency. To address these issues, voltage- and current-balancing circuits and decoupling networks should be integrated at the topology level, alongside optimization of equivalent loop and parasitic parameters [85]. Overall, the "two-winding transformer with power-stage combination" emphasizes the coordinated design of magnetic flux utilization and device/parameter decoupling among ports, while the "multi-module with series/parallel networking" approach focuses more on cross-module consistency and reliability design.

In hydrogen-based DC microgrids, the two aforementioned categories of "topology-derived isolated converters" each possess distinct application scenarios. The single-transformer, two-winding architecture, characterized by its compact structure and efficient reuse of power devices, is suitable for coupling multiple sources such as PV, FC, and BESS to either unipolar or bipolar DC buses via a centralized high-frequency link. This topology can be integrated with voltage balancers or polarity balancing networks to maintain mid-point voltage and mitigate imbalance in bipolar DC buses. This approach has already found engineering applications in hybrid energy microgrids and electric vehicle systems, serving as a multi-port interface and for power routing, benefiting from its high power density and reduced number of magnetic components [87,88]. For applications requiring high bus voltage, long feeder lines, or N + 1 redundancy and online capacity expansion, the modular architecture can meet voltage and insulation requirements through the free combination of output series/parallel and input series/parallel configurations, while facilitating power level standardization and reliability design [78,85,86]. This design concept has also been validated in DC systems incorporating hydrogen storage and electrolyzers, as well as in bipolar DC microgrids, demonstrating its feasibility and scalability [89,90].

3.2.2. Multi-Winding Transformer-Derived Type

The isolated "Multi-Winding Transformer Derived Type" multi-port converter linearly expands DC ports by increasing the number of windings on the common high-frequency magnetic link. Each port is typically coupled via an active full-bridge circuit to a multi-winding high-frequency transformer. Therefore, power transmission between ports can be achieved through phase-shift control, along with the coupling inductance provided by transformer leakage or an external series inductor. This design inherently supports bidirectional power flow, fixed-frequency operation, and electrical isolation. Figure 13 illustrates a representative three-port configuration. Port 1 interfaces the primary through a full bridge, while two secondary windings (1:N_1 and 1:N_2) transfer power to Ports 2 and 3 via their respective full bridges and filters. Power sharing among ports is governed by phase-shift control, which allows the energy storage system to operate bidirectionally, enabling charge and discharge [91].

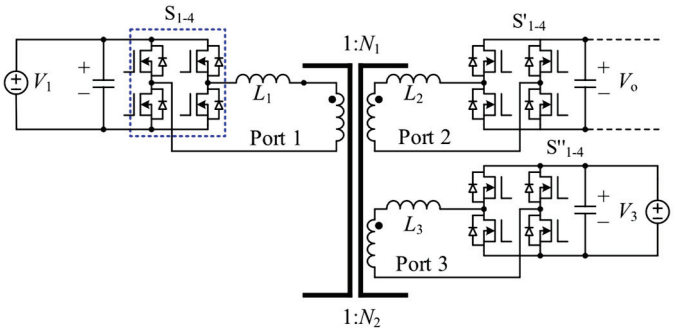


Figure 13. Multi-winding transformer-derived topology.

Current research on isolated multi-winding transformer-derived multi-port converters concentrates on four themes. (1) Power–flow decoupling: the power transfer matrix of the multi-winding transformer-derived type is inherently coupled, so port voltages and phase-shift variables are mutually dependent [92]. To address this, control frameworks based on continuous time averaged (state-space) models, look-up table decoupling matrices, and model–reference decoupling have been proposed to enhance independent port regulation and dynamic stability [93]. (2) Multi-winding transformer design: The allocability of inter-winding leakage inductance and coupling coefficients determines soft-switching boundaries and transmissible power. Recent work has proposed collaborative design/calculation methods and equivalent modeling for multi-port leakage inductance, enhancing design prediction accuracy [94–96]. (3) Zero-sequence circulating current: Three-winding configurations or those incorporating delta/center-tap structures may generate zero-sequence paths and circulating currents, introducing additional losses and port recoupling. Comprehensive suppression measures are required through winding connections and shielding, equivalent modeling, and control strategies [96,97]. (4) High efficiency and wide ZVS range: In transformers with three or more windings, connection arrangements such as star (Y), delta (Δ), or stabilizing windings introduce zero-sequence paths and circulating currents, resulting in undesirable coupling between ports. Current research addresses this issue through careful design of magnetizing inductances, multi-phase modulation strategies, and phase-shift optimization techniques to extend full-port ZVS, thereby reducing RMS currents and conduction losses [98,99]. Although notable progress has been made in this direction, a systematic and unified design and validation approach balancing the three-dimensional trade-off among high port-count, high power-density, and manufacturability remains an open research gap.

In hydrogen-based microgrids and hydrogen-coupled systems, the multi-winding transformer-derived (MWTD) architecture has been employed to simultaneously couple multiple ports, including FC, EL, and BESS, within a common high-frequency magnetic link to achieve single-stage energy aggregation and flexible power distribution [91]. Specifically, this topology utilizes a single multi-winding high-frequency transformer to realize electrical isolation and flexible power exchange among different ports, making it particularly suitable for scenarios requiring frequent bidirectional power flows between electrochemical storage devices and renewable energy units. Furthermore, MWTD topologies also show promising application prospects in renewable energy electric vehicle charging stations and onboard vehicle charging and discharging systems [100,101].

4. Comparative Analysis and Considerations

Building upon the classification and detailed analysis of isolated and non-isolated MPC topologies presented above, this section presents a comparative evaluation highlighting their

key performance characteristics, structural complexities, and suitability for hydrogen-based DC microgrid applications. Furthermore, considerations are presented regarding the impacts of current ripple and ramp rate on hydrogen-based distributed energy resources, the selection of optimal control strategies, and the impact of emerging semiconductor technologies on MPC topologies. Moreover, existing challenges and targeted recommendations for future research directions are discussed within each of these subsections.

4.1. Comparative Analysis of MPCs

Table 2 summarizes the key parameters of typical multi-port converters (MPCs) within the previously discussed non-isolated and isolated architectures, including output voltage expressions, topological complexity, typical efficiency, estimated power density, and bidirectional power-flow capability. In general, non-isolated topologies feature simpler structures and fewer components than isolated counterparts, which makes them attractive in applications that are sensitive to cost or require high power density. Owing to the absence of isolation windings, non-isolated MPCs usually achieve a relatively higher estimated power density. By contrast, isolated topologies tend to exhibit slightly lower power density because transformers or multi-winding magnetic components increase both volume and structural complexity. Both categories can reach high efficiency, although the exact values depend on device ratings, control strategy, and operating conditions. The lack of galvanic isolation in non-isolated configurations, however, limits system-level safety and scalability. Isolated MPCs, on the other hand, provide electrical isolation and modular expansion through transformers or multi-winding structures, at the expense of higher device count and more intricate control. Moreover, isolated topologies often rely on more complex modulation schemes, such as phase-shift modulation, whereas non-isolated MPCs typically employ simpler PWM-based control. Finally, while bidirectional power-flow capability significantly enhances system flexibility, it also increases control and design complexity; this trade-off should be carefully evaluated in practical engineering applications, motivating future research into hybrid structures that combine the advantages of both isolated and non-isolated MPCs.

According to the topology structure analysis shown in Table 3, non-isolated multi-port converters (MISO, SIMO, MIMO) generally exhibit characteristics such as low current ripple and high power density. However, as the number of ports increases, their control complexity and component count also rise accordingly. For example, MISO topologies like ISOS-Buck offer the advantages of simple circuitry and low cost, making them more suitable for unidirectional step-down applications such as PEMEL. The SIMO structure (e.g., ISOS-Boost) employs independent rectification outputs for each port, making it suitable for PV, WT, and FC interfaces, but it faces challenges such as cross-regulation between ports and current sharing, alongside increased switching components. MIMO structures (e.g., IPOS-Boost) possess multi-level output capability, suitable for various energy storage devices such as BESS and SC, but with further increased control complexity. In contrast, isolated multi-port converters (TD and MWTD) demonstrate outstanding performance in galvanic isolation, safety, and reliability. These topologies typically employ phase-shift modulation (PSM) to achieve soft-switching and reduce switching losses. For instance, hybrid topologies feature DC bus voltage adaptive balancing capability, suitable for most distributed energy interfaces, albeit accompanied by complex control strategies and high costs. Additionally, TAB structures can achieve bidirectional power flow between arbitrary ports and are suitable for soft-switching operation, particularly appropriate for applications requiring flexible configuration and high safety. However, these structures are constrained by magnetic component dependency and control strategy complexity, increasing the difficulty of design and application.

Table 2. Key parameters of typical topologies in multi-port converter architecture.

MPCs		Output Voltage	NP	S	D	L	C	W	EF	PD	BPF
MISO	ISOS-Buck [30]	$V_o = D_1V_1 + D_2V_2$	3	2	2	1	1	×	94.16%	*****	×
	ISOS-Boost [31]	$V_o = \frac{V_1D_1+V_2D_2}{D_y} = \frac{V_1D_1+V_2D_2}{1-D_x}$	3	4	4	2	1	×	92–95%	****	×
	IPOS-Boost [40]	$V_o = \frac{V_1}{1-D_1} = \frac{V_2}{1-D_2} = \frac{V_3}{1-D_3}$	4	4	2	3	1	×	90–95%	****	×
	IPOS-Cuk [41]	$V_o = \frac{D_1}{1-D_1}V_1 + \frac{D_2(D_2-D_1)}{(1-D_1)(1-D_2)}V_2$	3	2	1	3	3	×	94.13%	****	×
SIMO	ISOS-Boost [53]	$V_i = \frac{D_b}{1-D_b}\sum_{i=1}^{n} V_{oi}$	3	3	6	2	2	×	90%	****	×
	ISOP-Switched-Boost [57]	$V_{o1} = \frac{V_{in}}{1-D}; V_{o2} = \frac{D(\lambda-1)V_{in}}{1-D}$	3	2	1	2	2	×	94–96%	****	×
MIMO	IPOS-Boost [69]	$\begin{bmatrix} V_{O1} & V_{in2}-V_{in1} & V_{O2} \\ R_1I_b & V_{O1} & 0 \\ 0 & V_{O2} & R_2I_b \end{bmatrix}\begin{bmatrix} D_1 \\ D_3 \\ D_4 \end{bmatrix} = \begin{bmatrix} V_{O2}+V_{O1}-V_{in1} \\ R_1I_b \\ R_2I_b \end{bmatrix}$	4	4	4	1	2	×	80.5%	*****	×
	ISOS-Buck-Boost [70]	$\begin{cases} V_{o1} = \frac{D_3}{1-D_3}V_3 + \frac{D_1-D_3}{1-D_3}(V_1+V_2) \\ V_{o2} = \frac{1}{1-D_3}V_3 + \frac{1+D_1-2D_3}{1-D_3}(V_1+V_2) \\ V_{o1} = \frac{D_3}{1-D_3}V_3 + \frac{D_3-D_1}{1-D_3}(V_1+V_2) \\ V_{o2} = \frac{1}{1-D_3}V_3 + \frac{1-D_1}{1-D_3}(V_1+V_2) \end{cases}$	5	4	×	3	5	×	×	***	√
TD	Hybrid [77]	$V_3 = V_1(1-D_3); V_2 = V_1(1-D_2)$	5	8	4	3	5	1	95.37%	***	√
	Hybrid [78]	$V_o = \frac{(D-k)U_1^2T}{L_sI_o}$	3	14	8	5	4	2	×	***	√
MWTD	TAB [91]	$\begin{cases} i_1 = \frac{V_2'}{\omega L_{21}}\varphi_{21}\left(1-\frac{\lvert\varphi_{21}\rvert}{\pi}\right) + \frac{V_3'}{\omega L_{31}}\varphi_{31}\left(1-\frac{\lvert\varphi_{31}\rvert}{\pi}\right) \\ i_2 = \frac{V_1}{\omega L_{21}}\varphi_{21}\left(1-\frac{\lvert\varphi_{21}\rvert}{\pi}\right) - \frac{V_3'}{\omega L_{32}}\varphi_{32}\left(1-\frac{\lvert\varphi_{32}\rvert}{\pi}\right) \\ i_3 = \frac{V_1}{\omega L_{31}}\varphi_{31}\left(1-\frac{\lvert\varphi_{31}\rvert}{\pi}\right) + \frac{V_2'}{\omega L_{32}}\varphi_{32}\left(1-\frac{\lvert\varphi_{32}\rvert}{\pi}\right) \end{cases}$	3	12	×	3	3	3	94–96%	***	√

NP: number of ports, S: switch, D: diode, L: inductor, C: capacitor, W: Winding, EF: efficiency, PD: power density(***–*****: qualitative level from low to excellent), BPF: bidirectional power flow (√: yes, ×: no).

Table 3. Comparison of typical MPC topologies and DER suitability.

	MPCs	MS	Merits	Limits	MSDP
MISO	ISOS-Buck [30]	PWM	Simple circuitry; low cost.	Coupled duty cycle allocation among sources; step-down only.	PEMEL
	ISOS-Boost [31]	PWM	Low input current ripple; dynamic power sharing.	Input port coupling and circulating current boundary; parameter mismatch degrades dynamic and steady-state performance.	PV; WT; FC;
	IPOS-Boost [40]	PWM	Scalable to additional ports.	Magnetic design complexity; higher control complexity and cost.	PV; WT; FC
	IPOS-Cuk [41]	PWM	Continuous port currents; low ripple.	More involved control; high stress on the coupling capacitor.	PV; WT; FC

Table 3. *Cont.*

	MPCs	MS	Merits	Limits	MSDP
SIMO	ISOS-Boost [53]	PWM	Independent rectification and output capacitors per port; strong extensibility.	Cross-regulation and current sharing issues among outputs; higher switch count.	PV; WT; FC
	ISOP-Switched-Boost [57]	PWM	Low current ripple; reduced device count; supports simultaneous step-up/step-down.	Multiple coupled control variables; port coupling; operating region constrained by λ.	PV; WT; FC; PEMEL
MIMO	IPOS-Boost [69]	PWM	High power density; multi-level DC bus.	Multi coupled control variables; complex control.	PV; WT; FC; BESS; SC
	ISOS-Buck-Boost [70]	PWM	Good adaptability to power level; fewer devices.	Coupling with bipolar DC bus; complex control.	Most DERs
TD	Hybrid [77]	PSM	Galvanic isolation; automatic balancing of bipolar bus voltages.	Complex control strategy; higher cost.	Most DERs
	Hybrid [78]	PSM	Modular architecture; graceful degradation under single-module faults.	High cost; multi-module control complexity.	Most DERs
MWTD	TAB [91]	PSM	Bidirectional power flow between any ports; soft switching.	Large number of magnetic components; reliance on leakage-inductance design; complex control.	Most DERs

MS: modulation strategy, MSDP: most suitable DER ports.

In summary, non-isolated topologies are more suitable for low-voltage applications or scenarios with cost and space constraints, while isolated topologies are better suited for high-voltage levels, bidirectional power transfer, or complex energy systems with higher safety requirements. However, each category faces specific challenges in practical engineering. The key challenge for non-isolated topologies lies in dynamic cross-regulation issues, where mutual interference between ports affects stable system operation. This challenge can be addressed by introducing optimized control strategies such as dual-loop control, distributed coordinated control, or model predictive control to achieve precise coordination and effective decoupling of power between ports. Isolated topologies primarily face challenges in high-frequency transformer design complexity and soft-switching technology implementation. Although galvanic isolation enhances system safety and reliability, challenges such as precise control of transformer leakage inductance, thermal management of magnetic components, and extending the operational range of soft-switching techniques remain critical and require further investigation. Therefore, future research should focus on the collaborative optimization of magnetic integration design and soft-switching control strategies and further explore novel transformer structures and materials to reduce transformer design difficulty and cost, thereby promoting broader practical applications of isolated multi-port converters.

4.2. Discussion and Consideration

4.2.1. Impact of Current Ripple and Ramp on Electrochemical DER

Current ripple, an inherent dynamic characteristic of power electronic converters, significantly impacts the performance and longevity of PEMFC and PEMEL in hydrogen-

based distributed energy systems. During PEMFC operation, ripple superimposed on DC current induces periodic charge accumulation and fluctuations in reactant concentrations at the membrane electrode assembly (MEA) interface. Specifically, low-frequency ripple (approximately 100–300 Hz) disrupts the oxygen reduction reaction (ORR) at the cathode catalyst layer, resulting in cyclic increases in interfacial charge transfer impedance and reductions in double-layer capacitance [102]. These dynamic electrochemical disturbances manifest as pronounced I–V hysteresis in the MEA polarization curves, causing delays in operating voltage response to current changes and consequently introducing additional activation polarization losses. Furthermore, frequent load fluctuations compel the fuel supply system to operate at elevated hydrogen flow rates to meet instantaneous peak current demands, decreasing hydrogen utilization efficiency and indirectly increasing overall fuel consumption. High-frequency ripple (>10 kHz), although too rapid for complete electrochemical reaction responses within the MEA, generates additional internal ohmic losses within the membrane and electrode structure [103]. These losses elevate local temperatures within the MEA, accelerating thermal aging effects on catalyst layers and membrane materials and thus negatively affecting the long-term performance of fuel cells.

Proton exchange membrane electrolyzers exhibit operational characteristics similar to PEMFCs; however, ripple-induced mechanisms differ distinctly. In PEMEL systems, low-frequency current ripple typically exerts negligible short-term effects on hydrogen production since the hydrogen yield primarily depends on the average current. Conversely, high-frequency current ripple adversely affects long-term PEMEL operation by inducing rapid potential fluctuations at the anode, causing frequent oxidation-reduction cycles on electrode materials. This phenomenon accelerates passivation processes in critical components such as titanium-based electrode meshes, incrementally raising the electrolyzer's internal high-frequency resistance (HFR). Additionally, increased HFR restricts gas bubble detachment and water mass transport, further diminishing the electrolyzer's operational stability and durability over extended operation periods [104].

Specifically, the impact of current ripple on hydrogen-based distributed energy performance has been validated in multiple experimental studies. In an experimental investigation of a prototype 300 W fuel cell UPS system, when continuous 100–120 Hz low-frequency ripple with approximately 24.3% amplitude was present, the MEA electrochemical characteristics underwent periodic disturbances, resulting in significant voltage output lag effects, ultimately leading to reduced system operating efficiency and accelerated fuel cell lifespan degradation [105]. Another study on high-frequency ripple effects on a 1100 W rated fuel cell stack demonstrated that at a 10 kHz frequency, even a 2% current ripple could reduce stack output voltage by approximately 2 V, with voltage drop further intensifying to over 4 V when ripple amplitude increased to 20% [103]. This voltage drop forces the fuel cell to increase hydrogen supply to maintain the same power output, increasing fuel consumption. Additionally, durability experiments on long-term PEMEL operation indicate that while high-frequency (10 kHz) ripple does not significantly reduce hydrogen production efficiency in the short term, over 3000 h of testing it increased internal high-frequency resistance to more than twice that of low-frequency and ripple-free conditions, while exacerbating titanium mesh electrode passivation [106]. This demonstrates the negative impact of high-frequency ripples on PEMEL system long-term operational lifespan.

To address current ripple effects in PEMFC and PEMEL-based distributed energy systems, the specific constraints inherent to hydrogen applications should be carefully considered during converter selection and design. Because of the pronounced ripple sensitivity and relatively slow dynamic response of hydrogen-based electrochemical devices, converters should provide highly continuous input current and effective transient

buffering capability. Continuous-current topologies, such as Ćuk and SEPIC converters, inherently possess advantages in this respect, as inductors placed on both the input and output sides naturally smooth the currents, significantly reducing ripple propagation toward hydrogen equipment and thus protecting the electrochemical interface. However, these topologies require separate inductors for each port or additional coupling capacitors (such as in the Ćuk topology), resulting in reduced power density and increased magnetic complexity in high-power scenarios. In comparison, conventional single-inductor topologies, such as boost or buck converters, offer simpler circuits, fewer magnetic components, and higher power density. Nevertheless, these topologies typically produce pulsating currents on one side, necessitating large filtering capacitors to suppress ripple, which increases losses and the risk of parasitic resonances and may affect the long-term reliability and stability of the system. For MPC topology selection in hydrogen-based applications, the trade-off among topology complexity, component count, power density, and ripple performance should therefore be carefully assessed and optimized. It is noteworthy that, at the present stage, requirements on admissible current-ripple levels at PEMFC and PEMEL interfaces are predominantly formulated as device or stack-level operating guidelines and optimization targets reported in the literature, rather than as universally harmonized standards. A technology-wide standard defining admissible ripple thresholds across hydrogen-based electrochemical applications has not yet been established. Therefore, future research could focus on developing unified ripple metrics and interface specifications for hydrogen-based MPC systems. Such standardized criteria would explicitly relate the electrochemical ripple sensitivity inherent to PEM devices to the ripple characteristics associated with different multi-port converter topologies, thereby supporting converter designs that preserve high operational efficiency and enhance the durability of hydrogen-based electrochemical systems.

Additionally, interleaving technology utilizes multiple parallel phases whose ripple components partially cancel each other, effectively reducing the ripple seen by hydrogen-based equipment without significantly increasing the number of magnetic components. Consequently, this enhances the practical applicability of interface converters. Furthermore, the applicability of active power-decoupling circuits and active filtering techniques for handling low-frequency current ripple should be more thoroughly evaluated. These methods, through coordination of circuit topology and control algorithms, can achieve a more stable system input current, thereby reducing dynamic disturbances at the MEA interface. In summary, establishing unified ripple standards for hydrogen-based electrochemical devices and minimizing current ripple through optimized converter topologies and advanced control strategies represent key future research directions in hydrogen-based distributed energy systems.

4.2.2. Effect of Current Ramp on Electrochemical

Elevated current slew rate, as a critical variable in the dynamic operation of electrochemical devices, affects the performance and lifespan of PEMFC and PEMEL in hydrogen-based distributed energy systems. From a fundamental perspective, both types of device contain electrode double-layer capacitance that can provide instantaneous response during current transients; however, the lag in reactant supply and product removal typically induces transient voltage overshoot or undershoot phenomena. Specifically, when current slew rate rises rapidly, the cathode ORR rate in PEMFC increases instantaneously, but the required oxygen supply often cannot meet the demand in time, leading to local oxygen concentration depletion at the cathode catalyst layer, increased charge transfer impedance, and resulting instantaneous voltage undershoot. Meanwhile, temporary hydrogen insufficiency

at the anode may trigger side reactions such as carbon support oxidation, accelerating catalyst and membrane degradation [107]. Similarly, in PEMEL systems, rapid current increase causes the anode oxygen evolution reaction (OER) to intensify rapidly, generating substantial oxygen bubbles that accumulate on the electrode surface, impeding timely water reactant transport and bubble detachment, reducing the effective catalytic area, thus manifesting as voltage overshoot phenomena [108]. Furthermore, the response characteristics of both types of devices differ during rapid current slew rate decrease. In PEMFC, when current decreases rapidly, the abrupt reduction in water production combined with gas supply inertia may cause temporary drying at the membrane–electrode interface, resulting in reduced membrane conductivity and voltage fluctuations. In PEMEL systems, rapid current decrease leads to swift reduction in anode reaction rate, with corresponding decrease in bubble generation at the electrode surface, causing drastic changes in water content at the membrane–electrode interface, potentially inducing periodic fluctuations in mechanical stress and accelerating material aging.

Current research has experimentally validated the adverse effects of high current slew rates on PEM systems. Dynamic load cycling experiments conducted on a PEMFC prototype single cell with an active area of 25 cm^2 and rated power of 250 W demonstrated that, after 2000 cycles at a high current slew rate of 1.0 $A/cm^2/s$, cell output performance decreased by approximately 20.67%, roughly twice the performance loss observed with low slew rate cycling at 0.3 $A/cm^2/s$ [107]. Additionally, in a PEMEL electrolyzer prototype with an active area of 5 cm^2, after 700 cycles at a high current slew rate of approximately 2.9 $A/cm^2/s$, the internal HFR increased to approximately 1.6 times its initial value [109]. This confirms the direct negative impact of severe current slew rate fluctuations on the internal electrical performance of PEMEL.

To mitigate the adverse effects of excessive current slew rates, improvements can be implemented through power electronic converter control strategies. First, current slew rate limiting functionality can be incorporated into the converter controller by setting maximum allowable current change rates (di/dt limiting), preventing transient issues in hydrogen-based distributed energy sources through gradual regulation of current change rates. Second, introducing advanced control strategies such as feedforward control and model predictive control to optimize current rise and fall trajectories can avoid abrupt changes, smoothing current transitions and reducing the impact of transient overshoot/undershoot on the system.

4.2.3. Selection of Optimal Control Strategies

Control strategies for multi-port converters also have a direct impact on the performance and equipment lifespan in hydrogen-based DC microgrids. From a control complexity perspective, basic control strategies such as conventional PI and droop control are suitable for remote areas or cost-constrained scenarios due to their simple structure and good economic feasibility. However, these control methods are limited by fixed parameter settings and exhibit limited dynamic response speed and control accuracy under severe load variations or significant nonlinearity, making it difficult to effectively suppress current ripple and current slew rate in PEMEL and PEMFC, potentially leading to reduced equipment lifespan during long-term operation.

To address these shortcomings, several improved control strategies such as dual-loop PI control, hierarchical coordinated control, sliding mode control, and active disturbance rejection control (ADRC) have increasingly been applied to multi-port converters in recent years [110]. These control strategies can significantly improve DC bus voltage stability and load disturbance adaptability while maintaining moderate costs by enhancing local

control and system anti-disturbance capability. For instance, sliding mode control, with its robustness to parameter uncertainties and fast dynamic response, can effectively reduce DC bus voltage fluctuations and current ripple caused by inter-port power interactions, alleviating transient impacts on PEMEL and PEMFC ports. These control strategies have a moderate cost and control complexity, and are suitable for small industrial parks or hydrogen systems requiring frequent switching of operating modes.

In scenarios demanding extremely high control accuracy and dynamic performance, advanced intelligent control strategies such as MPC, neural networks, and meta-heuristic optimization algorithms have been extensively studied and applied. These strategies can effectively reduce the current ripple and current slew rate in PEMEL and PEMFC through real-time optimization of control variables and system prediction models, thereby avoiding the MEA degradation and electrolyzer efficiency decline caused by severe current variations. For example, recent research has demonstrated that combining MPC control with multi-phase interleaved topology can maintain PEM electrolyzer current ripple below 0.5%, significantly improving hydrogen system operational stability and equipment lifespan [111]. However, these control techniques involve high computational complexity and hardware costs, making them more suitable for high-precision applications such as large-scale hydrogen production facilities or grid-side DC microgrids.

Currently, reducing the computational complexity and implementation costs of advanced control strategies to promote their application in cost-constrained regions for hydrogen microgrids remains an important research topic. Additionally, to further ensure the lifespan of hydrogen-based distributed energy equipment, future control strategy design should incorporate equipment aging status and prognostics and health management (PHM) techniques into control strategies, achieving synergistic optimization of control performance and equipment durability.

4.2.4. Impact of Emerging Semiconductor Technologies on MPC Topologies

Emerging semiconductor technologies such as silicon carbide (SiC) and gallium nitride (GaN) devices offer significant advantages over traditional silicon devices, owing to their wide bandgap, low conduction losses, and fast switching characteristics. Furthermore, in terms of switching frequency and power density, wide bandgap semiconductor devices support higher switching frequencies, enabling MPC to substantially reduce the size of passive components such as filter inductors and transformers, thereby increasing power density.

The application of these novel devices has positively impacted multi-port converter performance. A study on a hybrid multimodule DC–DC converter demonstrated that using GaN transistors could achieve a peak efficiency of 99.25% at a high switching frequency of 100 kHz in simulation. In another research case, a three-port boost–buck converter employing SiC MOSFETs achieved 94.3% efficiency [112]. These experiments demonstrate the application prospects of novel semiconductor devices in hydrogen-based DC microgrids. However, the high manufacturing costs and process complexity of these novel devices remain key factors constraining their large-scale deployment. Therefore, future research should focus on exploring the design of multi-port DC converters that leverage advanced semiconductor devices to achieve high efficiency and high power density, balancing technical performance with economic feasibility to promote the practical application of hydrogen microgrids.

5. Conclusions

This review systematically analyzes the mainstream topologies and technical developments of MPCs in hydrogen-based DC microgrids. Based on an analysis of various DER interfaces, it is concluded that MPCs should possess flexible power distribution capabilities, wide-range high-voltage-gain conversion abilities, and low ripple current. The specific topology analysis reveals that non-isolated multi-port converters, with their compact structure and high efficiency and density, are suitable for small- and medium-scale applications and residential scenarios. In contrast, isolated multi-port converter topologies typically incorporate winding transformers to achieve electrical isolation. This feature makes them particularly suitable for scenarios demanding improved system safety and electrical isolation. Specific applications include high-voltage electrolytic hydrogen production systems and industrial hydrogen storage integration. Although existing topologies have achieved positive technological advancements, several critical issues still persist. These include power decoupling control between ports, optimization of soft-switching operating regions, balanced design between high-voltage gain and device stress, and coordinated optimization for system stability. The following future research directions are recommended: (i) advanced ripple mitigation through interleaving and active power decoupling techniques to improve PEMFC and PEMEL lifespan; (ii) current slew rate management via advanced control strategies and slew rate limiting to reduce transient impacts on electrochemical DERs; (iii) integration of hydrogen storage systems with BESS and supercapacitors to leverage complementary advantages; (iv) hybrid converter topologies integrating isolated and non-isolated advantages through optimized magnetic design and soft-switching technologies; and (v) emerging semiconductor integration emphasizing high-frequency operation and improved efficiency in hydrogen-based DC microgrid. Collectively, these proposed directions are expected to expedite the engineering translation and scalable deployment of multi-port converters in hydrogen-based DC microgrids.

Funding: This research received no external funding.

Data Availability Statement: No new data were created or analyzed in this study.

Conflicts of Interest: The authors declare no conflict of interest.

References

1. Lopez, G.; Aghahosseini, A.; Bogdanov, D.; Satymov, R.; Oyewo, A.S.; Breyer, C. Sustainable Energy Industry Systems in the United States and Canada Demonstrating the Value of Solar-to-X. *IEEE J. Photovolt.* **2025**, *15*, 215–222. [CrossRef]
2. IEA. *Global Energy Review 2025*; IEA: Paris, France, 2025. Available online: https://www.iea.org/reports/global-energy-review-2025 (accessed on 11 October 2025).
3. Dragičević, T.; Lu, X.; Vasquez, J.C.; Guerrero, J.M. DC Microgrids—Part II: A Review of Power Architectures, Applications, and Standardization Issues. *IEEE Trans. Power Electron.* **2016**, *31*, 3528–3549. [CrossRef]
4. Abdolahi, M.; Hosseinnataj, S.; Norouzian, M.; Adabi, J.; Pouresmaeil, E. Bidirectional Dual-Input Single-Output DC-DC Converter Based on Passivity Control Strategy. *IEEE Open J. Power Electron.* **2024**, *5*, 1227–1242. [CrossRef]
5. Memon, D.A.; Ali, K.H.; Memon, A.A.; Ansari, J.A.; Badar, J.; Alharbi, M.; Banatwala, A.Z.; Kumar, M. Comparative analysis and implementation of DC microgrid systems versus AC microgrid performance. *Front. Energy Res.* **2024**, *12*, 1370547. [CrossRef]
6. Chen, T.; Jin, Y.; Lv, H.; Yang, A.; Liu, M.; Chen, B.; Xie, Y.; Chen, Q. Applications of Lithium-Ion Batteries in Grid-Scale Energy Storage Systems. *Trans. Tianjin Univ.* **2020**, *26*, 208–217. [CrossRef]
7. R-Smith, N.A.-Z.; Moertelmaier, M.; Gramse, G.; Kasper, M.; Ragulskis, M.; Groebmeyer, A.; Jurjovec, M.; Brorein, E.; Zollo, B.; Kienberger, F. Fast method for calibrated self-discharge measurement of lithium-ion batteries including temperature effects and comparison to modelling. *Energy Rep.* **2023**, *10*, 3394–3401. [CrossRef]
8. Mekonnin, A.S.; Wacławiak, K.; Humayun, M.; Zhang, S.; Ullah, H. Hydrogen Storage Technology, and Its Challenges: A Review. *Catalysts* **2025**, *15*, 260. [CrossRef]

9. Saafan, A.A.; Khadkikar, V.; Moursi, M.S.E.; Zeineldin, H.H. A New Multiport DC-DC Converter for DC Microgrid Applications. *IEEE Trans. Ind. Appl.* **2023**, *59*, 601–611. [CrossRef]
10. Sameera; Tariq, M.; Rihan, M. Impact of shading heaviness on voltage, current and power of the solar photovoltaic string. *Next Sustain.* **2025**, *5*, 100062. [CrossRef]
11. Sullivan, C.R.; Awerbuch, J.J.; Latham, A.M. Decrease in Photovoltaic Power Output from Ripple: Simple General Calculation and the Effect of Partial Shading. *IEEE Trans. Power Electron.* **2013**, *28*, 740–747. [CrossRef]
12. AlLee, G.; Tschudi, W. Edison Redux: 380 Vdc Brings Reliability and Efficiency to Sustainable Data Centers. *IEEE Power Energy Mag.* **2012**, *10*, 50–59. [CrossRef]
13. Zhao, X.; Yan, Z.; Xue, Y.; Zhang, X.P. Wind Power Smoothing by Controlling the Inertial Energy of Turbines With Optimized Energy Yield. *IEEE Access* **2017**, *5*, 23374–23382. [CrossRef]
14. Peña-Alzola, R.; Campos-Gaona, D.; Ksiazek, P.F.; Ordonez, M. DC-Link Control Filtering Options for Torque Ripple Reduction in Low-Power Wind Turbines. *IEEE Trans. Power Electron.* **2017**, *32*, 4812–4826. [CrossRef]
15. Huang, Z.; Shen, J.; Chan, S.H.; Tu, Z. Transient response of performance in a proton exchange membrane fuel cell under dynamic loading. *Energy Convers. Manag.* **2020**, *226*, 113492. [CrossRef]
16. Benmouiza, K.; Cheknane, A. Analysis of proton exchange membrane fuel cells voltage drops for different operating parameters. *Int. J. Hydrogen Energy* **2018**, *43*, 3512–3519. [CrossRef]
17. Liu, X.; Li, H.; Wang, Z. A Fuel Cell Power Conditioning System With Low-Frequency Ripple-Free Input Current Using a Control-Oriented Power Pulsation Decoupling Strategy. *IEEE Trans. Power Electron.* **2014**, *29*, 159–169. [CrossRef]
18. Babu, B. Self-discharge in rechargeable electrochemical energy storage devices. *Energy Storage Mater.* **2024**, *67*, 103261. [CrossRef]
19. Xia, Z.; Qahouq, J.A.A. Lithium-Ion Battery Ageing Behavior Pattern Characterization and State-of-Health Estimation Using Data-Driven Method. *IEEE Access* **2021**, *9*, 98287–98304. [CrossRef]
20. Yan, Z.; Sun, S.; Fu, B.; Cen, D.; Yang, N.; Qi, H.; Hu, R.; Zeng, J.; Liu, J. Battery-Friendly DC–DC Converter With Ripple-Free Current Modulation Strategy. *IEEE J. Emerg. Sel. Top. Power Electron.* **2023**, *11*, 2300–2310. [CrossRef]
21. Diao, W.; Pecht, M.; Liu, T. Management of imbalances in parallel-connected lithium-ion battery packs. *J. Energy Storage* **2019**, *24*, 100781. [CrossRef]
22. Kothari, R.; Buddhi, D.; Sawhney, R.L. Optimization of electrolytic input power for the production of hydrogen. *Int. J. Hydrogen Energy* **2006**, *31*, 2329–2336. [CrossRef]
23. Mucci, S.; Mitsos, A.; Bongartz, D. Power-to-X processes based on PEM water electrolyzers: A review of process integration and flexible operation. *Comput. Chem. Eng.* **2023**, *175*, 108260. [CrossRef]
24. Lu, X.; Du, B.; Zhou, S.; Zhu, W.; Li, Y.; Yang, Y.; Xie, C.; Zhao, B.; Zhang, L.; Song, J.; et al. Optimization of power allocation for wind-hydrogen system multi-stack PEM water electrolyzer considering degradation conditions. *Int. J. Hydrogen Energy* **2023**, *48*, 5850–5872. [CrossRef]
25. Amiri, M.; Farzanehfard, H. A High-Efficiency Interleaved Ultra-High Step-Down DC–DC Converter With Very Low Output Current Ripple. *IEEE Trans. Ind. Electron.* **2019**, *66*, 5177–5185. [CrossRef]
26. Buitendach, H.P.C.; Gouws, R.; Martinson, C.A.; Minnaar, C.; Bessarabov, D. Effect of a ripple current on the efficiency of a PEM electrolyser. *Results Eng.* **2021**, *10*, 100216. [CrossRef]
27. Padmawansa, N.; Gunawardane, K.; Subasinghage, K. Fuel Cell and Supercapacitor Hybrid Energy Storage for Regulating DC Link Voltage in DC Microgrids. In Proceedings of the 2024 IEEE 9th Southern Power Electronics Conference (SPEC), Brisbane, QLD, Australia, 2–5 December 2024; pp. 1–6. [CrossRef]
28. Singh, A.K.; Mishra, A.K.; Gupta, K.K.; Siwakoti, Y.P. High Voltage Gain Bidirectional DC-DC Converters for Supercapacitor Assisted Electric Vehicles: A Review. *CPSS Trans. Power Electron. Appl.* **2022**, *7*, 386–398. [CrossRef]
29. Sengupta, A.; Pereira, T.; Liserre, M. Design Optimization of Dual Active Bridge Converter for Supercapacitor Application. *IEEE Trans. Power Electron.* **2024**, *39*, 11544–11557. [CrossRef]
30. Soldado-Guamán, J.; Herrera-Perez, V.; Pacheco-Cunduri, M.; Paredes-Camacho, A.; Delgado-Prieto, M.; Hernandez-Ambato, J. Multiple Input-Single Output DC-DC Converters Assessment for Low Power Renewable Sources Integration. *Energies* **2023**, *16*, 1652. [CrossRef]
31. Alhamrouni, I.; Salem, M.; Zahraoui, Y.; Ismail, B.; Jusoh, A.; Sutikno, T. Multi-input interleaved DC-DC converter for hybrid renewable energy applications. *Bull. Electr. Eng. Inform.* **2022**, *11*, 1765–1778. [CrossRef]
32. Tomar, A.; Mishra, S. Grid Interactive MISO Converter Based PV System. In Proceedings of the 2018 2nd IEEE International Conference on Power Electronics, Intelligent Control and Energy Systems (ICPEICES), New Delhi, India, 22–24 October 2018; pp. 642–647. [CrossRef]
33. Ramprasath, S.; Krishnakumar, C. High gain multi-input single-output DC-DC boost converter with enhanced circuit for photovoltaic applications. *J. Power Electron.* **2024**, *24*, 1843–1854. [CrossRef]

34. Alam, M.M.; Lu, D.C.; Siwakoti, Y. Small signal analysis of dual input buck converter. *Int. J. Smart Grid Clean Energy* **2020**, *9*, 8–16. [CrossRef]
35. Chen, Y.; Lu, Y.; Luo, W. Model predictive control of double-input buck converters. *J. Power Electron.* **2021**, *21*, 941–950. [CrossRef]
36. Gorji, S.A.; Sahebi, H.G.; Movahed, M.; Ektesabi, M. Multi-Input Boost DC-DC Converter with Continuous Input-Output Current for Renewable Energy Systems. In Proceedings of the 2019 IEEE 4th International Future Energy Electronics Conference (IFEEC), Singapore, 25–28 November 2019; pp. 1–5. [CrossRef]
37. Xian, L.; Wang, G.; Wang, Y. Subproportion control of double input buck converter for fuel cell/battery hybrid power supply system. *IET Power Electron.* **2014**, *7*, 2141–2150. [CrossRef]
38. Kang, S.H.; Kim, H.S.; Hwang, Y.S.; Lee, B.K. An Optimal DC–DC Converter for Fuel Cell-Supercap Series-Connected Powertrain in Fuel Cell Electric Vehicles. *IEEE Trans. Power Electron.* **2025**, *40*, 17384–17399. [CrossRef]
39. Vijayan, M.; Udumula, R.R.; Mahto, T.; Ravi Eswar, K.M. A novel multi-port high-gain bidirectional DC–DC converter for energy storage system integration with DC microgrids. *J. Energy Storage* **2024**, *87*, 111431. [CrossRef]
40. Sundarakamath, R.; Natarajan, S. Integration of multiple sources for fuel cell hybrid electric vehicles using single inductor multi-input converter. *Int. J. Hydrogen Energy* **2024**, *53*, 503–516. [CrossRef]
41. Chandrasekar, B.; Nallaperumal, C.; Dash, S.S. A Nonisolated Three-Port DC–DC Converter with Continuous Input and Output Currents Based on Cuk Topology for PV/Fuel Cell Applications. *Electronics* **2019**, *8*, 214. [CrossRef]
42. Hao, X.; Salhi, I.; Laghrouche, S.; Ait Amirat, Y.; Djerdir, A. Multiple inputs multi-phase interleaved boost converter for fuel cell systems applications. *Renew. Energy* **2023**, *204*, 521–531. [CrossRef]
43. Sivaram, N.V.; Lavanya, A.; Divya Navamani, J. Dual input single Output quadratic Boost converter for DC microgrid. *e-Prime-Adv. Electr. Eng. Electron. Energy* **2024**, *9*, 100683. [CrossRef]
44. Sun, Z.; Bae, S. Multiple-Input Soft-Switching DC–DC Converter to Connect Renewable Energy Sources in a DC Microgrid. *IEEE Access* **2022**, *10*, 128380–128391. [CrossRef]
45. Mahobiya, S.; Thankachan, J. Comparative Analysis of Multiport Boost Converter and Z-Source Multiport Converter for EV Charging. In Proceedings of the 2024 IEEE International Conference on Power Electronics, Drives and Energy Systems (PEDES), Karnataka, India, 18–21 December 2024; pp. 1–6. [CrossRef]
46. Shi, Y.; Che, Z.; Xie, B.; Xie, D.; Wang, L.; Yao, J. Topology and control method of interleaved parallel DC/DC converters with ripple compensation for fuel cell applications. *J. Power Electron.* **2025**, *25*, 642–653. [CrossRef]
47. Harini, S.; Chellammal, N.; Chokkalingam, B.; Mihet-Popa, L. A Novel High Gain Dual Input Single Output Z-Quasi Resonant (ZQR) DC/DC Converter for Off-Board EV Charging. *IEEE Access* **2022**, *10*, 83350–83367. [CrossRef]
48. Faraji, R.; Farzanehfard, H.; Esteki, M.; Khajehoddin, S.A. A Lossless Passive Snubber Circuit for Three-Port DC–DC Converter. *IEEE J. Emerg. Sel. Top. Power Electron.* **2021**, *9*, 1905–1914. [CrossRef]
49. Kardan, F.; Alizadeh, R.; Banaei, M.R. A New Three Input DC/DC Converter for Hybrid PV/FC/Battery Applications. *IEEE J. Emerg. Sel. Top. Power Electron.* **2017**, *5*, 1771–1778. [CrossRef]
50. Hernandez, F.D.; Samanbakhsh, R.; Mohammadi, P.; Ibanez, F.M. A Dual-Input High-Gain Bidirectional DC/DC Converter for Hybrid Energy Storage Systems in DC Grid Applications. *IEEE Access* **2021**, *9*, 164006–164016. [CrossRef]
51. Pradhan, S.K.; Sekaran, S.; Chakraborty, I. A novel non-isolated high gain multiport DC-DC converter for integrating fuel cell/solar PV and battery energy storage system. *Energy Sources Part A Recovery Util. Environ. Eff.* **2023**, *45*, 1994–2012. [CrossRef]
52. Reddy, B.N.; Alsaif, F.; Reddy, C.R.; Sunil Kumar, S. Development of multiple input supply based modified SEPIC DC–DC converter for efficient management of DC microgrid. *Sci. Rep.* **2024**, *14*, 11066. [CrossRef]
53. Fong, Y.C.; Cheng, K.W.; Raman, S.R.; Wang, X. Multi-Port Zero-Current Switching Switched-Capacitor Converters for Battery Management Applications. *Energies* **2018**, *11*, 1934. [CrossRef]
54. Markkassery, S.; Saradagi, A.; Mahindrakar, A.D.; Lakshminarasamma, N.; Pasumarthy, R. Modeling, Design and Control of Non-isolated Single-Input Multi-Output Zeta–Buck–Boost Converter. *IEEE Trans. Ind. Appl.* **2020**, *56*, 3904–3918. [CrossRef]
55. Anagha, E.B.; Bos, M.J.; Boby, K.; Gibi, M. Multiple output high gain DC-DC converter. *Mater. Today Proc.* **2022**, *58*, 540–546. [CrossRef]
56. Aranda, E.D.; Litrán, S.P.; Prieto, M.B.F. Combination of interleaved single-input multiple-output DC-DC converters. *CSEE J. Power Energy Syst.* **2022**, *8*, 132–142. [CrossRef]
57. Bansal, R.; Tokas, V.; Bansal, R.; Kumar, M. Characterization and Steady State Analysis of Multiport Switched Boost Converter. In Proceedings of the 2023 IEEE 3rd International Conference on Sustainable Energy and Future Electric Transportation (SEFET), Bhubaneswar, India, 9–12 August 2023; pp. 1–6. [CrossRef]
58. Dhananjaya, M.; Ponuru, D.; Babu, T.S.; Aljafari, B.; Alhelou, H.H. A New Multi-Output DC-DC Converter for Electric Vehicle Application. *IEEE Access* **2022**, *10*, 19072–19082. [CrossRef]

59. Malik, M.Z.; Farh, H.M.H.; Al-Shaalan, A.M.; Al-Shamma'a, A.A.; Alhelou, H.H. A Novel Single-Input-Multi-Output Converter for Flexible-Order Power-Distributive With MPPT Capability. *IEEE Access* **2021**, *9*, 131020–131032. [CrossRef]
60. Abishek, M.; Amutha Prabha, N.; Goyal, J.K.; Vaithilingam, C.A. A Non-Isolated Single-Input Multiple-Output DC-DC Converter for Auxiliary Power Loads in Electric Vehicle Applications. In Proceedings of the 2023 Innovations in Power and Advanced Computing Technologies (i-PACT), Kuala Lumpur, Malaysia, 8–10 December 2023; pp. 1–5. [CrossRef]
61. Wai, R.J.; Jheng, K.H. High-Efficiency Single-Input Multiple-Output DC–DC Converter. *IEEE Trans. Power Electron.* **2013**, *28*, 886–898. [CrossRef]
62. Hasanpour, S.; Siwakoti, Y.P.; Blaabjerg, F. A new soft-switching high gain DC/DC converter with bipolar outputs. *IET Power Electron.* **2024**, *17*, 144–156. [CrossRef]
63. Qureshi, M.A.; Torelli, F.; Mazza, A.; Chicco, G. Application of Artificial Dynamics to Represent Non-isolated Single-Input Multiple-Output DC-DC Converters with Averaged Models. In Proceedings of the 2021 56th International Universities Power Engineering Conference (UPEC), Middlesbrough, UK, 31 August–3 September 2021; pp. 1–6. [CrossRef]
64. Ye, J.; Guo, H.; Wang, B.; Zhang, X. Deep Deterministic Policy Gradient Algorithm Based Reinforcement Learning Controller for Single-Inductor Multiple-Output DC–DC Converter. *IEEE Trans. Power Electron.* **2024**, *39*, 4078–4090. [CrossRef]
65. Elbakly, A.M.; Abdelsalam, I.; Marei, M.I. Interleaved Multi-Port Non-Isolated DC/DC Converter for Green Hydrogen Production with PV/PEM Electrolyzer System. In Proceedings of the 2025 7th International Youth Conference on Radio Electronics, Electrical and Power Engineering (REEPE), Moscow, Russia, 8–10 April 2025; pp. 1–5. [CrossRef]
66. Arulmozhiyal, R.; Murali, M.; Thirumalini, P. Single Input Multi-Output DC-DC converter for Sustinable energy applications. In Proceedings of the 2022 Second International Conference on Advances in Electrical, Computing, Communication and Sustainable Technologies (ICAECT), Bhilai, India, 21–22 April 2022; pp. 1–5. [CrossRef]
67. Suresh, K.; Chellammal, N.; Bharatiraja, C.; Sanjeevikumar, P.; Blaabjerg, F.; Nielsen, J.B.H. Cost-efficient nonisolated three-port DC-DC converter for EV/HEV applications with energy storage. *Int. Trans. Electr. Energy Syst.* **2019**, *29*, e12088. [CrossRef]
68. Ramesh, M.; Mallikarjuna, B.; Rajasekar, T. A Novel Investigation on Single-Input Three-Output DC-DC Buck Converter For Electrical Vehicles. In Proceedings of the 2021 7th International Conference on Electrical Energy Systems (ICEES), Online, 11–13 February 2021; pp. 141–146. [CrossRef]
69. Nahavandi, A.; Hagh, M.T.; Sharifian, M.B.B.; Danyali, S. A nonisolated multiinput multioutput DC–DC boost converter for electric vehicle applications. *IEEE Trans. Power Electron.* **2015**, *30*, 1818–1835. [CrossRef]
70. Saafan, A.A.; Khadkikar, V.; Moursi, M.S.E.; Zeineldin, H.H. A New Multiport DC-DC Converter for DC Microgrid Applications. In Proceedings of the 2021 IEEE Industry Applications Society Annual Meeting (IAS), Vancouver, BC, Canada, 10–14 October 2021; pp. 1–7. [CrossRef]
71. Puppala, S.; Singh, P.P.; Potnuru, D. Design and experimental validation of multi-input–multi-output DC–DC converter for a remote village DC microgrid application. *J. Power Electron.* **2025**, *25*, 1833–1844. [CrossRef]
72. Prabhakaran, P.; Agarwal, V. Novel Four-Port DC–DC Converter for Interfacing Solar PV–Fuel Cell Hybrid Sources With Low-Voltage Bipolar DC Microgrids. *IEEE J. Emerg. Sel. Top. Power Electron.* **2020**, *8*, 1330–1340. [CrossRef]
73. Filsoof, K.; Lehn, P.W. A Bidirectional Multiple-Input Multiple-Output Modular Multilevel DC–DC Converter and its Control Design. *IEEE Trans. Power Electron.* **2016**, *31*, 2767–2779. [CrossRef]
74. Azmoon-Asmarood, S.; Maalandish, M.; Shoghli, I.; Nazemi-Oskuee, S.H.R.; Hosseini, S.H. A non-isolated high step-up MIMO DC–DC converter for renewable energy applications. *IET Power Electron.* **2022**, *15*, 953–962. [CrossRef]
75. Prieto, M.B.F.; Litran, S.P.; Aranda, E.D.; Gomez, J.M.E. New Single-Input, Multiple-Output Converter Topologies: Combining Single-Switch Nonisolated dc-dc Converters for Single-Input, Multiple-Output Applications. *IEEE Ind. Electron. Mag.* **2016**, *10*, 6–20. [CrossRef]
76. Suresh, K.; Bharatiraja, C.; Chellammal, N.; Tariq, M.; Chakrabortty, R.K.; Ryan, M.J.; Alamri, B. A Multifunctional Non-Isolated Dual Input-Dual Output Converter for Electric Vehicle Applications. *IEEE Access* **2021**, *9*, 64445–64460. [CrossRef]
77. Koroglu, T.; Ekici, E.; Savrun, M.M. Five-Port Isolated Bidirectional DC-DC Converter for Interfacing a Hybrid Photovoltaic–Fuel Cell–Battery System with Bipolar DC Microgrids. *Electronics* **2024**, *13*, 1036. [CrossRef]
78. Cai, X.; Liu, Y.; Zhu, Y.; Zhou, Y.; Luo, C.; Liu, Q. ISOS-SAB DC/DC Converter for Large-Capacity Offshore Wind Turbine. *Energies* **2024**, *17*, 5071. [CrossRef]
79. Liu, X.; Wu, X.; Zhao, X. A multi-port DC–DC–AC system based on CLLC resonant converter and FSBB converter. *Electr. Eng.* **2024**, *106*, 5557–5578. [CrossRef]
80. Aghajani, A.A.; Eldoromi, M.; Nakhaei, B.; Birjandi, A.A.M. Multi-Port Dual-Active-Bridge DC-DC Converter for Bi-Polar DC Microgrid Application Using Buck-Boost Voltage Balancer. In Proceedings of the 2023 14th Power Electronics, Drive Systems, and Technologies Conference (PEDSTC), Babol, Iran, 31 January–2 February 2023; pp. 1–5. [CrossRef]

81. Wu, H.; Zhang, J.; Qin, X.; Mu, T.; Xing, Y. Secondary-Side-Regulated Soft-Switching Full-Bridge Three-Port Converter Based on Bridgeless Boost Rectifier and Bidirectional Converter for Multiple Energy Interface. *IEEE Trans. Power Electron.* **2016**, *31*, 4847–4860. [CrossRef]
82. Chen, D.; Yang, Z. Research on the Switch Reuse Dual Buck/Boost-DAB Four-Port DC/DC Converter. In Proceedings of the 2024 IEEE 10th International Power Electronics and Motion Control Conference (IPEMC2024-ECCE Asia), Chengdu, China, 17–20 May 2024; pp. 1198–1203. [CrossRef]
83. ElMenshawy, M.; Massoud, A. Modular Isolated DC-DC Converters for Ultra-Fast EV Chargers: A Generalized Modeling and Control Approach. *Energies* **2020**, *13*, 2540. [CrossRef]
84. Sun, X.; Shen, Y.; Li, W.; Wu, H. A PWM and PFM Hybrid Modulated Three-Port Converter for a Standalone PV/Battery Power System. *IEEE J. Emerg. Sel. Top. Power Electron.* **2015**, *3*, 984–1000. [CrossRef]
85. Lee, J.-Y.; Lee, J.-S.; Kim, H.-S.; Jung, J.-H. Enhanced Four-Port-Based DAB Converter for Interlinking and Balancing Bipolar DC Buses of DC Distribution Systems. *J. Electr. Eng. Technol.* **2025**, *20*, 2233–2247. [CrossRef]
86. Lei, Y.; Liu, F.; Zhuang, Y.; Liu, Q.; Zhu, H.; Huang, Y. A Dual LC Interleaved Four-Port Converter for Bipolar DC Microgrids. *IEEE Trans. Ind. Electron.* **2024**, *71*, 10783–10794. [CrossRef]
87. Sun, X.; Shen, Y.; Li, W. A novel LLC integrated three-port DC-DC converter for stand-alone PV/battery system. In Proceedings of the 2014 IEEE Conference and Expo Transportation Electrification Asia-Pacific (ITEC Asia-Pacific), Beijing, China, 31 August–3 September 2014; pp. 1–6. [CrossRef]
88. Mira, M.C.; Zhang, Z.; Knott, A.; Andersen, M.A.E. Analysis, Design, Modeling, and Control of an Interleaved-Boost Full-Bridge Three-Port Converter for Hybrid Renewable Energy Systems. *IEEE Trans. Power Electron.* **2017**, *32*, 1138–1155. [CrossRef]
89. Hashemzadeh, S.M.; Zhu, B. A multi-port high step-up converter integrating coupled inductor and high-frequency transformer with hybrid isolated/non-isolated outputs for renewable energy-based DC micro grids. *Energy* **2025**, *335*, 138350. [CrossRef]
90. Nalamati, C.S.; Gupta, R. Analytical investigation of interleaved input/output parallel DAB converter for grid scale battery storage. *J. Energy Storage* **2024**, *99*, 113400. [CrossRef]
91. Duarte, J.L.; Hendrix, M.; Simoes, M.G. Three-Port Bidirectional Converter for Hybrid Fuel Cell Systems. *IEEE Trans. Power Electron.* **2007**, *22*, 480–487. [CrossRef]
92. Zhao, C.; Round, S.D.; Kolar, J.W. An Isolated Three-Port Bidirectional DC-DC Converter With Decoupled Power Flow Management. *IEEE Trans. Power Electron.* **2008**, *23*, 2443–2453. [CrossRef]
93. Heo, K.-W.; Yun, C.-W.; Jung, G.-G.; Lee, J.-S.; Kim, H.-S.; Jung, J.-H. Enhanced four-port dual-active-bridge converter employing power decoupling capability for DC microgrid islanding mode operation. *J. Power Electron.* **2024**, *24*, 171–180. [CrossRef]
94. Dey, S.; Reece, C.; Irabor, O.P.; Mallik, A. Comparative Analysis and Optimization of Triple Active Bridge Transformer Configuration With Integrable Leakage Inductance. *IEEE J. Emerg. Sel. Top. Power Electron.* **2023**, *11*, 5102–5119. [CrossRef]
95. Chakkalakkal, S.; Kozielski, K.; Taha, W.; Wang, Y.; Anand, A.; Emadi, A. Loss-Optimized Design of a Triple Active Bridge DC-DC Converter for an Electric Vehicle Application. In Proceedings of the 2025 IEEE Applied Power Electronics Conference and Exposition (APEC), Atlanta, GA, USA, 16–20 March 2025; pp. 3147–3154. [CrossRef]
96. Alam, M.D.; Rahman, M.M.; Husain, I.; Lukic, S. Circulating Power and Winding Current Minimization in a Triple Active Bridge DC-DC Converter with Optimized Leakage Inductance Design. In Proceedings of the 2024 IEEE Applied Power Electronics Conference and Exposition (APEC), Long Beach, CA, USA, 25–29 February 2024; pp. 474–480. [CrossRef]
97. Jiang, W.; Ma, W.; Wang, J.; Wang, W.; Zhang, X.; Wang, L. Suppression of Zero Sequence Circulating Current for Parallel Three-Phase Grid-Connected Converters Using Hybrid Modulation Strategy. *IEEE Trans. Ind. Electron.* **2018**, *65*, 3017–3026. [CrossRef]
98. Kim, D.U.; Dong, D.; Kim, B.; Kim, S. A New Asymmetric Leakage Inductance for Enhancing Zero-Voltage Switching Performance in Asymmetric Triple-Active-Bridge Converters. *IEEE Trans. Power Electron.* **2024**, *39*, 11187–11203. [CrossRef]
99. Purgat, P.; Bandyopadhyay, S.; Qin, Z.; Bauer, P. Zero Voltage Switching Criteria of Triple Active Bridge Converter. *IEEE Trans. Power Electron.* **2021**, *36*, 5425–5439. [CrossRef]
100. di Benedetto, M.; Lidozzi, A.; Solero, L.; Crescimbini, F.; Bifaretti, S. Hardware design of SiC-based Four-Port DAB Converter for Fast Charging Station. In Proceedings of the 2020 IEEE Energy Conversion Congress and Exposition (ECCE), Detroit, MI, USA, 11–15 October 2020; pp. 1231–1238. [CrossRef]
101. Dao, N.D.; Lee, D.C.; Phan, Q.D. High-Efficiency SiC-Based Isolated Three-Port DC/DC Converters for Hybrid Charging Stations. *IEEE Trans. Power Electron.* **2020**, *35*, 10455–10465. [CrossRef]
102. Choi, W.; Enjeti, P.N.; Howze, J.W.; Joung, G. An experimental evaluation of the effects of ripple current generated by the power conditioning stage on a proton exchange membrane fuel cell stack. *J. Mater. Eng. Perform.* **2004**, *13*, 257–264. [CrossRef]

103. Valdez-Resendiz, J.E.; Rosas-Caro, J.C.; Sanchez, V.M.; Lopez-Nuñez, A.R. Experimental study of a fuel cell stack performance operating with a power electronics converter with high-frequency current ripple. *Int. J. Hydrogen Energy* **2025**, *108*, 66–75. [CrossRef]
104. Puranen, P.; Hehemann, M.; Järvinen, L.; Ruuskanen, V.; Kosonen, A.; Ahola, J.; Kauranen, P. Experimental study on the influence of a PEM water electrolyzer cell's impedance on its power consumption under impaired power quality. *IET Renew. Power Gener.* **2024**, *18*, 4480–4496. [CrossRef]
105. Zhan, Y.; Guo, Y.; Zhu, J.; Li, L. Performance comparison of input current ripple reduction methods in UPS applications with hybrid PEM fuel cell/supercapacitor power sources. *Int. J. Electr. Power Energy Syst.* **2015**, *64*, 96–103. [CrossRef]
106. Parache, F.; Schneider, H.; Turpin, C.; Richet, N.; Debellemanière, O.; Bru, É.; Thieu, A.T.; Bertail, C.; Marot, C. Impact of Power Converter Current Ripple on the Degradation of PEM Electrolyzer Performances. *Membranes* **2022**, *12*, 109. [CrossRef]
107. Chandran, M.; Palaniswamy, K.; Karthik Babu, N.B.; Das, O. A study of the influence of current ramp rate on the performance of polymer electrolyte membrane fuel cell. *Sci. Rep.* **2022**, *12*, 21888. [CrossRef]
108. Endrődi, B.; Trapp, C.A.; Szén, I.; Bakos, I.; Lukovics, M.; Janáky, C. Challenges and Opportunities of the Dynamic Operation of PEM Water Electrolyzers. *Energies* **2025**, *18*, 2154. [CrossRef]
109. Weiß, A.; Siebel, A.; Bernt, M.; Gasteiger, H.A. Impact of Intermittent Operation on the Lifetime and Performance of a PEM Water Electrolyzer. *ECS Meet. Abstr.* **2018**, *MA2018-02*, 1606. [CrossRef]
110. Gevorkov, L.; Domínguez-García, J.L.; Romero, L.T.; Martínez, À.F. Modern MultiPort Converter Technologies: A Systematic Review. *Appl. Sci.* **2023**, *13*, 2579. [CrossRef]
111. Yu, Q.; Sun, Z.; Han, Y.; Zhang, T.; Zhang, R.; Lin, M. High-Performance Two-Stage DC/DC Converter Based on LADRC-PI Hybrid Control for PEM Electrolyzer Hydrogen Production. *Micromachines* **2025**, *16*, 665. [CrossRef]
112. Mostafa, H.H.; Ibrahim, A.M.; Amer, F.Z.; Sawires, E.F. Multiport bidirectional converters for off board charging stations of electric vehicles. *Sci. Rep.* **2025**, *15*, 36128. [CrossRef]

Disclaimer/Publisher's Note: The statements, opinions and data contained in all publications are solely those of the individual author(s) and contributor(s) and not of MDPI and/or the editor(s). MDPI and/or the editor(s) disclaim responsibility for any injury to people or property resulting from any ideas, methods, instructions or products referred to in the content.

energies

MDPI

Article

Economic Feasibility of Using Municipal Solid Waste and Date Palm Waste for Clean Energy Production in Qatar

Ahmad Mohamed S. H. Al-Moftah [1,2], Mohammad Alnajideen [1,*], Fatima Alafifi [3,4], Pawel Czyzewski [5], Hao Shi [1,6], Mohammad Alherbawi [3], Rukshan Navaratne [1] and Agustin Valera-Medina [1]

[1] College of Physical Sciences and Engineering, Cardiff University, Cardiff CF24 3AA, UK
[2] Qatar National Research Fund (QNRF), Qatar Foundation, Doha P.O. Box 5825, Qatar
[3] College of Science and Engineering, Hamad Bin Khalifa University, Doha P.O. Box 5825, Qatar
[4] Qatar Environment and Energy Research Institute, Hamad Bin Khalifa University, Doha P.O. Box 5825, Qatar
[5] Institute of Thermal Engineering, Poznan University of Technology, 60-965 Poznan, Poland
[6] The Institute of Reactive Flows and Diagnostics, Technical University of Darmstadt, 64287 Darmstadt, Germany
* Correspondence: alnajideenmi@cardiff.ac.uk

Abstract

The transition to clean energy is crucial for mitigating the impacts of climate change and achieving sustainable development. Reliance on fossil fuels, which are integral to manufacturing and transportation, remains a major contributor to greenhouse gas (GHG) emissions. Biomass gasification presents a renewable energy alternative that can significantly reduce emissions. However, proper disposal of municipal solid waste (MSW) and agricultural residues, such as date palm waste (DPW), is an increasing global challenge, including in Qatar. This study evaluates the economic feasibility of implementing an MSW and DPW gasification plant for clean electricity generation in Qatar. The country's growing population and economic development have led to substantial waste production, making it an ideal location for waste-to-energy (WTE) initiatives. Using discounted cash flow (DCF) analysis, the study estimates the capital cost of a 373 MW_{th} facility at approximately $12.07 million, with annual operating costs of about $4.09 million and revenue of $26.88 million in 2023. The results indicate a net present value (NPV) of $245.77 million, a return on investment (ROI) of 84.80%, a payback period of approximately 5 years over a 20-year project lifetime and a net reduction of 206,786 tonnes CO_2 annually. These findings demonstrate the economic viability of biomass gasification in Qatar while contributing to reduced GHG emissions and advancing the country's sustainability goals under Qatar National Vision 2030.

Keywords: biomass gasification; municipal solid waste; date palm waste; economic feasibility; Qatar National Vision 2030

1. Introduction

Decarbonising power and transport sectors necessitates reducing reliance on fossil fuels and transitioning to clean, renewable energy sources that produce nearly zero carbon emissions. This ambition has been championed by international agreements like the Paris Agreement and efforts under the United Nations Framework Convention on Climate Change [1–3]. The urgency of achieving net-zero emissions by 2050 was reaffirmed during the COP28 summit in 2023 [3–5]. However, transitioning to clean energy

sources presents significant challenges, including maintaining stable and affordable energy supplies, fostering economic growth, and ensuring universal energy access [6,7].

Amongst the sustainable approaches, adopting low-carbon energy alternatives, such as replacing natural gas with bioenergy fuels like bio-methane for heating and electricity production, has gained prominence. Bioenergy, derived from biomass, encompasses a wide range of organic materials, including crop residues, agricultural waste, and industrial by-products [8]. Its diverse applications include bio-jet kerosene for air travel, liquid biofuel for road transport, and fuels for industrial processes and electricity generation [9]. As a renewable energy source, biomass has significant potential to reduce harmful emissions [10].

Globally, bioenergy constitutes 55% of renewable energy use and 6% of the global energy supply [11,12]. In 2023, electricity generated from bioenergy is reached nearly 750 TWh and is projected to increase to approximately 1350 TWh by 2030, meeting around 3.5% of global electricity demand [12]. While bioenergy plays a vital role globally, its integration into waste management practices presents unique opportunities, particularly in regions with significant waste generation. Solid waste, for instance, reached approximately 2.24 billion tonnes globally in 2022, equating to 0.79 kg per person per day [13]. The World Bank estimates that solid waste will increase by 73% to 3.88 billion tonnes by 2050, driven by rapid population growth and urbanisation [13].

In Qatar, a nation heavily reliant on fossil fuels, more than 2.5 million tonnes of municipal solid waste (MSW) are generated annually [14,15]. This waste, comprising agricultural residues, animal waste, and household organic material, predominantly ends up in landfills, contributing to air and water pollution through the emission of methane (CH_4), carbon dioxide (CO_2), and other harmful gases [16,17]. While these challenges are significant, Qatar's large-scale production of MSW and date palm waste (DPW) offers a substantial opportunity to adopt waste-to-energy (WTE) technologies. These issues are not unique to Qatar; in the broader Middle East and North Africa (MENA) region, urban waste exceeds 150 million tonnes annually [14].

Sweden is among the global leaders in WTE and waste management, having successfully utilised gasification technology to significantly reduce landfilling and emissions. For instance, the GoBiGas project [18], conducted in Gothenburg, exemplifies this approach by converting biomass and waste into syngas. The syngas is then processed into bio-methane, which can be used for heating and as a fuel source. In addition, Sweden has achieved remarkable success in waste management, with only 1% of its MSW ending up in landfills [19]. This waste is utilised in gasification technology, which generates clean energy from resources that cannot be recycled, thereby reducing emissions. Sweden's GoBiGas project serves as an excellent example of how landfill waste can be minimised through a combination of WTE, recycling, composting, and the recovery of materials and energy. These efforts have resulted in lower greenhouse gas (GHG) emissions, reduced reliance on fossil fuels, and increased use of clean energy sources within the country [18]. The amounts and share of waste deposited in landfills across Europe are presented by the European Environment Agency [19]. Qatar could adopt similar technologies to minimise landfill use and emissions, paving the way for a more sustainable future.

Besides MSW and agricultural residues, food waste from restaurants represents the third-largest contributor to landfills [20]. Landfills in Qatar and across the MENA region present environmental concerns, releasing CH_4, CO_2, and other gases such as ammonia (NH_3) [21], leading to soil degradation, groundwater pollution, and greenhouse gas emissions [22]. CH_4 and CO_2, which account for 90–98% of landfill gases, are the primary contributors to GHG pollution [23,24].

Qatar's economy has grown significantly, but one of its key challenges is the management of MSW [15]. A notable issue is the regular turnover of the expatriate community, which increases the waste stream and landfill pressures. The Ministry of Municipality and Environment faces the task of managing waste from various sources, highlighting the need for a detailed, integrated MSW management plan that addresses residential, industrial, construction, and commercial waste streams. One challenge of implementing biomass gasification technology in Qatar is the development of material recovery facilities (MRFs) that can separate MSW and produce solid fuels for gasification, such as Refuse-Derived Fuel (RDF) or Solid Recovered Fuel (SRF). Furthermore, constructing biorefineries for producing bioproducts, including biomaterials and biochemicals, is essential [15].

The use of MSW and DPW in Qatar for clean energy generation is particularly appealing, as it addresses the dual challenge of increasing energy needs and growing waste management issues. However, implementing such projects faces numerous obstacles and constraints, which can be categorised as technical, economic, social, political, and environmental. Technical barriers include the conditions and equipment required to process waste into energy, as well as the absence of proper waste segregation structures [23]. Economically, the establishment and operation of Waste-to-Energy (WTE) plants entail high costs, and there is a need for a stable policy regime to support these projects. Currently, Qatar lacks policies or incentives to attract private sector investment or collaboration in financing WTE projects [25,26]. Politically, the absence of clear backing increases uncertainty and risks, further hampering the pursuit and implementation of such initiatives.

To mitigate the above-mentioned impacts, the Qatari government has implemented programmes focused on increasing recycling and adopting sustainable waste management practices, such as WTE incineration and composting.

This study evaluates the feasibility of using a biomass plant to generate clean electricity from MSW and DPW through gasification in Qatar. This evaluation will determine whether this technology can be successfully implemented as a source of clean energy while assessing its economic and environmental impacts. The study also supports Qatar's National Vision 2030 and serves as a benchmark for neighbouring countries and regions with similar characteristics to evaluate the financial feasibility of adopting biomass gasification technology.

1.1. Energy Outlook

The State of Qatar, a small peninsular nation covering approximately 11.571 km^2, is located in the Middle East, bordered by Saudi Arabia and surrounded by the Arabian Gulf. Despite its small size, Qatar has a population of around 3 million people, with 72% residing in the capital city, Doha, one of the country's eight municipalities [27]. Qatar is well known for its high-income economy, primarily supported by oil and natural gas production, which contribute significantly to its status as one of the wealthiest nations globally. As a leading producer and exporter of natural gas and oil, Qatar plays a vital role in the global energy market [28,29]. However, in recent years, Qatar has made concerted efforts to diversify its energy sources, investing in renewable energy to reduce its dependence on fossil fuels and align with its national development vision [30].

Since 1965, Qatar has relied heavily on fossil fuels to meet its energy demands. By 2022, natural gas had become the dominant energy source, accounting for 87.3% of the country's energy mix, followed by oil at 12.6%. Renewable energy, while growing, still represented a small fraction at 0.1% [12,31]. This heavy reliance on fossil fuels has significantly contributed to the country's carbon footprint. Energy-related CO_2 emissions from Qatar accounted for 0.27% of global emissions, marking a 327% increase since 2000. This rise

reflects the rapid industrial and economic growth in Qatar and highlights the urgent need to diversify energy sources to address environmental challenges [31].

Figure 1 provides an overview of key metrics related to Qatar's energy landscape, including total energy supply, production, consumption and CO_2 emissions. As of the most recent data [12,31], 99% of Qatar's electricity generation comes from natural gas, with a total electricity production reaching 54,623 GWh—a 498% increase since 2000. On a per capita basis, electricity consumption is 19.11 MWh, reflecting a 45% rise over the same period. The country's electricity generation is primarily powered by natural gas, with a peak demand of approximately 9000 MW and a total installed capacity exceeding 12,000 MW [32]. This rapid growth in electricity demand is largely driven by Qatar's rapid economic development and the need for air conditioning due to its hot climate. Electricity is priced at 0.10 Qatari Riyals (approximately 0.027 USD) per kWh, with the cost remaining consistent regardless of usage. However, the increasing demand for cooling is expected to drive future energy costs higher [15,33,34].

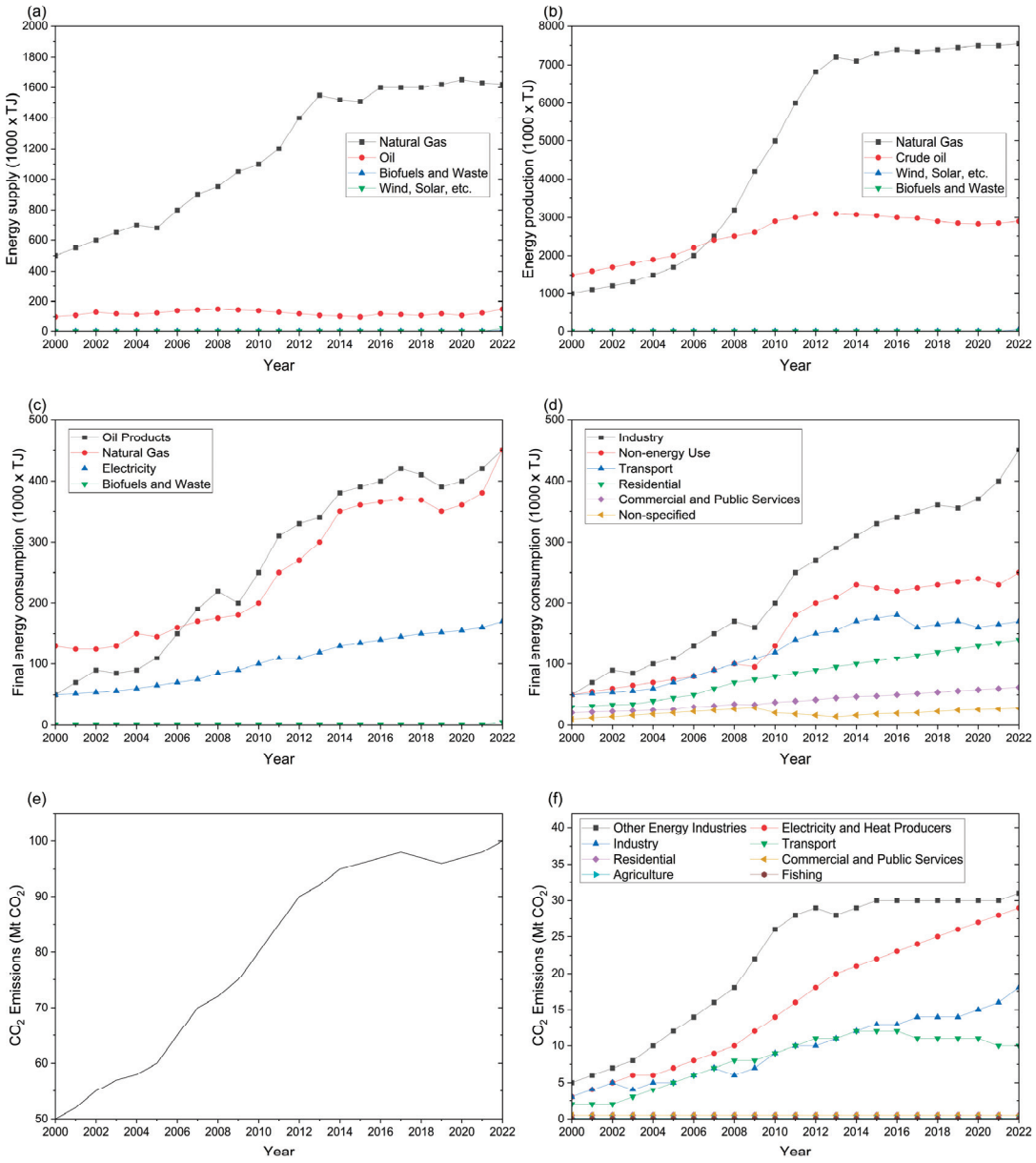


Figure 1. Qatar's key metrics for 2022; (**a**) total energy supply; (**b**) domestic energy production; (**c**) total final consumption by fuel source; (**d**) total final consumption by sector; (**e**) CO_2 emissions from fuel combustion; and (**f**) CO_2 emissions by sector. Data from [31], adjusted by authors.

In alignment with its national targets for environmental sustainability, Qatar implemented a carbon offsetting and mitigation framework during the FIFA World Cup Qatar 2022. This initiative supported the country's long-term energy goals by introducing low-carbon solutions such as energy-efficient stadiums powered by renewable energy sources, including solar power. The carbon-neutral approach also encompassed broader initiatives, such as renewable energy projects, forest conservation, and enhanced waste management systems that promote recycling and energy conservation [35–37]. These integrated strategies not only addressed the immediate environmental impacts of the tournament but also underscored Qatar's commitment to a more sustainable energy future.

Qatar's population growth, coupled with increasing urbanisation and industrialisation, has led to a significant surge in energy demand. For example, the Qatar General Electricity and Water Corporation (Kahramaa) reported a 10% growth in power consumption in 2019 alone [38]. In response to this growing demand and to mitigate its carbon footprint, Qatar has been making substantial investments in renewable energy. By 2030, the country aims to generate 20% of its electricity from renewable sources [39]. Key initiatives include solar power projects such as Al-Kharsaah, Mesaieed, Ras Laffan, and Dukhan, which are projected to produce around 4000 MW of electricity by 2030 [40,41]. These projects are expected to contribute 30% of Qatar's total power generation capacity and reduce CO_2 emissions by 4.7 million tonnes annually [39,42]. These efforts align with Qatar's broader objective of diversifying its energy mix, improving efficiency, and transitioning toward more sustainable energy solutions.

1.2. MSW and DPW in Qatar

1.2.1. Gasification Plant Statistics

Biomass conversion methods are broadly classified into thermochemical and biochemical processes. Thermochemical methods include gasification, carbonisation, pyrolysis, combustion, and catalytic liquefaction, whereas biochemical processes encompass anaerobic digestion and fermentation [25]. Both approaches break down feedstock molecules to produce biofuels, which can serve as renewable energy sources. Gasification converts carbon-based materials like MSW and DPW into syngas, a mixture of hydrogen, carbon monoxide, and methane [43]. This process offers a cleaner alternative to conventional waste disposal methods while generating energy.

Gasification is particularly suitable for Qatar as a means of producing clean energy from MSW and DPW. The country's climatic conditions result in waste with high moisture levels, particularly DPW, which poses challenges for conventional combustion processes. Gasification, however, can tolerate high moisture content and convert it into useful syngas, making it ideal for Qatar. The gasification process involves steps such as pyrolysis, partial oxidation, and gasification. In the pyrolysis stage, the waste material is thermally decomposed without oxygen to produce syngas with high levels of carbon monoxide, hydrogen, and methane. This syngas can subsequently be used in a gas turbine or processed through combined heat and power (CHP) systems to generate electricity [44]. MSW and DPW are high-calorific-value feedstocks that are abundantly available in Qatar, making them ideal for renewable energy production through gasification technology.

Qatar is actively exploring the gasification of MSW and DPW as a viable clean energy solution [45]. The adoption of gasification aligns with Qatar's National Vision 2030 [46], which aims to diversify the economy, reduce GHG emissions, and enhance environmental sustainability. Qatar National Vision 2030 outlines the country's long-term strategy for sustainable development, focusing on economic, social, human, and environmental pillars. It aims to transform Qatar into an advanced society capable of sustaining its development

and providing a high standard of living for its people [47]. By 2030, it is estimated that gasification technology could supply 9.4% of Qatar's power consumption [48]. Waste-to-energy (WTE) projects, such as biomass gasification, provide Qatar with opportunities to enhance energy security and reduce its dependence on landfills. The gasification process breaks down waste materials in a low-oxygen environment to produce syngas, which can be used for electricity generation, heating, and industrial processes [49]. By-products such as tar and char from gasification can also be utilised in other industries, contributing to a circular economy.

The date palm is a vital cultural and economic asset in Qatar, producing various by-products, including leaflets, rachis, fruit stalk trimmings, and trunks, which are often discarded as waste. However, these by-products present significant opportunities for reuse, recycling, and energy recovery. Similarly, Qatar's MSW primarily consists of food scraps, yard waste, plastic, and paper. In 2023, the country generated over 2.5 million tonnes of MSW, as reported in the Qatar National Development Plan 2018–2022 [50,51].

Landfilling remains the predominant method of waste disposal, with approximately 95% of MSW ending up in landfills. This reliance on landfills poses environmental risks, including soil and water contamination, GHG emissions, and potential health hazards for nearby communities [52]. To address these challenges, Qatar has implemented the Qatar Integrated Waste Management Project (QIWMP), which includes landfill gas recovery, composting and recycling facilities, and a WTE plant to mitigate the environmental impact of MSW disposal [53].

Qatar's estimated 700,000 date palm trees produce approximately 26,000 metric tonnes of dates annually, with each tree generating around 250 kg of waste [54]. This results in an annual production of about 175,000 metric tonnes of DPW [55]. Although Qatar's date production is modest compared to regional producers like Saudi Arabia and Iran, leveraging DPW for energy recovery could significantly contribute to its National Vision 2030 [56,57]. Globally, the production of date palms has increased from 6.83 million metric tonnes in 2011 to 9.66 million metric tonnes in 2021 [58,59]. Qatar dedicates around 2598 hectares to date palm cultivation, with significant production in municipalities like Al-Rayyan, Umm Salal, Al-Khor, and Al-Shamal. Al-Rayyan alone accounts for 27% of national production, amounting to about 8419 tonnes annually, followed closely by Umm Salal and Al-Khor at 25.7% each. Al-Shamal contributes 21.6%, producing approximately 6735 tonnes annually across 561.3 hectares [60], as shown in Table 1.

Table 1. Municipalities and date palm statistics in Qatar [60].

Municipality (Region)	Date Palm (Number)	Production (Tonnes/Year)	Production (%)	Area (Hectare)
Al-Rayyan	175,396	8419.1	27.0	701.6
Umm Salal	166,951	8013.8	25.7	667.8
Al-Khor	166,951	8013.8	25.7	667.8
Al-Shamal	140,317	6735.0	21.6	561.3
Total	649,616	31,182	100	2598.5

At the pre-processing stage for WTE initiatives, MSW and DPW must undergo several key processes to optimise gasification efficiency. Waste collection, segregation, pre-treatment, transportation, and storage are critical steps in preparing feedstock for the gasification plant. Dedicated trucks and containers ensure waste is collected separately from residential, industrial, and agricultural sites, maintaining the integrity of the waste

streams. Proper segregation at the source eliminates contaminants that could reduce the effectiveness of the gasification process. Collected waste undergoes pre-treatment, including shredding and grinding to reduce material size and sorting to remove non-combustible components [61,62]. These steps enhance the calorific value of the feedstock and improve gasification efficiency. Moisture reduction during pre-treatment is also crucial to optimise energy output. Once prepared, the feedstock is transported to the gasification plant, where storage facilities near the plant preserve the quality of the materials and prevent contamination. This systematic approach ensures the effective use of MSW and DPW for energy production, contributing to Qatar's efforts to achieve sustainable waste management and energy diversification [30].

1.2.2. Energy Production from MSW and DPW

According to Yayha et al. [53], a mature data palm tree produces approximately 20 kg of dry leaves annually. On average, an acre of land contains between 80 and 130 date palm trees. Each tree's trunk has an average mass of 60 kg, as shown in Table 2. In any given year, around 2–3 trees die per acre die and are replaced with newly planted ones. Currently, most of this waste is discarded in landfills, exacerbating pollution and contributing to CO_2 emissions.

Table 2. Energy potential and applications of DPW and MSW [63–65].

Waste Type	Weight (kg/Tree/Year)	Applications
Leaflets	9.2	Baskets, crates, carpets, food covers, fans etc.
Rachis	10.8	Timber, wood, furniture, mats, fuel etc.
Trunk	60.0	Poles, beams, girders, etc.
Fruit pruning	0.5	Cages, trays, cords, vases, twine etc.
Date stone	90.0	Medicinal usage, body temperature coolant etc.

To address this issue, various initiatives have been introduced to promote the utilisation of DPW for electricity generation and other purposes [66–69]. For instance, the Qatar National Research Fund, under the Qatar Foundation, has supported numerous studies investigating the potential of DPW for producing biofuels, biogas, and other valuable products [68,70]. Research by Sait et al. [71], employing thermogravimetric analysis (TGA), examined the thermochemical properties of date palm biomass. The study revealed that date palm seeds and leaves possess high calorific values and significant volatile content, making them well-suited for energy production. Specifically, the calorific value of date palm seeds was found to be 18.97 MJ/kg, while the leaves and trunk exhibited calorific values of 17.9 MJ/kg and 17.4 MJ/kg, respectively, as detailed in Table 3. This high energy potential highlights the promise of DPW as a bioenergy resource.

Table 3. DPW and MSW higher heating values (HHV) [15,71,72].

Residue Type	HHV ($MJkg^{-1}$)
Leaflets	17.9
Rachis	10.9
Trunk	17.4
Date stone	18.97
MSW	13.4

2. Methodology

2.1. Measurement of Total Residues

The residue-to-product ratio (RPR) is used to estimate the volume of residues generated by a tree or a particular area of land [71]. The RPR is typically derived from field data and adjusted to align with local conditions, such as climate, soil characteristics, and farming practices. In this study, both the RPR and the higher heating values (HHV) are actual measured values obtained from literature that represent climates similar to Qatar [44,73]. These values have been calculated based on global averages to ensure their applicability and reliability under the studied conditions.

The total date palm residue in Qatar, R_{Ti}, is calculated by multiplying the number of date palm trees in the country (649,616) by the average amount of residues each tree produces annually, as listed in Table 4. In 2021, Qatar produced over 2.5 million tonnes of MSW from commercial and household sources, equating to 1.6 kg of waste per capita per day [53].

Table 4. Estimation of total date palm residues in Qatar [53].

Residue Type	Residue Weight (kg/Tree/Year)	Number of Date Palm Trees	Total Residues (kg $\times$ 10^6/Year)
Leaf	9.2	649,616	5.976
Rachis	10.8	649,616	7.015
Trunks	60.0	649,616	38.967
Date stone	90.0	649,616	58.465

2.2. Total Potential Energy

Based on the findings by Hiloidhari et al. [74] and Tolessa [75], the gross crop residue potential ($GCRP$) is calculated using factors such as the area under cultivation, the amount of crop produced, and the residue-to-product ratio (RPR), as given by Equation (1):

$$GCRP = \sum_{i=1}^{t} CA_{(i)} \times CY_{(i)} \times RPR_{(i)} \quad (1)$$

where; $GCRP$ is the potential of gross crop residue, t represents the total number of crops (tonnes), $CA_{(i)}$ is the cultivated area of the i^{th} crop (hectares), $CY_{(i)}$ is the crop yield of the i^{th} crop (hectares), and $RPR_{(i)}$ is the residue-to-product ratio of the i^{th} crop.

For date palm trees, Equation (1) can be rewritten as:

$$GCRP = \sum_{i=1}^{t} RA_{(i)} HHV_{(i)} \quad (2)$$

where; $RA(i)$ represents the quantity of available residues from the i^{th} crop per hectare per year (in MJ/year) and $HHV(i)$ is the high heating value (in MJ/kg).

Using Equation (2), the total energy potential of date palm residues in Qatar is calculated based on the weight of the residues and their respective high heating values.

The capital cost of the power plant is calculated using the following scaling Equation (3) [76]:

$$C_b = C_r \left(\frac{S}{S_r} \right)^n \quad (3)$$

where; C_b is the estimated capital cost of the new power plant (in 2016), C_r is the reference plant capital cost, S is the capacity of the new power plant, S_r is the reference plant capacity, and n is the standard scaling factor of 0.6, obtained from historical data for similar-scale economic analysis [73]. It was chosen based on the work of (Tribe, M.A. and Alpine,

R.L.W., 1986) [77]. This selection was influenced by various factors, including technological constraints, economic feasibility, environmental sustainability, and regulatory requirements.

To adjust for inflation to 2023, Equation (4) is used:

$$\frac{C_a}{C_b} = \frac{l_a}{l_b} \tag{4}$$

where C_a and C_b represent the estimated capital costs of the new plant in 2023 and 2016, respectively. l_a and l_b are the chemical engineering plant cost indices for 2023 and 2016, respectively. Therefore, we can derive:

$$\frac{C_{2023}}{C_{2016}} = \frac{l_{2023}}{l_{2016}} \tag{5}$$

Rearrange Equation (5):

$$C_a = C_{2023} = \frac{l_{2023}}{l_{2016}} \times C_{2016} \tag{6}$$

$$\text{Biomass cost = Collection cost + Storage cost + Transportation cost} \tag{7}$$

$$\text{Operating cost = Fixed cost (inclusive of biomass cost) + Variable cost} \tag{8}$$

To assess the project's financial viability, discounted cash flow (DCF) analysis is used to calculate the Net Present Value (NPV), as given by Equation (9) [74]:

$$NPV = \sum_{t=0}^{N} \frac{C_t}{(1+i)^t} \tag{9}$$

where Ct is net cash flow over the year, i is the financial discount rate, N is the total number of years and t is the time of the cash flow. The Return on Investment (ROI) for a power plant with an operating life of 20 years in Qatar can be calculated using Equation (10) [76]:

$$ROI = \frac{\mathrm{P} \times (1 - \mathrm{TR})}{(\mathrm{TPC} \times \mathrm{CRF} + \mathrm{TVC})} \tag{10}$$

where; P is the profit, TR is the tax rate (10% for Qatar), TPC is the total plant cost, CRF is the capital recovery factor, and TVC is the total variable cost. It is worth noting that the typical operating time of a power plant is much longer than 20 years. However, for market reasons, i.e., a satisfactory rate of return for investors, a period of 20 years is conducive to acquiring them. Moreover, after 20 years, significant modernisation investments may be necessary, changing the investment balance. CRF can be found in Equation (11):

$$CRF = \frac{i}{1 - (1-i)^{-n}} \tag{11}$$

The payback period can be calculated using Equation (12) [78]:

$$Payback\ Period = Y + \frac{N}{P} \tag{12}$$

where; Y is the last year with negative cumulative NPV, N is the absolute value of the negative cumulative NPV at the end of the year, and P is the annual cash flow during the year after Y.

3. Results and Discussions

3.1. Qatar's Energy Potential from DPW and MSW

The total energy potential of date palm residues in Qatar is summarised in Table 5. The total residues were calculated by multiplying residues weight by the number of date palm trees (see Table 4), while the total energy was calculated by multiplying the higher heating value (HHV) by the total residues, as given in Sections 2.1 and 2.2. The data shows that date stones have the highest energy potential among the residues, contributing a total energy of 1.109×10^9 MJ. Trunks follow as the second-largest contributor, providing 0.678×10^9 MJ. Leaflets contribute 0.106×10^9 MJ, while rachis residues account for the lowest contribution at 76.46×10^9 MJ. MSW in Qatar contributes 33.4×10^6 MJ to the total energy potential. The combined total energy potential of DPW and MSW reaches 2.01×10^9 MJ annually, demonstrating the significant renewable energy resource represented by these waste streams.

Table 5. Total energy of date palm residue and MSW in Qatar.

Type of Residue	Total Residues (kg $\times$ 10^6 /year)	HHV (MJ/kg)	Total Energy (MJ $\times$ 10^6)
Leaflets	5.976	17.90	106.97
Rachis	7.015	10.90	76.46
Trunks	38.967	17.41	678.42
Date stone	58.465	18.97	1109.08
MSW	2.5000	13.40	33.40
Total	112.923		2004.43

Biomass HHV, such as trunks and date stones, is influenced by moisture content, chemical composition (cellulose, hemicellulose, lignin, ash, and oil), and environmental factors [79]. The type of biomass residues, such as trunks or date stones, also impacts variations in energy potential. When evaluating HHV, it is essential to consider not only the material's inherent composition but also the drying and storage processes that affect moisture content [71]. The HHV serves as an indicator of the energy content of residues from DPW, as well as MSW available in Qatar. Consequently, the coefficients of variation for these residues are affected by factors including chemical identity, the amount of water-soluble compounds, and the polymerisation of organic substances present in the residues.

In general, the HHV values for trunks and date stones are higher than those for leaflets and rachis due to the former's higher carbon content and lower hydrogen content [71]. Moisture content is a key factor significantly affecting HHV differences. A direct relationship has been observed: higher moisture content correlates with lower HHV, as part of the energy content is used to vaporise the water [80,81]. For instance, the HHV of trunks (see Table 5) is approximately 17.41 MJ/kg, while for date stones, it is 18.97 MJ/kg. This disparity is attributed to the lower moisture content in date stones compared to trunks.

It is worth mentioning that, for the majority of the year, the climate of Qatar is classified as dry due to low relative air humidity [82]. This, coupled with high temperatures, significantly facilitates the drying process of biomass, including trunks and date stones. Compared to the climatic conditions of European countries such as Sweden, where natural drying of biomass can take several years, Qatar's climate provides a considerable advantage. This natural drying capability reduces the cost of biomass conditioning required for thermochemical conversion processes such as gasification and combustion.

3.2. Economic Analysis

In this study, the economic analysis of biomass gasification was conducted using the discounted cash flow (DCF) methodology. This approach estimates the project's future cash flows, discounts them to their present value, and determines the net present value (NPV). By accounting for the time value of money, the DFC method provides a comprehensive evaluation of the project's financial viability.

3.2.1. Capital Costs

The initial capital cost represents the total expense required to install the project, including power plant construction, auxiliary systems (e.g., transformers, evacuation lines), and all upfront costs necessary for development construction, and commissioning [74,83]. These costs typically include land acquisition, equipment and materials procurement, legal and regulatory fees, labour, construction, and associated engineering and design fees.

This study estimates costs for a 373 MW_{th} gasification-based biomass electricity generation facility, processing MSW and DPW. The plant configuration includes a single steam generator, condensing steam turbine, biomass storage and handling systems, and a post-emissions control system. The operational specifications of the facility include the reception, storage, and gasification of MSW and DPW with moisture content ranging between 20% and 50% [84]. It is worth noting that the 373 MW_{th} capacity for the biomass gasification plant proposed in this study represents a mid-sized, economically viable facility capable of efficiently managing substantial feedstock volumes while aligning with regional energy and resource availability.

To estimate costs, the Chemical Engineering Plant Cost Index (CEPCI) is employed. This index provides cost projections for chemical process industries, including equipment, construction labour, engineering processes, and supervision activities [85]. The CEPCI values for 2016 and 2023 are \$541.7 and \$808.7, respectively [85]. The facility is designed to start up using either natural gas or diesel fuel. Considering local conditions in Qatar, such as biomass production and treatment costs, the average capital cost is estimated at \$3669/kW [84]. For a nominal capacity of 112 MW_e (373 MW_{th}), the total estimated capital cost of the power plant is \$183,450,000 [84]. By applying Equations (3)–(6), the capital cost of the power plant ($C_{b,2016}$) in 2016 is \$8,083,008.04, while the estimated cost for a 373 MW_{th} biomass power plant in 2023 ($C_{b,2023}$) is \$12,067,064.06.

3.2.2. Operating Cost

The operating cost of the biomass gasification facility includes expenditures for biomass feedstock, labour, maintenance, and other operational expenses. These costs are influenced by system availability and the biomass consumption rate. Using the exponential method, the fixed cost is estimated at \$110/kW annually based on 2016 values, while the variable cost is calculated as \$4.2/MWh. Additional operational costs include the collection, storage, and transportation of biomass feedstock to Qatar's Dukhan biomass plant, with an average transportation distance of 150 km. The transportation cost is estimated at \$100 per 9 tonnes, while collection and storage costs are \$80 and \$25 per 9 tonnes, respectively [76]. Using Equations (3) and (6), the fixed cost for a 373 MW_{th} biomass power plant in 2023 is \$263,113.96, and the variable cost amounts to \$1,251,022.58. Furthermore, the biomass process cost, calculated using Equation (7), is \$2,572,135. Combining these expenditures, the total operating cost of the biomass power plant, using Equation (8), is \$4,086,271.54.

The cost of biomass feedstock required to supply the power plant is also considered in the operating expenses. It is important to note that the proposed facility would be

pioneering in nature, providing a real database for calculating and designing subsequent biomass energy investments in Qatar [86]. At present, biomass pricing in Qatar remains predictive. However, due to the waste-derived nature of biomass in the country, its price is expected to be lower than global market prices [68]. Potential suppliers may view the facility as an effective disposal site for post-production waste, further reducing costs. It is essential to note that the analysed residues, while suitable for energy production, could also have alternative applications, potentially impacting their availability and pricing as energy carriers [87,88]. However, Qatar's uniform energy and industrial structure–primarily based on oil and gas–along with its geographic isolation from global biomass waste markets, minimise the likelihood of such price pressures [89,90]. Consequently, the steady and wide availability of the analysed biomass types can be anticipated for the facility, ensuring a reliable and cost-effective feedstock supply for energy production.

3.2.3. Revenue and Cash Flow

In the electricity sector, the primary source of revenue comes from selling generated power to the distribution grid, as illustrated in Figure 2. Revenue is determined by the electricity price and the plant's capacity factor. In this study, the biomass plant operates with an electricity generation efficiency of 30%, with an average capacity factor of 0.8, and an average electricity price of \$30/MWh [83]. The facility, rated at 373 MW_{th} and generating 112 MW_e of power, is expected to maintain consistent annual sales revenue. The annual revenue can be calculated as follows [73]:

$$\text{Annual Revenue} = 112\ MW_e \times 8000\ h/year \times \$30/MWh = \$26{,}880{,}000 \quad (13)$$

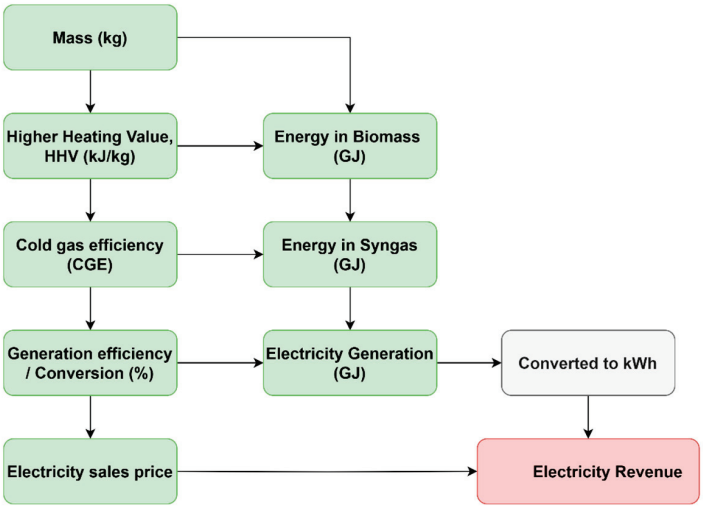


Figure 2. Sales revenue computation for MSW and DPW gasification power plant. Adjusted from [73].

This calculation assumes stable operation of the plant under the given capacity factor and electricity price conditions.

The discounted cash flow (DCF) method is employed to assess the financial feasibility of the biomass gasification plant. The DCF analysis calculates key financial metrics, including the net present value (NPV), return on investment (ROI), and payback period. The total investment for the biomass plant comprises the capital cost and operating cost, amounting to \$16,153,335.6. Additional costs include the working capital cost, which is estimated at 15% of the total investment, equalling \$2,243,000.34 [91]. The decommissioning cost of the plant is approximately \$2,900,000 [78]. The average inflation rate in Qatar is reported at 1.47% [92], and the expected completion period for the plant is two years.

Given Qatar's structural financing policies and commitment to renewable energy, it is assumed that the project will be self-financed. This approach eliminates the need for debt servicing costs, which are often included in operating expenses under alternative financing scenarios. Assuming a discount rate of 8% and a project lifetime of 20 years, the NPV of the biomass gasification power plant is calculated using Equation (9) [76]. The resulting NPV is $245,765,864.05.

Figure 3 illustrates the projected cash flow over the plant's 20-year operational period, highlighting the NPV derived from the relationship between operating costs and revenue. The NPV shown in Figure 3 exhibits high values starting after the first two years, reflecting the commencement of operations for the MSW and DPW gasification plant. This trend indicates a positive economic outlook, as revenue inflows progressively outweigh operating cost outflows over the project's lifetime. The widening gap between the positive inflows (revenue) and negative outflows (operating costs) underscores the plant's ability to generate significant surplus revenue in the long run.

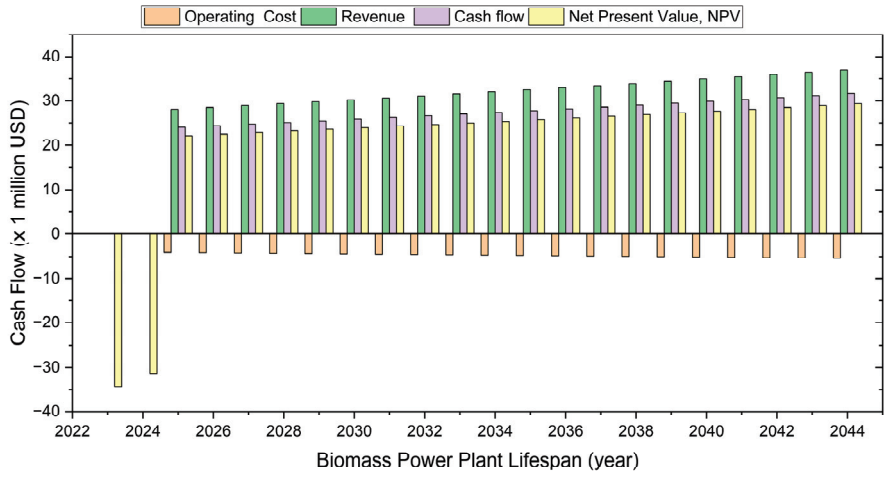


Figure 3. Projected cash flow over 20 years of biomass gasification plant operation in Qatar.

The capital recovery factor (CRF), estimated using Equation (11), was found to be 0.1. Additionally, the return on investment (ROI) is calculated using Equation (10), which considers the total revenue return and the CRF, applying a discount rate of 8% and a plant lifetime of 20 years. The results are depicted in Figure 4, which demonstrates the ROI progression and further highlights the plant's financial feasibility and profitability under the assumed conditions.

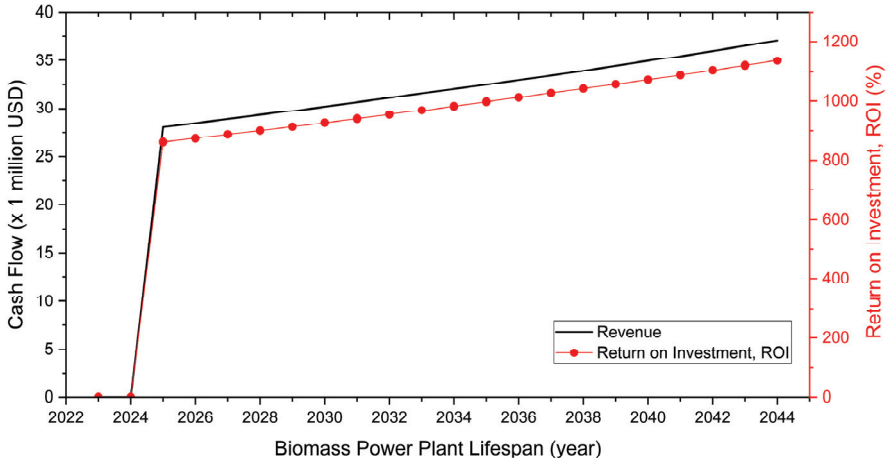


Figure 4. Return on investment, ROI, of the plant operation over 20 years.

The return on investment (ROI) is projected to increase annually over the plant's lifetime, aligning with the revenue growth. The calculated ROI for the biomass gasification power plant is 84.78%, which indicates that for every dollar invested (USD, $), the project is expected to generate a return of 84.78 cents over its operational lifetime. The combination of a high NPV and significant ROI underscores the financial feasibility of the biomass gasification power plant in Qatar. These results also highlight the project's strong potential to deliver long-term economic benefits and contribute to the country's renewable energy initiatives.

The payback period for the biomass gasification plant is estimated using Equation (12) and is found to be approximately 5 years, as illustrated by the intersection point in Figure 5. This intersection represents the moment when the total investment is fully recovered through accumulated profits. Furthermore, the cumulative NPV grows at a significantly faster rate than the annualised NPV due to the effect of compounded profits over time. This results in intersecting plots, where the intersection highlights the point at which accumulated annual profits equal the initial investment. The rapid growth of cumulative NPV and the relatively short payback period further emphasise the plant's high-profit potential and its strong financial viability.

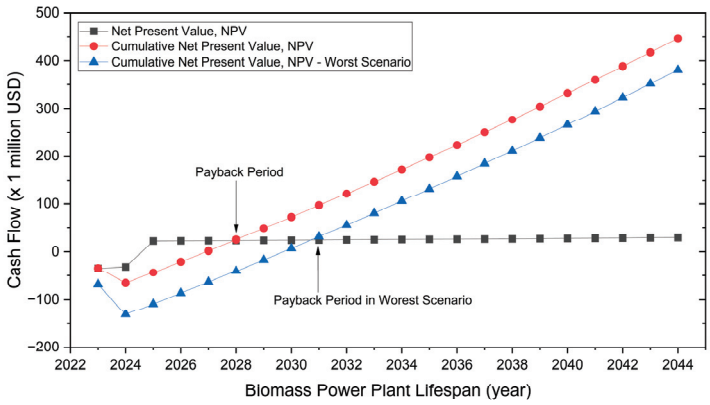


Figure 5. Overview of financial indicators: NPV as a function of power plant lifetime and payback period.

Examples from other countries suggest that for thermal power plants, actual investment costs can substantially surpass initial estimates, sometimes by as much as 300% for nuclear facilities [93]. For facilities utilising fuels such as biomass or coal, cost overruns are generally less extreme but remain common.

The proposed biomass gasification project in Qatar demonstrates promising economic metrics, including a total capital cost of $12.07 million ($3669/kW), annual operational costs of $4.09 million, and an expected revenue of $26.88 million annually. The plant achieves a net present value (NPV) of $245.77 million, a return on investment (ROI) of 84.80%, and a payback period of 5 years. To ensure a fair comparison, power plants must share similar capacities, technologies, processes, and environmental conditions. However, as an illustrative example here is; a biomass gasification project in Portugal, with a capacity of 11 MW, relies on forestry residues as feedstock [78]. The project's capital cost is €2500/kW ($2800/kW at 2019 exchange rates), with an NPV of €2.367 million, an internal rate of return (IRR) of 8.66%, and a payback period of 23 years [78]. The Portuguese project faces challenges such as high feedstock transportation costs and lower plant efficiency due to climatic and logistical constraints. While both plants achieve a 30% efficiency in electricity conversion, Qatar's dry climate reduces biomass drying costs, enhancing operational profitability compared to wetter regions like Portugal. Qatar's project offers economic viability, making it an attractive model for waste-to-energy initiatives in the MENA region.

For analysis of the given data, it is assumed that the biomass power plant in Qatar operates at an efficiency of 30% for electricity generation. This efficiency rate is critical in evaluating the viability and success of the project, as it directly influences revenue, operational costs, and the overall profitability of the plant. The amount of energy produced from biomass depends on factors such as the type of biomass resource utilised, the plant layout, and the methods employed during operations [94]. One empirical example is the biomass power plant in Copenhagen, Denmark, where the conversion efficiency is also 30% [95]. This plant uses both straw and wood waste as feedstocks to generate electricity. Similarly, a review of Alkhathami (2022) [73] and related literature indicates [16,96–98] that a 30% efficiency rate is a realistic assumption for the biomass power plant, which utilises MSW and DPW as feedstocks.

In this study, a worst-case scenario assumes investment cost overruns of up to two times the original estimate. This assumption has been incorporated into the profitability calculations and reflected in Figure 5. Even under this scenario, the estimated payback period extends to approximately 8 years, which remains a highly favourable value for this type of investment. This result further highlights the project's resilience and economic feasibility, even under less optimal conditions.

3.2.4. Emissions

The implementation of the MSW and DPW gasification plant offers a significant reduction in carbon emissions. The gasification process prevents the release of methane (CH_4) and carbon dioxide (CO_2), which are typically emitted from decomposing waste in landfills. Methane, with a global warming potential (GWP) of 28–34 times that of CO_2, represents a critical emission to mitigate. The avoidance of 72,500 tonnes of CO_2-equivalent emissions annually highlights the environmental advantage of this approach.

The electricity generated by the plant, approximately 896,000 MWh annually, replaces natural gas-based electricity, avoiding an estimated 358,400 tonnes of CO_2 emissions each year. While the plant generates emissions during syngas combustion and through operational activities such as transportation and pre-treatment, these are relatively modest. Total emissions from the gasification process amount to approximately 224,114 tonnes of CO_2 annually.

By balancing avoided emissions against generated emissions, the gasification plant achieves a net reduction of 206,786 tonnes of CO_2 annually. This result highlights the plant's role as a cleaner alternative to landfill disposal and fossil fuel-based energy production, contributing significantly to Qatar's National Vision 2030. Table 6 provides a breakdown of carbon footprint calculations, and further details are available in the Appendix A.

An annual net reduction of 206,786 tonnes of CO_2 represents approximately 0.2% of Qatar's total CO_2 emissions. According to data from the International Energy Agency (IEA) [99], Qatar's CO_2 emissions from fuel combustion were approximately 90.667 million tonnes in 2022. While this percentage may seem modest, it is a meaningful step towards mitigating climate change. Every reduction contributes to the global effort to lower greenhouse gas concentrations in the atmosphere. Moreover, implementing measures that achieve such reductions can set a precedent for further environmental initiatives, potentially leading to more substantial decreases in emissions over time.

Table 6. Carbon footprint calculation for MSW and DPW gasification [33,53,71,74,100]. The detailed calculations are available in the Appendix A.

	Source	Calculation Assumptions	Result (Tonnes CO_2/Year)
Carbon emissions from current practices	Methane from landfills	2.50 million tonnes MSW/year, 1 kg CH_4/tonne, GWP = 28–34	70,000 (CO_2-eq from CH_4)
	CO_2 from landfills	1:1 ratio with CH_4	2500 (CO_2 from landfills)
	Total landfill emissions avoided.	CH_4 + CO_2	72,500
Emissions from biomass gasification	Fossil fuel displacement	896,000 MWh electricity, 0.4 tonnes CO_2/MWh	358,400
	Syngas Combustion	112.9 M kg feedstock, 50% carbon, 1 tonne C = 3.67 CO_2	207,176
	Transportation	150 km, 100 kg CO_2/tonne	11,292
	Pre-treatment Operations	0.05 tonnes CO_2/tonne	5646
	Total Gasification Emissions	Syngas + Transportation + Pre-treatment	224,114

Category	Result (Tonnes CO_2/year)
Total Avoided Emissions	430,900
Total Gasification Emissions	224,114
Net Carbon Reduction	206,786

4. Conclusions

The gasification of municipal solid waste (MSW) and date palm waste (DPW) offers a sustainable and economically viable solution to Qatar's waste management challenges. This study demonstrates that the proposed biomass gasification plant can effectively reduce landfill dependency while generating clean energy, thereby contributing significantly to Qatar's National Vision 2030.

Qatar generates approximately 2.5 million tonnes of MSW annually, a figure projected to rise to 4.4 million tonnes by 2023, according to the Ministry of Municipality and Environment. This feasibility study estimates that the capital cost of a 373 MW_{th} biomass gasification power plant in 2023 is $12.07 million, with fixed operating costs of $263.11 million and variable costs of $1.25 million. The total cost for the collection, transportation, and storage of MSW and DPW is estimated at $2.57 million, resulting in total annual operating costs of $4.09 million. The analysis further reveals a net present value (NPV) of $245.77 million and an annual revenue of $26.88 million, with a payback period of approximately 5 years. Additionally, the gasification plant achieves a net reduction of 206,786 tonnes of CO_2 annually.

This study also highlights critical challenges to implementing MSW and DPW gasification, such as ensuring sufficient feedstock availability and managing the costs of collection, transportation, and pre-treatment. Despite these challenges, the results underline the potential for scalability and replication of this technology in Qatar and other regions with similar waste profiles.

Future research should focus on exploring the co-gasification of MSW with other waste streams, utilising syngas, produced during gasification, for gas turbine power generation, assessing applications for by-products, investigating additional strategies for reducing carbon footprints, and optimising process efficiencies to enhance economic and environmental outcomes. Addressing these areas will enable the proposed technology to play an even greater role in advancing Qatar's renewable energy objectives and reducing greenhouse gas (GHG) emissions from conventional energy sources.

Author Contributions: Conceptualization, A.M.S.H.A.-M. and M.A. (Mohammad Alnajideen); Data curation, A.M.S.H.A.-M. and M.A. (Mohammad Alnajideen); Formal analysis, A.M.S.H.A.-M., M.A. (Mohammad Alnajideen) and P.C.; Funding acquisition, A.V.-M.; Investigation, A.M.S.H.A.-M., M.A. (Mohammad Alnajideen), F.A., P.C., H.S. and M.A. (Mohammad Alherbawi); Methodology, A.M.S.H.A.-M., M.A. (Mohammad Alnajideen), P.C., H.S. and M.A. (Mohammad Alherbawi); Project administration, M.A. (Mohammad Alnajideen), R.N. and A.V.-M.; Resources, M.A. (Mohammad Al-

najideen); Supervision, M.A. (Mohammad Alnajideen), R.N. and A.V.-M.; Validation, A.M.S.H.A.-M., M.A. (Mohammad Alnajideen), F.A., P.C. and H.S.; Visualization, A.M.S.H.A.-M., M.A. (Mohammad Alnajideen), F.A., P.C. and M.A. (Mohammad Alherbawi); Writing—original draft, A.M.S.H.A.-M.; Writing—review & editing, M.A. (Mohammad Alnajideen), R.N. and A.V.-M. All authors have read and agreed to the published version of the manuscript.

Funding: This research received no external funding.

Data Availability Statement: No new data were created or analysed in this study. Data sharing is not applicable to this article.

Acknowledgments: Cardiff University authors gratefully acknowledge the support from the EPSRC through the projects Ocean-REFuel—Ocean Renewable Energy Fuels (EP/W005018/1) and Storage of Ammonia For Energy (SAFE)—AGT Pilot (EP/T009314/1). The author (A.M.) gratefully acknowledges the support provided by the Qatar National Research Fund under the doctoral project (GSRA5-1-0404-18034).

Conflicts of Interest: The authors declare no conflict of interest.

Nomenclature

CEPCI	Chemical Engineering Plant Cost Index
CO_2	Carbon Dioxide
CRF	Capital Recovery Factor
DCF	Discounted Cash Flow
DPW	Date Palm Waste
GCRP	Potential of Produced Crop Residue
GHG	Greenhouse Gases
HHV	High Heating Value
kg	Kilogram
MSW	Municipal Solid Waste
MW_e	Megawatt electrical
MW_{th}	Megawatt thermal
NPV	Net Present Value
ROI	Return on Investment
USD	United States Dollar
WTE	Waste-to-Energy

Appendix A

Carbon Footprint Calculation for MSW and DPW Gasification [33,53,71,74,100].

1. Carbon Emissions from Current Practices

   A. Methane (CH_4) and CO_2 Emissions from Landfills

- Annual MSW generation: 2.5 million tonnes
- CH_4 emission factor: Approx. 1 kg CH_4 per tonne of MSW/year (based on IPCC guidelines).
- Methane Global Warming Potential (GWP): 28–34 times more impactful than CO_2 over 100 years (IPCC AR6).
- Landfill gas composition: 50% CH_4, 50% CO_2 (by volume).

Calculation:
CH_4 emissions = 2.5 million tonnes MSW $\times$ 1 kg CH_4/tonne = 2500 tonnes CH_4.
CH_4 emissions in CO_2 equivalent = 2500 $\times$ 28 = 70,000 tonnes CO_2-eq/year.
CO_2 from landfill = Approx. 2500 tonnes/year (assuming a 1:1 ratio with CH_4).

Total landfill emissions: 72,500 tonnes CO_2-eq/year.

B. Avoided Emissions from Fossil Fuels

- Electricity generation potential: 373 MW_{th} plant with 30% efficiency = 112 MW_e.
- Displacement of natural gas: Approx. 0.4 tonnes CO_2/MWh for gas-based power.

Calculation:
Annual electricity generation = 112 MW × 8000 h = 896,000 MWh.
Avoided CO_2 emissions = 896,000 MWh × 0.4 tonnes CO_2/MWh = 358,400 tonnes CO_2/year.

2. Emissions from Biomass Gasification

A. Direct Emissions from Syngas Combustion

- The carbon content of MSW and DPW: Approximately. 50% by weight (literature value).
- Annual MSW and DPW usage: 112.9 million kg.
- Carbon to CO_2 conversion: 1-tonne carbon = 3.67 tonnes CO_2.

Calculation:

- Carbon content = 112.9 million kg × 50% = 56.45 million kg.
- CO_2 emissions = 56.45 × 3.67 = 207,176 tonnes CO_2/year.

B. Emissions from Transportation, Pre-treatment, and Operations

- Transportation: 150 km average distance; 100 kg CO_2/tonne (literature estimate).
- Pre-treatment energy use: Approx. 0.05 tonnes CO_2/tonne (based on similar studies).

Calculation:
Transportation emissions = 112,923 tonnes × 0.1 tonnes CO_2/tonne = 11,292 tonnes CO_2/year.
Pre-treatment emissions = 112,923 tonnes × 0.05 tonnes CO_2/tonne = 5646 tonnes CO_2/year.
Total operational emissions: 11,292 + 5646 = 16,938 tonnes CO_2/year.

C. Total Gasification Emissions:

Total emissions = 207,176 (syngas combustion) + 16,938 (operations) = 224,114 tonnes CO_2/year.

3. Calculate the Net Carbon Footprint

Net Emissions Saved:
Avoided landfill emissions: 72,500 tonnes CO_2-eq/year.
Avoided fossil fuel emissions: 358,400 tonnes CO_2/year.
Total avoided emissions: 430,900 tonnes CO_2/year.
Net Carbon Emissions from Gasification:
Total emissions: 224,114 tonnes CO_2/year.
Net Carbon Footprint Reduction:
Emissions saved − emissions generated = 430,900 − 224,114 = 206,786 tonnes CO_2/year.

References

1. Mor, S.; Aneja, R.; Madan, S.; Ghimire, M. Kyoto Protocol and Paris Agreement: Transition from Bindings to Pledges–A Review. *Millenn. Asia* **2023**, *15*, 690–711. [CrossRef]
2. Gan, K.E.; Taikan, O.; Gan, T.Y.; Weis, T.; Yamazaki, D.; Schüttrumpf, H. Enhancing renewable energy systems, contributing to Sustainable Development Goals of United Nation and building resilience against climate change impacts. *Energy Technol.* **2023**, *11*, 2300275. [CrossRef]
3. Nevitt, M. Assessing COP 28: The New Global Climate Deal in Dubai, NYU: New York University. United States of America. 2023. Available online: https://coilink.org/20.500.12592/xd25800 (accessed on 15 February 2025).
4. Molitor, M.R. The United Nations Climate Change Agreements. In *The Global Environment*; Routledge: Abingdon, UK, 2023; pp. 210–235.
5. Jiang, T.; He, X.; Su, B.; Havea, P.H.; Wei, K.; Kundzewicz, Z.W.; Liu, D. COP 28: Challenge of coping with climate crisis. *Innovation* **2024**, *5*, 100559. [CrossRef] [PubMed]
6. Kabeyi, M.J.B.; Olanrewaju, O.A. Sustainable energy transition for renewable and low carbon grid electricity generation and supply. *Front. Energy Res.* **2022**, *9*, 743114. [CrossRef]
7. Akpan, J.; Olanrewaju, O. Sustainable energy development: History and recent advances. *Energies* **2023**, *16*, 7049. [CrossRef]
8. Bioenergy, I. *Bioenergy–A Sustainable and Reliable Energy Source*; International Energy Agency Bioenergy: Paris, France, 2009.
9. Wang, W.-C.; Tao, L. Bio-jet fuel conversion technologies. *Renew. Sustain. Energy Rev.* **2016**, *53*, 801–822. [CrossRef]
10. Kalak, T. Potential use of industrial biomass waste as a sustainable energy source in the future. *Energies* **2023**, *16*, 1783. [CrossRef]
11. Duarah, P.; Haldar, D.; Patel, A.K.; Dong, C.-D.; Singhania, R.R.; Purkait, M.K. A review on global perspectives of sustainable development in bioenergy generation. *Bioresour. Technol.* **2022**, *348*, 126791. [CrossRef]
12. IEA. Tracking Clean Energy Progress 2023. 2023. Available online: https://www.iea.org/reports/tracking-clean-energy-progress-2023 (accessed on 14 October 2024).
13. Valavanidis, A. *Global Municipal Solid Waste (MSW) in Crisis. Two Billion Tonnes of MSW Every Year, a Worrying Worldwide Environmental Problem*; National and Kapodistrian University of Athens: Athens, Greece, 2023; Volume 1, pp. 1–28.
14. Zafar, S. Waste management outlook for the Middle East. In *The Palgrave Handbook of Sustainability: Case Studies and Practical Solutions*; Springer: Berlin/Heidelberg, Germany, 2018; pp. 159–181.
15. Mariyam, S.; Cochrane, L.; Zuhara, S.; McKay, G. Waste management in Qatar: A systematic literature review and recommendations for system strengthening. *Sustainability* **2022**, *14*, 8991. [CrossRef]
16. Al-Moftah, A.M.S.; Marsh, R.; Steer, J. Life cycle assessment of solid recovered fuel gasification in the state of Qatar. *ChemEngineering* **2021**, *5*, 81. [CrossRef]
17. Al-Moftah, A.M.S.; Marsh, R.; Steer, J. Thermal decomposition kinetic study of non-recyclable paper and plastic waste by thermogravimetric analysis. *ChemEngineering* **2021**, *5*, 54. [CrossRef]
18. Larsson, A.; Gunnarsson, I.; Tengberg, F. *The GoBiGas Project-Demonstration of the Production of Biomethane from Biomass via Gasification*; Göteborg Energi: Gothenburg, Sweden, 2018; Volume 10.
19. Diversion of Waste from Landfill in Europe. Indicators. Available online: https://www.eea.europa.eu/en/analysis/indicators/diversion-of-waste-from-landfill?activeAccordion=ecdb3bcf-bbe9-4978-b5cf-0b136399d9f8 (accessed on 19 January 2025).
20. Lazić, B.; Batinić, B.; Tot, B.; Vujić, G. Assessment of Restaurants Food Waste Towards Circular Economy in Transition Country Cities. *Environ. Eng. Manag. J. EEMJ* **2022**, *21*, 1147–1156.
21. Siddiqua, A.; Hahladakis, J.N.; Al-Attiya, W.A.K. An overview of the environmental pollution and health effects associated with waste landfilling and open dumping. *Environ. Sci. Pollut. Res.* **2022**, *29*, 58514–58536. [CrossRef]
22. Mishra, P.; SINGP, N.; Shrama, C.; Pathak, A.K. Landfill emissions and their impact on the environment. *Int. J. Eng. Res. Technol.* **2020**, *9*, 617–622.
23. Gupta, J.; Ghosh, P.; Kumari, M.; Thakur, I.S. *Solid Waste Landfill Sites for the Mitigation of Greenhouse Gases, in Biomass, Biofuels, Biochemicals*; Elsevier: Amsterdam, The Netherlands, 2022; pp. 315–340.
24. Aziz, H.A.; Rosli, N.A.; Hung, Y.-T. Landfill Methane Emissions. In *Handbook of Environment and Waste Management: Acid Rain and Greenhouse Gas Pollution Control*; World Scientific: Singapore, 2020; pp. 397–454.
25. Adams, P.; Bridgwater, T.; Lea-Langton, A.; Ross, A.; Watson, I. Biomass Conversion Technologies. In *Greenhouse Gas Balances of Bioenergy Systems*; Elsevier: Amsterdam, The Netherlands, 2018; pp. 107–139.
26. Abdmouleh, Z.; Alammari, R.A.; Gastli, A. Recommendations on renewable energy policies for the GCC countries. *Renew. Sustain. Energy Rev.* **2015**, *50*, 1181–1191. [CrossRef]
27. Qatar, N.P.C. 2024. Available online: https://www.psa.gov.qa/en/statistics1/pages/default.aspx (accessed on 16 October 2024).

28. Kırşanlı, F. Good Governance, Democracy, and Economic Resilience in the Gulf Region: A Post-Pandemic Analysis. Democracy, and Economic Resilience in the Gulf Region: A Post-Pandemic Analysis (21 May2024). 2024. Available online: https://papers.ssrn.com/sol3/papers.cfm?abstract_id=4850644 (accessed on 16 October 2024).
29. Bonaparte, Y. Qatar 2050: The Race to the Top! SSRN 4084114. 2022. Available online: https://papers.ssrn.com/sol3/papers.cfm?abstract_id=4084114 (accessed on 16 October 2024).
30. Tan, T.; Al-Khalaqi, A.; Al-Khulaifi, N. Qatar national vision 2030. *Sustain. Dev. Apprais. Gulf Reg.* **2014**, *19*, 65–81.
31. IEA. 2024. Available online: https://www.iea.org/countries/qatar (accessed on 16 October 2024).
32. Cochrane, L.; Al-Hababi, R. *Sustainable Qatar: Social, Political and Environmental Perspectives*; Springer Nature: London, UK, 2023.
33. Zafar, S. Solid Waste Management in Qatar. 2022. Available online: https://www.ecomena.org/solid-waste-management-in-qatar/ (accessed on 16 October 2024).
34. Perumal, S.V. Doha's Waste Management Market Offers "Unique" Opportunities: Invest Qatar. 2023. Available online: https://www.gulf-times.com/article/656656/business/dohas-waste-management-market-offers-unique-opportunities-invest-qatar (accessed on 16 October 2024).
35. Thaker, H.M.T.; Sakti, M.R.P.; Qoyum, A.; Thaker, M.A.M.T.; Hosen, M. Recent SDGs and ESG Implementation by Qatar. *J. Environ. Assess. Policy Manag.* **2023**, *25*, 2350017. [CrossRef]
36. Al Mohannadi, F. *Critical Analysis of the Environmental Component of the Sustainable Stadiums Built for the 2022 FIFA World Cup in Qatar*; Hamad Bin Khalifa University: Ar-Rayyan, Qatar, 2023.
37. Lundberg, O. FIFA World Cup 2022 as a Catalyst for Environmental Sustainability in Qatar. In *Sustainable Qatar: Social, Political and Environmental Perspectives*; Springer Nature: Singapore, 2022; pp. 55–72.
38. Electricity, Q.G.; Water Corporation "KAHRAMAA". *KAHRAMAA and Siraj Energy Sign Agreements for Al-Kharsaah Solar PV Power Plant*; KAHRAMAA: Doha, Qatar, 2020.
39. Nassar, A.K. Identifying and explaining public preferences for renewable energy sources in Qatar. *Sustainability* **2022**, *14*, 13835. [CrossRef]
40. Ali, B. Comparative sustainability assessment of energy storage technologies in Qatar. *J. Energy Storage* **2023**, *67*, 107534. [CrossRef]
41. Abdallah, I.; Alhosin, H.; Belarabi, M.; Chaouki, S.; Mahmoud, N.; Tayah, J. A Pan-Asian Energy Transition? The New Rationale for Decarbonization Policies in the World's Largest Energy Exporting Countries: A Case Study of Qatar and Other GCC Countries. *Energies* **2024**, *17*, 3776. [CrossRef]
42. Bhattacharjee, S.; Panja, A.; Kumar, R.; Ram, H.; Meena, R.K.; Basak, N. Municipal solid waste compost: A comprehensive bibliometric data-driven review of 50 years of research and identification of future research themes. *Environ. Sci. Pollut. Res.* **2023**, *30*, 86741–86761. [CrossRef]
43. Tahir, M.H.; Chen, D. Integrated approach for H2-Rich syngas production from wastes using carbon-based catalysts and subsequent CO2 adsorption by carbon-based adsorbents: A review. *Int. J. Hydrogen Energy* **2024**, *59*, 679–696. [CrossRef]
44. Al-Moftah, A.M.S. *Thermal Kinetics Study of Paper and Plastic Waste Gasification*; Cardiff University: Cardiff, UK, 2022.
45. AlNouss, A.; Alherbawi, M.; Parthasarathy, P.; Al-Thani, N.; McKay, G.; Al-Ansari, T. Waste-to-energy technology selection: A multi-criteria optimisation approach. *Comput. Chem. Eng.* **2024**, *183*, 108595. [CrossRef]
46. Al-Maadeed, A.; Abu-Bader, S. An Overview of Qatar. In *The Routledge International Handbook of Social Development, Social Work, and the Sustainable Development Goals*; Routledge: Abingdon, UK, 2023.
47. Qatar National Vision 2030: A Roadmap for Transformation. 2022. Available online: https://www.gco.gov.qa/en/state-of-qatar/qatar-national-vision-2030/our-story/ (accessed on 19 January 2025).
48. Abdullah, Z.T. Sustainable Business Assessment of the Gasification of Solid Recovered Fuel for Bread Making. *Energy Nexus* **2024**, *16*, 100326. [CrossRef]
49. Porshnov, D. Evolution of pyrolysis and gasification as waste to energy tools for low carbon economy. *Wiley Interdiscip. Rev. Energy Environ.* **2022**, *11*, e421. [CrossRef]
50. Sebastian, J.K.; Nagella, P.; Mukherjee, E.; Dandin, V.S.; Naik, P.M.; Jain, S.M.; Al-Khayri, J.M.; Johnson, D.V. *Date Palm: Genomic Designing for Improved Nutritional Quality, in Compendium of Crop Genome Designing for Nutraceuticals*; Springer: Berlin/Heidelberg, Germany, 2023; pp. 1–64.
51. Perry-Givens, S. *Navigating Second Chances: A Qualitative Exploration of the Role Higher Education Plays in Supporting Justice-Impacted Individuals*; California State University: Fresno, CA, USA, 2024.
52. Kiehbadroudinezhad, M.; Merabet, A.; Hosseinzadeh-Bandbafha, H. Landfill Source of Greenhouse Gas Emission. In *Advances and Technology Development in Greenhouse Gases: Emission, Capture and Conversion*; Elsevier: Amsterdam, The Netherlands, 2024; pp. 123–145.
53. Talballa, H.M.; Gichuru, J. Toward the Circular Qatari Zero-Waste Management Sector. In *Sustainable Qatar*; Springer: Berlin/Heidelberg, Germany, 2023; p. 305.

54. Rani, G.M.; Pathania, D.; Umapathi, R.; Rustagi, S.; Huh, Y.S.; Gupta, V.K.; Kaushik, A.; Chaudhary, V. Agro-waste to sustainable energy: A green strategy of converting agricultural waste to nano-enabled energy applications. *Sci. Total Environ.* **2023**, *875*, 162667.
55. Shahbaz, M.; Rashid, N.; Saleem, J.; Mackey, H.; McKay, G.; Al-Ansari, T. A review of waste management approaches to maximise sustainable value of waste from the oil and gas industry and potential for the State of Qatar. *Fuel* **2023**, *332*, 126220. [CrossRef]
56. East, M.; Initiative, C.C. *The Green Economy and Innovation*; The Cyprus Institute: Nicosia, Cyprus, 2022.
57. Phan, M.H.; Stive, M.J. Managing mangroves and coastal land cover in the Mekong Delta. *Ocean Coast. Manag.* **2022**, *219*, 106013. [CrossRef]
58. Alotaibi, K.D.; Alharbi, H.A.; Yaish, M.W.; Ahmed, I.; Alharbi, S.A.; Alotaibi, F.; Kuzyakov, Y. Date palm cultivation: A review of soil and environmental conditions and future challenges. *Land Degrad. Dev.* **2023**, *34*, 2431–2444. [CrossRef]
59. Statista. Production of Dates Worldwide from 2010 to 2022 (in Million Metric Tons)*. 2024. Available online: https://www.statista.com/statistics/960247/dates-production-worldwide/ (accessed on 17 October 2024).
60. Al-Khayri, J.M.; Jain, S.M.; Johnson, D.V. *Date Palm Genetic Resources and Utilization*; Springer: Berlin/Heidelberg, Germany, 2015; Volume 1.
61. Hinchliffe, D.; Frommann, J.; Gunsilius, E. *Waste to Energy Options in Municipal Solid Waste Management*; GIZ: Eschborn, Germany, 2017.
62. Consonni, S.; Viganò, F. Waste gasification vs. conventional Waste-To-Energy: A comparative evaluation of two commercial technologies. *Waste Manag.* **2012**, *32*, 653–666. [CrossRef]
63. Al-Alawi, R.A.; Al-Mashiqri, J.H.; Al-Nadabi, J.S.; Al-Shihi, B.I.; Baqi, Y. Date palm tree (*Phoenix dactylifera* L.): Natural products and therapeutic options. *Front. Plant Sci.* **2017**, *8*, 845. [CrossRef]
64. Awad, S.; Zhou, Y.; Katsou, E.; Li, Y.; Fan, M. A critical review on date palm tree (*Phoenix dactylifera* L.) fibres and their uses in bio-composites. *Waste Biomass Valorization* **2021**, *12*, 2853–2887. [CrossRef]
65. Alotaibi, M.D.; Alshammari, B.A.; Saba, N.; Alothman, O.Y.; Sanjay, M.; Almutairi, Z.; Jawaid, M. Characterization of natural fiber obtained from different parts of date palm tree (*Phoenix dactylifera* L.). *Int. J. Biol. Macromol.* **2019**, *135*, 69–76. [CrossRef]
66. Castillo, A.B.; Cortes, D.J.D.; Sorino, C.F.; Soriño, C.K.P.; El-Naas, M.H.; Ahmed, T. Bioethanol production from waste and nonsalable date palm (*Phoenix dactylifera* L.) fruits: Potentials and challenges. *Sustainability* **2023**, *15*, 2937. [CrossRef]
67. Basha, J.S.; Jafary, T.; Vasudevan, R.; Bahadur, J.K.; Ajmi, M.A.; Neyadi, A.A.; Soudagar, M.E.M.; Mujtaba, M.A.; Hussain, A.; Ahmed, W. Potential of utilization of renewable energy technologies in gulf countries. *Sustainability* **2021**, *13*, 10261. [CrossRef]
68. Parthasarathy, P.; Alherbawi, M.; Shahbaz, M.; Al-Ansari, T.; McKay, G. Developing biochar from potential wastes in Qatar and its revenue potential. *Energy Convers. Manag. X* **2023**, *20*, 100467. [CrossRef]
69. Clarke, S.F.; Almannai, S. Sustainable Waste Management in Qatar. In *Sustainable Development: An Appraisal from the Gulf Region.*, 1st ed.; Berghahn Books: Oxford, NY, USA, 2014; pp. 367–390.
70. Alherbawi, M.; Parthasarathy, P.; Al-Ansari, T.; Mackey, H.R.; McKay, G. Potential of drop-in biofuel production from camel manure by hydrothermal liquefaction and biocrude upgrading: A Qatar case study. *Energy* **2021**, *232*, 121027. [CrossRef]
71. Sait, H.H.; Hussain, A.; Salema, A.A.; Ani, F.N. Pyrolysis and combustion kinetics of date palm biomass using thermogravimetric analysis. *Bioresour. Technol.* **2012**, *118*, 382–389. [CrossRef]
72. Umar, H.; Sulaiman, S.; Ahmad, R.; Tamili, S. Characterisation of Oil Palm Trunk and Frond as Fuel for Biomass Thermochemical. In *IOP Conference Series: Materials Science and Engineering*; IOP Publishing: Bristol, UK, 2020.
73. Alkhathami, H.M. *Reaction Kinetics in Biomass Gasification (Chemical Engineering)*; Cardiff University: Cardiff, UK, 2022.
74. Hiloidhari, M.; Das, D.; Baruah, D. Bioenergy Potential Crop Residue Biomass India. *Renew. Sustain. Energy Rev.* **2014**, *32*, 504–512. [CrossRef]
75. Tolessa, A. Bioenergy potential from crop residue biomass resources in Ethiopia. *Heliyon* **2023**, *9*, e13572. [CrossRef]
76. Huang, Y.; Zhao, Y.-j.; Hao, Y.-h.; Wei, G.-q.; Feng, J.; Li, W.-y.; Yi, Q.; Mohamed, U.; Pourkashanian, M.; Nimmo, W. A feasibility analysis of distributed power plants from agricultural residues resources gasification in rural China. *Biomass Bioenergy* **2019**, *121*, 1–12. [CrossRef]
77. Tribe, M.; Alpine, R. Scale economies and the "0.6 rule". *Eng. Costs Prod. Econ.* **1986**, *10*, 271–278. [CrossRef]
78. Cardoso, J.; Silva, V.; Eusebio, D. Techno-economic analysis of a biomass gasification power plant dealing with forestry residues blends for electricity production in Portugal. *J. Clean. Prod.* **2019**, *212*, 741–753. [CrossRef]
79. EL-Mously, H.; Midani, M.; Darwish, E.A. Date Palm Byproducts for Green Fuels and Bioenergy Production. In *Date Palm Byproducts: A Springboard for Circular Bio Economy*; Springer: Berlin/Heidelberg, Germany, 2023; pp. 271–343.
80. Amen, R.; Hameed, J.; Albashar, G.; Kamran, H.W.; Shah, M.U.H.; Zaman, M.K.U.; Mukhtar, A.; Saqib, S.; Ch, S.I.; Ibrahim, M. Modelling the higher heating value of municipal solid waste for assessment of waste-to-energy potential: A sustainable case study. *J. Clean. Prod.* **2021**, *287*, 125575. [CrossRef]

81. Kumar, A.; Samadder, S.R. Development of lower heating value prediction models and estimation of energy recovery potential of municipal solid waste and RDF incineration. *Energy* **2023**, *274*, 127273. [CrossRef]
82. Badran, A. Eco-farming policies and sustainable food security in Qatar: The role of hydroponics. *Adv. Mod. Agric.* **2025**, *6*, 3039. [CrossRef]
83. Beaty, H.W. *Handbook of Electric Power Calculations*; McGraw-Hill: New York City, NY, USA, 2001.
84. Cost, C. *Performance Characteristic Estimates for Utility Scale Electric Power Generating Technologies*; US Energy Information Administration: Washington, DC, USA; Sargent and Lundy: Chicago, IL, USA, 2020.
85. Maxwell, C. Towering Skills, Cost Indices. 2022. Available online: https://toweringskills.com/financial-analysis/cost-indices/ (accessed on 17 December 2024).
86. Kaur, P.; Kaur, G.J.; Routray, W.; Rahimi, J.; Nair, G.R.; Singh, A. Recent advances in utilization of municipal solid waste for production of bioproducts: A bibliometric analysis. *Case Stud. Chem. Environ. Eng.* **2021**, *4*, 100164. [CrossRef]
87. Alherbawi, M.N. *Development of Novel Integrated Systems to Produce Drop-In Jet Biofuel from Multi-Biomass in Qatar*; Hamad Bin Khalifa University: Ar-Rayyan, Qatar, 2022.
88. Makkawi, Y.; Khan, M.; Pour, F.H.; Moussa, O.; Mohamed, B.; Alnoman, H.; Elsayed, Y. A comparative analysis of second-generation biofuels and its potentials for large-scale production in arid and semi-arid regions. *Fuel* **2023**, *343*, 127893. [CrossRef]
89. Sulaiti, F. *Identifying Qatar's Potential for Carbon Sequestration*; Swansea University: Swansea, UK, 2023.
90. Van de Graaf, T.; Sovacool, B.K. *Global Energy Politics*; John Wiley & Sons: Hoboken, NJ, USA, 2020.
91. Sorrels, J.L.; Walton, T.G. *Cost Estimation: Concepts and Methodology*; US Environmental Protection Agency: Washington, DC, USA, 2017.
92. Statista. Qatar: Inflation Rate from 1989 to 2029. 2023. Available online: https://www.statista.com/statistics/379995/inflation-rate-in-qatar/ (accessed on 17 December 2024).
93. Wealer, B.; Bauer, S.; Goeke, L.; von Hirschhausen, C.R.; Kemfert, C. *Economics of Nuclear Power Plant Investment: Monte Carlo Simulations of Generation III/III+ Investment Projects*; DIW Discussion Papers, No. 1833; German Institute for Economic Research (DIW Berlin): Berlin, Germany, 2019.
94. De Meyer, A.; Cattrysse, D.; Rasinmäki, J.; Van Orshoven, J. Methods to optimise the design and management of biomass-for-bioenergy supply chains: A review. *Renew. Sustain. Energy Rev.* **2014**, *31*, 657–670. [CrossRef]
95. Mathiesen, B.V.; Lund, R.S.; Connolly, D.; Ridjan, I.; Nielsen, S. *Copenhagen Energy Vision: A Sustainable Vision for Bringing a Capital to 100% Renewable Energy*; Aalborg University: Aalborg, Denmark, 2015.
96. Faaij, A. Modern biomass conversion technologies. *Mitig. Adapt. Strateg. Glob. Chang.* **2006**, *11*, 343–375. [CrossRef]
97. Goffé, J.; Ferrasse, J.-H. Stoichiometry impact on the optimum efficiency of biomass conversion to biofuels. *Energy* **2019**, *170*, 438–458. [CrossRef]
98. Matsakas, L.; Gao, Q.; Jansson, S.; Rova, U.; Christakopoulos, P. Green conversion of municipal solid wastes into fuels and chemicals. *Electron. J. Biotechnol.* **2017**, *26*, 69–83. [CrossRef]
99. IEA. How Much CO2 Does Qatar Emit? 2025. Available online: https://www.iea.org/countries/qatar/emissions (accessed on 18 January 2025).
100. Eggleston, H.; Buendia, L.; Miwa, K.; Ngara, T.; Tanabe, K. *2006 IPCC Guidelines for National Greenhouse Gas Inventories*; IPCC: Geneva, Switzerland, 2006. Available online: https://www.osti.gov/etdeweb/biblio/20880391 (accessed on 16 October 2024).

Disclaimer/Publisher's Note: The statements, opinions and data contained in all publications are solely those of the individual author(s) and contributor(s) and not of MDPI and/or the editor(s). MDPI and/or the editor(s) disclaim responsibility for any injury to people or property resulting from any ideas, methods, instructions or products referred to in the content.

energies

MDPI

Article

Study on Determining the Efficiency of a High-Power Hydrogenerator Using the Calorimetric Method

Elisabeta Spunei [1], Dorian Anghel [1], Gheorghe Liuba [1], Cristian Paul Chioncel [1,*] and Mihaela Martin [2]

[1] Department of Engineering Sciences, Faculty of Engineering, Babes-Bolyai University, 400028 Cluj-Napoca, Romania; elisabeta.spunei@ubbcluj.ro (E.S.); dorian.anghel@ubbcluj.ro (D.A.); gheorghe.liuba@ubbcluj.ro (G.L.)

[2] Department of Public Administration and Management, Faculty of Political, Administrative and Communication Sciences, Babes-Bolyai University, 400028 Cluj-Napoca, Romania; mihaela.martin@ubbcluj.ro

* Correspondence: cristian.chioncel@ubbcluj.ro; Tel.: +40-0746-946282

Abstract

The global energy crisis demands efficient electricity production solutions, especially for isolated communities where hydraulic energy can be harnessed sustainably. This paper presents a case study analyzing the efficiency of a 13,330 kW hydrogenerator, consisting of a bulb-type hydro-aggregate using the calorimetric method—a viable alternative when testing at nominal load is not feasible due to technical limitations. The method involves measuring the thermal energy absorbed by the cooling water under three operating conditions: no-load unexcited, no-load excited, and symmetric three-phase short-circuit. Measurements followed IEC standards and were conducted with high-precision instruments for temperature, flow, voltage, and current. The results quantify mechanical, ventilation, iron, and copper losses, as well as additional losses via radiation and convection. Thermal analysis revealed significant heat accumulation in the rotor and stator windings, indicating the need for improved cooling solutions. The calorimetric method enables efficiency evaluation without interrupting generator operation, offering a valuable tool for diagnostics, predictive maintenance, and informed decisions on modernization. Furthermore, integrating an intelligent operational control system could enhance efficiency and improve the quality of the supplied energy, supporting long-term sustainability in hydroelectric power generation.

Keywords: synchronous generator; calorimetric method; energy losses; efficiency

1. Introduction

Considering the electricity crisis faced by all countries, increasing energy production and reducing energy consumption are requirements being implemented through various national and international strategies. In the case of isolated communities that do not benefit from electricity transport and distribution networks but have a flowing water source, establishing a micro-hydropower plant can solve the issue of electricity supply. Thus, pico-hydro energy systems are being developed and implemented, featuring one or two Pelton turbines with different numbers of buckets, which provide lighting for communities and power for small consumers [1].

A study conducted by the International Energy Agency (*IEA*) found that electricity consumption in industry accounts for 37% of global energy consumption, while approximately 30% of global energy is consumed in buildings [2].

Moreover, if we refer to electricity production, in 2019, about 11% of global primary energy came from renewable sources. Hydropower is included in renewable energy sources, and it is transformed in hydropower plants into electricity. This energy source accounts for over 60% of renewable energy production [3].

At the European level, through the REPowerEU plan, the goal for renewable energy production has been proposed to increase from the current 40% to 45% by 2030 [4]. This goal can be achieved through the construction of new small or large hydropower facilities, maintaining the operation of hydropower plants and micro-hydropower plants at high efficiency, as well as modernizing/repairing hydroenergy systems in various stages of construction or taken out of operation.

For both operating and new hydro-aggregates, it is necessary to determine the efficiency of each component (turbine, generator) as well as the overall efficiency of the hydro-aggregate. In the case of operating hydro-aggregates, determining efficiency can lead to solutions for more efficient operation of the entire system, considering that most hydropower plants have been in operation for a considerable time and that modern equipment and solutions available on the market can contribute to increased efficiency.

Since, in most cases, the rotor speed of the turbines in micro-hydropower plants ranges from 75 to 400 rpm, while the generator speed is often above 750 rpm, a mechanical transmission is necessary between these components. If the turbine has fixed blades and the generator is of the asynchronous type, then the efficiency of the hydro-aggregate is lower than that estimated by calculations. To eliminate this disadvantage and increase efficiency, a synchronous generator with permanent magnets directly coupled to the turbine can be used. With a synchronous generator, it is possible to control the turbine rotor speed based on the water flow that can be turbine-fed [5]. It has been demonstrated that, in the case of low-power turbines, hydro-aggregates have higher efficiency when equipped with permanent magnet generators compared to those with asynchronous generators [6].

Depending on the characteristics of the hydroenergy installation, the type of turbine, and the optimal design of the blades, a higher or lower efficiency of the entire hydroenergy system can be achieved [7,8]. Additionally, if the hydropower plant operates at a power level lower than its nominal power, its efficiency decreases due to significant losses occurring in the electric generator [9]. In this situation, increasing efficiency can be achieved by reducing the value of the stator voltage [10]. Other methods used to increase the efficiency of generators in hydroenergy systems include the use of autotransformers or frequency converters, each with its advantages and disadvantages [11].

Regardless of the type of generator used, its efficiency is very important in hydropower systems, necessitating the establishment of its efficiency by determining loss values, using provisions from current standards [12,13]. The loss values depend on the constructive type of the hydrogenerator and its operating mode.

Loss values are usually determined by testing the generator under no-load and short-circuit conditions, determining core losses, mechanical and ventilation losses, and copper losses [9]. The value of iron losses can be determined through magnetic circuit methods and finite element methods when the generator operates at no load [14], separately analyzing the various parts of the magnetic cores of the rotor and stator [15,16]. In the case of large synchronous generators, mechanical losses caused by friction in bearings can be determined by analyzing the variation in speed during mechanical and electrical braking [17].

When Roebel bars are used, internal circulating currents between conductors occur, causing additional losses, which represent approximately 2% of nominal losses [18]. Another category of additional losses is determined by the stamping of laminations, which can lead to an increase in iron losses of up to 4% in the case of high-power hydrogenerators [19]. All these additional losses should not be neglected, as they determine the decrease in the efficiency of the hydrogenerator.

A modern method used for determining losses consists of infrared thermography of the mechanical parts of the generator, aimed at identifying the heat emitted through them. The method involves the use of multiple sensors that communicate with the monitoring system, thereby reducing the time needed to determine efficiency compared to other methods used [20,21].

When determining the efficiency of the generator using the calorimetric method, it is considered that all losses in the machine are transformed into heat. Thus, the temperature and flow rate of the cooling fluid must be measured, along with the temperatures along the surface of the machine. Based on the heat transfer coefficient, the losses and input power, as well as the efficiency of the generator, are calculated [22–24]. Research has shown that the temperature on the rotor is higher than that in the stator. This fact was demonstrated through analysis with an infrared sensor installed on the stator side to measure the temperature of each rotor pole [25]. A similar study presents the same methodology for determining the efficiency of a 90 MW synchronous generator with apparent poles and a vertical axis. The results obtained from measurements were compared with those provided by the generator manufacturer [26]. Although the same methodology for determining generator efficiency is used, in the present case study, the calorimetric method is applied to a bulb-type generator. While the 90 MW generator dissipates part of its losses through cooling air, this type of hydro unit has a much lower capacity for heat evacuation via air, and the method for measuring the expelled air flow is less accurate than measuring the cooling agent—water—circulating through the cooling system's pipes.

The same method is also used to determine the efficiency of a 60 MW hydrogenerator, where emphasis is placed on the arrangement of measuring equipment required for capturing the necessary parameters [27]. It was found that the performance and calibration of the measuring system significantly affect the quality of the measurements, potentially introducing errors of up to 5% [28].

The advantage of using the calorimetric method lies in the fact that it does not require stopping the hydro unit and does not require direct access to internal components, using only external sensors such as thermoresistances, thermal cameras, and flow meters. It has been demonstrated that this method allows for the determination of efficiency without affecting the operation of the facility, thus being useful for early fault detection and predictive maintenance [29].

If the cooling agent is water, to meet measurement uncertainty requirements, flow meters must be correctly installed, and the discharge of cooling water should be reduced to a low value so that the measurement uncertainty is within 3% [30].

To increase the efficiency of hydrogenerators, during the repair stage of hydro units, the use of modern materials and high-performance systems for controlling their operation is essential. Another method used to increase the efficiency of an asynchronous generator involves the automatic modification of the winding connections from a delta to a star connection [9].

In all cases of using electric generators, the waveforms of the voltages, currents, frequency variations, and harmonic levels must be monitored and analyzed, as any variation in load or water flow leads to a transient regime of the entire hydro unit, influencing

the quality of the energy supplied to the consumer [31]. If an asynchronous generator is used in the hydroelectric system, which supplies electricity in an unbalanced system, the unbalanced system will negatively influence the performance of the generator and will also affect the quality of the supplied energy [32].

In situations where the micro-hydroelectric plant operates autonomously, the determination of the performance of the hydro unit must take into account the use of battery banks, as well as the inverter, necessary for controlling frequency during variations in load or water flow [33]. These components also influence the efficiency of the hydro unit.

The operation of the electric generator at maximum efficiency requires that an optimal choice of variable values be made from the design stage to ensure the fulfillment of this objective [34], followed by verification in the simulation stage.

If an Intelligent Energy Control System (*IECS*) is implemented at the micro-hydroelectric plant, used for adjusting the voltage and frequency supplied by the generator and for monitoring load variations, it ensures the quality indicators of the energy provided to the consumer, achieving maximum efficiency at different loads [35] and operating regimes, while ensuring safe operation [36].

This paper presents a case study in which the calorimetric method is applied to determine the efficiency of a high-power hydrogenerator, consisting of a bulb-type hydroaggregate, presented in Figure 1.

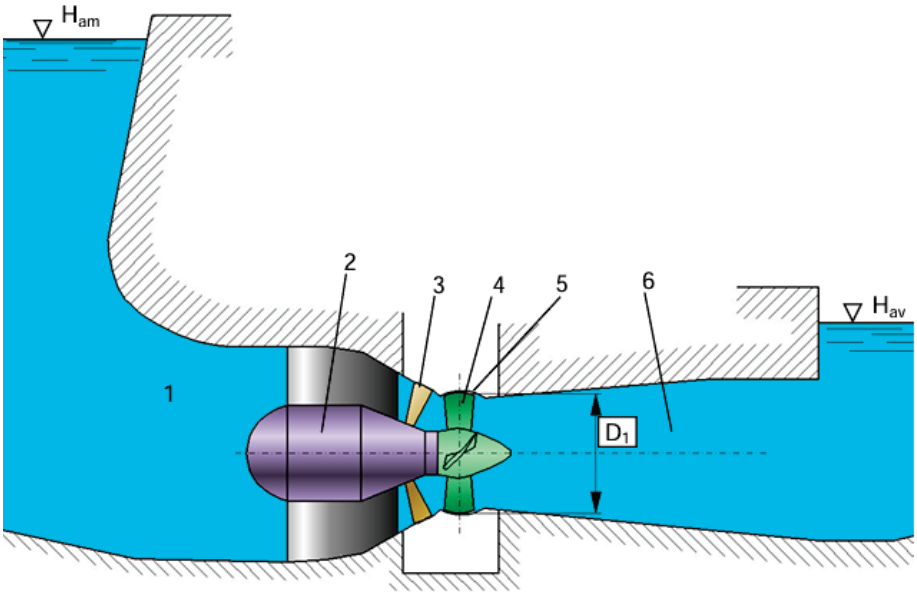


Figure 1. Cross-section view of a hydroelectric facility with a bulb-type turbine.

In this figure, H_{am} represents the upstream water level and H_{av} represents the downstream level. The components are labeled as follows: 1—intake chamber; 2—turbine capsule; 3—guide apparatus; 4 and 5—turbine rotor and rotor chamber, respectively; 6—draft tube. The hydroelectric facility/arrangement housing the analyzed hydro unit is designed for low head and high flow rates. Initially, the plant featured a unique upstream bulb-type hydro unit (with the generator positioned upstream of the turbine rotor), built by a Romanian manufacturer. Given its long operational life, the need arose to improve the unit's energy efficiency, leading to the generator's refurbishment. Based on this upgrade, in situ measurements were conducted to determine efficiency, aiming to validate the guaranteed performance provided by the manufacturer using the most accurate method available.

This method is employed because it does not subject the hydrogenerator to demands that could jeopardize its proper functioning over time, and because load testing is not feasible due to the high power of the hydrogenerator. Determining the efficiency after a certain operational period is a mandatory requirement to identify any critical points and areas where intervention can ensure efficient long-term operation of the hydrogenerator.

For the analyzed hydrogenerator, cooling is ensured by using water as the cooling agent. Measurements were carried out for three operating conditions/regimes of the generator: no-load unexcited, no-load excited, and three-phase short-circuit. For these regimes, both transmitted and non-transmitted energy losses through the cooling systems were calculated.

This method is being applied for the first time in Romania. The existing research does not include studies where the calorimetric method is used to determine the efficiency of a bulb-type hydro unit cooled by water rather than air, as is typical for most hydrogenerators. The method was chosen for its higher precision since the water flow rate can be measured more accurately than air flow, especially considering the large surface area of the hydrogenerator.

The results obtained allow for the identification of critical energy loss areas and provide a complete picture of the thermal behavior of the generator. The study confirms that the calorimetric method is reliable, precise, and can be applied without disrupting the operation of the equipment, making it suitable for the periodic assessment of efficiency and for supporting decisions regarding maintenance and modernization of hydroelectric installations. The case study was not intended to certify the efficiency of the refurbished hydrogenerator but rather to validate its performance using the calorimetric method under specific operating conditions.

2. Testing Method

2.1. Generalities and Objectives in Determining Efficiency

Determining the efficiency of the generator using the calorimetric method involves measuring the temperature of the cooling agent, which can be either water or air.

In the presented case study, the cooling agent is water. This determination method was chosen because, under normal operating conditions, it was not possible to run the generator at its nominal parameters (voltage, current, power, and speed). The determination of efficiency was carried out in accordance with the provisions of the IEC standards 34-2, 34-2A, and 34-4, taking into account all losses from the generator, from its radial and radial–axial bearings [37–39].

To determine the efficiency of the generator, the same power factor value is maintained while the value of the active load is modified, and the efficiency is determined with the general formula

$$\eta_G = \frac{P}{P + \sum P} \quad (1)$$

where η_G is the efficiency of the generator, P is its active power supplied by the generator, and ΣP represents the measured and calculated losses from the generator corresponding to the active power.

The operating regimes used for determining losses in the generator are

- No-load unexcited operation (the excitation winding is not powered), when the generator operates at nominal speed;
- No-load excited operation, when the excitation winding is powered at nominal voltage and the rotor speed is nominal;
- Three-phase short-circuit operation, when the current value in the stator winding is at its nominal value.

Determining the generator's efficiency involves carrying out measurements and constructing characteristics such as

- Measuring the ohmic resistances of the stator and rotor windings;
- Measuring the flow rate and the inlet and outlet temperatures of the coolant in the cooling units;
- Determining the nominal excitation current by directly measuring it at the generator's nominal apparent power;
- Determining the loss values in the axial and radial bearings of the generator;

Determining the adjustment characteristics of the generator by establishing the excitation current value at P = 0.25, 0.50, 0.75, 1.00, and 1.1% of the nominal current for nominal power factor and unit power factor.

Preliminary operations before measurements included the following:

- Selecting and installing the measurement transducers according to the manufacturer's technical specifications;
- Connecting the transducers to the data acquisition systems;
- Calibrating the equipment in accordance with required standards.

2.2. Measuring Devices Used

2.2.1. Devices for Measuring Electrical Quantities

Electrical measurements in the generator's primary circuits were carried out using current transformers and shunts, along with measuring instruments that featured a precision class of at least 0.5 in alternating current circuits and a precision class of 0.5 in direct current circuits. For secondary circuits, measurements were made with devices having a precision class of 0.2.

To measure electrical parameters in the stator of the synchronous generator, the Chauvin Arnoux (France) CA8336 network analyzer was used, with a sampling rate of 256 samples per period, compliant with IEC 61000-4-30 Class B [40]. Measurements for the excitation winding were taken using the Chauvin Arnoux (France) CA PEL 113 logger. Instrument errors were as follows: voltage and current < 0.25%, power calculations (active, reactive, apparent) < 0.3%, and power factor < 1%.

2.2.2. Devices for Measuring Temperatures

To measure the cooling air, platinum thermoresistances are used. Thus, for each cooler unit, a *PT* 100 Ω thermoresistance at 0 °C is used to measure the temperature of the warm air, while the cold air temperature is measured with an identical thermoresistance placed in the middle of the cooler unit. The thermoresistances are mounted in copper sheaths to reduce the effect of air currents on measurement precision. The measurement error of the thermoresistances must be a maximum of ±0.5 °C at 0 °C and a maximum of ±0.35 °C at 100 °C.

The cooling water temperature at the inlet and outlet of the cooling circuit for the axial and radial bearings of the generator is measured using *PT* 100 Ω thermoresistances at 0 °C, adapted for mounting on pipes and for operation in water environments, with a precision of ±0.1 °C.

To measure temperatures in the stator windings of the generator, thermoresistances are also used, and the value taken into account is determined as the average value of the maximum measured temperatures.

To measure the temperatures of the generator casing, as well as the temperatures on the outer and inner surfaces of the generator pit, *PT* 100 Ω thermoresistances or laser measuring devices are used.

Ambient temperatures, air temperatures in the generator pit, in the machine room, and outside the generator pit are also measured using *PT* 100 Ω thermoresistances.

2.2.3. Devices for Measuring the Cooling Water Flow in Bearings

Ultrasonic flow meters are used to measure the cooling water flow for each of the separate cooler units, which are mounted on pipes. For remote monitoring, it is necessary for each flow meter to be equipped with an analog output in a unified current signal (4–20 mA) or voltage (0–10 V).

In the analyzed situation, the flows of 5 cooler units were monitored. The total flow of cooling water Q_A is determined as the sum of the flows of the "*i*" cooler units:

$$Q_A = \sum Q_{Ai} \tag{2}$$

Ultrasonic flowmeters were installed on the cooling system pipes, following the manufacturer's installation guidelines. These MAGFLOW-type meters have an accuracy of ±0.5%, repeatability of 0.1%, and an auto-calibration function. Systematic errors considered during flow measurement included transducer repeatability ± 0.1%, transducer non-linearity ± 0.25%, and pipe length-induced error ± 0.2%.

2.3. Determination of Efficiency Using the Calorimetric Method

2.3.1. Determination of Losses Transmitted by the Cooling Agent Water

The determination of losses transmitted by the cooling agent water is carried out for three distinct operating modes of the hydrogenerator: no-load unexcited operation, no-load excited operation, and short-circuit operation.

For the determination of losses in no-load unexcited mode, the measured values of the cooling water flow rate and the temperatures of the water at the inlet and outlet of the cooler unit are used. By calculating the temperature difference between the hot water at the outlet and the cold water at the inlet of the cooler unit, the amount of heat released by the hot air from the generator, converted into power losses P_{10}, is determined:

$$P_{10} = \sum \left(Q_{Ai0} \cdot \Delta T_{i0} \cdot \rho_A \cdot C_{pA} \right) \tag{3}$$

where

- Q_{Ai0} is the flow rate of the cooling water through cooler unit *i* (L/min);
- ΔT_{i0} is the temperature difference between hot and cold water *i* (°C);
- ρ_A is the density of the cooling water (997 kg/m^3);
- C_{pA} is the specific heat of water (4176 J/kg·°C).

The density of water ρ_A is selected according to the IEC 34-2A [38] provisions, and the average temperature of the cooling water T_{Am} is calculated using the following formula:

$$T_{Am} = \frac{T_{ACm} + T_{ARm}}{2} \tag{4}$$

where

- T_{ARm}—average temperature of cold water, at the cooler inlet, was calculated for all cooler units (°C);
- T_{ACm}—average temperature of hot water at the cooler outlet, was calculated for all cooler units (°C);
- T_{Am}—average temperature of the cooling water for all cooler units calculated from the average temperatures of cold and hot water (°C).

2.3.2. Determination of Non-Transmitted Losses Through the Cooling Agent

Some of the generator's losses are not transmitted to the cooling agent—in this case, water. The losses that are not transmitted are losses due to radiation and convection P_2 transmitted through the generator shields.

These losses are determined using the following formula:

$$P_2 = \sum(h_i \cdot \Delta T_{i0} \cdot A_i) \quad (5)$$

where

- P_2—losses due to radiation and convection [W];
- h_i—heat transfer coefficient through surface i [W/m^2·°C];
- A_i—surface area i [m^2];
- ΔTi—the temperature difference between surface i and the ambient temperature at 1 m distance [°C].

The value of the coefficient h_i is selected according to the IEC provisions, and in this case, it is 15 W/m^2·°C.

The surfaces for which measurements are required are

- A_1—area of the downstream shield of the generator, with a value of 20.68 m^2;
- A_2—area of the upstream shield of the generator, with a value of 17.33 m^2.

For the upstream shield, temperatures were measured with 4 thermoresistances, and for the downstream shield, 2 thermoresistances were used. These temperature values were determined for each of the modes: no-load unexcited, no-load excited, and short-circuit. For the calculations, temperature values under stabilized conditions were used.

After calculating the heat transfer for each individual surface, the losses are determined by algebraic summation.

2.3.3. Determination of Separate Losses of the Generator

The determination of separate losses of the generator is also based on the three distinct operational modes of the hydrogenerator: no-load unexcited operation, no-load excited operation, and short-circuit operation.

3. Results

The measurements were taken on a bulb-type hydro unit. The hydrogenerator is directly and rigidly coupled to the hydraulic turbine via the rotor, with the entire unit submerged in water.

The nominal data of the generator are

- Nominal apparent power, S_n = 13,330 kVA;
- Nominal voltage, U_n = 6300 V ± 5%;
- Nominal stator current, I_n = 1221.6 A;
- Nominal excitation voltage, U_{En} = 300 V;
- Nominal excitation current, I_{En} = 288 A;
- Speed, n = 107.1 r.p.m.;
- Power factor, $cos\varphi$ = 0.975.

3.1. Measurements for the No-Load Unexcited Operating Mode

For the no-load unexcited operation test of the generator, its rotor will be driven at nominal speed and maintained at this speed throughout the tests. During operation,

temperature values will be monitored until the thermal steady-state condition in the generator is reached.

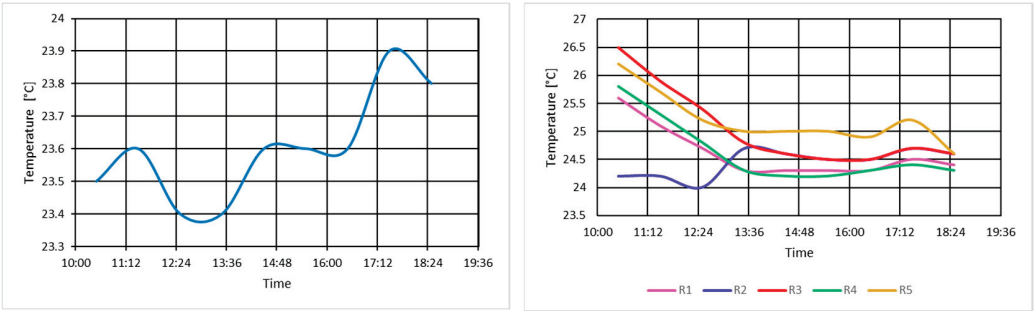
3.1.1. Determination of Mechanical and Ventilation Losses by Measuring Cold and Hot Water Temperatures in No-Load Unexcited Mode

The flow rates of the water that circulated through the five cooling units were as follows: 230 L/min, 200 L/min, 190 L/min, 215 L/min, 200 L/min (Table 1).

Table 1. Values of losses during no-load unexcited operation based on flow rate and water temperatures through each cooling unit.

Cooling Unit Number	Water Flow Rate [L/min]	Water Temperature [°C]			Losses P_{1i0} [kW]
		T_{i0Ac}	T_{i0Ar}	ΔT_{i0}	
1	230	24.4	23.8	0.6	9.576
2	200	24.6	23.8	0.8	11.103
3	190	24.6	23.8	0.8	10.548
4	215	24.3	23.8	0.5	7.460
5	200	24.6	23.8	0.8	11.103
Total losses P_{10} [kW]					49.788

For each cooler unit, the average temperatures of the cold water at the inlet and hot water at the outlet were calculated. The time variation in the temperature of the cold water is presented in Figure 2a, and that of the hot water in Figure 2b. For all cooler units, the value of the cooling water temperature was the same, with measurements being taken every 60 min from 10:30 to 18:30.



(**a**) (**b**)

Figure 2. Variation in the cooling agent temperature during the generator operation in no-load unexcited mode: (**a**) water at the inlet of the cooler unit; (**b**) water at the outlet of the 5 cooler units.

The losses evacuated through the cooling water correspond to mechanical and ventilation losses, and their values corresponding to each cooler unit are presented in Table 1.

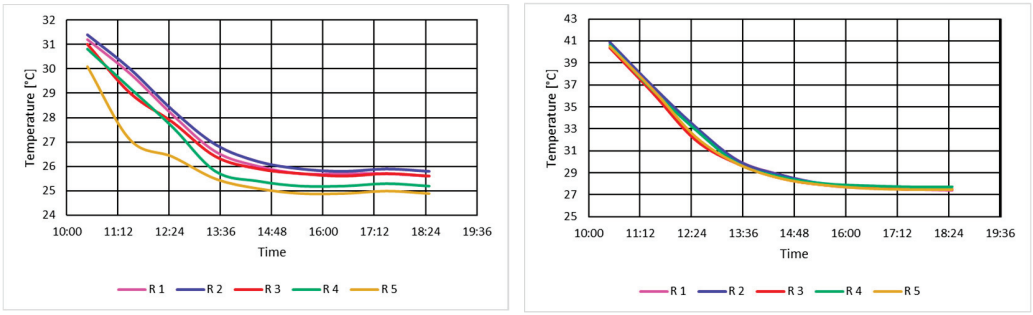
The total value of mechanical losses due to ventilation and friction with air determined in the no-load unexcited operation mode P_{10} is 49.788 kW.

3.1.2. Determination of Air Temperatures Through Cooler Units in No-Load Unexcited Mode

For this measurement, the temperature of the cold air entering the five cooler units and the hot air exiting the same cooler units was recorded. These measurements were taken at the same moments in time and intervals as those used for the cooling water temperature measurements. The variation in the temperatures of cold air T_{Arr} and the air at the outlet of the cooler units (hot air T_{Arc}) is presented in Figure 3a,b.

It is noted that toward the end of the monitoring period, the temperatures through the five cooler units stabilize. With the stabilized values of the temperatures of the cold air

and the hot air, the average temperature for the cold air T_{medArr} = 25.42 °C and the average temperature for the hot air T_{medArc} = 27.52 °C were calculated.



(**a**) (**b**)

Figure 3. Variation in the cooling agent temperature during the generator operation in no-load unexcited mode: (**a**) air at the inlet of the cooler unit; (**b**) air at the outlet of the 5 cooler units.

3.1.3. Determination of Winding Temperatures in No-Load Unexcited Mode

For this measurement, the temperature of the rotor winding and the temperatures of the stator winding were recorded using the temperature monitoring system of the hydrogenerator located in the hydroelectric power plant. The measured temperature values were noted at the same intervals and during the same time periods as those used for measuring the water temperature in the cooler units.

The variation in the temperatures of the stator winding *BS*, measured through thermoresistances, and the rotor winding *BR* is presented in Figure 4. It is observed that the temperature stabilizes at the rotor winding level T_{BR} at a value of 28.1 °C, and at the stator winding level T_{BS} at a value of 27.95 °C, which was obtained as the arithmetic mean of the last measured temperature values from the six thermoresistances.

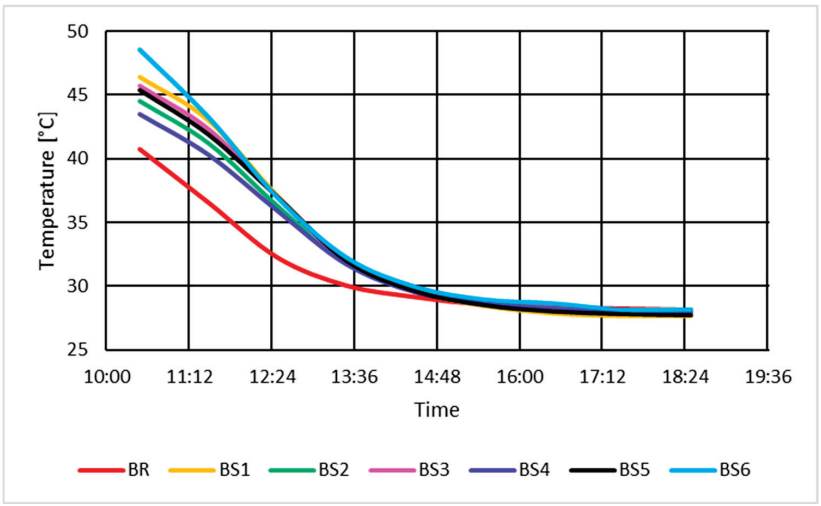


Figure 4. Variation in generator winding temperatures in no-load unexcited condition.

In the no-load unexcited regime, at the beginning of the tests, the temperature measured in the rotor winding was lower than in the stator winding due to the temperature difference between the interior and exterior of the hydro unit and the ventilation caused by rotor movement. By the end of the test period, when stator temperatures stabilized, the rotor winding temperature also decreased and stabilized at a value close to that of the stator.

3.1.4. Determination of Magnetic Core Temperatures in No-Load Unexcited Condition

For this measurement, the temperature of the magnetic core was recorded using the measuring system integrated into the hydro unit. The same measurement period and time interval were maintained.

The variation in the magnetic core temperature T_M is presented in Figure 5.

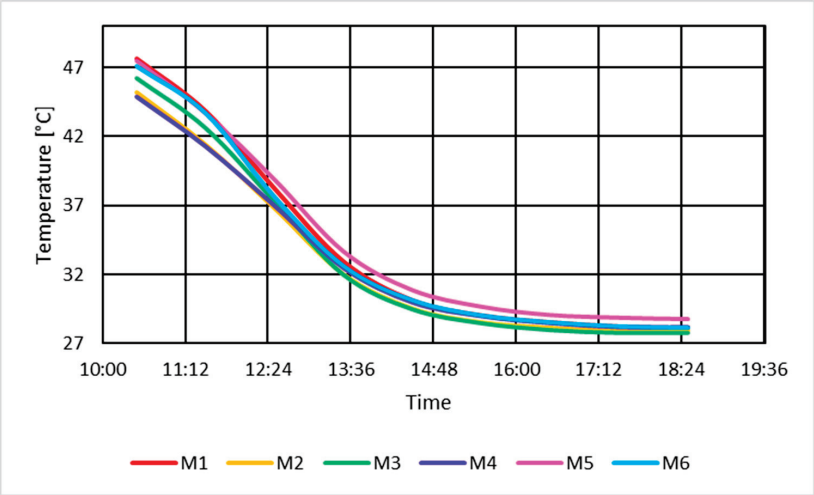
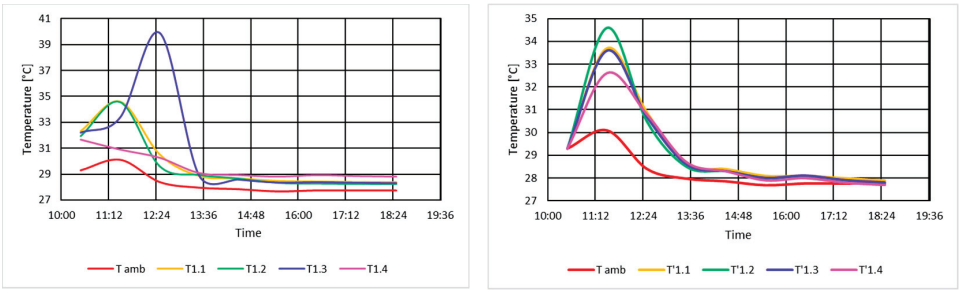


Figure 5. Variation in magnetic core temperatures of the generator in no-load unexcited condition.

The stabilized temperature value at the level of the magnetic core (T_M) was 28.15 °C, obtained as the arithmetic mean of the most recent measured temperature values.

3.1.5. Determination of Measured Temperatures at the Upstream Shield and 1 m from the Shield in No-Load Unexcited Condition

The variation in the ambient temperature and the temperatures measured at the upstream shield and 1 m from this shield is shown in Figure 6a,b.



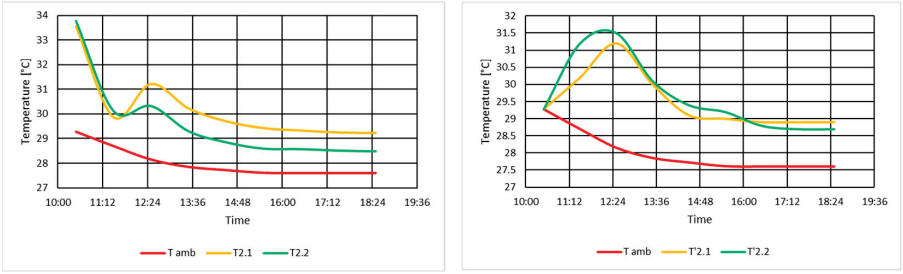
(**a**) (**b**)

Figure 6. Variation in temperatures measured for the upstream shield in no-load unexcited condition: (**a**) at the shield level; (**b**) at a distance of 1 m from the upstream shield.

For this shield, the average temperature T_{1m} at the shield level in the stabilized condition was 28.43 °C, the average temperature at 1 m from the upstream shield T'_{1m} was 27.78 °C, and the stabilized ambient temperature T_{amb} was 27.75 °C.

3.1.6. Determination of Measured Temperatures at the Downstream Shield and 1 m from the Shield in No-Load Unexcited Condition

For the downstream shield, and at a distance of 1 m from it, the variation in the measured temperatures is presented in Figure 7a,b, along with the variation in the ambient temperature.



(**a**) (**b**)

Figure 7. Variation in temperatures measured for the downstream shield in no-load unexcited condition: (**a**) at the shield level; (**b**) at a distance of 1 m from the downstream shield.

For this shield, the average temperature T_{2m} at the shield level in the stabilized condition was 28.86 °C, the average temperature at 1 m from the downstream shield T'_{2m} was 28.8 °C, and the stabilized ambient temperature T_{amb} was 27.6 °C.

For the no-load unexcited operating condition, the losses due to radiation and convection P_{20} through the two shields (upstream and downstream) are determined using the following formula:

$$P_{20} = (h_1 \cdot A_1 \cdot \Delta T_1) + (h_2 \cdot A_2 \cdot \Delta T_2) \quad (6)$$

where ΔT_1 is calculated as the difference between the average temperature T_{1m} at the upstream shield and the average temperature at 1 m from the upstream shield T'_{1m}, and ΔT_2 is calculated as the difference between the average temperature T_{2m} at the downstream shield and the average temperature at 1 m from the downstream shield T'_{2m}.

This results in

$$P_{20} = (15 \times 20.68 \times 0.66) + (15 \times 17.33 \times 0.555) = 349 \text{ [W]} \quad (7)$$

3.2. Measurements Conducted for the No-Load Excited Operating Condition

3.2.1. Determination of Mechanical and Ventilation Losses by Measuring Cold and Hot Water Temperatures in No-Load Excited Condition

To determine stabilized values of temperatures in this condition, the excitation winding of the generator is powered, and its rotor is driven at nominal speed.

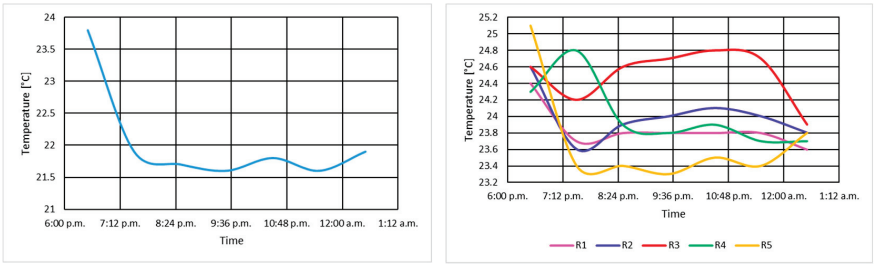
Measurements were recorded at a 60 min interval from 18:30 to 0:30. The water flow rates circulating through the five cooler units were 225 L/min, 200 L/min, 185 L/min, 215 L/min, and 200 L/min (Table 2). At each time interval, the temperature of the cold water at the cooler unit inlet and the hot water at the outlet was measured.

The stabilized temperature values measured in the no-load excited condition are presented in Table 2.

The time variation in the cold water temperature is shown in Figure 8a, and that of the hot water in Figure 8b.

Table 2. Values of losses during operation in no-load excited condition based on flow rate and water temperatures through each cooler unit.

Cooling Unit Number	Water Flow Rate [L/min]	Water Temperature [°C]			Losses P_{1i0e} [kW]
		T_{i0Ace}	T_{i0Are}	ΔT_{i0e}	
1	225	23.6	21.9	1.7	26.542
2	200	23.8	21.9	1.9	26.369
3	185	23.9	21.9	2.0	25.675
4	215	23.7	21.9	1.8	26.854
5	200	23.8	21.9	1.9	26.369
Total losses P_{10e} [kW]					131.809



(**a**) (**b**)

Figure 8. Variation in cooling agent temperature during generator operation in no-load excited condition: (**a**) water at cooler unit inlet; (**b**) water at outlet from the 5 cooler units.

The losses associated with the no-load excited condition P_{10e} are determined by the following formula:

$$P_{10e} = \sum \left(Q_{Ai0e} \cdot \Delta T_{i0e} \cdot \rho_A \cdot C_{pA} \right) \quad (8)$$

where

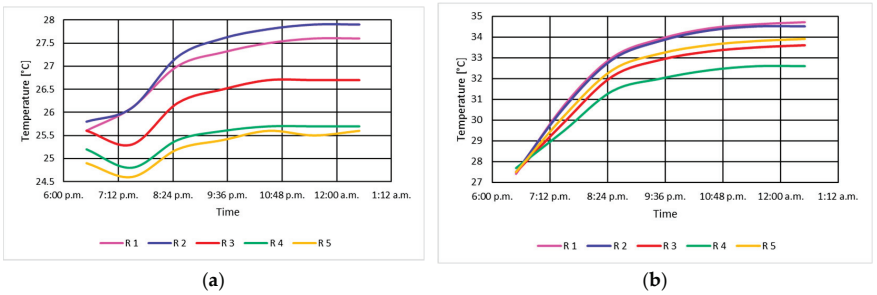
- Q_{Ai0e}—is the cooling water flow rate through cooler unit i (L/min) in the no-load excited condition;
- ΔT_{i0e}—is the temperature difference between hot and cold water for cooler unit i (°C) in the no-load excited condition.

The total value of mechanical losses due to ventilation and friction with air determined in the no-load excited operating condition P_{10e} is 131.809 kW.

3.2.2. Determination of Air Temperatures Through Cooler Units in No-Load Excited Condition

To determine the air temperatures, the same five cooler units were used, where the temperature of the cold air at the cooler unit inlet and the hot air at the outlet was measured in the no-load unexcited condition. Measurements were conducted at the same time intervals as for the cooling agent water. The variation in the cold air temperature T_{Arre} and the air at the outlet from the cooler units (hot air T_{Arre}) for the no-load excited condition is presented in Figure 9a,b.

It is noted that towards the end of the monitoring period, the temperatures through the five cooler units stabilize. The calculated average value of the air temperature at the inlet to the cooler units was $T_{medArre}$ = 26.7 °C, while the average temperature for the hot air was $T_{medArce}$ = 33.86 °C.



(**a**) (**b**)

Figure 9. Variation in the cooling agent temperature during the generator's no-load excitation operation: (**a**) air at the inlet of the cooler unit; (**b**) air at the outlet of the 5 cooler units.

3.2.3. Determination of Winding Temperatures in No-Load Excitation Mode

To determine the air temperatures, the same five cooler units were used, where the temperature of the cold air at the cooler unit inlet and the hot air at the outlet was measured in the no-load unexcited condition.

The temperature of the rotor winding and the temperatures of the stator winding were measured at the same measurement points and with the same instruments.

Figure 10 presents the variation in the stator winding temperatures *BS* and the rotor winding temperatures *BR*.

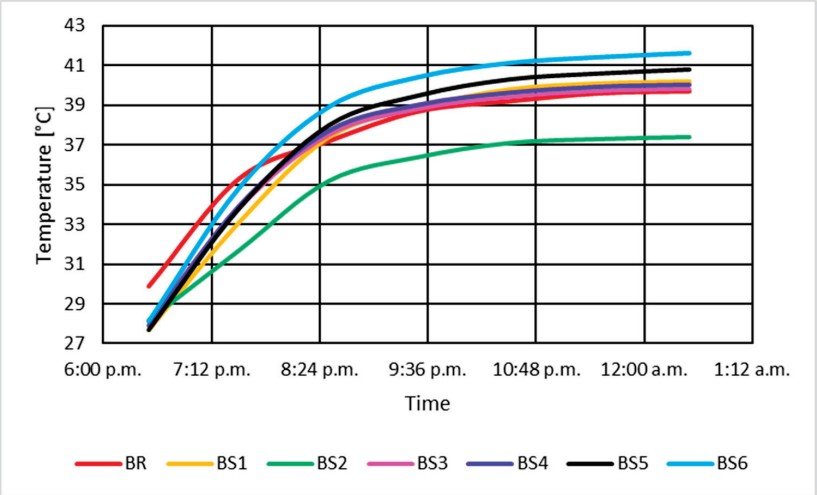


Figure 10. Variation in the generator winding temperatures in no-load excitation mode.

In no-load excitation mode, the stabilized temperature at the rotor winding level T_{BRe} was 39.7 °C, and at the stator winding level T_{BSe} was 39.97 °C—the value obtained as the arithmetic mean of the last measured temperatures on the stator winding.

In the no-load excited regime, the same trend was observed: the rotor winding temperature stabilized at a value similar to the stator winding temperature.

3.2.4. Determination of Magnetic Core Temperatures in No-Load Excitation Mode

The measurement of the magnetic core temperature of the generator in no-load excitation mode was carried out at the same measurement points and with the same instruments as in the case of no-load non-excitation mode. Figure 11 shows the variation in the temperatures measured between 18:30 and 00:30.

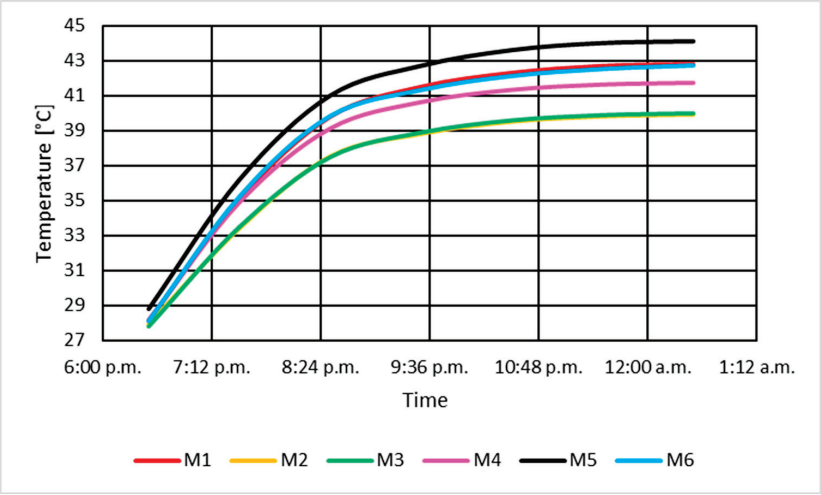
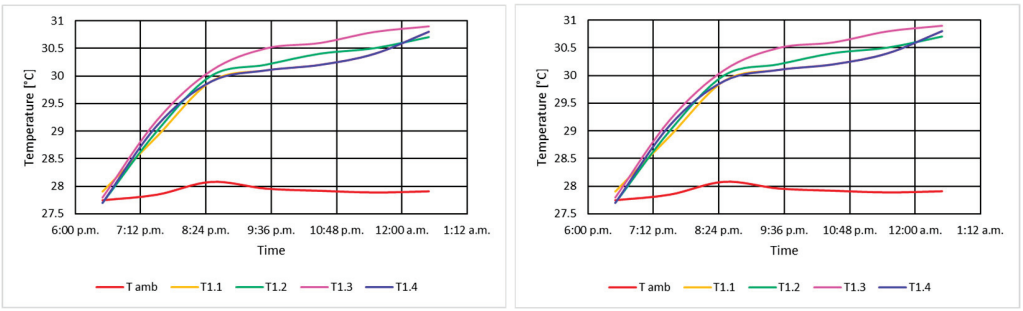


Figure 11. Variation in the magnetic core temperatures of the generator in no-load excitation mode.

The stabilized temperature value at the magnetic core level, in no-load excitation mode, T_{Me} was 41.87 °C, obtained as the arithmetic mean of the last measured temperatures.

3.2.5. Determination of Temperatures Measured at the Upstream Shield and 1 m from the Shield in No-Load Excitation Mode

The variation in the ambient temperature and the temperatures measured at the shield upstream and 1 m from this shield, for the no-load excitation mode, is presented in Figure 12a,b.



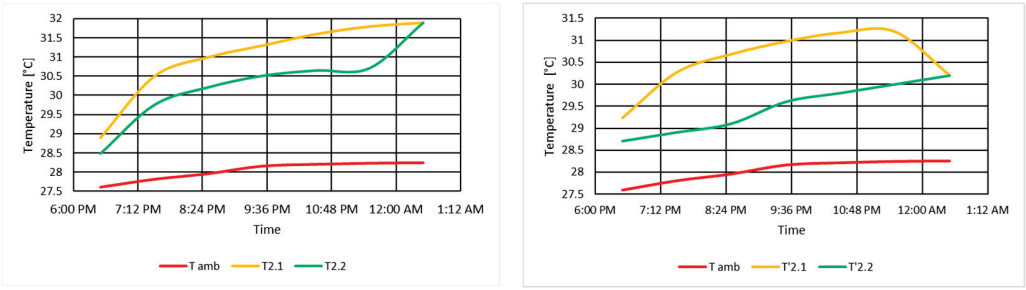
(**a**) (**b**)

Figure 12. Variation pattern of the measured temperatures for the upstream shield, under no-load excitation conditions: (**a**) at the level of the shield; (**b**) at a distance of 1 m from the upstream shield.

The average temperature T_{1me} in a stabilized mode at the shield level was 30.8 °C, while the average temperature 1 m from the upstream shield T'_{1me} was 29.61 °C, and the stabilized ambient temperature T_{amb} was 27.91 °C.

3.2.6. Determination of Temperatures Measured at the Shield Downstream and 1 m from the Shield in No-Load Excitation Mode

For the no-load excitation regime, the variation in the temperatures measured for the downstream shield and at a distance of 1 m from it is presented in Figure 13a,b, along with the variation in the ambient temperature.



(**a**) (**b**)

Figure 13. Variation pattern of the measured temperatures for the downstream shield, under no-load excitation conditions: (**a**) at the level of the shield; (**b**) at a distance of 1 m from the downstream shield.

For the no-load excitation regime, the average temperature T_{2me} at the shield level in stabilized mode was 31.9 °C, the average temperature 1 m from the downstream shield T'_{2me} was 30.2 °C, and the stabilized ambient temperature T_{amb} was 28.25 °C.

For the no-load excitation operating mode, the losses through radiation and convection P_{20e} through the two shields (upstream and downstream) are determined using the following Formula (6). Thus,

$$P_{20e} = (15 \times 20.68 \times 1.2) + (15 \times 17.33 \times 0.555) = 814.155 \text{ [W]} \quad (9)$$

3.3. Measurements Performed for the Short-Circuit Operating Mode

3.3.1. Determination of Mechanical and Ventilation Losses by Measuring the Temperatures of Cold and Hot Water in Short-Circuit Mode

For this regime, a symmetric three-phase short-circuit was made at the terminals of the stator winding of the generator, and the rotor was driven at nominal speed. Subsequently, the excitation winding was powered, adjusting the excitation current until the currents in the stator winding reached nominal values.

The same interval of 60 min was maintained between two successive measurements, with the measurement period being from 00:30 to 04:30. At each time interval, the value of the cold water temperature at the inlet of the cooler unit and the hot water temperature at the outlet was measured for each cooler unit. The variation over time of the hot water temperature is presented in Figure 14, with the cold water temperature being constant at 24.3 °C.

The losses associated with the short-circuit mode are determined by the following formula:

$$P_{1sc} = \sum (Q_{Aisc} \cdot \Delta T_{isc} \cdot \rho_A \cdot C_{pA}) \quad (10)$$

where

- Q_{Aisc} is the flow rate of cooling water through cooler unit i (L/min) in short-circuit mode;
- ΔT_{isc} is the temperature difference between hot and cold water for cooler unit i (°C) in short-circuit mode.

The stabilized temperature values measured during short-circuit operation are presented in Table 3, along with the flow rate values of water circulating through the five cooler units.

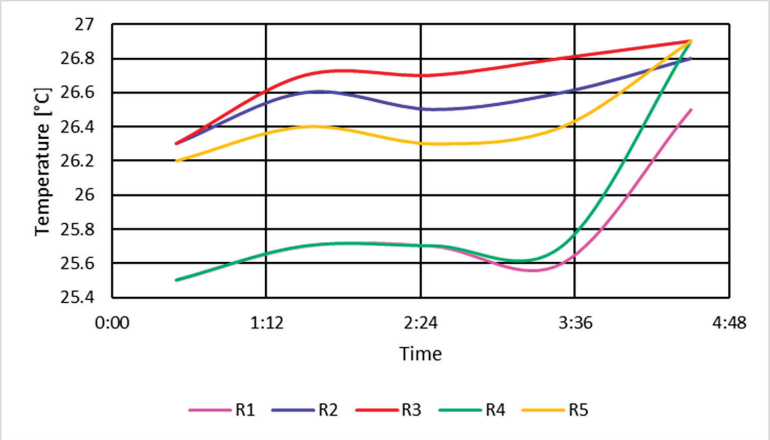


Figure 14. Variation in the water temperature at the outlet of the cooler units during generator operation in short-circuit.

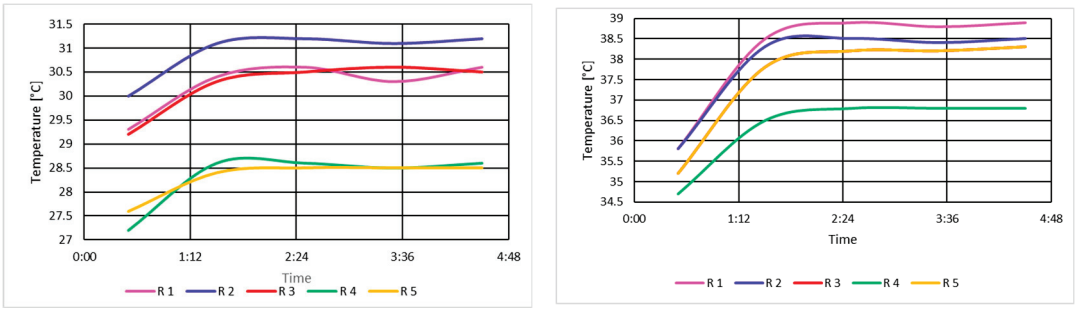
Table 3. Values of losses during short-circuit operation based on flow rates and water temperatures through each cooler unit.

Cooler Unit Number	Water Flow Rate [L/min]	Water Temperature [°C]			Losses P_{1isc} [kW]
		T_{iAcsc}	T_{iArsc}	ΔT_{isc}	
1	230	26.5	24.3	2.2	35.112
2	200	26.8	24.3	2.5	34.696
3	190	26.9	24.3	2.6	34.279
4	215	26.9	24.3	2.6	38.790
5	210	26.9	24.3	2.6	37.888
Total losses P_{1sc} [kW]					180.764

The total value of mechanical losses through ventilation and air friction determined in short-circuit mode P_{1sc} is 180.753 kW.

3.3.2. Determination of Air Temperatures Through Cooler Units in Short-Circuit Mode

For this regime, the air temperature values at the inlet and outlet of the five cooler units were also determined. The measurements were made at the same time intervals and at the same moments as in the case of measuring the cooling agent water. The variation in the cold air temperature T_{Arrsc} and the air at the outlet of the coolers (hot air T_{Arcsc}) for the short-circuit regime is presented in Figure 15a,b.



(**a**) (**b**)

Figure 15. Variation pattern of the cooling agent's temperature during generator operation in short-circuit conditions: (**a**) air at the entrance of the cooler units; (**b**) air at the exit of the cooler units.

For the short-circuit regime, the calculated average value of the air temperature at the inlet of the cooler units was $T_{medArrsc}$ = 29.88 °C, while the average temperature for the hot air was $T_{medArcsc}$ = 38.16 °C.

3.3.3. Determination of Winding Temperatures in Short-Circuit Mode

Similar to the other tests, the temperature of the rotor winding and the temperatures of the stator winding were measured at the same measurement points and with the same instruments. The variation in these temperatures is presented in Figure 16.

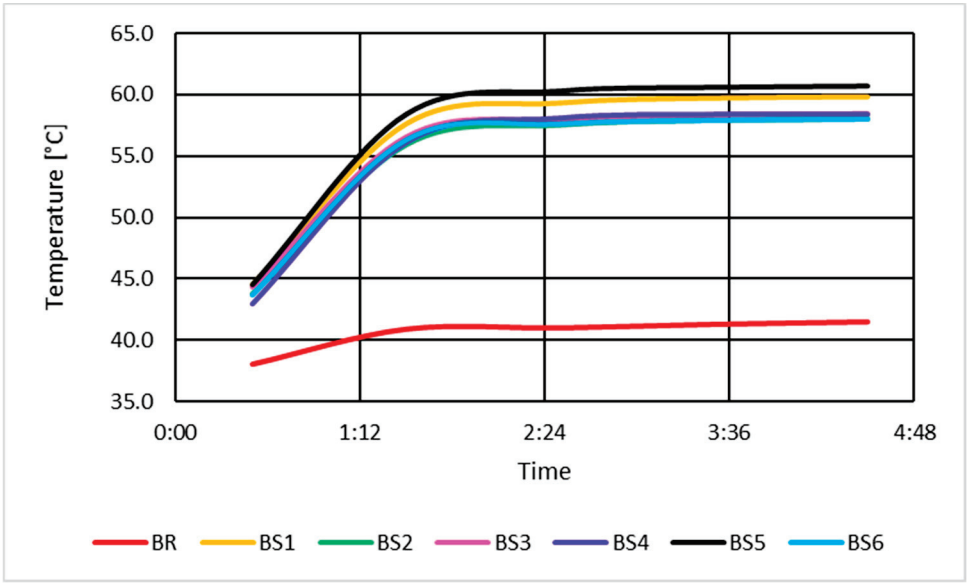


Figure 16. Variation in the generator winding temperatures in short-circuit mode.

For this regime, the stabilized temperature at the rotor winding level T_{BRsc} was 41.5 °C, while at the stator winding level T_{BSsc} it was 58.97 °C, a value obtained as the arithmetic mean of the last measured temperatures on the stator winding.

In the short-circuit regime, the stabilized rotor winding temperature was lower than the stator winding temperature due to the lower current in the rotor winding compared to the stator winding.

3.3.4. Determination of Magnetic Core Temperatures in Short-Circuit Mode

For this regime, the values of the magnetic core temperature of the generator were measured at the same measurement points and with the same instruments as in the case of no-load excitation mode. The variation in the magnetic core temperatures is presented in Figure 17.

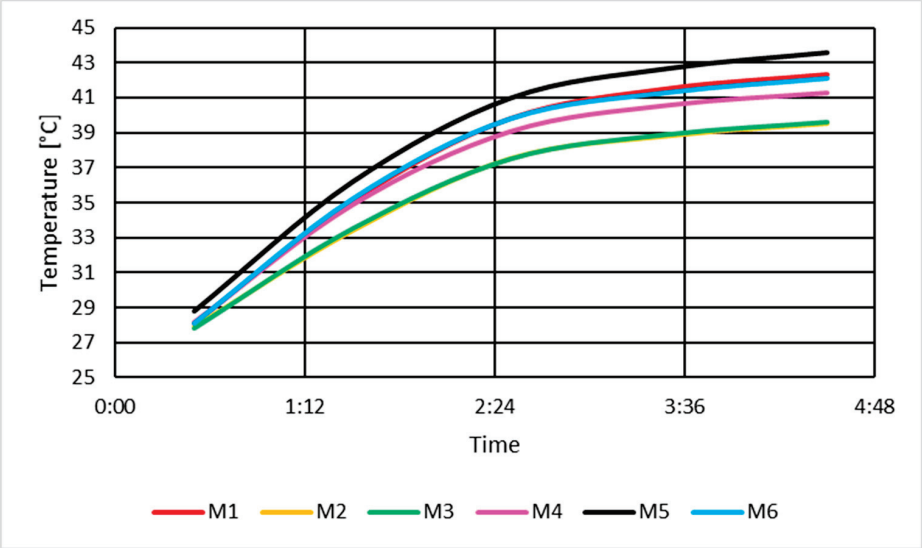
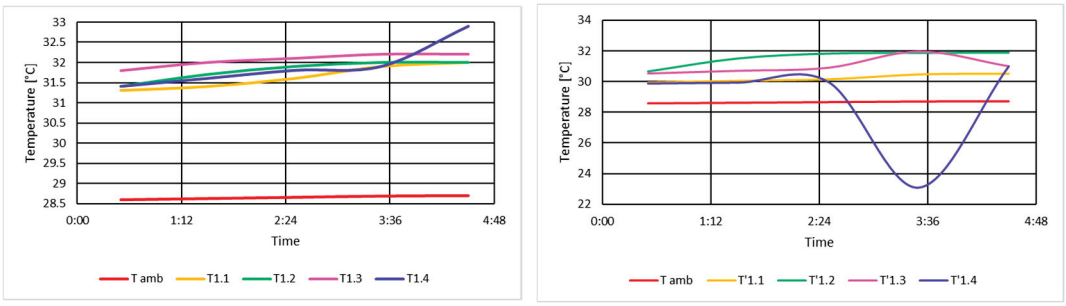


Figure 17. Variation module of the magnetic core temperatures of the generator under short-circuit conditions.

The stabilized temperature value at the magnetic core level T_{Msc} was 41.4 °C, obtained as the arithmetic mean of the last measured temperature values.

3.3.5. Determination of Measured Temperatures at the Upstream Shield and 1 m from the Shield Under Short-Circuit Conditions

For operation under short-circuit conditions, Figure 18a,b show the variation in ambient temperature, as well as the temperatures measured at the upstream shield and 1 m from this shield.



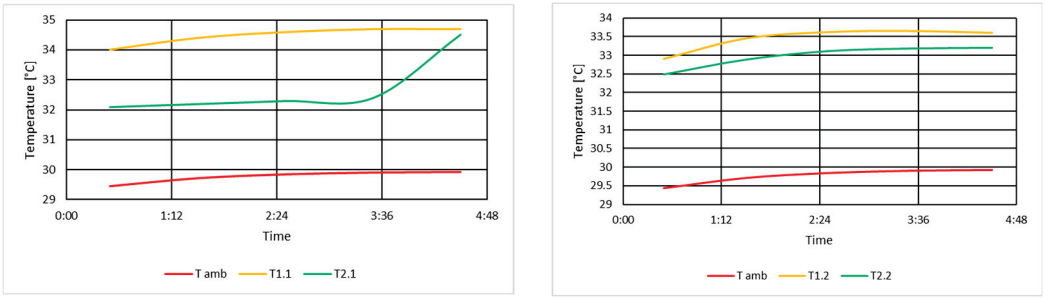
(**a**) (**b**)

Figure 18. Variation in measured temperatures for the upstream shield under short-circuit conditions: (**a**) at the shield level; (**b**) at a distance of 1 m from the upstream shield.

For this shield, the average temperature T_{1msc} at the shield level, under stabilized conditions, was 32.28 °C, the average temperature at 1 m from the upstream shield T'_{1msc} was 31.1 °C and the stabilized ambient temperature T_{amb} was 28.7 °C.

3.3.6. Determination of Measured Temperatures at the Downstream Shield and 1 m from the Shield Under Short-Circuit Conditions

For the downstream shield, as well as at a distance of 1 m from it, the variation in measured temperatures is presented in Figure 19a,b, alongside the variation in the ambient temperature.



(**a**) (**b**)

Figure 19. Variation in measured temperatures for the downstream shield under short-circuit conditions: (**a**) at the shield level; (**b**) at a distance of 1 m from the downstream shield.

For this regime, the average temperature T_{2msc} at the shield level, under stabilized conditions, was 34.6 °C, while the average temperature at 1 m from the downstream shield T'_{2msc} was 33.4 °C.

For the short-circuit operation regime, losses due to radiation and convection P_{2sc} through the two shields (upstream and downstream) are determined using the following Formula (6). This results in

$$P_{2sc} = (15 \times 20.68 \times 1.2) + (15 \times 17.33 \times 1.2) = 684.18 \text{ [W]} \quad (11)$$

3.4. Determination of the Separate Losses of the Generator

3.4.1. Determination of Losses During the Generator's Operation in No-Load Unexcited Mode

According to standard IEC 34-2A [38], after reaching a stabilized thermal regime in the generator, the following are determined:

- The amount of heat that the cooling water absorbs during passage through the cooler units, quantified as power losses P_{10};
- The amount of heat transmitted through radiation and convection, quantified as P_{20} losses.

Thus, for the unloaded unexcited operation regime, ventilation losses P_v were determined using the following formula:

$$P_v = P_{10} + P_{20} = 49.788 + 0.349 = 50.137 \text{ [kW]} \quad (12)$$

where P_{10} represents the mechanical losses through ventilation and air friction determined during the no-load unexcited operation of the generator, while P_{20} represents the losses through radiation and convection through the two shields (upstream and downstream) determined for the same regime.

3.4.2. Determination of Losses During the Generator's Operation in No-Load Excited Mode

For this operating regime of the generator, iron losses are determined. The test is performed at the nominal speed and at the nominal voltage of the generator.

After reaching the stabilized thermal regime in the generator IEC 34-2A, the following quantities are determined:

- The amount of heat that the cooling water absorbs during passage through the cooler units, transformed into P_{10e} power losses;
- Losses through radiation and convection, quantified as P_{20e} losses;
- The voltage at the stator terminals of the generator;
- The excitation voltage at the rotor terminals of the generator;
- The excitation current of the generator.

For the operation in no-load excited mode, the iron losses P_{Fe} were determined using the following formula:

$$P_{Fe} = P_{10e} + P_{20e} - P_v - I_{E0}^2 \cdot R_{E0e-40} \quad (13)$$

where

- P_{10e} represents the mechanical losses through ventilation and air friction determined during the no-load excited operation of the generator;
- P_{20e} represents the losses through radiation and convection through the two shields determined for the same regime;
- I_{E0} is the excitation current in no-load operation of the generator, which had a value of 186 A;
- $R_{E0e\text{-}20}$ is the resistance of the excitation winding at 20 °C, which in the analyzed case was 0.6941 Ω;
- $R_{E0e\text{-}40}$ is the resistance of the excitation winding at 40 °C during no-load operation of the generator, which in the analyzed case was 0.7485 Ω.

The value of iron losses P_{Fe} that resulted was:

$$P_{Fe} = 131.809 + 0.814 - 50.137 - 34.596 \times 0.7485 = 56.591 \text{ [kW]} \quad (14)$$

3.4.3. Determination of Losses During the Generator's Operation in Short-Circuit Mode

In short-circuit mode, the losses in copper at the temperature of the winding corresponding to the regime, together with additional losses from the generator, are determined.

The test was performed for the operation of the generator at nominal speed maintained by the speed regulator and at the nominal current in the generator's stator.

After reaching the stabilized thermal regime in the generator as per IEC 34-2A [38], the following quantities were determined:

- The amount of heat that the cooling water absorbs during passage through the cooler units, transformed into P_{1sc} power losses;
- The amount of heat transmitted through radiation and convection, quantified in P_{2sc};
- The voltages at the rotor terminals of the generator;
- The current in the generator's stator;
- The excitation current of the generator;
- The temperatures of the stator winding of the generator;
- The resistance of the generator's excitation winding at the temperature corresponding to the short-circuit regime;

- The resistance of the stator winding in the R_{1sc} phase corresponding to the short-circuit regime.

From the measurements performed on the generator in symmetric three-phase short-circuit, corresponding to the nominal current, the following results were obtained:

- The excitation current in short-circuit mode, at nominal current, I_{Esc} = 198 A;
- The current through the stator winding in short-circuit mode, at nominal current, I_{1sc} = 1221 A;
- The resistance of the excitation winding at 20 °C, $R_{Esc\text{-}20}$ = 0.6941 Ω;
- The resistance of the excitation winding at 42 °C, $R_{Esc\text{-}42}$ = 0.7539 Ω;
- The resistance of the excitation winding at 75 °C, $R_{Esc\text{-}75}$ = 0.8438 Ω;
- The resistance of the stator winding at 20 °C, $R_{1sc\text{-}20}$ = 0.01662 Ω;
- The resistance of the stator winding at 59 °C, $R_{1sc\text{-}59}$ = 0.0192 Ω.

The copper losses in the stator winding P_{Cu1} are determined using the following formula:

$$P_{Cu1} = m \cdot I_1^2 \cdot R_{1sc-59} = 3 \times 1492.307 \times 0.0192 = 85.957 \text{ [kW]} \quad (15)$$

where m is the number of phases of the generator.

The copper losses in the rotor winding P_{Cu2} are determined using the following formula:

$$P_{Cu2} = I_E^2 \cdot R_{Esc-42} = 39.204 \times 0.7539 = 29.556 \text{ [kW]} \quad (16)$$

For the operation regime in short-circuit mode, the additional losses P_{suplim} were determined using the following formula:

$$P_{\text{suplim}} = P_{1sc} + P_{2sc} - P_v - 3 \cdot I_{1sc}^2 \cdot R_{1sc-59} - I_{Esc}^2 \cdot \text{R}_{Esc-42} \quad (17)$$

The value of the additional losses P_{suplim} that resulted was

$$P_{\text{suplim}} = 181.764 + 0.684 - 50.137 - 3 \times 1490.841 \times 0.0192 - 39.204 \times 0.7539 \quad (18)$$

$$P_{\text{suplim}} = 16.883 \text{ [kW]} \quad (19)$$

The calculated value of mechanical losses P_m was 73.26 kW. The value of the total losses $\sum P$ is determined as the sum of all losses, using the following formula:

$$\sum P = P_m + P_{Fe} + P_{\text{Cu}1} + P_{\text{Cu}2} + P_{\text{suplim}} = 73.26 + 56.591 + 85.957 + 69.988 + 19.883 \quad (20)$$

$$\sum P = 302.679 \text{ [kW]} \quad (21)$$

3.5. Determination of the Generator's Efficiency

The determination of the generator's efficiency is based on the measured and calculated losses under conditions for different values of nominal power $0.25 \cdot P_n$, $0.5 \cdot P_n$, $0.75 \cdot P_n$, P_n, and $1.1 \cdot P_n$, depending on the value of the power factor.

The efficiency value η was determined using the following formula:

$$\eta[\%] = \frac{S_n \cdot \cos\varphi}{S_n \cdot \cos\varphi + \sum P} \cdot 100 = 97.724\% \text{ [kW]} \quad (22)$$

The values of the quantities used to determine the efficiency are presented in Table 4 for the nominal power factor.

Table 4. Values of the generator's quantities at $cos\varphi$ = 0.975.

Quantity	U.M.	$0.25 \cdot P_n$	$0.5 \cdot P_n$	$0.75 \cdot P_n$	P_n	$1.1 \cdot P_n$
Apparent power	kVA	3332.5	6665	9997.5	13,330	14663
Active power	kW	3249.19	6498.38	9747.56	12,996.75	14,296.43
Stator voltage	V	6300	6300	6300	6300	6300
Stator current	A	305.4	610.8	916.2	1221.6	1343.76
Excitation current	A	224	243	274	288	315
Mechanical losses	kW	73.26	73.26	73.26	73.26	73.26
Iron losses	kW	56.591	56.591	56.591	56.591	56.591
Stator copper losses	kW	5.372	21.489	48.351	85.957	104.008
Rotor copper losses	kW	42.339	49.826	63.349	69.988	99.225
Additional losses	KW	1.055	4.220	9.496	16.883	20.427
Total losses	kW	178.617	205.386	251.047	302.679	353.511
Efficiency	%	94.789	96.936	97.489	97.724	97.586

4. Discussion

Determining the efficiency of a high-power hydrogenerator using the calorimetric method proved to be a feasible and reliable approach in the context of the impossibility of testing under load. The method is compatible with international standards (IEC 34-2, 34-2A, 34-4) and allows a comprehensive evaluation of energy losses through temperature, flow, and electrical parameter measurements, under real operating conditions. The results obtained are comparable to those mentioned in the literature, confirming that mechanical, ventilation, and iron losses represent a significant proportion of total losses, especially in no-load regimes. In short-circuit mode, the increase in temperature in the stator windings highlights the need for effective cooling solutions and constant monitoring.

As a method based on standardized provisions for determining efficiency via calorimetry, its novelty lies in applying it to a bulb-type hydro unit where cooling is primarily achieved using water as the cooling agent. In conventional hydrogenerators, air plays a significant role in cooling and loss reduction.

Table 5 presents the loss values and efficiency guaranteed by the manufacturer of the refurbished hydro unit, as listed in the technical manual provided upon delivery, alongside the values obtained from the conducted analysis.

Table 5. Manufacturer-guaranteed values vs. values obtained through research.

Quantity	U.M.	Values	
		Guaranteed	Evaluated
Mechanical losses	kW	65	73.26
Iron losses	kW	65.25	56.591
Stator copper losses	kW	98.89	85.957
Rotor copper losses	kW	81.49	69.988
Additional losses	KW	11.303	16.833
Total losses	kW	321.946	302.676
Efficiency	%	97.58	97.724

It was found that the efficiency value determined via the calorimetric method and measured in situ is very close to the guaranteed value of the refurbished hydrogenerator, with a slight increase observed. This increase is attributed to reduced losses in the generator windings and magnetic core.

Compared to previous studies, where indirect or estimative methods dominate, this research offers a direct alternative, applicable without risks to operating equipment. Additionally, integrating an Intelligent Energy Control System (*IECS*) could contribute to

maintaining high efficiency under variable load and flow conditions, supporting the transition to a more flexible and sustainable energy system.

Depending on the complexity of the intelligent energy control system, it can continuously acquire signals related to temperature, flow rate, current, and voltage values, thereby reducing the time needed to install measurement equipment for determining hydrogenerator efficiency. The downside of this system is the need for periodic verification, calibration, and standardization, which incurs additional costs. Merely acquiring and processing signals from the *IECS* does not allow for efficiency determination but only for continuous monitoring of operational status to prevent failures and improper functioning.

Future research directions may include applying the method in power plants of different capacities, testing under diverse climatic conditions, or incorporating it into predictive maintenance models based on data.

5. Conclusions

The study demonstrated that the calorimetric method is a viable solution for determining the efficiency of a high-power hydrogenerator when load testing is not possible.

The novelty lies in applying the efficiency determination method to a unique bulb-type hydro unit with a closed-circuit ventilation system, where permanent access to the capsule is possible via a vertical shaft from the upstream head. Additionally, for this type of hydro unit, cooling is achieved using water as the cooling agent, unlike most hydrogenerators that use air.

By applying this method in three distinct regimes (no-load unexcited, no-load excited, and short-circuit), the main thermal losses in the system were identified, highlighting critical energy zones. The increased temperature value in the rotor and stator windings indicates the accumulation of losses in the active electromagnetic areas, suggesting the need for more effective cooling systems. The results obtained can serve as a basis for repair, modernization, or optimization interventions in operational regimes.

Furthermore, the paper shows that evaluating efficiency during the operational phase is essential for increasing energy efficiency and ensuring safe and sustainable operation. Implementing an intelligent monitoring system could complement the calorimetric method and contribute to maintaining optimal efficiency over time. Therefore, the proposed methodology is not only useful but also necessary in the current context of sustainable development in the hydroenergy sector.

Author Contributions: Conceptualization, G.L. and E.S.; methodology, G.L.; validation, E.S., D.A. and C.P.C.; formal analysis, C.P.C.; investigation, G.L. and D.A.; resources, E.S. and C.P.C.; data curation, M.M.; writing—original draft preparation, E.S.; writing—review and editing, E.S. and C.P.C.; visualization, D.A., M.M. and C.P.C.; supervision, E.S. and G.L.; project administration, E.S., C.P.C. and M.M.; funding acquisition, E.S., C.P.C. and M.M. All authors have read and agreed to the published version of the manuscript.

Funding: The publication of this article was supported by the 2024 Development Fund of the UBB.

Data Availability Statement: The data presented in this study are available on request from the first author.

Conflicts of Interest: The authors declare no conflicts of interest. The funders had no role in the design of the study; in the collection, analyses, or interpretation of data; in the writing of the manuscript; or in the decision to publish the results.

Abbreviations

The following abbreviations are used in this manuscript:

IEC	International Electrotechnical Commission
IEA	International Energy Agency
IECS	Intelligent Energy Control System
η_G	Efficiency of the generator
P	Active power
Σp	Losses from the generator
PT	Sensor made of platinum
Q_A	Total flow of cooling water
Q_{Ai0}	Flow rate of the cooling water through cooler unit
ΔT_{i0}	Temperature difference between hot and cold water
ρ_A	Density of the cooling water
C_{pA}	Specific heat of water
T_{ARm}	Average temperature of cold water, at the cooler inlet, calculated for all cooler units
T_{ACm}	Average temperature of hot water at the cooler outlet, calculated for all cooler units
T_{Am}	Average temperature of the cooling water for all cooler units
P_2	Losses due to radiation and convection transmitted through the generator shields
h_i	Heat transfer coefficient through surface
A_i	Surface area i
ΔTi	Temperature difference between surface i and the ambient temperature at 1 m distance
A_1	Area of the downstream shield of the generator
A_2	Area of the upstream shield of the generator
S_n	Nominal apparent power
U_n	Nominal voltage
I_n	Nominal stator current
U_{En}	Nominal excitation voltage
I_{En}	Nominal excitation current
m	Number of phases of the generator
n	Speed
$cos\varphi$	Power factor
P_{10}	Total value of mechanical losses due to ventilation and friction with air determined in the no-load unexcited operation mode
T_{Arr}	Temperatures of cold air
T_{Arc}	Temperatures of hot air at the outlet of the cooler units
BS	Stator winding
BR	Rotor winding
T_{BR}	Temperatures of rotor winding in no-load unexcited stabilized condition
T_{BS}	Temperatures of stator winding in no-load unexcited stabilized condition
T_M	Temperatures of magnetic core in no-load unexcited stabilized condition
T_{1m}	Average temperature at the upstream shield in no-load unexcited stabilized condition
T'_{1m}	Average temperature at 1 m from the upstream shield in no-load unexcited stabilized condition
T_{amb}	Stabilized ambient temperature
T_{2m}	Average temperature at the downstream shield in no-load unexcited stabilized condition
T'_{2m}	Average temperature at 1 m from the downstream shield in no-load unexcited stabilized condition
P_{20}	Losses due to radiation and convection through the two shields (upstream and downstream)
P_{10e}	Total value of mechanical losses due to ventilation and friction with air determined in the no-load excited condition
Q_{Ai0e}	Cooling water flow rate through cooler unit i, in no-load excited condition

ΔT_{i0e}	Temperature difference between hot and cold water for cooler unit i, in no-load excited condition
T_{Arre}	Temperatures of cold air in no-load excited condition
T_{Arce}	Temperatures of hot air at the outlet of the cooler units in no-load excited condition
T_{BRe}	Temperatures of rotor winding in no-load excited condition
T_{BSe}	Temperatures of stator winding in no-load excited condition
T_{M3}	Temperatures of magnetic core in no-load unexcited stabilized condition
T_{1me}	Average temperature at the upstream shield in no-load excited stabilized condition
T'_{1me}	Average temperature at 1 m from the upstream shield in no-load excited stabilized condition
T_{2me}	Average temperature at the downstream shield in no-load excited stabilized condition
T'_{2me}	Average temperature at 1 m from the downstream shield in no-load excited stabilized condition
P_{20e}	Losses due to radiation and convection through the two shields (upstream and downstream) in no-load excited condition
Q_{Aisc}	Flow rate of cooling water through cooler unit i in short-circuit mode
ΔT_{isc}	Temperature difference between hot and cold water for cooler unit i in short-circuit mode.
P_{1sc}	Total value of mechanical losses through ventilation and air friction determined in short-circuit mode
T_{Arrsc}	Temperatures of cold air in short-circuit condition
T_{Arcsc}	Temperatures of hot air at the outlet of the cooler units in short-circuit condition
T_{BRsc}	Temperatures of rotor winding in short-circuit condition
T_{BSsc}	Temperatures of stator winding in short-circuit condition
T_{Msc}	Temperatures of magnetic core in short-circuit stabilized condition
T_{1msc}	Average temperature at the upstream shield in short-circuit stabilized condition
T'_{1msc}	Average temperature at 1 m from the upstream shield in short-circuit stabilized condition
T_{2msc}	Average temperature at the downstream shield in short-circuit stabilized condition
T'_{2msc}	Average temperature at 1 m from the downstream shield in short-circuit stabilized condition
P_{2sc}	Losses due to radiation and convection through the two shields (upstream and downstream) in short-circuit condition
P_v	Ventilation losses
P_{Fe}	Iron losses
I_{Esc}	Excitation current in short-circuit mode
I_{1sc}	Current through the stator winding in short-circuit mode
$R_{Esc\text{-}20}$	Resistance of the excitation winding at 20 °C
$R_{1sc\text{-}20}$	Resistance of the stator winding at 20 °C
P_{Cu1}	Copper losses in the stator winding
P_{suplim}	Additional losses
P_m	Mechanical losses
$\sum P$	Total losses
η	Efficiency
H_{am}	Upstream water level
H_{av}	Downstream level

References

1. Yahya, A.K.; Munim, W.N.W.A.; Othman, Z. Pico-hydro power generation using dual pelton turbines and single generator. In Proceedings of the 8th IEEE International Power Engineering and Optimization Conference (PEOCO), Shah Alam, Malaysia, 24–25 March 2014.
2. Reducing Global Energy Consumption. Available online: https://www.agg-net.com/resources/articles/ancillary-equipment/reducing-global-energy-consumption (accessed on 12 July 2022).
3. Renewable Energy. Available online: https://ourworldindata.org/renewable-energy (accessed on 12 July 2022).
4. REPowerEU: Affordable, Secure and Sustainable Energy for Europe. Available online: https://ec.europa.eu/info/strategy/priorities-2019-2024/european-green-deal/repowereu-affordable-secure-and-sustainable-energy-europe_en (accessed on 12 July 2022).
5. Pistelok, P.; Baranski, M. Highly efficient synchronous generators with permanent magnets intended to small hydropower station. In Proceedings of the 5th International Conference on Clean Electrical Power (ICCEP), Taormina, Italy, 16–18 June 2015.
6. Rozowicz, S.; Goryca, Z.; Peczkis, G.; Korczak, A. Pico hydro generator as an effective source of renewable energy. *Prz. Elektrotechniczny* **2019**, *95*, 200–204.
7. Tanutwutthigorn, K.; Suntivarakorn, R. Efficiency improvement and economic analysis of micro hydro power plant by using twin vertical hydro turbine. In Proceedings of the 9th International Conference on Future Environment and Energy (ICFEE), Osaka, Japan, 9–11 January 2019.
8. Pomoja, F.; Manescu, T.S.; Hopota, A. Improving efficiency of an micro-hydro aggregate using a banky 10 kw micro-turbine, by blade design optimization. In Proceedings of the 7th International Symposium on Machine and Industrial Design in Mechanical Engineering (KOD 2012), Balatonfured, Hungary, 24–26 May 2012.
9. Rubes, O.; Cervinka, D. Efficiency optimization of small hydro power plant in low power operation. In Proceedings of the IEEE International Conference on Environment and Electrical Engineering and 2017 IEEE Industrial and Commercial Power Systems Europe (EEEIC/I&CPS Europe), Milan, Italy, 6–9 June 2017.
10. Rubes, O.; Cervinka, D. Increasing the Efficiency of Induction Generator in Small Hydro Power Plant for Varying River Flow Rate. In Proceedings of the 12th International Conference on Mechatronics, Brno, Czech Republic, 6–8 September 2017.
11. Rubes, O.; Knobloch, J.; Cervinka, D. Techniques to Increase the Efficiency of Small Hydro Power Plants with Induction Machine. In Proceedings of the IEEE International Conference on Environment and Electrical Engineering (EEEIC)/IEEE Industrial and Commercial Power Systems Europe (ICPS Europe), Palermo, Italy, 12–15 June 2018.
12. *IEEE Standard 115-2009*; IEEE Guide Test Procedures for Synchronous Machines, Acceptance and Performance Testing and Parameter Determination for Dynamic Analysis. IEEE: New York, NY, USA, 2010.
13. *IEC 60034-2-2*; Rotating Electrical Machines. Part 2-2: Specific Methods for Determining Separate Losses of Large Machines from Tests. IEC: Geneva, Switzerland, 2020.
14. Li, W.L.; Liang, D.W.; Zhang, Y. Calculation of Iron Loss in Large Hydro-Generator under Non-Load. In Proceedings of the International Conference on Materials Science and Information Technology (MSIT 2011), Singapore, 16–18 September 2011.
15. Merkhouf, A.; Guillot, E.; Hudon, C.; Desnoyers, M.; Aguiar, A.B.M.; Al-Haddad, K. Electromagnetic Loss Computation in Large Hydro Electrical Generator Using Different Existing Models. In Proceedings of the 20th International Conference on Electrical Machines (ICEM), Marseille, France, 2–5 September 2012.
16. Aguiar, A.B.M.; Merkhouf, A.; Al-Haddad, K. Influence of the Air Gap Length on the Magnetic Core Loss in Large Hydro Generator. In Proceedings of the 20th International Conference on Electrical Machines (ICEM), Marseille, France, 2–5 September 2012.
17. Ćalasan, M.; Ostojić, M.; Petrović, D. The retardation method for bearings loss determination. In Proceedings of the International Symposium on Power Electronics Power Electronics, Electrical Drives, Automation and Motion, Sorrento, Italy, 20–22 June 2012.
18. Rehfeldt, A.; Fricke, T.; Schwarz, B.; Bresemann, E.; Ponick, B. Measurement of Sub-Conductor Circulating Currents in Roebel Bars of a Hydro Generator. In Proceedings of the 13th International Conference on Electrical Machines (ICEM), Alexandroupoli, Greece, 3–6 September 2018.
19. Traxler-Samek, G.; Langmayr, D. Three-dimensional temperature distribution in large hydro-generators: Efficient simulation and optimization. *Elektrotechnik Informationstechnik* **2019**, *136*, 216–223. [CrossRef]
20. Bortoni, E.C.; Siniscalchi, R.T.; Jardini, J.A. Hydro Generator Efficiency Assessment using Infrared Thermal Imaging Techniques. In Proceedings of the IEEE-Power-and-Energy-Society General Meeting, Minneapolis, MN, USA, 25–29 July 2010.
21. Bortoni, E.C.; Siniscalchi, R.T.; Jardini, J.A. Determination of Hydro Generator Efficiency Using Infrared Thermal Imaging Techniques. *IEEE Trans. Energy Convers.* **2012**, *27*, 1134–1139.
22. Bortoni, E.C.; Siniscalchi, R.T. Hydro generators losses measurement in accordance to IEEE-STD-115 and IEC-60034-2. In Proceedings of the 2012 IEEE Power and Energy Society General Meeting, San Diego, CA, USA, 22–26 July 2012.

23. Baholo, B.; Mellor, P.H.; Howe, D.; Birch, T.S. An automated calorimetric method of loss measurement in electrical machines. *J. Magn. Magn. Mater.* **1994**, *133*, 433–436. [CrossRef]
24. Bertalanic, Z.; Pavlica, M.; Maljkovic, Z. Analysis of hydro-generator's losses determined by calorimetric method. In Proceedings of the XIX International Conference on Electrical Machines—ICEM 2010, Rome, Italy, 6–8 September 2010.
25. Hudon, C.; Levesque, M.; Torriano, F.; Gingras, S.; Picard, J.; Petit, A. On-Line Rotor Temperature Measurements. In Proceedings of the 32nd Electrical Insulation Conference (EIC), Philadelphia, PA, USA, 8–11 June 2014.
26. Guerrero, R.C.; Aller, J.M. Efficiency Calculation for a 90 MVA Vertical Shaft Hydro-Alternator using the Calorimetric Method. In Proceedings of the 2024 IEEE ANDESCON, Cusco, Peru, 11–13 September 2024.
27. Indra, B.B.; Suresh, R. Generator Efficiency Measurement by Calorimetric Method: Case of UT3A HEP 60MW. *Proc. IOE Grad. Conf.* **2019**, *7*, 29–36.
28. Rasilo, P.; Ekström, J.; Haavisto, A.; Belahcen, A.; Arkkio, A. Calorimetric System for Measurement of Synchronous Machine Losses. *IET Electr. Power Appl.* **2012**, *5*, 286–294. [CrossRef]
29. Battisti, L.; Tieghi, L.; Fattahi, S. Heat-Loss Based Method for Real-Time Monitoring Method for Hydroelectric Power Plant Efficiency. *Energies* **2025**, *18*, 2586. [CrossRef]
30. Xinjie, G.; Chunqiang, P.; Hongtao, L.; Xuhui, X.; Cuiwei, J. Measuring uncertainty of hydraulic generator efficiency by calorimetric method. In *Journal of Physics: Conference Series, Proceedings of the 4th IAHR Asian Working Group Symposium on Hydraulic Machinery and Systems, Kashgar, China, 12–16 August 2023*; IOP Publishing: Philadelphia, PA, USA, 2024; Volume 2752, p. 012218.
31. Widiyanto, P.; Irasari, P.; Hikmawan, M.F. Suitability Analysis of Cross-Flow Turbine and Synchronous Generator Characteristics for Very Low Head Hydro Power Application. In Proceedings of the International Conference on Sustainable Energy Engineering and Application (ICSEEA)—Innovative Technology Toward Energy Resilience, Tangerang, Indonesia, 23–24 October 2019.
32. Jiang, F.; Bo, Z.Q.; Li, R.M. Performance of induction generator in parallel with an unbalanced three phase system. In Proceedings of the 1998 International Conference on Power System Technology (POWERCON 98), Beijing, China, 18–21 August 1998.
33. Safdar, I.; Sultan, S.; Raza, H.A.; Umer, M.; Ali, M. Empirical analysis of turbine and generator efficiency of a pico hydro system. *Sustain. Energy Technol. Assess.* **2020**, *37*, 100605. [CrossRef]
34. Kunckel, S.; Klaus, G.; Liese, M. Calculation of eddy current losses and temperature rises at the stator end portion of hydro generators. In Proceedings of the International Conference on Electrical Machines (ICEM 2002), Brugge, Belgium, 26–28 August 2002.
35. Valsan, V.; Kanakasabapathy, P. Design and Implementation of Smart Energy Management System for Stand-alone Micro-hydro Systems. In Proceedings of the IEEE International Conference on Technological Advancements in Power and Energy (IEEE TAP Energy)—Exploring Energy Solutions for an Intelligent Power Grid, United Nat Acad Impact, Kollam, India, 21–23 December 2017.
36. Barboianu, I.; Grigoriu, M.; Popescu, M.C. Application Software for Analyzing the Dynamic Stability of Hydro-aggregates. *Int. J. Comput. Sci. Netw. Secur.* **2020**, *17*, 227–234.
37. *IEC 60034-2-1:2024*; Rotating Electrical Machines—Part 2-1: Standard Methods for Determining Losses and Efficiency from Tests (Excluding Machines for Traction Vehicles). IEC: Geneva, Switzerland, 2024.
38. *IEC 60034-2A:1974*; Rotating Electrical Machines—Part 2: Methods for Determining Losses and Efficiency of Rotating Electrical Machinery form Tests (Excluding Machines for Traction Vehicles)—Measurement of Losses by the Calorimetric Method. IEC: Geneva, Switzerland, 1974.
39. *IEC 60034-4:1967*; Recommendations for Rotating Electrical Machinery (Excluding Machines for Traction Vehicles)—Part 4: Methods for Determining Synchronous Machine Quantities from Tests. IEC: Geneva, Switzerland, 1967.
40. *IEC 61000-4-30 Consolidated version*; Electromagnetic Compatibility (EMC)—Part 4-30: Testing and Measurement Techniques—Power Quality Measurement Methods. IEC: Geneva, Switzerland, 2021.

Disclaimer/Publisher's Note: The statements, opinions and data contained in all publications are solely those of the individual author(s) and contributor(s) and not of MDPI and/or the editor(s). MDPI and/or the editor(s) disclaim responsibility for any injury to people or property resulting from any ideas, methods, instructions or products referred to in the content.

energies

MDPI

Article

Mitigating Energy Losses Under Incremental Load Variations in Distributed Power-Flow Systems While Ensuring User Comfort

Sadiq Muhammad [1], Saher Javaid [1,2], Iacovos Ioannou [3,4,5], Yuto Lim [1,*] and Yasuo Tan [1]

[1] Graduate School of Advanced Science and Technology, Japan Advanced Institute of Science and Technology, Nomi 923-1292, Ishikawa, Japan; saher@jaist.ac.jp or saher@kanazawa-gu.ac.jp (S.J.)
[2] Department of Information Engineering, Kanazawa Gakuin University, Kanazawa 920-1392, Ishikawa, Japan
[3] Department of Computer Science, University of Cyprus, Nicosia 1678, Cyprus; ioannou.iakovos@ucy.ac.cy or ia.ioannou@euc.ac.cy
[4] CYENS Centre of Excellence, Nicosia 1016, Cyprus
[5] Department of Computer Science and Engineering, European University of Cyprus, Nicosia 2404, Cyprus
* Correspondence: ylim@jaist.ac.jp

Abstract

Renewable energy sources (RESs) such as photovoltaic (PV) and fuel cells (FCs) introduce variability that complicates reliable, loss-aware operation of distributed power-flow systems (DPFSs) in smart homes. Frequent charge/discharge cycling of energy storage systems (ESSs) can inflate losses and jeopardize user comfort when generation and demand are mismatched. This paper addresses the gap in multi-load, multi-source coordination under fluctuating RESs by proposing a Multiple-Load Power-Flow Assignment (MPFA) framework that explicitly minimizes storage-related losses while maintaining demand satisfaction. We evaluate four logical interconnection scenarios among generators (PGs), loads (PLs), and storage (PSs), and compare three control algorithms—total-demand-based (TDPF), adaptive-demand-based (ADPF), and grid-based (GBPF). Using measured PV/FC data across seasons, MPFA consistently reduces storage-related losses as interconnections increase, with GBPF guaranteeing full daily demand satisfaction by flexibly supplementing local generation with grid power. ADPF performs strongly when grid support is limited by prioritizing critical loads and optimizing storage utilization. The results provide actionable guidance for designing smart-home energy management that emphasizes sustainability, reliability, and user comfort.

Keywords: energy storage systems; power flow control; renewable energy sources; smart homes; energy losses; reliability; user comfort; Multiple-Load Power-Flow Assignment (MPFA)

1. Introduction

The rapid advancement of smart home technologies and the increasing adoption of Renewable Energy Sources (RESs) have revolutionized the way energy is generated, stored, and consumed. Smart homes, equipped with intelligent energy management systems, enable efficient utilization of energy resources while enhancing user comfort and reducing operational costs. The urgent need to reduce CO_2 emissions and mitigate the impact of conventional energy sources on the environment has led to a global shift towards RES power generation. This transition addresses environmental concerns and the dwindling reserves of traditional energy sources such as oil and gas. RESs such as photovoltaic (PV),

biomass, and wind offer clean and efficient alternatives to conventional power generation methods [1,2].

Smart home systems have evolved significantly with advancements in the Internet, transforming traditional homes into interconnected spaces where appliances and devices communicate seamlessly [3]. Modern smart homes often incorporate RESs like PVs and Fuel Cells (FCs) alongside conventional appliances, creating more sustainable and efficient energy ecosystems [4]. Through integration with RESs, smart home systems can optimize energy usage, reduce dependence on fossil fuels, and minimize environmental impact. As these systems continue to evolve, they promise to revolutionize modern living by providing personalized, interconnected, and energy-efficient environments. These systems gather energy profiles and oversee automation controls, managing the ON/OFF operations of Home Appliances and Devices (HADs) efficiently [5].

However, the integration of RESs, such as solar PV systems and wind turbines, into the smart home environment introduces significant challenges due to their inherent variability and intermittency. Fluctuations in energy generation can lead to imbalances between supply and demand, resulting in energy losses, reduced system efficiency, and potential disruptions in power supply. These fluctuations in energy generation can lead to instability in the DPFS, making it difficult to maintain a reliable and consistent power supply [6].

Deploying Energy Storage Systems (ESSs) has emerged as a practical solution to mitigate power fluctuations and enhance power system reliability. To tackle the changes in power from renewable energy and the varying needs of electricity in a system, using ESSs is an effective solution [7,8]. This flexibility helps manage situations where we have too much power when demand is low or not enough power during peak times. Using ESSs to store surplus power and supply it when needed effectively mitigates these fluctuations.

This paper investigates the impact of fluctuating energy generation on multiple load operations in smart homes and evaluates energy loss within the DPFS. In this work, we introduce the Multiple-Load Power-Flow Assignment (MPFA) approach, which aims to minimize power storage losses and ensure the maximum demand of power loads is satisfied. The DPFS framework is designed to dynamically allocate power flows between energy generators, loads, and storage units, taking into account the variability of RESs and the diverse demand patterns of smart homes. Through extensive simulations, we explore four distinct scenarios of power flow interactions between generators, loads, and storage systems. Our results demonstrate significant reductions in primary and secondary storage losses, highlighting the effectiveness of the proposed MPFA approach. Furthermore, the framework ensures that the maximum demand of power loads is consistently met, even under fluctuating generation conditions.

Fluctuating renewable energy production leads to temporal mismatches between generation and demand in smart homes, causing intermittent under- or over-supply conditions. Such fluctuations can result in frequent charging/discharging of storage units, increasing energy losses and reducing system efficiency. The proposed MPFA framework addresses these challenges by dynamically re-allocating power flows among generators, storage systems, and multiple loads in real time. Through the integration of the ADPF and GBPF algorithms, the MPFA approach adaptively balances supply–demand mismatches, prioritizes critical loads, and leverages both local storage and grid power to maintain continuous operation with minimized losses.

2. Related Work

The integration of Renewable Energy Sources (RESs) into power systems has been extensively studied in recent years, driven by the global push toward sustainable and

resilient energy infrastructures. Researchers have explored various facets of RES integration, encompassing energy generation, storage, and consumption, with a sustained focus on optimizing power flow and minimizing energy losses. This section provides a comprehensive review of key studies in the field, highlighting seminal contributions and identifying persisting gaps that the current research aims to address.

For instance, one study examined the impact of solar irradiance fluctuations on power grid stability and proposed a dynamic energy management system to mitigate these effects [1]. In a related effort, another work introduced a linear programming-based approach to optimize energy storage sizing under operational safety conditions to ensure stable grid performance [7]. Similarly, a battery energy storage system (BESS) optimization model was developed with the primary objective of minimizing overall energy costs [9], while another contribution addressed dual power load scenarios by introducing novel load-shifting algorithms that significantly reduce energy losses [10]. Further discussions appear in studies that extend grid optimization [5,11].

More recently, researchers proposed an energy management approach that prioritizes the utilization of stored power in energy storage systems (ESSs) during periods when the System Marginal Price (SMP) is high, while also considering household appliance efficiency ratings and noise limitations [12,13]. In cases where ESS reserves are depleted, their strategy shifts toward operating high-power and high-efficiency appliances to achieve cost-effective energy consumption under conditions of low grid demand [3,11–15]. Another line of research advanced the field by applying ESS to mitigate photovoltaic (PV) fluctuations, introducing a control strategy that regulates the state of charge (SoC) and determines output power based on super short-term PV forecasts [16,17]. Similarly, ref. [18] presents an optimization-based sizing routine for battery energy storage systems (BESSs) aimed at ensuring adequacy and small-signal stability in hybrid power systems. These contributions highlight the growing importance of coordinated control and appropriate storage sizing—topics directly aligned with the objectives of this study. This method incorporates rolling prediction theory, ensuring real-time regulation at every sampling point, and further develops an ESS sizing framework to evaluate the combined technical and economic performance of the system [19,20]. Moreover, rolling, short-horizon forecasting has also been used to regulate PV-driven variability in real time [16], while recent work develops adequacy- and stability-oriented BESS sizing for hybrid microgrids [18].

The historical evolution of power system flexibility has also been explored, with one study emphasizing that cloud transients cause rapid PV output variations which significantly influence voltage levels in low-voltage (LV) grids with high PV penetration [21]. Such variations may cause power-quality violations; their effects were analyzed via load-flow assessments under multiple scenarios [21]. In addition, a comprehensive review highlighted the main characteristics of flexible power systems, identifying flexibility sources, evaluation parameters, and the broader impacts of variable renewable energy penetration on transient stability, small-signal stability, and frequency response [6]. A decentralized droop control method based on battery state of charge was proposed to enable reliable power exchange among clustered nanogrids without inter-unit communication, reducing line losses and ensuring scalability [22]. Building on droop concepts, adaptive droop control further enhances voltage regulation and coordinated power exchange in DC nanogrids [23]. Renewable-integrated DC nanogrids with distributed control have been shown suitable for rural/remote electrification scenarios [24]. To further improve resource sharing and transient control, a multi-agent distributed control strategy employing augmented Lagrangian optimization has been introduced, achieving optimal power distribution with minimized losses [24]. Additionally, cooperative game-theoretic approaches, such as Nash Bargaining

Solution (NBS) based energy management, have been applied to nanogrids to ensure fair and efficient allocation of resources, enhancing battery lifespan and renewable utilization while maintaining robust bus voltage regulation [25].

Despite substantial progress in the domains of RES integration, ESS optimization, and power flow management, several critical gaps persist in the literature. First, most existing studies focus on single-load scenarios, often neglecting the complexities inherent in multiple-load operations within smart homes. Second, the impact of fluctuating energy generation on energy losses in DPFS remains underexplored. Third, there is a lack of comprehensive frameworks that simultaneously integrate RESs, ESSs, and multiple loads to optimize power flow allocation and minimize energy losses. Finally and most importantly, the literature rarely considers user comfort or satisfaction, particularly when power demand cannot be fully met, an essential aspect for practical deployment in real-world smart home environments [11,14,15,26]. Recent works underscore these gaps. For example, presents a multi-objective optimization model for smart home energy management that incorporates user comfort as a critical constraint, revealing significant trade-offs between energy efficiency and occupant satisfaction [11,14,15,26]. One study investigates the coordinated operation of multiple loads, ESSs, and PV systems, and demonstrates that incorporating user preferences leads to both improved energy utilization and enhanced comfort [27,28]. Similarly, Kiani et al. introduce a demand-side management approach using reinforcement learning [29], where user comfort is explicitly modeled and optimized, further emphasizing the necessity of considering end-user experience in future smart grid research. While single-source or single-load optimization is well-studied, the coupling of multi-source–multi-storage–multi-load systems introduces complex energy loss and control challenges. Additionally, the risk of thermal runaway in ESSs poses reliability and safety concerns in residential applications [30,31]. Authors in [32] propose a shrinking-horizon control architecture for bidirectional home charging (V2H/H2V), improving load balancing and reducing operational costs within HEMS.

Due to the intermittent and fluctuating nature of renewable sources such as solar and wind, achieving a stable, large-scale energy supply remains challenging. Hydrogen energy offers significant potential as a complementary pathway in the clean energy transition. Through water electrolysis, surplus renewable power can be converted into hydrogen for long-term storage and later reconverted into electricity via proton-exchange-membrane fuel cells [33], with advances in PEMFC membrane materials (e.g., SPEEK) enabling this conversion step [34]. For a system-level overview of power-to-hydrogen and long-term storage, see [35]. This integrated hydrogen–electricity pathway supports deep decarbonization and enhances the flexibility of distributed energy systems.

The contributions of this research are threefold: (i) the development of a dynamic power flow allocation framework for smart home energy systems, (ii) the evaluation of energy losses under multiple operational scenarios, and (iii) the demonstration of the DPFS algorithm's capability to satisfy load demands while minimizing storage losses. By addressing key challenges of RES integration, this work provides an effective approach for optimizing energy management in future smart homes.

Table 1 summarizes the key contributions, strengths, and limitations of existing studies on multi-load or multi-source power flow control and energy management in smart homes. As shown, most prior works focus on single-load or cost-oriented optimization, whereas the proposed MPFA framework uniquely emphasizes multi-load coordination under fluctuating renewable conditions while ensuring user comfort.

Table 1. Summary of related work and strengths of the proposed MPFA framework.

Study	Main Focus	Strengths	Limitations
[1]	Dynamic EMS for PV fluctuation mitigation.	Improves grid stability; adaptive response to irradiance changes.	Focuses on single-load; ignores ESS losses.
[7]	ESS sizing via linear programming.	Ensures safe operation and SoC management.	Ignores multi-load and RES variability.
[9]	Cost minimization model for BESS.	Reduces operational cost; enhances ESS use.	Static model; lacks real-time adaptability.
[10]	Dual-load shifting algorithm.	Lowers losses under dual-load operation.	Limited scalability to multi-load systems.
[12,13]	Smart home scheduling with SMP pricing.	Considers appliance efficiency and user comfort.	Excludes RES uncertainty and loss modeling.
[21]	PV-induced voltage fluctuation in LV grids.	Highlights grid flexibility challenges.	No mitigation strategy provided.
[6]	Review of flexibility in RES systems.	Comprehensive theoretical overview.	Lacks quantitative smart home validation.
[22–25]	Nanogrid droop (SoC/adaptive) and cooperative microgrid control.	Improves DC-bus voltage regulation and fair power sharing ; enables rural/remote electrification and islanded operation; MPC-based optimal power flows for cooperative microgrids;	Droop does not explicitly optimize economics; cooperative/MPC methods can require more tuning/communication; scope often beyond single-home scale.
[11,14,15,27–29]	User comfort in multi-load energy management.	Balances comfort and energy efficiency.	Does not address DPFS losses or fluctuation effects.
Proposed MPFA	Multi-load power flow optimization under RES fluctuation.	Integrates RES, ESS, and loads; minimizes storage loss; maintains comfort and stability.	Current model omits degradation and converter losses (future work).

3. System Model

This section provides an in-depth description of the Distributed Power Flow System (DPFS) implemented in a smart home environment. The DPFS enables optimal energy management by coordinating multiple power generation sources, flexible energy storage systems, and diverse household loads. Through real-time power flow control and adherence to operational constraints, the DPFS ensures reliable, efficient, and sustainable operation of the residential microgrid.

3.1. Overview of System Architecture

As illustrated in Figure 1, the DPFS is architected around three fundamental subsystems:

- **Power Generation Systems (PGs)**: Responsible for producing electrical energy from renewable and conventional sources.
- **Power Storage Systems (PSs)**: Facilitate temporal balancing of supply and demand by storing surplus energy and discharging it as needed.
- **Power Loads (PLs)**: Represent the consumption profile of the household through various appliances and devices.

All subsystems are interconnected via a central electrical bus, supporting bidirectional energy transfer and intelligent coordination.

3.2. Performance Metrics

User comfort and demand satisfaction are used as system-level metrics. We define

$$U_c = 1 - \frac{T_{int}}{T_{tot}}, \qquad D_s = \frac{E_{\text{supplied}}}{E_{\text{demanded}}} \times 100\%,$$

where T_{int} is the total interruption time over the horizon T_{tot}, and E_{supplied}, E_{demanded} are cumulative energy supply and demand, respectively.

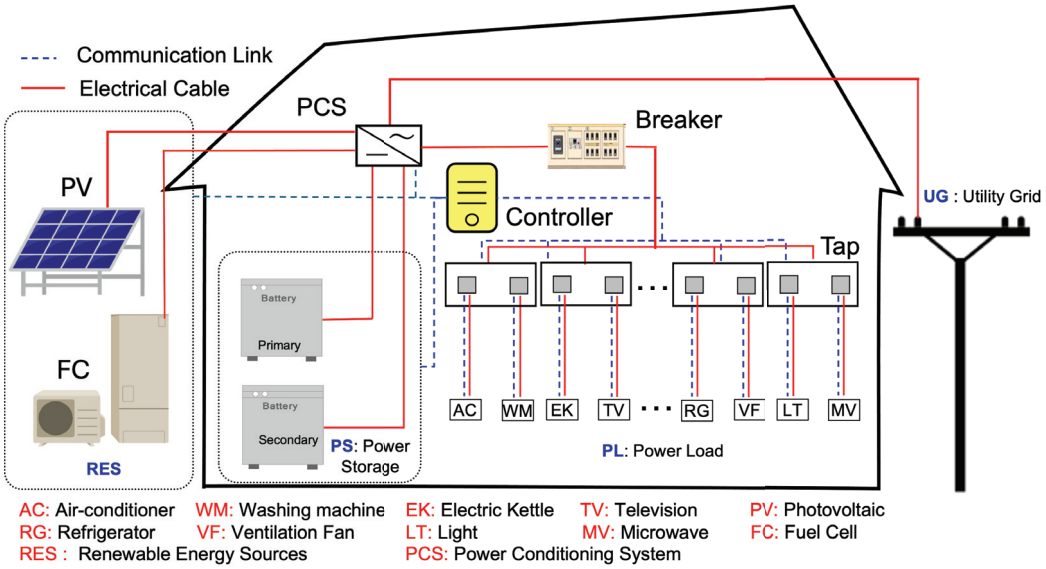


Figure 1. System model of the DPFS in a smart home environment, illustrating three power generation units (PV, FC, UG), two storage systems, and eight power loads.

3.3. Power Generation Systems (PGs)

The power generation subsystem comprises the following:

- **PV Panels**: Generate variable renewable energy based on solar irradiance.
- **Fuel Cells (FC)**: Provide semi-controllable renewable generation through hydrogen-based electrochemical reactions.
- **Utility Grid (UG)**: Functions as a fully controllable generator, supplementing local generation to guarantee demand satisfaction.

Let J be the total number of PGs. For the j-th PG at time t:

- $PG_j^f(t)$: Fluctuating RESs generation (e.g., PV, FC)
- $PG_j^c(t)$: Controllable generation (e.g., UG)

Subject to generation bounds:

$$\mathcal{P}_{PG_j^c}^{\min} \leq \mathcal{P}_{PG_j^c}(t) \leq \mathcal{P}_{PG_j^c}^{\max}, \tag{1}$$

$$\mathcal{P}_{PG_j^f}^{\min} \leq \mathcal{P}_{PG_j^f}(t) \leq \mathcal{P}_{PG_j^f}^{\max}. \tag{2}$$

3.4. Power Storage Systems (PSs)

The power storage subsystem introduces flexibility and robustness, enabling the DPFS to buffer renewable fluctuations and optimize energy usage. Each PS can be categorized as primary (PS_p) or secondary (PS_s), designed for different cycling profiles.

Let H denote the total number of PS units. Each storage system h at time t is defined by

- SoC_h^{ini}: Initial state of charge.
- SoC_h^{min}, SoC_h^{max}: Minimum and maximum SoC bounds.
- η_c: Charging efficiency.
- η_d: Discharging efficiency.
- ESS_h: Storage capacity (Wh or kWh).

3.4.1. Stored Energy and SoC Dynamics

Let n index time steps with step size Δt. The total stored energy in the h-th PS at time t is given by

$$E_{\mathrm{PS}_h}[n+1] = E_{\mathrm{PS}_h}[n] + \eta_c \, \mathcal{P}_{\mathrm{PS}_h^{in}}[n]\Delta t - \frac{1}{\eta_d} \, \mathcal{P}_{\mathrm{PS}_h^{out}}[n]\Delta t, \tag{3}$$

$$E_{\mathrm{PS}_h}[0] = SoC_h^{ini} \, ESS_h, \tag{4}$$

$$SoC_h[n+1] = SoC_h[n] + \frac{\eta_c \, \Delta t}{ESS_h} \, \mathcal{P}_{\mathrm{PS}_h^{in}}[n] - \frac{\Delta t}{\eta_d \, ESS_h} \, \mathcal{P}_{\mathrm{PS}_h^{out}}[n], \tag{5}$$

$$SoC_h^{min} \leq SoC_h[n] \leq SoC_h^{max}. \tag{6}$$

where $E_{\mathrm{PS}_h}^{ini}$ is the initial stored energy, $\mathcal{P}_{\mathrm{PS}_h^{in}}(t)$ is the charging power, and $\mathcal{P}_{\mathrm{PS}_h^{out}}(t)$ is the discharging power.

The initial stored energy is computed as

$$E_{\mathrm{PS}_h}^{ini} = SoC_h^{ini} \cdot ESS_h \tag{7}$$

The state of charge evolves according to

$$SoC_h(t) = SoC_h^{ini} + \frac{\eta_c}{ESS_h} \int_0^t \mathcal{P}_{\mathrm{PS}_h^{in}}(\tau) \, d\tau - \frac{1}{\eta_d \, ESS_h} \int_0^t \mathcal{P}_{\mathrm{PS}_h^{out}}(\tau) \, d\tau \tag{8}$$

The SoC is subject to operational limits:

$$SoC_h^{min} \leq SoC_h(t) \leq SoC_h^{max} \tag{9}$$

3.4.2. Charging and Discharging Constraints

Charging and discharging power are bounded:

$$\mathcal{P}_{\mathrm{PS}_h^{in}}^{\min} \leq \mathcal{P}_{\mathrm{PS}_h^{in}}(t) \leq \mathcal{P}_{\mathrm{PS}_h^{in}}^{\max}, \tag{10}$$

$$\mathcal{P}_{\mathrm{PS}_h^{out}}^{\min} \leq \mathcal{P}_{\mathrm{PS}_h^{out}}(t) \leq \mathcal{P}_{\mathrm{PS}_h^{out}}^{\max}, \tag{11}$$

and cannot occur simultaneously. A simple complementarity condition is

$$\mathcal{P}_{\mathrm{PS}_h^{in}}(t) \, \mathcal{P}_{\mathrm{PS}_h^{out}}(t) = 0, \tag{12}$$

or, equivalently, with binary auxiliaries $u_h^c(t), u_h^d(t) \in \{0, 1\}$,

$$u_h^c(t) + u_h^d(t) \leq 1, \tag{13}$$

$$\mathcal{P}_{\mathrm{PS}_h^{in}}(t) \leq u_h^c(t) \, \mathcal{P}_{\mathrm{PS}_h^{in}}^{\max}, \tag{14}$$

$$\mathcal{P}_{\mathrm{PS}_h^{out}}(t) \leq u_h^d(t) \, \mathcal{P}_{\mathrm{PS}_h^{out}}^{\max}. \tag{15}$$

3.4.3. Energy Loss Calculations

Energy losses occur inside storage during charge/discharge due to imperfect efficiencies:

$$P_{loss}^{h_c}(t) = \left(1 - \eta_c\right) \mathcal{P}_{\mathrm{PS}_h^{in}}(t), \tag{16}$$

$$P_{loss}^{h_d}(t) = \left(\tfrac{1}{\eta_d} - 1\right) \mathcal{P}_{\mathrm{PS}_h^{out}}(t). \tag{17}$$

where $P_{loss}^{h_c}(t)$ and $P_{loss}^{h_d}(t)$ denote charging and discharging losses, respectively.

Total storage-related loss at the bus.

$$P_{\text{loss,tot}}(t) \;=\; \sum_{h}\Big[P^{h_c}_{loss}(t) + P^{h_d}_{loss}(t)\Big] \;=\; \sum_{h}\Big[(1-\eta_c)\,\mathcal{P}_{\text{PS}^{in}_h}(t) + \big(\tfrac{1}{\eta_d}-1\big)\,\mathcal{P}_{\text{PS}^{out}_h}(t)\Big]. \quad (18)$$

To incorporate degradation, the aging cost C_{deg} is defined as

$$C_{deg}(t) = k_{cyc}\frac{E_{cyc}(t)}{E_{rated}} + k_T(T(t)-25)^2,$$

where k_{cyc} and k_T are empirically derived coefficients. This formulation captures cycle-life and temperature-induced capacity fade consistent with Li-ion models in [36]. Including C_{deg} allows evaluating long-term operational costs alongside instantaneous losses. The present storage model neglects degradation and temperature effects for simplicity.

3.5. Power Loads (PLs)

The PL subsystem models residential energy consumption through both controllable and fluctuating loads:

- **Controllable Loads (PL^c)**: Schedulable devices (e.g., air conditioner, washing machine).
- **Fluctuating Loads (PL^f)**: Non-shiftable, variable demand devices (e.g., refrigerator, lights).

Let K be the number of loads. The k-th load at time t is represented as

- $PL^c_k(t)$: Controllable demand.
- $PL^f_k(t)$: Fluctuating demand.

With respective power constraints:

$$\mathcal{P}^{\min}_{PL^c_k} \le \mathcal{P}_{PL^c_k}(t) \le \mathcal{P}^{\max}_{PL^c_k} \quad (19)$$

$$\mathcal{P}^{\min}_{PL^f_k} \le \mathcal{P}_{PL^f_k}(t) \le \mathcal{P}^{\max}_{PL^f_k} \quad (20)$$

3.6. Power Flow and System Balance

All components interact via a central power bus. The instantaneous system-wide power balance at time t is

$$\mathcal{P}_{\text{PG}}(t) + \sum_{h}\mathcal{P}_{\text{PS}^{out}_h}(t) \;=\; \mathcal{P}_{\text{PL}}(t) + \sum_{h}\mathcal{P}_{\text{PS}^{in}_h}(t) + P_{\text{loss,tot}}(t). \quad (21)$$

where $\mathcal{P}_{\text{PG}}(t)$ and $\mathcal{P}_{\text{PL}}(t)$ denote aggregate generated and consumed power, respectively, and $P_{\text{loss,tot}}(t)$ is the aggregate storage-related loss defined in the Section 3.4.3.

Cumulative energy for generation and consumption over time horizon $[0, t]$ is

$$E_{PG^c_j} = \int_0^t \mathcal{P}_{PG^c_j}(\tau)d\tau \quad (22)$$

$$E_{PG^f_j} = \int_0^t \mathcal{P}_{PG^f_j}(\tau)d\tau \quad (23)$$

$$E_{PL^c_k} = \int_0^t \mathcal{P}_{PL^c_k}(\tau)d\tau \quad (24)$$

$$E_{PL^f_k} = \int_0^t \mathcal{P}_{PL^f_k}(\tau)d\tau \quad (25)$$

3.7. Logical Connections in DPFS

We examine four power-flow assignment scenarios in Table 2 that differ in how power generators (PGs), power storage systems (PSs), and power loads (PLs) are interconnected. (1) **MPFA/S** (multi-load, single storage): multiple PLs are supplied via a single PS; a single RES-based PG (optionally backed by the UG) charges that PS (Figure 2). (2) **MPFA/SG** (multi-load, single generator): multiple PLs are connected to a single RES PG and a single PS (Figure 2). (3) **MPFA/MG** (multi-load, multiple generators): multiple PLs are supplied by multiple RES PGs and a single PS (Figure 3). (4) **MPFA/MSG** (multi-load, multiple generators and storages): multiple PL sets can draw from all RES PGs, the UG, and multiple PSs (Figure 3).

Table 2. Summary of MPFA scenarios in the DPFS.

Scenario	Power Generators (PGs)	Power Storages (PSs)	Description
MPFA/S	1	1	Single PG–single PS configuration
MPFA/SG	1	1	Single RES PG and single PS supplying multiple loads
MPFA/MG	3	1	Multiple PGs with single PS
MPFA/MSG	3	2	Multiple PGs and PSs, fully integrated DPFS

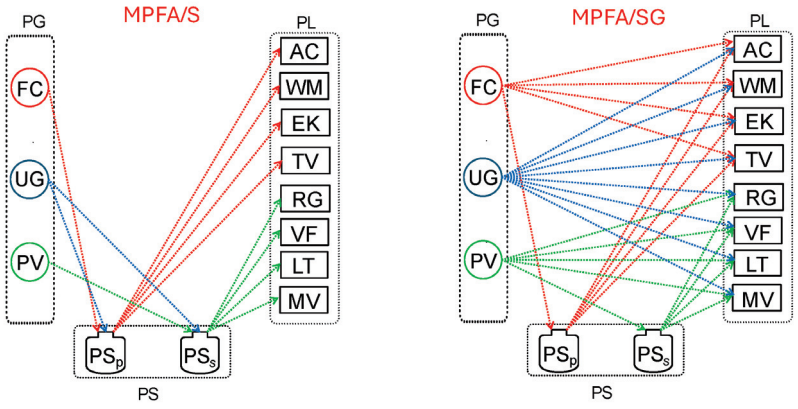


Figure 2. Logical connection for MPFA/S and MPFA/SG.

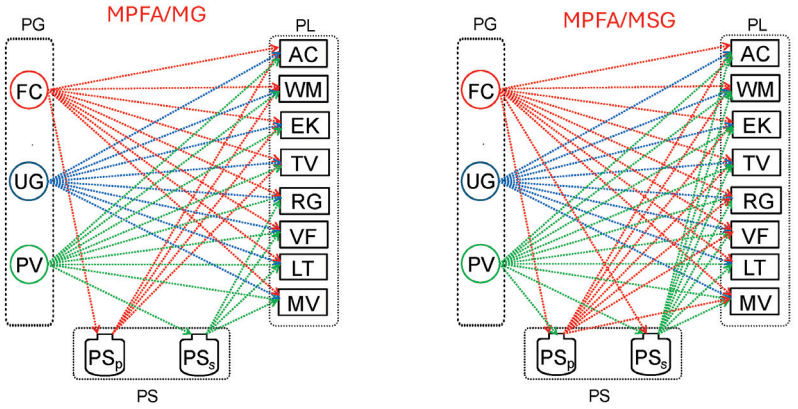


Figure 3. Logical connection for MPFA/MG and MPFA/MSG.

4. DPFS Algorithms

This section introduces three power flow algorithms designed for the DPFS: the Total-Demand-Based Power Flow (TDPF) algorithm, the Adaptive-Demand-Based Power Flow

(ADPF) algorithm, and the Grid-Based Power Flow (GBPF) algorithm. These algorithms are foundational for managing the smart home DPFS by dynamically balancing supply, demand, and storage resources in real time, optimizing energy usage, and prioritizing user comfort and system reliability.

4.1. Overview of Power Flow Algorithms

In Algorithm 1 represent the TDPF, ADPF, and GBPF algorithms differ in their operational logic, their handling of load priorities, and the manner in which they utilize available energy resources including renewable generation, energy storage, and the external utility grid. Their integration enables the DPFS to flexibly adapt to changes in renewable output, user demand, and energy storage status.

Algorithm 1 MPFA Power-Flow Management (bus-level allocation under TDPF/ADPF/GBPF).

Require: $\mathcal{P}_{PL_k}(t)$ for all k, $\mathcal{P}_{PG_j}(t)$ for all j, $\mathcal{P}_{\mathrm{PS}_h^{in}}(t)$ and $\mathcal{P}_{\mathrm{PS}_h^{out}}(t)$ for all h, and $\mathcal{P}_{\mathrm{grid}}(t)$

for each time step t **do**
  Compute total demand: $P_{\mathrm{demand,tot}}(t) = \sum_{k \in K} \mathcal{P}_{PL_k}(t)$
  Compute total supply: $P_{\mathrm{supply,tot}}(t) = \sum_{j \in J} \mathcal{P}_{PG_j}(t)$
  Compute available discharge from storage: $P_{\mathrm{storage,tot}}(t) = \sum_{h \in H} \mathcal{P}_{\mathrm{PS}_h^{out}}(t)$
  if TDPF or GBPF mode **then**
    if $P_{\mathrm{demand,tot}}(t) \leq P_{\mathrm{supply,tot}}(t)$ **then**
      Serve all $\mathcal{P}_{PL_k}(t)$, charge PSs subject to η_c and bounds
      Record charging losses
    else if $P_{\mathrm{demand,tot}}(t) \leq P_{\mathrm{supply,tot}}(t) + P_{\mathrm{storage,tot}}(t)$ **then**
      Discharge PSs with η_d to meet deficit, record losses
    else if GBPF mode and $P_{\mathrm{demand,tot}}(t) \leq P_{\mathrm{supply,tot}}(t) + P_{\mathrm{storage,tot}}(t) + \mathcal{P}_{\mathrm{grid}}(t)$ **then**
      Draw remaining deficit from grid
      Serve all $\mathcal{P}_{PL_k}(t)$, update energy accounting
    else
      Curtail loads (TDPF only; GBPF curtails only if a grid cap binds)
  else if ADPF mode **then**
    Sort loads by priority (essential $\rightarrow$ non-essential)
    Allocate $\mathcal{P}_{PG_j}(t)$ to high-priority $\mathcal{P}_{PL_k}(t)$ first
    If $\mathcal{P}_{PG_j}(t)$ is exhausted, use PSs
    If PSs are exhausted, curtail lowest priority $\mathcal{P}_{PL_k}(t)$ as needed
    Compute and record energy losses

4.1.1. Total-Demand-Based Power Flow (TDPF) Algorithm

The Total-Demand-Based Power Flow (TDPF) algorithm is depicted in Figure 4 and constitutes a baseline approach to power management in the DPFS. This algorithm operates by first evaluating the total power demand of the system at each discrete time interval and comparing it to the sum of the available power supply from Power Generation (PGs) and Power Storage Systems (PSs).

If the available supply is sufficient to meet the total demand, all household Power Loads (PLs) are powered accordingly, maximizing user comfort and uninterrupted operation of appliances. In this scenario, any surplus power after meeting demand is allocated to charging the PSs with a charging efficiency factor η_c, and any residual energy loss resulting from charging inefficiencies is computed and recorded for system analysis and optimization.

Conversely, if the supply is insufficient to meet the total demand, the algorithm suspends the operation of HADs, which may include flexible loads or critical appliances, to prevent over-discharge and ensure safe operation of the DPFS. Although this may lead to user discomfort due to interrupted appliance use, it preserves the integrity of storage systems and prevents excessive battery cycling or blackout conditions. This stepwise logic ensures that energy is allocated efficiently, losses are minimized, and system stability is maintained under varying operational and environmental conditions.

4.1.2. Adaptive-Demand-Based Power Flow (ADPF) Algorithm

The Adaptive-Demand-Based Power Flow (ADPF) algorithm, as illustrated in Figure 5, enhances flexibility by introducing adaptive load prioritization. Unlike the TDPF, which treats all loads equally, the ADPF algorithm recognizes the varying importance of different household appliances and assigns higher priority to essential or critical loads (such as medical equipment, refrigeration, or heating/cooling systems).

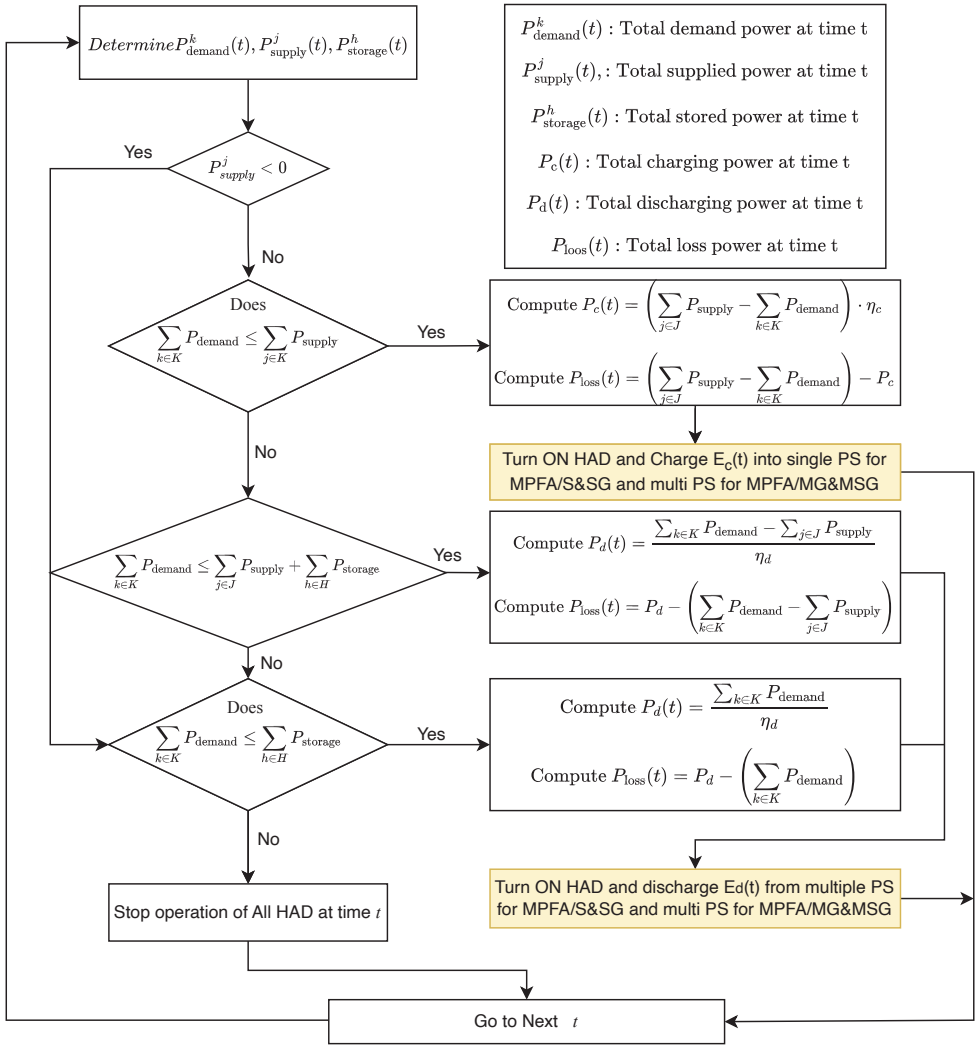


Figure 4. Flowchart of Total-Demand-Based Power Flow (TDPF) algorithm.

During each time step, the ADPF algorithm first attempts to satisfy the demand of prioritized loads using the available supply from RES PGs and PSs units. If the available supply is sufficient, the surplus is charged to PSs with efficiency η_c and losses are computed as before. If the available supply is not sufficient, the algorithm allocates stored energy (if

available) to power the remaining prioritized loads, discharging PSs with efficiency η_d and again computing corresponding losses. When neither PGs nor PSs can fully meet demand, the algorithm systematically turns off the lowest priority or non-critical loads, thereby minimizing user discomfort by ensuring that essential services remain operational. This adaptive approach optimizes energy usage and minimizes the impact of supply shortages on user comfort.

4.1.3. Grid-Based Power Flow (GBPF) Algorithm

The Grid-Based Power Flow (GBPF) algorithm, shown in Figure 6, introduces the external utility grid as an additional energy source to further enhance the reliability and resilience of the DPFS. This approach first allocates power from RES PGs and storage units, maximizing local RES PGs and PSs energy utilization. If the combined supply from local sources is insufficient to meet the full household demand, the GBPF algorithm automatically engages the external grid, which supplies the remaining demand and thus ensures that no load curtailment occurs. This operational paradigm guarantees user comfort and the seamless operation of all loads at all times.

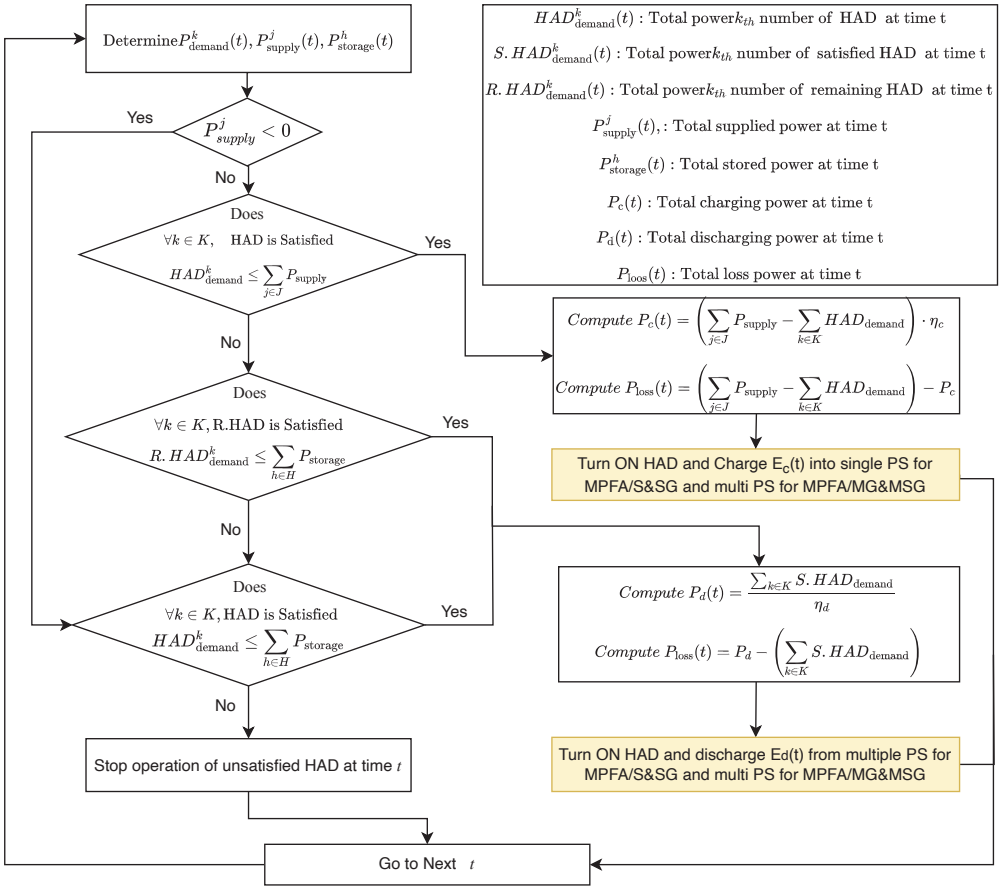


Figure 5. Flowchart of Adaptive-Demand-Based Power Flow (ADPF) algorithm.

By using the grid only when local sources are insufficient, the GBPF algorithm maximizes the economic and ecological benefits of RES energy while maintaining the capability to fully satisfy demand. This approach provides system-level reliability and stability, minimizes the risk of service interruptions, and can reduce storage cycling (lower storage-related losses) at the expense of potentially higher imported energy when RES are scarce.

4.2. Algorithmic Logic and Stepwise Description

The detailed operational logic of each algorithm is as follows:

Total-Demand-Based Power Flow (TDPF) Algorithm:

- At each time step t, the algorithm first checks whether there is any available power supply.
- If the total demand is less than or equal to the total supply, the surplus power is used to charge the storage units with efficiency η_c, and any residual energy loss is computed.
- If the demand exceeds the supply but remains less than or equal to the combined available power from supply and storage, the deficit is met by discharging storage with efficiency η_d, and corresponding losses are calculated.
- If only storage is available and sufficient to meet the demand, the storage discharges accordingly.
- If none of these conditions are satisfied, all HAD operations are suspended for that time step.
- This logic ensures that energy is allocated efficiently, minimizes losses, and maintains system stability under varying operational and environmental conditions.

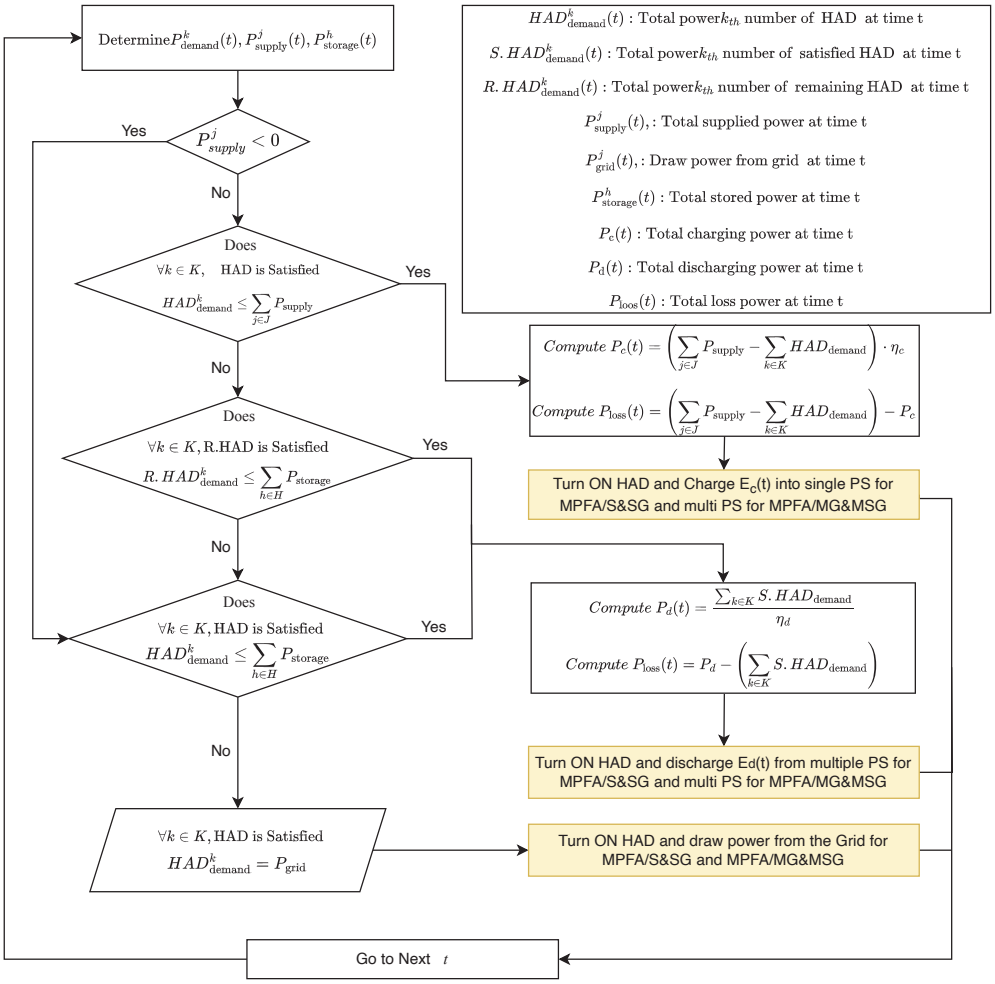


Figure 6. Flowchart of Grid-Based Power Flow (GBPF) algorithm.

Adaptive-Demand-Based Power Flow (ADPF) Algorithm:

- This algorithm governs the allocation of stored and supplied energy to meet demand in real time at each time step t.
- If supply is available and exceeds the total HAD demand, the surplus energy is stored after accounting for charging efficiency η_c, and any losses are computed.
- In the absence of sufficient supply, the algorithm checks whether the stored energy can satisfy the HAD demand. If so, the storage discharges energy based on the discharging efficiency η_d, with the corresponding energy loss calculated.
- In cases where stored energy is insufficient, the algorithm defaults to discharging what is available from the multiple power sources (e.g., MPFA/S&G or MPFA/MG&MSG configurations).
- This process ensures optimal utilization of energy resources and maintains the operation of HAD systems while minimizing energy losses.

Grid-Based Power Flow (GBPF) Algorithm:

- The GBPF algorithm manages energy distribution by coordinating supplied, stored, and demanded energy at each time step t.
- When there is a positive supply, the algorithm first checks if the total HAD demand is less than or equal to the available supply.
- If true, and the HAD demand is fully met by the supply, the excess supply is partially stored in the energy storage system after accounting for the charging efficiency η_c. The energy loss in this case is the difference between the remaining supply and the amount successfully stored.
- If the HAD demand exceeds the current supply but can still be met by combining supply with stored energy, the required deficit is discharged from storage based on the discharging efficiency η_d, and losses are computed accordingly.
- In both scenarios, HAD systems are activated and energy is either charged into or discharged from single or multiple power sources (e.g., MPFA/S&G or MPFA/MG&MSG).
- If the combined available supply and storage are insufficient to meet demand, all HAD operations are halted for that time step to prevent instability.
- This strategy ensures optimal grid-supported energy flow, maintains HAD operation when feasible, and prevents overuse of limited resources.

For completeness and reproducibility, a generic pseudocode structure encompassing the operational flow of these algorithms is presented below.

Figures 4–6 provide flowchart representations for the TDPF, ADPF, and GBPF algorithms, respectively, depicting their decision-making process and operational flow.

In summary, the TDPF, ADPF, and GBPF algorithms together provide a robust, flexible, and adaptive power management framework for the DPFS. By considering total demand, load priority, and grid integration, these algorithms enable real-time optimization of energy flows, minimize system losses, maintain user comfort, and ensure reliable smart home operation under a wide range of supply, storage, and demand scenarios. Their modular design allows for seamless integration and future extension within advanced residential energy management systems.

4.3. Computational Remarks and Guarantees

Each algorithm operates in a single pass per time step with arithmetic over J generators, H storages, and K loads. The per-step time is $O(J+H+K)$ for TDPF and GBPF; ADPF adds a priority sort of loads $O(K \log K)$ (or $O(K)$ with bucketed priorities). Feasibility is always achieved under GBPF (assuming $\mathcal{P}_{\text{grid}}(t)$ is adequate). Under fixed η_c, η_d, storage bounds, and complementarity, the energy state $E_{\text{PS}_h}[n]$ remains within

$[SoC_h^{\min} ESS_h,\ SoC_h^{\max} ESS_h]$ provided the charging/discharging limit constraints hold. Optimality (loss-minimality) is not claimed for TDPF/ADPF but is empirically evaluated; extending MPFA with optimization-based dispatch is left to future work.

5. Numerical Simulations

This section presents the simulation setup and scenarios considered to evaluate the proposed Multiple-Load Power Flow Assignment (MPFA) approach in a smart home environment. The Distributed Power Flow System (DPFS) consists of three key components: power generators (PGs), power loads (PLs), and power storage systems (PSs). The PGs include a photovoltaic (PV) array, a fuel cell (FC), and the utility grid (UG), each playing a crucial role in supplying energy to household appliances. The PLs comprise various essential household HADs, including an air conditioner (AC), washing machine (WM), ventilation fan (VF), light (LT), electric kettle (EK), microwave (MV), television (TV), and refrigerator (RG), all of which are modeled based on their real-time usage patterns in a smart home. The PSs include two dedicated storage units, PS1 and PS2, which manage fluctuations in energy demand and supply.

5.1. Simulation Scenarios and Setup

The simulation framework is developed using Python, incorporating real experimental data from both the FC and PV systems obtained from the *iHouse* setup. To comprehensively assess the impact of power flow strategies, the study explores four distinct MPFA scenarios: MPFA/S, MPFA/SG, MPFA/MG, and MPFA/MSG. These scenarios are designed to analyze how different energy sources and storage mechanisms contribute to energy distribution, loss minimization, and demand satisfaction. The evaluation is conducted using three power-flow algorithms—TDPF, ADPF, and GBPF—each offering unique insights into system performance under varying energy conditions.

The operation of the FC is modeled based on the ENE-FARM framework, in Table 3 with its active operational hours set from 00:00 to 05:00 and 16:00 to 23:59 across all seasons to optimize energy availability [10,37]. Although the current FC model assumes stable operation, in practice FC performance degrades due to component aging and reversible voltage losses. For PV generation, actual recorded data is used to reflect seasonal variations, with representative dates selected for each season: winter (11 January), spring (23 April), summer (14 June), and autumn (17 October). The utility grid is considered a controllable energy source and is available 24/7, providing an additional layer of stability to the energy supply.

Table 3. Main experimental parameters used in the simulation.

Component	Specification / Setting
PV system	Model: 1.0 kW mono-crystalline PV array; tilt angle: 30°; efficiency: 18%;
Fuel cell (FC)	Model: Toshiba ENE-FARM household FC system; type: PEMFC; rated electrical output: 700 W; thermal output: 1.0 kW; hydrogen supply pressure: 1.3 bar; reaction temperature: 70 °C; overall system efficiency: 90% (electric 40%, heat 50%).

Regarding household appliance PLs, the simulation considers the most relevant and frequently used HADs in a smart home environment. A detailed 24 h operational profile of these appliances is depicted in Figure 7 and Table 4, illustrating the variations in energy demand throughout the day. Notably, the air conditioner (AC) operates for 21 h, reflecting its significant role in maintaining indoor comfort, while the refrigerator (RG) remains

active continuously for 24 h to ensure food preservation. The operational schedules of other household appliances are also taken into account, aligning with the daily energy consumption patterns of typical users.

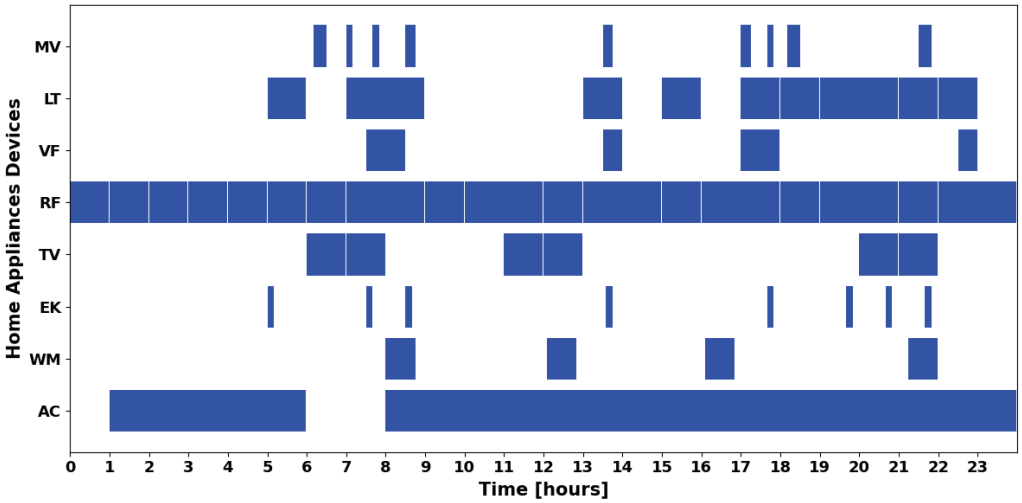


Figure 7. Household activity schedule for the operation of HADs.

For both PSs, the initial, minimum, and maximum state of charge (SoC) are 21%, 20%, and 94%, respectively. Both PSs have charging efficiency η_c and discharging efficiency η_d of 92%. This setup allows for a realistic assessment of power flow strategies and their effectiveness in balancing supply and demand while minimizing losses within the DPFS.

Table 4. Power ratings of home appliances across seasons.

Season	Home Appliance Power Ratings (W)							
	AC	WM	EK	TV	RG	VF	LT	MV
Winter	890	500	600	120	150	66	36.8	1000
Summer	790	350	600	120	250	111	36.8	1000
Autumn	380	450	600	120	200	36	36.8	1000
Spring	380	350	600	120	200	36	36.8	1000

5.2. Power Profile Results and Discussion

The simulation results presented in Figure 8 illustrate the power consumption and supply profiles for the first scenario for the winter season (MPFA/S). Both TDPF and ADPF algorithms achieve similar levels of demand fulfillment throughout the day. However, at 13:00, 14:00, 21:00, and 22:00 the ADPF algorithm exhibits higher demand satisfaction than TDPF. This indicates the effectiveness of ADPF in dynamically adjusting power allocation, ensuring better utilization of available storage energy.

In this section, power flow scenarios and algorithms are tested and verified for the winter season. The power supply and consumption profiles reflect the operational strategies of the implemented power flow algorithms. The total power supply in the ADPF and TDPF approaches is primarily sourced from FC, PV, and PSs, while the GBPF algorithm integrates power from PV, FC, PSs, and the UG to meet the power demand. The total daily power demand during winter is 24.51 kWh.

In Figure 9, the power demand satisfaction profile is analyzed throughout the day. During hours 08:00, 09:00, and 22:00, ADPF achieves higher demand fulfillment than TDPF does.

This suggests that ADPF is more effective in managing limited power resources from a single generator and storage, optimizing allocation to maintain supply during critical hours.

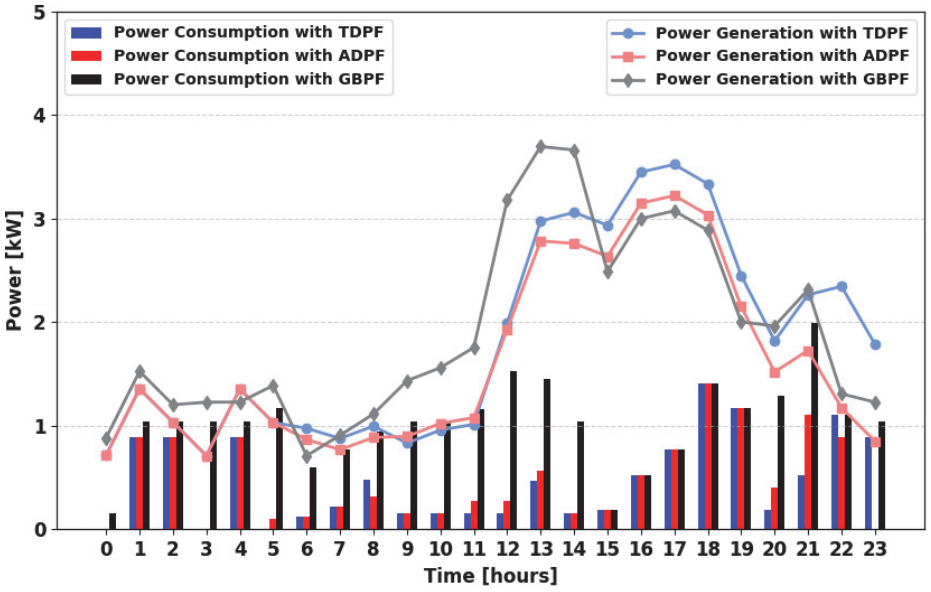


Figure 8. Power supply and consumption in winter with MPFA/S.

Figure 10 demonstrates an improvement in power availability due to the presence of multiple power generators. ADPF satisfies more demand at key intervals: 04:00, 08:00, 09:00, 12:00, 13:00, 21:00, 23:00, and 24:00, compared to TDPF.

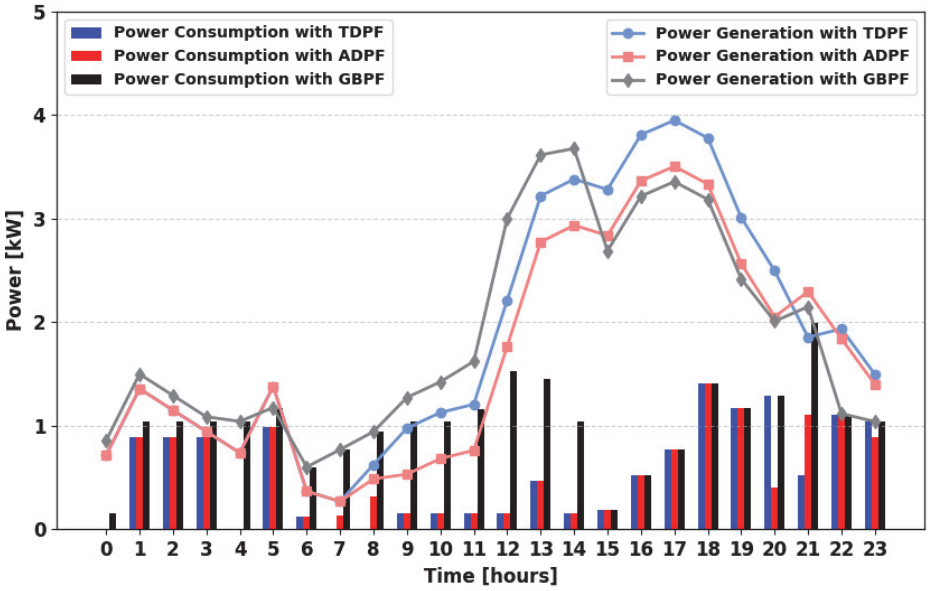


Figure 9. Power supply and consumption in winter with MPFA/SG.

Finally, Figure 11 shows the most efficient and balanced power supply scenario. Here, ADPF ensures greater demand satisfaction during multiple hours, particularly in the morning (08:00–11:00) and later in the evening (19:00, 22:00, and 24:00). The presence of multiple PSs allows surplus energy from PGs to be stored and redistributed effectively, further improving demand fulfillment.

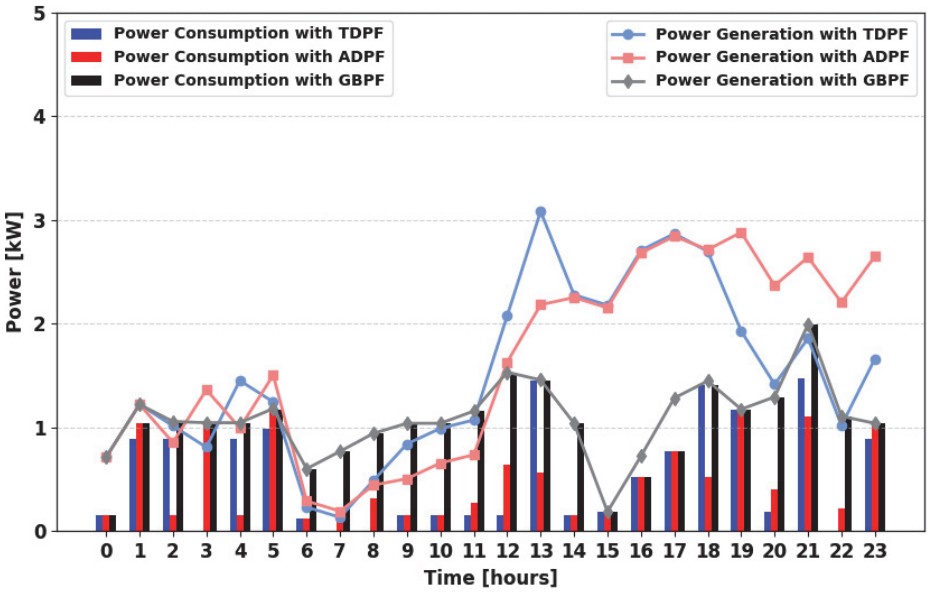


Figure 10. Power supply and consumption in winter with MPFA/MG.

Across all scenarios, the GBPF algorithm consistently meets the full daily power demand, highlighting its superior performance in ensuring reliable energy supply. The results further emphasize the importance of multi-source generation and grid integration in optimizing energy distribution and reducing supply gaps.

Figures 12 and 13 illustrate the power supply and consumption profiles during the summer season for the MPFA/S and MPFA/SG scenarios. In both cases, the ADPF and TDPF algorithms exhibit nearly identical performance in meeting demand, primarily due to the limited number of connections available. In Figure 14, with the increased number of connections in the MPFA/MG scenario, the TDPF algorithm outperforms ADPF. Specifically, demand satisfaction is higher at critical hours such as 02:00, 03:00, 04:00, 09:00, 10:00, 13:00, 19:00, and 22:00. Conversely, in Figure 15, the ADPF algorithm demonstrates better performance at 01:00, 03:00, 05:00, 20:00, 21:00, and 23:00. In the MPFA/MSG scenario, the ADPF algorithm nearly satisfies the maximum demand across all periods, while the TDPF algorithm either fully meets or intermittently fails to meet the demand at multiple times. Across all evaluated scenarios, the GBPF algorithm consistently achieves full daily power demand satisfaction, confirming its superior reliability and effectiveness during the summer season.

Figures 16 and 17 illustrate the power supply and consumption profiles for the autumn season. Given the relatively lower energy demand during this period, the MPFA/S, MPFA/SG, and MPFA/MG scenarios exhibit similar performance trends across all three evaluated algorithms. In particular, Figure 18, representing the MPFA/MG scenario, shows that during critical hours—specifically, 05:00, 08:00, 12:00, 13:00, and 17:00–20:00 the ADPF algorithm is able to satisfy a higher portion of the demand compared to the TDPF algorithm. Furthermore, Figure 19 highlights the MPFA/MSG scenario, where at hours 7:00–9:00, 20:00, and 21:00, the TDPF algorithm fails to meet the required load, whereas the ADPF algorithm successfully fulfills the demand based on available power supply. This distinction underlines the adaptability of the ADPF method under supply-constrained conditions. Across all considered scenarios, the GBPF algorithm consistently achieves full daily demand satisfaction, demonstrating its robustness and superior capability in ensuring reliable power delivery throughout the autumn season.

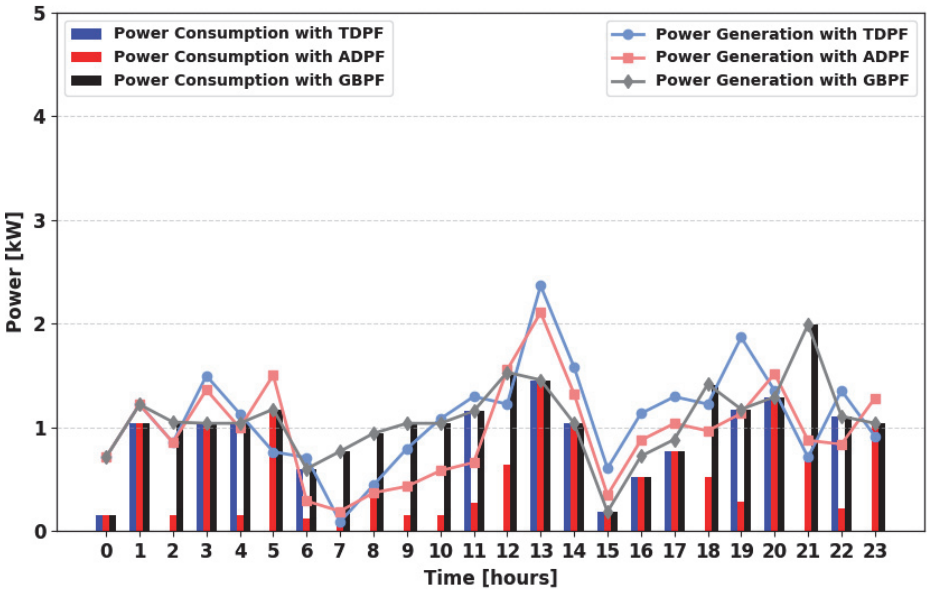


Figure 11. Power supply and consumption in winter with MPFA/MSG.

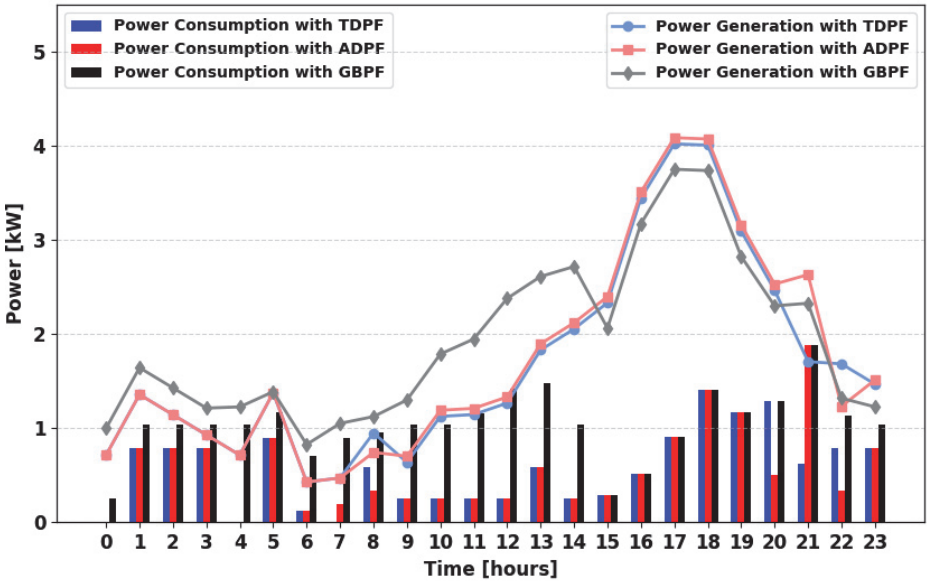


Figure 12. Power supply and consumption in summer with MPFA/S.

Figures 20–23 present the power supply and consumption profiles for the spring season, a period characterized by lower energy demand and relatively high photovoltaic (PV) energy supply. In the MPFA/S scenario, both the ADPF and TDPF algorithms demonstrate comparable performance in terms of demand satisfaction. However, the GBPF algorithm outperforms them during certain periods, leveraging the additional availability of grid power to meet the load requirements better. Specifically, Figure 21, which illustrates the MPFA/SG scenario, highlights that during the early morning hours from 1:00 to 5:00 and midday hours from 11:00 to 14:00, the TDPF algorithm is able to satisfy a greater portion of the demand compared to the ADPF algorithm, likely due to its effective load distribution strategy.

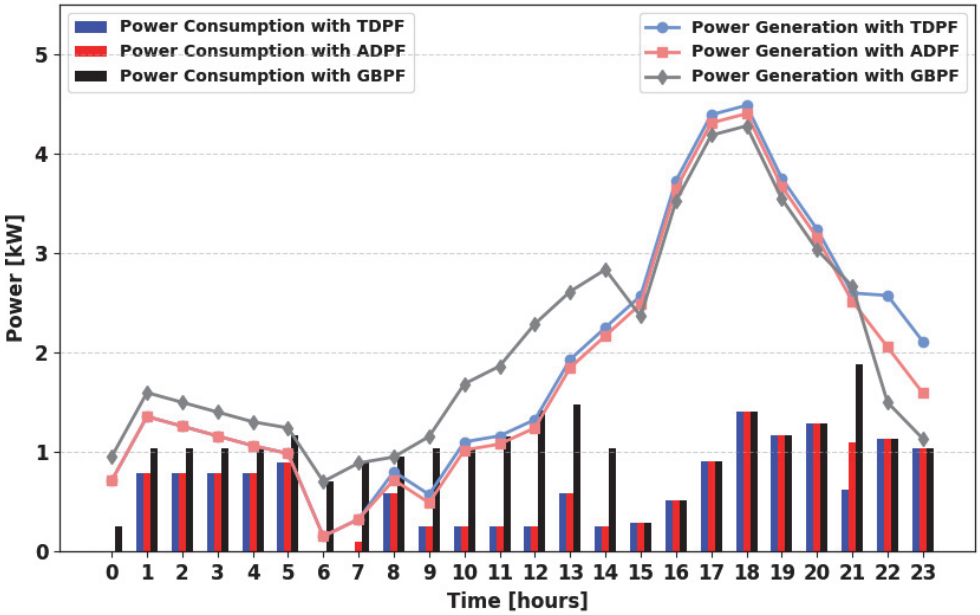


Figure 13. Power supply and consumption in summer with MPFA/SG.

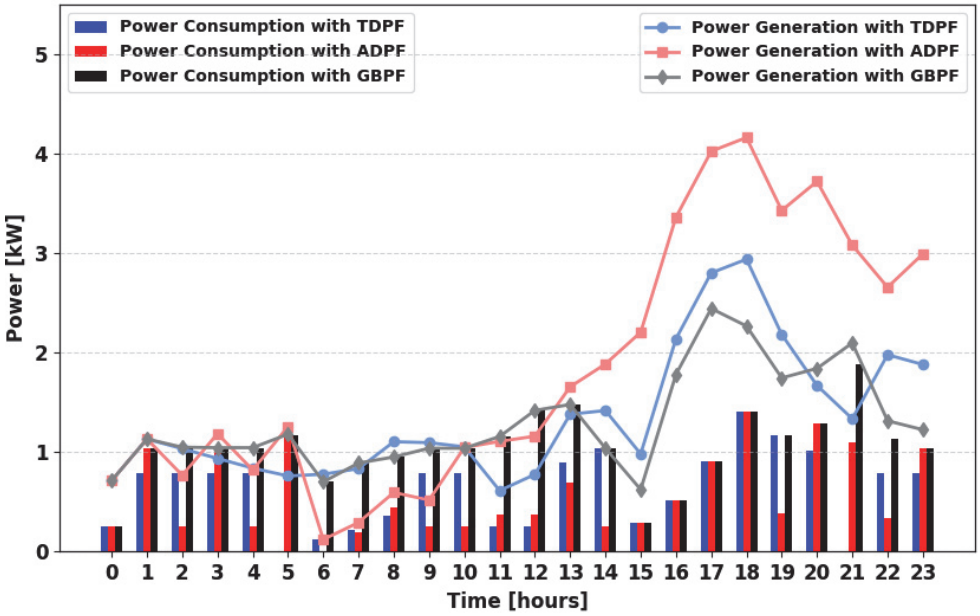


Figure 14. Power supply and consumption in summer with MPFA/MG.

Moreover, Figure 22, focusing on the MPFA/MG scenario, reveals that at 06:00, neither the TDPF nor the ADPF algorithm is able to fully satisfy the load, pointing to a temporary mismatch between supply availability and demand requirements. Nevertheless, as shown in Figure 23, under the more advanced MPFA/MG and MPFA/MSG scenarios, all three algorithms ADPF, TDPF, and GBPF successfully meet the full demand across all time periods. This is largely attributed to the abundant RES supply during the spring season and the extensive logical connections established between devices, which enhance load-sharing flexibility and system robustness. Overall, the results emphasize the importance of optimizing connectivity and leveraging renewable generation to ensure reliable and efficient microgrid operation under varying seasonal conditions.

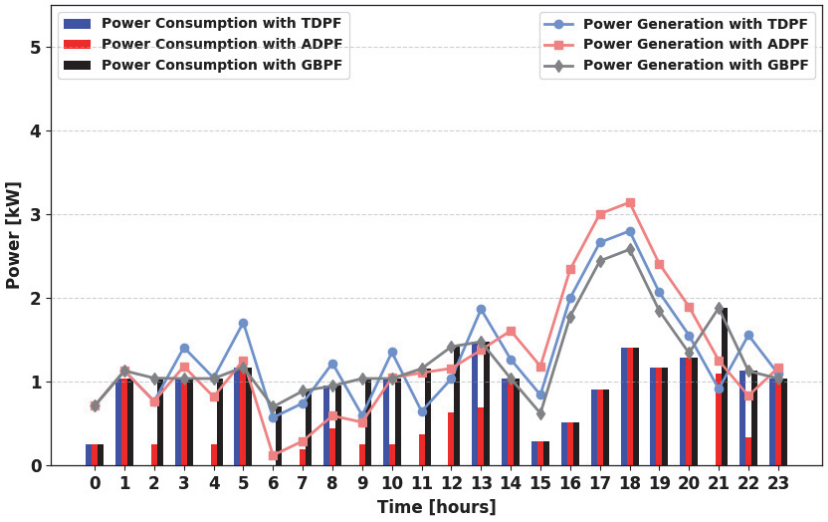


Figure 15. Power supply and consumption in summer with MPFA/MSG.

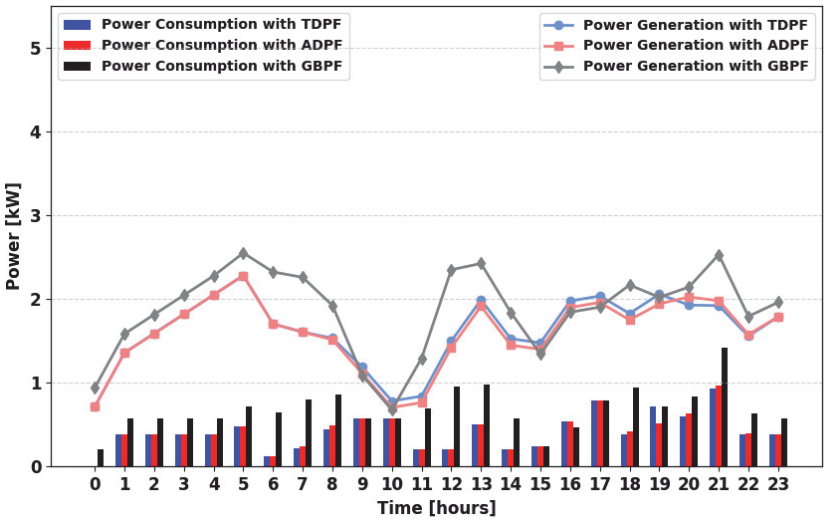


Figure 16. Power supply and consumption in autumn with MPFA/S.

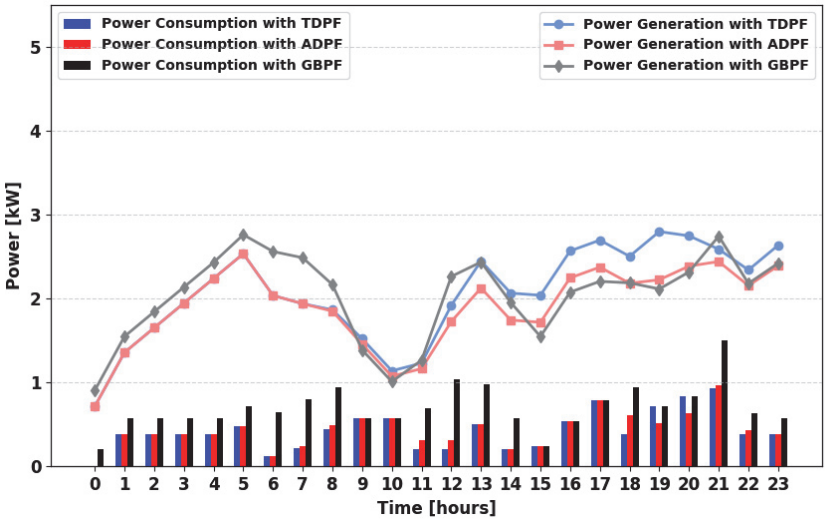


Figure 17. Power supply and consumption in autumn with MPFA/SG.

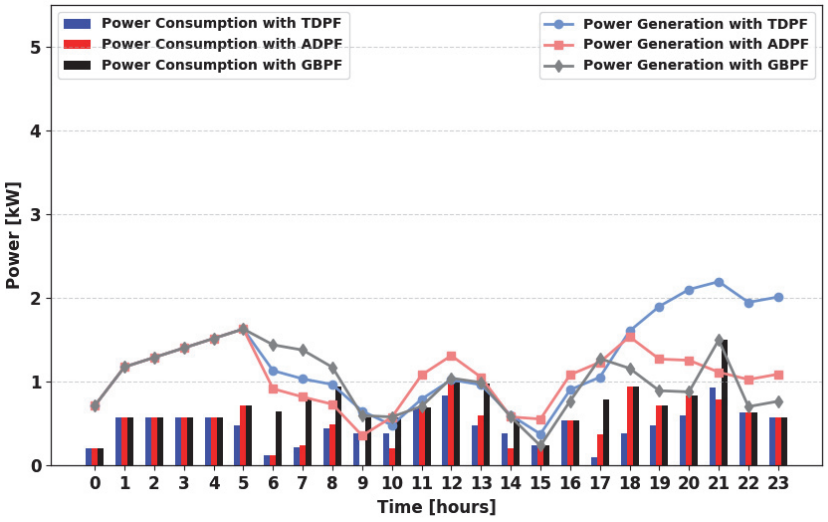


Figure 18. Power supply and consumption in autumn with MPFA/MG.

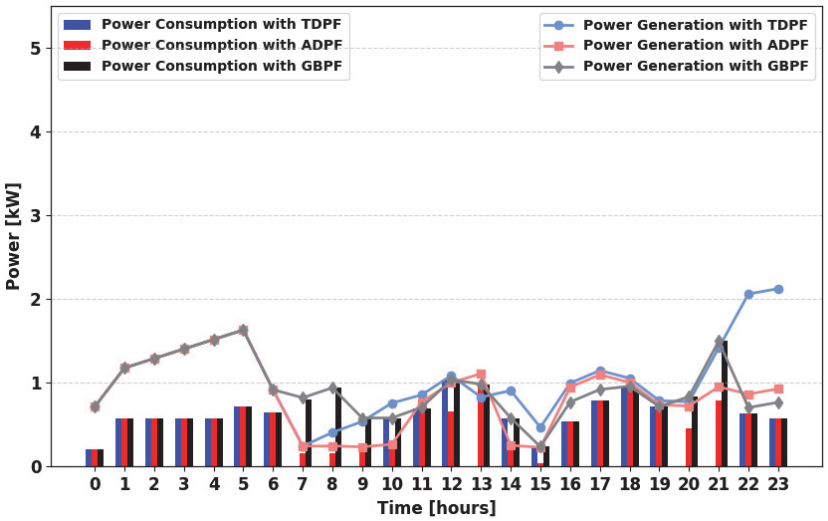


Figure 19. Power supply and consumption in autumn with MPFA/MSG.

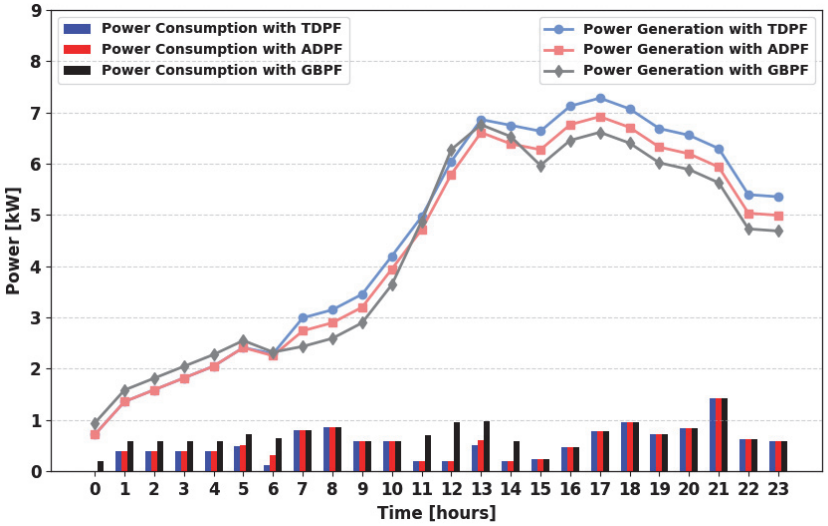


Figure 20. Power supply and consumption in spring with MPFA/S.

5.3. Power Loss Results and Discussion

This section analyzes the power loss in different scenarios using various power flow algorithms. For the winter season and in the MPFA/S scenario (Figure 24), the logical connection where power flows primarily from the PS leads to a high frequency of charging and discharging, resulting in significant storage losses. The TDPF and ADPF algorithms exhibit similar storage losses. Under GBPF, 100% demand is guaranteed; grid support often reduces battery cycling and thus storage-related losses, although total imported energy can increase when RES are scarce.

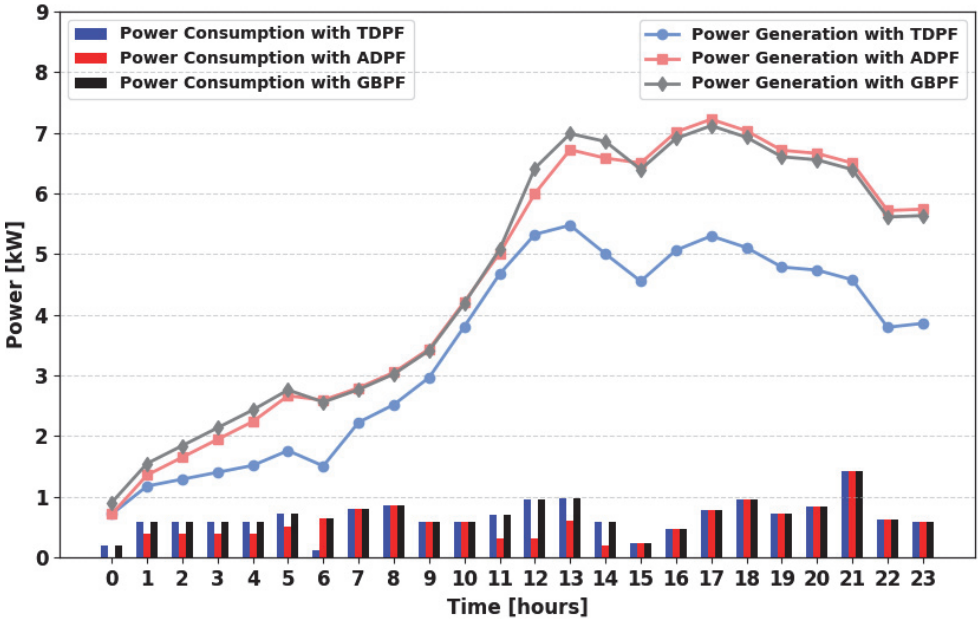


Figure 21. Power supply and consumption in spring with MPFA/SG.

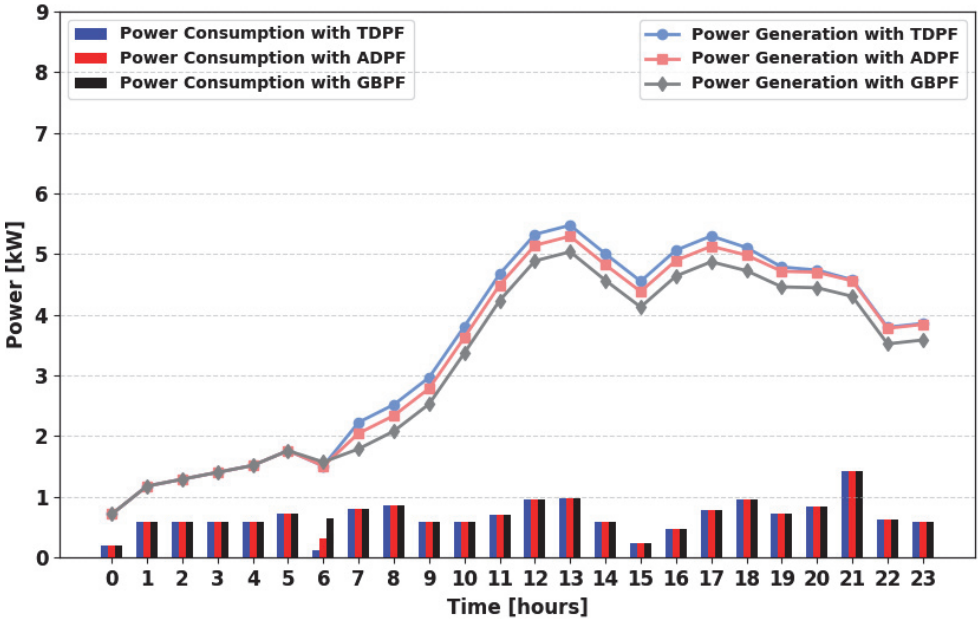


Figure 22. Power supply and consumption in spring with MPFA/MG.

For winter, Figure 25 represents the charging and discharging profile for the MPFA/SG scenario. Here, the logical connection allows power to be drawn from a single generator, reducing dependency on PS and significantly lowering power losses compared to MPFA/S. This highlights the impact of direct generation-based supply in minimizing inefficiencies.

In Figure 26 (MPFA/MG) and Figure 27 (MPFA/MSG), power loss continues to decrease rapidly across scenarios. The introduction of multiple generators and storage systems in these configurations enhances energy availability and distribution efficiency, resulting in further reductions in energy losses. Notably, across all scenarios except MPFA/S, the ADPF algorithm demonstrates lower power losses compared to TDPF. Across MPFA/SG–MPFA/MSG scenarios, power loss in GBPF is significantly lower than in ADPF, benefiting from grid integration that reduces cycling.

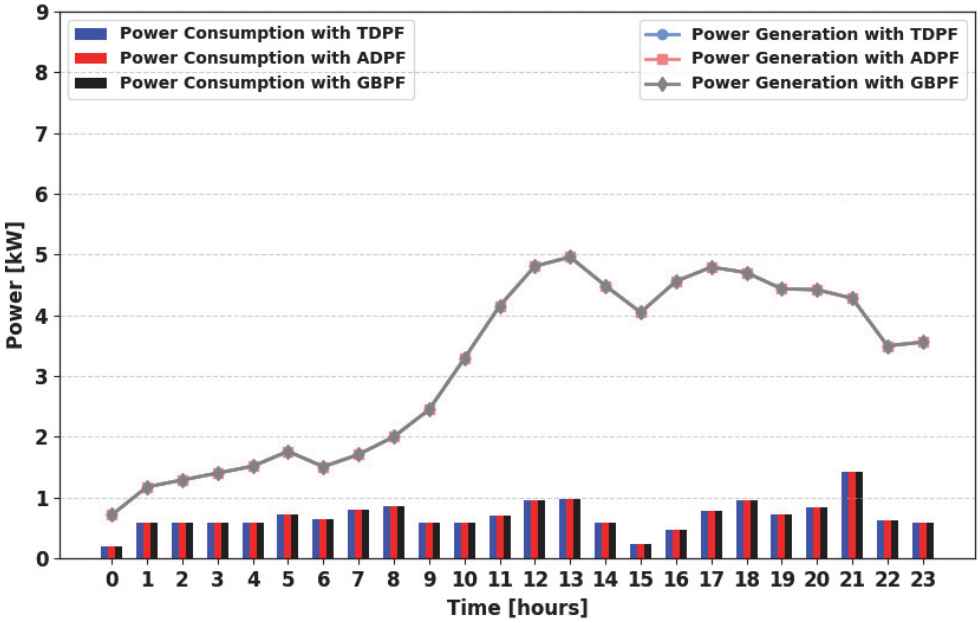


Figure 23. Power supply and consumption in spring with MPFA/MSG.

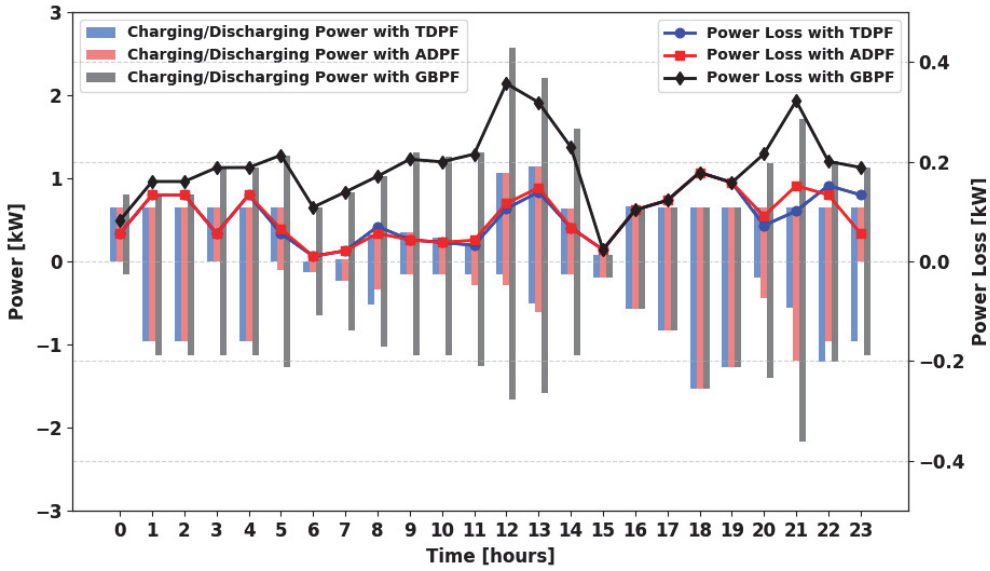


Figure 24. Power loss in winter with MPFA/S.

For the summer season, Figures 28–31 illustrate the charging/discharging profile and power loss across the three algorithms. In the MPFA/S scenario, limited logical connections lead to high power charging/discharging, resulting in significant losses. The GBPF algorithm ensures complete demand satisfaction and generally yields the lowest storage-related losses due to reduced cycling from grid support (though imported energy can increase when RES are scarce). In MPFA/SG, power loss remains similar across all three algorithms. In MPFA/MG and MPFA/MSG, ADPF exhibits lower losses than TDPF at all time periods, while GBPF consistently has the lowest losses compared to both TDPF and ADPF.

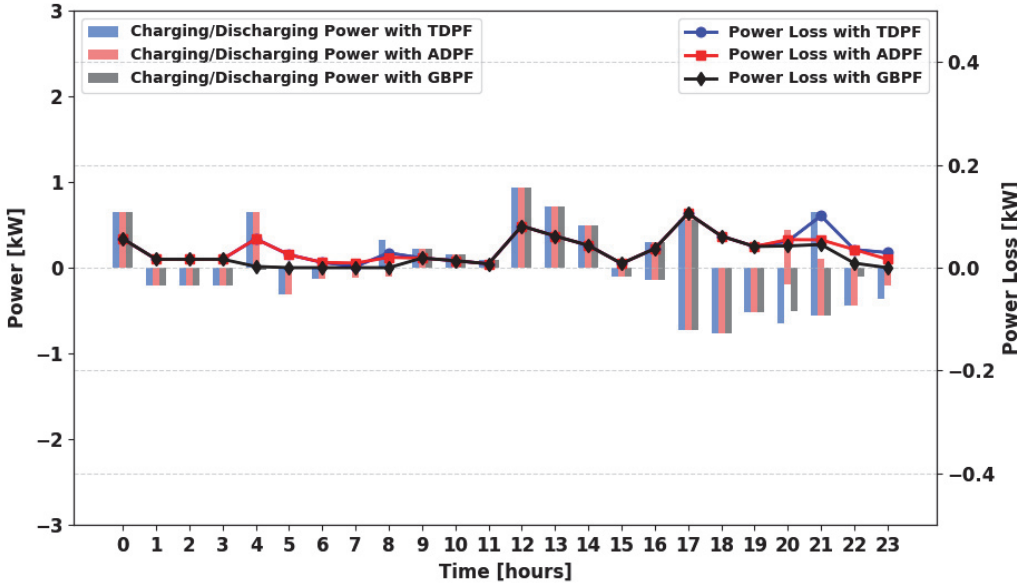


Figure 25. Power loss in winter with MPFA/SG.

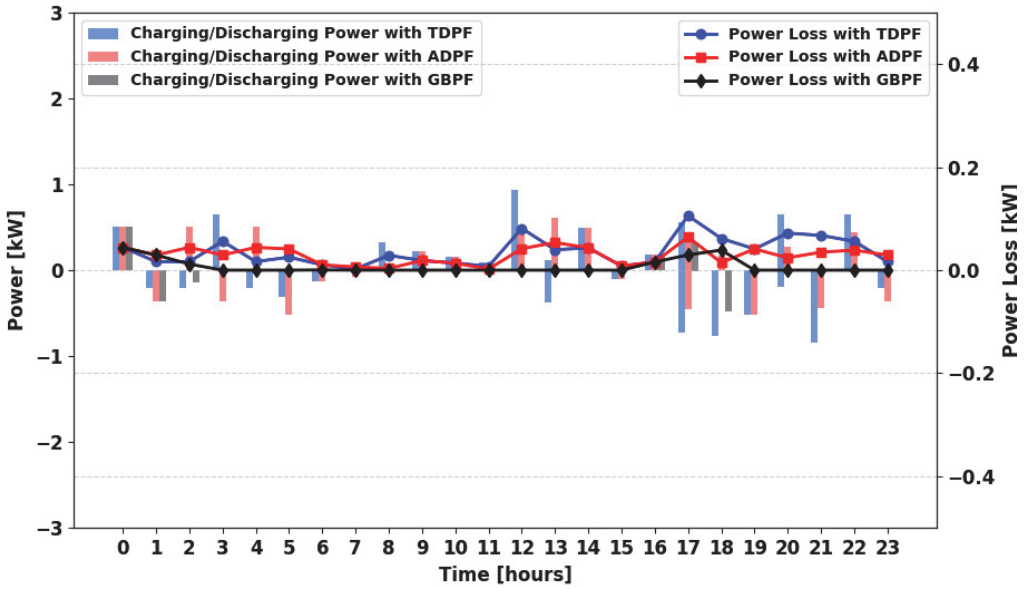


Figure 26. Power loss in winter with MPFA/MG.

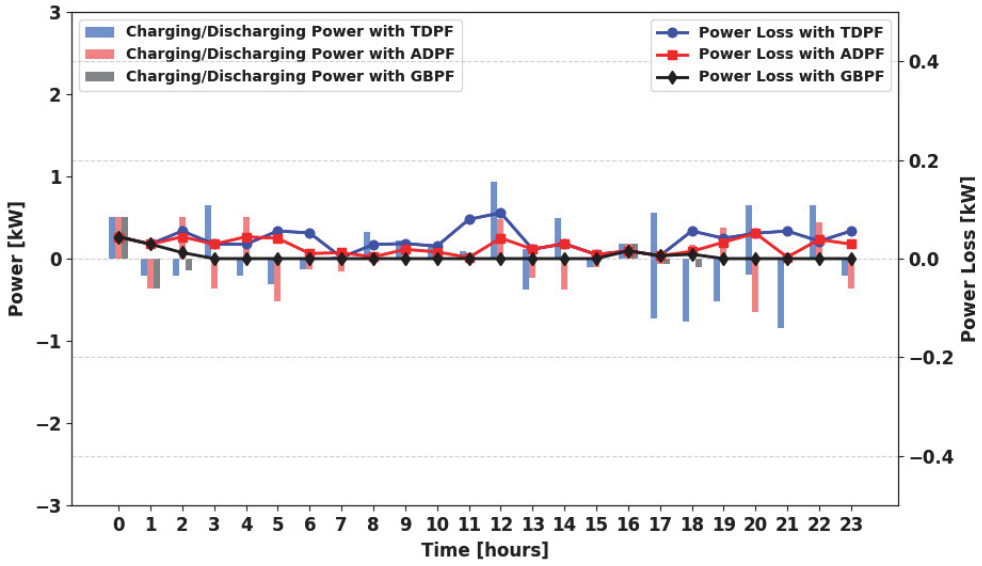


Figure 27. Power loss in winter with MPFA/MSG.

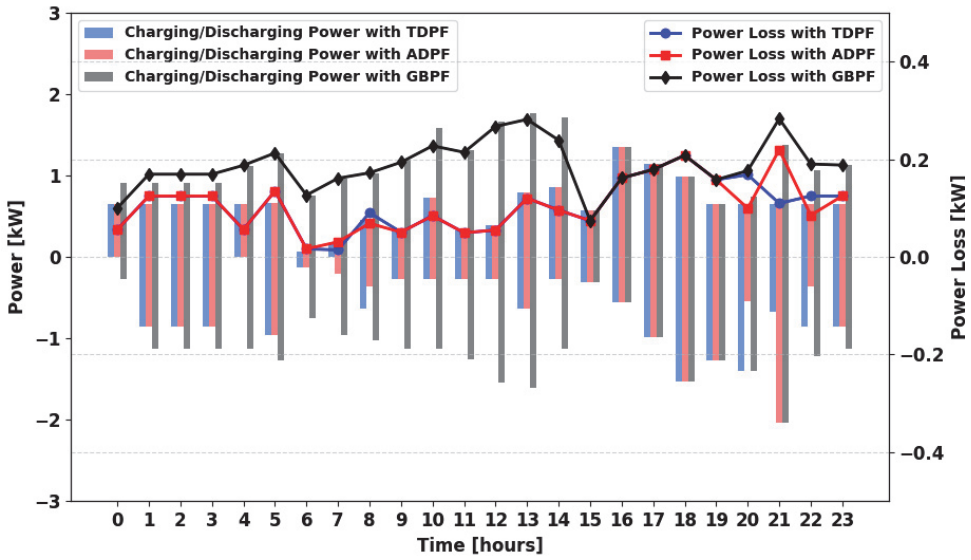


Figure 28. Power loss in summer with MPFA/S.

For the autumn season, Figures 32–35 present the charging/discharging profile and power loss. Similar to summer, MPFA/S experiences high losses due to frequent charging/discharging. With grid support, GBPF reduces storage cycling and typically yields the lowest storage-related losses while ensuring 100% demand satisfaction. In MPFA/SG, power loss remains similar across all algorithms. In MPFA/MG, ADPF has lower losses than TDPF, while in MPFA/MSG, TDPF exhibits higher losses compared to ADPF, and GBPF maintains the lowest losses.

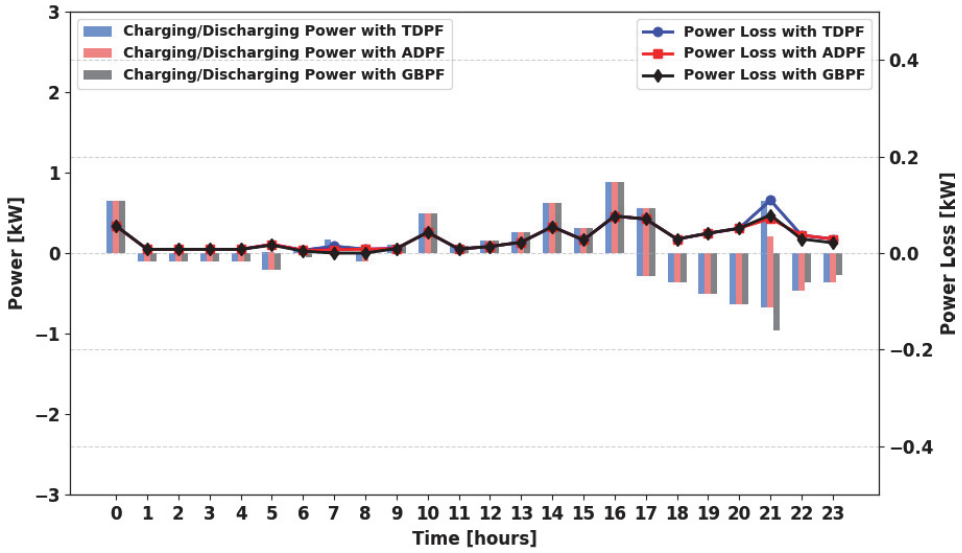


Figure 29. Power loss in summer with MPFA/SG.

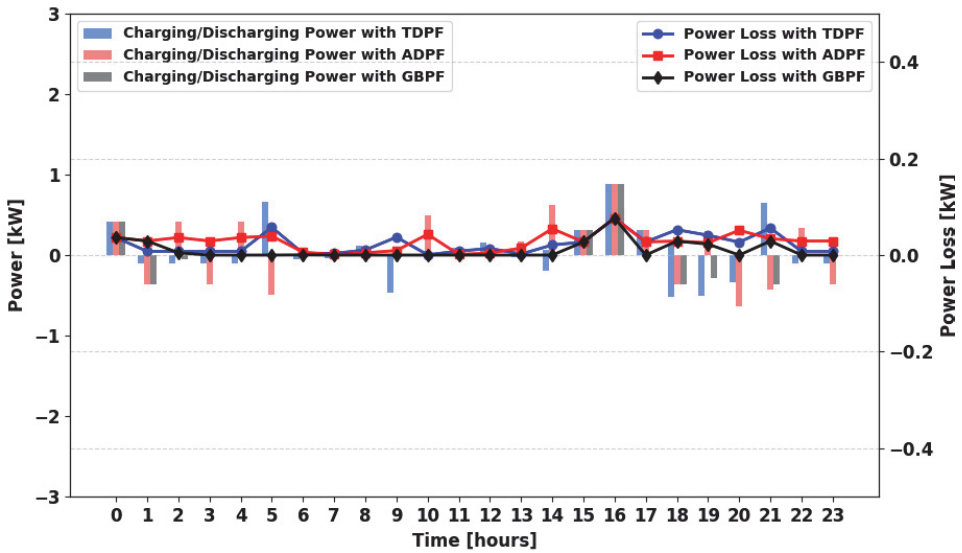


Figure 30. Power loss in summer with MPFA/MG.

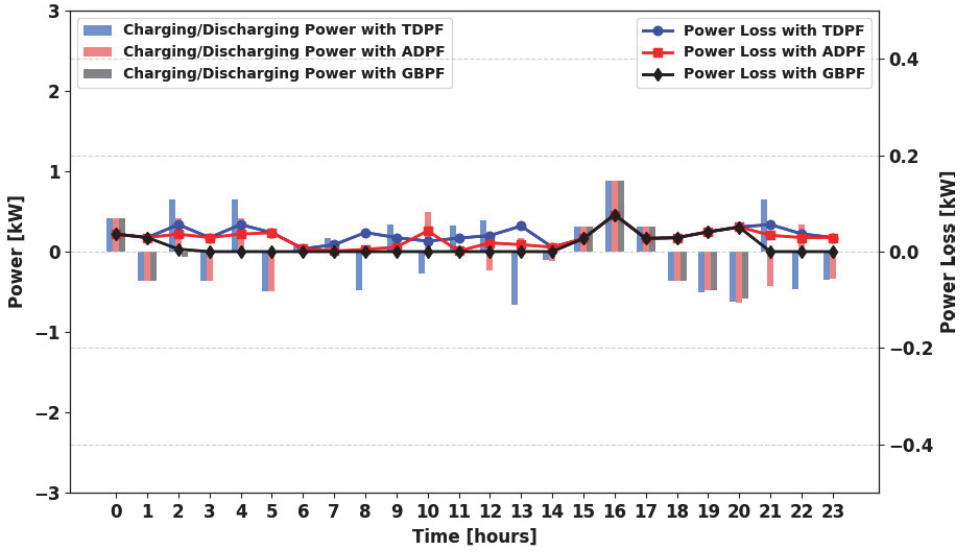


Figure 31. Power loss in summer with MPFA/MSG.

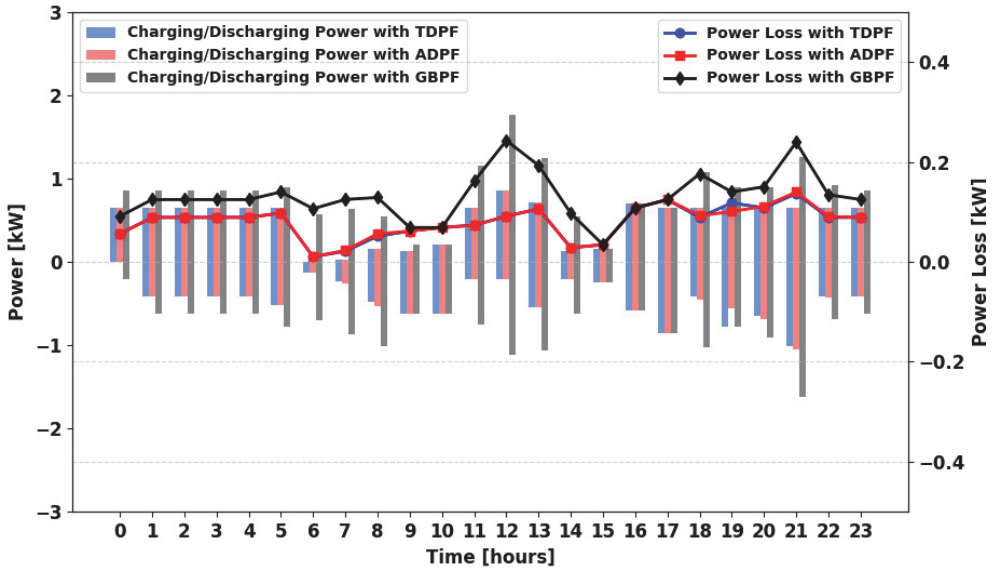


Figure 32. Power loss in autumn with MPFA/S.

For the spring season, Figures 36–39 show the charging/discharging profile and power loss. In MPFA/S, TDPF experiences the lowest losses due to lower demand satisfaction, ADPF has moderate losses, and GBPF achieves full demand satisfaction and generally the lowest storage-related losses; in spring, all three methods show similar losses due to ample RES supply. In MPFA/SG and MPFA/MSG, losses remain similar across algorithms due to the lower demand compared to supply. In MPFA/MG, GBPF outperforms the other two algorithms in minimizing power loss.

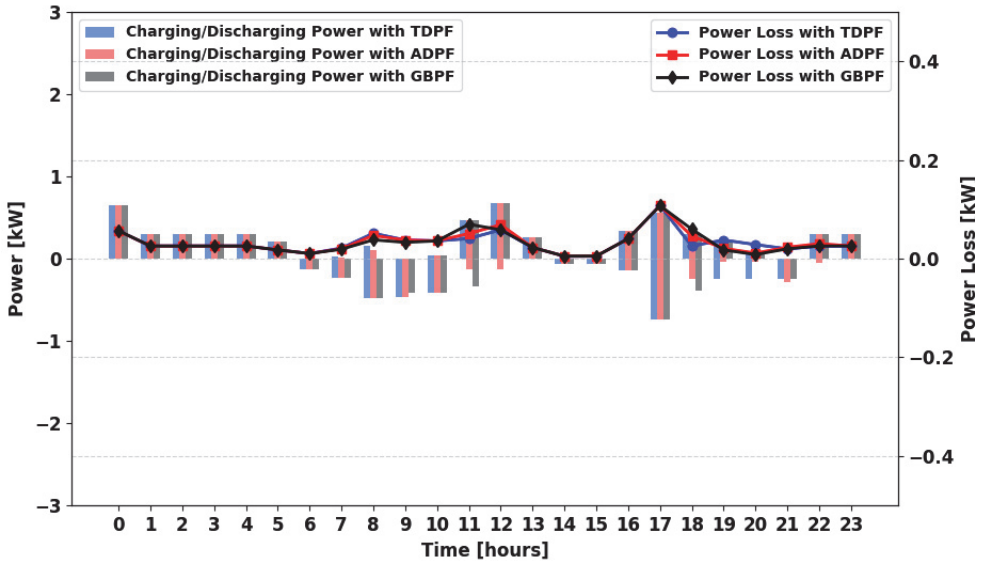


Figure 33. Power loss in autumn with MPFA/SG.

The comparative analysis in Figure 40 for the winter season shows that MPFA/SG achieves an energy loss reduction of 71.64% compared to MPFA/S, while MPFA/MG further reduces energy loss by 30.06% compared to MPFA/SG. The MPFA/MSG scenario provides an additional 9.61% reduction in energy loss compared to MPFA/MG. Regarding algorithm performance, in the MPFA/MSG scenario, the ADPF algorithm reduces energy loss by 32.47% compared to TDPF, whereas GBPF achieves a substantial 80.09% reduction in energy loss relative to ADPF. These results emphasize that energy loss is minimized as more

generation and storage units are incorporated into the system. Moreover, GBPF consistently outperforms other algorithms in reducing energy losses due to its ability to supplement local power with the grid, leading to a more efficient energy distribution strategy.

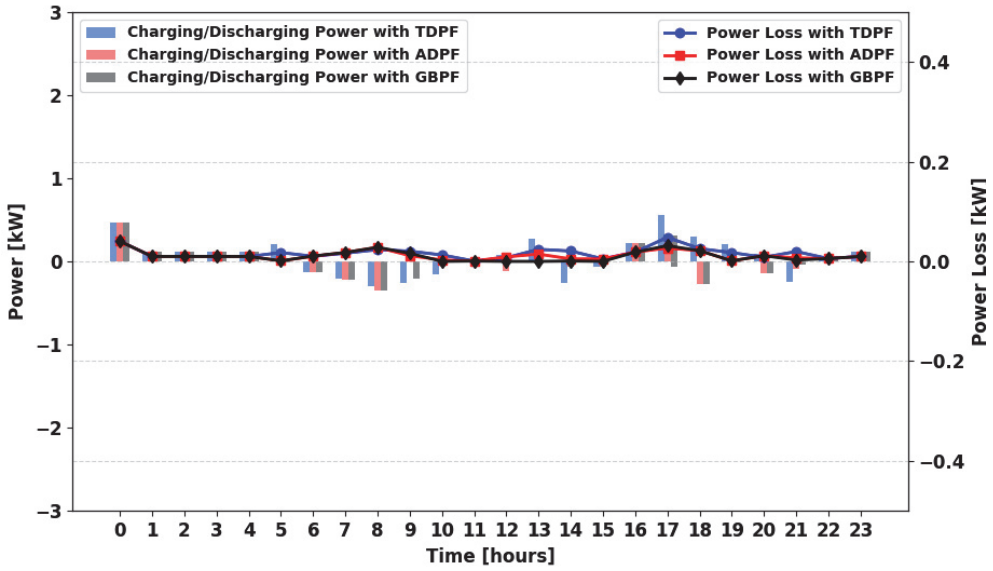


Figure 34. Power loss in autumn with MPFA/MG.

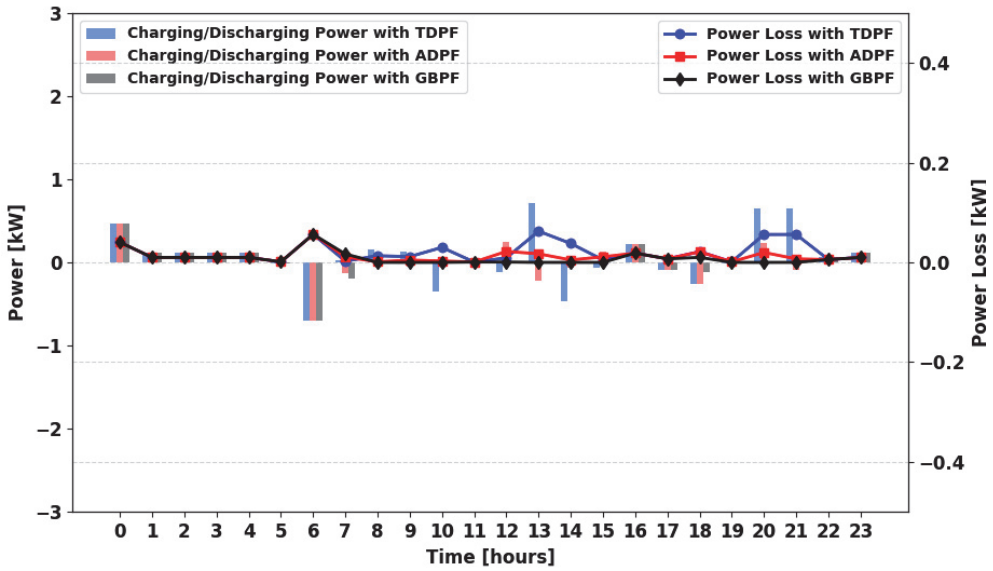


Figure 35. Power loss in autumn with MPFA/MSG.

For the summer season (Figure 41), MPFA/SG achieves a 77.38% energy loss reduction compared to MPFA/S, while MPFA/MG further reduces energy losses by 31.34% relative to MPFA/SG. In the MPFA/MSG scenario, ADPF reduces energy losses by 48.94% compared to TDPF, while GBPF achieves a 51.06% energy loss reduction compared to ADPF.

For the autumn season (Figure 42), MPFA/SG reduces energy losses by 66.60% compared to MPFA/S, and MPFA/MG achieves an additional 59.82% energy loss reduction relative to MPFA/SG. In MPFA/MSG, ADPF outperforms TDPF with a 68.20% energy loss reduction, while GBPF reduces energy losses by 31.80% compared to ADPF.

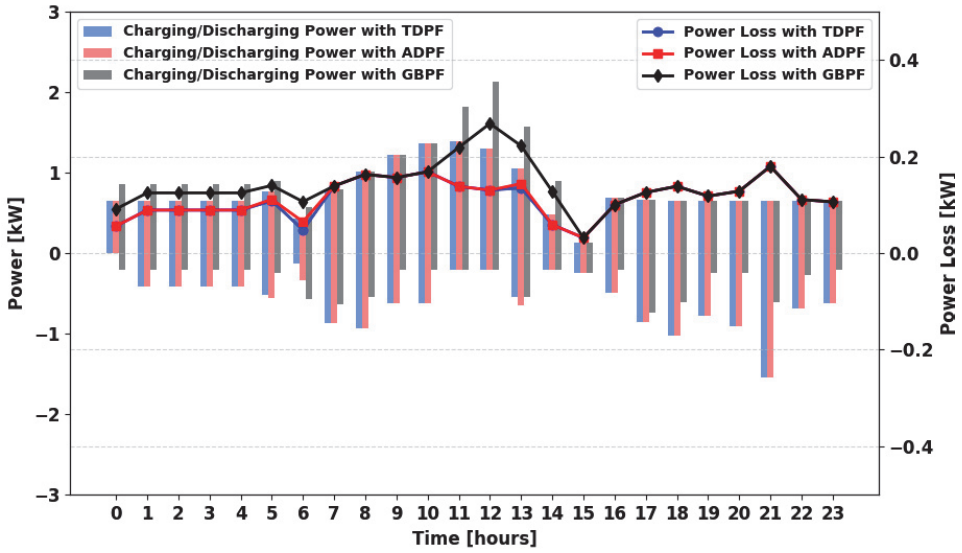


Figure 36. Power loss in spring with MPFA/S.

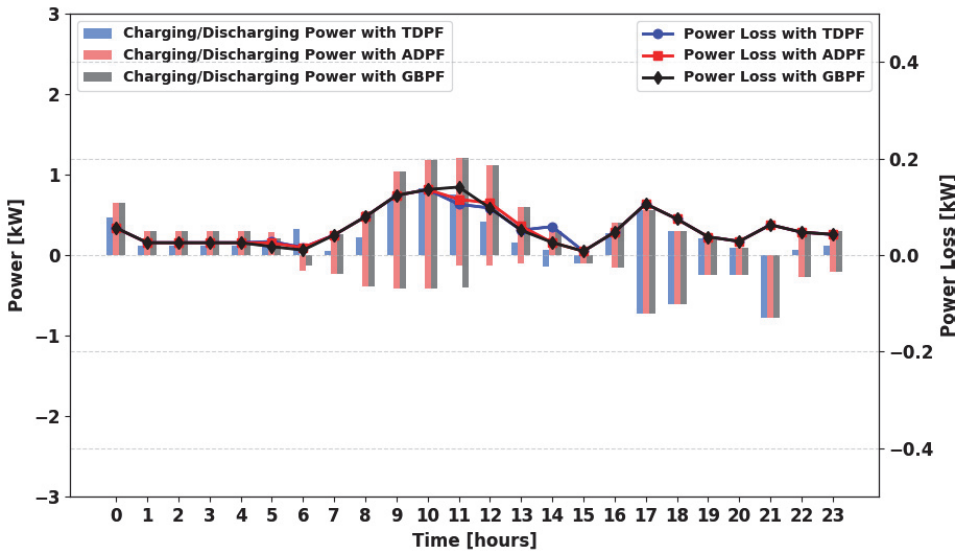


Figure 37. Power loss in spring with MPFA/SG.

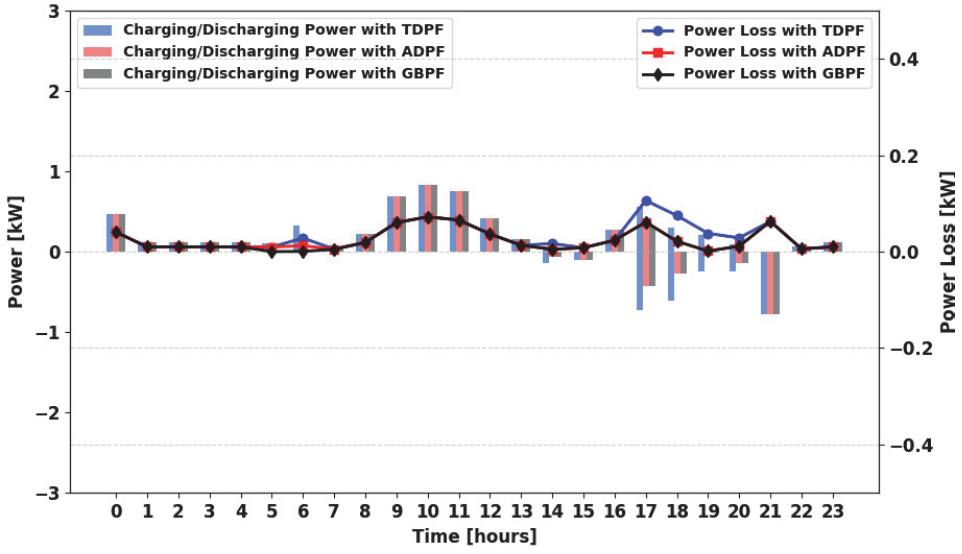


Figure 38. Power loss in spring with MPFA/MG.

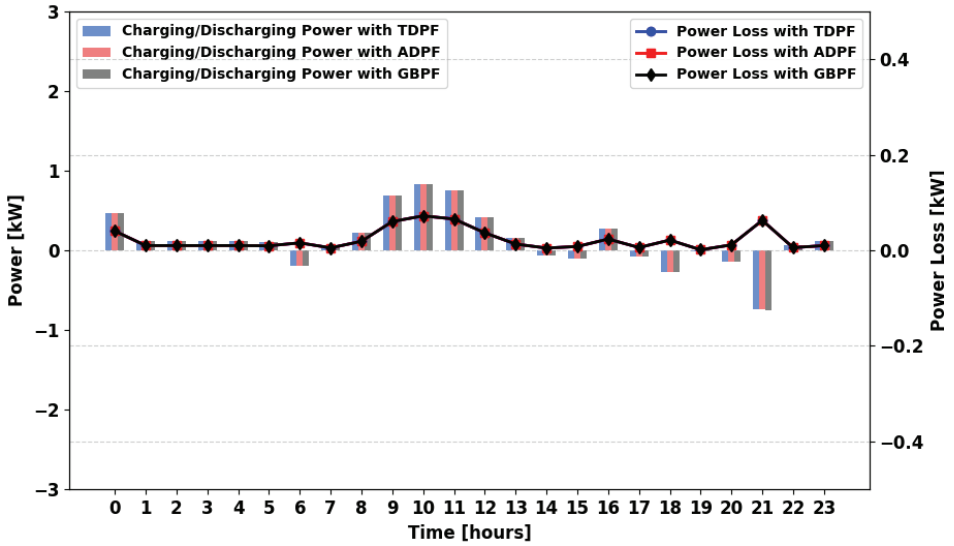


Figure 39. Power loss in spring with MPFA/MSG.

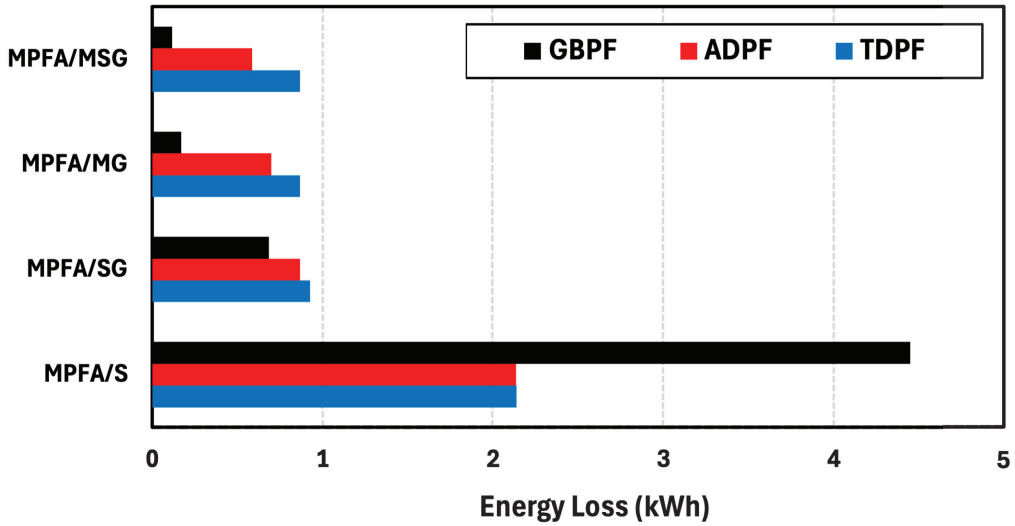


Figure 40. Energy loss for DPFS in winter.

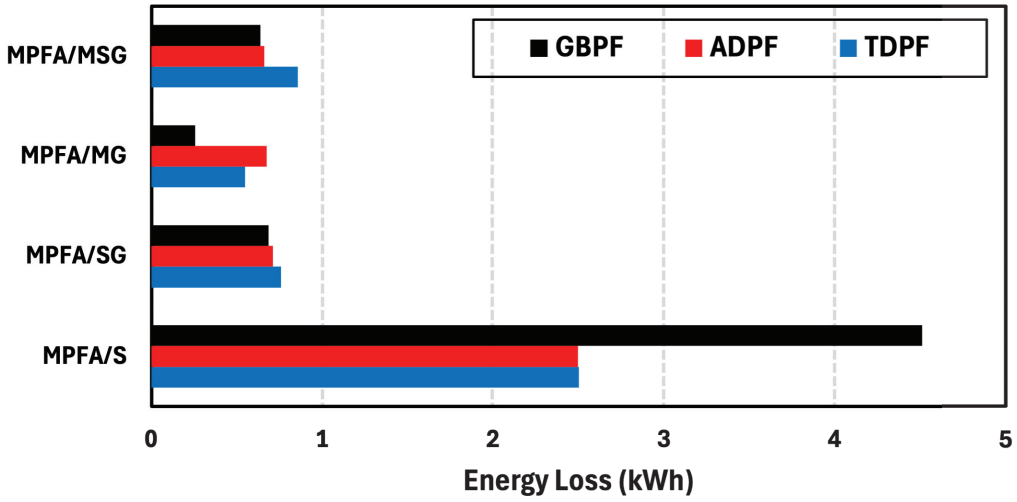


Figure 41. Energy loss for DPFS in summer.

For the spring season (Figure 43), MPFA/SG achieves a 53.94% energy loss reduction compared to MPFA/S, while MPFA/MG reduces energy losses by 52.73% relative to MPFA/SG. Additionally, MPFA/MSG achieves a 16.49% energy loss reduction compared to MPFA/MG. In this scenario, all three algorithms exhibit similar energy losses due to power consumption being lower than the available RES power supply.

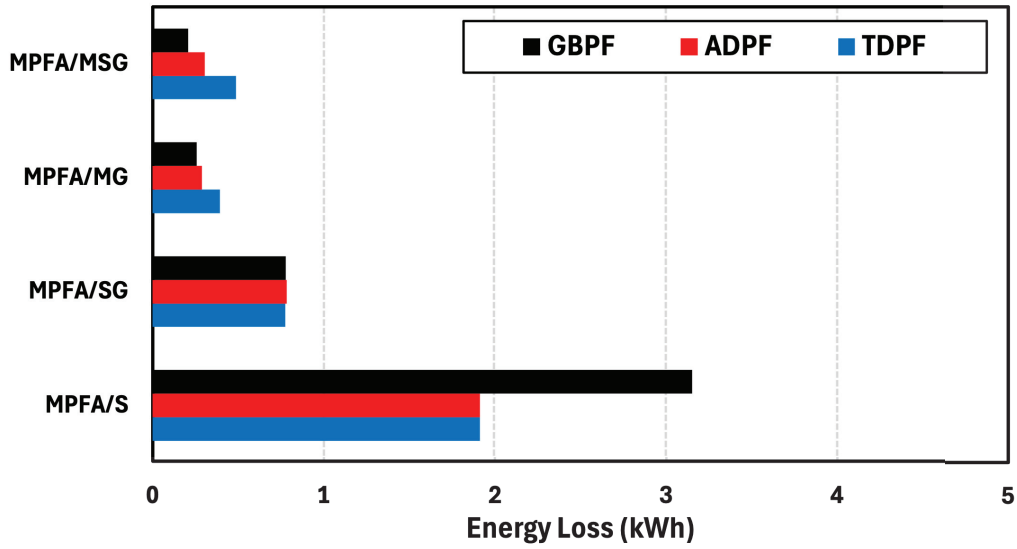


Figure 42. Energy loss for DPFS in autumn.

5.4. Cross-Season Summary

Across seasons, enlarging MPFA connectivity (S → SG → MG → MSG) consistently lowers storage-related energy losses and raises demand satisfaction. GBPF guarantees full daily demand and the lowest storage-related losses in most cases due to reduced cycling. ADPF outperforms TDPF under constrained local supply by prioritizing critical loads and smoothing storage usage. To avoid redundancy, detailed hour-by-hour plots are retained in the figures, while aggregate comparisons (daily energy demanded/supplied, daily energy loss, storage throughput) are summarized here.

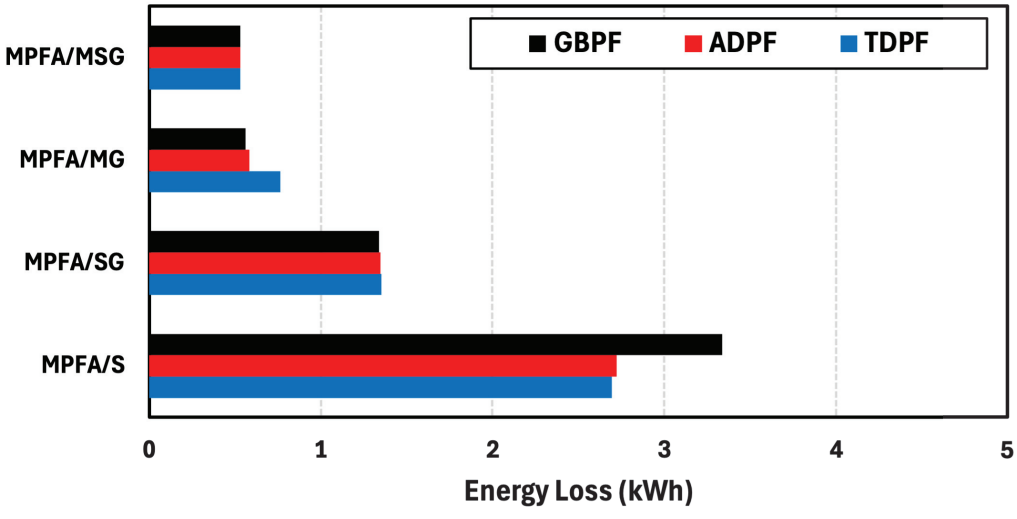


Figure 43. Energy loss for DPFS in spring.

5.5. Statistical Validation (Supplement)

We computed daily aggregates over multiple representative days per season. Variability across days (mean $\pm$ std) for demand satisfaction, daily energy loss, and storage throughput is provided in [8]; no material changes to the rank ordering of methods were observed.

5.6. Overall Results

The comprehensive numerical simulations demonstrate that the proposed MPFA approach, in conjunction with advanced power flow algorithms, significantly enhances the operational efficiency and reliability of smart home distributed power flow systems.

Across all seasonal scenarios, integrating multiple power generation sources and storage units proved crucial in minimizing storage-related losses and ensuring consistent demand fulfillment. Notably, the GBPF algorithm consistently achieved complete daily demand satisfaction; with grid support, it often reduces battery cycling and hence storage-related losses, though total imported energy can increase when RES are scarce. The ADPF algorithm also exhibited strong performance—especially when grid support is limited—by dynamically prioritizing loads and optimizing storage utilization and allocation. Furthermore, the results highlight the importance of leveraging renewable energy resources, optimizing connectivity among appliances, and deploying intelligent control algorithms to ensure stable and efficient power delivery under varying seasonal and operational conditions. Overall, the study validates the effectiveness of the MPFA framework and provides valuable insights for the design of future smart home energy management systems that prioritize sustainability, resilience, and cost-effectiveness.

5.7. Limitations and Practical Considerations

Large-scale hardware-in-the-loop (HIL) verification and dynamic grid-event testing are pending. Battery and hydrogen-system degradation were modeled empirically; converter and thermal losses beyond η_c, η_d are neglected. Cost modeling and scalability to larger feeder-level deployments are not included. Implementation-wise, GBPF requires reliable grid availability and metering; ADPF requires priority configuration and limited communications; both are compatible with edge controllers.

6. Conclusions and Future Work

This paper has presented a comprehensive investigation of power flow assignment scenarios and power flow algorithms within the DPFS for smart homes. Four distinct power-flow assignment scenarios—MPFA/S, MPFA/SG, MPFA/MG, and MPFA/MSG—were evaluated, each representing different logical interconnections between PGs, PLs, and PSs. The simulation framework incorporated real experimental data and accounted for seasonal variations to evaluate system performance under realistic and dynamic operating conditions. Simulation results consistently demonstrated that as the logical connectivity among generators, loads, and storage units is enhanced, particularly in the MPFA/MSG scenario, both power losses are minimized and demand satisfaction improves. Among the analyzed algorithms, the GBPF approach achieved the highest levels of demand fulfillment. It exhibited the lowest power losses across all scenarios and seasons, leveraging grid integration to ensure a reliable supply. The ADPF algorithm also provided significant improvements in power allocation efficiency and storage utilization, resulting in reduced user discomfort compared to the TDPF method, especially under supply-constrained conditions.

Overall, the findings highlight the importance of adopting multi-source, multi-storage power flow strategies and intelligent algorithmic control to optimize energy utilization, minimize losses, and enhance the reliability and resilience of smart home energy systems. The study offers a practical framework and actionable insights for future smart home energy management solutions, particularly as the share of RESs and distributed resources continues to rise. Future work includes: (i) optimization-based MPFA dispatch with explicit cost terms (tariffs, degradation), (ii) HIL validation under real grid events, (iii) stochastic PV/FC forecasts and uncertainty-aware scheduling, and (iv) scalability tests on multi-home feeders with communication delays and cyber-physical constraints.

Author Contributions: Conceptualization, S.M., S.J. and Y.L.; writing—original draft preparation, S.M.; writing—review and editing, S.M., S.J., I.I. and Y.L.; supervision, S.J., Y.L., I.I. and Y.T. All authors have read and agreed to the published version of the manuscript.

Funding: This research received no external funding.

Data Availability Statement: The original contributions presented in the study are included in the article, further inquiries can be directed to the corresponding author.

Acknowledgments: The authors have reviewed and edited the output and take full responsibility for the content of this publication.

Conflicts of Interest: The authors declare no conflicts of interest.

Abbreviations

The following abbreviations are used in this manuscript:

RES	Renewable energy sources
ESS	Energy storage system
BESS	Battery energy storage system
DPFS	Distributed power flow system
HAD	Home appliances and devices
PGs	Power generators
PLs	Power loads
PSs	Power storage systems
PV	Photovoltaic
FC	Fuel cell
UG	Utility grid
SoC	State of charge
MPFA	Multiple-Load Power-Flow Assignment
MPFA/S	Multiple-Load Power-Flow Assignment with single PS
MPFA/SG	Multiple-Load Power-Flow Assignment with single PG
MPFA/MG	Multiple-Load Power-Flow Assignment with multiple PGs
MPFA/MSG	Multiple-Load Power-Flow Assignment with multiple PGs and PSs
TDPF	Total-Demand-Based Power Flow algorithm
ADPF	Adaptive-Demand-Based Power Flow algorithm
GBPF	Grid-Based Power Flow algorithm

Nomenclature

The following nomenclature is used in this manuscript:

$PG_j^f(t)$	Fluctuating power generation
$PG_j^c(t)$	Controllable power generation

j	Index of PGs, $j = 1, \ldots, n_{PG}$
$PL_k^f(t)$	Fluctuating power loads
k	Index of PLs, $k = 1, \ldots, n_{PL}$
h	Index of PSs, $h = 1, \ldots, n_{PS}$
$\mathcal{P}_{\mathrm{PG}}(t)$	Power generation at time t
$\mathcal{P}_{\mathrm{PL}}(t)$	Power consumption at time t
$\mathcal{P}_{\mathrm{grid}}(t)$	Grid power at time t
$P_{\mathrm{loss,tot}}(t)$	Aggregate storage-related power loss at the bus at time t
$E_{\mathrm{PS}_h}^{ini}$	Initial energy stored of hth PS
$E_{\mathrm{PS}_h}(t)$	Energy stored of hth PS at time t
$\mathcal{P}_{\mathrm{PS}_h^{in}}(t)$	Charging power of hth PS at time t
$\mathcal{P}_{\mathrm{PS}_h^{out}}(t)$	Discharging power of hth PS at time t
$SoC_h(t)$	State of charge of hth PS at time t
SoC_h^{ini}	Initial state of charge of hth PS
SoC_h^{min}	Minimum state of charge of hth PS
SoC_h^{max}	Maximum state of charge of hth PS
$\mathcal{P}^{\min}_{\mathrm{PS}_h^{in}}$	Minimum charging power of hth PS
$\mathcal{P}^{\max}_{\mathrm{PS}_h^{in}}$	Maximum charging power of hth PS
$\mathcal{P}^{\min}_{\mathrm{PS}_h^{out}}$	Minimum discharging power of hth PS
$\mathcal{P}^{\max}_{\mathrm{PS}_h^{out}}$	Maximum discharging power of hth PS
$P_{loss}^{h_c}(t)$	Charging loss of hth PS at time t
$P_{loss}^{h_d}(t)$	Discharging loss of hth PS at time t
η_c	Charging efficiency of power storage
η_d	Discharging efficiency of power storage
$E_{PG_j^c}$	Cumulative energy of controllable power generation
$E_{PG_j^f}$	Cumulative energy of fluctuating power generation
$E_{PL_k^c}$	Cumulative energy of controllable power consumption
$E_{PL_k^f}$	Cumulative energy of fluctuating power consumption

References

1. Prakash, S.; Al Zaabi, O.; Behera, R.K.; Al Jaafari, K.; Al Hosani, K.; Muduli, U.R. Modeling and Dynamic Stability Analysis of the Grid-Following Inverter Integrated With Photovoltaics. *IEEE J. Emerg. Sel. Top. Power Electron.* **2023**, *11*, 3788–3802. [CrossRef]
2. Tailor, R.; Conka, Z.; Kolcun, M.; Bena, L. Electric Energy Flow Algorithm for Household in Smart Street Development. In Proceedings of the 2020 IEEE 3rd International Conference and Workshop in Obuda on Electrical and Power Engineering (CANDO-EPE), Budapest, Hungary, 18–19 November 2020; IEEE: Piscataway, NJ, USA, 2020; pp. 73–78. [CrossRef]
3. Han, B.; Zahraoui, Y.; Mubin, M.; Mekhilef, S.; Seyedmahmoudian, M.; Stojcevski, A. Home Energy Management Systems: A Review of the Concept, Architecture, and Scheduling Strategies. *IEEE Access* **2023**, *11*, 19999–20025. [CrossRef]
4. Sarker, S.; Rakib, M.A.; Islam, S.; Shafin, S.S. An IoT-based Smart Grid Technology: Bidirectional Power Flow, Smart Energy Metering, and Home Automation. In Proceedings of the 2021 International Conference on Maintenance and Intelligent Asset Management (ICMIAM), Ballarat, Australia, 12–15 December 2021; IEEE: Piscataway, NJ, USA, 2021; pp. 1–6. [CrossRef]
5. Lanouar, L.; Rekik, M.; Bouchaala, O.; Krichen, L. An optimal power supervising strategy for a smart home assessed based on BPMN Framework. In Proceedings of the 2020 21st International Conference on Sciences and Techniques of Automatic Control and Computer Engineering (STA), Monastir, Tunisia, 20–22 March 2020; IEEE: Piscataway, NJ, USA, 2020; pp. 406–411. [CrossRef]
6. Impram, S.; Varbak Nese, S.; Oral, B. Challenges of renewable energy penetration on power system flexibility: A survey. *Energy Strategy Rev.* **2020**, *31*, 100539. [CrossRef]
7. Javaid, S.; Lim, Y.; Tan, Y.; Ioannou, I.I. Safety-Based Optimal Storage Capacity Sizing for Power System with Renewable Energy Sources. In Proceedings of the 2024 20th International Conference on Distributed Computing in Smart Systems and the Internet of Things (DCOSS-IoT), Abu Dhabi, United Arab Emirates, 29 April–1 May 2024; IEEE: Piscataway, NJ, USA, 2024; pp. 462–468. [CrossRef]
8. Ioannou, I.; Javaid, S.; Tan, Y.; Vassiliou, V. Autonomous Reinforcement Learning for Intelligent and Sustainable Autonomous Microgrid Energy Management. *Electronics* **2025**, *14*, 2691. [CrossRef]

9. Karanja, J.M.; Hinga, P.K.; Ngoo, L.M.; Muriithi, C.M. Optimal Battery Location for Minimizing the Total Cost of Generation in a Power System. In Proceedings of the 2020 IEEE PES/IAS PowerAfrica, Nairobi, Kenya, 25–28 August 2020; IEEE: Piscataway, NJ, USA, 2020; pp. 1–5. [CrossRef]
10. Lim, Y.; Javaid, S.; Tan, Y.; Khwanrit, R. Minimizing Energy Loss for Multiple Load Power Flow Assignment in Smart Homes. In Proceedings of the 2023 International Conference on Energy, Power, Environment, Control, and Computing (ICEPECC), Gujrat, Pakistan, 8–9 March 2023; pp. 1–6. [CrossRef]
11. Hu, B.; Zhao, Z.; Jian, J.; Chen, Q.; Zhang, S.; Wang, L.; Yu, C.; Wang, Y.; Jiao, Y.; Xu, Y. Intelligent Power Trading Optimization Control System Based on Cloud-Cluster-Client Collaborative Architecture. In Proceedings of the 2024 IEEE 7th International Electrical and Energy Conference (CIEEC), Harbin, China, 10–12 May 2024; IEEE: Piscataway, NJ, USA, 2024; pp. 3633–3638. [CrossRef]
12. Li, H.; Eseye, A.T.; Zhang, J.; Zheng, D. Optimal energy management for industrial microgrids with high-penetration renewables. *Prot. Control Mod. Power Syst.* **2017**, *2*, 12. [CrossRef]
13. Alsolami, M.; Alferidi, A.; Lami, B. Real-Time Energy Management of a Microgrid Using MPC-DDQN-Controlled V2H and H2V Operations with Renewable Energy Integration. *Energies* **2025**, *18*, 4622. [CrossRef]
14. Marcos, J.; García, M.; Marroyo, L.; Lorenzo, E. Control Strategies to Smooth Short-Term Power Fluctuations in Large PV Plants Using Storage. *Energies* **2014**, *7*, 6593–6619. [CrossRef]
15. Ma, W.; Ma, M.; Li, Y.; Wang, C.; Li, Z.; Chen, Z. Control Strategy of a Hybrid Energy Storage System to Smooth Photovoltaic Power Fluctuations Considering Photovoltaic Output Power Curtailment. *Sustainability* **2019**, *11*, 1324. [CrossRef]
16. Zhao Zhen, Xuemin Zhang, Shengwei Mei, Xiqiang Chang, Hua Chai, Rui Yin, Fei Wang Ultra-short-term irradiance forecasting model based onground-based cloud image and deep learning algorithm and Deep Learning for Ramp-Rate Control. *IET Renew. Power Gener.* **2021**, *38*, 1825–1837. [CrossRef]
17. Gong, H.; Rallabandi, V.; McIntyre, M.L.; Ionel, D.M. On the Optimal Energy Controls for Large Scale Residential Communities including Smart Homes. In Proceedings of the 2019 IEEE Energy Conversion Congress and Exposition (ECCE), Baltimore, MD, USA, 29 September–3 October 2019; IEEE: Piscataway, NJ, USA, 2019; pp. 503–507. [CrossRef]
18. Cardenas, A.; Swinfen-Styles, L.; Rouse, J.; Garvey, S.D. Optimal sizing of battery energy storage systems for hybrid renewable energy system design. *J. Energy Storage* **2022**, *52*, 104774. [CrossRef]
19. Baidowi, P.A.; Mujaiyid, Z.; Hakim, M.D.; Nazrin, I.G.; Ramly, R.; Mohd Isa, M.R.; Darus, M.Y. Low-cost Modular Smart Home Controlling System for Minimising Energy Consumption: A Conceptual Study. In Proceedings of the 2022 International Visualization, Informatics and Technology Conference (IVIT), Kuala Lumpur, Malaysia, 1–2 November 2022; IEEE: Piscataway, NJ, USA, 2022; pp. 284–287. [CrossRef]
20. Wang, L.; Tian, W.; Madawala, U.K.; Yang, J. A Power Selective Control of Versatile Wireless Vehicle-Grid-Home Power Interface (VW–VGH–PI). In Proceedings of the 2021 IEEE Southern Power Electronics Conference (SPEC), Kigali, Rwanda, 6–9 December 2021; IEEE: Piscataway, NJ, USA, 2021; pp. 1–5. [CrossRef]
21. Brinkel, N.B.G.; Gerritsma, M.K.; AlSkaif, T.A.; Lampropoulos, I.; van Voorden, A.M.; Fidder, H.A.; van Sark, W.G.J.H.M. Impact of rapid PV fluctuations on power quality in the low-voltage grid and mitigation strategies using electric vehicles. *Int. J. Electr. Power Energy Syst.* **2020**, *118*, 105741. [CrossRef]
22. Samende, C.; Bhagavathy, S.M.; McCulloch, M. State of Charge Based Droop Control for Coordinated Power Exchange in Low Voltage DC Nanogrids. In Proceedings of the 2019 IEEE 13th International Conference on Power Electronics and Drive Systems (PEDS), Toulouse, France, 9–12 July 2019; IEEE: Piscataway, NJ, USA, 2019; pp. 1–6. [CrossRef]
23. Khan, O.; Abulanwar, S.; Aziz, M.; Khan, I.A. Voltage Regulation and Power Management of DC Nanogrids Using Adaptive Droop Control. In Proceedings of the 2020 IEEE International Conference on Power Electronics, Drives and Energy Systems (PEDES), Jaipur, India, 16–19 December 2020; IEEE: Piscataway, NJ, USA, 2020; pp. 1–6. [CrossRef]
24. Arsalan, A.; Ahmad, J.; Tahir, M.; Mazumder, S.K. Distributed Control and Power Management of Islanded DC Nanogrids with Applications to Rural Electrification. In Proceedings of the 2020 IEEE Energy Conversion Congress and Exposition (ECCE), Detroit, MI, USA, 11–15 October 2020; IEEE: Piscataway, NJ, USA, 2020; pp. 4662–4667. [CrossRef]
25. Ouammi, A.; Dagdougui, H.; Dessaint, L.; Sacile, R. Coordinated Model Predictive-Based Power Flows Control in a Cooperative Network of Smart Microgrids. *IEEE Trans. Smart Grid* **2015**, *6*, 2233–2244. [CrossRef]
26. Cui, C.; Xue, J. Energy and Comfort Aware Operation of Multi-Zone HVAC System Through Preference-Inspired Deep Reinforcement Learning. *Energy* **2024**, *292*, 130505. [CrossRef]
27. Fiorotti, R.; Fardin, J.F.; Rocha, H.R.O.; Rua, D.; Lopes, J.A.P. Day-ahead optimal scheduling considering thermal and electrical energy management in smart homes with photovoltaic–thermal systems. *Appl. Energy* **2024**, *374*, 124070. [CrossRef]

28. Liao, W.; Xiao, F.; Li, Y.; Zhang, H.; Peng, J. A comparative study of demand-side energy management strategies for building integrated photovoltaics-battery and electric vehicles (EVs) in diversified building communities. *Appl. Energy* **2024**, *361*, 122881. [CrossRef]
29. Wei, G.; Chi, M.; Liu, Z.W.; Ge, M.F.; Li, C.; Liu, X. Deep Reinforcement Learning for Real-Time Energy Management in Smart Home. *IEEE Syst. J.* **2023**, *17*, 2489–2499. [CrossRef]
30. Wang, Q.; Ping, P.; Zhao, X.; Chu, G.; Sun, J.; Chen, C. Thermal runaway caused fire and explosion of lithium ion battery. *J. Power Sources* **2012**, *208*, 210–224. [CrossRef]
31. Feng, X.; Ouyang, M.; Liu, X.; Lu, L.; Xia, Y.; He, X. Thermal runaway mechanism of lithium ion battery for electric vehicles: A review. *Energy Storage Mater.* **2018**, *10*, 246–267. [CrossRef]
32. Caminiti, C.M.; Merlo, M.; Fotouhi Ghazvini, M.A.; Edvinsson, J. optimHome: A Shrinking Horizon Control Architecture for Bidirectional Smart Charging in Home Energy Management Systems. *Energies* **2024**, *17*, 1963. [CrossRef]
33. Wang, Y.; Chen, K.S.; Mishler, J.; Cho, S.C.; Adroher, X.C. PEM fuel cell and electrolysis cell technologies: Current status and challenges. *Energy Environ. Sci.* **2022**, *15*, 1908–1959. [CrossRef]
34. Li, X.; Ye, T.; Meng, X.; He, D.; Li, L.; Song, K.; Jiang, J.; Sun, C. Advances in the Application of Sulfonated Poly(Ether Ether Ketone) (SPEEK) and Its Organic Composite Membranes for Proton Exchange Membrane Fuel Cells (PEMFCs). *Polymers* **2024**, *16*, 2840. [CrossRef]
35. Bielecki, A.; Ernst, S.; Skorek-Osikowska, A. The potential of Power-to-Hydrogen technology in the Visegrad Group region. *Int. J. Hydrog. Energy* **2021**, *46*, 29337–29356. [CrossRef]
36. Che, Y.; Hu, X.; Lin, X.; Guo, J.; Teodorescu, R. Health prognostics for lithium-ion batteries: Mechanisms, methods, and prospects. *Energy Environ. Sci.* **2023**, *16*, 338–371. [CrossRef]
37. Perera, M.K and Disanayaka, R.U.I and Kumara, E.M.C.S and Walisundara, W.M.C.S.B.; Priyadarshana, H.V.V.; Ekanayake, E.M.A.G.N.C.; Hemapala, K.T.M.U. Multi Agent Based Energy Management System for Microgrids. In Proceedings of the IEEE 9th Power India International Conference (PIICON), Sonepat, India, 28 February–1 March 2020. [CrossRef]

Disclaimer/Publisher's Note: The statements, opinions and data contained in all publications are solely those of the individual author(s) and contributor(s) and not of MDPI and/or the editor(s). MDPI and/or the editor(s) disclaim responsibility for any injury to people or property resulting from any ideas, methods, instructions or products referred to in the content. MDPI stays neutral with regard to jurisdictional claims in published maps and institutional affiliations.

energies

MDPI

Article

Forecast-Driven Climate Control for Smart Greenhouses: Energy Optimization Using LSTM Model

Abdulaziz Aborujilah [1], Mohammed Al-Sarem [2,3,*] and Marwan Alabed Abu-Zanona [4,*]

[1] Department of Management Information System, College of Commerce & Business Administration, Dhofar University, Salalah 211, Oman; aaborujilah@du.edu.om
[2] College of Computer Science and Engineering, Taibah University, Medina 41477, Saudi Arabia
[3] Energy, Industry, and Advanced Technologies Research Center, Taibah University, Madinah 41477, Saudi Arabia
[4] Department of Management Information Systems, King Faisal University, Al-Ahsa 31982, Saudi Arabia
* Correspondence: msarem@taibahu.edu.sa (M.A.-S.); mabozanoneh@kfu.edu.sa (M.A.A.-Z.)

Abstract

Greenhouses play a vital role in modern agriculture by providing controlled environments for year-round crop production. However, climate regulation within these structures accounts for a significant portion of their energy consumption, often exceeding 50% of operational costs. Current greenhouse systems predominantly rely on reactive control strategies, leading to energy inefficiency and unstable internal conditions. Addressing this gap, the present study develops a machine learning-based framework that leverages time series forecasting models—specifically Long Short-Term Memory (LSTM)—that predict key climate parameters and generate optimal actuator control recommendations. The system utilizes multivariate environmental data to forecast temperature, humidity, and CO_2 levels and minimize a composite energy proxy through proactive adjustments to heating, ventilation, and lighting systems. Experimental results demonstrate high prediction accuracy (R^2 = 0.9835) and significant improvements in energy efficiency. By integrating predictive analytics with real-time sensor feedback, the proposed approach supports intelligent, energy-aware decision-making and advances the development of smart agriculture through proactive greenhouse climate management.

Keywords: smart greenhouse; climate control optimization; time series forecasting; machine learning; LSTM neural networks; energy-efficient agriculture

1. Introduction

In modern agriculture, greenhouses are very useful as they offer controlled conditions for plant growth and increase productivity. They provide proper temperatures, humidity, light, and CO_2 levels for plant growth [1–3]. This enables cropping throughout the year irrespective of the outside weather [3]. Additionally, greenhouses protect crops from adverse climatic events, leading to improved crop quality and enhanced production [4,5]. Within greenhouses, climate control plays a decisive role in optimizing growth, improving yield, and maintaining high standards of quality, along with auguring greater technological integration. The importance of maintaining optimal temperature is critical since different crops have distinct thermal requirements during various growth phases [4]. In addition, the incorporation of renewable solar and geothermal energy systems enhances

the energy performance and lowers operational expenditure [6,7]. Controlling humidity is crucial for disease control [4,8], maintaining transpiration, and nutrient absorption essential to plant health [9]. Elevated CO_2 concentrations also increase photosynthesis and productivity [4,10], and automated systems can economize CO_2 in relation to yield profits [4]. Artificial lighting facilitates off-season production [11,12], and cost-effective lighting aids in energy conservation [13,14]. Greenhouses have integrated advanced sensors and real-data monitoring which enable access to automated integrated climate control systems [4,6]. These systems use refined algorithms such as neural networks, fuzzy logic, and predictive control for customizable, accurate regulation [6,15]. All these advancements reduce the amount of energy consumed, resources used, and overall negative impact on the environment which, in turn, promotes economic productivity and environmental health [4,6,13,16,17]. Furthermore, these innovations facilitate the adoption of climate-resilient agricultural systems [6,13]. Although these technologies offer multiple benefits, the current control systems in greenhouses heavily rely on reactive strategies, which result in enormous energy losses and inadequate conditions for plant development. Greenhouses have high energy consumption, especially those designed for off-season cultivation. Heating, cooling, and lighting systems can account for up to 50% of total production costs [18,19]. Increased operational costs occur due to fossil fuel dependency, the emission of greenhouse gases, and climate change [13,20]. One of the major inefficiencies of ventilation-induced heat loss can be solved with more modern techniques, such as air handling units, borehole thermal storage, and heat pumps [21]. Other technologies such as phase change materials (PCMs) have also proven to be effective by lowering gas consumption by 23.7% [6,7]. Internal environments in a house that are maintained by reactive control strategies tend to fail, which is harmful to plant growth. Uncontrolled temperature and moisture levels in plastic-covered structures are particularly bad examples and lead to crop loss due to overheating or cold stress, which has been observed in cucumber production [22–24]. The variation in microclimate conditions within greenhouse zones also impacts the uniformity and consistency of plant growth and yield. Solving such issues requires deploying real-time monitoring advanced sensor networks on a wider scale [23,25]. Lighting presents challenges too; dynamic lighting systems have the ability to reduce energy use by up to 20% without affecting yield [26]. However, passive greenhouses with inadequate lighting are likely to experience stunted growth unless supplemented with treatments like sucrose application [27].

Innovative optimal climate control strategies must be adopted to facilitate efficient and sustainable greenhouse systems. New techniques offer great potential. For example, some HVAC systems like rooftop greenhouses can reclaim heat energy from other buildings [28]. Solar, geothermal, and wind energy are renewable options that reduce fossil fuel dependence, and semi-transparent photovoltaics support light transmission as well as electricity generation [19]. Further, the sustainability of Closed-loop systems that recycle organic waste and drainage water is enhanced by the creation of renewable energy and organic fertilizers [5,29]. Sustainability in greenhouse farming is achieved with the combination of Internet of Things (IoT) and Machine Learning (ML) technologies that enable autonomous and preemptive decisions to be made based on real-time data. Crop yields, alongside resource use and productivity, are enhanced by the proactive, data-driven decision-making these technologies provide. Real-time data is critical during the growing season, and IoT devices can capture temperature, humidity, soil moisture, and light intensity [30–33]. Moreover, these sensors are usually bundled with actuators that regulate irrigation, lighting, and ventilation to adjust to the requirements of the plant and maintain a stable microclimate [30,31,33–35]. The automation of these processes helps with the

management of greenhouses because IoT platforms allow remote access and farmers can oversee and manage the systems from anywhere using web interfaces [30,31,33,35,36]. In addition to monitoring, ML has a major impact on predictive analytics. ML models predict growth, foresee disease outbreaks, and detect pest infestations utilizing data from IoT devices, permitting timely intervention [32,37–40]. Such models further analyze historical and real-time data to track water, nutrient, and energy use to maximize efficiency and minimize wastage [3,4,8–12]. ML decision-support systems provide relevant information for crop management, irrigation scheduling, and pest management [35,38]. These improvements allow the achievement of optimal environmental conditions for the plants at any time, as well as risk minimization and enhanced productivity, while ensuring a smaller ecological footprint [32,38,39,41]. Minimizing labor and resource waste drives down operational costs [37–39,41]. There are still unanswered questions, to be sure. Data privacy and security and expanding the IoT and ML infrastructure, as well as other concerns related to the integration of data, computation limits, complexity, and transparency of the models need attention [32,34]. Realizing the advantages of these technologies also requires one to adequately train the farmers and devise adoption strategies [32,34]. This study proposes a Clean Energy Smart Grid (CESG) design integrating demand response, energy storage, and forecasting to address renewable energy intermittency. A nested sizing framework is introduced, combining hourly optimal operation and annual optimal sizing for cost-effective, reliable system design. To overcome computational limits, the study replaces the inner Lotus Effect Algorithm (LEA) with a trained Artificial Neural Network (ANN), maintaining accuracy with a 98.92% time reduction. Results show demand response reduces costs by 28%, and the hybrid ANN-LEA approach accelerates convergence time by 43%, enhancing scalability and efficiency [42]. This review explores how artificial intelligence (AI) is transforming energy management in renewable-integrated smart grids by enhancing forecasting, fault detection, and control. It highlights advancements in machine learning and deep learning for grid observability, anomaly detection, and multi-agent optimization of energy dispatch and microgrids. Key barriers such as data sparsity, model transparency, and standardization are discussed, alongside emerging solutions like explainable AI and quantum-enhanced computing.

The study concludes that integrating AI with digital infrastructure and policy reform is essential for enabling intelligent, resilient, and low-carbon power systems [43]. This study analyzes solar energy forecasting in the U.S. using AI-based time-series models, focusing on Random Forest and XGBoost for predictive accuracy.

Both models demonstrated high reliability across hourly and daily datasets from major solar regions, enabling dynamic grid and storage management. Findings support the integration of AI forecasting in real-time dispatch, load planning, and policy-making to support decarbonization goals. Future research should explore hybrid deep learning models (LSTM, CNN-LSTM) and storage integration for enhanced accuracy and smart microgrid deployment [44]. This review examines the influence of uncertain factors on long-term energy system optimization models, essential for planning future energy transitions. Uncertainties are categorized into policy, economic, and technical domains, with a focus on carbon reduction and energy transformation challenges. The paper summarizes existing modeling approaches used to address these uncertainties in system evolution and planning. It concludes by highlighting key uncertainty factors and recommending future research directions for robust energy system modeling [45]. This study presents a web-based decision support tool for monitoring and upgrading HVAC systems using smart meter data. The tool enables real-time analysis of heating/cooling cycles, room-level efficiency, and retrofit energy-saving potential. Unlike traditional theoretical models, it adopts a

data-driven, building-specific approach to optimize HVAC performance. A case study in Athens demonstrates its effectiveness in enhancing energy efficiency and supporting sustainable building practices [46]. The paper presents a novel approach for controlling the climate of autonomous greenhouses by implementing a predictive, energy-efficient model using time-series machine learning techniques. The model achieves remarkable energy savings by preemptively adjusting control device (actuators) settings to optimal levels within the greenhouse based on its prediction for the temperature, humidity, and CO_2 equilibrium surge values. This self-sufficient, intelligent system fosters sustainability and greater crop yields through improved data analysis.

Review

Researchers have proposed advanced techniques that combine Machine Learning (ML), optimization, and IoT to facilitate the accurate prediction of critical climate variables and the control of greenhouse actuators. LSTM-based models offer predictive capabilities on the environment's sequential data loading, and climate forecasting using LSTM algorithms placed on IoT devices aids in making energy-conscious decisions [47]. In addition, temperature and humidity predictions have been made with great accuracy and minimal error using LSTM with Support Vector Machine (SVM) hybrids [48]. For more precise CO_2 predictions, some models use multi-model fusion methods with wavelet denoising, variational mode decomposition, and LSTMs, which successfully reduce noise in time-series data using feature extraction methods [49]. Forecasting of internal temperature and relative humidity has also successfully been performed using Adaptive Neuro-Fuzzy Inference System (ANFIS) models [50]. In climate management, optimization algorithms are instrumental on the control side. Using fuzzy logic modules, Differential Evolution (DE) can reduce energy consumption by 36% while optimizing climate parameters (1). Also, the combination of Convolutional Neural Networks (CNNs), LSTM with MPC, and other features have shown improvement concerning responsiveness, accuracy, and control within the temperature, humidity, and CO_2 control dimensions [51]. The impact of uncertain weather forecast monitoring is alleviated with robust data-driven MPC frameworks by retaining internal conditions through the use of dynamic models and optimization routines coupled with internal model control [52]. Using global optimization techniques like interpolation control and surrogate-based modeling techniques, dynamic setpoints are achieved, resulting in 27% energy savings and a 25% improvement in crop yield [53]. Superiority in multi-objective optimization enhances the tuning of PID controller setpoints in parallel with energy efficiency using Genetic Algorithms and RBFNN. As a result, overshoot and rise time are countered while maintaining the desired balance [54]. Furthermore, proactive microclimate control is made possible by real-time monitoring via IoT systems, which provides dependable and near-instantaneous communication between sensors and actuators [47]. The inclusion of crop physiological data into the control systems allows for more accurate decisions to be made, thus optimizing the advancement of the plant and the effectiveness of the resources used [55]. The combined effect of these approaches allows smart greenhouses to be accurately advanced and optimally eco-regulated, improving the energy efficiency and sustainability of agriculture. Different methods have also been tried in the prediction of greenhouse climate forecasting using time series analysis with varying advantages and disadvantages. Increasingly sophisticated models, notably LSTMs, continue to be used mainly because of their ability to capture intricate relationships over time, especially for estimating the cooling demand, temperature, and humidity levels [40,48,56,57]. These models perform exceptionally well, attaining RMSE values as low as 0.0766 and R^2 scores peaking at 0.982 [48,56]. On the other hand, LSTMs face challenges related to

high computational costs and extensive model optimization known as hyperparameter tuning [58]. On the other hand, temperature and evapotranspiration are often predicted using ARIMA models which are autoregressive chronologically integrated moving averages with a linear approach, resulting in R^2 values from 0.86 to 0.91 [59]. However, ARIMA models do not capture nonlinear trends well and are often highly customized in terms of data processing requirements [7,8]. Metaheuristics-based optimization of Moth-Flame algorithms to tree-based ensemble models have shown promise in forecasting numerous environmental factors including CO_2 and humidity with R^2 values exceeding 0.9929 using XGBoost [40,60,61]. Although XGBoost tends to be accurate, it can be inefficient computationally and susceptible to overfitting [61]. Lastly, time-series models like Prophet, which are made to accommodate strong seasonality, have been able to forecast droughts with an accuracy rate of 92.01% [62] but struggle more with weakly seasonal and irregular data. Table 1 shows a comparative analysis of time-series forecasting models.

Table 1. Comparative analysis of time-series forecasting models.

Model	Strengths	Limitations	Key References
LSTM (Long Short-Term Memory)	Captures long-term dependencies; handles nonlinear, multivariate sequences; robust to noise.	Requires large training data; computationally intensive; risk of overfitting.	[63]
XGBoost (Extreme Gradient Boosting)	Fast, scalable; handles missing data well; strong in tabular data; interpretable with SHAP.	Not ideal for sequential dependencies; lacks native time-series memory.	[64]
RNN (Recurrent Neural Network)	Learns temporal dynamics; simpler than LSTM; useful for short-term sequence modeling.	Struggles with long-term dependencies; vanishing gradients.	[65]
HMM (Hidden Markov Model)	Good for regime-switching and probabilistic modeling of states; interpretable transitions.	Limited in capturing complex nonlinear dynamics; assumes Markovian property.	[66]

2. Methodology

2.1. Problem Formulation

In this study, we aim to optimize greenhouse climate control by forecasting future climate states and minimizing energy consumption through intelligent actuator management. The system uses time-series data consisting of both environmental variables and actuator settings.

- $t \in \mathbb{N}$: Discrete time steps (e.g., hourly intervals);
- $x_t \in \mathbb{R}^n$: State time t.

State vector:

$= [Tair_t, Rhair_t, CO_2air_t, VentLee_t, Ventwind_t, PipeLow_t, PipeGrow_t, AssimLight_t, EnScr_t, BlackScr_t, Tot_PAR_t, co2_dos_t]$

1. Forecasting Climate Variables

The goal is to predict the future value of a climate (e.g., air temperature) h steps ahead using the previous k time steps:

$$\hat{y}_{t+h} = f(x_t, x_{t-1}, \ldots, x_{t-k})$$

where

- $\hat{y}_{t+h}$: Forecasted climate variable at time t + h;

- f(·): Forecasting (e.g., LSTM);
- k: Number of historical considerations.

2. Optimization

Given the forecast $\hat{y}_{t+h}$, the task is to determine settings u_{t+h} that meet the following requirements:

1. Maintain target climate conditions y*;
2. Minimize energy consumption proxy E_t.

The energy proxy is as follows:

$$_t = \alpha_1 \cdot \text{PipeLow}_t + \alpha_2 \cdot \text{PipeGrow}_t + \alpha_3 \cdot \text{AssimLight}_t$$

Optimization Problem

:E_{t+h}

$$\hat{y}_{t+h} = f(x_{t-k:t}, u_{t+h}) \approx y^*$$

$$u_min \leq u_{t+h} \leq u_max$$

2.2. Dataset Description

The GreenhouseClimate (https://community.data.4tu.nl/category/use-cases/, accessed on 23 October 2025) dataset is a comprehensive, high-frequency multivariate time series dataset designed to facilitate academic research in the domains of autonomous greenhouse climate control, energy optimization, and intelligent agricultural systems. It comprises 47,809 time-stamped records, captured at 5 min intervals, covering a wide array of environmental, mechanical, and control-related parameters within a controlled greenhouse setting. The dataset includes detailed measurements of internal climate conditions such as air temperature, relative humidity, carbon dioxide concentration, and humidity deficit. In addition, it documents the status of key actuators including heating pipes, ventilation systems, high-pressure sodium (HPS) and LED lighting, energy and blackout curtains, as well as irrigation volumes and drain water properties. One of the dataset's significant strengths lies in its inclusion of both control setpoints and realized values (VIPs) for each major system component, allowing for the precise evaluation of system performance and control accuracy. In addition, it offers information on photosynthetically active radiation (PAR), spectral light volumes, and water supply intervals, which increases its value in machine learning for time-series analysis, predictive control, and multi-objective optimization. The dataset focuses on 2020 as it offers the most complete and high-resolution data available for analysis. This ensures consistency and reliability for modeling greenhouse climate and control systems. The dataset underwent preprocessing for advanced time-series forecasting. Conversions from Excel timestamps to online MATLAB site (https://matlab.mathworks.com/) datetime format were performed. Significant climate and actuator variables were selected, converted to numerical values, and arranged in a time-indexed timetable. Data was aggregated to hourly intervals with the mean and imputed to remove missing values. An energy proxy was calculated by adding the values from PipeLow, PipeGrow, and AssimLight. All features were subsequently normalized using Z-score standardization to maintain model compatibility and performance.

2.3. Forecasting Models Implementation Experiments Workflow

As the main tool for implementing experimental procedures pertaining to greenhouse climate forecasting and control optimization, MATLAB was used in this study is https://matlab.mathworks.com/. The workflow started with reading and preprocessing raw

sensor data which included converting timestamps, selecting relevant environmental and actuator variables, and performing hourly resampling with timetable and retime functions. Gaps in the data were removed to maintain data quality, and an energy proxy was estimated from important actuator variables. Subsequently, the data were normalized to enable efficient training of the Long Short-Term Memory (LSTM) network. The MATLAB deep learning toolbox was utilized to define and train the LSTM model with the aid of trainNetwork, employing sequence generation designed for temporal pattern learning in climate data. Standard model evaluation metrics, including RMSE, MAE, and R^2, were calculated alongside visual regression and residual plots. The trained model was then used to forecast future temperature values, compute expected energy consumption, and generate actuator recommendations based on threshold rules, and all procedures were visualized and executed programmatically in MATLAB.

Appendix A show more details for algorithms and tables used in this paper.

3. Workflow

3.1. Climate Data Preprocessing Workflow

Figure 1 illustrates the sequential steps for preparing raw greenhouse sensor data for machine learning-based climate forecasting. Initially, the raw dataset is parsed by converting timestamps into datetime format, ensuring time-aware processing. Each variable is then cleaned and converted into numeric values to handle inconsistencies such as string entries. A time-indexed table is constructed, and the data is resampled into hourly averages to smooth fluctuations and reduce noise. Following this, all features are normalized using Z-score standardization to ensure uniform scale for effective model training. The result is a cleaned and normalized dataset (D_clean) ready for input into the LSTM-based forecasting pipeline. Figure 1 shows a climate data preprocessing workflow.

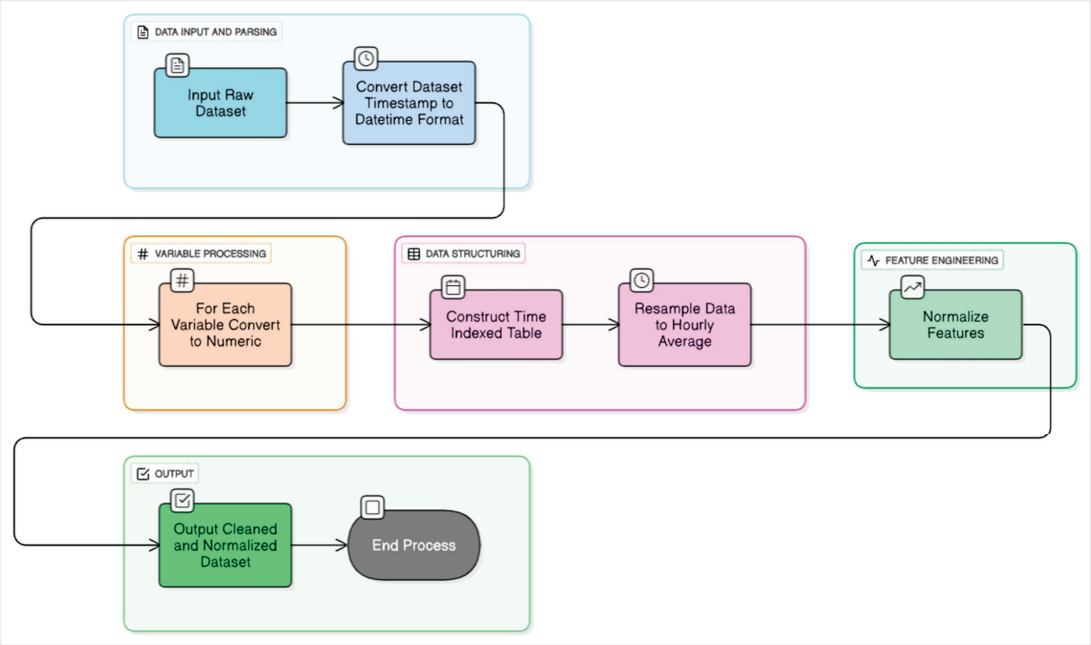


Figure 1. Climate data preprocessing workflow.

3.2. LSTM-Based Climate Forecasting Workflow

Figure 2 illustrates the full process of training and using an LSTM (Long Short-Term Memory) model for forecasting greenhouse climate variables. It begins with the preparation

phase, where input data is used to create training sequences. These sequences are passed to the model construction phase, which defines the LSTM architecture. The training phase then uses the architecture to train the model. Once trained, the model forecasts future steps and outputs predicted values, enabling proactive climate control in smart greenhouse systems. The process concludes after successful forecasting.

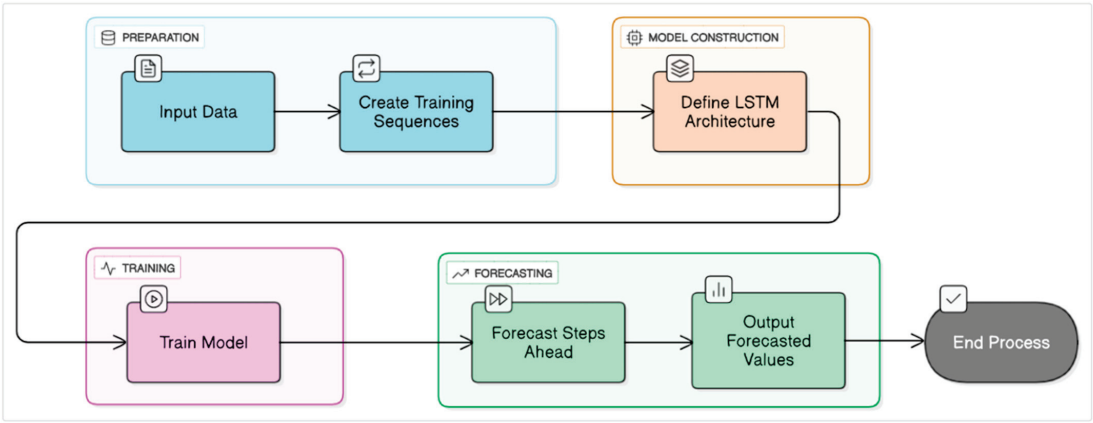


Figure 2. LSTM-based climate forecasting workflow.

3.3. Energy Proxy Computation and Actuator Recommendation

This process begins with the input of control variables such as PipeLow, PipeGrow, and AssimLight, which are essential for evaluating greenhouse energy consumption. For each time step, an energy proxy is computed by finding the sum of the values of these control variables, resulting in an energy vector that reflects total energy usage over time. In parallel, forecasted temperature values and a threshold (θ) are provided to guide actuator decisions. Each predicted temperature is assessed: if it is lower than $-\theta$, the system recommends increasing heating; if it exceeds $+\theta$, it suggests increasing ventilation; and if it falls within the threshold range, it is advised to hold the current settings. These decisions are collected and returned as actuator recommendations. The process ensures a data-driven approach to balancing energy efficiency with climate stability, ultimately supporting intelligent, real-time control in greenhouse environments. Figure 3 show Energy Proxy Computation and Actuator Recommendation process flow.

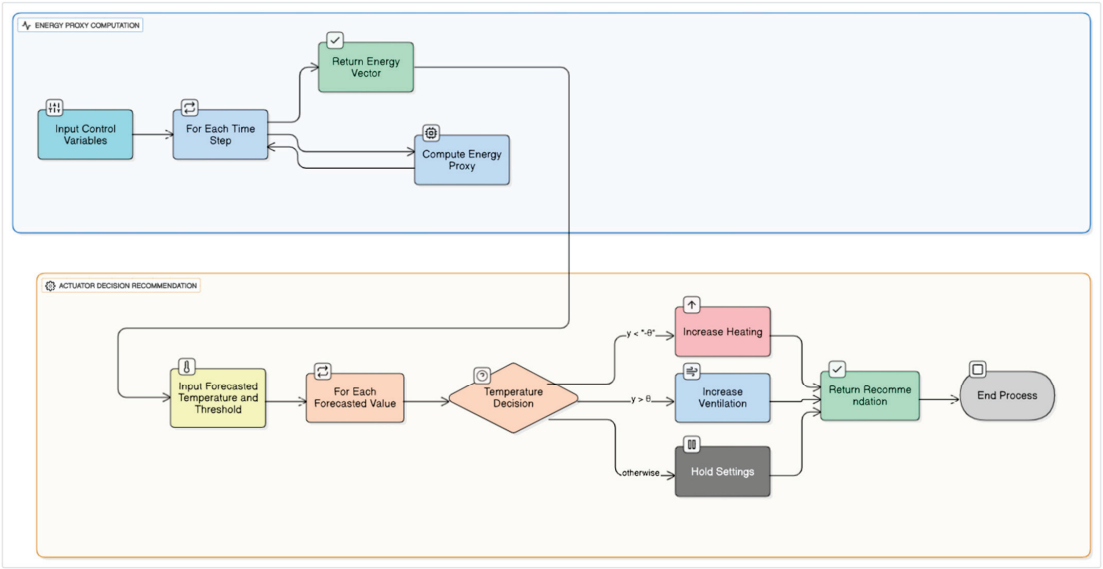


Figure 3. Energy proxy computation and actuator recommendation.

4. Results and Discussion

The presented figures collectively provide empirical evidence supporting the efficacy of the proposed Long Short-Term Memory (LSTM) model in facilitating predictive climate control and energy optimization within smart greenhouse systems. The temporal progression of key environmental parameters, as depicted in Figure 4, highlights the intrinsic variability and interdependence among air temperature (Tair), relative humidity (Rhair), and CO_2 concentration (CO_2air). These parameters exhibit both periodic and stochastic fluctuations, reinforcing the need for robust forecasting models capable of capturing nonlinear and long-range temporal dependencies. Building upon this, Figure 5 integrates actuator-related variables—namely PipeLow and PipeGrow (heating components), and AssimLight (artificial lighting)—with the aforementioned environmental parameters. This comprehensive representation illustrates the dynamic relationship between internal climate conditions and corresponding energy control actions. The observed patterns underscore the complexity of greenhouse climate regulation and the imperative for anticipatory rather than reactive control mechanisms. Figure 6 introduces an estimated energy proxy, serving as a synthesized indicator of cumulative energy consumption attributable to the operation of actuators. The presence of pronounced peaks and temporal irregularities across the observation period suggests inefficiencies under traditional control regimes. These findings validate the strategic rationale for implementing forecast-driven interventions aimed at preemptively regulating energy use. To examine system dynamics at a finer temporal resolution, Figure 7 focuses on a 48 h snapshot of core environmental variables. The short-term variability captured in this figure facilitates the detection of microclimatic shifts that are critical for responsive control. Complementarily, Figure 8 delineates the activation patterns of actuators alongside energy proxy levels. This alignment provides operational insights into the temporal synchronization between forecast-informed control decisions and actual energy deployment. The predictive capabilities of the LSTM model are visually demonstrated in Figure 9, which illustrates the forecasted trajectory of normalized air temperature over a 6 h horizon. The smooth transition between historical observations and forecasted values is evidence of the model's ability to learn and extrapolate temporal patterns effectively. The predictive fidelity is further substantiated by Figure 10, wherein the actual and predicted values over the training set exhibit close alignment, signifying high model accuracy and generalizability. Model performance is rigorously assessed through residual diagnostics in Figure 11, which plots the error distribution (actual minus predicted values). The residuals appear symmetrically centered around zero and lack discernible autocorrelation, indicating unbiased and homoscedastic predictions. This is corroborated by the regression analysis in Figure 12, where predicted values demonstrate a strong linear correlation with observed values. The tight clustering around the identity line reflects a high coefficient of determination (R^2), confirming the statistical validity of the model. Operational energy implications are further explored in Figure 13, which reveals a significant disparity between heating and ventilation energy requirements, with ventilation emerging as the dominant energy consumer. This insight informs strategic prioritization in actuator-level optimization to reduce overall energy expenditure. Lastly, Figure 14 visualizes deviations from optimal climatic conditions—specifically temperature and humidity—across time. The minimized deviation under the forecast-driven regime highlights the capacity of the proposed approach to maintain favorable microclimatic conditions while concurrently enhancing energy efficiency.

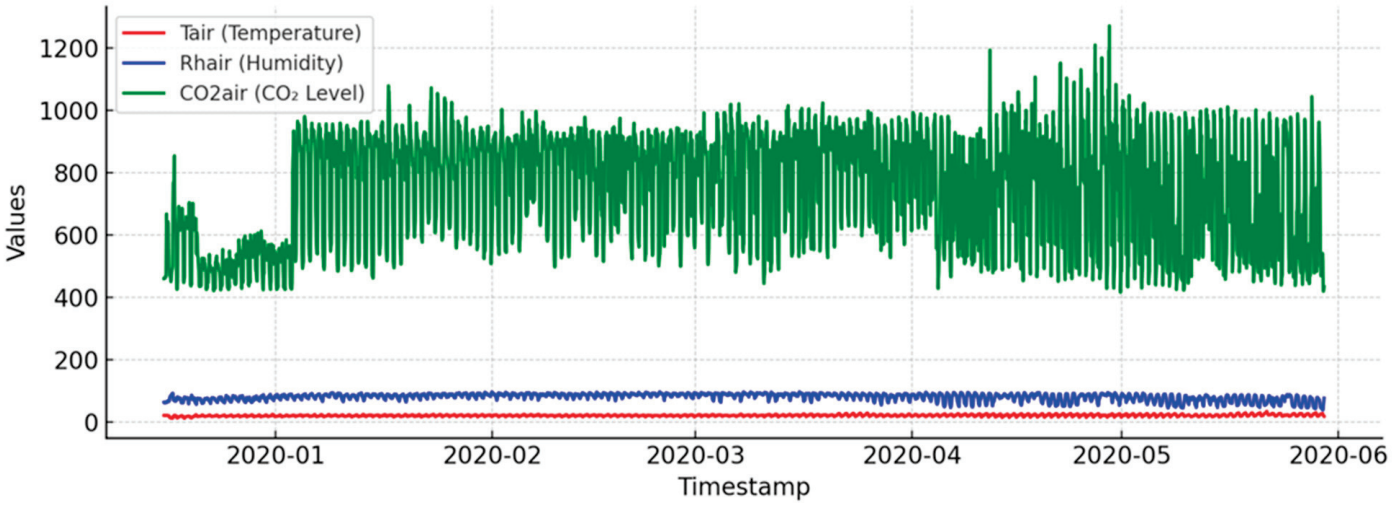


Figure 4. Climate variable trends over time.

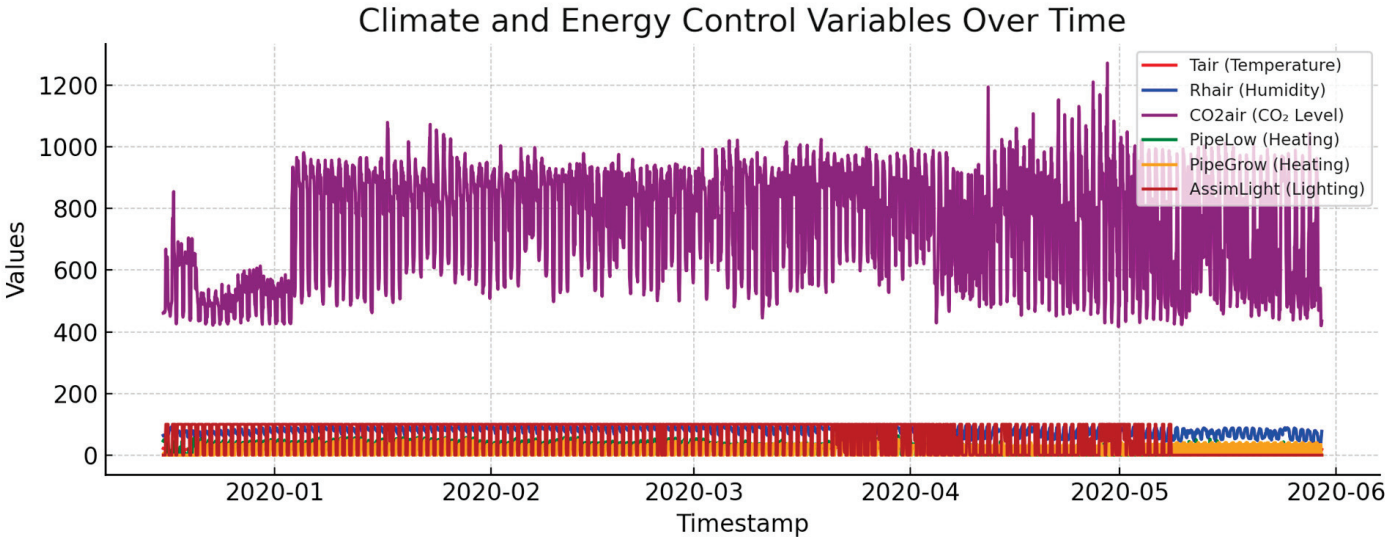


Figure 5. Climate and energy control variables over time.

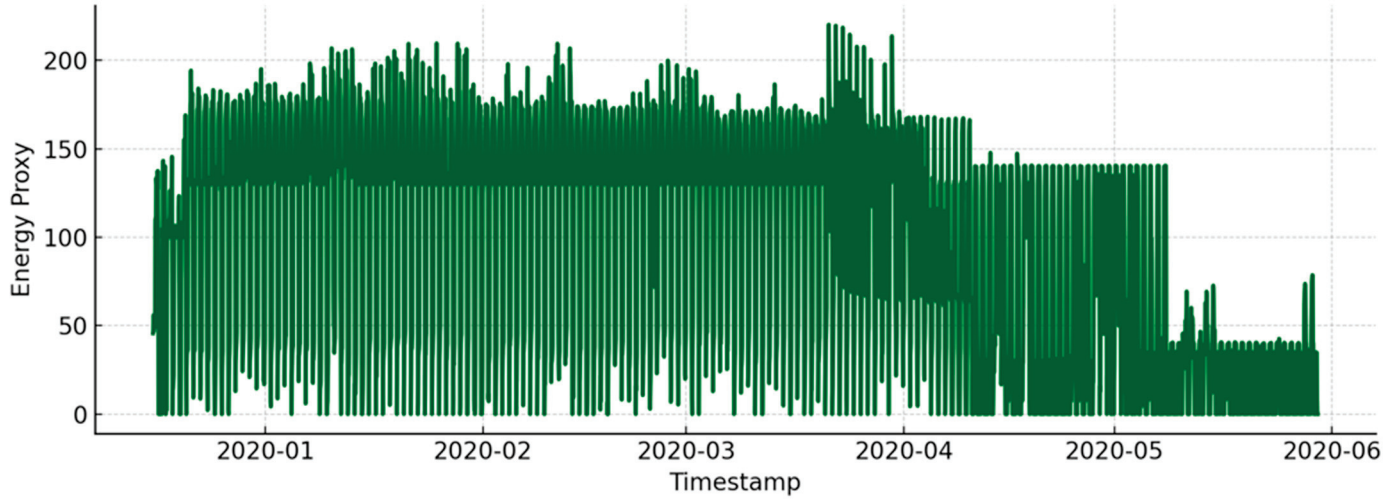


Figure 6. Estimated energy proxy over time.

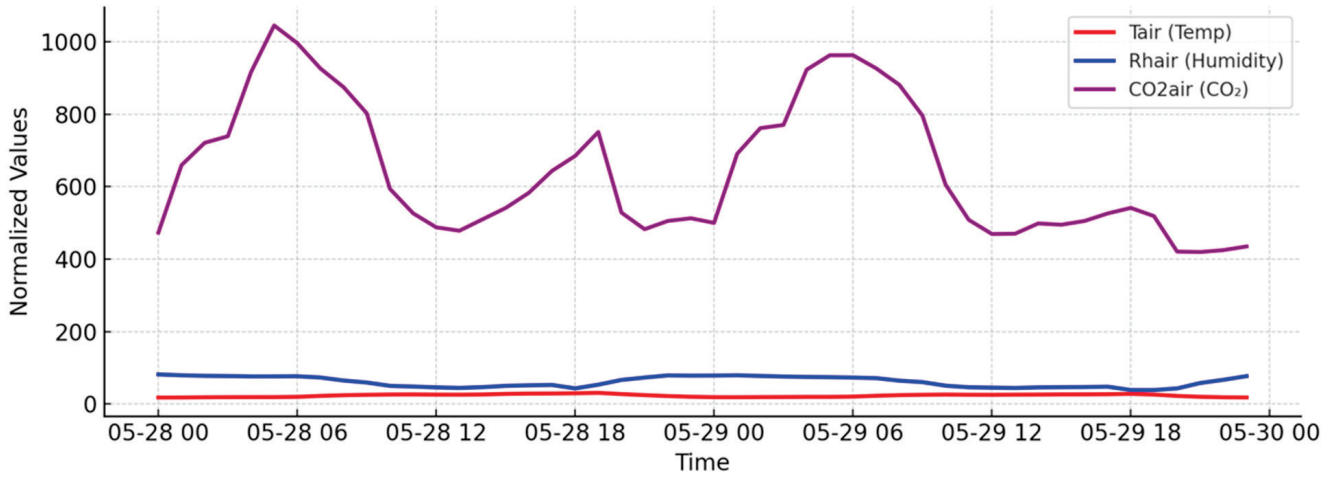


Figure 7. Climate variables (48 h).

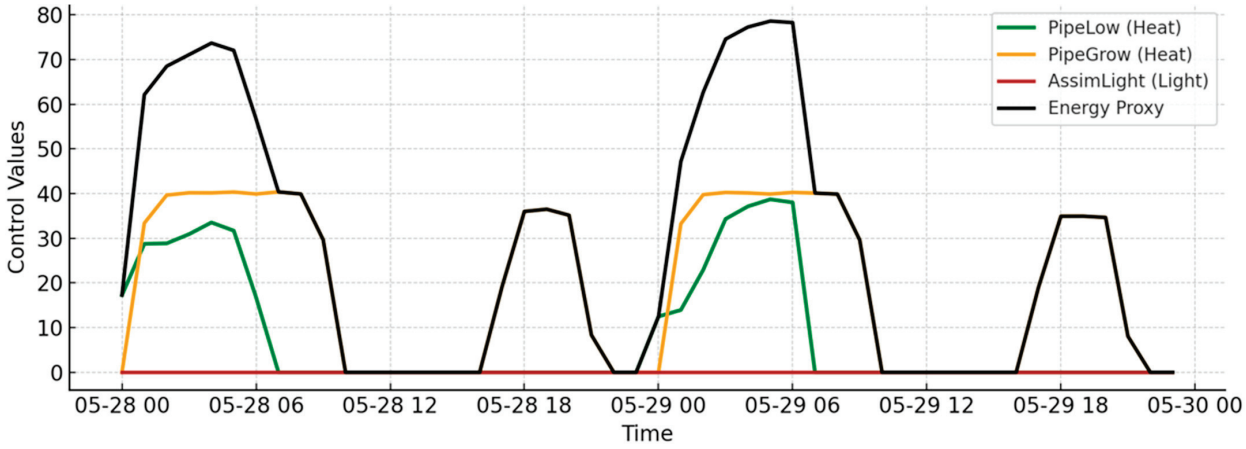


Figure 8. Recent energy control variables (48 h).

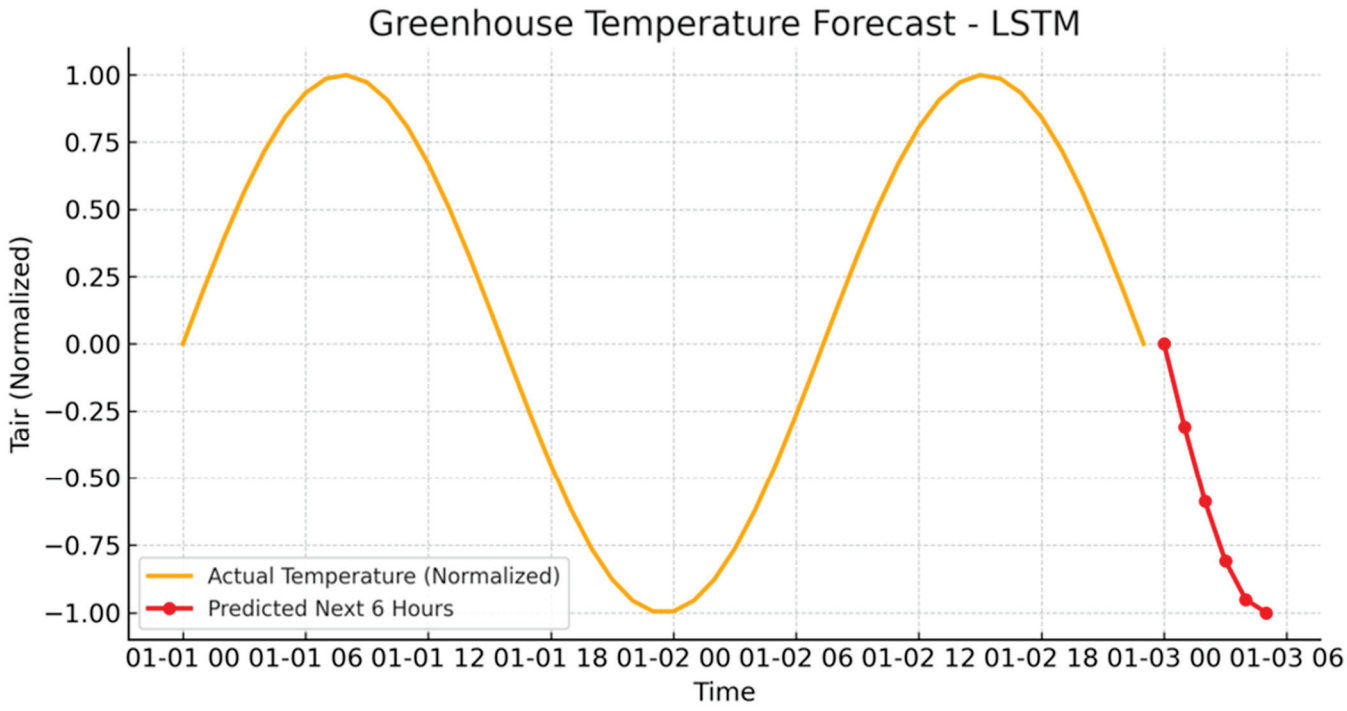


Figure 9. Greenhouse temperature forecast—LSTM.

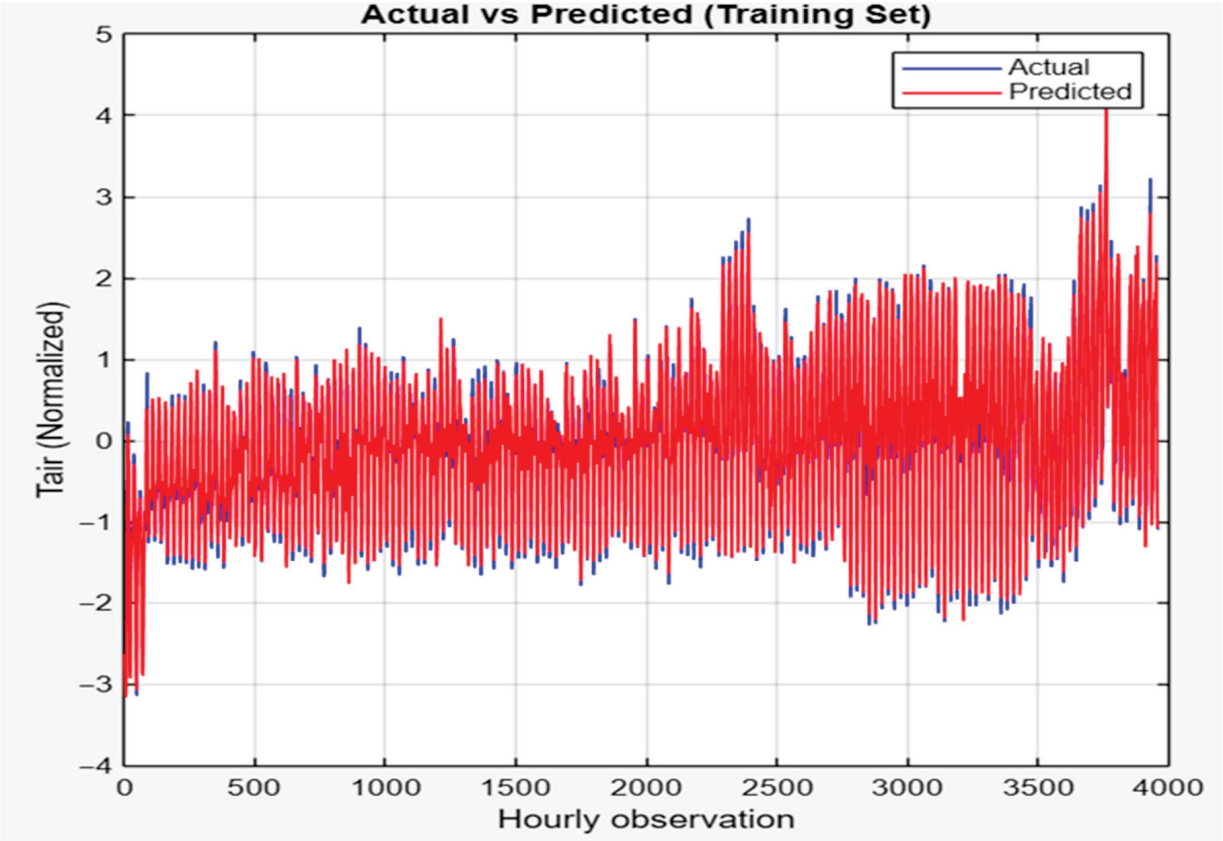


Figure 10. Comparison of actual vs. predicted greenhouse air temperature (training set).

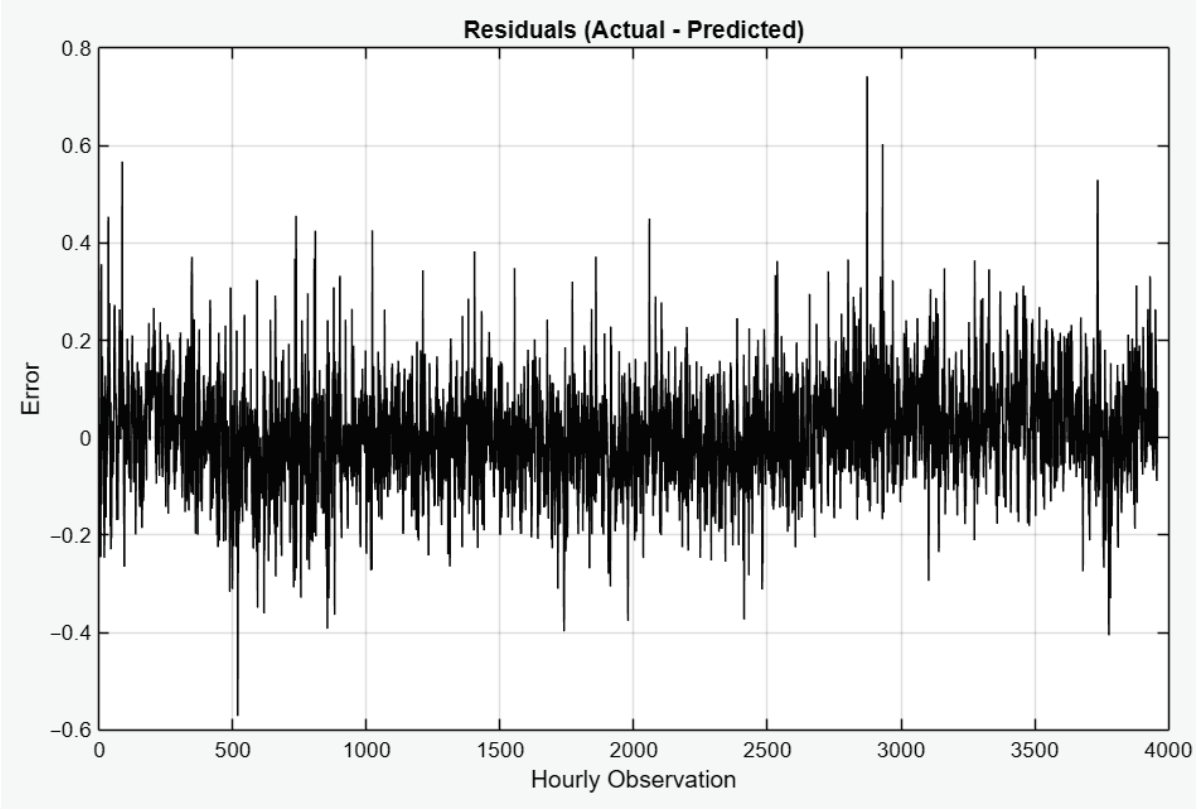


Figure 11. Residual errors between actual and predicted air temperature (training set).

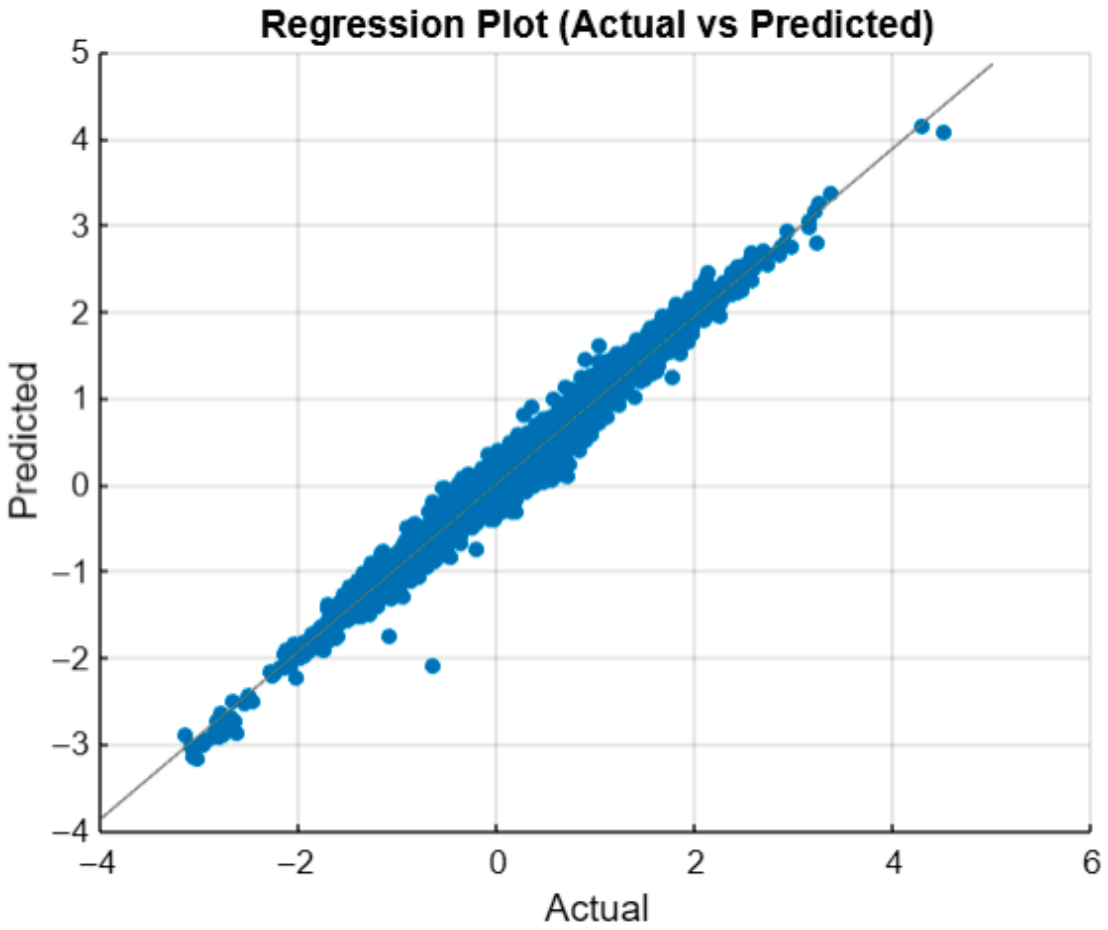


Figure 12. Regression plot of actual vs. predicted air temperature values.

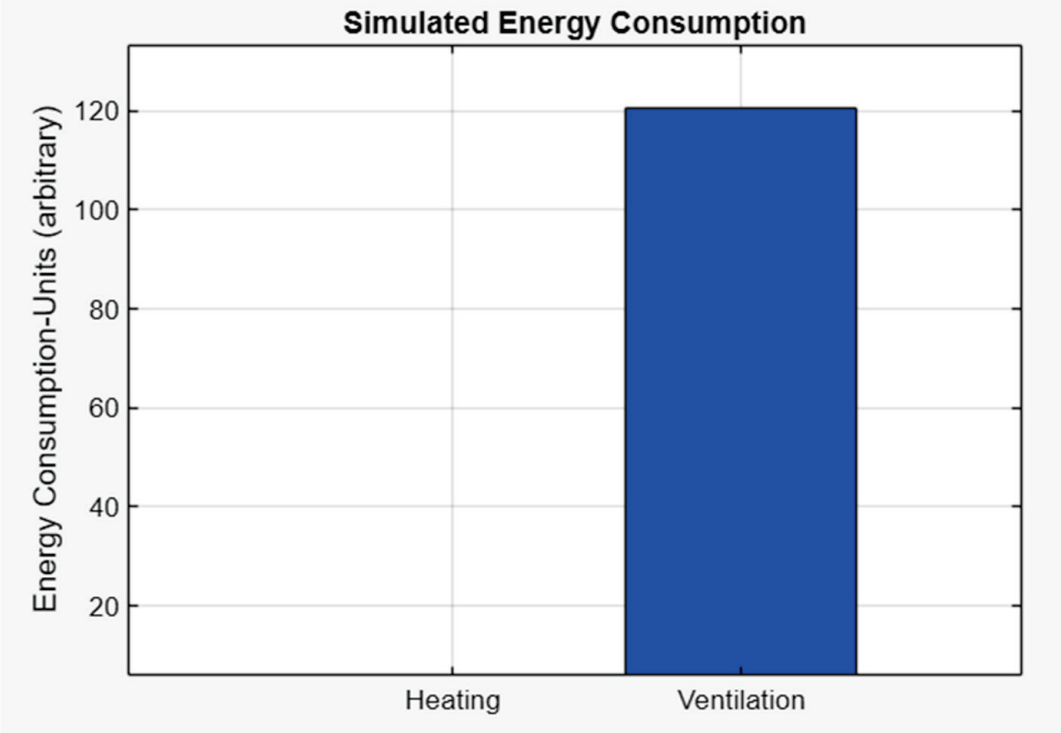


Figure 13. Simulated energy consumption comparison between heating and ventilation.

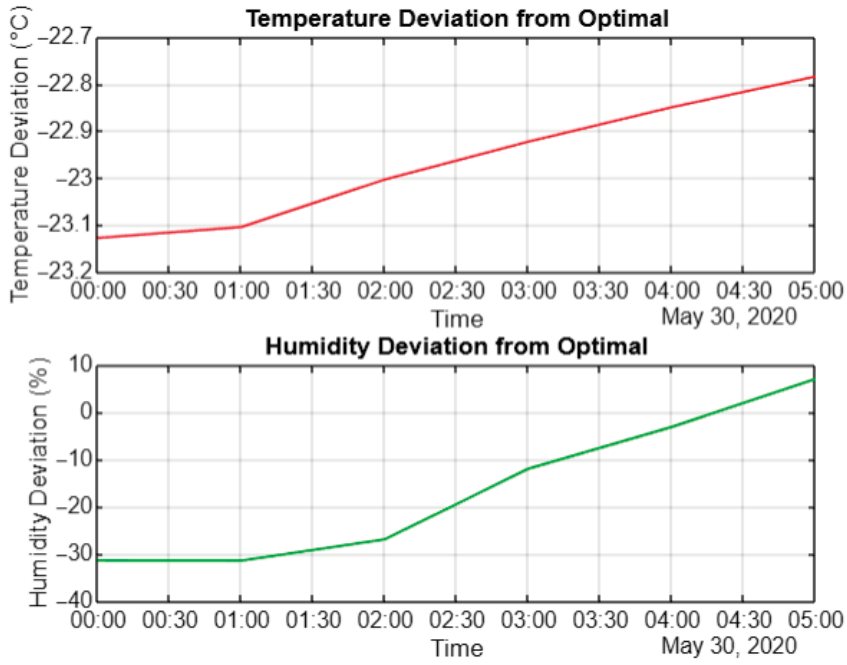


Figure 14. Deviation from optimal climate conditions: temperature and humidity over time.

5. Conclusions

This study presents a forecast-driven climate control strategy for smart greenhouses, leveraging the predictive power of Long Short-Term Memory (LSTM) models to enhance energy efficiency while maintaining optimal crop-growing conditions. The proposed system accurately forecasts key environmental variables—air temperature, relative humidity, and CO_2 concentration—and uses these predictions to proactively adjust control mechanisms such as heating, ventilation, and lighting. The experimental results and accompanying visual analyses, including regression plots, residual distributions, and actual versus predicted comparisons, confirm the reliability and precision of the LSTM model. The strong alignment between predicted and actual values, along with minimal residual error and high R^2 values, validates the effectiveness of the forecasting approach. Additionally, the analysis of energy proxy variables highlights significant energy-saving opportunities, particularly in ventilation, which was identified as the most energy-intensive operation. By enabling anticipatory control decisions based on real-time forecasts, the system shifts greenhouse management from reactive to predictive, thereby reducing unnecessary energy usage and contributing to sustainable agriculture practices. However, certain limitations must be acknowledged. First, the model's performance is dependent on the quality and granularity of historical sensor data, and noise or missing values may affect prediction accuracy. Second, the study focuses primarily on temperature forecasting; although CO_2 and humidity are considered, their direct forecast-based control integration remains limited. Third, the system was validated in a single controlled environment, and broader generalization across diverse greenhouse setups and crop types remains to be investigated. Future research should address these limitations by considering the following: (1) incorporating advanced data preprocessing techniques to handle real-world sensor noise; (2) extending the forecasting model to simultaneously predict and optimize multiple variables such as CO_2 enrichment and humidity; (3) deploying the framework in multiple greenhouse scenarios to evaluate adaptability across varying crops and climatic conditions. Furthermore, integration of reinforcement learning or hybrid optimization techniques could further enhance actuator control decisions, balancing energy efficiency with crop yield and plant health objectives. In conclusion, this work establishes

a robust foundation for intelligent, data-driven greenhouse climate control, with promising implications for scalable, sustainable, and resource-efficient smart farming systems.

Author Contributions: Methodology, A.A.; Validation, M.A.-S. and M.A.A.-Z.; Formal analysis, A.A.; Investigation, A.A.; Writing—original draft, A.A., M.A.-S. and M.A.A.-Z.; Funding acquisition, M.A.A.-Z. All authors have read and agreed to the published version of the manuscript.

Funding: This paper was funded by the Research, Development, and Innovation Authority (RDIA)—Kingdom of Saudi Arabia—Under supervision Energy, Industry, and Advanced Technologies Research Center, Taibah University, Madinah, Saudi Arabia with grant number (12979-iau-2023-TAU-R-3-1-EI-).

Data Availability Statement: The data presented in this study are openly available in [IUACAAS] [https://community.data.4tu.nl/category/use-cases/, accessed on 23 October 2025].

Acknowledgments: This article is derived from a research grant funded by the Research, Development, and Innovation Authority (RDIA)—Kingdom of Saudi Arabia—with grant number (12979-iau-2023-TAU-R-3-1-EI-).

Conflicts of Interest: The authors declare no conflict of interest.

Appendix A

Table A1. Climate control stages and equations.

Stage	Task	Mathematical Action
Forecasting	Predict future climate state	$\hat{y}_{t+h} = f(x_{t-k:t})$
Energy Proxy	Estimate energy usage	$E_t = \alpha_1 \cdot u_1 + \alpha_2 \cdot u_2 + \alpha_3 \cdot u_3$
Optimization	Recommend actuator settings	Minimize E_{t+h}, subject to $\hat{y}_{t+h} \approx y^*$
Decision	Generate control action	If $\hat{y}_t < y^*$, then increase heating; else ventilate

Table A2. Dataset description.

Dataset Item	Data Type	Typical Range/Unit
Air Temperature (Tair)	Float	10–35 °C
Relative Humidity (Rhair)	Float	30–90%
CO_2 Concentration (CO_2air)	Integer	300–1500 ppm
Humidity Deficit (HumDef)	Float	4–12 g/m^3
Heating Pipes (PipeLow, PipeGrow)	Float	25–60 °C
Ventilation (VentLee, Ventwind)	Float	0–100% (opening percentage)
Lighting Status (AssimLight)	Integer (binary)	0 or 100 (on/off)
Curtain Positions (EnScr, BlackScr)	Float	0–100%
Irrigation Volume (water_sup)	Float	0–15 L/m^2/day
Drain Conductivity and pH	Float	1–5 dS/m; pH 5.5–7.5
PAR (Tot_PAR)	Float	0–1500 µmol/m^2/s
LED Light Intensities (int_*_sp/vip)	Integer	0–1000 (proportional control)
Control Setpoints (*_sp)	Float	Varies by actuator type
Realized Values (*_vip)	Float	Matches corresponding control setpoint range

Table A3. Forecasted temperature and heating actions.

Forecast Time	Predicted Tair	Recommendation
30-May-2020 00:00:00	−1.1283	Increase Heating
30-May-2020 01:00:00	−1.1050	Increase Heating
30-May-2020 02:00:00	−1.0037	Increase Heating
30-May-2020 03:00:00	−0.9231	Increase Heating
30-May-2020 04:00:00	−0.8496	Increase Heating
30-May-2020 05:00:00	−0.7842	Increase Heating

Algorithm A1: Climate Data Preprocessing

Input: Raw dataset D_raw with timestamp and variables
Output: Cleaned and normalized hourly dataset D_clean

1. Convert Excel timestamps to datetime: T ← datetime(D_raw.timestamp)
2. For each variable x in D_raw:
    x ← convert to numeric (handle strings)
3. Construct time-indexed table: D_time ← timetable(T, D_raw)
4. Resample to hourly average: D_hourly ← retime(D_time, 'hourly', 'mean')
5. Normalize features: x_norm ← (x—mean(x))/std(x)
6. Return D_clean ← normalized D_hourly

Algorithm A2: Forecasting Using LSTM

Input: Normalized dataset D_clean, lookback steps k
Output: Forecasted values Y_pred

1. Create training sequences:
    For i = k+1 to N:
        X_train[i] ← D_clean[i-k:i-1]
        Y_train[i] ← D_clean.Tair[i]
2. LSTM modelin:
    Layers ← [Input, LSTM(100), FullyConnected(1), Regression]
3. Train model: net ← trainNetwork(X_train, Y_train, Layers)
4. Forecast h steps:
    For t = 1 to h:
        Y_pred[t] ← predict(net, X_test_t)
        Update X_test_t with Y_pred[t]
5. Return Y_pred

Algorithm A3: Energy Proxy Computation

Input: Control variables (PipeLow, PipeGrow, AssimLight)
Output: Energy proxy E_t

1. For each time t:
    E_t ← PipeLow_t + PipeGrow_t + AssimLight_t
2. Return vector E

Algorithm A4: Actuator Decision Recommendation

Input: Forecasted temperature Y_pred, threshold θ
Output: Recommendation R

1. For each y in Y_pred:
   If y < −θ: R[y] ← 'Increase Heating'
   Else if y > θ: R[y] ← 'Increase Ventilation'
   Else: R[y] ← 'Hold Settings'
2. Return R

References

1. Ben-Lhachemi, N.; Benchrifa, M.; Nasrdine, S.; Mabrouki, J.; Slaoui, M.; Azrour, M.A. Effect of IoT Integration in Agricultural Greenhouses. In *Technical and Technological Solutions Towards a Sustainable Society and Circular Economy*; World Sustainability Series; Springer: Cham, Switzerland, 2024; Volume Part F2854, pp. 435–445. [CrossRef]
2. Iddio, E.; Wang, L.; Thomas, Y.; McMorrow, G.; Denzer, A. Energy efficient operation and modeling for greenhouses: A literature review. *Renew. Sustain. Energy Rev.* **2020**, *117*, 109480. [CrossRef]
3. El-Gayar, S.; Negm, A.; Abdrabbo, M. Greenhouse Operation and Management in Egypt. In *Conventional Water Resources and Agriculture in Egypt*; Handbook of Environmental Chemistry; Springer: Cham, Switzerland, 2019; Volume 74, pp. 489–560. [CrossRef]
4. Bailey, B. Natural and mechanical greenhouse climate control. *Acta Hortic.* **2006**, 43–53. [CrossRef]
5. Vox, G.; Teitel, M.; Pardossi, A.; Minuto, A.; Tinivella, F.; Schettini, E. Sustainable greenhouse systems. In *Sustainable Agriculture: Technology, Planning and Management*; Oxford University Press: New York, NY, USA, 2010; pp. 1–80. Available online: https://www.scopus.com/inward/record.uri?eid=2-s2.0-84892100708&partnerID=40&md5=a01ef38b80dd107112bceec8385e6473 (accessed on 23 October 2025).
6. Van Ooteghem, R.J.C. Optimal Control Design for a Solar Greenhouse. In *IFAC Proceedings Volumes (IFAC-PapersOnline)*; Wageningen University: Wageningen, The Netherlands, 2010. Available online: https://www.scopus.com/inward/record.uri?eid=2-s2.0-80051911906&partnerID=40&md5=aa4f585232c6834a6f50d7d457fd8cdc (accessed on 23 October 2025).
7. Ahsan, T.M.A.; Rahman, M.S.; Ahamed, M.S. Geothermal energy application for greenhouse microclimate management: A review. *Geothermics* **2025**, *127*, 103209. [CrossRef]
8. Kempkes, F.; de Zwart, H.; Munoz, P.; Montero, J.; Baptista, F.; Giuffrida, F.; Gilli, C.; Stepowska, A.; Stanghellini, C. Heating and dehumidification in production greenhouses at northern latitudes: Energy use. *Acta Hortic.* **2017**, 445–452. [CrossRef]
9. Dik, D.; Polyakova, E.; Chelovechkova, A.; Moskvin, V.; Nikiforova, T. The System of Environment Control of Botanic Garden Greenhouses. In Proceedings of the 2018 International Multi-Conference on Industrial Engineering and Modern Technologies, FarEastCon 2018, Vladivostok, Russia, 3–4 October 2018. [CrossRef]
10. Dumitrascu, A. Methods and software tools for greenhouse climate. In Proceedings of the 8th International Scientific Conference on Modern Management of Mine Producing, Geology and Environmental Protection, SGEM 2008, Albena, Bulgaria, 16–20 June 2008; pp. 301–308. Available online: https://www.scopus.com/inward/record.uri?eid=2-s2.0-84890259918&partnerID=40&md5=9f2011a65f4ac4bb3c1c6b885aa882da (accessed on 23 October 2025).
11. Tawalbeh, M.; Aljaghoub, H.; Alami, A.H.; Olabi, A.G. Selection criteria of cooling technologies for sustainable greenhouses: A comprehensive review. *Therm. Sci. Eng. Prog.* **2023**, *38*, 101666. [CrossRef]
12. Ajagekar, A.; Decardi-Nelson, B.; You, F. Energy management for demand response in networked greenhouses with multi-agent deep reinforcement learning. *Appl. Energy* **2024**, *355*, 122349. [CrossRef]
13. Dieleman, J.A.; Hemming, S. Energy saving: From engineering to crop management. *Acta Hortic.* **2011**, 65–74. [CrossRef]
14. Altes-Buch, Q.; Quoilin, S.; Lemort, V. A modeling framework for the integration of electrical and thermal energy systems in greenhouses. *Build. Simul.* **2022**, *15*, 779–797. [CrossRef]
15. Rodríguez, F.; Berenguel, M.; Guzmán, J.L.; Ramírez-Arias, A. Climate and irrigation control. *Adv. Ind. Control* **2015**, *171*, 99–196. [CrossRef]
16. Xu, L.; Su, Y.; Liang, Y. Requirement and current situation of control-oriented microclimate environmental model in greenhouse system. *Nongye Gongcheng Xuebao/Trans. Chin. Soc. Agric. Eng.* **2013**, *29*, 1–15. [CrossRef]
17. Katzin, D.; van Mourik, S.; Kempkes, F.L.K.; van Henten, E.J. Energy saving measures in optimally controlled greenhouse lettuce cultivation. *Acta Hortic.* **2020**, 265–272. [CrossRef]

18. Banakar, A.; Montazeri, M.; Ghobadian, B.; Pasdarshahri, H.; Kamrani, F. Energy analysis and assessing heating and cooling demands of closed greenhouse in Iran. *Therm. Sci. Eng. Prog.* **2021**, *25*, 101042. [CrossRef]
19. Kavga, A.; Petrakis, T.; Thomopoulos, V. The contribution of innovative semi-transparent photovoltaics for energy autonomy in the field of greenhouse systems. *VDI Berichte* **2022**, *2022*, 61–68. [CrossRef]
20. Arabhosseini, A. Application of clean energies in agricultural greenhouses. In Proceedings of the 2023 8th International Conference on Technology and Energy Management, ICTEM 2023, Babol, Iran, 8–9 February 2023. [CrossRef]
21. Ghaderi, M.; Reddick, C.; Sorin, M. A Systematic Heat Recovery Approach for Designing Integrated Heating, Cooling, and Ventilation Systems for Greenhouses. *Energies* **2023**, *16*, 5493. [CrossRef]
22. Zhang, Q.; Zhang, X.; Yang, Z.; Huang, Q.; Qiu, R. Characteristics of Plastic Greenhouse High-Temperature and High-Humidity Events and Their Impacts on Facility Tomatoes Growth. *Front. Earth Sci.* **2022**, *10*, 848924. [CrossRef]
23. Joshi, A.; Saxena, A.; Das, S.K. Effect of Greenhouse Microclimate on Crop Performance. In *Protected Cultivation: Structural Design, Crop Management Modeling, and Automation*; Apple Academic Press: New York, NY, USA, 2024; pp. 135–159. [CrossRef]
24. Bai, L.; Deng, H.; Zhang, X.; Yu, X.; Li, Y. Gibberellin is involved in inhibition of cucumber growth and nitrogen uptake at suboptimal root-zone temperatures. *PLoS ONE* **2016**, *11*, e0156188. [CrossRef]
25. Šalagovič, J.; Vanhees, D.; Verboven, P.; Holsteens, K.; Verlinden, B.; Huysmans, M.; Van de Poel, B.; Nicolaï, B. Microclimate monitoring in commercial tomato (*Solanum Lycopersicum* L.) greenhouse production and its effect on plant growth, yield and fruit quality. *Front. Hortic.* **2024**, *3*, 1425285. [CrossRef]
26. Pinho, P.; Hytönen, T.; Rantanen, M.; Elomaa, P.; Halonen, L. Dynamic control of supplemental lighting intensity in a greenhouse environment. *Light. Res. Technol.* **2013**, *45*, 295–304. [CrossRef]
27. Gómez-Cabezas, M.; España, Á. Exogenous Sucrose Enhances Growth and Physiological Performance of Tomato Seedlings Under Suboptimal Light Conditions in Passive Greenhouses. *Horticulturae* **2024**, *10*, 1337. [CrossRef]
28. Muñoz-Liesa, J.; Royapoor, M.; Cuerva, E.; Gassó-Domingo, S.; Gabarrell, X.; Josa, A. Building-integrated greenhouses raise energy co-benefits through active ventilation systems. *Build. Environ.* **2022**, *208*, 108585. [CrossRef]
29. Dorais, M.; Dubé, Y. Managing greenhouse organic wastes: A holistic approach. *Acta Hortic.* **2011**, 183–198. [CrossRef]
30. Săcăleanu, D.-I.; Matache, M.-G.; Roșu, Ș.-G.; Florea, B.-C.; Manciu, I.-P.; Perișoară, L.-A. IoT-Enhanced Decision Support System for Real-Time Greenhouse Microclimate Monitoring and Control. *Technologies* **2024**, *12*, 230. [CrossRef]
31. Ardiansah, I.; Bafdal, N.; Suryadi, E.; Bono, A. Greenhouse monitoring and automation using Arduino: A review on precision farming and internet of things (IoT). *Int. J. Adv. Sci. Eng. Inf. Technol.* **2020**, *10*, 703–709. [CrossRef]
32. Saraswat, S.; Khan, R.; Gupta, A.; Mehta, A. Mechanized functioning of tomato and lettuce greenhouses using IoT and machine learning techniques. In *Convergence of Cloud Computing, AI, and Agricultural Science*; IGI Global Scientific Publishing: Hershey, PA, USA, 2023; pp. 261–279. [CrossRef]
33. Tripathy, N.; Tripathy, S.S.; Rath, M.; Swain, J. An IoT Assisted Fog Enabled Framework for Smart Green House. In Proceedings of the Proceedings—International Conference on Computational Intelligence and Networks, Bhubaneswar, India, 1–3 December 2022. [CrossRef]
34. Debdas, S.; Pandey, S.; Gupta, S.; Dash, R.K.; Patnaik, M.C.; Singh, A.A. Optimizing Resource Efficiency in Smart Greenhouses through IoT. In Proceedings of the 2024 5th International Conference for Emerging Technology, INCET 2024, Belgaum, India, 24–26 May 2024. [CrossRef]
35. Jain, H. Data analytics enabled by the Internet of Things and artificial intelligence for the management of Earth's resources. *Data Anal. Artif. Intell. Earth Resour. Manag.* **2024**, 19–36. [CrossRef]
36. Rokade, A.; Singh, M.; Malik, P.K.; Singh, R.; Alsuwian, T. Intelligent Data Analytics Framework for Precision Farming Using IoT and Regressor Machine Learning Algorithms. *Appl. Sci.* **2022**, *12*, 9992. [CrossRef]
37. Pugazh, M.P.; Xavier, V.M.A.; Shyni, S.S. Design of Greenhouse System with Internet of Things and Machine Learning. In Proceedings of the 10th International Conference on Advanced Computing and Communication Systems, ICACCS 2024, Coimbatore, India, 14–15 March 2024; pp. 1921–1926. [CrossRef]
38. Hazra, S.; Mondal, A.; Dey, P.; Prabhakar, S.; Jha, A.K.; Rakshit, N. Future Prospects of Agriculture Using IoT and Machine Learning. In Proceedings of the 2024 IEEE International Conference on Smart Power Control and Renewable Energy, ICSPCRE 2024, Rourkela, India, 19–21 July 2024. [CrossRef]
39. Gomathy, G.; Esther, C.; Manaswini, S.; Swedharani, R.V.; Hyden, J.J.; Anand, A.A. Effective Farming for Zero Wastage and Enhancement of Farmer's Income. In Proceedings of the 4th International Conference on Power, Energy, Control and Transmission Systems: Harnessing Power and Energy for an Affordable Electrification of India, ICPECTS 2024, Chennai, India, 8–9 October 2024. [CrossRef]

40. Bavana, H.S.; Kummara, S.; Pranutha, S.S.K.; Vijayalakshmi, V.; Farooqui, N.A. An Investigation of the Utilizations of Machine Learning Methods in Precision Agriculture. In Proceedings of the 2nd IEEE International Conference on IoT, Communication and Automation Technology, ICICAT 2024, Gorakhpur, India, 23–24 November 2024; pp. 880–887. [CrossRef]
41. Apuroop, I.; Sandhu, R.; Krishnamraju, D.E.S.; Singh, G.; Shikhar, S.; Kumar, S.; Jakkampud, S. Applying Machine Learning Approaches in Fertilizer Optimization and Yield Prediction for Smart Agriculture. In Proceedings of the 2025 International Conference on Automation and Computation, AUTOCOM 2025, Dehradun, India, 4–6 March 2025; pp. 53–58. [CrossRef]
42. Eltamaly, A.M.; Almutairi, Z.A. Nested Optimization Algorithms for Accurately Sizing a Clean Energy Smart Grid System, Considering Uncertainties and Demand Response. *Sustainability* **2025**, *17*, 2744. [CrossRef]
43. Egbuna, I.K.; Salihu, F.B.; Okara, C.C.; Emmanuel, D. Advances in AI-powered energy management systems for renewable-integrated smart grids. *World J. Adv. Eng. Technol. Sci.* **2025**, *15*, 2300–2325. [CrossRef]
44. Ahmed, I.; Khan, M.A.U.H.; Islam, M.D.; Hasan, S.; Jakir, T.; Hossain, A.; Hasnain, K.N. Optimizing Solar Energy Production in the USA: Time-Series Analysis Using AI for Smart Energy Management. *arXiv* **2025**, arXiv:2506.23368. [CrossRef]
45. Feng, S.; Ren, H.; Zhou, W. A review of uncertain factors and analytic methods in long-term energy system optimization models. *Glob. Energy Interconnect.* **2023**, *6*, 450–466. [CrossRef]
46. Stoian, D.; Spiliotis, E.; Stamatopoulos, E.; Sarmas, E.; Marinakis, E. A web-based decision support tool for efficiently monitoring and upgrading HVAC systems. In Proceedings of the 2024 IEEE 15th International Conference on Information, Intelligence, Systems & Applications (IISA), Chania Crete, Greece, 17–19 July 2024; pp. 1–7.
47. Rizwan, A.; Khan, A.N.; Ahmad, R.; Kim, D.H. Optimal Environment Control Mechanism Based on OCF Connectivity for Efficient Energy Consumption in Greenhouse. *IEEE Internet Things J.* **2023**, *10*, 5035–5049. [CrossRef]
48. Tung, Y.-C.; Syahputri, N.W.; Diputra, I.G.N.A.S. Greenhouse Environment Sentinel with Hybrid LSTM-SVM for Proactive Climate Management. *AgriEngineering* **2025**, *7*, 96. [CrossRef]
49. Guo, J.; Zhang, B.; Lin, L.; Xu, Y.; Zhou, P.; Luo, S.; Zhuo, Y.; Ji, J.; Luo, Z.; Hassan, S.G. Multi-model fusion method for predicting CO_2 concentration in greenhouse tomatoes. *Comput. Electron. Agric.* **2024**, *227*, 109623. [CrossRef]
50. Hamidane, H.; El Faiz, S.; Rkik, I.; El Khayat, M.; Guerbaoui, M.; Ed-Dhhak, A.; Lachhab, A. Application analysis of ANFIS strategy for greenhouse climate parameters prediction: Internal temperature and internal relative humidity case of study. In *E3S Web of Conferences*; EDP Sciences: Les Ulis, France, 2021. [CrossRef]
51. Shao, X.; Chen, Y.; Chen, X.; Zhu, F. Research on intelligent monitoring and optimization control system model of greenhouse environment based on deep learning. In Proceedings of the 2024 4th International Conference on Electronic Information Engineering and Computer Communication, EIECC 2024, Wuhan, China, 13–15 December 2024; pp. 1246–1250. [CrossRef]
52. Chen, W.-H.; You, F. Semiclosed Greenhouse Climate Control Under Uncertainty via Machine Learning and Data-Driven Robust Model Predictive Control. *IEEE Trans. Control Syst. Technol.* **2022**, *30*, 1186–1197. [CrossRef]
53. Su, Y.; Xu, L. Global Optimization and Control of Greenhouse Climate Setpoints for Energy Saving and Crop Yield Increase. *Agriculture* **2025**, *15*, 939. [CrossRef]
54. Abbood, H.M.; Nouri, N.M.; Riahi, M.; Alagheband, S.H. An intelligent monitoring model for greenhouse microclimate based on RBF Neural Network for optimal setpoint detection. *J. Process Control.* **2023**, *129*, 103037. [CrossRef]
55. Yu, W.; Körner, O.; Schmidt, U. Crop Photosynthetic Performance Monitoring Based on a Combined System of Measured and Modelled Chloroplast Electron Transport Rate in Greenhouse Tomato. *Front. Plant Sci.* **2020**, *11*, 1038. [CrossRef]
56. Mahmood, F.; Govindan, R.; Yang, D.; Bermak, A.; Al-Ansari, T. Forecasting cooling load and water demand of a semi-closed greenhouse using a hybrid modelling approach. *Int. J. Ambient. Energy* **2022**, *43*, 8046–8066. [CrossRef]
57. Kim, J.; Kim, K.-J.; Kim, J.; Choi, Y.; Yun, B.-J.; Kwon, S.-G. Evaluating Deep Learning Models for Prediction of Climate Conditions in Greenhouse. In Proceedings of the 2024 IEEE International Conference on Consumer Electronics-Asia, ICCE-Asia 2024, Danang, Vietnam, 3–6 November 2024. [CrossRef]
58. Wijayaningrum, V.N.; Haniah, M.; Al Hadid Firdaus, V. Advanced Predictive Analytics for Agricultural Weather Forecasting Using Machine Learning. In Proceedings of the IEIT 2024—2024 International Conference on Electrical and Information Technology, Malang, Indonesia, 12–13 September 2024; pp. 182–187. [CrossRef]
59. Hendy, Z.M.; Abdelhamid, M.A.; Gyasi-Agyei, Y.; Mokhtar, A. Estimation of reference evapotranspiration based on machine learning models and timeseries analysis: A case study in an arid climate. *Appl. Water Sci.* **2023**, *13*, 216. [CrossRef]
60. Jeon, Y.-J.; Kim, J.Y.; Hwang, K.-S.; Cho, W.-J.; Kim, H.-J.; Jung, D.-H. Machine Learning-Powered Forecasting of Climate Conditions in Smart Greenhouse Containing Netted Melons. *Agronomy* **2024**, *14*, 1070. [CrossRef]
61. Dai, Z.; Huang, T. Enhancing the prediction accuracy of greenhouse temperatures through hybrid machine learning models: An in-depth comparative analysis of RBF, RF, and XGBoost techniques combined with SMA and MFO optimization strategies. *Multiscale Multidiscip. Model. Exp. Des.* **2024**, *8*, 311. [CrossRef]

62. Shetty, S.V.; Bharath, M.S.; Chandan, R.; Divya, V.; Nayak, S.S. Prediction of Drought—A Machine Learning Approach using Time Series Data. In Proceedings of the International Conference on Applied Intelligence and Sustainable Computing, ICAISC 2023, Dharwad, India, 16–17 June 2023. [CrossRef]
63. Wen, X.; Liao, J.; Niu, Q.; Shen, N.; Bao, Y. Deep learning-driven hybrid model for short-term load forecasting and smart grid information management. *Sci. Rep.* **2024**, *14*, 13720. [CrossRef]
64. Yadav, D.K.; Kaushik, A.; Yadav, N. Predicting machine failures using machine learning and deep learning algorithms. *Sustain. Manuf. Serv. Econ.* **2024**, *3*, 100029.
65. Mienye, I.D.; Swart, T.G.; Obaido, G. Recurrent neural networks: A comprehensive review of architectures, variants, and applications. *Information* **2024**, *15*, 517. [CrossRef]
66. Soltani, A. An Overview of Hidden Markov Models. Bachelor's Thesis, University of Padua, Padua, Italy, 2024.

Disclaimer/Publisher's Note: The statements, opinions and data contained in all publications are solely those of the individual author(s) and contributor(s) and not of MDPI and/or the editor(s). MDPI and/or the editor(s) disclaim responsibility for any injury to people or property resulting from any ideas, methods, instructions or products referred to in the content.

energies

MDPI

Article

Multi-Criteria Model Predictive Controller for Hybrid Heating Systems in Buildings

Ali Soleimani [1,2], Paul Davidsson [1,2,*], Reza Malekian [1,2] and Romina Spalazzese [1,2]

[1] Sustainable Digitalisation Research Centre, Malmö University, 205 06 Malmö, Sweden; ali.soleimani@mau.se (A.S.); reza.malekian@mau.se (R.M.); romina.spalazzese@mau.se (R.S.)
[2] Department of Computer Science and Media Technology, Malmö University, 205 06 Malmö, Sweden
* Correspondence: paul.davidsson@mau.se

Abstract

With more hybrid heating systems available, there is a need to optimize energy use intelligently from the end-consumer perspective. This paper focuses on a multi-criteria heating system optimization to optimize cost, carbon emission, and comfort level of building occupants. A discrete Multi-Objective Model Predictive Controller (MO-MPC) algorithm is proposed to optimally utilize two heating sources connected to a building, namely district heating (DH) and a building-integrated electrical heat pump (HP). The model is tested on a real-world building case simulated with a gray box building model. The results are compared to a conventional PID controller as well as the MPC scheme, each with a single heating input, and eight different cases are constructed to make this comparison more visible. The results indicate that, using MO-MPC, a cost saving of up to 10% and emission saving of up to 13% can be reached without additional thermal discomfort, while the potential savings on cost and emission with the hybrid system can be up to 25% and 77%, respectively. Further, a sensitivity analysis on price and emission parameters is conducted to investigate the changes in the provided solution.

Keywords: heat pump; district heating; model predictive control; multi-objective optimization; gray-box modeling; hybrid heating

1. Introduction

Building heating systems, used in commercial and residential buildings, are crucial and inseparable parts of our societal and individual lives. They provide us with comfortable—or near comfortable—indoor conditions needed to perform daily activities. At the same time, indoor heating and cooling account for more than 50% of energy consumption in Europe [1]. While it specifies a great amount of energy consumption, it also entails that, on a domestic scale, this sector holds a huge opportunity to save energy.

Centralized heating resources are among the most popular means of domestic heating. District heating as a traditional supplier is still well-established as a primary means of heating in urban areas in Europe. However, increasing energy prices over the past few years, lower availability, and environmental concerns surrounding this system threaten the supply of clean and uninterrupted energy in a desired indoor environment for the end-user. Environmentally speaking, in the EU, the second major heat production sources are natural and manufactured gases, accounting for 31.5%, right after renewable energies at 33.5% [2]. This signifies the heavy reliance of the district heating system on highly CO_2-emitting and

polluting sources. Secondly, the average price of DH in European countries has almost doubled between 2000 and 2015 [3].

A heating supply with a single centralized resource can be inadequate and unreliable. The recent advancement and application of hybrid heating systems, providing flexibility and higher energy efficiency, can be proposed as a solution to these issues. Building-integrated heat pumps (HPs) are one of these systems that have been proven to operate well with the central DH systems. They are rapidly gaining popularity in countries with cold winter climates, such as Germany, Sweden, Denmark, and Austria, due to their decreasing costs and government incentives [4]. The number of buildings supplied by HP has reached 16% of buildings across European countries, with 20 million installed units by 2022 [5]. Not only are they able to assist in supplying the heating demand in cold seasons, but these units also provide a highly efficient source of heating for end-users [5]. This generally results in lower energy bills for building managers and, more importantly, a lower environmental footprint. It is to be noted that in the literature, there are two main categories of hybrid heating systems. In the first type, the HP is working not separately but as a part of a low-temperature DH, otherwise known as 5th-generation DH, which is not the focus of this paper. We assume that HP and DH are working in parallel, and each can individually deliver heat to the consumers.

With hybrid heating systems in place, the control of the system becomes increasingly challenging. Single-resource heating systems are generally controlled by Rule-Based Controllers (RBC)—e.g., on–off controllers—and Proportional–Integral–Derivative (PID) controllers [6], whose main aim is to regulate indoor temperature rather than energy saving. Additionally, the conventional controllers not only have an inherent response delay but also perform poorly under changing systems, which makes them not fully efficient in heating systems with volatile inputs [7]. Furthermore, While these control algorithms are adequate for single heating systems, hybrid systems require a more sophisticated controller to find the optimal heating resources. Model Predictive Controller (MPC) is a superior alternative that offers future control action prediction and fast response and solves an optimization algorithm, all at the cost of being more computationally expensive. In this study, we try to adapt and make a fair comparison of this controller's performance with the PID algorithm in a hybrid heating context.

1.1. Related Work

The co-existence of building-level HP and DH has been investigated in many studies, especially as a means for energy and cost saving. Reda et al. [8] investigated the hybrid DH and solar-assisted HP hybrid system to provide heat to an office building in Finland. Their results revealed that a 19% renewable heating share in the heating season can be achieved. Hermansen et al. [9] investigate the cost-saving of an MPC-controlled hybrid heating system with both DH and HP, based on time-varying electricity prices. A 23% cost was saved, while authors argue that flexible taxes and fees on the Danish energy market on both DH and electricity prices can make this even more significant and encourage customers to take more energy-efficient decisions. A hybrid solar-assisted DH with local HP and auxiliary gas heater is modeled by Abokersh et al. [10] in TRNSYS 18, a transient system simulation software. Thermal energy efficiency and economic cost of the system are assessed in two different RBC strategies. In another research by Liu et al. [11], a DH coupled with geothermal HP is considered with different heat control loops in place. The capacity and investment cost were considered in this study, and the hybrid system's viability and competitiveness are compared with a normal DH. Liu et al. [12] studied a solar-assisted HP and DH hybrid heating system to lower operating cost and maximize renewable energy use. TRNSYS 18 is used to model the heating system with an RBC for the solar and heat

loop. They have reached economic savings of at least 72% in the latter by leveraging solar energy. A DH, borehole thermal energy storage, and HP were studied by Fiorentini et al. [13] to investigate the effect of the hybrid system on the cost and carbon emission of the system. The most savings they can achieve compared to a storage-less system are nearly 10% and 44% for the emission and cost. A ground-source HP and DH is optimized in several cases by Xue et al. [14], prioritizing cost or maximum demand reduction in resources. Their analysis gave a 2.2% reduction in cost in a hybrid solution while increasing the CO_2 emissions slightly due to the higher DH emission levels. A comparison of the reviewed literature and the current study is summarized in Table 1.

The control algorithm is the core of hybrid heating systems. MPCs, as a means of thermal system control, have been widely researched. Knudsen et al. [15], a bi-objective MPC algorithm, is used to control the energy consumption considering the cost and CO_2 emission of the system on a Danish electrical-based heating system. The findings show that, by leveraging demand response, a significant cost saving can be made compared to a PID-controlled system. In another study by Tarragona et al. [16], an MPC-controlled building connected to an HP, solar panels, and a storage tank was tested under several simulation scenarios. It was concluded that the hybrid system with the controller has significant economic savings compared to the rule-based controller. Baeten et al. [17] investigated using a multi-objective MPC to optimize comfort, cost, and carbon emission separately. They targeted an electrical-based HP and natural gas boiler, aiming to optimize the building's energy scheme by adopting a demand response program. Finck et al. [18] proposed an economic MPC on an HP and thermal storage heating system in one house. A rule-based controller, as a base case, and two different MPC pricing scenarios are considered to show the demand flexibility capturing of the latter cases and optimize the energy consumption and the total consumer heating cost. Aruta et al. [19] proposed a bi-objective MPC penalizing energy cost and thermal discomfort (using aggregated deviation temperature as the index). A genetic algorithm is used to find the optimal solutions, and the model is tested on a nearly zero experimental building. Apart from the MPC, the fuzzy-logic algorithm has been considered for achieving similar goals. Qi et al. [20] used this concept to control a ground-source HP aiming to save energy and improve thermal comfort. The results show a significant improvement compared to a PID controller. In another study by Underwood et al. [21], the fuzzy-logic controller was used for the same purpose and optimal setpoint tracking.

Gray-box modeling has been used extensively to model building thermal characteristics for MPC applications. In terms of the order of the model (which is specified by the number of capacitors in the model), many studies exist to find the right order. The authors in [22] investigated the Resistor–Capacitor (RC) models used for small and large applications. The review identifies that the commonly used models for building energy simulation are the ISO 13790 (5R1C) [23] and VDI 6007 (7R2C) [24] suggested building models. Another study by Vivian et al. [25] made a comparison between the two mentioned models and realized that the second-order one (7R2C) substantially lowers the Root Mean Square Error (RMSE) by up to 53%, capturing the dynamics of the building more accurately, both for cooling and heating seasons. A study by Yu et al. [26] concluded that the second-order models perform more robustly, while the third-order models are prone to overfitting. The models were tested on a real-world, experimental building [27]. Klanatsky et al. [28] focused on the methods of parameter estimation on a test case and provided a comparison with RC models of different orders, concluding that the third-order model is the most suitable building model to feed predictive controllers. Other studies [29,30] observed that, for both heating and cooling applications in longer periods, first-order models are more accurate than the second-order ones. The complexity of the RC models is

quite flexible, and based on the application, higher-order models can be used for specific cases. However, most reviewed research realized that 2nd-order and 3rd-order RC models are adequate for the MPC application of small-scale buildings in heating seasons. Another important aspect of gray-box models is the number of states. Bacher et al. [31] investigated RC models with several states and realized that the two-state and three-state models (where usually one state represents the measurable indoor air temperature and the remaining states correspond to latent, unmeasured thermal dynamics) are performing the best in terms of model robustness—using statistical metrics such as the auto-correlation function and residuals—for simulating a single-zone building heating system.

Table 1. Summary of the recent related literature and their major focuses compared with the current study.

Ref.	Method	Building Model	Energy Type(s)	Objective(s)	Results
[8]	Rule-based	White	District heating, heat pump, solar energy	Energy efficiency, renewable use	Up to 25% on-site renewable use in solar-assisted heat pump scenario and lowering heat pump input temperature from 5 to 10 degrees.
[9]	MPC, rule-based	White	Low-temperature district heating, heat pump, thermal storage	Economic	23% cost saving with dynamic electricity prices. As a result of load shifting with the multiple input energies and thermal storage.
[10]	Rule-based	White	District heating, heat pump, thermal storage, gas boiler, solar fields	Economic	Solar fields, electricity grid, and natural gas resources are optimally allocated. In the best case, 7% economic savings and 75% use of solar fields are achieved.
[11]	Rule-based	White	District heating, heat pump	Energy efficiency, resource sizing, investment	The setting and optimal size of a heat pump that has the most efficiency coupled with the district heating.
[12]	Rule-based	White	District heating, heat pump, thermal storage, solar energy	Economic, renewable use	Solar-assisted heat pump compared to a normal one can save up to 50.9% energy and 28% cost.
[13]	Rule-based	White	District heating, heat pump, thermal storage, solar energy	Economic, Environment	More than 27% reduction in CO_2 emission of electricity use when using the thermal storage and load shifting, and an extra 3.9–9.7% reduction potential when using solar-assisted heat pumps.
[14]	Rule-based	White	District heating, heat pump,	Economic, environment	A 2.2% reduction in annual energy cost while increasing the CO_2 emission slightly, in the optimal solution.
[15]	MPC, PID	White	Heat pump	Economic, environment	An MPC with different penalty weights was assessed. Depending on the weights, savings on cost and emissions can be achieved.
[16]	MPC, rule-based	White	Heat pump, solar energy, thermal storage	Economic, renewable use	MPC strategy has 16–22% cost savings compared to rule-based algorithm while significantly decreasing the power purchased from grid and promoting on-site renewable use.
[17]	MPC	Gray	Heat pump	Economic, Environment, Sizing	Adding the thermal storage increases the load-shifting abilities, while decreasing the peak demand by 11%.
[18]	MPC, rule-based	Black	Heat pump, thermal storage, solar energy	Economic, demand prediction	The MPC, compared to the rule-based strategy, enables demand flexibility and optimize energy consumption, leading to lower overall energy cost.
[19]	MPC	Black		Economic, comfort	A cost savings of up to 26% with an improved comfort level is achieved through the proposed GA- and ANN-based MPC strategy compared to the reference control strategy.
[20]	Fuzzy-logic, PID	White	Ground source heat pump, thermal storage	Energy efficiency	With the optimal control strategy, more than 200 kWh has been saved while the predicted mean vote (PMV) index has improved greatly.
[21]	Fuzzy-logic	-	Heat pump, thermal storage	Energy efficiency	The fuzzy multi-variable controller can achieve 20% energy saving while improving the temperature set-point tracking.
This paper	MPC, PID	Gray	District heating, heat pump	Economic, environment, comfort	(refer to Section 3).

1.2. Research Aims and Contributions

In the existing literature, the MPC is used extensively in building energy control. However, there is a gap in using the controller to incorporate more optimization criteria.

Addressing hybrid energy systems from a consumer perspective is another shortcoming observed in the literature. The result of this study will help building simulators, energy providers, and most importantly, building managers in operating buildings to make a more optimal decision locally while reflecting the energy supply chain constraints and advantages. The main contributions of this paper are as follows:

1. A multi-objective predictive controller designed to consider cost, emissions, and comfort level of the building's indoor environment. The hybrid heating system is supplied by a heat pump and district heating.
2. Proposing an MPC and a system architecture to assist the process of applying it to real-world hybrid-heated buildings
3. Competitiveness analysis of district heating versus heat pumps in the Swedish energy market using real-world data.
4. In a sensitivity analysis, investigating the control behavior under different cost, emission and outdoor weather condition scenarios.

The rest of the paper is organized as follows: Section 2 provides a detailed framework and system architecture of the hybrid heating system considered in this study. It further explains the minimum necessary data for the controller to operate and how they can be obtained. Section 3 shows the simulation results under different generated case studies and compares them against one another. Section 4 discusses the results and authors' findings based on the findings in this paper. Section 5 provides a summary and possible future study paths based on our research. Finally, Appendix A describes detailed building simulation parameters that are used in this study.

2. Materials and Methods

2.1. System Overview—Hybrid Heating System

The system under study is a hybrid heating system, including centralized DH and a building-integrated HP, connected to a single-family building with a single heating zone. The overall system framework is depicted in Figure 1. Each system has separate heat delivery pipes, meaning that they work independently. The HP considered in the study is an air-to-water system based on a commercial model in [32], and it is powered by electricity. It was assumed that the maximum building heat demand in the simulated week is smaller than each heat supplier's capacity, meaning that one heating unit can supply the entire demand at any time.

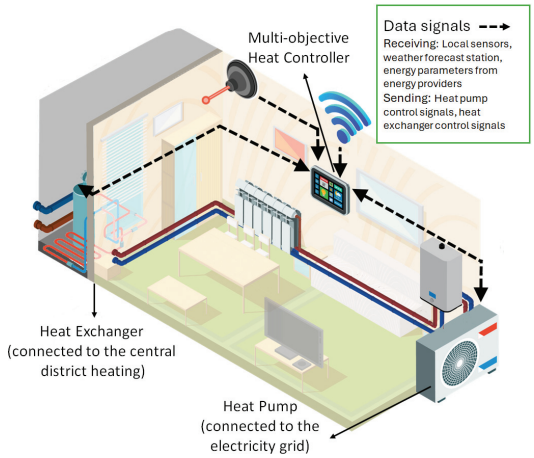


Figure 1. General framework of the studied system.

The energy parameter signals, namely emission and cost, are received from energy providers. The DH delivers heating with pipelines and a heat exchanger unit connected to the building. Based on the study location, it is assumed that the DH prices are fixed throughout the year, while the emission level is changing with one-hour resolution. As for the electricity, both prices and emission levels follow hourly time-series data. More details on the energy prices are explained in Section 3.1.

2.2. System Architecture: Cloud and Local Data

In the application of the control system described here, it is assumed that the controller has access to several data sources. These data are received either locally through the sensors installed in the case study or through communication with data providers. We have identified several signals that are transmitted from the energy providers and weather stations, which are (1) The day-ahead dynamic prices/emissions from the electricity provider; (2) the day-ahead heating prices/emissions from the DH provider (considered as fixed-price contracts over a year); and (3) the day-ahead ambient temperature/solar irradiance forecast.

The rest of the data is measured locally in the case study, which includes (1) the flow of the air handling unit (AHU) or exhaust air flow and its temperature to calculate the ventilation losses; (2) the estimated process energy, based on occupancy and indoor activity, to calculate the process energy input; and (3) the indoor temperature recordings to fine-tune the model predictions according to the subject building.

2.3. State-Space Building Model

At the core of the MPC algorithm is the system modeling, which arguably determines the overall accuracy and efficiency of the controller. A state-space model of the building is adopted to represent the building's thermal characteristics in this study. This study uses a discrete linear state-space model formulated as a Stochastic Differential Equation (SDE), shown in (1), as part of the controller. It is to be noted that the continuous state-space model of the building is discretized using the exponential discretization method.

$$\begin{cases} X(k+1) = AX(k) + B_u U(k) + B_w \epsilon(k) \\ Y(k) = CX(k) + D_u U(k) + D_w \epsilon(k) \end{cases}, \tag{1}$$

where k is the discrete time-step index, X is the state vector of the building, U is the system input vector (measured disturbances), ϵ is a vector with the system noises (unmeasured disturbances), and Y is a scalar with the output (indoor temperature prediction).

The mentioned state-space model is based on a physical gray-box modeling of the building, approximated by RC electrical networks. A more in-depth description of the 3R2C model can be found in Appendix A. The model and the estimated parameters were obtained from [26], which can be referred to for the exact estimated parameters.

2.4. Multi-Objective Model Predictive Controller (MO-MPC)

One of the benefits of the MPC is the capability to solve an optimization problem. Here, a discrete, non-linear MO-MPC is chosen as the core controller. The goal of the problem is to incorporate three elements to find the optimal solution, which includes the total operating cost of the heating system, the carbon emission of the heating system, and the comfort deviation of the occupants.

A multi-objective formulation is developed to tackle this, and a weighted-sum method is used to solve the problem shown in Equation (2). Equations (3)–(5) indicate each

mentioned objective expression. It is worth noting that in (5), the operative temperature of the heating zone is chosen to represent the thermal comfort. More detailed information on this comfort index is explained in Appendix B. In Equation (6), the Coefficient of Performance (COP) of the HP is calculated based on outdoor temperature according to the manufacturer's datasheet [32]. Equation (7) is the relation between HP electrical power and heating power. Finally, Equations (8)–(10) are the DH power limits, HP electrical power limits, and indoor temperature bounds, respectively.

Normalization techniques are usually used in these problems with different objective ranges to ensure an equal effect on the decision variables. Here, a common approach in MPC, namely the min–max normalization, is utilized. Each objective is normalized using min–max normalization, as in $x_{norm} = (x - x_{min})/(x_{max} - x_{min})$, to fall between (0, 1). The minimum and maximum values are determined by a series of pre-simulations on one objective at a time. By running the simulation single-objectively, we found the minimum and maximum of each objective as follows:

- The cost objective has a value between 251 and 368.
- The emission objective has a value between 2.0 and 17.2.
- The discomfort index objective has a value between 1 and 192.

The above information was used as the mix–max normalization bounds to normalize the objectives as explained above.

$$min \quad MOBJ = \sum_{k=1}^{N_k} w_1 Co_{norm}(k) + w_2 Em_{norm}(k) + w_3 DC_{norm}(k) \tag{2}$$

subject to: Equation (1),

$$Co(k) = \left(c_{HP}(k) \frac{Q_{HP}(k)}{COP_{HP}(k)} + c_{DH}(k) \frac{Q_{DH}(k)}{\eta_{DH}} \right) \Delta k \ , \forall k \in [1, 2, \ldots, N_k] \tag{3}$$

$$Em(k) = (p_{HP}(k) P_{HP}(k) + p_{DH}(k) Q_{DH}(k)) \Delta k \ , \forall k \in [1, 2, \ldots, N_k] \tag{4}$$

$$DC(k) = \begin{cases} (T_{op}(k) - T_{set+}^{comf}) \Delta k & T_{set+}^{comf} \leq T_{op}(k) \\ (T_{set-}^{comf} - T_{op}(k)) \Delta k & T_{op}(k) \leq T_{set-}^{comf} \\ 0 & \text{otherwise} \end{cases} \ , \forall k \in [1, 2, \ldots, N_k] \tag{5}$$

$$COP_{HP}(t) = 3 - \frac{5}{100}(7 - T_a(k)) \ , \forall k \in [1, 2, \ldots, N_k] \tag{6}$$

$$P_{HP}(k) = \frac{Q_{HP}(k)}{COP_{HP}(k)} \tag{7}$$

$$0 \leq Q_{DH}(k) \leq \overline{Q}_{max} \ \forall k \in [1, 2, \ldots, N_k] \tag{8}$$

$$0 \leq P_{HP}(k) \leq \overline{P}_{max} \ \forall k \in [1, 2, \ldots, N_k] \tag{9}$$

$$T_{set}^{low} \leq T_{op}(k) \leq T_{set}^{up} \tag{10}$$

where Co, Em, and DC are the cost index in (SEK), carbon emission index in (kg CO_2) and discomfort index in (°Ch), and the *norm* specifies the normalized values; N_k is the number of time steps in the simulation horizon; c_{HP} and c_{DH} are the electricity and DH time-series energy prices in (SEK/kWh); p_{HP} and p_{DH} are the electricity and district heating network time-series CO_2 emission levels in (kg CO_2/kWh); COP_{HP} and η_{DH} are the COP of HP and the DH efficiency; T_a and T_{op} are the outdoor (ambient) and the operative temperature in

(°C); Q_{DH}, Q_{HP}, and P_{HP} are the efficient heating power delivered by DH and HP and the electrical power of HP (in kW); T_{set}^{up} and T_{set}^{low} and T_{set}^{up} are the lower and upper temperature setpoints; T_{set}^{comf} is the thermal comfort temperature set.

It is worth noting that T_{set}^{comf}—standing between T_{set}^{up} and T_{set}^{low}—is considered as the ideal temperature for the occupants and is focused on in (5) as a soft constraint. Additionally, broader hard constraint bounds are applied to make sure the temperature does not protrude beyond certain levels. Generally, thermal comfort is a broad topic measured by many indoor air quality indices. Here, the operative temperature is chosen to represent this (refer to Appendix B). w_1, w_2, and w_3 in (2) are the weighted sum average coefficients and are determined as follows. The problem is solved iteratively with different weights. In all solutions, the sum of the three equals to 1, and the interval of change is 0.1. For instance, in one scenario with weights equal to $w_1 = 1$, $w_2 = 0$, and $w_3 = 0$, the simulation is focused on total cost minimization, and the other two objectives are not considered. The algorithm of the adopted controller is shown in Algorithm 1. In this algorithm, k and l are discrete time steps and control horizon indices. X_{ini} is the initial state equal to $[21 \;\; 21]^T$.

Algorithm 1 Multi-Objective Model Predictive Controller

Initialize time $k = 0$ and sampling time Δk
Initialize state variables and input variables X and U with zero vectors, $0_{N_X \times 1}$ and $0_{N_U \times 1}$
Receive the multi-objective weights and set as constants w_1, w_2, and w_3
for $k = 0, 1, 2, ..., N_k$ **do**
  Update current system states $X(k)$
  if $k == 0$ **then**
    $X(k) = X_{ini}$
  end if
  for $l = 0, 1, 2, ..., N_c$ **do**
    Update weather forecast data, T_a and I_{sol}, as constants from k to $k + l$
    Update price data for DH and HP, c_{DH} and c_{HP}, as constants from k to $k + l$
    Update emission data for DH and HP, p_{DH} and p_{HP}, as constants from k to $k + l$
    Construct the control horizon equation based on Equation (2): $\sum_{l=1}^{N_c} MOBJ$
    Solve the local optimization problem above with the SDE in Equation (1) and constraints in Equation (3)–(10) and find the optimal $u(k)$-$u(k + l)$ vector
  end for
  Save the results, $u(k)$ and $x(k)$, in vectors X and U
  Communicate the candidate solution vector of $U(k)$ to the heating resources separate controllers
  discard $u(k + 1)$-$u(k + l)$ controls
  Calculate the next state and outputs, $X(k + 1)$ and $Y(k)$, with the gray-box model explained in Appendix A
  Wait until $t = (k + 1)\Delta k$
  $k = k + 1$
end for

The simulation was conducted on an online notebook in the Google Colaboratory environment [33], using the Python programming language version 3.11 [34]. The Casadi library package is used to model the controller and the optimization problem with the in-built non-linear IPOPT solver [35].

3. Results

This section highlights the results of the simulation-based study in this work. It is worth noting that several assumptions are made in our work, which are as follows:

- The changes in building insulation wear and tear and efficiency of the heating systems are negligible during the simulation period.
- The size of the heating systems is selected in the sense that each heating resource can independently supply the building's heating demand.
- The heating demand consists only of the space heating, and the domestic hot water demand is not considered.

3.1. Case Study

The simulation result of the proposed controller is compared against PID controllers. To do so, several cases are constructed to make the comparison more tangible. These cases are defined based on the used heating resource and the objective of the simulation and are shown in Table 2. Cases A and B represent PID-controlled heating systems with a single input—HP in Case A and DH in Case B—and serve as the baselines. Cases C and D are MPC-controlled single-input (either HP or DH) with all three objectives and equal weights. Cases E, F, and G are single-objective MPCs with hybrid input (both HP and DH), with the objective focusing on cost, carbon emission, or comfort level one at a time. Finally, case H is one optimal multi-objective hybrid input case with equal weights ($w_1 = 0.33$, $w_2 = 0.33$, $w_3 = 0.33$).

Table 2. Simulation cases based on the model, objective(s), and input source(s).

Case	Description	Energy Source(s)		Objective(s)		
		Heat Pump	District Heating	Cost	Emission	Comfort
A	PID-HP	✓	-	-	-	-
B	PID-DH	-	✓	-	-	-
C	MPC-HP	✓	-	✓	✓	✓
D	MPC-DH	-	✓	✓	✓	✓
E	MPC-Cost	✓	✓	✓	-	-
F	MPC-Emission	✓	✓	-	✓	-
G	MPC-Comfort	✓	✓	-	-	✓
H	MO-MPC	✓	✓	✓	✓	✓

The simulation is conducted over a week in the cold season, the first week of December 2023, with the weather conditions [36] and local energy prices of Malmö, Sweden, in the mentioned period. Figure 2 illustrates weather data and energy-related input signals (also known as measured disturbances in the control context). The dynamic spot market electricity prices [37] and the fixed DH prices for small buildings [38] located in southern Sweden are obtained from open data sources. As the paid electricity bill for the private customer includes certificates and additional network charges, a 66% electricity cost is added to the hourly spot market costs. The electricity emission data [39] are available online, and the DH emission factor according to the Swedish National Board of Housing (Boverket) equals 56 g CO_2/kWh [40]. Since this study focuses on creating added value on the changing energy parameters, a dynamic DH emission is required. Therefore, a Gaussian random hourly emission scenario with the mean equal to 56 g CO_2/kWh and sigma equal to 7.5 g CO_2/kWh is generated, with the assumption that the emission levels are the highest in the daily coldest hours and peak usage of DH, and is illustrated in Figure 2. This assumption is grounded on the fact that in early morning hours and late afternoon, due to colder outdoor temperatures and typical social patterns, energy demand for space heating and hot water surges. Consequently, more air-polluting and lower-priority centralized heating sources are used, resulting in higher carbon emissions of the DH system [41].

The building, heating system, and controller are also other components that require modeling data for simulation. The building data is obtained from the ZEB living lab project, an experimental building developed for thermal analysis of buildings and their energy resources. The gray-box modeling of this building and estimated thermal parameters are

presented in Appendix A. The heating system parameters considered in this study are shown in Table 3. Additionally, the MPC setpoints, determined based on the data availability and project needs, and PID set parameters, based on the guidelines in [42], are shown in Table 4. It is worth mentioning that the PID set point is considered with a dead band between 21 and 23 °C so that it is comparable with the MPC comfort zone, which has the same thresholds.

Table 3. Heating systems specification.

	Definition	Symbol	Value
HP	Model	-	F2050-6 [32]
	Type	-	air-to-water [32]
	Max. electrical power [kW]	$\overline{P}_{max}$	6 [32]
	Min. power [kW]	-	0
	Coefficient of Performance	COP_{HP}	Acc. to Equation (6) [32]
DH	Max. heating power [kW]	$\overline{Q}_{max}$	6
	Min. power [kW]	-	0
	Heat exchanger efficiency	η_{DH}	0.98

Table 4. Controller setpoints and parameters for the model predictive and the PID controller.

	Definition	Symbol	Value
MPC	Type	-	Discrete MPC
	Optimization type	-	Non-Linear
	Operative temp. low/up setpoint [°C]	T_{set}^{low} / T_{set}^{up}	20/24
	Comfort zone operative temp. [°C]	T_{set-}^{comf} / T_{set+}^{comf}	21/23
	Simulation Horizon [hr]	N_k	168
	Simulation Sample time [min]	Δk	15
	Control horizon [hr]	N_c	6
	Control signal interval [min]	-	30
PID	Operative temp. setpoint [°C]	-	21–23
	Proportional factor	-	5.0
	Integral factor	-	0.1
	Derivative factor	-	0.05
	Control signal interval [min]	-	30

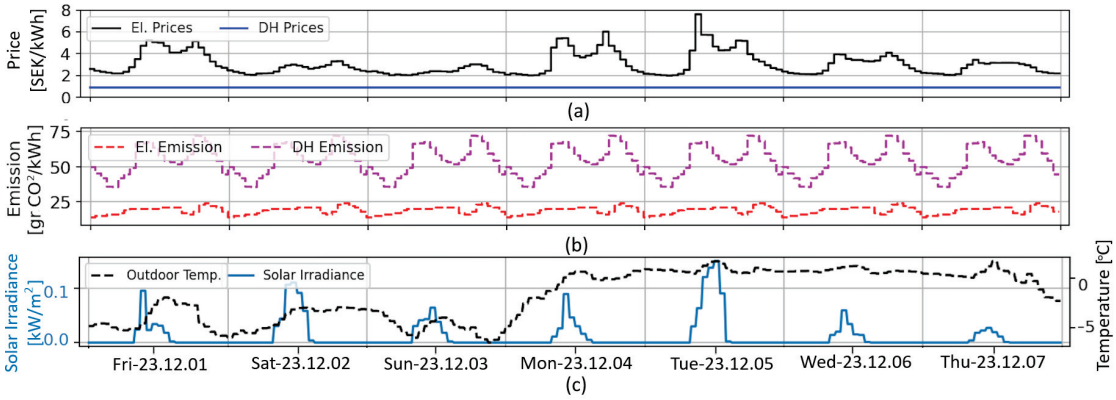


Figure 2. Input signals (also known as measured disturbances) including (**a**) electricity and district heating hourly prices, (**b**) electricity and district heating hourly emissions, and (**c**) hourly outdoor temperature and global horizontal solar irradiance.

3.2. Simulation Results

The simulation results of the eight constructed cases are presented in Table 5, and the scaled values of each objective for these cases are illustrated and compared in Figure 3. The heat output and operative temperature profile of each case are illustrated in Figure 4. Table 5 shows the objective values for each considered case. Cases A–D all have a single heating input. Cases A and B focus on keeping the temperature at a certain level, while C and D consider all three objectives simultaneously. The data shows that the HP-based

PID controller has the highest cost, while the DH-based PID controller case has the highest emission level (almost eight times the former), with both having quite low discomfort. Cases C and D decrease the cost and emission slightly, compared to A and B, compromising the comfort level slightly more. This fact is also reflected in Figure 4a–d.

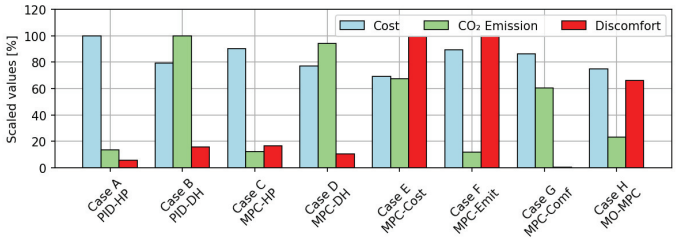


Figure 3. Scaled cost, carbon emission, and discomfort index of the studied cases using the max-scaling method.

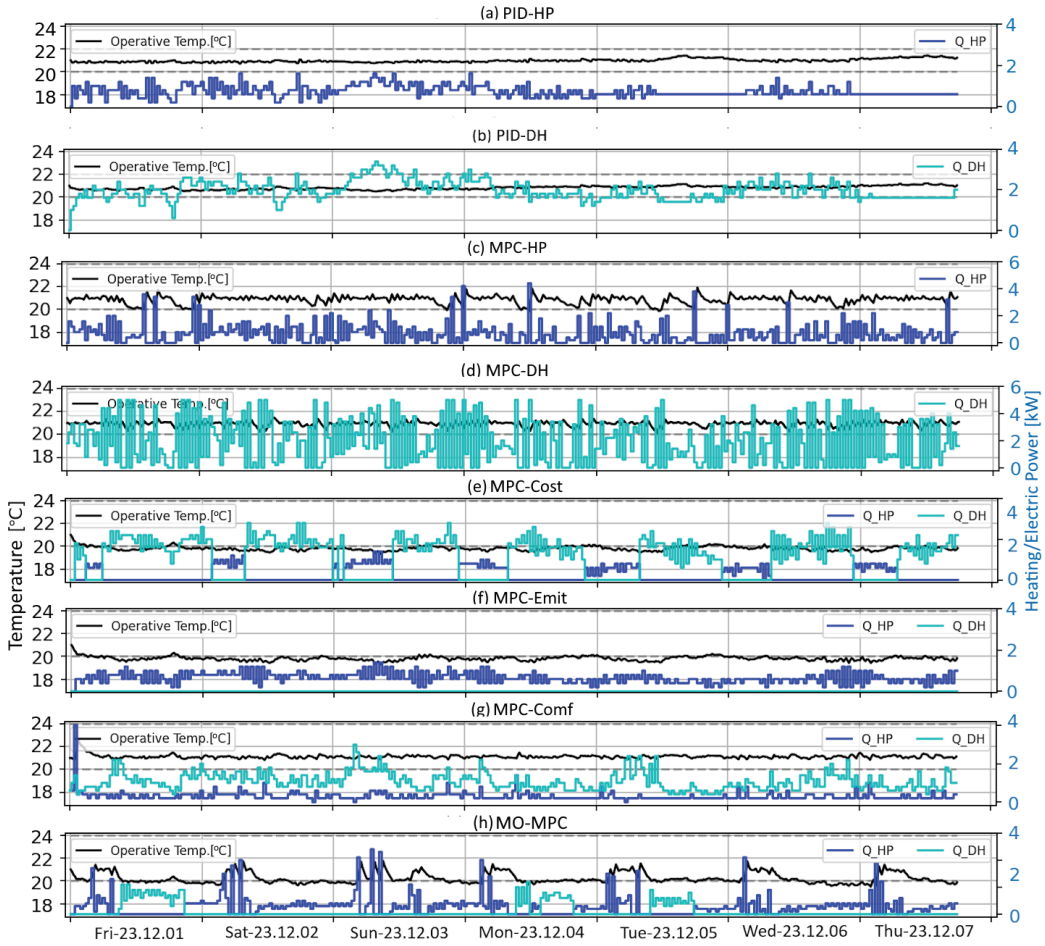


Figure 4. One-week simulation result, the heating, and the operative temperature profiles for the considered cases.

The rest of the cases are considered to focus on one or a mixture of objective statements (as mentioned in Equation (2)), with hybrid input, trying to minimize their value in cases E-H. Case E demonstrates the least cost while having the highest emission, after Cases B and D. Additionally, Cases E and F each have the lowest comfort. Compared to E and F, Case G has the smallest discomfort level while having relatively high cost and emission objectives. Finally, the results of case H stand between the extreme cases, considering all criteria at once, as discussed before, with equal penalty weights.

Table 5. Numerical results for the studied cases with model predictive controllers and PID controllers in one week of simulation.

Case	Objective			Energy Consumption			Operative Temp.	
	Cost [SEK]	Emission [kg CO_2]	Discomfort Index [°Ch]	District Heating [kWh]	Heat Pump [kWh]	Total [kWh]	Min. [°C]	Max. [°C]
A.PID-HP	363	2.3	11	0	120	120	20.6	21.7
B.PID-DH	288	17.2	30	317	0	317	20.5	21.4
C.MPC-HP	327	2.1	32	0	115	115	19.8	21.4
D.MPC-DH	280	16.2	20	308	0	308	20.1	21.4
E.MPC-Cost	251	11.6	191	184	38	222	19.7	21.0
F.MPC-Emit	325	2.0	192	0	107	107	19.7	21.0
G.MPC-Comf	313	10.4	1	175	51	226	20.8	24.3
H.MO-MPC	272	4.0	127	96	38	134	19.8	23.6

The data in the table reveals that, in terms of cost, the base case (case A) is the most expensive operation of the system, while case E has the lowest expense, followed by cases H, D, and B. In terms of emissions, case F has the lowest carbon footprint, followed closely by the base case. Finally, comparing the comfort level of the generated cases indicates that case G has the lowest discomfort, while cases E and F have the highest. Finally, case H considers the three objectives simultaneously, and it is observed that the objective values are positioned between the single-objective cases. With 9% more cost compared to case E, case H has half the emission of this case with a higher comfort level. Additionally, the results shown in Figure 3 indicate that in the last-mentioned case (Case H), approximately a 25% saving on cost and 75% saving on carbon emission can be achieved compared to the extreme cases while lowering the comfort slightly (equal to 65% of the least comfortable case).

After conducting the above simulation, to obtain a better perspective of the influence of each objective and multiple criteria-based solutions, we focused on a multi-objective simulation. The problem was initially solved using two objectives at a time by setting the weight of the third objective to zero. The weights of the remaining two objectives were varied in 0.1 increments from 0 to 1, ensuring they always summed to 1. The results for three different combinations of bi-objective problems are calculated and illustrated in Figure 5. Some specific weighted scenarios are highlighted, and further, the results are compared to PID controller cases in these figures.

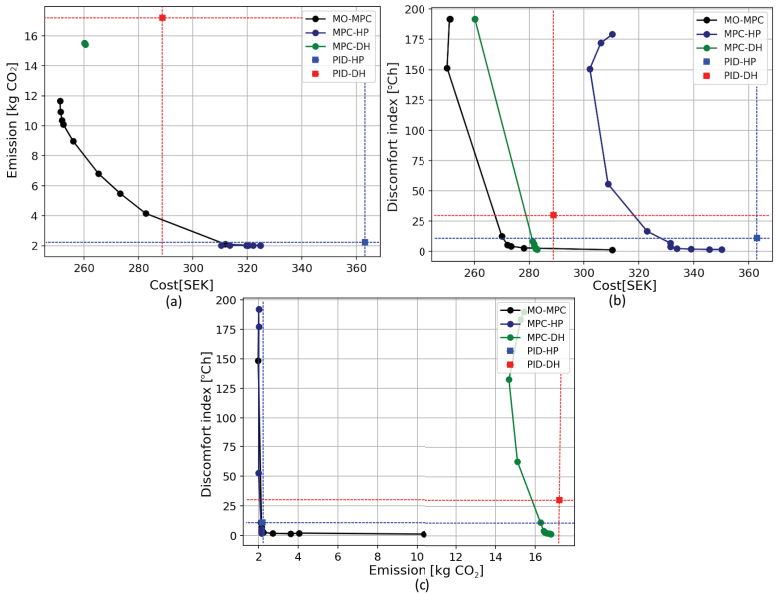


Figure 5. The Pareto Frontier of MO-MPC bi-objective problem solution with different combinations of weights from 0.1 to 1 for (**a**) cost versus carbon emission minimization with $w_3 = 0$, (**b**) cost versus

discomfort minimization with $w_2 = 0$, and (**c**) carbon emission versus discomfort with $w_1 = 0$. The results are compared with the PID controller values(the dashed line are guide lines to specify the PID case positions in the figure.

Finally, the problem was solved with all three objectives explained previously in Section 2, and the results are shown in a 3D plot in Figure 6. The figure is generated as a dotted line and a surface and compared to the values of PID controllers in cases A and B. In the right figure, the color map is the discomfort index, coloring the z-axis. In the left figure, the red triangle is a reference plane.

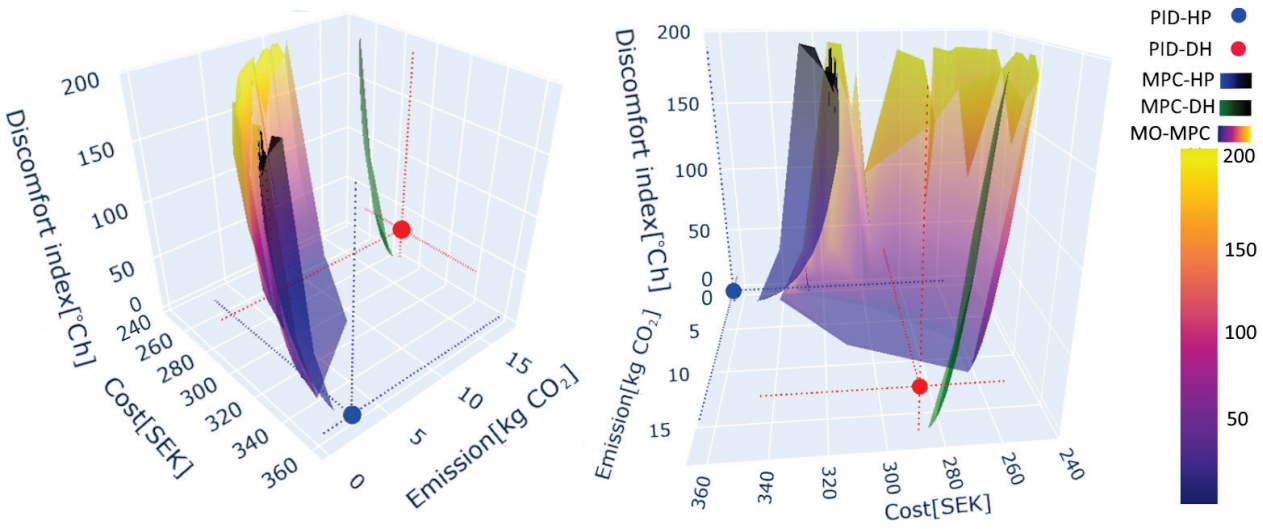


Figure 6. The Pareto Frontier of MO-MPC and single-input MPC (MPC-HP and MPC-DH cases) of the system with three objectives, namely cost, carbon emission, and discomfort index, in 3D plots (from two perspectives of the same plot).

3.3. Sensitivity Analysis

In this subsection, we present the change in the output objectives, namely cost, emission, and discomfort index, and the use of energy resources and their dependency on the input signals and external conditions.

3.3.1. Price Changes

One of the simulation's uncertainties is the dynamic electricity prices in Sweden. These prices are often volatile and dependent on network constraints, demand, renewable energy production, and weather forecasts. It is to be noted that, at the time of writing this article, the DH prices are fixed for one year and do not change until the year after, in the Swedish context [38]. Here, we conducted the sensitivity analysis by fixing the DH prices and changing the electricity prices. Scenarios are constructed by changing the electricity price signal proportionally from −50% to +50%. It is worth noting that the results can be perceived as the changes representing the ratio between two price signals. For example, a +20% electricity prices (c_{HP}) scenario is the same as a 1.2 ratio between electricity and DH prices (c_{HP}/c_{DH}). The results are shown in Figure 7a–c. Figure 7b,c represent the share of HP and DH in each case. It is worth noting that Cases A–D with the PID controller and single-input MPC do not display changes in their energy use and therefore are not considered in price and emission changes in this and the following subsection.

The results in this illustration indicate that, in case D, a 20% increase in electricity prices results in a sharp decrease of 82% in HP, meaning that it drives the algorithm to virtually always prioritize DH over HP. The price reduction of over 40%, on the other hand,

results in shifting to HP for most of the time, and cheaper electricity prices will make DH almost impractical to use at all times. In case H, however, the shift in energy sources is more moderate. A 40% electricity price decrease has more effects on this case, presumably because the HP has lower emissions; this case prioritizes HP even more than case E.

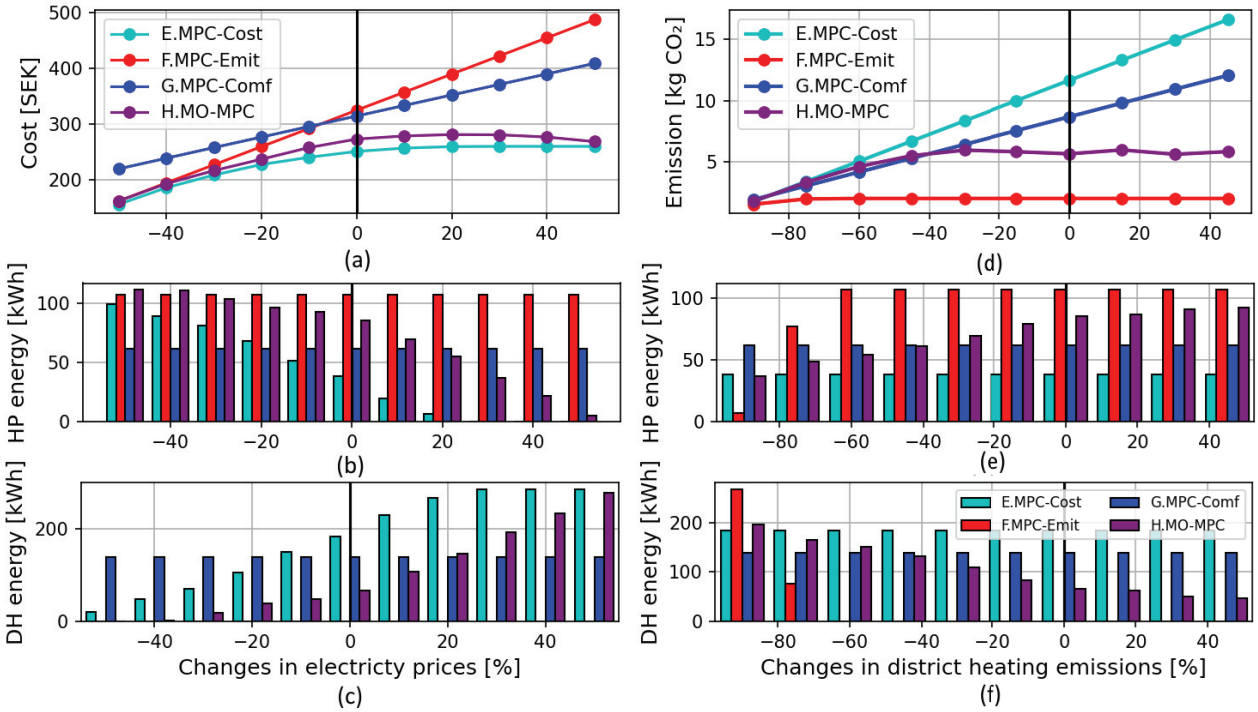


Figure 7. Sensitivity analysis: (**a**–**c**) showing the system cost changes and heating resources' share when electricity prices change, while (**d**–**f**) show the emission changes and heating resources' shares when the emission level of district heating changes.

3.3.2. Emission Changes

Another case-sensitive parameter is the level of network emissions. Hourly emission data, reflecting the resource mix of the DH and electricity, were more difficult to access at the time of publishing this paper. The electricity emission, while it might differ to some extent, is generally quite low in Sweden and considered unchanged. The DH emission, however, can vary substantially based on the season or the sources of heating that are used. To consider these changes, scenarios changing the emission from −90% to +40% are considered. It is worth noting that according to [40], the DH emission level can be more volatile, and therefore higher changes compared to the previous analysis on electricity have been considered. The results, such as the changes in the emission and the share of heating systems, are shown in The results are shown in Figure 7d–f.

The results show that the emissions in cases E and G are quite proportional to the increased emission factor of DH, and the share of HP and DH stays unchanged (the cyan and blue bars in Figure 7e,f. This reflects the fact that emission is not considered in their objective function. In cases F and H, however, the controller behaves differently. In case F, it changes the energy use only for scenarios where emission is lowered more than 80% (the red bars in Figure 7e,f). This is due to the fact that the HP emissions are drastically lower than the DH's. In case H, the changes in energy mix happen across all emission scenarios. In other words, the DH is gradually being used more, lowering the emission levels. This reflects the fact that the three objective values should be equal in all scenarios in this case.

3.3.3. Weather Changes

The alterations in weather conditions—especially outdoor temperature—can affect the results in two ways. Firstly, since the efficiency of the HP is weather-dependent (see Equation (6)), the HP is less efficient at lower temperatures. Secondly, the heating load of the entire system will increase when the temperature drops. Consequently, a sensitivity analysis is conducted to demonstrate the heating system's behavior in response to changes in temperature.

To evaluate the controller's performance under different weather conditions, six temperature scenarios were created, varying the outdoor temperature in 5 °C increments from −15 °C to +10 °C relative to the base case. In the base case, the outdoor temperature ranges between −5 °C and 0 °C; therefore, the coldest scenario corresponds to temperatures between −20 °C and −15 °C, while the warmest scenario represents conditions between +5 °C and +10 °C. The reason for this range is that the assumed HP's minimum operating temperature stands at −20 °C, and the heating system is usually utilized not above +10 °C ambient temperature. The value of each objective and the share of DH and HP in each case over the simulation horizon are depicted in Figures 8 and 9, respectively. In the latter figure, the bars corresponding to DH and HP are marked.

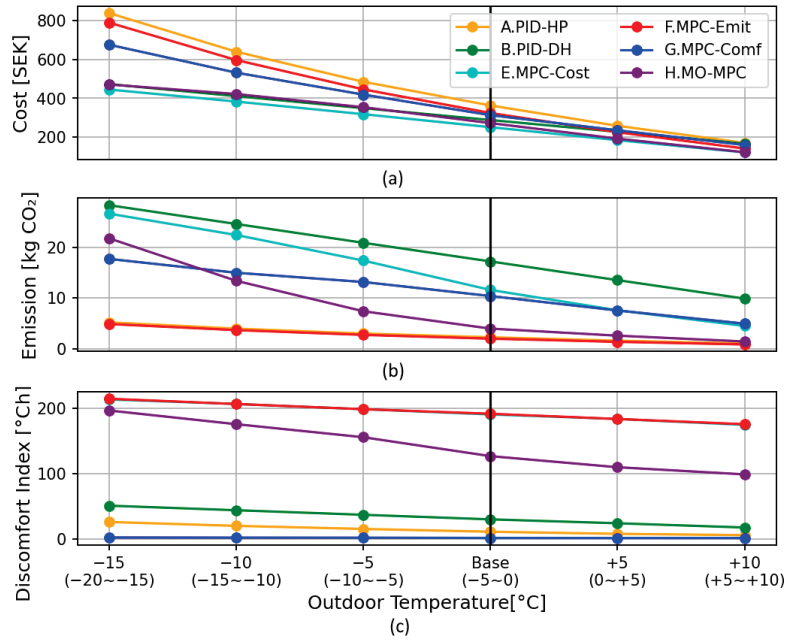


Figure 8. Sensitivity analysis on the outdoor temperature showing the value of (**a**) cost, (**b**) emission, and (**c**) discomfort index for the simulation cases when the outdoor temperature varies.

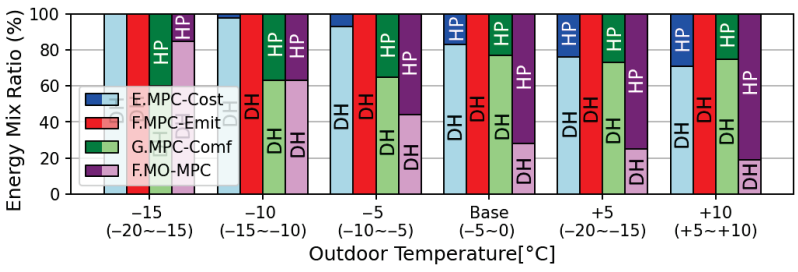


Figure 9. Sensitivity analysis on the outdoor temperature showing the share of HP and DH in percentage for the simulation cases when the outdoor temperature varies.

The results in Figure 8 show that with the drop in temperature, all objective criteria increase. In terms of cost, the increase is more moderate in cases E and H, which prioritize cost and mix of objectives. The emission increases steadily for all scenarios, with case F being less pronounced. In terms of comfort, cases A, B, and G have retained almost the same level of comfort with the changes in temperature. It is worth noting that in this graph, cases C and D, which involve only a single input, are excluded to avoid overcrowding the figure.

The share of energy resources shown in Figure 9 demonstrates that at lower temperatures, cases E and H experience more DH use, where at a -15 temperature drop, almost all load is supplied by the DH. The reason, as mentioned earlier, is the lower COP of HP in colder climates. Case F supplies the entire demand with HP regardless of the temperature since the emission level of HP is still much lower than that of DH. The only scenario where HP use stays unchanged and even increases slightly with the drop in temperature is case G. In this comfort-based case, the cost and emission factors are excluded, which makes the input sources unimportant to the algorithm, as long as the discomfort is minimized. The slight increase in HP use could be the effect of its higher efficiency in general. It is worth noting that cases A, B, C, and D are excluded since they are single-input cases, wherein cases A and C, HP share is always 100%, and in cases B and D, DH share is always 100%.

4. Discussion

The prioritization of objectives is a key consideration in addressing multi-objective problems. The results in Table 5 suggest that the three objective goals are virtually in "contrast", a term proposed by Sameti and Haghighat [43]. This means that an increase in one will lead to a decline in the other. In other words, opting for cost minimization will increase the emissions and discomfort, while opting for carbon minimization will increase the cost and thermal discomfort, and so on. Here, case H is merely an example of a candidate Pareto frontier, which considers equal weights and importance for all three objectives. Overall, a strategy must be taken by the stakeholder (building manager, network operator, or both) to determine the weights and make a compromise with the less important objectives. In the literature, there are several articles addressing the weight assignment in such problems. In [6], a standard weighting method is described in which objectives are given equal weights, yielding the initial results. After that, start changing the weights in a way that the sum will still add up to 1 until it has the expected prioritization. Another research [44] has used a lexicographic formulation in an attempt to rank the objectives based on importance. Afterwards, solving the problem with one objective at a time and adding the results as constraints, trying to solve the problem with the next objective. This method is specifically useful when there are many objectives involved in a multi-objective problem.

From another perspective, the significance of input parameters on the results is monitored during the simulation. Parameters such as the efficiency of each heating system, the difference between the cost and emission signals, and the weights definition are the main link between the results and inputs. The ratio between the efficiencies (COP_{HP}/η_{DH}) determines at what ratio between input signals the heating sources are switched on. For instance, if this ratio equals three, it means in cost-based cases the HP is activated when the electricity cost is less than three times the DH cost. This argument is valid for emission levels and the emission signal as well. On top of that, the weighting factors decide which heating source to switch on based on a certain input signal. For example, a higher cost objective weight will prioritize the electricity and DH costs over their emission level.

In terms of the numerical results and the optimal strategy, the proposed MO-MPC outperforms the PID controllers and single-input MPCs. These solutions are compared to

MPC cases in 2D and 3D Pareto figures in Figures 5 and 6. Ideally, the solution on the depicted line is optimal, and the ones in the dominated region (above and to the right of the Pareto frontier line) are suboptimal, since at least one Pareto-optimal solution exists that improves one or more objectives without worsening the others. The PID solutions fall into the dominated region, which suggests that they are suboptimal solutions. The single-input MPCs are almost aligned with the MO-MPC curve, which shows they are superior solutions compared to the PID ones. This shows that the algorithm successfully optimizes the hybrid heating system, taking advantage of the price and emission levels during the simulation period.

In terms of the thermal comfort in simulation results, in PID-controlled systems (cases A and B), which prioritize the operative temperature, it has led to a fairly comfortable environment. The discomfort index, however, increases drastically in MPC cases E and F and to some extent in case H. While high discomfort is observed in some MPC cases, the MO-MPC provides this advantage to set how much importance should be given to the discomfort index, since other criteria can play a role. For instance, in case H, the discomfort has increased less intensely while lowering the cost and emission of the system at the same time.

Another remark is that while the proposed controller is functional in other hybrid systems in different contexts, the share of the heating resources might vary. This depends on the input energy parameters, namely the price and emission levels in the target geographical location. The MO-MPC algorithm is otherwise guaranteed to make optimal heating decisions based on the system inputs.

The solution requires both energy systems to be in standby mode and the prices to be meticulously chosen by the operators. In many buildings with hybrid heating sources, HP is merely a backup resource for when the demand is high or sometimes manually switched on by the building manager based on individual preferences. Additionally, for such a system to exist and make decisions automatically, energy prices ought to be determined more competitively by the energy provider, taking network and environmental constraints in energy use into account.

Another point of discussion is how to determine the "right" weights (in this context, w_1, w_2, and w_3). Something that has not been fully addressed in the previous multi-objective research is the authority to tamper with the weights of the proposed solution from different stakeholder perspectives. Based on the theory of Pareto Optimality, the multi-objective solutions in the discussed cases (cases E–H) are at the front of all "Pareto Optimal" solutions with different objective prioritization [45]. However, the "right" weights are often subjectively different—if not in conflict—from a consumer perspective versus a network operator perspective. For instance, the consumer might opt for a maximum comfort level, which, according to our simulation results, has a high cost and emission level. This might be entirely different from the network operation goals. This will raise the question of the level of authority in determining the weights from a consumer perspective. More research is required on how and to what extent each stakeholder can determine the optimization weights.

A further aspect to consider is the scalability of the proposed approach. In this study, we focused on a single-family, single-zone building; however, two distinct scenarios arise when extending the framework to multi-zone buildings. In the first scenario, where each household is equipped with its own heat pump (HP), the algorithm remains scalable, as each apartment can independently benefit from an MO-MPC system. In the second scenario, involving shared heating resources—specifically a common HP—a distributed or centralized MPC architecture would be required. Although several studies have explored such control strategies, the scalability of the present model for these types of buildings still requires validation in further studies.

The results illustrate the prioritization of chosen energies in the Swedish energy market. While the method is general and applicable in any setting and climate, the share of each energy resource is dependent on the input signals (cost and emission) of that market. The relation between these energies can be further assessed in other heat-requiring countries. The heating demand consists of space heating only in this paper. The domestic hot water is another major heat demand. It usually requires a prediction model based on consumers' living patterns and regulating the hot storage tank temperature/flow accordingly [46,47]. This was out of the scope of this paper but should be highlighted as a future direction in a mixed-method study.

We have identified some limitations in this study. The sum of operative temperature deviations as a thermal discomfort index cannot fully reflect this criterion. It indeed penalizes the higher deviations (especially above one °C) exponentially. This will force the optimization to keep the deviations within one °C. However, this method assumes symmetric discomfort (e.g., 2 °C hotter is considered as uncomfortable as 2 °C too cold), while this does not reflect reality, as some individuals may tolerate higher temperatures more easily than colder. Another limitation is that the comfort level criteria do not account for humidity, air movement, or clothing level, which are part of more advanced thermal comfort models, such as predicted mean vote.

Finally, in this study, both the air-to-water HP and the DH system were modeled with sufficient capacity to individually meet the entire heating demand. This assumption was made to focus on the operational performance of the MPC algorithm, allowing it to determine the optimal allocation between the two heat sources without constraints from component sizing. In practice, the HP would typically operate up to a defined bivalence point, and the DH would supply the remaining load. The MPC framework can easily be extended to include such a capacity limitation, which will be addressed in future research.

5. Conclusions and Future Directions

This paper investigates a hybrid heating system control and provides a practical framework to apply in real-world scenarios. The performance of a Multi-Objective Model Predictive Controller (MO-MPC) that applies different combinations of cost, emission, and comfort level of a hybrid heating system in an individual building. The heating system is composed of a central district heating (DH) with a controllable heat exchanger and a building-integrated heat pump (HP). The results are compared to a conventional PID controller with a single heating resource. The simulation is conducted using electricity and DH market data for a week in the cold season in the Swedish energy market.

Eight cases with different inputs and goals are constructed to compare the systems against one another. The results demonstrate that the MO-MPC algorithm outperforms the PID controller from several viewpoints. The cost saving and emission saving of the MO-MPC can be as high as 10% and 13% compared to the single-input PID system, while the achievable savings on cost and emission with the hybrid system advantage are up to 25% and 77%, respectively. Further, sensitivity analysis shows that changes in electricity prices can heavily affect the optimal solution. Only a 20% increase in electricity prices makes DH virtually always superior to HP in a cost-based solution. This emphasizes the importance of dynamic cost determination by energy providers to have a hybrid solution.

For further development of this research, several elements should be considered or improved to make the system more robust and closer to reality. Here, thermal comfort is measured by the operative temperature. More indices (qualitative and quantitative) will improve the accuracy and validity of this heating system objective. Additionally, the multi-objective weights considered here are essentially examples of the final solution. As

discussed in the discussion section, very few studies have investigated consumer choices and heating priorities and how they might affect the energy network. The consideration of domestic hot water prediction was not in the scope of this paper; however, it can add value in terms of making the model more realistic through a mixed-method approach.

Author Contributions: Conceptualization, A.S., P.D., R.M. and R.S.; methodology, A.S.; software, A.S.; validation, A.S.; formal analysis, A.S.; data curation, A.S.; writing—original draft preparation, A.S.; writing—review and editing, A.S., P.D., R.M. and R.S.; visualization, A.S.; supervision, P.D., R.M. and R.S.; project administration, R.M.; funding acquisition, P.D. and R.M. All authors have read and agreed to the published version of the manuscript.

Funding: This research is partially supported by the Knowledge Foundation (Stiftelsen för kunskaps- och kompetensutveckling) for the project titled "Intelligent and Trustworthy IoT Systems" under Grant No. 20220087-H-01.

Data Availability Statement: The original contributions presented in this study are included in the article. Further inquiries can be directed to the corresponding author(s).

Conflicts of Interest: The authors declare no conflicts of interest.

Abbreviations

The following abbreviations are used in this manuscript:

DH	District Heating
HP	Heat Pump
MPC	Model Predictive Controller
MO-MPC	Multi-Objective Model Predictive Controller
PID	Proportional–Integral–Derivative
RBC	Rule-Based Controller
RC	Resistor–Capacitor
AHU	Air Handling Unit
COP	Coefficient of Performance
I.I.D.	Independent and Identically Distributed

Appendix A. Gray-Box Model of the Building

In this section, the building simulation model is described. To capture the thermal characteristics of the case study—the "ZEB Living Lab" experimental building [48]—a gray-box model is used. Yu et al. in [26] experimented with different RC networks applied to the same case study with different orders and numbers of parameters and realized that the stochastic 3R2C model, depicted in Figure A1, exhibited the least residual error and performed more robustly on the validation dataset. The same model and parameters are used in this study, which are listed in Table A1.

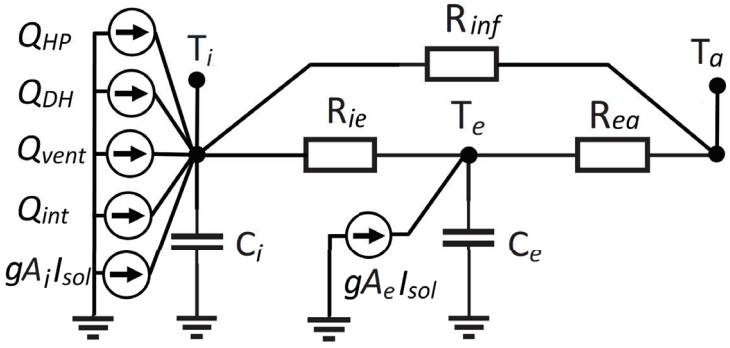


Figure A1. Gray-box model representation of the building.

Equations (A1)–(A5) describe the details of the building state-space model previously mentioned in Equation (1) in this study. Model states, inputs, and disturbances are shown in (A1). The model parameter matrices are detailed in (A2). Equations (A3) and (A4) are the SDEs of the building. Finally, Equation (A5) is the heat loss through ventilation (or gained through an air handling unit).

$$X = \begin{bmatrix} T_i & T_e \end{bmatrix}^T,\ U = \begin{bmatrix} Q_{HP} & Q_{DH} & Q_{vent} & Q_{int} & I_{sol} & T_a \end{bmatrix}^T \\ \epsilon = \begin{bmatrix} \epsilon_{Ti} & \epsilon_{Te} \end{bmatrix}^T \tag{A1}$$

$$A = \begin{bmatrix} -\frac{1}{C_i R_{ie}} - \frac{1}{C_i R_{inf}} & \frac{1}{C_i R_{ie}} \\ \frac{1}{C_e R_{ie}} & -\frac{1}{C_e R_{ie}} - \frac{1}{C_e R_{ea}} \end{bmatrix} \\ B_u = \begin{bmatrix} \frac{1}{C_i} & \frac{1}{C_i} & \frac{1}{C_i} & \frac{1}{C_i} & \frac{gA_i}{C_i} & \frac{1}{C_i R_{inf}} \\ 0 & 0 & 0 & 0 & \frac{gA_e}{C_e} & \frac{1}{C_e R_{ea}} \end{bmatrix} \\ C = \begin{bmatrix} 1 & 0 \end{bmatrix},\ D_u = \begin{bmatrix} 0 & 0 & 0 & 0 & 0 & 0 \end{bmatrix} \\ B_w = \begin{bmatrix} 1 & 0 \\ 0 & 1 \end{bmatrix},\ D_w = \begin{bmatrix} 1 & 0 \end{bmatrix} \tag{A2}$$

$$C_i \frac{dT_i}{dt} = \frac{T_e - T_i}{R_{ie}} + \frac{T_a - T_i}{R_{inf}} + Q_{HP} + Q_{DH} \\ + Q_{vent} + Q_{int} + (gA_i) I_{sol} + \epsilon_{Ti} \tag{A3}$$

$$C_e \frac{dT_e}{dt} = \frac{T_i - T_e}{R_{ie}} + \frac{T_a - T_e}{R_{ea}} + (gA_e) I_{sol} + \epsilon_{Te} \tag{A4}$$

$$Q_{vent} = \dot{m} C_p (T_{sup} - T_{ex}) \tag{A5}$$

where T_i, T_e, and T_a are the indoor, envelope, and outdoor (ambient) temperatures, respectively; ϵ_{Ti} and ϵ_{Te} are the indoor and envelope temperature disturbances; R_{ie}, R_{ea}, and R_{inf} are the heat resistance between indoor and envelope, envelope and outdoor, and indoor and outdoor through windows and doors, respectively; C_i and C_e are the heat capacity of indoor thermal mass and the heat capacity of the external walls; Q_{vent} is the heat lost (or gained) through ventilation (or air handling unit); Q_{int} is the indoor activity and process energy; gA_i and gA_e are the active area times the heat gain through windows and through walls based on each surface area; $\dot{m}$ and C_p are the air mass and the air heat unit; and, finally, $T_{sup}(t)$ and $T_{ex}(t)$ are the supplying and exhausting air temperatures of the system.

It is worth noting that the Q_{int} and Q_{vent} are considered constant and neutralize one another; therefore, they are not used in this study. ϵ_{Ti} and ϵ_{Te} are generated based on the residuals of the RC model. The one-step predictions (residuals) are estimates of the system noise (i.e., the realized values of the incremental Wiener process) added together with the observation noise. They are assumed to be white noise, i.e., Independent and Identically Distributed (I.I.D.).

Table A1. Gray-box model thermal parameters used in this study.

Model Name	R_{ie} [°C/kWh]	R_{ea} [°C/kWh]	R_{inf} [°C/kWh]	C_i [kWh/°C]	C_e [kWh/°C]	gA_i [m^2]	gA_e [m^2]
3R2Csto	58.49	1.15	15.75	1.15	4.22	1.56	0.122

Appendix B. Discomfort Index—Operative Temperature

In order to choose a simple yet efficient index to calculate the discomfort of the building occupants, operative temperature was chosen. This index is related to the indoor temperature (T_i) and the mean radiant temperature and is calculated by Equation (A6) according to ISO 7726:1998 [49]. When the metabolic rate is between 1.0 met and 1.3 met and the indoor air velocity is less than 0.1 m/s (which is valid for normal indoor activity and indoor air movement), the expression can be simply approximated by Equation (A7).

$$T_{op} = \frac{h_r T_{mrt} + h_c T_i}{h_r + h_c} \tag{A6}$$

$$T_{op} \simeq \frac{T_{mrt} + T_i}{2} \tag{A7}$$

where T_{mrt} is the mean radiant temperature, and h_r and h_c are the convective heat transfer coefficient and linear radiative heat transfer coefficient, respectively.

Since the chosen model described in Appendix A does not record the T_{rmt}, we have made a fair assumption that this temperature can be approximated by the envelope temperature. The envelope temperature is the building surface temperature on the walls, while the mean radiant temperature is defined as the uniform temperature of an imaginary enclosure on walls, ceiling, and floor, which corresponds to the radiant heat transfer between the surface and the human body. Therefore, the new operative temperature is calculated as shown in Equation (A8) and used in the simulations in this paper. To be able to compare the cases considered in this article, the sum of all the operative temperature deviations is calculated in (°Ch) [50].

$$T_{op} \simeq \frac{T_e + T_i}{2} \tag{A8}$$

References

1. European Heat Pump Association. Decarb Heat. 2023. Available online: https://www.ehpa.org/news-and-resources/campaigns/decarb-heat (accessed on 20 April 2025).
2. Eurostats. Electricity and Heat Statistics. 2024. Available online: https://www.ec.europa.eu/eurostat/statistics-explained/index.php?title=Electricity_and_heat_statistics (accessed on 20 April 2025).
3. Werner, S. European District Heating Price Series, DiVA Portal. 2016. Available online: https://www.diva-portal.org/smash/record.jsf?pid=diva2%3A1067605 (accessed on 30 October 2025).
4. Sayegh, M.A.; Jadwiszczak, P.; Axcell, B.; Niemierka, E.; Bryś, K.; Jouhara, H. Heat pump placement, connection and operational modes in European district heating. *Energy Build.* **2018**, *166*, 122–144. [CrossRef]
5. European Heat Pump Association. European Heat Pump Market Statistics Report. 2023. Available online: https://www.ehpa.org/wp-content/uploads/2023/06/EHPA_market_report_2023_Executive-Summary.pdf (accessed on 20 April 2025).
6. Drgoňa, J.; Arroyo, J.; Figueroa, I.C.; Blum, D.; Arendt, K.; Kim, D.; Ollé, E.P.; Oravec, J.; Wetter, M.; Vrabie, D.L.; et al. All you need to know about model predictive control for buildings. *Annu. Rev. Control* **2020**, *50*, 190–232. [CrossRef]
7. Maddalena, E.T.; Lian, Y.; Jones, C.N. Data-driven methods for building control—A review and promising future directions. *Control Eng. Pract.* **2020**, *95*, 104211. [CrossRef]
8. Reda, F.; Paiho, S.; Pasonen, R.; Helm, M.; Menhart, F.; Schex, R.; Laitinen, A. Comparison of solar assisted heat pump solutions for office building applications in Northern climate. *Renew. Energy* **2020**, *147*, 1392–1417. [CrossRef]
9. Hermansen, R.; Smith, K.; Thorsen, J.E.; Wang, J.; Zong, Y. Model predictive control for a heat booster substation in ultra low temperature district heating systems. *Energy* **2022**, *238*, 121631. [CrossRef]
10. Abokersh, M.H.; Valles, M.; Saikia, K.; Cabeza, L.F.; Boer, D. Techno-economic analysis of control strategies for heat pumps integrated into solar district heating systems. *J. Energy Storage* **2021**, *42*, 103011. [CrossRef]
11. Liu, D.x.; Lei, H.Y.; Li, J.S.; Dai, C.s.; Xue, R.; Liu, X. Optimization of a district heating system coupled with a deep open-loop geothermal well and heat pumps. *Renew. Energy* **2024**, *223*, 119991. [CrossRef]

12. Liu, X.; Wang, X.; Huang, K.; Feng, G.; Li, X.; Cui, Y. Research on solar-air source heat pump coupled heating system based on heat network in severe cold regions of China. *Energy Built Environ.* **2024**. [CrossRef]
13. Fiorentini, M.; Heer, P.; Baldini, L. Design optimization of a district heating and cooling system with a borehole seasonal thermal energy storage. *Energy* **2023**, *262*, 125464. [CrossRef]
14. Xue, T.; Jokisalo, J.; Kosonen, R. Cost-Effective Control of Hybrid Ground Source Heat Pump (GSHP) System Coupled with District Heating. *Buildings* **2024**, *14*, 1724. [CrossRef]
15. Knudsen, M.D.; Petersen, S. Demand response potential of model predictive control of space heating based on price and carbon dioxide intensity signals. *Energy Build.* **2016**, *125*, 196–204. [CrossRef]
16. Tarragona, J.; Fernández, C.; Cabeza, L.F.; de Gracia, A. Economic evaluation of a hybrid heating system in different climate zones based on model predictive control. *Energy Convers. Manag.* **2020**, *221*, 113205. [CrossRef]
17. Baeten, B.; Rogiers, F.; Helsen, L. Reduction of heat pump induced peak electricity use and required generation capacity through thermal energy storage and demand response. *Appl. Energy* **2017**, *195*, 184–195. [CrossRef]
18. Finck, C.; Li, R.; Zeiler, W. Optimal control of demand flexibility under real-time pricing for heating systems in buildings: A real-life demonstration. *Appl. Energy* **2020**, *263*, 114671. [CrossRef]
19. Aruta, G.; Ascione, F.; Bianco, N.; Mauro, G.M.; Vanoli, G.P. Optimizing heating operation via GA-and ANN-based model predictive control: Concept for a real nearly-zero energy building. *Energy Build.* **2023**, *292*, 113139. [CrossRef]
20. Qi, D.; Liu, Y.; Zhao, C.; Dong, Y.; Song, B.; Li, A. Thermal response and performance evaluation of floor radiant heating system based on fuzzy logic control. *Energy Build.* **2024**, *313*, 114232. [CrossRef]
21. Underwood, C. Fuzzy multivariable control of domestic heat pumps. *Appl. Therm. Eng.* **2015**, *90*, 957–969. [CrossRef]
22. Yang, J.; Wang, H.; Cheng, L.; Gao, Z.; Xu, F. A review of resistance–capacitance thermal network model in urban building energy simulations. *Energy Build.* **2024**, *323*, 114765 . [CrossRef]
23. *ISO 13790:2008*; Energy Performance of Buildings—Calculation of Energy Use for Space Heating and Cooling. 2nd ed. ISO: Geneva, Switzerland, 2008.
24. *VDI 6007-1*; Calculation of Transient Thermal Response of Rooms and Buildings—Modelling of Rooms. German Association of Engineers (VDI): Düsseldorf, Germany, 2012.
25. Vivian, J.; Zarrella, A.; Emmi, G.; De Carli, M. An evaluation of the suitability of lumped-capacitance models in calculating energy needs and thermal behaviour of buildings. *Energy Build.* **2017**, *150*, 447–465. [CrossRef]
26. Yu, X.; Skeie, K.S.; Knudsen, M.D.; Ren, Z.; Imsland, L.; Georges, L. Influence of data pre-processing and sensor dynamics on grey-box models for space-heating: Analysis using field measurements. *Build. Environ.* **2022**, *212*, 108832. [CrossRef]
27. Knudsen, M.D.; Georges, L.; Skeie, K.S.; Petersen, S. Experimental test of a black-box economic model predictive control for residential space heating. *Appl. Energy* **2021**, *298*, 117227. [CrossRef]
28. Klanatsky, P.; Veynandt, F.; Heschl, C. Grey-box model for model predictive control of buildings. *Energy Build.* **2023**, *300*, 113624. [CrossRef]
29. Wang, X.; Tian, S.; Ren, J.; Jin, X.; Zhou, X.; Shi, X. A novel resistance-capacitance model for evaluating urban building energy loads considering construction boundary heterogeneity. *Appl. Energy* **2024**, *361*, 122896. [CrossRef]
30. Kastner, P.; Dogan, T. Towards Auto-Calibrated UBEM Using Readily Available, Underutilized Urban Data: A Case Study for Ithaca, NY. *Energy Build.* **2024**, *317*, 114286. [CrossRef]
31. Bacher, P.; Madsen, H. Identifying suitable models for the heat dynamics of buildings. *Energy Build.* **2011**, *43*, 1511–1522. [CrossRef]
32. NIBE. F2050 Air Source Heat Pump. Available online: https://www.nibe.eu/en-gb/products/heat-pumps/air-source-heat-pumps/f2050 (accessed on 20 April 2025).
33. Google. Google Colaboratory. Available online: https://colab.research.google.com/ (accessed on 30 October 2025).
34. *Python Language Reference*, Version 3.11; Python Software Foundation: Wake Forest, NC, USA, 2025. Available online: http://www.python.org (accessed on 30 October 2025).
35. Andersson, J.A.E.; Gillis, J.; Horn, G.; Rawlings, J.B.; Diehl, M. CasADi—A software framework for nonlinear optimization and optimal control. *Math. Program. Comput.* **2019**, *11*, 1–36. [CrossRef]
36. The Joint Research Centre: EU Science Hub. Photovoltaic Geographical Information System (PVGIS). 2023. Available online: https://joint-research-centre.ec.europa.eu/photovoltaic-geographical-information-system-pvgis_en (accessed on 20 April 2025).
37. E.on. Electricity Prices Hour by Hour. 2023. Available online: https://www.eon.se/el/elpriser/aktuella (accessed on 20 April 2025).
38. E.on. District Heating Small Home 2023. 2023. Available online: https://www.eon.se/fjarrvarme/priser (accessed on 20 April 2025).

39. Nowtricity. Real Time Live Emissions from Energy Production by Country. 2023. Available online: https://www.nowtricity.com/country/sweden (accessed on 20 April 2025).
40. Piltz Vitanc, L.; Hinsegård, M. Emission Factors and Methods Used in Climate Impact Assessments of Energy Use in Swedish Heated Buildings-Assessing District Heating and Electricity as Energy Source. 2023. Available online: https://lup.lub.lu.se/student-papers/search/publication/9122136 (accessed on 30 October 2025).
41. Gadd, H.; Werner, S. Daily heat load variations in Swedish district heating systems. *Appl. Energy* **2013**, *106*, 47–55. [CrossRef]
42. Paris, B.; Eynard, J.; Grieu, S.; Talbert, T.; Polit, M. Heating control schemes for energy management in buildings. *Energy Build.* **2010**, *42*, 1908–1917. [CrossRef]
43. Sameti, M.; Haghighat, F. Optimization approaches in district heating and cooling thermal network. *Energy Build.* **2017**, *140*, 121–130. [CrossRef]
44. O'Dwyer, E.; De Tommasi, L.; Kouramas, K.; Cychowski, M.; Lightbody, G. Prioritised objectives for model predictive control of building heating systems. *Control Eng. Pract.* **2017**, *63*, 57–68. [CrossRef]
45. Mattson, C.A.; Messac, A. Pareto frontier based concept selection under uncertainty, with visualization. *Optim. Eng.* **2005**, *6*, 85–115. [CrossRef]
46. Ritchie, M.; Engelbrecht, J.; Booysen, M. A probabilistic hot water usage model and simulator for use in residential energy management. *Energy Build.* **2021**, *235*, 110727. [CrossRef]
47. Gelažanskas, L.; Gamage, K.A. Forecasting hot water consumption in residential houses. *Energies* **2015**, *8*, 12702–12717. [CrossRef]
48. Sartori, I.; Walnum, H.T.; Skeie, K.S.; Georges, L.; Knudsen, M.D.; Bacher, P.; Candanedo, J.; Sigounis, A.M.; Prakash, A.K.; Pritoni, M.; et al. Sub-hourly measurement datasets from 6 real buildings: Energy use and indoor climate. *Data Brief* **2023**, *48*, 109149. [CrossRef]
49. *ISO 7726:1998*; Ergonomics of the Thermal Environment—Instruments for Measuring Physical Quantities. ISO: Geneva, Switzerland, 1998.
50. Olesen, B.W.; Wang, H.; Kazanci, O.B. The Effect of Room Temperature Control by Air-Or Operative Temperature on Thermal Comfort and Energy Use. In *Proceedings of the Building Simulation 2019*; IBPSA: Brussels, Belgium, 2019; Volume 16, pp. 2086–2093.

Disclaimer/Publisher's Note: The statements, opinions and data contained in all publications are solely those of the individual author(s) and contributor(s) and not of MDPI and/or the editor(s). MDPI and/or the editor(s) disclaim responsibility for any injury to people or property resulting from any ideas, methods, instructions or products referred to in the content.

energies

MDPI

Article

Carbon Black–Enhanced Polyethylene Wax Phase Change Materials for Efficient Photothermal Energy Conversion and Storage in Mobile Heating Systems

Martyna Szatkowska [1], Piotr Szatkowski [1], Katarzyna Suchorowiec [1], Ewelina Radomska [2] and Kinga Pielichowska [1,*]

[1] Department of Glass Technology and Amorphous Coatings, Faculty of Materials Science and Ceramics, AGH University of Krakow, Al. Mickiewicza 30, 30-059 Krakow, Poland; szatkowska@agh.edu.pl (M.S.); pszatko@agh.edu.pl (P.S.)

[2] Department of Thermal and Fluid Flow Machines, Faculty of Energy and Fuels, AGH University of Krakow, Al. Mickiewicza 30, 30-059 Krakow, Poland; radomska@agh.edu.pl

* Correspondence: kinga.pielichowska@agh.edu.pl or kingapie@agh.edu.pl

Abstract

Organic phase change materials (PCMs) have been used and studied for many years. In this work, we focus on an industrially available PCM—polyethylene waxes (PEW) modified with seven types of carbon black (CB) exhibiting different properties. Carbon black (CB) was selected as a more cost-effective modifier compared to carbon nanomaterials, as it is easier to implement industrially and capable of converting and storing thermal energy. The experiments were designed to evaluate the thermal properties and photothermal conversion efficiency of PCMs modified with different grades of carbon black. The influence of carbon black on selected PCM properties was investigated using differential scanning calorimetry (DSC), thermogravimetric analysis (TG), scanning electron microscopy (SEM), and laser flash analysis (LFA). Furthermore, the photothermal conversion capability was evaluated. The results indicate that modification with carbon black decreases the phase transition enthalpy for most formulations, with reductions ranging from 8 to 12% for 1 wt.% CB to 10–15% for 2.5 wt.% CB. At the same time, an improvement in the thermal conductivity of PCMs modified with carbon black was observed, with the best performance achieved for N234 carbon black, showing an increase of approximately 17–18% in the 25–55 °C temperature range. The ratio of the heat of solidification to the heat of melting (Qs/Qm) for most samples was approximately 0.90–0.98, indicating excellent thermal cycling stability. The highest photothermal conversion efficiency was observed for samples modified with N234 and N330; these materials exhibited the greatest temperature rise, reaching approximately 135 °C in about 15 min, due to enhanced light absorption of PCMs by carbon black. Overall, the results confirm that PEW/CB systems demonstrate a good balance between absorption, heat generation, and controlled phase-change behavior, making them promising candidates for solar–thermal energy storage and conversion applications.

Keywords: phase-change material (PCM); carbon black; thermal analysis; photothermal conversion; thermal conductivity

1. Introduction

The rapidly growing demand for mobile heating systems, portable thermal energy storage devices, and integrated photothermal conversion applications motivates the de-

velopment of optimized organic PCM formulations with enhanced thermal conductivity and photothermal performance. Phase change materials (PCMs) constitute an attractive class of materials for thermal energy storage and energy conversion systems. PCMs store thermal energy both as sensible heat—from the initial temperature to the melting point and further to the final temperature—and as latent heat during phase transitions, such as solid–liquid or solid–solid transformations [1,2]. Compared to conventional sensible heat thermal energy storage systems, PCM-based systems offer the advantage of storing significantly larger amounts of heat within a relatively small material volume [3–5].

In general, phase change materials are classified as organic or inorganic [6]. Organic PCMs are considered chemically stable, safe, noncorrosive, and cost-effective. They are characterized by high phase transition enthalpy and good thermal reliability over numerous melting–solidification cycles [7,8]. Paraffin waxes are relatively inexpensive, safe to use, chemically inert, noncorrosive, and thermally stable up to 300 °C; however, they are flammable and exhibit low thermal conductivity (0.1–0.3 W/(m·K)). Paraffins demonstrate excellent thermal stability even after 1500 thermal cycles [8].

Paraffin- and polyethylene-based PCMs have been investigated in numerous combinations due to their structural and chemical similarities [8,9]. Zauner et al. [10] evaluated several promising polymers, including polyethylene (PE), polyoxymethylene (POM), and various polyamides (PAs), and selected high-density polyethylene (HDPE) for detailed investigation. Their results showed that HDPE exhibits a high phase transition enthalpy and remains thermally stable over more than 1000 heating–cooling cycles. The authors also designed a suitable heat exchanger, constructed a laboratory-scale storage prototype, and characterized its energy capacity and power profiles under various operating conditions. Navarro et al. [11] investigated HDPE spheres impregnated with a paraffin mixture with a melting point of 58 °C for domestic hot water applications. In their experimental system, polyethylene spheres containing embedded PCM were placed at the top of a water tank to enhance thermal stratification and increase energy density. The results demonstrated that PCM had a beneficial effect on maintaining the water temperature for an extended period. However, the presence of PE prolonged the PCM melting time as a result of its low thermal conductivity. Additionally, PCM leakage from the spheres was observed, and the PCM content would require optimization to enable safe use in drinking water tanks [11].

The primary limitation of organic PCMs is their inherently low thermal conductivity. A commonly proposed strategy to overcome this drawback is the incorporation of carbon-based additives—such as carbon black, graphene, graphite, or carbon nanotubes—to enhance heat transfer. Fikri et al. [12] proposed paraffin wax PCM with functionalized multi-walled carbon nanotubes (FMWCNTs). They reported that the addition of 1 wt.% non-functionalized MWCNTs increased thermal conductivity by 9.5%, while functionalized MWCNTs resulted in an improvement of 50.7% compared to the unmodified PCM. Feng et al. [13] investigated poly(ethylene glycol) infiltrated in porous carbon skeletons of diamond foam (DF) and dual three-dimensional carbon nanotube–diamond foam (CDF), both with a porosity of 70%. The use of DF improved thermal conductivity by 505% compared to pure PCM, whereas CDF achieved an improvement of 550%. Mishra [14] studied carbon black-modified lauric acid (LA) as a PCM. The addition of 2 wt.% carbon black increased thermal conductivity from 0.219 W/(m·K) for pure LA to 0.241 W/(m·K); a 5 wt.% loading resulted in an approximately 50% improvement compared to unmodified LA. Efforts to enhance thermal conductivity are primarily driven by the need to accelerate the PCM charging and discharging processes.

Different approaches have been investigated to enhance the thermal conductivity of PCMs. Afaynou et al. [15] proposed the use of metal foam as a partial filler in a hybrid heat

https://doi.org/10.3390/en19051162

sink (HS). While this strategy increases thermal conductivity, it suppresses natural convection within the PCM, thereby limiting the effective heat storage capacity and increasing the cost of the system. N-eicosane was used as the PCM in numerical simulations. The optimal configuration was identified as two-thirds of the metal foam, resulting in a 33.82% reduction in eicosane temperature, a 12.67% increase in efficiency, a 57.54% increase in thermal energy storage, and a 33.33% reduction in the cost and weight compared to a fully filled metal foam configuration [15]. Mishra et al. [16] proposed the incorporation of lauric acid modified with 4 wt.% carbon black nanoparticles or 4 wt.% graphene nanoplatelets into a biomass-derived porous matrix obtained from coffee or turmeric powder. The incorporation of 25 wt.% of the porous matrix significantly improved structural stability by effectively suppressing PCM leakage while maintaining a high latent heat storage capacity of approximately 130 J/g. Solid–solid composite PCMs exhibited high photothermal conversion efficiency (106%) and notable thermal regulation capability, reducing the superheating temperature by approximately 10 °C compared with the pristine PCM. These enhancements were attributed to improved light absorption and increased energy conversion efficiency [16]. The thermal conductivity in organic PCMs can also be improved by incorporating boron nitride, as demonstrated by Yu et al. [17]. The authors constructed thermally conductive boron nitride (BN) networks within a paraffin wax (PW) matrix supported by poly(styrene-b-ethylene-butylene-b-styrene) (SEBS). The composite with a 20/80 SEBS to PW mass ratio and containing 30 wt.% BN exhibited excellent dimensional stability, a high latent heat capacity (129.8 J/g), and significantly enhanced thermal conductivity of 1.51 W/(m·K), representing a 293% increase compared to the unfilled material [17].

Despite the superior thermal enhancements achievable with carbon nanomaterials, carbon black represents a more cost-effective and industrially viable alternative for PCM modification. In this work, polyethylene waxes modified with seven distinct types of carbon black were investigated. The influence of carbon black properties, such as particle size, specific surface area, and conductivity characteristics, on thermal behavior, thermal conductivity, and photothermal performance was systematically assessed. The resulting materials were characterized using differential scanning calorimetry (DSC), thermogravimetric analysis (TG), scanning electron microscopy (SEM), laser flash analysis (LFA), and photothermal conversion measurements.

In this work, polyethylene waxes modified with seven distinct types of carbon black with different parameters and characteristics were investigated. The influence of carbon black properties, such as particle size, specific surface area, and conductivity, on thermal behavior and thermal conductivity to find structure–properties relationships, has been investigated. Moreover, photothermal performance was systematically assessed to identify the most effective CB grades for solar–thermal energy conversion and storage applications and mobile heating.

2. Materials and Methods

The polyethylene waxes (PEW) were obtained from EuroCeras Sp. z o.o. (Cerelane 1100, Kędzierzyn Koźle, Poland), carbon black N220, N330, N234, conductive (Konin, Poland), carbon black HCS-2, HCS-165, HCS-200S (Hangzhou, China)—Table 1.

Samples of PEW were heated at a temperature of 130 °C to melting, then 1, 2.5, and 5% of modifiers (carbon blacks) were added to the melted PEW and homogenized using an ultrasonic homogenizer to obtain a homogenous dispersion. Homogenization time was 30 s. It was observed that too long a homogenization process generates intense heat and significantly reduces the efficiency of the process by causing excessive cavitation. The material designations used in the tests are described in Table 2.

https://doi.org/10.3390/en19051162

Table 1. Properties of CBs.

Carbon Black	Particle Size [nm]	Total Specific Surface [10^3 m^2/kg]	Ash (Mass Fraction) [%]
N220	20–25	101–111	0.50
N330	26–30	107–117	0.50
N234	19–23	70–80	0.50
conductive	20–50	65.0 ± 5.0	0.50
HCS-2	20–25	200–600	≤0.50
HCS-165	16	80–200	≤0.20
HCS-200S	24–28	150–300	≤0.50

Table 2. Samples description.

Sample	Name Used in the Article	CB Content [%]
PEW	PCM	-
PEW + electroconductive carbon black	PCM+E_CB	1.0 2.5 5.0
PEW + carbon black N220	PCM+CB_N220	1.0 2.5 5.0
PEW + carbon black N234	PCM+CB_N234	1.0 2.5 5.0
PEW + carbon black N330	PCM+CB_N330	1.0 2.5 5.0
PEW + carbon black HCS2	PCM+CB_HCS2	1.0 2.5 5.0
PEW + carbon black HCS165	PCM+CB_HCS165	1.0 2.5 5.0
PEW + carbon black HCS200	PCM+CB_HCS200	1.0 2.5 5.0

Differential scanning calorimetry (DSC) measurements were conducted using the DSC 1 calorimeter from Mettler Toledo (Greifensee, Switzerland), equipped with an intracooler. Prior measurements, DSC was calibrated with indium and zinc standards. The temperature program involved a heating–cooling–heating cycle within a temperature range of 25 to 130 °C, with a heating and cooling rate of 10 °C/min in a nitrogen atmosphere (30 mL/min). Samples with mass ca. 3 mg were closed in pierced aluminum pans. The first heating run was performed for the removal of the samples' thermal history resulting from the preparation and processing.

Additionally, DSC 1 was utilized for modulated temperature DSC measurements in TOPEM mode, with parameters set at an amplitude of 0.5 K, a switching time of 15 s, and a base heating rate of 1 K/min over the temperature range of 25 to 130 ° C.

Additionally, DSC250 from TA Instruments (New Castle, DE, USA), was used, which featured a refrigerated cooling system to analyze the phase change material after 20 cycles

https://doi.org/10.3390/en19051162

of heating–cooling within a temperature range of 25 to 130 °C, with a rate of 10 °C/min in a nitrogen atmosphere (340 mL/min).

Fourier transform infrared (FTIR) measurements were performed using a spectrophotometer from ThermoFisher Scientific (Waltham, MA, USA) model: Nicolet iS20 Nicolet Apex with an Attenuated Total Reflection (ATR) adapter, operating with OMNIC 9.16.188 software. Spectra were collected in absorbance mode of 4000–400 cm^{-1} after 32 scans at 4 cm^{-1}.

Thermogravimetric analyses were performed using a TGA 550 Discovery analyzer (TA Instruments, New Castle, DE, USA). The samples were examined in a temperature range of 40–600 °C, with a heating rate of 10 K/min under a nitrogen atmosphere.

Scanning electron microscopy (SEM) was carried out using a NOVA NANO SEM 200 system (FEI, Hillsboro, OR, USA) equipped with EDS. Before imaging, the sample was coated with a carbon layer and examined at magnifications of approximately 2000× and 10,000×.

Thermal diffusivity was measured using the laser flash analysis (LFA) method with an LFA 467 HyperFlash instrument (Netzsch, Selb, Germany). All measurements were performed in an inert nitrogen atmosphere with a gas flow rate of 50 mL/min. The tests were carried out at 25 °C, 40 °C, 55 °C, and 70 °C (solid state). For each temperature, the chamber was first stabilized, followed by a 300 s equilibration period before the laser pulse to ensure uniform temperature throughout the sample. Three measurements were carried out at each temperature step. The samples were cylindrical (height: 1.55 mm; diameter: 15 mm) and placed in a holder, externally secured with stainless-steel spacers coated with graphite, as shown in Figure 1. Heating was carried out at 5 K/min to the target temperature, after which a laser pulse of known energy was applied. From the moment of irradiation, the temperature response on the rear surface of the sample was recorded. The resulting signals were analyzed using LFA Proteus 8.0.3 software, and thermal diffusivity was determined using the selected three-layer model. Then, the thermal conductivity (λ, W/(m·K)) was calculated as follows:

$$\lambda = \alpha \rho c_p \tag{1}$$

where α, ρ, and c_p stand for thermal diffusivity (mm^2/s), density (g/cm^3), and specific heat capacity (J/g). The density was determined from the Archimedes method, while the specific heat capacity was obtained from the DSC measurements. The uncertainty of the thermal conductivity was estimated from the general formula for error propagation [18]:

$$\delta\lambda = \sqrt{\left(\frac{\partial\lambda}{\partial\alpha}\delta\alpha\right)^2 + \left(\frac{\partial\lambda}{\partial\rho}\delta\rho\right)^2 + \left(\frac{\partial\lambda}{\partial c_p}\delta c_p\right)^2} \tag{2}$$

where δ stands for the uncertainty of a specific variable. According to the producers, the uncertainties of $\delta\alpha$, $\delta\rho$, and δc_p are 3% [19], 0.4% [20], and 2% [21], respectively. Thus, the estimated uncertainty of the thermal conductivity is 3.6%.

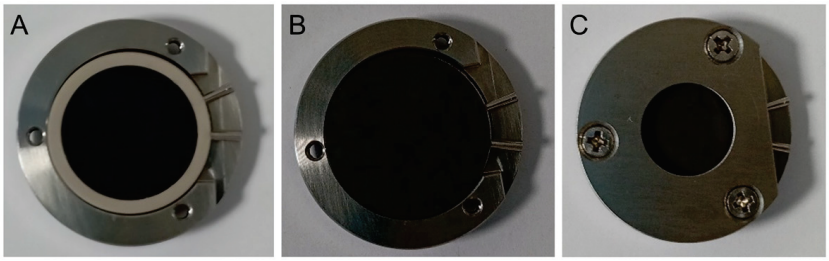


Figure 1. A sample during the preparation for the LFA measurements: (**A**) the sample in a PEEK ring; (**B**) the sample secured with a graphite-coated stainless-steel spacer; (**C**) the complete measurement holder.

https://doi.org/10.3390/en19051162

The photothermal conversion performance was investigated using the LED Ossila Solar Simulator (Ossila, Sheffield, UK), with a light spectrum ranging from 350 to 1050 nm at a working distance of 8.5 cm and output power of 1 Sun for 36 min at room temperature. Following the experiment, the samples were placed in a customized experimental setup for photothermal conversion evaluation according to Figure 2.

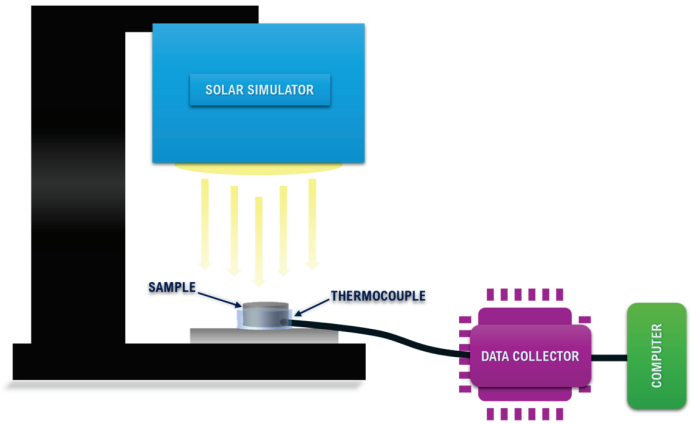


Figure 2. Scheme of the experimental setup for photothermal conversion evaluation.

The temperature of the sample was recorded through a thermocouple connected with a PicoLog TC-08 high-resolution thermocouple data logger (Pico Technology, St Neots, UK) connected to the computer. The temperature of the sample was recorded during the exposition to the simulated solar light and when the simulated solar source was switched off. When the experiment (solar exposition) time reached 36 min, the simulated solar light source was turned off, allowing the sample to cool down naturally to the room temperature. The photothermal conversion efficiency was calculated following Equation (3) [22–24]:

$$\eta = \frac{m \cdot \Delta H_m}{I \cdot S \cdot (T_e - T_s)} \cdot 100\% \quad (3)$$

where η denotes the photothermal conversion efficiency; m is the mass of the phase-change material (PCM); ΔH represents the enthalpy of the PCM; I corresponds to the optical power density (1000 W/m^2); S denotes the irradiated surface area; T_s is defined as the onset time of the phase transition, and T_e is defined as the termination time of the phase transition.

3. Results and Discussion

To evaluate the material's ability to absorb and release heat, DSC measurements were performed using a heating–cooling–heating cycle. Data from the second heating run were analyzed, as the first run was used to eliminate the thermal history of the samples. The DSC results are presented in Figure 3 and Table 3.

The addition of carbon black only slightly affects the shifts in melting or crystallization peaks. The differences are typically around one degree between the pure PCM and the modified sample. There is no clear relationship between the temperature changes in individual peaks and either the carbon black content or the specific type of carbon black used.

Phase transition temperatures are intensive properties of the polyethylene wax matrix phase, determined exclusively by molecular composition and thermodynamic equilibrium. The physical dispersion of non-interacting carbon black cannot alter this intrinsic thermodynamic property. Consistent values of Tm and Ts across all formulations (95–96 °C and 90–91 °C, respectively) thus demonstrate strong thermal compatibility and the absence of interfacial chemical reactions, as it was confirmed in FTIR results.

https://doi.org/10.3390/en19051162

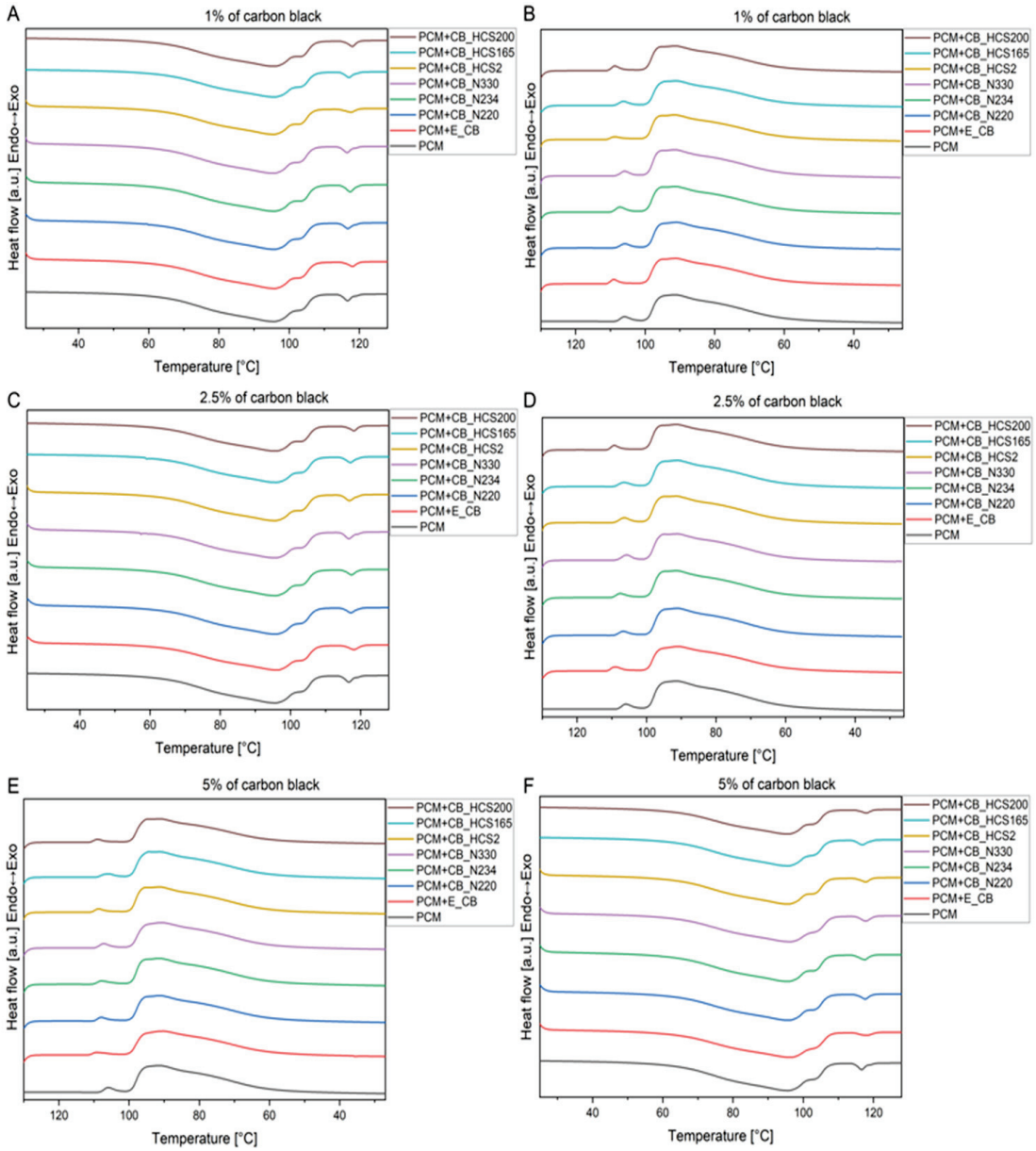


Figure 3. DSC curves for PCM with carbon black 1% (**A**,**B**), 2.5% (**C**,**D**), and 5% (**E**,**F**), and heating (**A**,**C**,**E**) and cooling (**B**,**D**,**F**).

Table 3. Temperature and heat of melting and solidification of PCM/CB (Q_m—the heat of fusion, Q_s—the heat of solidification).

Sample	CB Content [%]	T_{monset} [°C]	T_{m1} [°C]	T_{m2} [°C]	T_{m3} [°C]	Q_m [J/g]	T_{sonset} [°C]	T_{s1} [°C]	T_{s2} [°C]	T_{s3} [°C]	Q_s [J/g]
PCM	-	62	95	104	117	242.84	99	106	91	77	242.57
PCM+E_CB	1	62	96	104	118	227.39	100	109	91	77	226.53
	2.5	62	96	104	118	213.67	100	109	91	77	210.68
	5	62	96	104	115	214.51	100	109	90	77	213.35
PCM+CB_N220	1	62	96	104	115	227.85	99	106	91	77	224.50
	2.5	62	96	104	115	223.42	99	107	91	77	218.22
	5	62	96	104	118	221.30	99	108	91	77	217.18

https://doi.org/10.3390/en19051162

Table 3. *Cont.*

Sample	CB Content [%]	T_{monset} [°C]	T_{m1} [°C]	T_{m2} [°C]	T_{m3} [°C]	Q_m [J/g]	T_{sonset} [°C]	T_{s1} [°C]	T_{s2} [°C]	T_{s3} [°C]	Q_s [J/g]
PCM+CB_N234	1	62	96	104	117	232.38	100	109	91	78	227.52
	2.5	62	95	104	117	223.83	99	108	91	78	219.19
	5	62	96	103	117	225.84	99	108	91	77	221.03
PCM+CB_N330	1	61	95	103	116	230.08	99	108	91	78	226.09
	2.5	62	95	104	117	222.77	100	106	91	78	218.20
	5	62	96	104	118	228.82	99	107	90	78	225.92
PCM+CB_HCS2	1	62	95	104	118	219.85	100	109	92	77	215.24
	2.5	62	95	104	117	223.97	100	106	91	78	219.02
	5	62	96	103	118	223.64	100	109	91	77	219.79
PCM+CB_HCS165	1	62	96	104	117	219.93	99	106	91	77	220.36
	2.5	62	96	104	117	221.89	99	107	91	76	222.42
	5	62	95	104	117	222.82	99	106	91	78	222.96
PCM+CB_HCS200	1	62	96	104	118	226.13	100	109	91	77	226.55
	2.5	61	96	104	118	223.60	100	109	91	78	223.60
	5	62	95	104	118	212.93	99	109	91	77	213.20

In contrast, enthalpy values are extensive properties directly proportional to the mass of active phase change material in the composite. The observed enthalpy reductions (8–15%) result from: (i) effective PCM mass reduction due to space occupancy by carbon black (~1% for 1 wt.% loading), (ii) crystallization hindrance caused by CB particles, (iii) surface-mediated perturbation of local crystal order. This combined effect stay with good agreement with the literature data on carbon-modified paraffin systems and represents an optimized engineering trade-off: accepting modest enthalpy reduction in exchange for substantial thermal conductivity improvement (up to 22% for optimal CB grades) [25–27]. This strategy enables faster energy transfer during charging/discharging cycles, partially compensating for lower absolute storage capacity per unit mass.

The latent heat of fusion represents the thermal energy storage capacity of a material and is directly measured by DSC. For the pure PCM, the heat of melting was 242.84 J/g, which is characteristic of paraffin-based PCMs. Modification with carbon black leads to a systematic decrease in enthalpy across most formulations [28], ranging from 8 to 12% for 1 wt.% CB to 10–15% for 2.5 wt.% CB. The reduction in melting heat with increasing CB content is consistent with reports in the literature on nanoparticle-enhanced PCMs. Studies on carbon-modified paraffin systems have demonstrated similar trends, in which the addition of carbon-based fillers—such as carbon nanotubes, graphene, or activated carbon—results in a slight decrease in latent heat capacity [29–31]. In general, for polymer-based PCMs, the thermal energy storage capacity is directly connected to the degree of crystallinity. The incorporation of micro- or nanometric-sized additives leads to changes in the polymer matrix crystallization process. Depending on the type, size, shape, chemical composition, and concentration, incorporated additives have different effects on the crystallization process. Polymer chains can interact with fillers by chemisorption or occlusion, that trigger the macromolecule nucleation process [32]. In the most widely accepted paracrystalline model for different types of carbon black, continuous layers of hexagonally arranged carbon atoms form the basic building blocks. These carbon layers are concentrically arranged around one

https://doi.org/10.3390/en19051162

or more growth nuclei, resulting in adjacent layers orientated parallel to each other and creating ordered, parallel stacked layers known as a turbostratic structure, and finally forming nearly spherical particles and aggregates [33]. In polymer systems, paracrystalline CB structures can act as nucleating sites for polymer chains; however, the opposite confinement effect may also influence the crystallization ability of PEW. The mobility of PEW polymer chains can be restricted because of chain trapping within the narrow spaces between CB particles or adsorption onto high surface-area CB particles, which limits the crystallization process of PEW. This leads to a decrease in PEW crystallinity and a reduction in the heat of phase transition of the PCM system. The reduction in phase change enthalpy can also be attributed to a decrease in the effective PCM volume fraction within the composite, as carbon black nanoparticles occupy space in the material and thereby reduce the mass fraction of active PCM available for thermal energy storage [34–36]. However, the magnitude of the decrease (8–15%) is relatively modest, suggesting good compatibility between the carbon black particles and the PEW matrix. Previous studies on paraffin composites containing various carbon-based nanofillers have reported comparable or even larger enthalpy reductions (ranging from 3 to 40%, depending on filler type and concentration), indicating that the carbon black modifications applied in this study preserve thermal storage capacity to a satisfactory extent [37,38].

The solidification temperature (Ts) remained constant at 90–91 °C for all samples during the cooling cycle, demonstrating excellent thermal reversibility. This consistency is particularly important for applications requiring long-term cycling stability, as it indicates reliable phase transitions during repeated thermal cycles. The heat of solidification (Qs) ranged from 210 to 227 J/g and closely matched the corresponding melting enthalpy values, further confirming the reversibility of the phase transitions and the absence of significant material degradation during DSC measurements. The ratio of the heat of solidification to the heat of melting (Qs/Qm) for most samples was approximately 0.90–0.98, indicating excellent thermal cycling behavior. This observation is supported by literature on paraffin-based PCMs, where similar ratios have been reported for properly functioning phase change materials. Minor asymmetries between melting and crystallization enthalpies are common and can be attributed to nucleation effects and slight differences in heat transfer rates during heating and cooling cycles [39,40].

The melting temperatures observed in this study (95–96 °C) and the corresponding latent heats (212–243 J/g) are consistent with the reported values for paraffin waxes used as phase change materials. The literature data for standard paraffin PCMs with comparable melting points typically indicate latent heats in the range of 200–280 J/g. Polyethylene wax used in this work represents a mid-range paraffin formulation, and the measured thermal properties align well with those of commercially available PCM products and other paraffin-based thermal energy storage materials [41,42].

The influence of carbon black on the melting temperature was minimal, which contrasts with some reports from the literature that describe temperature shifts of ±2–5 °C upon the addition of certain nanofillers. This thermal stability is advantageous for mobile heating system applications, as it ensures consistent operating temperatures regardless of the specific carbon black formulation used [43].

Based on the obtained data, the relationship between the specific surface area (SSA) of CB and the investigated parameters can be found. In general, better results have been revealed for CB with lower SSA. Samples with carbon black N330 and N234 were characterized by slightly higher phase transition. Based on DSC data, the degree of crystallinity of the PEW matrix has been calculated to check the effect of SSA and the crystallinity of the polymer matrix—Figure 4.

https://doi.org/10.3390/en19051162

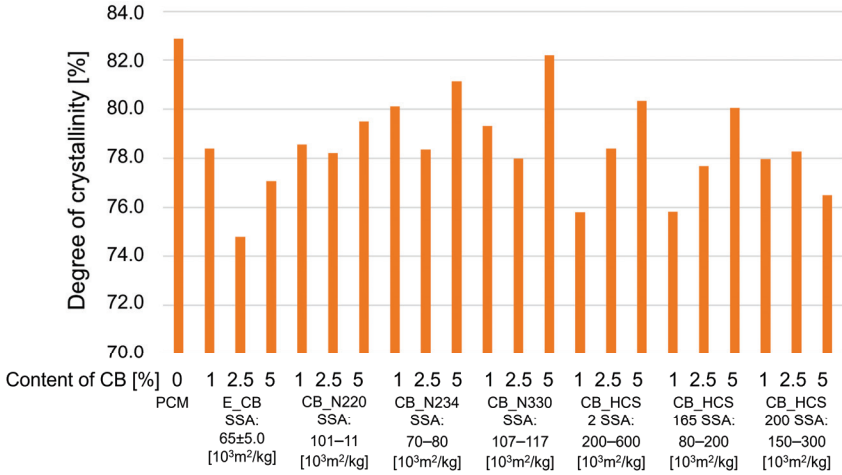


Figure 4. Degree of crystallinity of PEW vs. carbon black SSA and content [%].

From Figure 4 can be seen that in such systems polymer matrix can reach a slightly higher degree of crystallinity in systems modified with CB, characterized by lower SSA.

In Table 4 we shown DSC results after 20 heating–cooling cycles for the PCM base material and the two best formulations revealed that the best thermal behavior and repeatability were exhibited by the PCM+CB_N330 sample, where the values of heat of phase transition were on a similar level as before thermal cycling. For unmodified PCM and PCM+CB_N234, some decrease in phase transition enthalpy was found, but the obtained values are still above 200 J/g.

Table 4. DSC results after 20 heating–cooling cycles.

Sample	CB Content [%]	T_{monset} [°C]	T_{m1} [°C]	T_{m2} [°C]	T_{m3} [°C]	Q_m [J/g]	T_{sonset} [°C]	T_{s1} [°C]	T_{s2} [°C]	T_{s3} [°C]	Q_s [J/g]
PCM	-	63	97	105	115	204.38	98	102	89	76	209.42
PCM+CB_N330	1	64	96	103	116	231.63	98	104	89	76	217.09
PCM+CB_N234	1	63	97	104	117	208.00	98	104	89	76	208.25

Analysis of the FTIR results for both neat PCM, PCM/CB samples, and CB indicates no changes in PEW in the presence of carbon black, which indicates no chemical reaction between the PCM and the carbon additive (Figures 5 and 6).

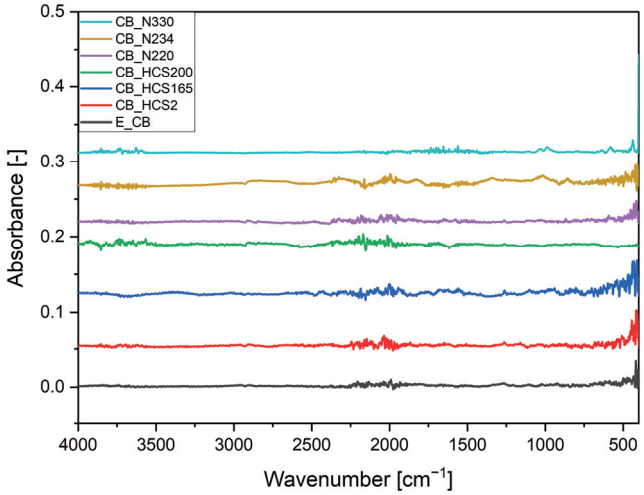


Figure 5. FTIR spectra of carbon black.

https://doi.org/10.3390/en19051162

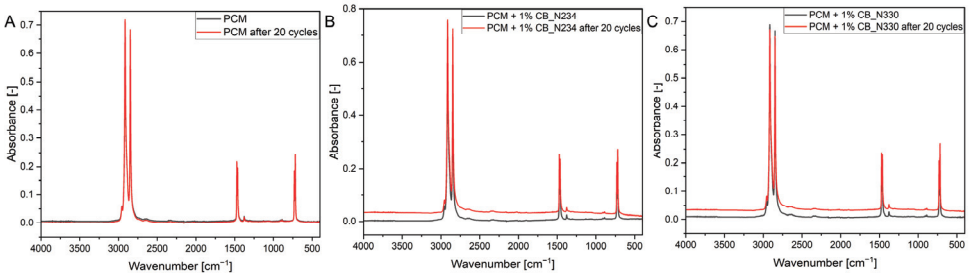


Figure 6. FTIR spectra of PCM before and after 20 heating–cooling cycles (**A**), PCM + 1% CB_N234 before and after 20 heating–cooling cycles (**B**), PCM + 1% CB_N330 before and after 20 heating–cooling cycles (**C**).

There are no characteristic absorption bands in the spectrum that could be associated with functional groups in carbon black. Only absorption bands typical for polyethylene wax were found (at 718 and 730 cm^{-1} from CH_2 rocking vibration [44], at 1462 and 1472 cm^{-1} from CH_2 bending [45], at 2847 and 2914 cm^{-1} from C-H stretching in alkanes [46]. Moreover, Fourier transform infrared spectroscopy analysis has been performed for samples after 20 thermal cycles and showed that the PCM before phase transitions and after 20 phase transition cycles (20 heating–cooling cycles) exhibits peaks originating from chemical bonds at the same positions and with the same intensities as before thermal cycling. In the same figure, we can see that a similar relationship is observed for samples modified with one percent of carbon black in B-CB 234 and in C-CB-330.

The thermal stability of the carbon black modified PCMs was further evaluated by thermogravimetric (TG) analysis; the results are presented in Table 5 and Figure 7.

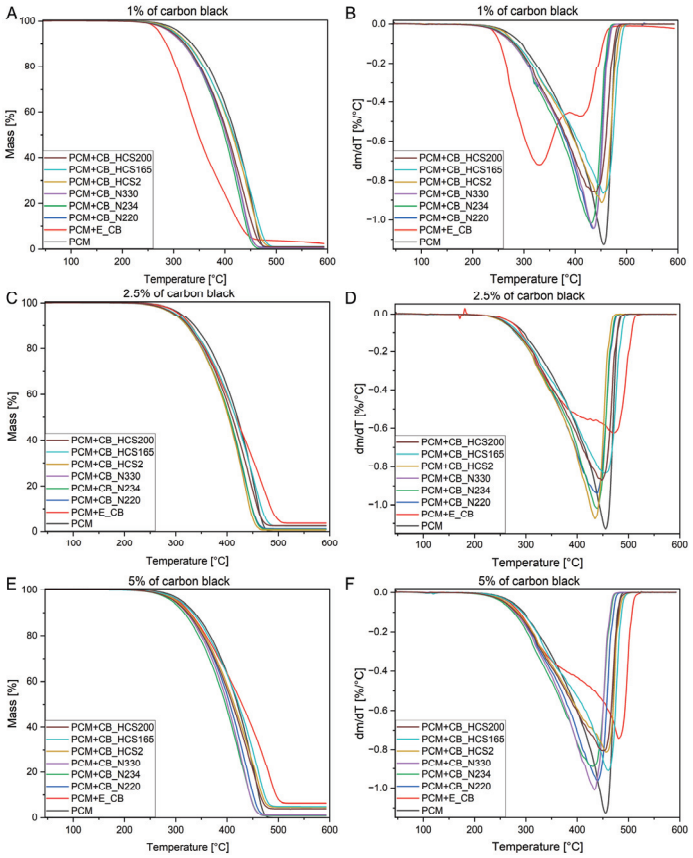


Figure 7. TG (**A**,**C**,**E**) and DTG (**B**,**D**,**F**) curves for PCM (Cerelane 1100) with carbon black 1% (**A**,**B**), 2.5% (**C**,**D**), and 5% (**E**,**F**).

https://doi.org/10.3390/en19051162

The unmodified PEW exhibited excellent thermal stability, with the onset of mass loss ($T_{1\%}$) occurring at 267 °C. This high initial decomposition temperature ensures safe operation in heating applications up to moderate temperatures. The temperature corresponding to 10% mass loss ($T_{10\%}$) was 336 °C, while the temperature at 50% mass loss ($T_{50\%}$) reached 420 °C, indicating a relatively broad window of thermal stability. The maximum decomposition rate (T_{DTGmax}) occurred at 462 °C. The residual char at 600 °C was negligible (0.002%), confirming nearly complete decomposition of the organic paraffin material at elevated temperatures. These values are in excellent agreement with the data from the literature for paraffin waxes. Studies on conventional paraffin-based PCMs typically report $T_{10\%}$ values in the range of 300–350 °C and $T_{50\%}$ values between 400 and 450 °C, indicating that the PEW formulation used in this study is representative of commercially available paraffin products [42,47].

Table 5. Thermal stability of PCM with carbon black.

Sample	CB Content [%]	$T_{1\%}$	$T_{2\%}$	$T_{3\%}$	$T_{5\%}$	$T_{10\%}$	$T_{50\%}$	T_{DTGmax}	Char Residue at 600 °C
		[°C]	[°C]	[°C]	[°C]	[°C]	[°C]	[°C]	[%]
PCM	-	267	285	297	312	336	420	462	0.002
PCM+E_CB	1	251	260	265	273	286	348	328	2.405
	2.5	269	286	296	309	330	417	475	3.432
	5	263	280	291	305	328	429	481	6.344
PCM+CB_N220	1	257	274	284	299	321	403	431	0.754
	2.5	259	275	285	299	322	404	440	1.093
	5	258	275	286	301	324	406	440	1.026
PCM+CB_N234	1	257	273	284	299	321	399	431	0.143
	2.5	255	271	282	298	321	405	441	0.859
	5	250	267	278	293	316	397	426	0.882
PCM+CB_N330	1	252	269	280	295	319	403	436	0.507
	2.5	255	272	283	298	322	403	433	0.654
	5	257	273	283	298	321	401	433	1.105
PCM+CB_HCS2	1	265	280	290	305	329	415	452	1.135
	2.5	260	278	289	304	329	415	451	2.269
	5	258	275	286	301	326	414	456	4.62
PCM+CB_HCS165	1	258	275	286	302	327	417	454	1.111
	2.5	259	276	288	303	328	416	452	2.276
	5	261	280	292	308	333	423	460	4.943
PCM+CB_HCS200	1	253	271	282	298	322	405	440	0.961
	2.5	258	274	285	300	325	410	450	2.365
	5	253	271	282	298	323	411	451	3.941

The addition of carbon-black nanoparticles has a complex, nonuniform effect on thermal stability:

- Electroconductive carbon black (E_CB) exhibited the most pronounced influence on thermal decomposition behavior. At a 1 wt.% loading, the onset temperature of mass loss ($T_{1\%}$) decreased to 251 °C, while at higher loadings it increased to the range of 263–269 °C. The temperatures corresponding to 50% mass loss ($T_{50\%}$) varied between 348 and 429 °C,

https://doi.org/10.3390/en19051162

depending on the concentration of carbon black. In particular, this formulation showed the highest char residue at 600 °C (2.405–6.344%), indicating incomplete decomposition and the possible accumulation of carbonaceous residue. This behavior can be attributed to the presence of conductive carbon black particles, which do not fully decompose and remain as stable carbon-rich residues at elevated temperatures.

- Carbon black grades N220, N234, and N330 exhibited more moderate effects on the thermal stability of PEW. The onset temperatures of mass loss ($T_{1\%}$) ranged from 250 to 257 °C at a 1 wt.% loading, while the temperatures corresponding to 50% mass loss ($T_{50\%}$) remained relatively stable at 399–406 °C, only slightly lower than those of the pure PCM. The char residue for these formulations was minimal (0.143–1.105%), indicating more complete thermal degradation compared to electroconductive variants. This behavior, which closely resembles that of the unmodified PCM, suggests that conventional carbon black grades exhibit good thermal compatibility with paraffin-based matrices [48,49].
- Carbon Black HCS series: The HCS formulations (HCS2, HCS165, and HCS200) exhibited an intermediate influence on the thermal stability of PEW. The onset temperatures of mass loss ($T_{1\%}$) ranged from 253 to 265 °C, while the temperatures at 50% mass loss ($T_{50\%}$) were between 405 and 423 °C, remaining very close to the pure PCM baseline. The char residue at 600 °C varied from 0.961 to 4.943%, which is higher than that observed for standard carbon black grades but lower than for electroconductive variants. This behavior suggests that specialty carbon black grades may form more thermally stable interactions with the paraffin matrix, contributing to enhanced thermal resistance at elevated temperatures.

The observed thermal behavior can be understood in the context of carbon-paraffin interactions. Studies on PCMs enhanced with carbon nanoparticles have demonstrated that carbon additives can enhance or slightly reduce thermal stability depending on their surface properties and degree of dispersion [34,35].

The reduction in $T_{1\%}$ (initial decomposition temperature) observed in this study stay with good agreement with literature findings. Research on graphene-enhanced paraffin systems reported $T_{1\%}$ reductions of 5–15 °C compared to pure paraffin, similar to the 8–16 °C reduction observed with carbon black in this study. This phenomenon is attributed to surface-catalyzed decomposition, where the high surface area of nanoparticles can catalyze the thermal decomposition of nearby paraffin molecules at lower temperatures [48–50].

The formation of a carbonaceous residue (char) at elevated temperatures is a characteristic feature of carbon-filled composites. The increase in char residue with increasing carbon black content observed in this study follows the expected trend: for a composite containing N wt.% of non-decomposable carbon black, the theoretical char yield should approach N wt.%. However, the experimentally observed values (0.002–6.344%) are generally lower than the nominal carbon black loadings (up to 5 wt.%), suggesting partial pyrolysis of carbon black into gaseous products and/or interactions with paraffin decomposition products. Previous studies on the thermogravimetric behavior of carbon-filled polymers indicate that char formation at 600 °C may account for 40–100% of the initial carbon black content, depending on the carbon black grade and thermal processing conditions. The relatively low char yields observed in this work—particularly for standard carbon black grades—suggest good dispersion and integration of carbon black within the paraffin macromolecular structure, as well as possible partial degradation of the carbon filler under the applied measurement conditions [48].

For applications in mobile heating systems, the thermal stability demonstrated by all formulations is excellent. According to the DSC results, the melting point was determined at ca. 90–96 °C, well below the $T_{1\%}$ values (251–269 °C) observed in TG analysis. This

https://doi.org/10.3390/en19051162

margin ensures that these PCM will maintain their thermal storage functionality throughout the design life of mobile heating systems that operate in typical temperature ranges (up to 60–100 °C) [41].

The observed carbon black aggregate sizes (in the range of 100–500 nm) are consistent with those of industrial carbon black products commonly used in thermal and electrical applications. Literature on carbon black nanostructure indicates that commercial carbon blacks consist of primary particles aggregated into larger structures, with aggregate sizes typically ranging from tens of nanometers to several micrometers, depending on the manufacturing process. The size range identified in this study places carbon black within the nanoparticle regime, which is advantageous for achieving property enhancement while maintaining adequate dispersion stability [51]. The uniformity of particle distribution observed at the micrometer scale compares favorably with reports on other nanoparticle–polymer systems. Studies on graphene oxide–paraffin and carbon nanotube–paraffin composites frequently describe localized agglomeration and clustering, particularly at higher filler loadings. The superior dispersion observed in the present carbon black–based systems may be attributed to the spherical or near-spherical morphology of carbon black aggregates, which pack more efficiently than the highly anisotropic structures of carbon nanotubes or graphene sheets [34,52,53].

For mobile heating system applications, the microstructural characteristics revealed by SEM analysis are highly advantageous. The homogeneous distribution of carbon black throughout the paraffin matrix ensures uniform material properties, which are critical for reliable thermal energy storage and heat transfer. In addition, good interfacial contact between the filler and the matrix reduces thermal resistance at the particle–matrix interfaces, which would typically be expected to enhance thermal conductivity. However, the LFA results indicate an unexpected decrease in thermal conductivity, suggesting that other effects—such as particle-induced phonon scattering or disruption of the paraffin crystalline structure—may dominate over the benefits of improved interfacial contact in this system [54].

Figure 8 shows SEM images of carbon black modified samples, and Figure 9 also shows EDS analysis.

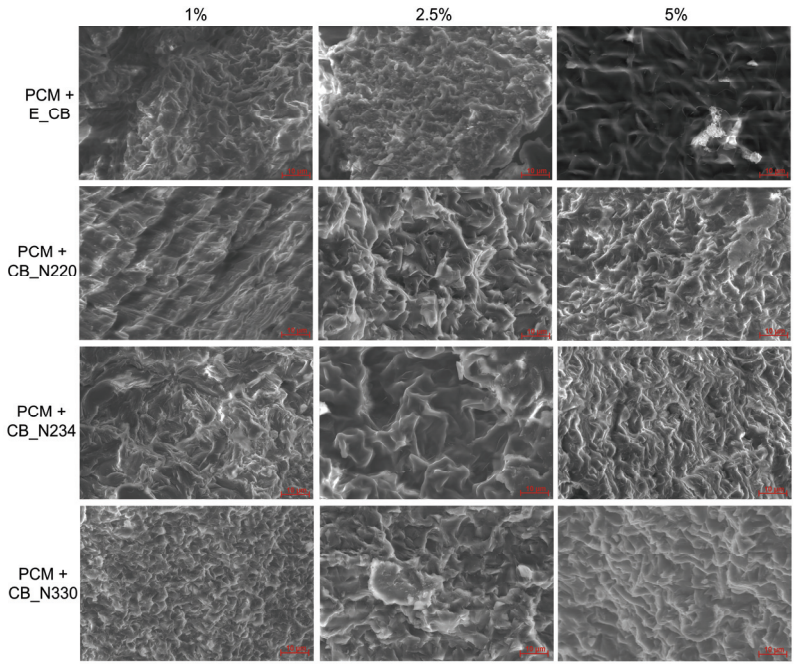


Figure 8. SEM 5000× images of PCM + 1%, 2.5%, 5% E_CB (**first row**) PCM + 1%, 2.5%, 5% CB_N220 (**second row**), PCM + 1%, 2.5%, 5% CB_N234 (**third row**), and PCM + 1%, 2.5%, 5% CB_N330 (**forth row**).

https://doi.org/10.3390/en19051162

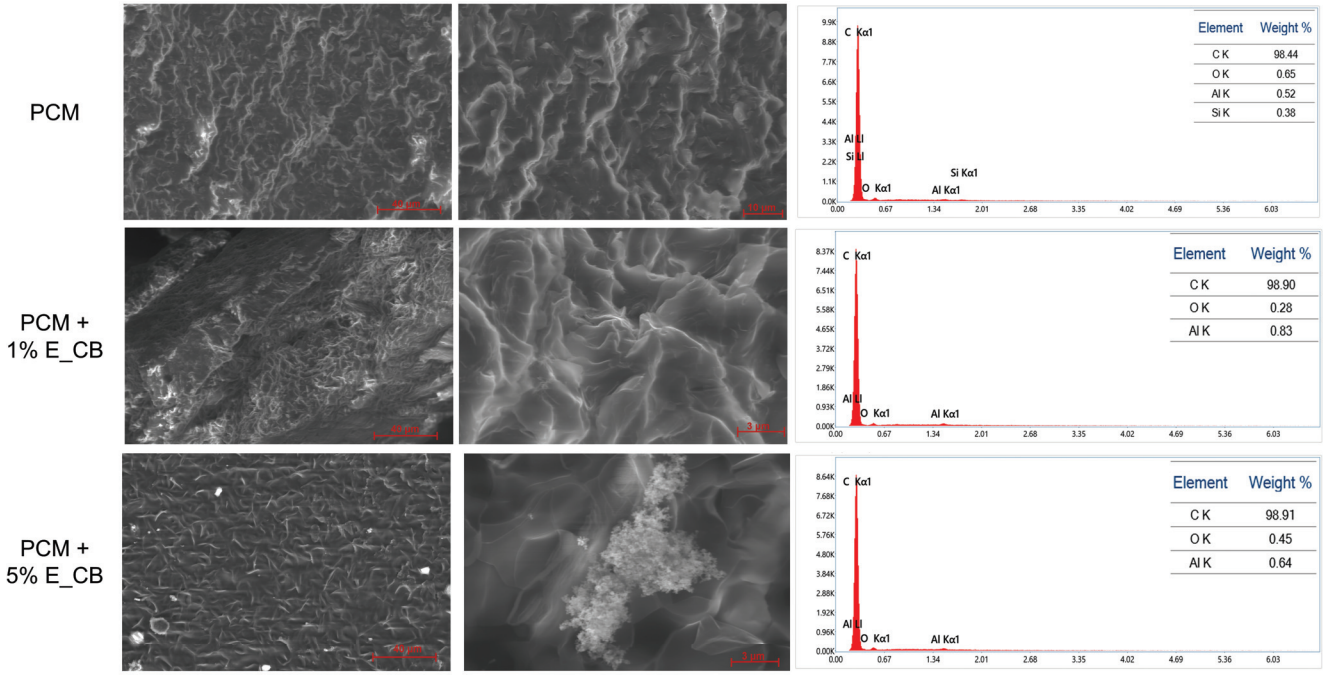


Figure 9. SEM images, from left to right respectively: PCM 2000×, 5000×, EDS (**first row**) PCM + 1% E_CB 2000×, 10,000×, EDS (**second row**), PCM + 5% E_CB 2000×, 10,000×, EDS (**third row**).

The absence of pronounced agglomeration or clustering in the SEM images further suggests that the composites are likely to maintain microstructural integrity during repeated thermal cycling. Such stability is essential for the durability and long-term reliability of phase change materials subjected to multiple heating and cooling cycles. Previous studies on PCM composites have emphasized the importance of microstructural stability in preserving long-term performance [55].

Figure 10 shows graphs of the specific heat capacity obtained using TOPEM DSC measurements. During phase transitions, the specific heat is highest [56]. Additionally, the highest heat of fusion is observed for materials with the highest carbon black content.

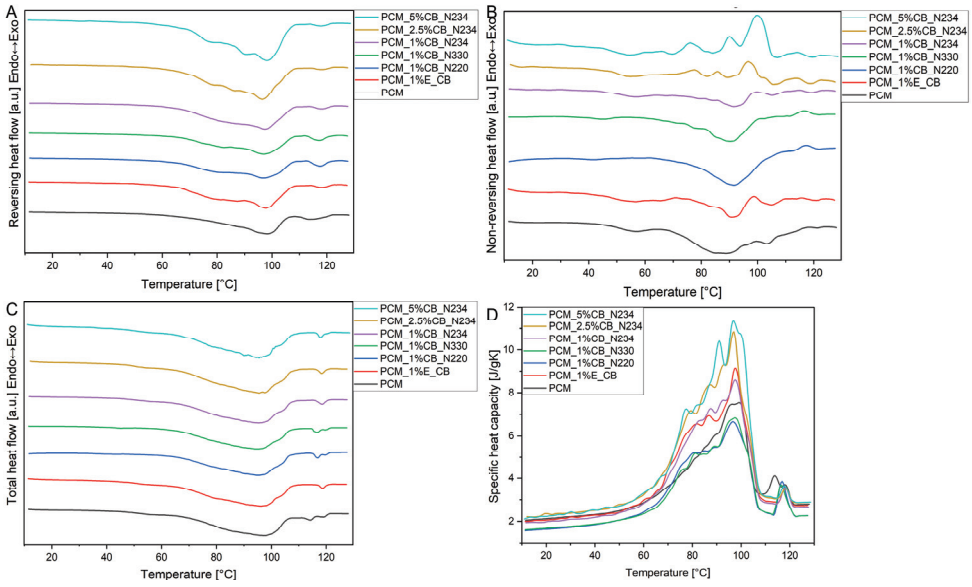


Figure 10. TOPEM DSC results: (**A**) reversing heat flow curves, (**B**) non-reversing heat flow curves, (**C**) total heat flow curves of TPCMs mixtures, (**D**) specific heat capacity curves of PCM with carbon black mixtures.

https://doi.org/10.3390/en19051162

Figure 10 shows that the reversing heat flow curves (A) indicate melting during heating as a reversible process. In contrast, the non-reversing heat flow (B) exhibits exothermic signals associated with recrystallization, followed by a peak corresponding to complete melting (C). Samples with higher carbon black mass fractions show a greater extent of recrystallization, which leads to an increased number of crystal defects. As a result, the enthalpy of the phase transition may be reduced. Overall, the heat flow profiles closely resemble those obtained from conventional DSC measurements. The specific heat capacity (C_p) values were determined from the TOPEM DSC measurements. The results of the thermal conductivity measurements were calculated using Equation (1) and are presented in Table 6.

Table 6. Results of thermal diffusivity and thermal conductivity of PCM with carbon black.

Sample	Thermal Diffusivity, mm^2/s				Thermal Conductivity, W/(m·K)			
	Temperature, °C				Temperature, °C			
	25	**40**	**55**	**70**	**25**	**40**	**55**	**70**
PCM	0.1480	0.1345	0.1180	0.0915	0.3030	0.2930	0.2950	0.3095
PCM + 1% CB_N234	0.1675	0.1475	0.1275	0.0930	0.3235	0.3090	0.3140	0.3620
Percentage improvement, %	13.2	9.7	8.1	1.6	6.8	5.5	6.3	17.0
PCM + 2.5% CB_N234	0.1570	0.1400	0.1200	0.0900	0.3450	0.3240	0.3260	0.3780
Percentage improvement, %	6.1	3.7	1.3	−2.2	13.9	10.6	10.5	22.0
PCM + 5% CB_N234	0.1610	0.1430	0.1220	0.0910	0.3580	0.3450	0.3450	0.3730
Percentage improvement, %	8.4	5.9	3.4	−1.1	18.0	17.6	16.8	20.5

The results obtained indicate an improvement in thermal conductivity with the addition of carbon black, with the most pronounced enhancement observed for N234 carbon black. Therefore, further measurements were conducted for composites containing 2.5 and 5 wt.% of this nanoadditive. The average, in the temperature range of 25–55 °C, thermal conductivity improvement is 6.2% for PCM + 1% CB_N234, 11.7% for PCM + 2.5% CB_N234, and 17.4% for PCM + 5% CB_N234 as compared to the base PCM. The deviating value of the thermal conductivity at 70 °C can be attributed to the proximity of this temperature to the phase transition, which compromises the thermal equilibrium of the sample during measurement and results in anomalous thermal conductivity behavior.

A detailed description of the microscopic mechanisms of conductive heat transfer and heat transfer enhancement can be found in the work of Wu et al. [57]. In general, the role of CB particles in enhancing heat transfer can be attributed to the fact that, in organic PCMs, heat conduction occurs primarily through lattice vibrations, with phonons acting as the main carriers of thermal energy [58]. The presence of CB particles within the PCM provides additional pathways for phonon transport, thereby improving the effective thermal conductivity of the composite material [59]. However, poor dispersion of the additive and/or a too low mass fraction may prevent the formation of a continuous conductive network and may introduce thermal contact resistance, resulting in only a modest improvement in thermal conductivity [59]. Consequently, the literature suggests that only additive mass fractions exceeding a certain threshold—dependent on the type of PCM and the additive used—can effectively enhance thermal conductivity. The results obtained in the present study suggest that the threshold mass fraction of CB particles in the PCM is 1 wt.% or lower, as an improvement in thermal conductivity is already

https://doi.org/10.3390/en19051162

observed at this concentration. Nevertheless, further studies are required to evaluate thermal conductivity enhancement at even lower additive mass fractions.

PEW/CB systems offer superior advantages versus graphene and CNT: comparable thermal conductivity gains (18–22% vs. 15–30%) with significantly lower cost ($2–5/kg vs. $50–500/kg), making them industrially viable for large-scale thermal energy storage applications [14,60–62].

Figure 11A presents the temperature evolution curves of the investigated composites. The pure PCM sample does not exhibit a clear phase change transition; instead, only a small and nearly linear temperature increase is observed, reaching approximately 10 °C by the end of irradiation. Upon switching off the light source, an immediate temperature decrease occurs. In contrast, the composite samples show a rapid temperature rise from the onset of irradiation, accompanied by a characteristic inflection point associated with the phase change transition, particularly evident for the N220, N330, and N234 samples. This inflection point corresponds to the transition region in which the temperature increases at a reduced rate due to latent heat absorption during the phase change process.

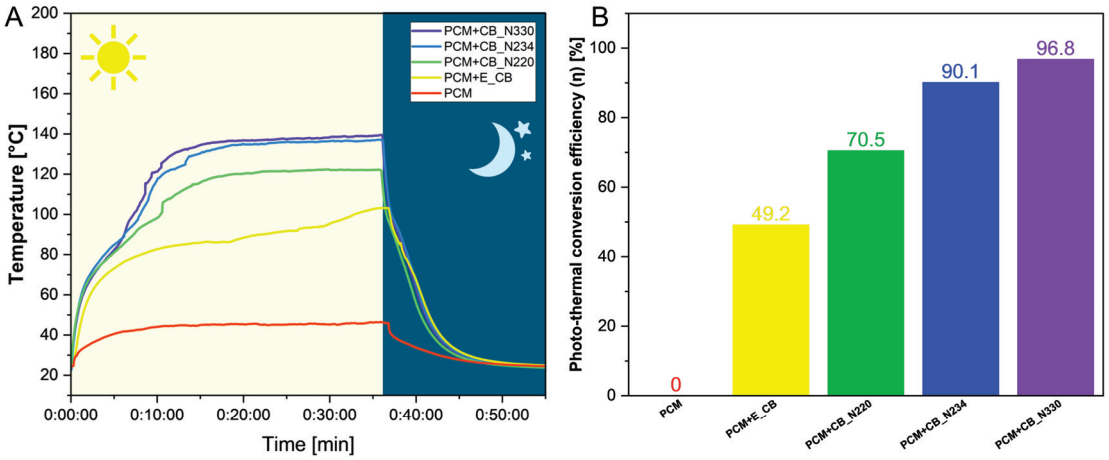


Figure 11. (**A**) Temperature evolution curves composites during solar–thermal conversion test, (**B**) calculated photothermal conversion efficiency.

The SE sample exhibited a rapid increase in temperature in the initial stage of irradiation; however, after reaching approximately 75 °C, the subsequent temperature increase was significantly lower compared to that of the N-series samples. In addition, this sample required a substantially longer irradiation time for the phase change transition to occur. The N330 and N234 samples showed the highest temperature increases, reaching approximately 135 °C within about 15 min. These values are high not only compared to the other samples studied here, but also relative to previously reported results [22,23]. Furthermore, the inflection point associated with the phase change transition appeared earlier and was shorter in duration for the N330 and N234 samples than for the N220 and SE samples. The thermal performance observed under the solar simulator is directly reflected in the photothermal conversion efficiency (Figure 11B). The highest photothermal conversion efficiencies were obtained for the N234 and N330 samples, resulting from their favorable combination of high thermal conductivity and high fusion enthalpy, determined by DSC measurements. In contrast, the SE and N234 samples exhibited lower photothermal conversion efficiencies, likely due to poorer light absorption and conversion performance. This behavior can be attributed to their lower thermal conductivity and the reduced enthalpy of melting observed in the DSC tests, possibly arising from less effective dispersion of the additive and the formation of agglomerates that hinder smooth phase transformation.

https://doi.org/10.3390/en19051162

Overall, the results confirm that carbon-based additives with strong optical absorption and adequate thermal conductivity are critical for optimizing photothermal performance in PEW-based composites. The N series formulations, particularly N330 and N234, demonstrate the best balance between absorption, heat generation, and controlled phase change behavior, making them highly promising candidates for solar–thermal energy storage and conversion applications. In the literature, Luo X. et al. [60] used expanded graphite and carbon nanotubes to modify paraffin. Expanded graphite greatly improves the thermal conductivity of paraffin. Carbon black nanoparticles endow the paraffin satisfied light absorption capacity. The intrinsic photothermal conversion efficiency is up to 60.1% at 1000 W/m^2. Mishra et al. [26] examined that CBNP increases both conductivity and photothermal conversion by ~134% due to improved radiation absorption and the carbon scattering effect. In turn, Zhang et al. [63] show that composites with graphene foam can effectively convert light into heat, accumulating energy in the PCM and extending the heat release period. In a comprehensive review of carbon-based PCMs [64], the authors discuss various carbon additives (CNTs, CFs, graphene/rGO, expanded graphite, biocarbon) and their impact on solar-to-thermal conversion and other energy conversions. They point out that photothermal conversion in graphene/rGO-based PCMs typically exceeds that of simple carbon additives due to improved absorption and heat transfer networks.

4. Conclusions

This study presents a comprehensive evaluation of polyethylene wax–based phase change materials modified with seven distinct types of carbon black, focusing on their thermal behavior during phase transitions, thermal stability, microstructural characteristics, and photothermal performance. The results demonstrate that carbon black modification leads to modest reductions in the enthalpy of fusion (8–15% across the investigated formulations), which can be attributed to the space-occupying nature of the nanoparticles and their interference with the crystallization process of the PEW matrix. Importantly, the melting and solidification temperatures remained stable (95–96 °C), ensuring predictable thermal behavior and good reliability. Moreover, the ratio of solidification to melting enthalpy (Qs/Qm ≈ 0.90–0.98) confirms excellent thermal cycling performance, which is critical for reliable operation in practical mobile heating systems. Among the evaluated carbon black grades, N234 exhibited the most pronounced improvement in thermal conductivity, with a 6.8% enhancement at 1 wt.% loading at 25 °C and a 17.0% increase at 70 °C. These improvements directly translate into faster charging and discharging rates in thermal energy storage applications. Thermogravimetric analysis showed that all the systems investigated possess good thermal stability, with onset decomposition temperatures ($T_{1\%}$) in the range of 250–269 °C, well above the typical operating temperatures (90–100 °C) of mobile heating systems. SEM analysis revealed a uniform distribution of carbon black within the PEW matrix, with aggregate sizes in the range of 100 to 500 nm, characteristic of commercial carbon black products. Photothermal conversion experiments demonstrated particularly high efficiency for the N234 and N330 formulations, which exhibited rapid temperature increases, reaching approximately 135 °C within about 15 min under solar simulator irradiation. This performance can be attributed to the strong optical absorption of carbon black combined with enhanced thermal conductivity. Overall, the results confirm that carbon black is a viable and cost-effective additive for enhancing the thermal properties and photothermal conversion capability of PEW-based PCM systems, while maintaining excellent thermal stability and cycling performance. Consistent Tm and Ts values across all PCM/CB systems (95–96 °C and 90–91 °C, respectively) demonstrated strong thermal compatibility and the absence of interfacial chemical reactions, as it was confirmed in FTIR

https://doi.org/10.3390/en19051162

results. Analysis of the FTIR results for both neat PCM, PCM/CB samples, and CB indicates no changes in PEW in the presence of carbon black, which indicates no chemical reaction between the PCM and the carbon additive. DSC results after 20 heating–cooling cycles for the PCM base material and the two best formulations revealed that the best thermal behavior and repeatability were exhibited by the PCM+CB_N330 sample, where the values of heat of phase transition were on a similar level as before thermal cycling.

Author Contributions: Conceptualization, M.S. and K.P.; methodology, M.S. and K.P.; formal analysis, M.S., P.S., K.S., E.R. and K.P.; investigation, M.S., P.S., K.S. and E.R.; data curation, M.S., P.S., K.S. and E.R.; writing—original draft preparation, M.S., P.S., E.R. and K.S.; writing—review and editing, M.S. and K.P.; visualization, M.S. and K.S.; supervision, K.P.; project administration, K.P.; funding acquisition, K.P. All authors have read and agreed to the published version of the manuscript.

Funding: The authors are grateful to the National Center for Research and Development for financial support under Contract No. NTE2/0004/2022 with the acronym MMC. This work was also supported by a subsidy from the Ministry of Science and Higher Education for the AGH University of Krakow (Project No. 16.16.160.557).

Data Availability Statement: The original contributions presented in this study are included in the article. Further inquiries can be directed to the corresponding author.

Conflicts of Interest: The authors declare no conflicts of interest.

References

1. Lawag, R.A.; Ali, H.M. Phase change materials for thermal management and energy storage: A review. *J. Energy Storage* **2022**, *55*, 105602. [CrossRef]
2. Pielichowska, K.; Szatkowska, M.; Pielichowski, K. Thermal Energy Storage in Bio-Inspired PCM-Based Systems. *Energies* **2025**, *18*, 3548.
3. Zhang, S.; Ocłoń, P.; Klemeš, J.J.; Michorczyk, P.; Pielichowska, K.; Pielichowski, K. Renewable energy systems for building heating, cooling and electricity production with thermal energy storage. *Renew. Sustain. Energy Rev.* **2022**, *165*, 112560. [CrossRef]
4. Zalba, B.; Marín, J.M.; Cabeza, L.F.; Mehling, H. Review on thermal energy storage with phase change: Materials, heat transfer analysis and applications. *Appl. Therm. Eng.* **2003**, *23*, 251–283. [CrossRef]
5. Pielichowska, K.; Pielichowski, K. Phase change materials for thermal energy storage. *Prog. Mater. Sci.* **2014**, *65*, 67–123. [CrossRef]
6. Mehling, H. Review of Classification of PCMs, with a Focus on the Search for New, Suitable PCM Candidates. *Energies* **2024**, *17*, 4455. [CrossRef]
7. Yang, G.; Yim, Y.J.; Lee, J.W.; Heo, Y.J.; Park, S.J. Carbon-Filled Organic Phase-Change Materials for Thermal Energy Storage: A Review. *Molecules* **2019**, *24*, 2055. [CrossRef]
8. Dash, L.; Mahanwar, P. A Review on Organic Phase Change Materials and Their Applications. *Int. J. Eng. Appl. Sci.* **2021**, *5*, 268–284.
9. Krupa, I.; Sobolčiak, P.; Abdelrazeq, H.; Ouederni, M.; Al-Maadeed, M.A. Natural aging of shape stabilized phase change materials based on paraffin wax. *Polym. Test.* **2017**, *63*, 567–572. [CrossRef]
10. Zauner, C.; Hengstberger, F.; Etzel, M.; Lager, D.; Hofmann, R.; Walter, H. Experimental characterization and simulation of a fin-tube latent heat storage using high density polyethylene as PCM. *Appl. Energy* **2016**, *179*, 237–246. [CrossRef]
11. Navarro, L.; Barreneche, C.; Castell, A.; Redpath, D.A.G.; Griffiths, P.W.; Cabeza, L.F. High density polyethylene spheres with PCM for domestic hot water applications: Water tank and laboratory scale study. *J. Energy Storage* **2017**, *13*, 262–267. [CrossRef]
12. Fikri, M.A.; Pandey, A.K.; Samykano, M.; Kadirgama, K.; George, M.; Saidur, R.; Selvaraj, J.; Abd Rahim, N.; Sharma, K.; Tyagi, V.V. Thermal conductivity, reliability, and stability assessment of phase change material (PCM) doped with functionalized multi-wall carbon nanotubes (FMWCNTs). *J. Energy Storage* **2022**, *50*, 104676. [CrossRef]
13. Feng, X.; Zhang, Y.; Yang, Z.; Zhao, Z.; Zhu, F.; Wei, X.; Chen, L.; Liu, J.; Feng, Y.; Li, C.; et al. Polyethylene glycol with dual three-dimensional porous carbon nanotube/diamond: A high thermal conductivity of composite PCM. *Nanotechnology* **2024**, *35*, 095702.
14. Mishra, A.K.; Ribezzo, A.; Morciano, M.; Bergamasco, L.; Campagnoli, E.; Giaretto, V.; Fasano, M.; Chiavazzo, E. Thermal conductivity enhancement in carbon black composite PCM for thermal energy storage. *J. Phys. Conf. Ser.* **2025**, *2940*, 012012.

 https://doi.org/10.3390/en19051162

15. Afaynou, I.; Faraji, H.; Choukairy, K.; Djebali, R.; Rezk, H. Comprehensive Analysis and Thermo-Economic Optimization of a Hybrid Phase Change Material-Based Heat Sink for Electronics Cooling. *Heat Transf.* **2025**, *54*, 3754–3774. [CrossRef]
16. Mishra, A.K.; Morciano, M.; Campagnoli, E.; Giaretto, V.; Fasano, M.; Chiavazzo, E. Coffee and turmeric bio-based shape-stabilized composite PCMs for thermal and solar energy storage applications. *Sol. Energy Mater. Sol. Cells* **2026**, *297*, 114136. [CrossRef]
17. Yu, J.; Feng, J. Form-stable phase change materials with enhanced thermal conductivity via segregated BN network within SEBS-supported paraffin wax for electronics thermal management. *Compos. Part A Appl. Sci. Manuf.* **2025**, *199*, 109187. [CrossRef]
18. Taylor, J.R. *An Introduction to Error Analysis: The Study of Uncertainties in Physical Measurements*; University Science Books: Melville, NY, USA, 1997.
19. Light Flash Apparatus LFA 467 HyperFlash® Series. 2026. Available online: https://analyzing-testing.netzsch.com/_Resources/Persistent/3/6/7/f/367f54b9bc7fc3a5b36f6b41191f5dbaf802ecb7/LFA_467_HyperFlash_en_web.pdf (accessed on 30 January 2026).
20. Analytical Balance. 2026. Available online: https://radwag.com/en/waga-analityczna-xa-82-220-5y,w1,9QF,114-107-100 (accessed on 30 January 2026).
21. Specific Heat Capacity Measurement. 2026. Available online: https://www.mt.com/be/nl/home/applications/Application_Browse_Laboratory_Analytics/Application_Browse_thermal_analysis/specific-heat-capacity-measurement.html (accessed on 30 January 2026).
22. Huang, Y.; Zou, M.; Chen, W.; Luo, W.; Hu, X.; Zhu, G.; Tan, S.; Jiang, X. A Novel Room-Temperature Flexible Phase Change Material for Solar Energy Photothermal Conversion and Battery Thermal Management. *ACS Sustain. Chem. Eng.* **2024**, *12*, 4662–4675. [CrossRef]
23. Cheng, G.; Wang, X.; He, Y. 3D graphene paraffin composites based on sponge skeleton for photo thermal conversion and energy storage. *Appl. Therm. Eng.* **2020**, *178*, 115560. [CrossRef]
24. Han, Z.; Zhao, Y.; Hu, S.; Zhou, Z.; Yan, Y.; Wang, C. Preparation and application of composite PCM with combined radiative cooling and photothermal conversion capabilities for building energy management. *Energy Build.* **2025**, *347*, 116363. [CrossRef]
25. Bharathiraja, R.; Ramkumar, T.; Selvakumar, M. Studies on the thermal characteristics of nano-enhanced paraffin wax phase change material (PCM) for thermal storage applications. *J. Energy Storage* **2023**, *73*, 109216. [CrossRef]
26. Mishra, A.K.; Lahiri, B.B.; Philip, J. Carbon black nano particle loaded lauric acid-based form-stable phase change material with enhanced thermal conductivity and photo-thermal conversion for thermal energy storage. *Energy* **2020**, *191*, 116572. [CrossRef]
27. Singh, R.P.; Sze, J.Y.; Kaushik, S.C.; Rakshit, D.; Romagnoli, A. Thermal performance enhancement of eutectic PCM laden with functionalised graphene nanoplatelets for an efficient solar absorption cooling storage system. *J. Energy Storage* **2021**, *33*, 102092. [CrossRef]
28. Fan, Z.; Zhao, Y.; Liu, X.; Shi, Y.; Jiang, D. Thermal Properties and Reliabilities of Lauric Acid-Based Binary Eutectic Fatty Acid as a Phase Change Material for Building Energy Conservation. *ACS Omega* **2022**, *7*, 16097–16108. [CrossRef] [PubMed]
29. Mishra, A.K.; Lahiri, B.B.; Philip, J. Effect of Surface Functionalization and Physical Properties of Nanoinclusions on Thermal Conductivity Enhancement in an Organic Phase Change Material. *ACS Omega* **2018**, *3*, 9487–9504. [CrossRef]
30. Colla, L.; Fedele, L.; Mancin, S.; Danza, L.; Manca, O. Nano-PCMs for enhanced energy storage and passive cooling applications. *Appl. Therm. Eng.* **2017**, *110*, 584–589. [CrossRef]
31. Rolka, P.; Lackowski, M. The effect of graphene nanoparticles on the thermal conductivity enhancement of organic phase change material and its energy storage properties. *Arch. Thermodyn.* **2024**, *44*, 103–121.
32. Diby, I.C.P.; Belkhiri, N.; Nohair, B.; Kazeruni, M.; Ruiz, E.; Kaliaguine, S. HDPE crystalline lamellae in composites involving pyrolytic carbon black: Effect on elastic modulus. *Polym. Compos.* **2025**, *46*, 38–53.
33. Spahr, M.E.; Rothon, R. Carbon Black as a Polymer Filler. In *Fillers for Polymer Applications*; Springer: Cham, Switzerland, 2017; pp. 261–291.
34. Fredi, G.; Dorigato, A.; Fambri, L.; Pegoretti, A. Wax Confinement with Carbon Nanotubes for Phase Changing Epoxy Blends. *Polymers* **2017**, *9*, 405. [CrossRef]
35. Pasupathi, M.K.; Alagar, K.; Stalin, P.M.J.; Matheswaran, M.M.; Aritra, G. Characterization of Hybrid-nano/Paraffin Organic Phase Change Material for Thermal Energy Storage Applications in Solar Thermal Systems. *Energies* **2020**, *13*, 5079. [CrossRef]
36. Ahmad, I.A.; Kim, H.K.; Deveci, S.; Kumar, R.V. Non-Isothermal Crystallisation Kinetics of Carbon Black- Graphene-Based Multimodal-Polyethylene Nanocomposites. *Nanomaterials* **2019**, *9*, 110. [CrossRef] [PubMed]
37. Yadav, D.K.; Rathore, P.K.S.; Singh, R.K.; Gupta, A.K.; Sikarwar, B.S. Experimental Study on Paraffin Wax and Soya Wax Supported by High-Density Polyethylene and Loaded with Nano-Additives for Thermal Energy Storage. *Energies* **2024**, *17*, 2461. [CrossRef]
38. Sharma, A.; Singh, P.K.; Sharma, K. Synergistic Effects of Heated Walnut Shell Powder and Reduced Graphene Oxide in Paraffin Wax Composites for Marine Thermal Applications. *Int. J. Marit. Eng.* **2024**, *1*, 277–286. [CrossRef]

https://doi.org/10.3390/en19051162

39. Nejman, A.; Gromadzińska, E.; Kamińska, I.; Cieślak, M. Assessment of Thermal Performance of Textile Materials Modified with PCM Microcapsules Using Combination of DSC and Infrared Thermography Methods. *Molecules* **2019**, *25*, 122. [CrossRef]
40. Sun, X.; Lee, K.O.; Medina, M.A.; Chu, Y.; Li, C. Melting temperature and enthalpy variations of phase change materials (PCMs): A differential scanning calorimetry (DSC) analysis. *Phase Transit.* **2018**, *91*, 667–680.
41. Kumari, P.; Raj, A.; Ghosh, D. Selection of Phase Change Material for Latent Heat Thermal Energy Storage Using a Hairpin Heat Exchanger: Numerical Study. *J. Therm. Sci. Eng. Appl.* **2024**, *16*, 091005. [CrossRef]
42. Nazari, S.M.; Caggiano, A.; Mankel, C.; Koenders, E. A Comparative Study on the Thermal Energy Storage Performance of Bio-Based and Paraffin-Based PCMs Using DSC Procedures. *Materials* **2020**, *13*, 1705. [CrossRef]
43. Mane, N.S.; Kodancha, P.; Hemadri, V.; Tripathi, S. Investigation on Cooling Performance of Composite PCM and Graphite Fin for Battery Thermal Management System of Electric Vehicles. *Energy Storage* **2024**, *6*, e70024. [CrossRef]
44. Dogan, O.M.; Keskin, S.; Dogan, A.; Ataman, H.; Usanmaz, A. Structure-property Relation of a Soft Liner Material Used in Denture Applications. *Dent. Mater. J.* **2007**, *26*, 329–334. [CrossRef] [PubMed]
45. Zhuang, J.; Li, M.; Pu, Y.; Ragauskas, A.; Yoo, C. Observation of Potential Contaminants in Processed Biomass Using Fourier Transform Infrared Spectroscopy. *Appl. Sci.* **2020**, *10*, 4345. [CrossRef]
46. Bacher, D.A. Infrared Spectroscopy n.d. Available online: https://webspectra.chem.ucla.edu/irtable.html (accessed on 6 September 2024).
47. Kim, H.B.; Mae, M.; Choi, Y. Thermal Performance Measurement Procedure and Its Accuracy for Shape-Stabilized Phase-Change Material and Microcapsule Phase-Change Material Combined with Building Materials. *Sustainability* **2021**, *13*, 6671. [CrossRef]
48. Öner, G.A. Flexural strength and thermal properties of carbon black nanoparticle reinforced epoxy composites obtained from waste tires. *Open Chem.* **2022**, *20*, 863–872. [CrossRef]
49. Yu, J.; Li, H.; Kong, L.; Zhu, H.; Zhu, Q.; Wang, H. Effects of Nanofilled Particle Forms and Dispersion Modes on Properties of Carbon-Based Energy Storage Composites. *Adv. Polym. Technol.* **2020**, *2020*, 6865497. [CrossRef]
50. Laghari, I.A.; Pandey, A.K.; Samykano, M.; Aljafari, B.; Kadirgama, K.; Sharma, K.; Tyagi, V.V. Thermal energy harvesting of highly conductive graphene-enhanced paraffin phase change material. *J. Therm. Anal. Calorim.* **2023**, *148*, 9391–9402. [CrossRef]
51. Singh, M.; Vander Wal, R.L. Nanostructure Quantification of Carbon Blacks. *C* **2018**, *5*, 2. [CrossRef]
52. Almousa, N.H.; Alotaibi, M.R.; Alsohybani, M.; Radziszewski, D.; AlNoman, S.M.; Alotaibi, B.M.; Khayyat, M.M. Paraffin Wax [As a Phase Changing Material (PCM)] Based Composites Containing Multi-Walled Carbon Nanotubes for Thermal Energy Storage (TES) Development. *Crystals* **2021**, *11*, 951. [CrossRef]
53. Feng, L.; Wu, J.; Sun, W.; Cai, W. Effects of Pore Structure and Pore Size of Expanded Graphite on the Properties of Paraffin Wax/Expanded Graphite Composite Phase Change Materials. *Energies* **2022**, *15*, 4201. [CrossRef]
54. Aslan, O.; Atalar, T.; Yılmaz, G.A.; Özkan, N. Enhancing the performance of HTPB-IPDI-based polyurethane composite liner through effective carbon black dispersion. *Propell. Explos. Pyrotech.* **2023**, *48*, e202300107. [CrossRef]
55. Samuel, J.; Yussuf, A.A.; Al-Zufairi, R.; Al-Banna, A.; Al-Shammary, T.; Abraham, G. High density polyethylene hybrid nanocomposites reinforced with carbon nanofiber and nanoclay. *J. Elastomer Plast.* **2024**, *56*, 713–731. [CrossRef]
56. Fan, R.; Wan, M.; Zheng, N.; Sun, Z. Simultaneously enhanced light absorption and heat transfer capability of melamine foam stabilized phase change composites by carbon black and metal fins for photothermal conversion and storage. *J. Energy Storage* **2022**, *54*, 105278. [CrossRef]
57. Wu, S.; Yan, T.; Kuai, Z.; Pan, W. Thermal conductivity enhancement on phase change materials for thermal energy storage: A review. *Energy Storage Mater.* **2020**, *25*, 251–295. [CrossRef]
58. Li, Z.R.; Hu, N.; Fan, L.W. Nanocomposite phase change materials for high-performance thermal energy storage: A critical review. *Energy Storage Mater.* **2023**, *55*, 727–753.
59. Cheng, P.; Chen, X.; Gao, H.; Zhang, X.; Tang, Z.; Li, A.; Wang, G. Different dimensional nanoadditives for thermal conductivity enhancement of phase change materials: Fundamentals and applications. *Nano Energy* **2021**, *85*, 105948. [CrossRef]
60. Luo, X.; Hao, B.; Xiang, H.; Li, H.; Tao, Z. A novel phase change materials used for direct photothermal conversion and efficient thermal storage. *Sol. Energy Mater. Sol. Cells* **2023**, *251*, 112142. [CrossRef]
61. Leong, K.Y.; Hasbi, S.; Ku, A.K.Z.; Mat, J.N.; Ong, H.C.; Din, M.F. Thermal properties evaluation of paraffin wax enhanced with carbon nanotubes as latent heat thermal energy storage. *J. Energy Storage* **2022**, *52*, 105027. [CrossRef]
62. Lu, X.; Liu, H.; Murugadoss, V.; Seok, I.; Huang, J.; Ryu, J.E.; Guo, Z. Polyethylene Glycol/Carbon Black Shape-Stable Phase Change Composites for Peak Load Regulating of Electric Power System and Corresponding Thermal Energy Storage. *Eng. Sci.* **2020**, *9*, 25–34. [CrossRef]

https://doi.org/10.3390/en19051162

63. Zhang, L.; Li, R.; Tang, B.; Wang, P. Solar-thermal conversion and thermal energy storage of graphene foam-based composites. *Nanoscale* **2016**, *8*, 14600–14607. [CrossRef]
64. Chen, X.; Cheng, P.; Tang, Z.; Xu, X.; Gao, H.; Wang, G. Carbon-Based Composite Phase Change Materials for Thermal Energy Storage, Transfer, and Conversion. *Adv. Sci.* **2021**, *8*, 2001274. [CrossRef]

Disclaimer/Publisher's Note: The statements, opinions and data contained in all publications are solely those of the individual author(s) and contributor(s) and not of MDPI and/or the editor(s). MDPI and/or the editor(s) disclaim responsibility for any injury to people or property resulting from any ideas, methods, instructions or products referred to in the content.

https://doi.org/10.3390/en19051162

energies

MDPI

Article

Effect of Illumination Colour on the Growth and Energetic Properties of *Chlorella vulgaris* for Bioenergy Applications

Pawel Czyzewski [1], Przemyslaw Matuszak [1], Marcelina Malecka [1], Joanna Jojka [1], Ahmad M. S. H. Al-Moftah [2,3], Hao Shi [2,4,*], Mohammad Alnajideen [2,*] and Agustin Valera-Medina [2]

[1] Institute of Thermal Engineering, Poznan University of Technology, 60-965 Poznan, Poland; pawel.czyzewski@put.poznan.pl (P.C.); joanna.jojka@put.poznan.pl (J.J.)
[2] College of Physical Sciences and Engineering, Cardiff University, Cardiff CF24 3AA, UK; al-moftaha@cardiff.ac.uk (A.M.S.H.A.-M.); valeramedinaa1@cardiff.ac.uk (A.V.-M.)
[3] Qatar National Research Fund (QNRF), Qatar Foundation, Doha P.O. Box 5825, Qatar
[4] Cambridge CARES, University of Cambridge, 1 Create Way, Singapore 138602, Singapore
* Correspondence: hao.shi@cares.cam.ac.uk (H.S.); alnajideenmi@cardiff.ac.uk (M.A.)

Abstract

Microalgae are a promising third-generation biomass resource due to their high photosynthetic efficiency, rapid growth rates, capacity to accumulate energy-rich biochemical fractions, and efficient utilisation of carbon dioxide (CO_2). In this study, the effect of illumination colour on the growth and energetic properties of *Chlorella vulgaris* cultivated in laboratory-scale photobioreactors was investigated. Four independent cultivation cycles were conducted under controlled conditions using a 16 h light/8 h dark photoperiod, temperatures of 20–30 °C, and aeration with air enriched with 10% CO_2. Cultures were illuminated using six light colours: plant-specific, white, green, red, blue, and ultraviolet. Biomass productivity was quantified, and the higher heating value (HHV) of the produced biomass was determined by bomb calorimetry. In addition, proximate (technical) analysis was performed for *Chlorella vulgaris* and compared with *Chlorella pyrenoidosa*, *Spirulina*, and *Fucus vesiculosus* (bladderwrack). The results showed that white illumination promoted both the highest biomass growth and the highest HHV for *Chlorella vulgaris* (15.08 $MJ \cdot kg^{-1}$), while ultraviolet illumination had a disruptive effect, leading to the lowest growth and calorific value (11.49 $MJ \cdot kg^{-1}$). Comparative analysis revealed that *Chlorella pyrenoidosa* exhibited the most favourable energetic properties; however, *Chlorella vulgaris* remains attractive for cultivation due to its robustness and broad tolerance to operating conditions.

Keywords: microalgae bioenergy; *Chlorella vulgaris*; photobioreactor cultivation; illumination colour; proximate analysis; algal biomass; *Chlorella pyrenoidosa*; *Fucus vesiculosus*

1. Introduction

The transition towards low-carbon and renewable energy systems has intensified interest in biomass as a sustainable energy resource. Biomass encompasses organic matter derived from plants, animals, and microorganisms, and is widely regarded as carbon-neutral due to its ability to assimilate atmospheric carbon dioxide (CO_2) through photosynthesis [1]. Beyond conventional lignocellulosic feedstocks, microalgae have attracted increasing attention as a third-generation biomass resource because of their high photosynthetic efficiency, rapid growth rates, and capacity to accumulate energy-rich biochemical fractions such as lipids and carbohydrates [2,3].

Unlike first- and second-generation bioenergy crops, microalgae cultivation does not compete directly with food production or require arable land and can be implemented in controlled systems such as photobioreactors or open ponds [4–6]. Furthermore, microalgae exhibit high CO_2 uptake rates and can be integrated with industrial emission streams, positioning them as a promising platform for combined bioenergy production and carbon capture [7,8]. As a result, microalgal biomass has been investigated for a range of thermochemical and biochemical conversion pathways, including combustion, gasification, pyrolysis, hydrothermal liquefaction, and anaerobic digestion, yielding products such as heat, electricity, syngas, bio-oil, hydrogen, and biochar [9–14].

From an energy systems perspective, the suitability of microalgal biomass as a fuel is governed not only by biomass productivity but also by its physicochemical and energetic properties [15]. Parameters such as moisture content, ash content, volatile matter, fixed carbon, and higher heating value (HHV) directly influence combustion behaviour, conversion efficiency, and overall energy yield [16,17]. In particular, higher lipid and volatile matter contents are generally associated with increased calorific value, while elevated ash and moisture contents can adversely affect thermochemical conversion routes [17–19]. Consequently, cultivation conditions that influence both biomass yield and biochemical composition are critical in determining the net energy potential of microalgae [20].

Among the key cultivation parameters, CO_2 availability and light conditions play a dominant role in regulating microalgal growth and composition. Numerous studies have demonstrated that *Chlorella vulgaris* can tolerate and effectively utilise elevated CO_2 concentrations, with reported optimal growth occurring over a wide range (2–12% CO_2), and some strains remaining viable even at substantially higher concentrations [21–23]. This robustness makes *Chlorella vulgaris* particularly attractive for coupling algal cultivation with industrial CO_2 sources, including flue gas and biogas upgrading streams [24–26].

Light is the primary energy input driving photosynthesis, and its characteristics—intensity, photoperiod, and spectral quality—strongly impact microalgal physiology and productivity [27,28]. While light intensity and photoperiod have been extensively investigated, the role of light spectral composition remains less systematically explored, particularly in the context of energy-relevant biomass properties [29]. Microalgae possess photosynthetic pigments, such as chlorophylls *a* and *b* and accessory carotenoids, whose absorption spectra are concentrated primarily in the blue (400–500 nm) and red (600–700 nm) regions of the visible spectrum [30]. Consequently, illumination wavelength can influence not only growth kinetics but also metabolic pathways associated with lipid, protein, and carbohydrate synthesis.

Previous studies have shown that specific wavelengths can enhance biomass accumulation or alter biochemical composition, depending on species and cultivation conditions [30–32]. For example, red and blue light have been reported to stimulate growth in certain green microalgae, while excessive exposure to short-wavelength or ultraviolet [3] radiation can induce photoinhibition and cellular damage [33–36]. However, much of the existing literature focuses primarily on biomass productivity, pigment content, or nutrient uptake, with limited attention paid to how spectral quality translates into downstream energy properties such as calorific value and fuel proximate composition [37–40].

In addition, most comparative studies assess energy content on a mass basis alone, without explicitly accounting for biomass yield per unit culture volume [41–44]. From a systems and process design perspective, the recoverable energy per unit reactor volume is a critical metric, as it integrates both growth performance and fuel quality. The impact of illumination wavelength on this combined energy yield remains insufficiently quantified [27,45].

https://doi.org/10.3390/en19061572

Against this background, the present study investigates the effect of light colour on the growth behaviour and energetic properties of *Chlorella vulgaris* cultivated in laboratory-scale photobioreactors under controlled conditions. Six lighting colours—plant-specific, white, green, red, blue, and ultraviolet—were examined over multiple cultivation cycles to assess biomass growth dynamics, stability, and reproducibility. Light spectrum plays a critical role in microalgal cultivation because different wavelengths influence photosynthetic efficiency, biomass productivity, and cellular metabolism [30]. Previous studies have shown that illumination conditions can also affect the biochemical composition of microalgae, including lipid, protein, and carbohydrate content, which are important parameters for bioenergy applications [27,46–48]. In the present study, the primary focus was placed on evaluating the influence of illumination colour on biomass growth kinetics and the resulting energetic properties of the produced biomass. Although detailed biochemical characterisation was beyond the scope of this work, the observed differences in biomass productivity and higher heating value provide an indication of how illumination conditions may affect the energy potential of microalgal biomass. To place the results in a broader energy-biomass context, the energetic and proximate properties of cultivated *Chlorella vulgaris* were compared with those of other algal species commonly discussed in bioenergy applications, namely *Chlorella pyrenoidosa*, *Spirulina*, and *Fucus vesiculosus* (bladderwrack). This comparative approach enables an assessment of trade-offs between biomass productivity, fuel quality, and species-specific cultivation constraints.

The novelty of this work lies in linking illumination wavelength not only to algal growth performance but also to fuel-relevant energetic characteristics and volumetric energy yield, thereby providing insights that are directly applicable to the design and optimisation of algal bioenergy systems. The findings contribute to a more integrated understanding of how cultivation strategies influence both biomass production and its suitability for thermochemical energy conversion.

2. Materials and Methods

2.1. Experimental Design and Scope of the Study

To address the research objectives, the study was structured into three interconnected experimental stages:

1. Investigation of the effect of illumination colour on the growth dynamics of *Chlorella vulgaris* cultivated in laboratory-scale photobioreactors.
2. Determination of the energetic properties (higher heating value, HHV) of the biomass obtained under different lighting conditions.
3. Comparative proximate (technical) analysis of cultivated *Chlorella vulgaris* biomass against selected algal species commonly discussed in bioenergy applications.

All experiments were conducted under controlled laboratory conditions to ensure reproducibility and comparability between cultivation cycles.

2.2. Algal Species and Culture Medium

The primary species investigated in this study was *Chlorella vulgaris*, selected due to its rapid growth, broad tolerance to environmental conditions, and documented suitability for energy applications, including combustion and anaerobic digestion [49–52]. The algae were cultivated using Wright's Cryptophyte (WC) medium, a well-established nutrient solution for freshwater microalgae [53].

The WC medium was prepared prior to each cultivation cycle and consisted of macronutrients, trace metals, vitamins, and a buffering agent. The spectral characteristics

https://doi.org/10.3390/en19061572

and nominal luminous flux of the light sources used in the experiments are summarised in Table 1. The composition of the WC culture medium used for algal cultivation is provided in Table 2. It includes components of the trace element solution added to the WC medium. The vitamin solution was composed of thiamine (3.36 $g \cdot L^{-1}$) and biotin (3.15 $g \cdot L^{-1}$). To maintain nutrient availability during cultivation, additional WC medium was supplied on the seventh day of each cycle at a rate of 5 mL per 50 mL of culture suspension. The initial concentration of algal biomass in the culture suspension (seston) did not exceed 0.2 $g \cdot L^{-1}$. All components were dissolved sequentially following the order reported in the tables, using continuous stirring. Sodium bicarbonate was used as a buffering agent, and the initial pH was adjusted to 7.0 ± 0.1.

Table 1. Spectral characteristics and nominal luminous flux of light sources used for algal cultivation.

	Colour of Bulbs	Wavelength [nm]	Luminous Flux [lm]
1.	Plant	450–630	1250 lm for all lamps
2.	White	608	
3.	Green	535	
4.	Red	625	
5.	Blue	450	
6.	UV	400	

Table 2. Composition of the WC culture medium used for *Chlorella vulgaris* cultivation (macronutrients, trace elements (microelements) and buffer).

Component	Amount [$g \cdot L^{-1}$]	Type
$CaCl_2 \cdot 2H_2O$	36.8	macronutrients
$MgSO_4 \cdot 7H_2O$	37.0	
$NaHCO_3$	12.6	
$K_2HPO_4 \cdot 3H_2O$	11.4	
$NaNO_3$	85.0	
$NaSiO_3 \cdot 9H_2O$	21.2	
Microelement solution	1.0	
Vitamin solution	1.0	
TED buffer	0.12	
Na_2EDTA	4.360	trace elements (microelement)
$FeCL_3 \cdot 6H_2O$	3.150	
$CuSO_4 \cdot 5H_2O$	0.001	
$ZnSO_4 \cdot 7H_2O$	0.010	
$COCl_2 \cdot 6H_2O$	0.022	
$MnCl_2 \cdot 4H_2O$	0.010	
$Na_2MoO_4 \cdot 2H_2O$	0.006	
H_3BO_3	1.000	

2.3. Photobioreactor Setup and Cultivation Conditions

Algae were cultivated in laboratory-scale glass photobioreactors with a working volume of 900 mL (1000 mL of the total volume). Each reactor was equipped with an aeration system supplying air enriched with 10 vol.% CO_2 to support algal growth and simulate intensified carbon capture conditions. The photobioreactor consisted of a glass cylinder with a height of 190 mm and a diameter of 90 mm. Daily mechanical mixing was applied to prevent sedimentation of biomass and to improve mass transfer of CO_2 and nutrients. The aeration flow rate (20 $L \cdot min^{-1}$) was kept constant throughout the experiment and maintained using a low-flow rotameter.

https://doi.org/10.3390/en19061572

The photobioreactors were placed inside six isolated chambers designed to minimise spectral cross-illumination between different light sources. A photograph of the cultivation system and lighting arrangement is shown in Figure 1a, while a representative photobioreactor during operation is presented in Figure 1b.

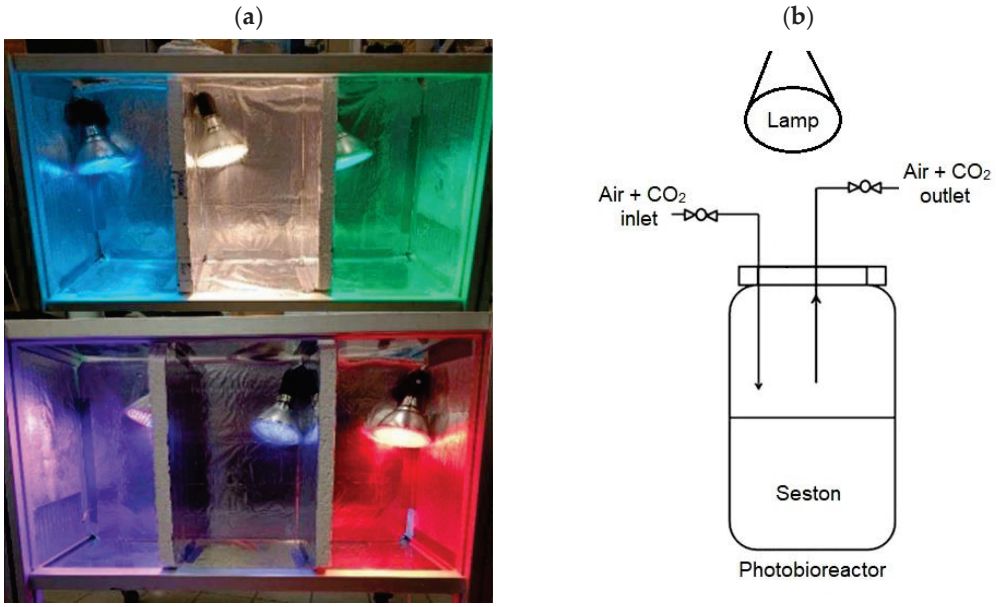


Figure 1. (**a**) Experimental test rig comprising six isolated illumination chambers for photobioreactor cultivation under different light colours: Blue, white, green, UV, plant and red (from left to right). (**b**) Photobioreactor during cultivation under white illumination (representative diagram).

Cultivation was conducted under the following controlled conditions:

- Temperature: maintained within the range of 20–30 °C
- Photoperiod: 16 h light/8 h dark
- Cultivation duration: 14 days per cycle

Each cultivation cycle was terminated after 14 days, as preliminary observations showed a significant reduction in biomass growth beyond this period. This approach also reflects practical constraints relevant to semi-continuous algal production systems, where periodic harvesting and medium reuse may enhance overall productivity.

The experimental system consisted of six identical laboratory-scale photobioreactors operating in parallel. Each reactor had the same geometry, working volume, aeration rate, and mixing conditions. The reactors were operated under controlled laboratory conditions to minimise variability between cultivation units. The only intentionally varied parameter was the illumination spectrum applied to each reactor, allowing evaluation of the influence of light wavelength on microalgal growth and biomass properties.

To ensure experimental consistency, all reactors were inoculated with the same initial biomass concentration and cultivated using the same culture medium composition. Temperature, aeration rate, and photoperiod were maintained constant throughout the experiments.

The experiments were performed in several independent cultivation cycles, allowing replication of the measurements. For each illumination condition, the obtained values were analysed using the specific growth rate (μ), calculated by linear regression of $\ln(X)$ versus cultivation time for each illumination condition and cultivation cycle.

This approach enabled evaluation of variability between independent cultivation runs and improved the reliability of the obtained results. All cultivation experiments were

https://doi.org/10.3390/en19061572

conducted independently under each illumination condition, and the resulting growth parameters were used for subsequent statistical analysis of the illumination effects.

2.4. Illumination Conditions and Light Sources

Six different illumination colours were investigated to evaluate their effect on algal growth and energy properties: Plant-specific light (combined red and blue spectrum), white, green, red, blue and Ultraviolet [3]. All light sources were 15 W lamps positioned at a fixed distance from the photobioreactors, as shown in Figure 1a. The nominal wavelength ranges and luminous flux values provided by the lamps' datasheets are summarised in Table 1.

The plant-specific lamp consisted of 126 surface-mounted diodes (SMDs), including 90 red and 36 blue LEDs, designed to support photosynthetic activity in higher plants. The white lamp had a correlated colour temperature of 2700 K, corresponding broadly to solar illumination.

It should be noted that illumination was characterised based on wavelength range and electrical power rather than photon flux density (μmol photons·m^{-2}·s^{-1}). While photon-based metrics are more directly relevant to photosynthesis, maintaining identical lamp power and reactor geometry allowed for a controlled comparative assessment of spectral effects. This limitation is acknowledged and considered in the interpretation of results.

2.5. Biomass Growth Measurement

Algal growth was monitored by periodic determination of dry biomass content. Every 3–5 days, approximately 5 mL of culture suspension was extracted from each reactor. The samples were placed in laboratory dishes and dried using an electric dryer until a constant mass was achieved. Representative samples during the drying process are shown in Figure 2.

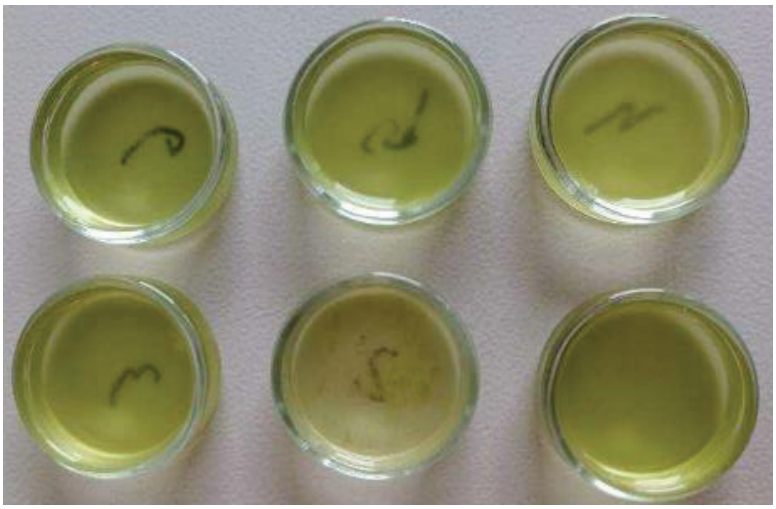


Figure 2. Laboratory dishes are used for drying culture samples to determine dry biomass during cultivation.

The mass of dry biomass obtained per litre of culture suspension was used to quantify growth dynamics and calculate percentage increases relative to the initial biomass concentration. Four independent cultivation cycles were conducted under identical conditions to account for biological variability. Final growth values were obtained by averaging results across these cycles.

https://doi.org/10.3390/en19061572

2.6. Biomass Drying and Sample Preparation

Following completion of each cultivation cycle, the algal biomass was separated from the culture medium and dried at 90 °C for six hours. To enhance evaporation efficiency and ensure uniform drying, the biomass suspension was distributed over a large surface area before drying. The dried biomass was subsequently homogenised and stored in airtight containers until further analysis.

2.7. Determination of Higher Heating Value

The higher heating value (HHV) of the algal biomass was determined using a bomb calorimeter in accordance with Polish Standard PN-C-04375-3:2013 [54,55]. The tests were conducted using a KL 14 calorimeter manufactured by Precyzja Bit, Bydgoszcz, Poland. The measurement method fully complies with the requirements of the relevant standard [54]. The measurement procedure involves the complete combustion of a fuel sample in an oxygen atmosphere under pressure in a calorimetric bomb immersed in water, followed by measurement of the resulting temperature increase of the water. The heat of combustion of the fuel is calculated automatically and displayed on the computer screen. The accuracy of the temperature increase measurement is approximately 0.001 °C.

For each measurement, approximately 1 g of dried biomass was pressed into a pellet and fitted with an ignition wire. Biomass obtained from individual cultivation cycles under identical illumination conditions was thoroughly homogenised prior to palletisation and HHV determination to minimise batch-to-batch variability. A representative biomass pellet before and after preparation is shown in Figure 3.



Figure 3. Biomass sample preparation for bomb calorimetry: dried algal biomass (**left**); and pressed pellet with ignition wire (**right**).

The calorimetric bomb was charged with oxygen, sealed, and placed in the calorimetric vessel. The heat of combustion was calculated analytically based on temperature rise and calibration constants of the calorimeter. For each lighting condition, multiple measurements were conducted and averaged to ensure reliability.

2.8. Proximate (Technical) Analysis

Proximate analysis of algal biomass included determination of analytical moisture content (W_a), ash content [8], volatile matter (VM), and fixed carbon (FC). Analyses were performed according to relevant Polish standards [56,57]. The measurements were carried out using the mass difference method after thermal treatment of the samples under controlled conditions. The prepared samples are presented in Figure 4.

https://doi.org/10.3390/en19061572

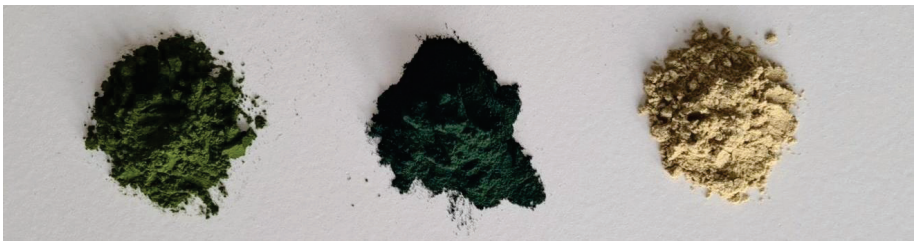


Figure 4. Algal biomass used for comparative analysis (**left** to **right**): *Chlorella pyrenoidosa*, *Spirulina*, and bladderwrack (*Fucus vesiculosus*).

Analytical moisture was determined by drying approximately 1 g of biomass at 105–110 °C for 90 min, followed by cooling in a desiccator and repeated weighing until mass stabilisation. The moisture content was calculated using the following Equation (1):

$$W_a = \frac{m_0 - m_1}{m_0} \cdot 100\% \quad (1)$$

where m_0 and m_1 are the initial mass of the sample before drying (g) and the mass of the sample after drying, respectively.

Ash content A_a was measured by heating samples to 500 °C and subsequently to 815 ± 10 °C under controlled conditions, with a final holding time of 90 min. The ash content was calculated as (2):

$$A_a = \frac{m_2}{m_0} \cdot 100\% \quad (2)$$

where m_2 is the mass of ash remaining after combustion (g).

Volatile matter (VM) was determined by heating samples in covered crucibles at 850 °C without air access for 3 min according to Equation (3):

$$VM = \frac{m_2 - m_3}{m_0} \cdot 100\% \quad (3)$$

where m_3 is the mass of the sample after volatile matter determination (g).

Fixed carbon (FC) was calculated indirectly using Equation (4):

$$FC = 100\% - (W_a + A_a + VM) \quad (4)$$

To contextualise the energetic performance of *Chlorella vulgaris*, proximate analysis was also conducted for *Chlorella pyrenoidosa*, *Spirulina*, and *Fucus vesiculosus*.

2.9. Data Processing and Averaging

Due to the biological nature of algal cultivation, variability between individual cultivation cycles was expected. To mitigate this effect, all reported growth and energetic values represent averages obtained from four independent cultivation cycles. This approach allows for a more robust comparison of illumination conditions while maintaining experimental feasibility at the laboratory scale.

2.10. Specific Growth Rate Analysis

The specific growth rate (μ) was determined using exponential biomass growth during the cultivation period. Under exponential growth conditions, biomass concentration can be described as [58]:

$$X(t) = X_0 e^{\mu t} \quad (5)$$

https://doi.org/10.3390/en19061572

where $X(t)$ is the biomass concentration at time (t), X_0 is the initial biomass concentration, and μ is the specific growth rate.

Taking the natural logarithm of Equation (5) gives:

$$\ln X(t) = lnX_0 + \mu t \quad (6)$$

This transformation produces a linear relationship between $\ln(X)$ and time, where the slope corresponds to the specific growth rate μ.

In this study, μ was determined using linear regression of $\ln(X)$ versus cultivation time based on all available experimental data points within each cultivation cycle. The slope of the regression line obtained using the least-squares method was taken as μ (day^{-1}), while the coefficient of determination (R^2) was used to evaluate the goodness of fit and verify the validity of the exponential growth assumption. The use of linear regression instead of a two-point estimation method reduces the influence of individual measurement errors, avoids subjective selection of exponential growth phase boundaries, and ensures reproducibility of the analysis.

To assess whether illumination colour had a statistically significant effect on the specific growth rate, a one-way analysis of variance (ANOVA) was performed using the calculated μ values obtained from the independent cultivation experiments conducted under different illumination colours.

3. Results and Discussion

3.1. Growth Response of Chlorella vulgaris to Illumination Colour

Figures 5–7 summarise the growth dynamics of *Chlorella vulgaris* over the 14-day cultivation period for four independent cultivation cycles and six illumination colours. Across all cycles, biomass increased rapidly during the initial cultivation phase, with the most pronounced growth typically observed within the first 3–5 days. This behaviour is characteristic of microalgal cultures under nutrient-replete conditions, where early exponential growth is followed by a gradual reduction as light availability, self-shading, or nutrient limitations begin to constrain further biomass accumulation.

Figure 5 presents the temporal biomass growth profiles for each cultivation cycle, while Figure 6 shows the corresponding culture volume increase. When illumination colours are compared over the full cultivation period, white light consistently produced the highest final biomass concentration, whereas UV illumination resulted in the lowest biomass yield across all cycles (Figures 5–7). The averaged final biomass concentrations, calculated from four independent cultivation cycles and reported in Table 3, confirm this trend, with white light yielding 0.71 $g{\cdot}L^{-1}$ and UV yielding only 0.51 $g{\cdot}L^{-1}$.

Table 3. Averaged dry biomass concentration of *Chlorella vulgaris* obtained under different illumination colours (mean values across four cultivation cycles) as well as Higher heating value (HHV) under different illumination colours (averaged values).

Colour	Amount [$g{\cdot}L^{-1}$]	Heating Value [MJ/kg]
Plant	0.64	12.94
White	0.71	15.08
Green	0.61	13.83
Red	0.62	14.21
Blue	0.59	13.41
UV	0.51	11.49

Note: Values represent mean concentrations averaged over four cultivation cycles.

https://doi.org/10.3390/en19061572

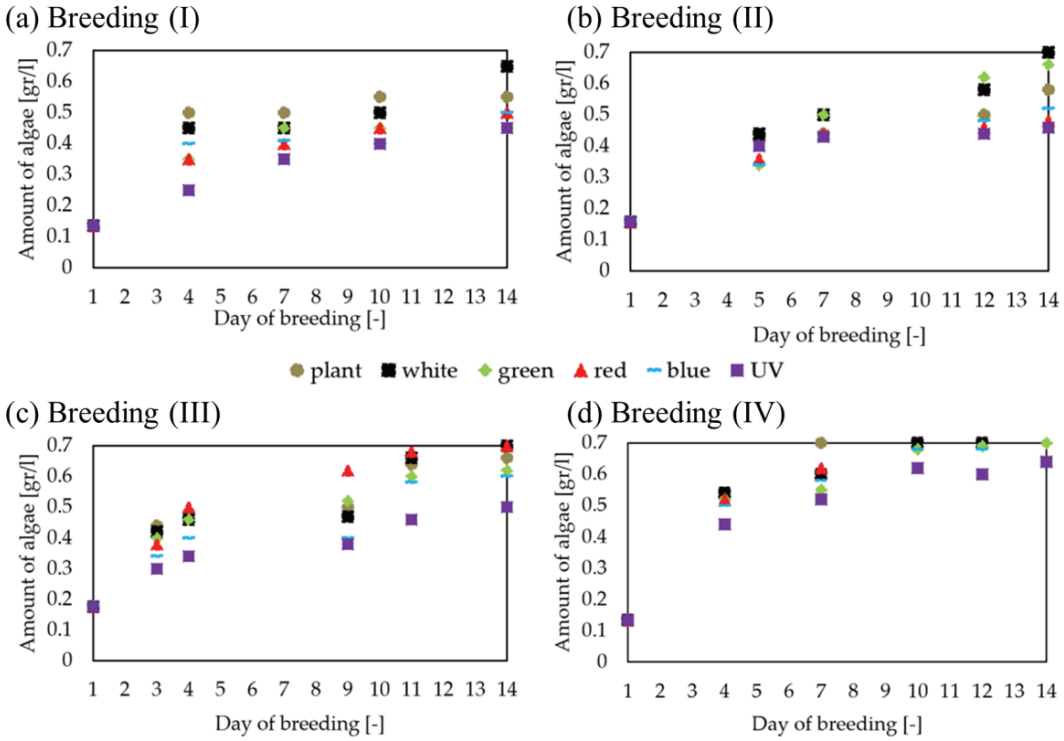


Figure 5. Biomass growth characteristics of *Chlorella vulgaris* across four cultivation cycles under six illumination colours: (**a**) breeding I; (**b**) breeding II; (**c**) breeding III; (**d**) breeding IV.

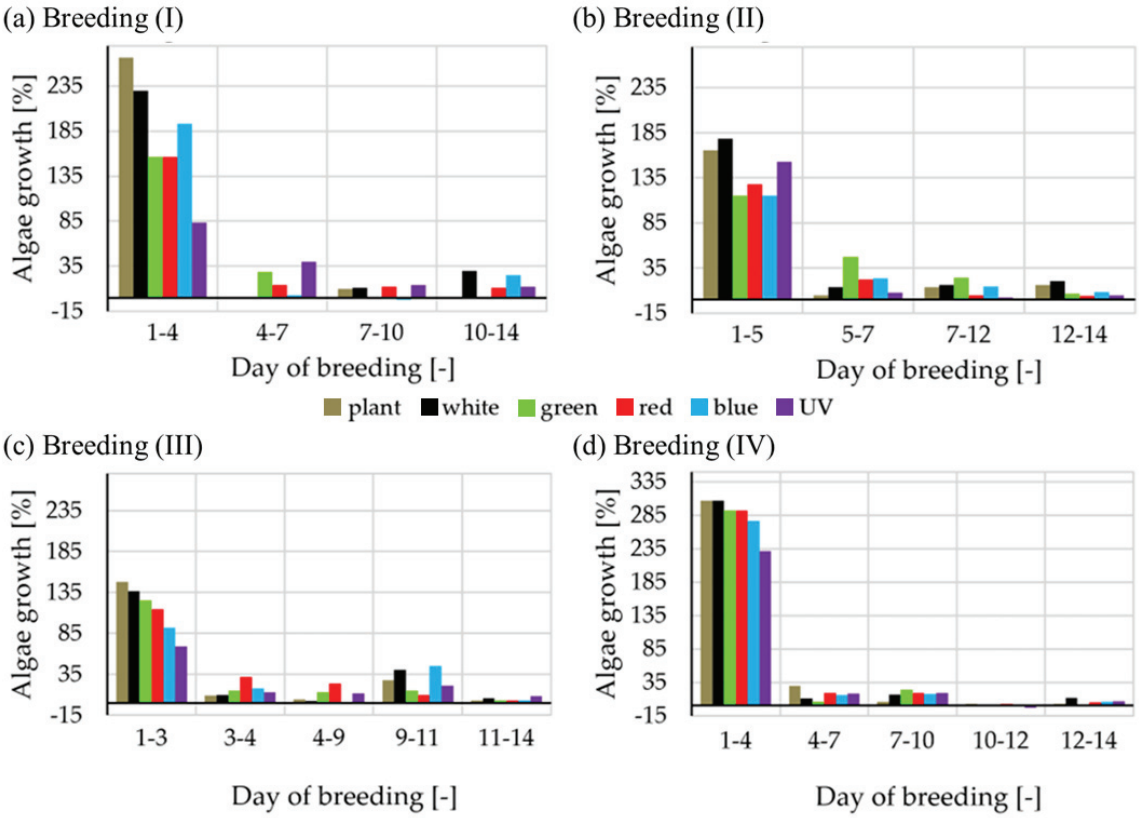


Figure 6. Culture volume increase characteristics across four cultivation cycles under six illumination colours: (**a**) breeding I; (**b**) breeding II; (**c**) breeding III; (**d**) breeding IV.

https://doi.org/10.3390/en19061572

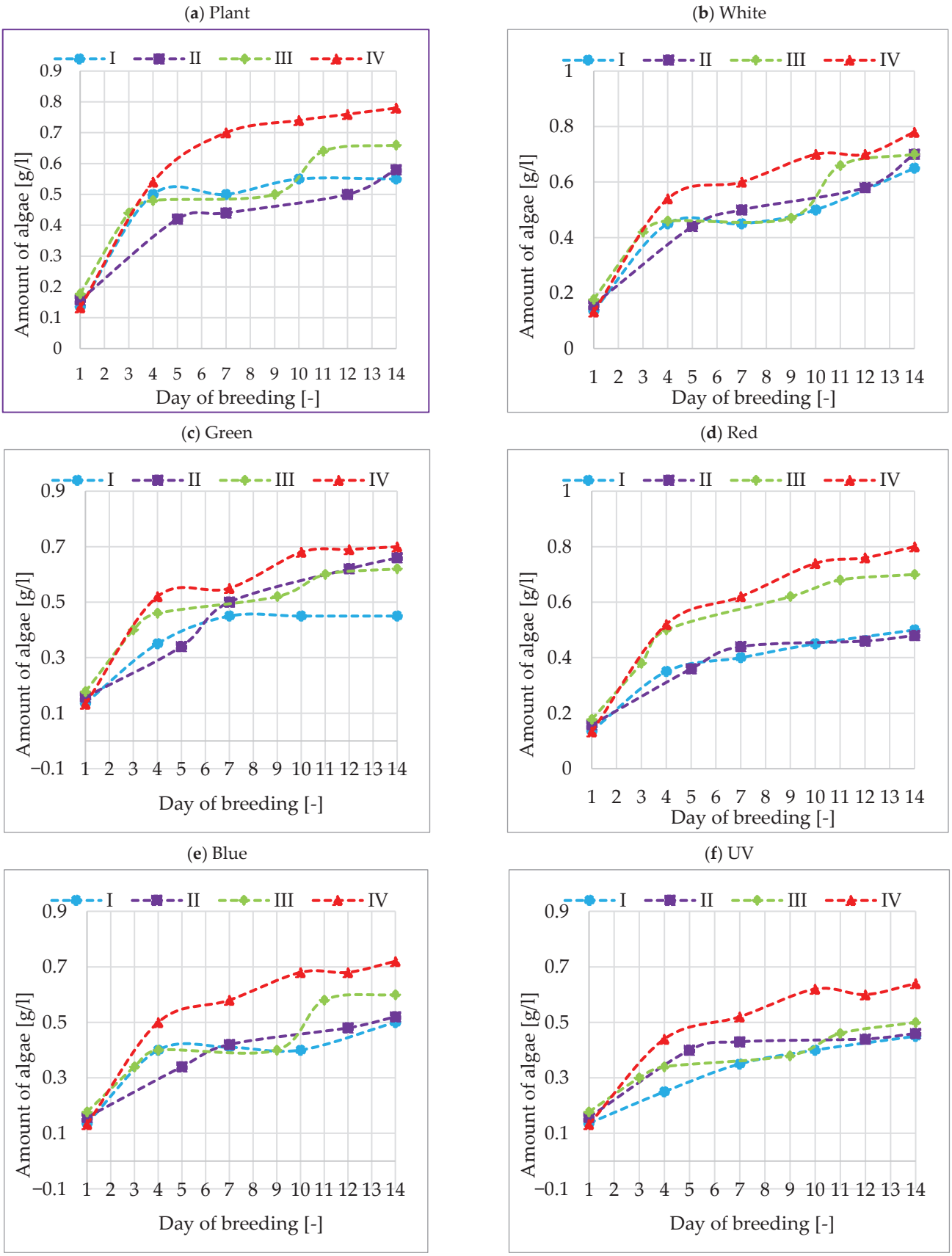


Figure 7. Biomass growth characteristics of *Chlorella vulgaris* grouped by illumination colour across four independent cultivation cycles: (**a**) plant-specific; (**b**) white; (**c**) green; (**d**) red; (**e**) blue; (**f**) ultraviolet [3]. In each panel, the four curves represent replicate cultivation cycles (breeding I–IV) conducted under identical operating conditions (temperature, CO_2 concentration, photoperiod, mixing, and culture medium).

https://doi.org/10.3390/en19061572

Although the relative ranking of intermediate colours (plant-specific, green, red, and blue) varied modestly between cultivation cycles, the white-light condition exhibited the greatest stability, indicating reduced sensitivity to inter-cycle biological variability (see Figure 7). In two cycles (breeding III and IV), red illumination produced final biomass levels comparable to white light, suggesting that under favourable conditions, red wavelengths can also support strong *Chlorella vulgaris* productivity.

The consistently poor performance observed under UV illumination is consistent with the known disruptive effects of UV radiation on photosynthetic organisms, including damage to cellular components and impairment of photosynthetic efficiency, ultimately suppressing growth [59]. In contrast, visible-spectrum illumination supports photosynthesis through absorption by chlorophylls and accessory pigments, and the observed differences between visible colours likely reflect both spectral matching to pigment absorption bands and physiological acclimation under each illumination regime [60].

It should be noted that illumination was controlled by lamp power and reactor geometry, and lamp specifications were characterised using nominal wavelength ranges and luminous flux rather than photon flux density. Consequently, the observed differences are interpreted as comparative spectral effects within the constraints of the adopted characterisation approach, rather than absolute wavelength-specific quantum efficiency.

Despite maintaining constant culture parameters (temperature, pH, light intensity, mixing, and substrate composition), differences in biomass growth were observed between individual cultivation cycles. The most probable cause of this variability is biological heterogeneity of the inoculum, including differences in the physiological state of cells at the time of inoculation. As culture density increased, self-shading effects may have contributed to a gradual reduction in effective light availability; however, this was mitigated through regular mixing of the cultures. Final biomass accumulation may have also been influenced by the extent of nutrient depletion, particularly nitrogen and phosphorus, as well as minor variations in hydrodynamic conditions and CO_2 mass transfer. These observations confirm that even under controlled laboratory conditions, microalgal growth exhibits inherent biological variability, thereby justifying the use of repeated cultivation cycles.

Based on averaged final biomass concentrations, the illumination performance can be ranked as: white, red, plant-specific, green, blue and ultraviolet, respectively.

The specific growth rate (μ) of *Chlorella vulgaris* was determined as described in Section 2.10. The obtained regression coefficients and coefficients of determination (R^2) are presented in Table 4.

Table 4. Specific growth rate (μ) of *Chlorella vulgaris* determined by linear regression of ln(X) versus cultivation time under different illumination spectra.

			Colour					
		Parameter	**Plant**	**White**	**Green**	**Red**	**Blue**	**UV**
Cultivation	1	R^2	0.800	0.808	0.600	0.997	0.593	0.929
		μ (day^{-1})	0.0127	0.0403	0.0251	0.0396	0.0215	0.0632
	2	R^2	0.943	0.954	0.870	0.767	0.920	0.869
		μ (day^{-1})	0.0334	0.0464	0.0665	0.0265	0.0424	0.0130
	3	R^2	0.868	0.834	0.933	0.859	0.816	0.950
		μ (day^{-1})	0.0361	0.0453	0.0380	0.0508	0.0488	0.0440
	4	R^2	0.820	0.968	0.898	0.952	0.938	0.893
		μ (day^{-1})	0.0340	0.0359	0.0337	0.0436	0.0365	0.0369

https://doi.org/10.3390/en19061572

The calculated μ values varied between 0.0127 and 0.0665 day^{-1} depending on the illumination spectrum and cultivation cycle. In most cases, the coefficient of determination exceeded $R^2 > 0.80$, indicating a good agreement between the experimental data and the exponential growth model. Lower R^2 values were observed for several treatments in the first cultivation cycle, particularly under green and blue light, suggesting a less pronounced exponential growth phase.

Across all cultivation cycles, relatively higher μ values were generally observed under white, red, and green illumination, while lower values were obtained under the plant spectrum. The UV treatment showed higher variability between cultivation cycles, with μ values ranging from 0.013 to 0.0632 day^{-1}. These results indicate that while the illumination spectrum influences the observed growth dynamics, the overall exponential growth behaviour of the culture is reasonably well described by the applied regression model.

The specific growth rates (μ) calculated for the different illumination conditions were compared using one-way ANOVA. Although variations in μ values were observed between the tested light spectra, the statistical analysis indicated that these differences were not significant ($F = 0.47$, $p = 0.796$). This suggests that, under the investigated experimental conditions, illumination colour did not significantly influence the intrinsic growth kinetics of *Chlorella vulgaris*. Nevertheless, differences in final biomass concentration were still observed between treatments. These results suggest that illumination conditions may primarily affect metabolic pathways and biomass composition rather than the intrinsic growth kinetics of the microalgal cells [61].

3.2. Higher Heating Value as a Function of Illumination Colour

The higher heating values (HHV) of *Chlorella vulgaris* biomass cultivated under each illumination colour are summarised in Table 5. The results demonstrate that illumination colour influenced not only biomass growth but also the energetic quality of the produced biomass. The highest HHV was obtained under white light (15.08 MJ·kg^{-1}), followed by red (14.21 MJ·kg^{-1}) and green illumination (13.83 MJ·kg^{-1}). In contrast, UV illumination resulted in the lowest HHV (11.49 MJ·kg^{-1}).

Table 5. Higher heating values (HHV) of different algal species were used for comparative analysis.

Algae Type	Heating Value [MJ/kg]
Chlorella pyrenoidosa	23.31
Spirulina	21.25
Bladderwrack	12.66
Chlorella vulgaris	15.08

The reduced HHV associated with UV-grown biomass aligns with the suppression of growth and likely reflects stress-induced changes in cellular composition and/or increased degradation of energy-rich biochemical fractions under UV exposure [60,62]. Conversely, the higher HHV obtained under white light suggests that broader-spectrum illumination promoted biomass with more favourable fuel characteristics. Although ultimate (CHNS/O) analysis and detailed biochemical fractionation were not performed in this study, previous research has shown that cultivation conditions can significantly influence lipid, protein, and carbohydrate allocation in microalgae, thereby affecting calorific value [63,64].

An unexpected but informative observation was the relatively low HHV obtained under the plant-specific lamp (12.94 MJ·kg^{-1}), despite its design to enhance photosynthetic growth in higher plants. This may indicate that illumination spectra optimised for terrestrial plant development do not necessarily maximise microalgal fuel quality under the present

https://doi.org/10.3390/en19061572

reactor configuration, and that enhanced growth does not directly translate into higher energy content when compositional shifts occur. The observed differences in HHV are consistent with the proximate analysis results, where higher volatile matter and lower ash and moisture contents are associated with higher calorific values, explaining the superior energetic performance under white illumination. Although detailed biochemical fractionation was not performed, the proximate analysis provides indirect evidence that the higher HHV observed under white illumination is associated with increased volatile matter and reduced ash and moisture contents.

3.3. Volumetric Energy Yield and Implications for Bioenergy Systems

To interpret the results from a bioenergy systems perspective, HHVs were combined with biomass yield to calculate recoverable energy per unit culture volume, as shown in Figure 8. This volumetric energy metric integrates productivity and fuel quality and is directly relevant to photobioreactor sizing, cultivation strategy selection, and downstream energy conversion processes. Unlike most previous studies that report calorific value on a mass basis alone, this work evaluates volumetric energy yield, which integrates biomass productivity and fuel quality and is directly relevant to photobioreactor and process design.

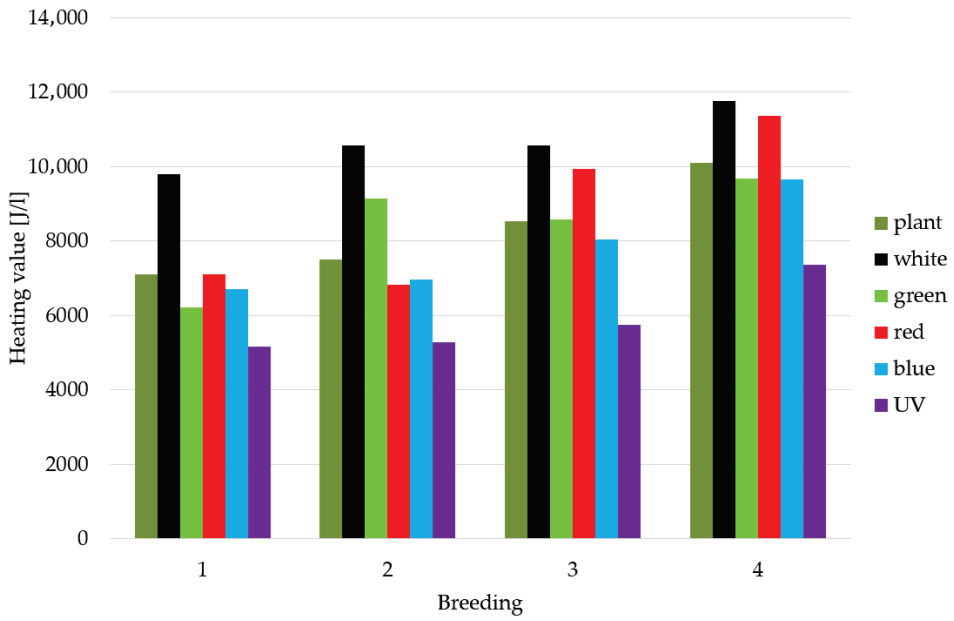


Figure 8. Summary of growth and energy results for *Chlorella vulgaris* cultivated under different illumination colours, including energy yield normalised per culture volume.

The analysis confirms that white illumination delivers the highest volumetric energy yield, combining both high biomass productivity and the highest HHV. In contrast, UV illumination produces the lowest energy per litre of culture, reflecting simultaneous reductions in growth and energetic quality. Notably, blue illumination, despite yielding lower biomass concentrations than most other visible colours, produced a volumetric energy yield comparable to several alternatives. This indicates that illumination colour influences biomass composition, as inferred from proximate analysis and HHV trends, and that biomass yield alone is insufficient to predict recoverable energy. These results highlight the importance of reporting both mass-based and volumetric energy metrics when evaluating algal cultivation strategies for energy applications, particularly in systems where reactor volume and cultivation time represent key constraints.

https://doi.org/10.3390/en19061572

3.4. Cross-Species Comparison of Energetic and Proximate Properties

To place the performance of cultivated *Chlorella vulgaris* within a broader biomass context, a comparative analysis of energetic and proximate (technical) properties was conducted for *Chlorella pyrenoidosa*, *Spirulina*, and *Fucus vesiculosus* (bladderwrack). It should be noted that the comparative species were not cultivated under identical conditions; therefore, this analysis is intended to contextualise energetic potential rather than provide a direct productivity comparison. The HHVs for these species are presented in Table 5, while the corresponding proximate analysis results are summarised in Table 6.

Table 6. Proximate analysis results of selected algal species, including analytical moisture (W_a), ash content (A_a), fixed carbon (FC), and volatile matter (VM).

Algae Type	Analytical Moisture, W_a [%]	Ash Content, A_a [%]	Fixed Carbon, *FC* [%]	Volatile Matter, *VM* [%]
Chlorella pyrenoidosa	4.09	4.37	14.94	76.61
Spirulina	6.28	7.47	13.55	72.70
Bladderwrack	10.48	17.86	9.03	62.63
Chlorella vulgaris	7.36	14.92	7.81	69.91

Among the assessed species, *Chlorella pyrenoidosa* exhibited the most favourable fuel properties, with the highest HHV (23.31 MJ·kg^{-1}), the lowest analytical moisture content (4.09%), the lowest ash content (4.37%), and the highest volatile matter fraction (76.61%). These characteristics are advantageous for thermochemical energy conversion, as high volatile matter content enhances ignition and combustion behaviour, while low moisture and ash contents reduce energy losses and mitigate ash-related operational challenges.

Spirulina also demonstrated a high HHV (21.25 MJ·kg^{-1}) but exhibited higher moisture and ash contents than *Chlorella pyrenoidosa*, which may partially offset its energetic advantage during conversion. In contrast, bladderwrack displayed the least favourable energy characteristics, with the lowest HHV (12.66 MJ·kg^{-1}), the highest moisture content, and the highest ash content, all of which are detrimental to efficient combustion-based energy recovery.

The proximate analysis results provide a mechanistic explanation for the observed HHV trends. Species with higher volatile matter fractions and lower ash contents exhibited higher calorific values, while increased moisture and ash contents were associated with reduced energetic performance. Fixed carbon values further support this interpretation, as higher fractions of slowly reacting carbonaceous material can prolong combustion but do not necessarily compensate for reduced volatile release in terms of overall energy efficiency.

While *Chlorella pyrenoidosa* appears superior from a fuel-quality perspective, *Chlorella vulgaris* remains attractive for large-scale cultivation due to its wider tolerance window and rapid growth, which may compensate for lower HHV in high-throughput production systems. Consequently, the selection of algal species and illumination strategy should be guided by the intended system objective: maximising fuel quality per unit mass or maximising recoverable energy per unit reactor volume under realistic operational constraints.

The calorific value and proximate composition of the biomass obtained in this study indicate that *Chlorella vulgaris* biomass may represent a promising feedstock for thermochemical bioenergy conversion technologies such as pyrolysis, gasification, or hydrothermal processing. The observed differences in biomass characteristics under different illumination conditions suggest that light spectrum may influence not only biomass growth but also its energetic properties.

https://doi.org/10.3390/en19061572

It should also be acknowledged that the comparative species analysed in this work were not cultivated under identical experimental conditions. Therefore, the comparison is intended to provide contextual insight into the energetic potential of the biomass rather than a direct productivity benchmark between species. Furthermore, illumination conditions may influence the biochemical composition of microalgal biomass, including lipid and protein fractions that are relevant for biofuel production pathways such as biodiesel or biohydrogen generation. Although the present study focused primarily on biomass productivity and energy content, future investigations should include detailed biochemical characterisation in order to better understand the relationship between illumination spectrum, cellular composition, and the resulting bioenergy conversion potential.

4. Conclusions

This study investigated the influence of illumination colour on the growth behaviour and energetic properties of *Chlorella vulgaris* cultivated in laboratory-scale photobioreactors, with the aim of linking cultivation conditions not only to biomass productivity but also to fuel-relevant energy characteristics. In addition, a comparative energetic and proximate analysis was conducted to contextualise the performance of *Chlorella vulgaris* against other algal species commonly discussed in bioenergy applications.

The results demonstrate that illumination colour significantly affects both biomass yield and energetic quality. Among the tested conditions, white illumination consistently produced the highest biomass concentration and the highest higher heating value, resulting in the greatest recoverable energy per unit culture volume. In contrast, ultraviolet illumination led to the poorest performance, characterised by suppressed growth and reduced calorific value, confirming its unsuitability for productive algal cultivation under the investigated conditions. Red and green illumination supported intermediate performance, while blue light, despite lower biomass yield, delivered a volumetric energy output comparable to several other visible-light conditions, highlighting that growth alone is insufficient to predict energy recovery potential.

By explicitly relating biomass productivity to calorific value, this work shows that volumetric energy yield is a critical metric for assessing algal cultivation strategies from an energy systems perspective. This integrated metric captures trade-offs between growth rate and fuel quality and is particularly relevant for photobioreactor-based systems where reactor volume and cultivation time are key design constraints.

The cross-species comparison further illustrates the importance of biomass composition in determining energy performance. *Chlorella pyrenoidosa* exhibited the most favourable fuel characteristics, with high calorific value, low moisture and ash contents, and high volatile matter fraction, making it well suited for thermochemical energy conversion. However, despite its lower HHV, *Chlorella vulgaris* remains attractive for large-scale applications due to its rapid growth, broader tolerance to cultivation conditions, and operational robustness, which may compensate for lower energy density in high-throughput production systems. These findings emphasise that species selection should be guided by system objectives, balancing fuel quality against cultivation feasibility and productivity.

The results obtained in this study indicate that illumination conditions can influence biomass growth and energetic properties, which is relevant for the optimisation of microalgal biomass production for bioenergy applications.

It should be noted that illumination conditions in this study were characterised based on nominal wavelength ranges and electrical power rather than photon flux density. While this approach enables controlled comparative assessment of spectral effects, future work would benefit from photon-based characterisation and from incorporating ultimate

https://doi.org/10.3390/en19061572

(CHNS/O) analysis or detailed biochemical fractionation to further elucidate the mechanisms underlying the observed differences in calorific value. Future research should focus on extended cultivation experiments, a broader characterisation of biochemical composition, and optimisation of illumination parameters such as light intensity, photoperiod, and spectral distribution. Further studies may also investigate the applicability of optimised illumination strategies in larger-scale photobioreactors and evaluate their potential for improving biomass productivity and energy-related properties of microalgae.

Overall, this study provides experimental evidence that illumination wavelength influences not only algal growth but also biomass energetic properties and volumetric energy yield. By linking cultivation strategy to fuel-relevant metrics, the results contribute to the optimisation of algal bioenergy systems and support more informed design decisions for photobioreactor-based biomass production targeting thermochemical energy conversion. The main merit of this work lies in the comparative experimental evaluation of several illumination spectra and their influence on the cultivation performance of *Chlorella vulgaris*. The results contribute to a better understanding of how light conditions may affect biomass productivity and the potential energetic properties of microalgal biomass.

Author Contributions: Conceptualization, P.C., P.M. and M.A.; Data curation, P.C. and P.M.; Formal analysis, M.A., P.C. and P.M.; Funding acquisition, M.A. and A.V.-M.; Investigation, P.C., P.M., M.M., J.J., A.M.S.H.A.-M. and M.A.; Methodology, P.C., P.M., M.A. and A.M.S.H.A.-M.; Project administration, P.C. and M.A.; Resources, P.C., A.V.-M. and M.A.; Software, J.J. and H.S.; Supervision, P.C., M.A. and A.V.-M.; Validation, P.C., M.M., J.J. and H.S.; Visualization, M.A., M.M., A.M.S.H.A.-M., A.V.-M. and P.C.; Writing—original draft; P.C., P.M., M.M., J.J., A.M.S.H.A.-M. and M.A.; Writing—review & editing, M.A. All authors have read and agreed to the published version of the manuscript.

Funding: This research received no external funding.

Data Availability Statement: The data presented in this study are contained within the article.

Acknowledgments: Cardiff University authors gratefully acknowledge the support from the EPSRC through the projects Ocean-REFuel—Ocean Renewable Energy Fuels (EP/W005018/1) and Storage of Ammonia For Energy (SAFE)—AGT Pilot (EP/T009314/1). The author (A.M.) gratefully acknowledges the support provided by the Qatar National Research Fund under the doctoral project (GSRA5-1-0404-18034).

Conflicts of Interest: The authors declare no conflicts of interest.

Abbreviations

Aa	Ash content (%, analytical basis)
CO_2	Carbon dioxide
FC	Fixed carbon (%)
HHV	Higher heating value ($MJ \cdot kg^{-1}$)
LED	Light-emitting diode
SMD	Surface-mounted diode
UV	Ultraviolet
VM	Volatile matter (%)
Wa	Analytical moisture content (%)
WC medium	Woods Hole Chu culture medium

References

1. Al-Moftah, A.M.S.; Alnajideen, M.; Alafifi, F.; Czyzewski, P.; Shi, H.; Alherbawi, M.; Navaratne, R.; Valera-Medina, A. Economic feasibility of using municipal solid waste and date palm waste for clean energy production in Qatar. *Energies* **2025**, *18*, 988. [CrossRef]

2. Zhang, S.; Zhang, L.; Xu, G.; Li, F.; Li, X. A review on biodiesel production from microalgae: Influencing parameters and recent advanced technologies. *Front. Microbiol.* **2022**, *13*, 970028. [CrossRef] [PubMed]
3. Behera, S.; Singh, R.; Arora, R.; Sharma, N.K.; Shukla, M.; Kumar, S. Scope of algae as third generation biofuels. *Front. Bioeng. Biotechnol.* **2015**, *2*, 90. [CrossRef]
4. Singh, J.; Gu, S. Commercialization potential of microalgae for biofuels production. *Renew. Sustain. Energy Rev.* **2010**, *14*, 2596–2610. [CrossRef]
5. Radican, E.; Luo, Y.; Xiao, Z. Microalgae Applications in the Agricultural and Food Sector: Towards a Sustainable Future. *Molecules* **2026**, *31*, 457. [CrossRef]
6. Alazaiza, M.Y.; Albahnasawi, A.; Al Maskari, T.; Abujazar, M.S.S.; Bashir, M.J.; Nassani, D.E.; Abu Amr, S.S. Biofuel production using cultivated algae: Technologies, economics, and its environmental impacts. *Energies* **2023**, *16*, 1316. [CrossRef]
7. Li, G.; Yao, J. A review of algae-based carbon capture, utilization, and storage (Algae-Based CCUS). *Gases* **2024**, *4*, 468–503. [CrossRef]
8. Deshmukh, M.; Kothawade, T.R.; Pathan, A.; Behera, U.S.; Sangwai, J.S.; Byun, H.-S. A Review on Sustainable Microalgae-Based Approaches for CO_2 Capture, Bioenergy, and Value-Added Products. *Korean J. Chem. Eng.* **2026**, 1–38. [CrossRef]
9. Xu, W.; Ding, K.; Hu, L. A mini review on pyrolysis of natural algae for bio-fuel and chemicals. *Processes* **2021**, *9*, 2042. [CrossRef]
10. Osman, A.I.; Lai, Z.Y.; Farghali, M.; Yiin, C.L.; Elgarahy, A.M.; Hammad, A.; Ihara, I.; Al-Fatesh, A.S.; Rooney, D.W.; Yap, P.-S. Optimizing biomass pathways to bioenergy and biochar application in electricity generation, biodiesel production, and biohydrogen production. *Environ. Chem. Lett.* **2023**, *21*, 2639–2705. [CrossRef]
11. Bora, A.; Thondi Rajan, A.S.; Ponnuchamy, K.; Muthusamy, G.; Alagarsamy, A. Microalgae to bioenergy production: Recent advances, influencing parameters, utilization of wastewater—A critical review. *Sci. Total Environ.* **2024**, *946*, 174230. [CrossRef]
12. Raheem, A.; Wan Azlina, W.A.K.G.; Taufiq Yap, Y.H.; Danquah, M.K.; Harun, R. Thermochemical conversion of microalgal biomass for biofuel production. *Renew. Sustain. Energy Rev.* **2015**, *49*, 990–999. [CrossRef]
13. Parakh, S.K.; Tian, Z.; Wong, J.Z.E.; Tong, Y.W. From Microalgae to Bioenergy: Recent Advances in Biochemical Conversion Processes. *Fermentation* **2023**, *9*, 529. [CrossRef]
14. Hidalgo, D.; Urueña, A.; Martín-Marroquín, J.M.; Díez, D. Integrated Approach for Biomass Conversion Using Thermochemical Routes with Anaerobic Digestion and Syngas Fermentation. *Sustainability* **2025**, *17*, 3615. [CrossRef]
15. Hasan, M.; Mofijur, M.; Uddin, M.; Kabir, Z.; Badruddin, I.A.; Khan, T.Y. Insights into anaerobic digestion of microalgal biomass for enhanced energy recovery. *Front. Energy Res.* **2024**, *12*, 1355686. [CrossRef]
16. Esteves, B.; Sen, U.; Pereira, H. Influence of chemical composition on heating value of biomass: A review and bibliometric analysis. *Energies* **2023**, *16*, 4226. [CrossRef]
17. Wang, Y.; Wu, J.J. Thermochemical conversion of biomass: Potential future prospects. *Renew. Sustain. Energy Rev.* **2023**, *187*, 113754. [CrossRef]
18. Quan, C.; Ravelomanantsoa, V.S.; Olazar, L.; Santamaria, L.; Lopez, G.; Liu, L.; Gao, N. Thermochemical conversion of waste into energy: A review. *Environ. Chem. Lett.* **2025**, *24*, 295–320. [CrossRef]
19. Jha, S.; Nanda, S.; Acharya, B.; Dalai, A.K. A Review of Thermochemical Conversion of Waste Biomass to Biofuels. *Energies* **2022**, *15*, 6352. [CrossRef]
20. Yang, L.; Chen, J.; Qin, S.; Zeng, M.; Jiang, Y.; Hu, L.; Xiao, P.; Hao, W.; Hu, Z.; Lei, A. Growth and lipid accumulation by different nutrients in the microalga *Chlamydomonas reinhardtii*. *Biotechnol. Biofuels* **2018**, *11*, 40. [CrossRef] [PubMed]
21. Clément-Larosière, B.; Lopes, F.; Gonçalves, A.; Taidi, B.; Benedetti, M.; Minier, M.; Pareau, D. Carbon dioxide biofixation by Chlorella vulgaris at different CO_2 concentrations and light intensities. *Eng. Life Sci.* **2014**, *14*, 509–519. [CrossRef]
22. Li, S.F.; Wang, C.C.; Taidi, B. Effective CO_2 capture by the fed-batch culture of Chlorella vulgaris. *J. Environ. Chem. Eng.* **2023**, *11*, 110889. [CrossRef]
23. Anjos, M.; Fernandes, B.D.; Vicente, A.A.; Teixeira, J.A.; Dragone, G. Optimization of CO_2 bio-mitigation by *Chlorella vulgaris*. *Bioresour. Technol.* **2013**, *139*, 149–154. [CrossRef]
24. Ashour, M.; Mansour, A.T.; Alkhamis, Y.A.; Elshobary, M. Usage of Chlorella and diverse microalgae for CO_2 capture-towards a bioenergy revolution. *Front. Bioeng. Biotechnol.* **2024**, *12*, 1387519. [CrossRef]
25. Chou, H.-H.; Su, H.-Y.; Song, X.-D.; Chow, T.-J.; Chen, C.-Y.; Chang, J.-S.; Lee, T.-M. Isolation and characterization of Chlorella sp. mutants with enhanced thermo-and CO_2 tolerances for CO_2 sequestration and utilization of flue gases. *Biotechnol. Biofuels* **2019**, *12*, 251. [CrossRef]
26. Omokaro, G.O.; Nafula, Z.S.; Iloabuchi, N.E.; Chikukula, A.A.; Osayogie, O.G.; Nnoli, E.C. Microalgae as biofactories for sustainable applications: Advancing carbon sequestration, bioenergy, and environmental remediation. *Sustain. Chem. Clim. Action* **2025**, *7*, 100098. [CrossRef]

https://doi.org/10.3390/en19061572

27. Maltsev, Y.; Maltseva, K.; Kulikovskiy, M.; Maltseva, S. Influence of light conditions on microalgae growth and content of lipids, carotenoids, and fatty acid composition. *Biology* **2021**, *10*, 1060. [CrossRef]
28. Songserm, R.; Nishiyama, Y.; Sanevas, N. Light influences the growth, pigment synthesis, photosynthesis capacity, and antioxidant activities in Scenedesmus falcatus. *Scientifica* **2024**, *2024*, 1898624. [CrossRef] [PubMed]
29. Tarakanov, I.G.; Tovstyko, D.A.; Lomakin, M.P.; Shmakov, A.S.; Sleptsov, N.N.; Shmarev, A.N.; Litvinskiy, V.A.; Ivlev, A.A. Effects of light spectral quality on photosynthetic activity, biomass production, and carbon isotope fractionation in lettuce, *Lactuca sativa* L. plants. *Plants* **2022**, *11*, 441. [CrossRef] [PubMed]
30. Esteves, A.F.; Pardilhó, S.; Gonçalves, A.L.; Vilar, V.J.P.; Pires, J.C.M. Unravelling the impact of light spectra on microalgal growth and biochemical composition using principal component analysis and artificial neural network models. *Algal Res.* **2025**, *85*, 103820. [CrossRef]
31. Trofimchuk, O.A.; Yakovlev, A.N.; Turanov, S.B.; Trigub, M.V.; Romanenko, S. IOP Conference Series: Materials Science and Engineering. In *The Influence of Diverse Optical Wavelengths on Growth Rate of Chlorella Vulgaris Microalgae*; IOP Publishing: Bristol, UK, 2020; p. 012005.
32. Esteves, A.F.; Soares, O.S.G.P.; Vilar, V.J.P.; Pires, J.C.M.; Gonçalves, A.L. The Effect of Light Wavelength on CO_2 Capture, Biomass Production and Nutrient Uptake by Green Microalgae: A Step Forward on Process Integration and Optimisation. *Energies* **2020**, *13*, 333. [CrossRef]
33. Wongsnansilp, T.; Khamcharoen, M. The Effects of Red–Blue Light on the Growth and Astaxanthin Production of a Haematococcus pluvialis Strain Isolated from Southern Thailand. *Appl. Microbiol.* **2024**, *4*, 1745–1756. [CrossRef]
34. Baidya, A.; Akter, T.; Islam, M.R.; Shah, A.K.M.A.; Hossain, M.A.; Salam, M.A.; Paul, S.I. Effect of different wavelengths of LED light on the growth, chlorophyll, β-carotene content and proximate composition of *Chlorella ellipsoidea*. *Heliyon* **2021**, *7*, e08525. [CrossRef]
35. Zhang, X.; Tang, X.; Zhou, B.; Hu, S.; Wang, Y. Effect of enhanced UV-B radiation on photosynthetic characteristics of marine microalgae *Dunaliella salina* (Chlorophyta, Chlorophyceae). *J. Exp. Mar. Biol. Ecol.* **2015**, *469*, 27–35. [CrossRef]
36. Sydney, T.; Marshall-Thompson, J.-A.; Kapoore, R.V.; Vaidyanathan, S.; Pandhal, J.; Fairclough, J.P.A. The effect of high-intensity ultraviolet light to elicit microalgal cell lysis and enhance lipid extraction. *Metabolites* **2018**, *8*, 65. [CrossRef] [PubMed]
37. Sweiss, M.; Assi, S.; Barhoumi, L.; Al-Jumeily, D.; Watson, M.; Wilson, M.; Arnot, T.; Scott, R. Qualitative and quantitative evaluation of microalgal biomass using portable attenuated total reflectance-Fourier transform infrared spectroscopy and machine learning analytics. *J. Chem. Technol. Biotechnol.* **2024**, *99*, 92–108. [CrossRef]
38. Ahmad, A.; W Hassan, S.; Banat, F. An overview of microalgae biomass as a sustainable aquaculture feed ingredient: Food security and circular economy. *Bioengineered* **2022**, *13*, 9521–9547. [CrossRef]
39. Sun, H.; Zhao, W.; Mao, X.; Li, Y.; Wu, T.; Chen, F. High-value biomass from microalgae production platforms: Strategies and progress based on carbon metabolism and energy conversion. *Biotechnol. Biofuels* **2018**, *11*, 227. [CrossRef] [PubMed]
40. Varghese, S.; Ralph, P.; Kuzhiumparambil, U. Sustainable carbon-rich materials from algae and biomass: Synthesis, characterisation, and applications. *Results Eng.* **2025**, *27*, 106439. [CrossRef]
41. Niu, Y.; Hemashini, T.; Leh, C.P. Comparative energy assessment and net energy return analysis of non-wood lignocellulosic bioethanol systems. In *Cellulose*; Springer: Berlin/Heidelberg, Germany, 2025; pp. 1–35.
42. Dunca, E.C.; Ioniță, M.F.; Varga, L.A.; Radu, S.M.; Ionel, I.; Halmaciu, I.A.; Istrate, I.A.; Cocârță, D.M.; Botoran, O.R.; Irimie, S.I. Assessment of the Energy Recovery Potential of Biomass Obtained from Non-Productive Lands in the Jiu Valley, Romania. *Sustainability* **2025**, *17*, 9380. [CrossRef]
43. Banerjee, N.; Sukichandran, P.; Chaudhari, P.; Thakur, A.K.; Kumar, R. Energy analysis and feasibility studies for algal biomass and biofuels. *Mater. Today Proc.* **2022**, *57*, 1448–1454. [CrossRef]
44. Chen, M.; Chen, Y.; Zhang, Q. A Review of Energy Consumption in the Acquisition of Bio-Feedstock for Microalgae Biofuel Production. *Sustainability* **2021**, *13*, 8873. [CrossRef]
45. Zhang, J.; Liu, F.; Wang, Q.; Gong, Q.; Gao, X. Effect of Light Wavelength on Biomass, Growth, Photosynthesis and Pigment Content of *Emiliania huxleyi* (Isochrysidales, Cocco-Lithophyceae). *J. Mar. Sci. Eng.* **2023**, *11*, 456. [CrossRef]
46. Esteves, A.F.; Salgado, E.M.; Vilar, V.J.P.; Gonçalves, A.L.; Pires, J.C.M. A growth phase analysis on the influence of light intensity on microalgal stress and potential biofuel production. *Energy Convers. Manag.* **2024**, *311*, 118511. [CrossRef]
47. Zhu, T.; Guan, G.; Huang, L.; Wen, L.; Li, L.; Ren, M. Transcriptomic and metabolomic analysis reveal the effects of light quality on the growth and lipid biosynthesis in Chlorella pyrenoidosa. *Biomolecules* **2024**, *14*, 1144. [CrossRef]
48. Chunzhuk, E.A.; Grigorenko, A.V.; Kiseleva, S.V.; Chernova, N.I.; Vlaskin, M.S.; Ryndin, K.G.; Butyrin, A.V.; Ambaryan, G.N.; Dudoladov, A.O. Effects of light intensity on the growth and biochemical composition in various microalgae grown at high CO_2 concentrations. *Plants* **2023**, *12*, 3876. [CrossRef]

https://doi.org/10.3390/en19061572

49. Ru, I.T.K.; Sung, Y.Y.; Jusoh, M.; Wahid, M.E.A.; Nagappan, T. Chlorella vulgaris: A perspective on its potential for combining high biomass with high value bioproducts. *Appl. Phycol.* **2020**, *1*, 2–11. [CrossRef]
50. Trisakti, B.; Sidabutar, R.; Irvan, I.; Munir, E.; Sarah, M.; Hanum, F.; Syahputra, M.R.; Michael, M.; Vanness, V.; Sinamo, G.C.; et al. Sustainable lipid production from Chlorella vulgaris USU1 strain using packed absorption column-derived effluent as carbon source for biomass generation. *Results Eng.* **2025**, *26*, 105383. [CrossRef]
51. Johnson, F.A.; Patel, B.; Ikotun, B.D. Enhanced biomass production from Chlorella micro-algae species: A review of new technologies towards sustainable energy development. *RSC Adv.* **2025**, *15*, 49809–49825. [CrossRef]
52. Mendes, A.R.; Spínola, M.P.; Lordelo, M.; Prates, J.A. Advances in bioprocess engineering for optimising Chlorella vulgaris fermentation: Biotechnological innovations and applications. *Foods* **2024**, *13*, 4154. [CrossRef] [PubMed]
53. Bilad, M.R.; Discart, V.; Vandamme, D.; Foubert, I.; Muylaert, K.; Vankelecom, I.F.J. Coupled cultivation and pre-harvesting of microalgae in a membrane photobioreactor (MPBR). *Bioresour. Technol.* **2014**, *155*, 410–417. [CrossRef] [PubMed]
54. Porowski, R. Analiza metod określania ciepła spalania i wartości opałowej paliw. *Zesz. Nauk. SGSP* **2016**, *59*, 45–70.
55. *PN-C-04375-1:2013-07*; Testing of Solid and Liquid Fuels-Calorimetric Bomb Calorimetry and Calorific Value Determination-Part 1: General, Apparatus, Methods. The Polish Committee for Standardization: Warsaw, Poland, 2013.
56. Racero-Galaraga, D.; Rhenals-Julio, J.D.; Sofan-German, S.; Mendoza, J.M.; Bula-Silvera, A. Proximate analysis in biomass: Standards, applications and key characteristics. *Results Chem.* **2024**, *12*, 101886. [CrossRef]
57. Jabeen, S.; Gao, X.; Altarawneh, M.; Hayashi, J.-I.; Zhang, M.; Dlugogorski, B.Z. Analytical procedure for proximate analysis of algal biomass: Case study for Spirulina platensis and Chlorella vulgaris. *Energy Fuels* **2019**, *34*, 474–482. [CrossRef]
58. Richmond, A. *Handbook of Microalgal Culture: Biotechnology and Applied Phycology*; Wiley Online Library: Hoboken, NJ, USA, 2004; Volume 577.
59. Kataria, S.; Jajoo, A.; Guruprasad, K.N. Impact of increasing Ultraviolet-B (UV-B) radiation on photosynthetic processes. *J. Photochem. Photobiol. B Biol.* **2014**, *137*, 55–66. [CrossRef] [PubMed]
60. Liu, J.; Van Iersel, M.W. Photosynthetic physiology of blue, green, and red light: Light intensity effects and underlying mechanisms. *Front. Plant Sci.* **2021**, *12*, 619987. [CrossRef] [PubMed]
61. Bialevich, V.; Zachleder, V.; Bišová, K. The effect of variable light source and light intensity on the growth of three algal species. *Cells* **2022**, *11*, 1293. [CrossRef] [PubMed]
62. Shahzaidi, Z.S.; Tackallou, S.H.; Amjad, L.; Zali, H.; Iranbakhsh, A. Analysis of UV radiation-induced changes: Effects on morpho-physiological, and biochemical traits of Portulaca Oleracea. *BMC Plant Biol.* **2025**, *25*, 1318. [CrossRef]
63. Brindhadevi, K.; Mathimani, T.; Rene, E.R.; Shanmugam, S.; Chi, N.T.L.; Pugazhendhi, A. Impact of cultivation conditions on the biomass and lipid in microalgae with an emphasis on biodiesel. *Fuel* **2021**, *284*, 119058. [CrossRef]
64. Juneja, A.; Ceballos, R.M.; Murthy, G.S. Effects of environmental factors and nutrient availability on the biochemical composition of algae for biofuels production: A review. *Energies* **2013**, *6*, 4607–4638. [CrossRef]

Disclaimer/Publisher's Note: The statements, opinions and data contained in all publications are solely those of the individual author(s) and contributor(s) and not of MDPI and/or the editor(s). MDPI and/or the editor(s) disclaim responsibility for any injury to people or property resulting from any ideas, methods, instructions or products referred to in the content.

https://doi.org/10.3390/en19061572

MDPI AG
Grosspeteranlage 5
4052 Basel
Switzerland
Tel.: +41 61 683 77 34

Energies Editorial Office
E-mail: energies@mdpi.com
www.mdpi.com/journal/energies



Disclaimer/Publisher's Note: The title and front matter of this reprint are at the discretion of the Guest Editors. The publisher is not responsible for their content or any associated concerns. The statements, opinions and data contained in all individual articles are solely those of the individual Editors and contributors and not of MDPI. MDPI disclaims responsibility for any injury to people or property resulting from any ideas, methods, instructions or products referred to in the content.





Academic Open
Access Publishing

mdpi.com

ISBN 978-3-7258-9070-5